The radial step of microtubules as a pre-preprophase band structure in plant cell division

Isaty Melogno

THESE

en vue de l'obtention du grade de Docteur, délivré par

l'ECOLE NORMALE SUPERIEURE DE LYON

Ecole Doctorale N° 340
BMIC – Biologie Moléculaire Intégrative et Cellulaire

Discipline : Sciences de la vie et de la santé (Biologie végétale)

Soutenue publiquement le 08/11/2024, par :

Isaty MELOGNO

The radial step of microtubules as a pre-preprophase band structure in plant cell division

Une organisation radiale de microtubules précède la formation de l'anneau de préprophase dans la division cellulaire des plantes

---

Sous la direction de : M. Christophe TREHIN et M. Olivier HAMANT

Devant le jury composé de :

Robert SABLOWSKI, Professeur, John Innes Centre	Rapporteur
Manuel THERY, Chercheur, CEA	Rapporteur
Marie-Cécile CAILLAUD, Directrice de recherche, ENS Lyon	Examinatrice
Bénédicte CHARRIER, Directrice de recherche, ENS Lyon	Examinatrice
Sabine MULLER, Chercheuse, Université de Tübingen	Examinatrice
Christophe TREHIN, Maître de conférences-HDR, ENS Lyon	Directeur de thèse

Summary

Cell division is a highly important process for growth and development. The orientation of cell division, as well as the different rules regulating division plane positioning, has been a wide question in plant biology. The pre-prophase band (PPB) is a plant-specific structure positioned and predicting the position of the future division plane, appearing right before mitosis. The PPB is notably formed by cortical microtubules (CMTs), forming a ring around the cell. However, the dynamics of the CMTs, and their transitioning process towards forming the PPB has not been studied in detail. Tensile stress has been shown to play a role in the organization of interphasic CMTs, as well as the orientation of the cell division plane. This project aims to study the transition of CMTs from interphase to PPB, using the stem as a model, where the tension is both highly directional and stable. We noticed a transient re-organization of the microtubules array between the highly aligned interphasic array, and the PPB stage. During this stage, the microtubules are organized in a radial array, losing their anisotropy. We could link this "radial step" with a pre-mitotic increase in cytoplasmic microtubules, around two to three hours before the formation of the PPB. The *trm678* mutant is a PPB-deficient mutant, and displays a longer and clearer "radial step". The variability in daughter cells volume ratio is also highly reduced in the mutant, compared to the wild type, and the pre-mitotic accumulation of cytoplasmic microtubules much higher. With these observations, we propose that the "radial step" is a crucial step for the formation of the PPB, and reflects the internal accumulation of microtubules. This could help shield transiently the cell from external mechanical cues, and therefore allow a symmetry, in terms of volume, between the two daughter cells. To go further in the investigation of the role of the "radial step", we studied the behavior of cell divisions and/or CMT dynamics in other genetic backgrounds, affected in microtubules and actin, and in cell wall composition. We also studied the behavior of microtubules in other systems. Notably, using protoplasts and callus, tobacco leaves, and developing lateral roots.

Aknowledgements

J'ai eu la chance d'être entourée de personnes incroyables pendant cette thèse, qui m'ont fait évoluer aussi bien sur le plan scientifique que personnel, et qui ont participé à rendre cette aventure enrichissante et épanouissante.

Tout d'abord, je voulais remercier Christophe et Olivier pour m'avoir accueillie en stage puis en thèse au sein de l'équipe, et pour avoir été des encadrants formidables. Même avec un emploi du temps chargé, vous avez réussi à trouver du temps pour moi, et à toujours garder un esprit d'encouragement et de positivité. Merci à Olivier d'avoir rendu ma thèse possible en me finançant avec la bourse d'ERC, mais surtout merci pour ton enthousiasme et le débordement d'idées dont tu as fait preuve à chaque réunion. Je voulais remercier tout particulièrement Christophe, qui m'a plus suivie pendant ma thèse, et qui a vraiment été un repère pour moi. C'est difficile de réduire à quelques phrases toute la gratitude que j'ai pour toi. J'aurais difficilement pu espérer mieux de la part d'un encadrant. J'ai adoré travailler avec toi, et je me suis sentie vraiment soutenue et guidée pendant toute ma thèse, et en particulier durant les périodes compliquées.

Je voulais ensuite remercier Shogo Takatani, avec qui j'ai effectué mon stage de Master, et qui a su me transmettre ses connaissances en microscopie et en biologie cellulaire avec beaucoup de patience et de pédagogie. Je suis très heureuse et fière de la tournure qu'a pris le projet. Je voulais également remercier les collaborateur.ices sur le projet, et en particulier Magalie Uyttewaal pour le regarde critique que tu as porté sur mon travail.

J'ai eu l'opportunité et la chance d'encadrer deux stagiaires pendant ma thèse: Bastien Pouget et Camille Gauthier. Je voulais remercier Bastien, qui a un peu essuyé les plâtres de mon début de thèse et qui a partagé ma frustration sur les protoplastes. Même si ce projet n'a pas abouti, j'espère t'avoir montré que la recherche peut aussi prendre la forme de tâtonnements… Camille, j'ai adoré travailler avec toi sur le projet de transformation de tabac. En plus d'avoir fait du super travail, de t'être montrée autonome et motivée, tu as fait preuve d'enthousiasme et de bonne humeur qui ont vraiment participé à rendre cette expérience super!

L'équipe MechanoDevo, au sein de laquelle j'ai effectué ma thèse, a beaucoup changé depuis le temps où j'y suis entrée, mais elle a gardé un esprit de diversité et de créativité qui est, à mon sens, extrêmement précieux. Je voulais remercier tous les membres de cette équipe, passés et présents, pour leurs conseils et remarques sur mon travail, mais aussi pour l'aide technique. En particulier Claire, qui est essentielle au travail de beaucoup dans cette équipe, et qui est un monstre de la microscopie et de l'analyse d'images.

Plus largement, j'aimerais remercier l'ensemble du laboratoire du RDP pour être un super environnement de travail. L'organisation et la structure du laboratoire facilitent vraiment le travail, et les scientifiques qu'il regroupe sont tou.tes plus doué.es les un.es que les autres! Je voulais en particulier remercier les personnes du couloir du GN1 pour la super ambiance qui règne dans cette partie reculée du RDP, pour les mots croisés, les midis jeux, le stretching club et j'en passe… Un petit merci spécial pour Philippe Dupuis et Philippe Vergne qui ont respectivement fait et fourni les mots croisés du Monde.

Je voulais avoir un petit mot aussi pour Alice et Marianne, qui ont partagé mon bureau pendant la totalité de ma thèse (même si juste la moitié pour Marianne, mais tu étais avec nous dans notre cœur), et avec qui j'ai traversé le quotidien, les moments cools et moins cools.

Et enfin, merci à tous mes proches de m'avoir soutenu pendant ces trois ans. Merci à tous.tes les ami.es que j'ai pu me faire au sein du laboratoire (c'est impossible de nommer chacun.e sans avoir des remerciements de 15 pages). Merci aussi à toutes celles et ceux que je me suis fait plus largement à Lyon. Merci à mes ami.es d'avant. Merci à mes meilleures amies de toujours. Merci à ma famille, ma sœur et mes parents. Je suis tellement chanceuse de vous avoir eu à mes côtés pendant ma thèse, mais plus largement, de vous avoir dans ma vie.

Preamble

This manuscript contains three main parts: (i) a general introduction, (ii) a results section, and (iii) a general discussion around the results, followed by a detail of the material and methods used, and an annexes section.

The introduction is first dedicated to the description of morphogenesis from a geometrical and mechanical point of view, at a global scale. It then describes the cellular drivers of morphogenesis, firstly the effectors (cell wall and cytoskeleton), and secondly the regulators (cell cycle and mitosis).

The results section is divided in three main parts. First, it describes the characterization of the radial step, a work that has been published in Proceedings of the National Academy of Sciences of the United States of America (PNAS) in 2024. The second part explores the function of this radial step, through the analysis of various mutants. The last part is an exploratory approach to study specific contributions to the radial step, and describes the use of various alternative model systems.

The discussion reflects on the results obtained, and on the possible implications of the radial step in division plane positioning and volume partitioning. It also emphasizes the conservation of this step amongst organs and genetic perturbations.

The annexes contain the protocols used for the protoplast experiments, the internship report of Camille Gauthier (and more detailed explanation on the tobacco mesophyll cell system), and the PNAS article mentioned above.

Table of contents

List of Abbreviations

ABP: Actin-binding protein

ACM: Apex culture medium

ACT: Actin

ADF: Actin depolymerization factor

AF: Actin filament

AM: Arabidopsis medium

BR: Brassinosteroid

CDK: Cyclin-dependent kinase

CDZ: Cortical division zone

CESA: Cellulose synthase

CLASP: Cytoplasmic linker-associated protein

CMT: Cortical microtubule

CSC: Cellulose synthase complex

CYC: Cyclin

EB: End-binding

GCP: γ-tubulin complex proteins

γTuRC: γ-tubulin ring complex

GMC: Guard mother cell

HG: Homogalacturonan

IQR: Interquartile rang

KTN: Katanin

LatB: Latrunculin B

MAP: Microtubule-associated protein

MBD: Microtubule binding domain

MT: Microtubule

MTOC: Microtubule organizing center

NEK: NIMA-related protein kinase

NIMA: Never-in-mitosis

NPA: Naphtylphtalamic acid

PCNA: Proliferating cell nuclear antigen

PDF: Protodermal factor

PI: Propidium iodide

PIN: Pin-formed protein

PME: Pectin methylesterase

PMEI: Pectin methylesterase inhibitor

PPB: Pre-prophase band

RB: retinoblastoma

RBR: retinoblastoma-related

SAM: Shoot Apical Meristem

SPR: Spiral

TRM: Tonneau-recruiting motif

TTP: TON1-TRM-PP2A

XXT: Xyloglucan transferase

Introduction

Etymologically, "development" comes from "desvelopmens", the action of unfolding what was rolled up on itself (late 14th century) (Logé *et al.*, 2010). In biology, the development of an organism has a broader sense, and can be defined by the changes in size, shape and function it undergoes during its life. Within biological development, morphogenesis refers to the shape changes, associated with the development of an organism, an organ, or a cell, and is closer to the original meaning of development. Biologists, as well as scientists from other disciplines, have been fascinated by morphogenesis for centuries, and modern biology has unraveled many mysteries, and raised many more.

Morphogenesis is a process differentially regulated between kingdoms. Indeed, most mobile animals develop their organs during embryo development, and little post-embryonic shape changes are observed, besides growth (Heidstra and Sabatini, 2014). Plants are sessile organisms, meaning that they lack the ability to move, and therefore are unable to escape stressful environmental challenges. They are highly exposed to light and temperature changes, drought and biotic stresses. Most plant organogenesis is post-embryonic, thanks to the presence of primary meristems at their apex (Heidstra and Sabatini, 2014). Meristems are structures containing pools of stem cells (undifferentiated cells), that replenish themselves continuously, and allow the plant to generate new organs (Heidstra and Sabatini, 2014). Secondary meristems generate new tissues, like the wood, and allow growth in thickness and adaptation to the increasing size of the plant as it gets taller (for mechanical support and hydraulics mainly) (Plavcová *et al.*, 2019). In this introduction, the focus will be on morphogenesis in plants, with some echoes from animal development when relevant.

Morphogenesis raises two main, and apparently contradictory, questions:

(i) How can organs with more or less complex shapes emerge?

(ii) How can organs with reproducible shapes emerge?

I. Morphogenesis: a question of geometry

1. Shape and size descriptors

A shape refers to the form or external boundary, outline, or surface of an object (e.g. a cell, a tissue, an organ), distinct from properties like color, texture, or material properties. On the other hand, size denotes the magnitude or dimensions of an object, which can be quantified in terms of length, width, height, diameter, perimeter, area, volume, or mass (Paluch and Heisenberg, 2009; Klingenberg, 2010; Balduzzi *et al.*, 2017). Shape and size reflect adaptation and functional relevance in living organisms. For shape, this can be observed in the flatness of plant leaves, adapted to photosynthesis (Liu *et al.*, 2010), or in the villi of the small intestine, adapted for nutrient and water absorption (Walton *et al.*, 2016). The functional relevance of form is emphasized by the reproducibility observed in organ shapes between organisms. Taxonomy is based on organisms

and organs with comparable shapes, and is the result of their morphogenesis (Viscosi and Cardini, 2011).

Relevant geometric quantitative parameters are required to describe shape at all scales, and are called shape descriptors. They can be quite simple, such as the length of a stem (for unidimensional forms, shape and size overlap), or the angle of a branch with respect to the stem axis, in one dimension (Figure I1A). Two-dimensional shape descriptors encompass circularity, perimeter and area. PaCeQuant, for example, is an analytic tool that has been develop to quantify various features of epidermal cells from leaves forming jigsaw puzzle forms and called pavement cells (Möller *et al.*, 2017; Figures I1B and I2). Other morphometrics analysis rely on landmarks localized at distinctive parts of the specimen (for example the intersection of veins) that can be collected in two or three dimensions (Klingenberg, 2002). After superimposing the landmarks from various specimen, or timepoints, for example, the variation in their coordinates informs on the shape changes, and thus the dynamics of development (Klingenberg, 2010; Figure I1C).

2. Growth

Morphogenesis is indeed a dynamic process. The associated shape changes can be referred to as elastic (reversible) or plastic (irreversible) deformations. Growth is a plastic deformation, and can be defined as an irreversible increase in volume. It can be measured by four parameters: growth rate, growth anisotropy, direction and rotation (Coen *et al.*, 2004; Figure I1D). Growth rate defines the rate at which a region changes in size. Growth anisotropy refers to how much the growth occurs preferentially in any direction. Direction is the angles at which preferential growth is oriented. Rotation is the angles from which a region rotates from another region.

One can describe growth by the velocities at which landmark points move, which can be represented as vectors (Coen *et al.*, 2004). Vector fields are a more accurate description of growth, as it may vary from point to point, and account for growth rate and direction (Coen *et al.*, 2004). Growth, and especially growth rates, is classically measured by tracking the position of landmarks on a region over time (Gould and Lord, 1989; Young *et al.*, 2010). These kinetic analyses are referred to as kinematics (quantification of the position changes over time) (Moulia and Fournier, 2009). Furthermore, as growth may vary between regions, it is more generally characterized in smaller, local regions (Coen *et al.*, 2004), even though more global kinematic measurements can be found (such as leaf area and elongation rate) (Kheibarshekan Asl *et al.*, 2011; Bertels and Beemster, 2020). For example, growth quantification of the shoot apical meristem (SAM) surface in plants involves measurements of growth rates for the cells making up the SAM, using cell vertices (tricellular junctions) as landmarks (Dumais and Kwiatkowska, 2001). The *Drosophila* wing disk growth can be measured through local tissue deformations of cell clusters or domains (Blanchard *et al.*, 2009; Heemskerk *et al.*, 2014).

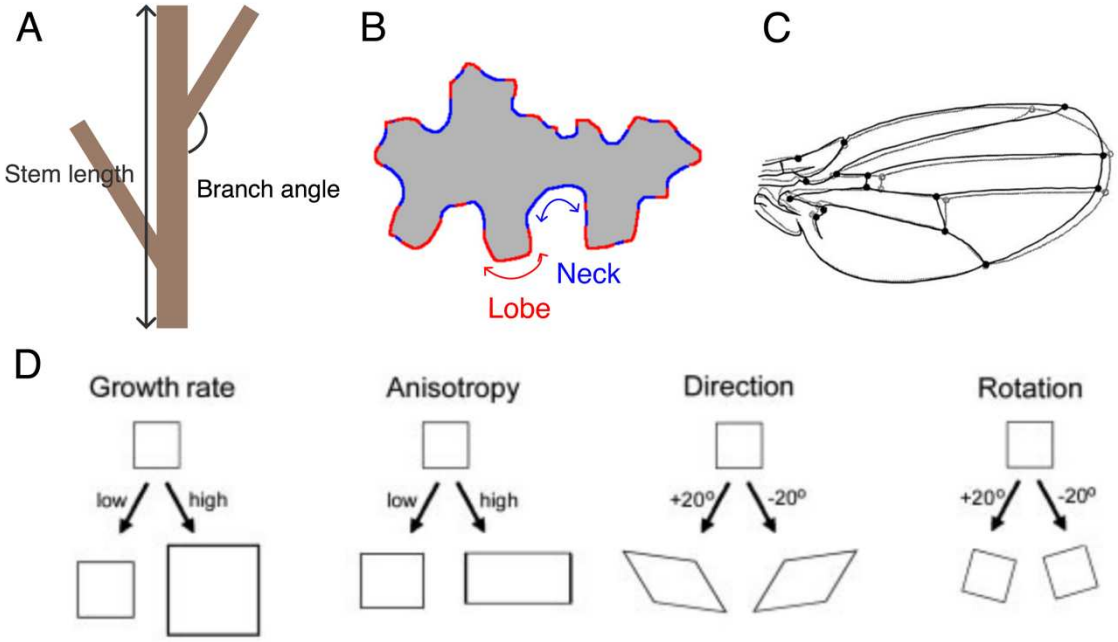

Figure I1: Examples of shape and growth descriptors. (A) Examples of simple measurements on a stem: stem length and branching angle from the stem. (B) (Adapted from Möller *et al.*, 2017) Scheme of a pavement cell with its lobe (red) and neck (blue) regions determined based on the curvature of the cell's outline. (C) (Adapted from Klingenberg, 2002) Example of two overlapping *Drosophila* wings, with landmark points (dots). The distances between landmarks inform on the shape changes between the two wings. (D) (Adapted from Coen *et al.*, 2004) Scheme of different parameters describing growth properties: growth rate, anisotropy, direction and rotation.

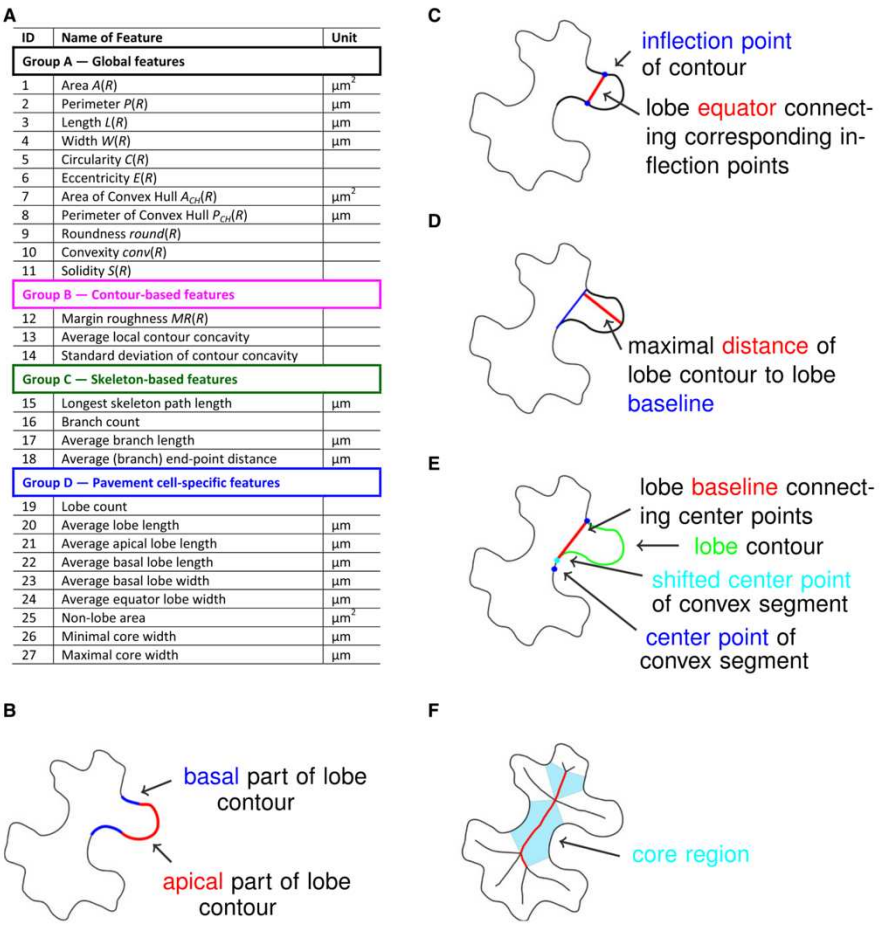

Figure I2: (Adapted from Möller *et al.*, 2017) Extent of the parameters that can be extracted from a pavement cell, using PaCeQuant.

3. Growth conflicts behind shape complexity

The differences in local growth patterns generate diverse shapes. The flatness of a leaf, for example, does not occur by default: it results from coordinated differential growth, with a key role of growth arrest at the leaf margins (Nath *et al.*, 2003; Figure I3B). Conversely, complex three-dimensional shapes emerge from growth conflicts within a tissue. Snapdragon flowers, for example, acquire their shape through local differences in growth rates and directions (Rebocho *et al.*, 2017). Similarly, the shape of traps arises from differential growth in *Utricularia* (Lee *et al.*, 2019).

If these types of studies reflect growth patterns and their impact on morphogenesis, they do not provide any mechanistic insight into how such shape changes emerge. In other words, one might wonder how shape changes occur upon growth conflicts. To answer this, we need to explore the mechanics behind the geometry.

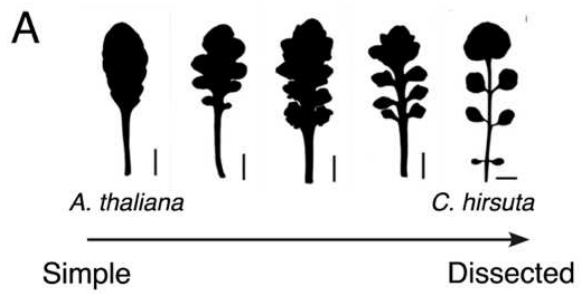
A
A. thaliana
C. hirsuta
Simple
Dissected

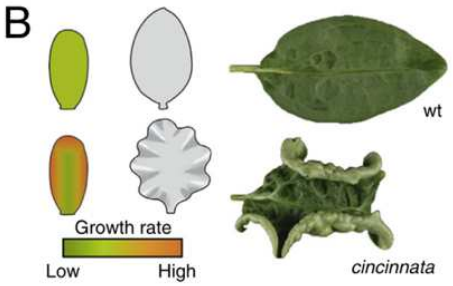
B
wt
Growth rate
Low
High
cincinnata

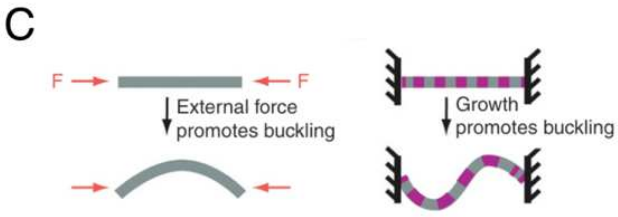
C
F
F
External force
promotes buckling
Growth
promotes buckling

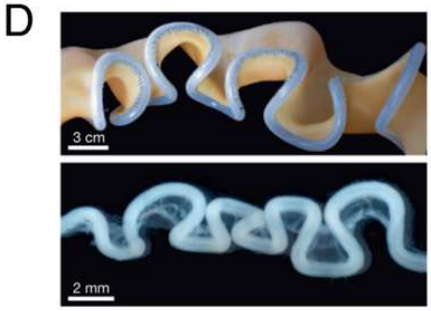
D
3 cm
2 mm

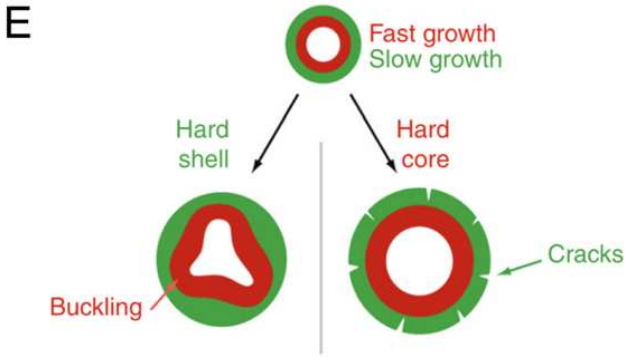
E
Fast growth
Slow growth
Hard
shell
Hard
core
Buckling
Cracks

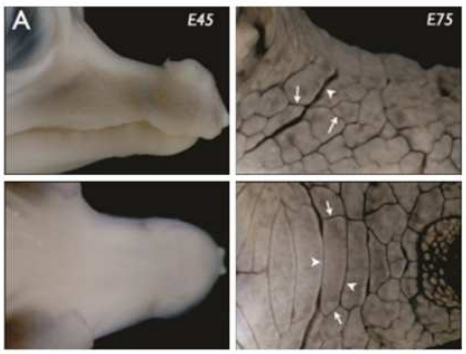
F
A
E45
E75

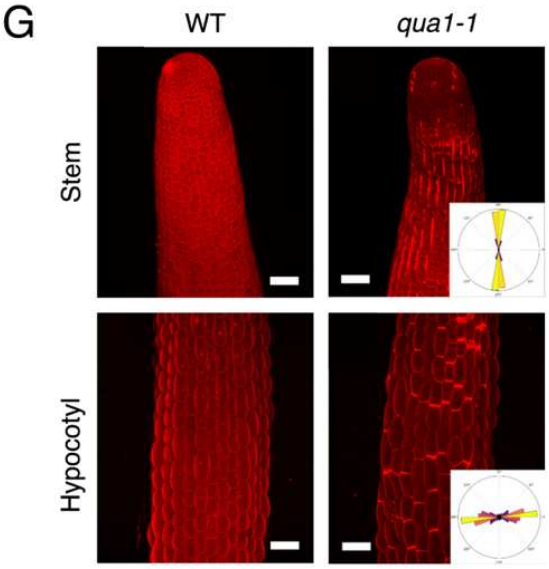
G
WT
qua1-1
Stem
Hypocotyl

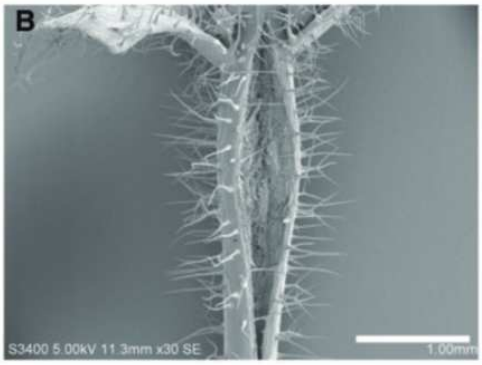
H
B
S3400 5.00kV 11.3mm x30 SE
1.00mm

Figure I3: Differential growth and material properties produce complex shapes. (A) (Adapted from Kierzkowski *et al.*, 2019) Various leaf dissection levels, from simple (*Arabidopsis thaliana*) to highly dissected (*Cardamina hirsuta*). (B) (Adapted from Trinh *et al.*, 2021, and Nath *et al.*, 2003) The leaf flatness is controlled by growth. If the margins grow more than the rest of the leaf, buckling occurs. (C) (Adapted from LeGoff and Lecuit, 2016) Buckling of rod-like structure might appear if an elastic rod is subjected to compressive forces (left image), or if it grows while constrained at both ends. (D) (Adapted from Savin *et al.*, 2011) The looping of the gut arises from differential growth between the gut tube and the mesentery. These growth differences, coupled with differential material elasticity, create the looping observed (bottom image), as shown by mimicking model, made from two rubbers with different Young's moduli (top image). (E) (Adapted from LeGoff and Lecuit, 2016) Scheme showing how three-dimensional structures may come from differential growth, coupled with differential material properties. When considering a fast-growing inner layer surrounded by a slow growing outer layer, the inner layer will buckle if the outer layer behaves as a hard shell (left), while the outer will crack if it is more brittle than the inner one (right). (F) (Adapted from Milinkovitch *et al.*, 2013) This latter mode has been shown to give rise to the cracks on the crocodiles' skins. During early development, no cracking is observed, while cracks in all directions are observed later on. (G-H) Cracks are also observed in the stem and hypocotyl of *Arabidopsis*. (G) (Adapted from Verger *et al.*, 2018) In the *qua1-1* mutant grown on 2.5% agar, vertical (stem) and longitudinal (hypocotyl) cracks are observed, revealing a brittle epidermis with fast-growing inner tissues. The scale bars are 50 µm. (H) (Adapted from Maeda *et al.*, 2014) A large vertical crack is observed in stems of *clv3 det3-1* double mutants. These mutants show increased inner tissue growth and defective cell expansion, resulting in the cracking of the outermost layer. The scale bar is 1 mm.

II. Morphogenesis: a question of mechanics

1. Mechanics as a restraining law

Mechanics is a branch of physics that studies the behavior of bodies when subjected to force. Mechanics is the sum of kinematics (the description of motion without considering the cause of motion) and dynamics (the description of the force behind motion). In other words, mechanics aims to study how forces act on a body, and how this body reacts as a result (Bidhendi and Geitmann, 2019). Living organisms can be considered as objects subjected to physical constraints. In particular, depending on the size of the organisms, gravity will dominate (fore large organisms), or surface tension will dominate (for small organisms, in the cell range) (D'Arcy Thompson, 1917). In that way, mechanics constrain the range of shapes. For example, the maximum height for sequoia trees is 110 meters, and this limit is the combined result of gravity, water coherence and wind (Koch *et al.*, 2004; Williams *et al.*, 2017; Niklas, 1998).

Resistance to gravity and upright growth (i.e. resisting one's own weight) can also be achieved by specific structures (Moulia *et al.*, 2006). For example, terrestrial arthropods' exoskeletons provide support against gravity (Weihmann, 2020). Its properties are modified upon hypergravity treatments (Stamm and Dirks, 2023), and relate with the organism's body size (Lease and Wolf, 2010). Similarly, the endoskeleton of vertebrates resists gravitational loading (Ross, 1984), and responds to mechanical stresses (Burr *et al.*, 2002). Wood provides mechanical resistance to trunks of dicots and gymnosperms (Thibaut *et al.*, 2001; Anten and Schieving, 2009; Williamson and Weimann, 2010). Growth implies the addition of new material (and weight), and therefore a stronger resistance to gravity (Morey-Holton, 2003).

Furthermore, as plants are sessile organisms, they are highly exposed to various stresses. Mechanical challenges can also arise from physical perturbations such as wind, raindrops or touch (Kouhen *et al.*, 2023). As a response, plants are extremely adaptable and show incredible plasticity in response to such stresses. Tree architecture, for example, is shaped by mechanical loads such as wind (Jaffe and Forbes, 1993; Eloy, 2011). The height of *Arabidopsis thaliana* plants is regulated by mechanical cues, as repeated touch inhibits inflorescence elongation (Braam, 2004). Morphological adaptations to mechanical cues are also observed in roots, that modify their growth trajectories in response to physical barriers (such as differences in soil architecture) (Wilson, 1967; Massa and Gilroy, 2003).

2. Mechanics behind growth

Overall growth at the organism or organ level is driven by cellular expansion and division. Plant cells have a stiff cell wall, containing a highly pressurized protoplast, at a pressure of around 1 MPa

(Beauzamy *et al.*, 2015; Coen and Cosgrove, 2023). Their growth is driven by a combination of water uptake (increasing the pressure inside the cell) and cell wall relaxation, yielding to the generated turgor pressure (Coen and Cosgrove, 2023; Figures I4 and I5).

To bridge geometry and mechanics, one needs to explicitly describe growth in mechanical terms. The Lockhart model mathematically links the growth rate to turgor pressure and cell wall extensibility, and is the most accepted model to describe plant growth, even though other models have been proposed (Heyn, 1940). Lockhart's equation also includes a threshold pressure at which the cell wall will yield and deform.

$$\text{Lockhart's equation : } r = \frac{\phi L}{\phi + L}(\Delta\pi\text{-}Y) = \phi\,(P\text{-}Y)$$

In this equation, r is the growth rate, L represents the hydraulic conductance, $\Delta\pi$ the differences in osmotic pressure, P the turgor pressure, ϕ the wall yielding coefficient and Y the yield threshold, which together make up for the wall extensibility (Lockhart, 1965; Cosgrove, 1993; Ali *et al.*, 2023). The turgor pressure P is therefore the force that is driving cell expansion in plants.

The cell wall growth is mediated by plastic (irreversible) deformation, through a process called creep. Creep describes this irreversible deformation, where cellulose microfibrils (cell wall components) can slide against each other, by a transient relaxation of the cell wall when yielding under the tension generated by the pressurized protoplast (Cosgrove, 2016).

Beyond magnitude, forces also have directions. Tensors inform on the deformation of a continuous object, either predictable or not, as well as the orientation of this deformation when subjected to the force. Plant growth is continuous (it is not localized to one edge, but is distributed along all sides, each with a particular growth rate) and oriented, and can therefore be viewed as a tensor field (Hernández-Hernández *et al.*, 2014). As the plant grows over time, the tensor field changes. Growth can be referred to as "isotropic" or "anisotropic". These terms are not restricted to growth, as they mean that "a property is the same in all directions" (isotropic) or "a property differs with angular orientation" (anisotropic) (Hamant and Moulia, 2016) and refer to the amplitude, or the norm, of the tensor. Mechanical cues (and growth) are defined by stress and strain. Stress (often noted σ) is the force applied on a body (its surface section), and is expressed as a force per area unit. Strain (often noted ε) is a unitless measure of the deformation (for a one-dimensional object: $\varepsilon = (l\text{-}l_0)/l_0$) experienced by this body, under the external force. Stress-strain relations are used to define the response of a material to stress (Hernández-Hernández *et al.*, 2014). Similar to Hooke's law which relates force (F) and deformation ($l\text{-}l_0$) through the stiffness (k) of a 1D spring ($F=k(l\text{-}l_0)$), stress and strain are related by the stiffness (E, also called elastic modulus or Young modulus) of a deforming 3D object: $\sigma = E\varepsilon$ (Mirabet *et al.*, 2011). Principal stresses are quantitative values, summarizing the different stresses in a three-dimensional space.

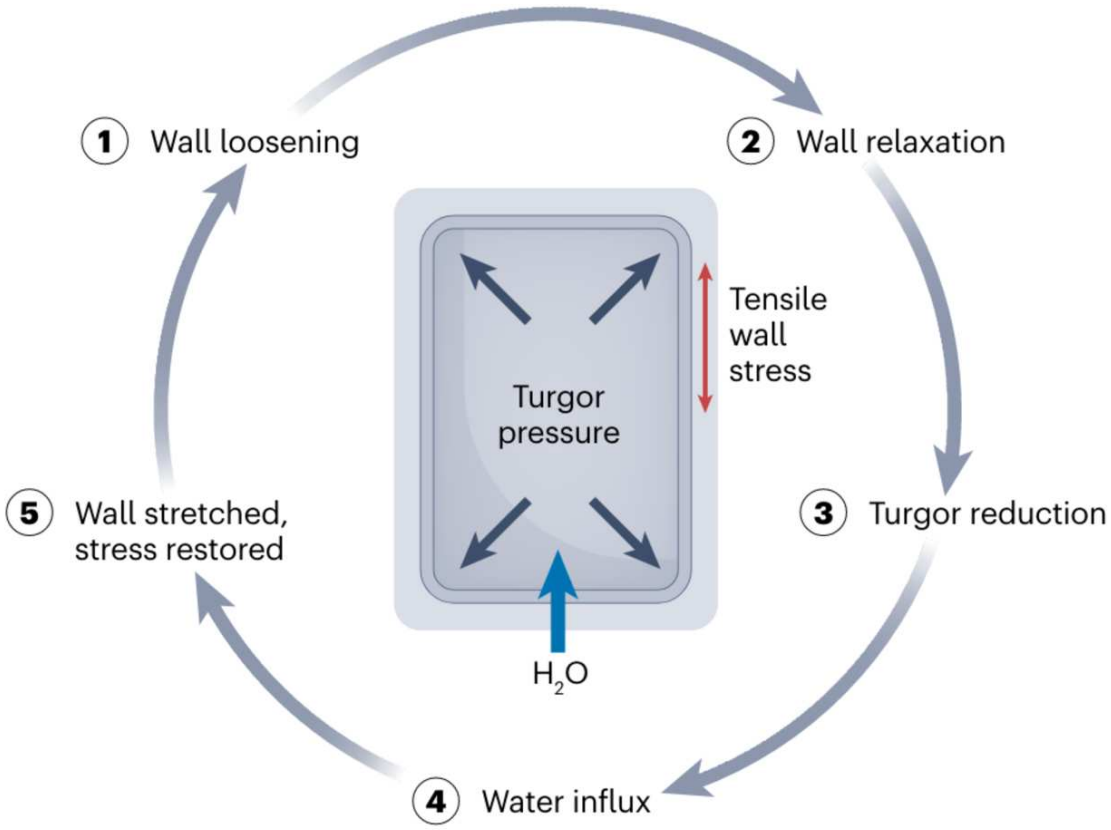

Figure I4: (Adapted from Cosgrove, 2024) Scheme representing the model of plant cell growth through wall relaxation. (1) The wall loosens, yielding under the tension it bears. (2) This leads to wall stress relaxation. (3) With the wall relaxed, the turgor pressure decreases. (4) This decrease in turgor pressure promotes the influx of water inside the protoplast, and leads to cell expansion. (5) This increase in size restores the turgor pressure, and the tension imposed on the cell wall by the protoplast.

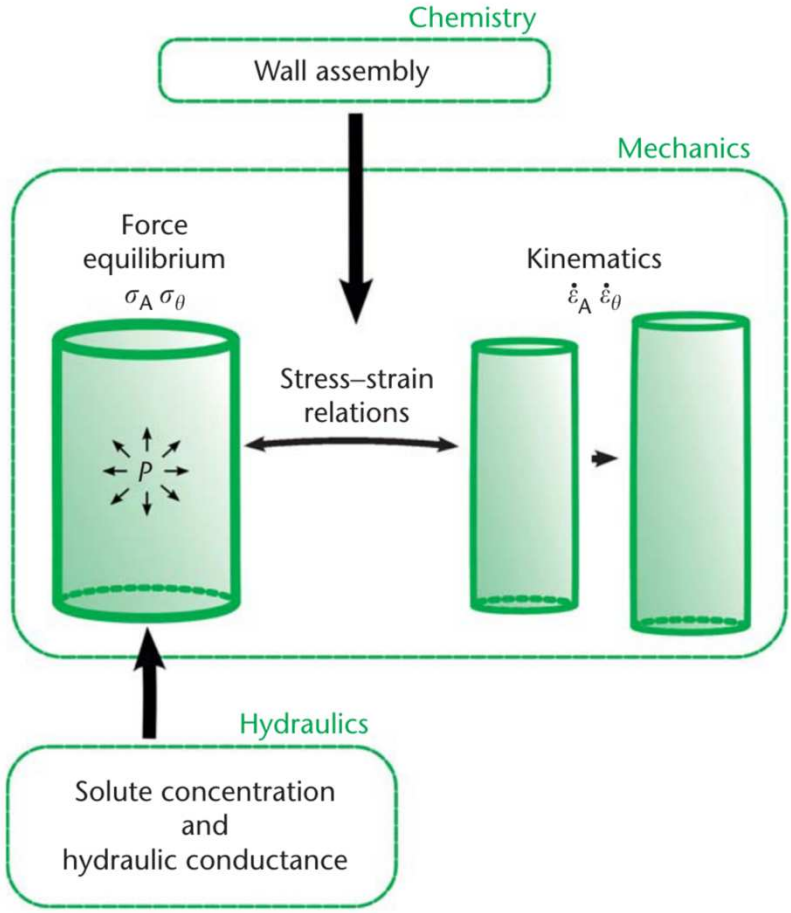

Figure I5: (Adapted from Jordan and Dumais, 2010) Cellular morphogenesis through wall chemistry and mechanics, and cellular hydraulics. Wall chemistry prescribes the wall material and properties. The wall is deformed through stress-strain relations, at the core of wall mechanics. As the cell expands, water must enter to maintain the turgor pressure and drive growth, involving cellular hydraulics.

3. Growth-derived stress

The relation between stress and strain through elastic moduli illustrates that morphogenesis arises from differences in material properties as well as differences in growth. If an elastic rod is subjected to forces compressing it on both extremities, it will buckle under a certain threshold (Figure I3C). Similarly, if this rod grows fast and is constrained on both extremities, buckling could be a way of relaxing the stress, giving rise to three-dimensional structures (Drasdo, 2000; Gjorevski and Nelson, 2010; LeGoff and Lecuit, 2024; Figures I3C and I3E). This has been proposed to be a driver in the formation of villi in the gut (Hannezo *et al.*, 2011), with experimental evidence that the surrounding muscle tissue of the gut constrains the fast growth of the lumen, giving rise to the villi (Shyer *et al.*, 2013; Figure I3D). However, there is a maximum threshold of force beyond which the material breaks. This is called the "strength" of the material. If an inner layer grows faster than a stiff outer layer, the latter will experience deformations and eventually crack (Figure I3E). This mechanism is for example giving rise to the scales on the crocodile skin (Milinkovitch *et al.*, 2013;

Figure I3F). Cracks emerging from differential growth and insufficiently stiff properties can also be observed in the bark of trees.

More interestingly for the study of morphogenesis, cracks in plant tissues can be induced artificially to reveal the stress pattern. The *quasimodo1* (*qua1*) mutant in *Arabidopsis* is affected in cell-to-cell adhesion (Bouton *et al.*, 2002; Mouille *et al.*, 2007). This mutant exhibits cracks in the epidermis of stems and hypocotyls, revealing that the inner tissues push on the epidermis, that is subsequently put under tension (Verger *et al.*, 2018; Figure I3G). A similar phenotype is observed in stems of *de-etiolated3-1 clavata2-1* double mutants of *Arabidopsis*, that present thicker piths and weaker epidermal walls (Maeda *et al.*, 2014; Figure I3H).

Mechanical constraints arising from tissue organizations have been studied for a long time in plants, with a seminal contribution of Hofmeister in the 19th century (Hofmeister, 1859; Hofmeister, 1963; Peters and Tomos, 1996). Quite early on, the outer tissues have been considered as limiting for growth. The idea was that the differences in growth between the pith and the outer tissues (when considering the stem) induce differences in tissue tension (Kraus, 1867; Thimann and Schneider, 1938). Indeed, the outer layer (epidermis) of areal tissues in plants is usually under tension. This phenomenon can be illustrated by peeling experiments on stems (Figure I6A). In sunflower hypocotyls (embryonic stem), after peeling in water (to avoid deformation through dehydration), when the stress relaxes, the outer tissues contract by around -9 % while the inner tissues expand by about +15 %, both within 2 hours (Kutschera and Niklas, 2007; Figure I6A). This shows that the inner tissues were under compression, and the outer tissues were under tension, before peeling.

While differential growth between tissue layers induce mechanical heterogeneities and mechanical stresses within an organ, such conflicts can also occur at local scales, between adjacent cells. Trichomes are hair-like protrusions with various functions in plants. In *Arabidopsis*, the growth of a trichome occurs first in the tissue plane, before its outgrowth perpendicular to the tissue plane (Hervieux *et al.*, 2017; Figure I7A). During its first stage of development, the trichome grows much faster than its neighboring cells. This was proposed to locally modify the maximal tension pattern to become circumferential around the trichome (Hervieux *et al.*, 2017; Figures I7B and Figure I7C) and validated later on, using the cracking mutant *qua1* (Verger *et al.*, 2018).

If differential growth between organs, or tissues, or even regions in the tissues, induce mechanical stresses, this is under the condition that cells are attached together, and have no motility, or slow enough to prevent the stress relaxation (Shraiman, 2005). The cell wall surrounding plant cells glues them together, making plants simpler model systems to study the role of such mechanical conflicts in morphogenesis: there is no cell displacement or intercalation in plants.

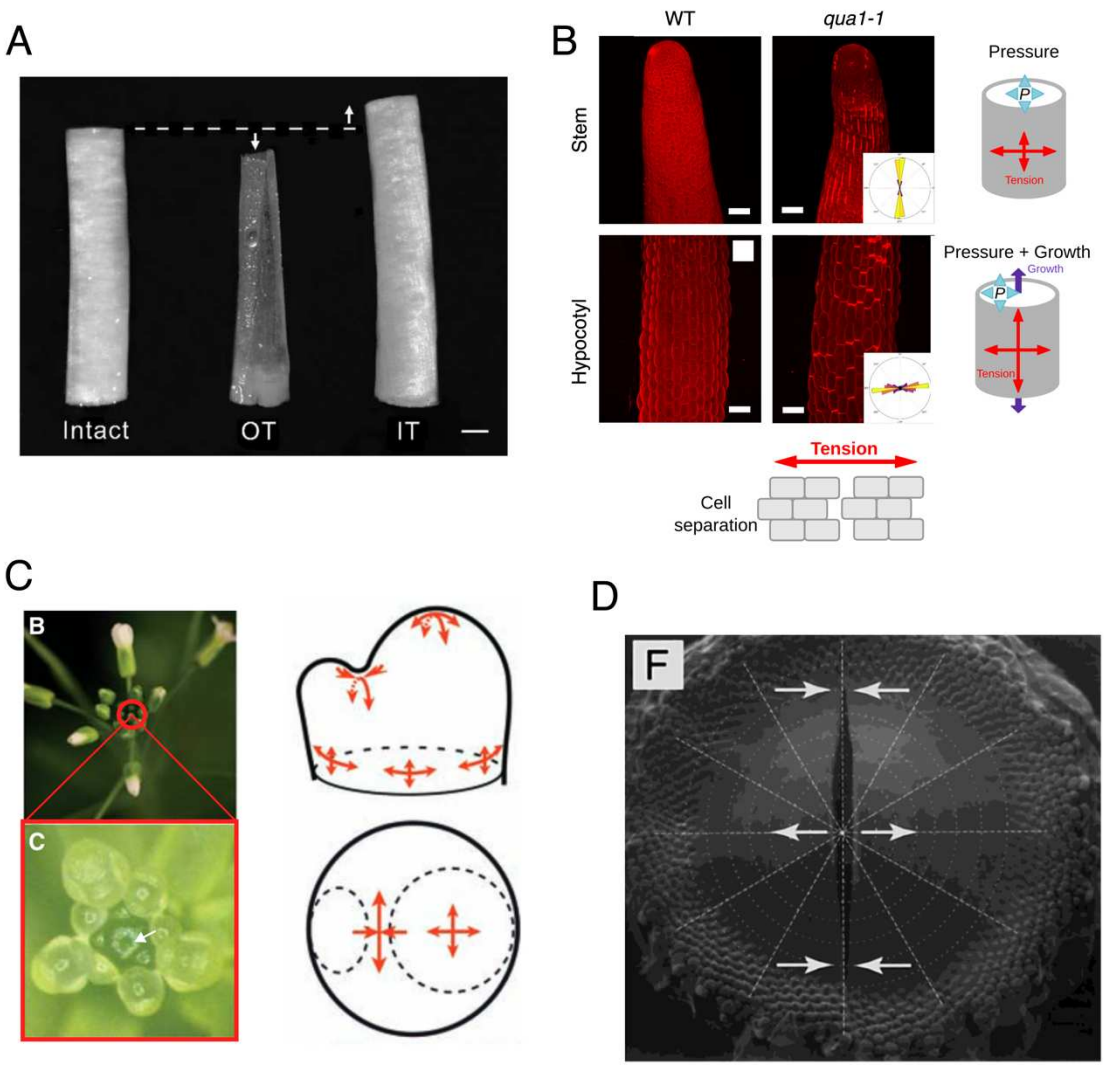

Figure I6: Tissue-derived mechanical stress in plants. (A) (Adapted from Kutschera and Niklas, 2007) Peeling experiment made on a sunflower hypocotyl, showing the size differences between the intact segment, and the isolated outer tissues (OT) and inner tissues (IT). Compared to the intact segment, the OT retract while the IT expand upon stress relaxation. This indicates that the OT are under tension and the IT under compression. The scale bar is 1 mm. (B) (Adapted from Verger *et al.*, 2018) The vertical cracks in the stem and longitudinal cracks in the hypocotyl of *qua1-1* mutants of *Arabidopsis* coincide with the maximal tension patterns modelled for a cylinder under pressure (stem) and combined with vertical growth (hypocotyl). As the cracks would form perpendicularly to the tension orientation, this confirms a transverse maximal tension in the stem, and a vertical maximal tension in the hypocotyl. The scale bars are 50 µm. (C) (Adapted from Vernoux *et al.*, 2010 and Hamant *et al.*, 2008) Left images: inflorescence of *Arabidopsis* with a zoom on the SAM (white arrow) and surrounding organ primordia. Right scheme: Modelling of tension patterns at the SAM from a side view (top) or top view (bottom). Tension is isotropic at the tip of the SAM, and anisotropic at the boundary between the SAM and the primordium. (D) (Adapted from Dumais and Steele, 2000) Shallow cut on a sunflower capitulum. The cut expands more in the center than in the generative regions on the edges. The white arrows indicate the forces acting on these different regions. The dashed lines show the radial and circumferential stress acting on the capitulum.

4. Shape-derived stress

With the assumption that the epidermis is under tension in plant aerial organs, shape in turn prescribes mechanical stress patterns. Indeed, an inflated sphere, for example, will present an isotropic tension pattern at its surface while a cylinder will present a tension twice as high transversely than axially (Jordan and Dumais, 2010; Verger *et al.*, 2018; Colin *et al.*, 2020). When coupled with axial growth, however, the maximal tension in a cylinder changes from transverse to longitudinal (Verger *et al.*, 2018). Stems can be represented as pressurized cylinders (Figure I6B). The predicted maximal tension was experimentally confirmed in *qua1*'s stems that display vertical cracks (reflecting transverse maximal tension) (Verger *et al.*, 2018; Figure I6B). In other words, the cylindrical shape of the stem prescribes maximal tensile stress in the transverse direction.

While modelling of maximal tension is quite easy for simple shapes, it can become harder to predict when they are more complex, with folding and buckling events, and when growth is integrated. Experimental evidence with indentation show that the SAM epidermis is under tension, because it is pressurized by tissues underneath (Beauzamy *et al.*, 2015). A mechanical model representing the SAM as a thin shell under pressure, derives tension orientations in the epidermis according to its shape (Hamant *et al.*, 2008). In this model the center of the meristem (a dome-like structure) presents an isotropic tension pattern, like an inflated half-sphere (Figure I6C). This could be validated experimentally with razorblade cuts in the sunflower capitulum (inflorescence), leading to gap opening (Dumais and Steele, 2000; Figure I6D). Organ emergence on the SAM's side perturbs this dome-like structure, and, based on shape-derived tension, reorganizes the tensile stress pattern to be circumferential around the emerging organ (Hamant *et al.*, 2008; Figure I6C). Furthermore, the fold induced at the boundary between the meristem and the primordium is predicted to induce a highly anisotropic tension pattern, combined with compressive stress (Hamant *et al.*, 2008; Burian *et al.*, 2013; Figure I6C). This could be validated by observing nuclei being squeezed in boundary cells (Fal *et al.*, 2021). Compression also occurs in the margin of the sunflower capitulum, through complex tissue deformation, as shown with razorblade cuts leading to gap closing in this region (Dumais and Steele, 2000; Figure I4D).

Shape-derived mechanical stresses are not restricted to the organ scale. Indeed, plant cells are also pressurized objects, putting their cell wall under tension (Coen and Cosgrove, 2023). Stress directions have been computed for the complex jigsaw puzzle-shaped pavement cells of *Arabidopsis* purely based on shape and curvature (Sampathkumar *et al.*, 2014; Figure I7D). While the cell wall is under tension, the cortical curvature in pressurized, isolated protoplasts (wall-less plant cells) has also been used to compute maximal tension (Colin *et al.*, 2020; Figure I7E). This was modelled for pressurized and confined protoplasts in rectangular microwells to induce an ellipsoidal shape, with a locally cylindrical shape (Colin *et al.*, 2020).

5. The mechanics behind proprioception

So far, we have seen how shape and force constrain each other. However, deformation, like buckling, appears as a passive response to force. Could there also be a more biologically active response to stress? Can cells perceive the stress pattern and actively resist to it?

In chick embryos, lack of mechanical stimulations due to muscle paralysis induce severe defects in bone development (Nowlan *et al.*, 2010). During heart maturation in zebrafish, the proper development of heart valves depends on the blood flow in the heart (Vermot *et al.*, 2009). In sunflowers, the emergence of an organ primordium at the capitulum has been proposed to be a consequence of differential growth between inner and outer layers. The compressive stress generated on the outer layer would be released by the formation of a bulge (the organ primordium) (Dumais and Steele, 2000). Although still debated, this was further supported by local application of expansin (leading to wall softening) inducing new organ emergence (Fleming *et al.*, 1997; Figure I8E).

These different examples show that cells and tissues can respond to stress patterns, and modify their properties and their growth accordingly. This is a form of proprioception. Proprioception is the perception, or sensing, of different body parts (their position, size and shape) (Hamant and Moulia, 2016). As organs grow and generate mechanical forces, adaptation to resist these forces is required. Proprioception requires movement, as evidenced by the loss of one's perception of their arm, when kept still for too long (Hamant and Moulia, 2016). Indeed, skin and muscles have been described as proprioceptors (Winter *et al.*, 2005; Macefield, 2021). In development, proprioception channels morphogenesis, and contributes to explain organ shape complexity and reproducibility. Skeletal muscles have been shown to be involved in developing the circumferential shapes of long bones, through mechanical signals (Sharir *et al.*, 2011). Mechanical forces are therefore part of the proprioceptive response. In plants, they have been proposed to help sepal shape reproducibility in *Arabidopsis* (Hervieux *et al.*, 2017). Mechanical forces are also restrictors of growth, as shown for *Arabidopsis* sepals (Hervieux *et al.*, 2016).

Gravitropic responses (the reorientation of growth in response to gravity) imply a proprioception of the curvature in response to gravity, and may involve mechanical sensing (Bastien *et al.*, 2013). This proprioceptive response to gravity is correlated with mechanical signaling in birch trees (Alonso-Serra *et al.*, 2020).

These different examples show that plants, like all kingdoms of life, have evolved molecular pathways to perceive and respond to mechanical stress. This opens the question of the biochemistry behind morphogenesis.

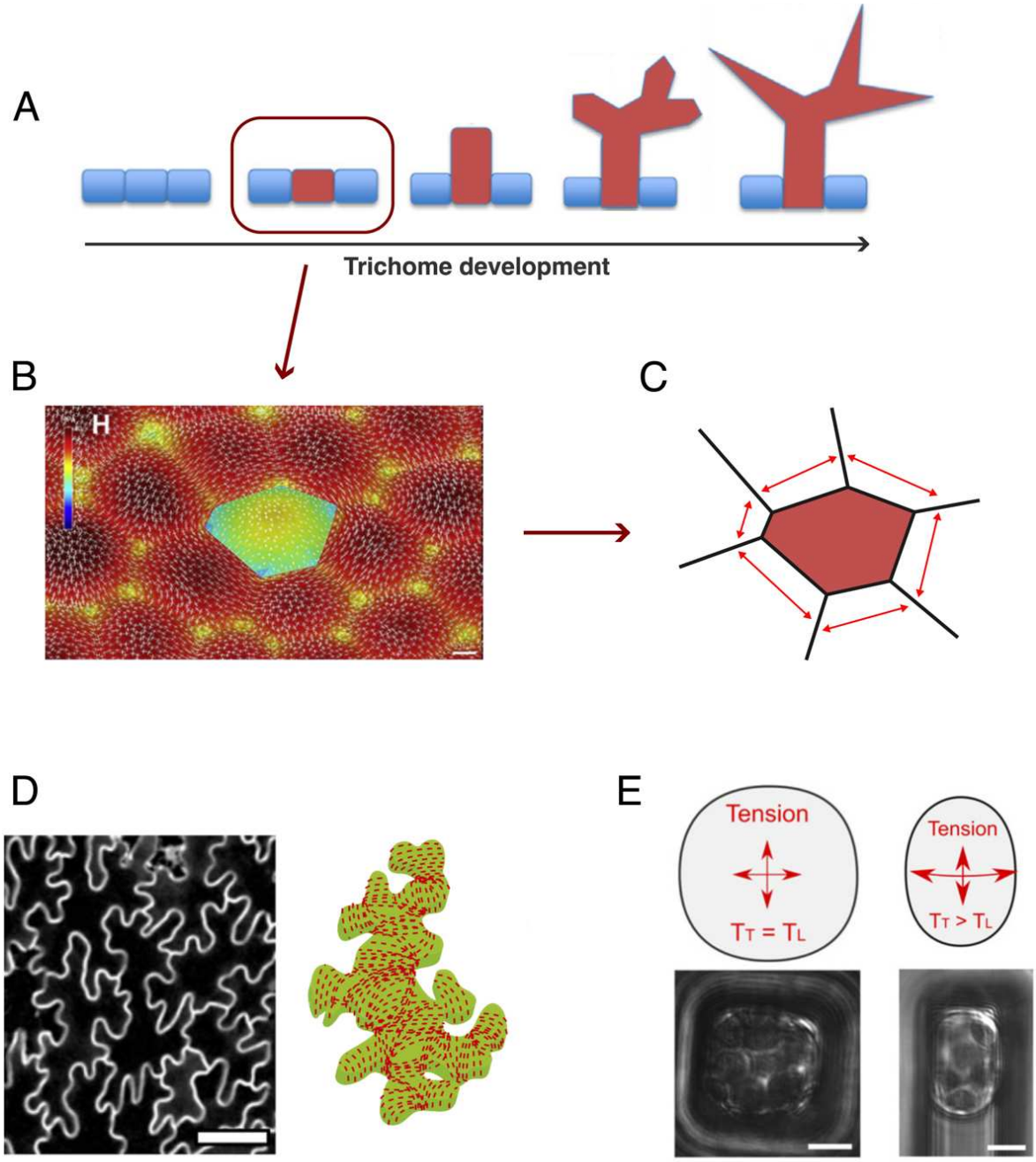

Figure I7: Local and cellular stress patterns in plants. (A) (Adapted from Hülskamp, 2019) Scheme of the different phases of trichome development. First, the trichome grows in plane, before an outgrowth at 90° from the tissue plane. Then, branching patterns emerge and give rise to the trichome shape. (B) (Adapted from Hervieux *et al.*, 2017) Computer simulation of the stress pattern distribution during the first step of trichome development. A central cell growing faster than its neighbors induce a radial reorganization of the stress around the fast-growing cell, as summarized in (C). The scale bar is 20 µm. (D) (Adapted from Carter *et al.*, 2017 and Sampathkumar *et al.*, 2014) Image of pavement cells of *Arabidopsis* leaves (left), and their prescribed maximal tension patterns (right). Maximal tension seems to be localized between two neck regions of the cell. The scale bar is 50 µm. (E) (Adapted from Colin *et al.*, 2020) Tension patterns prescribed by pressurized protoplasts with isodiametric (left) or oval (right) shapes. In the isodiametric scenario, the prescribed tension pattern is isotropic. In the oval scenario, the maximal tension is transverse to the axis of the cell. The scale bars are 5 µm.

III. Morphogenesis: a question of biochemistry

1. Positional information

If the generation of form can be viewed as a purely mechanical process based on differential growth, it cannot explain differential growth. Indeed, purely stress-based mechanisms are constantly changing, due to the feedback caused by growth, and are incompatible with the reproducible shapes observed in nature (Coen *et al.*, 2017). Even though they have been proposed to generate pattern formation at the cellular level (Hayashi and Carthew, 2004; Dumais, 2007), mechanics alone cannot generate differences in growth patterns.

Molecular and hormonal factors are involved in giving positional cues during morphogenesis (Wieschaus, 1995; Ali *et al.*, 2020). Signaling molecules functioning in a concentration-dependent manner are called morphogens (Bhalerao and Bennett, 2003). Morphogen gradients provide positional information during animal development (Gurdon *et al.*, 1994; Entchev *et al.*, 2000). While the use of the term "morphogen" is still debated in plants, phytohormones regulate cellular responses in a dose-dependent manner. The phytohormone auxin is especially regarded as a potential morphogen (Bhalerao and Bennett, 2003; Benková *et al.*, 2009). Indeed, the distribution of auxin fluxes determines lateral root and embryo developments, and lateral organ initiation at the shoot apical meristem (Teale *et al.*, 2006; Sauer *et al.*, 2013; Barbier de Reuille *et al.*, 2006; Figure I8A). Impairment of auxin fluxes results in organ-less shoots, notably in the *pin-formed/pin1* mutant, affected in polar auxin transport within cells (Gälweiler *et al.*, 1998; Figure I8C). On top of regulating organ initiation, auxin also controls organ shape by promoting growth. In the leaf, for example, the blade form is shaped by WUSCHEL-RELATED HOMEOBOX 5 (WOX5) protein gradients, involved in auxin biosynthesis (Zhang *et al.*, 2020), and leaf dissection (Figure I3A) is regulated by the position of auxin maxima at the leaf margins (Scarpella *et al.*, 2010). Moreover, the ratio between auxin and cytokinin, another phytohormone, determine the shoot or root identity in most cases, although there are some exceptions (Schaller *et al.*, 2015). An intermediate ratio of these two hormones induce the formation of a mass of disorganized cells, called a callus. A higher ratio of auxin to cytokinin induces shoot formation, while a higher ratio of cytokinin to auxin induces root formation (Ikeuchi *et al.*, 2013).

2. Polarity

In morphogenesis, the generation of axiality is required to generate one dimensional shapes like stems or petioles, or flat two dimensional shapes like leaves or petals, which can then combine to give rise to three-dimensional shapes. *Arabidopsis* and *Antirrhinum* leaves, for example, are planar structures that present adaxial-abaxial (upper-lower), dorso-ventral, and proximo-distal domains (McConnell and Barton, 1998; Waites and Hudson, 1995; Kidner and Timmermans, 2007). The

development of non-planar leaves, such as *Utricularia* traps, requires growth oriented by a polarity field (Whitewoods *et al.*, 2020). Definition of axiality depends on the establishment of polarity fields.

Polarity in tissues is generated by cellular asymmetries. Some factors are required for polarity establishment, and present a specific expression pattern within a cell, coordinated within a tissue to form a field of polarized cells. In animals, planar cell polarity (PCP) factors regulate tissue polarization (Simons and Mlodzik, 2007). Mutations in PCP genes disrupts the hair organization in *Drosophila* wing or in mouse fur, creating swirling patterns rather than the proximo-distal organization in wild types (Guo *et al.*, 2004; Vinson *et al.*, 1989). PCPs have also been shown to be involved in cell motility, and are involved in the establishment of the antero-posterior axis during zebrafish gastrulation and neurulation (Keller, 2022; Myers *et al.*, 2002). The sub-cellular localization of PCP factors varies between species and cell types, but is consistently polar. The PCP signaling pathway therefore acts in a tissue-specific manner, based on the asymmetric distribution of the PCP proteins (Simons and Mlodzik, 2007).

In plants, Pin-formed proteins (PINs), involved in auxin transport, are polarly localized at the sub-cellular scale (Feraru and Friml, 2008; Figure I8B). This polar localization regulates auxin fluxes, and this affects cell mechanics and growth. Thus, the initiation of lateral organs at the SAM is tightly linked with auxin patterning, and occurs at the local auxin maximum (Barbier de Reuille *et al.*, 2006; Galvan-Ampudia *et al.*, 2021; Figure I8A). Furthermore, the emergence of organ primordia is linked with local modifications of mechanical properties (Figure I8E). Hormonal fluxes induce a local modification of the cell wall composition and increase its elasticity (i.e. reduces its stiffness) (Peaucelle *et al.*, 2011). Combined with an increased growth rate, imposing pressure on the outer tissue, the tissue deforms and the organ is initiated, relaxing the stresses (Peaucelle *et al.*, 2011; Echevin *et al.*, 2019). *pin1* mutants result in organ-less shoots, due to an impairment in the polar transport of auxin (Gälweiler *et al.*, 1998; Figure I8C). A similar phenotype can be achieved with the naphtylphtalamic acid (NPA) drug, that inhibits auxin transport proteins (Abas *et al.*, 2021; Stieger *et al.*, 2002; Figure I8D).

Beside PINs, other polarly localized proteins have been identified in *Arabidopsis*. For example, SOSEKIs (SOKs) localize at cell edges in apico-basal, or radial polarity, when looking at the organism, and are thought to be involved in cell division orientation (Yoshida *et al.*, 2019). RabA5c is a small GTPase involved in vesicle trafficking and is localized at cell geometrical edges in young lateral roots. Impairing its expression results in highly affected lateral root development (Kirchhelle *et al.*, 2016). Similarly, CLASP proteins are localized at cell geometrical edges, and are involved in microtubule cytoskeleton regulations (Ambrose *et al.*, 2011). *clasp-1* mutants in *Arabidopsis* display defects in cell elongation (Ambrose *et al.*, 2007).

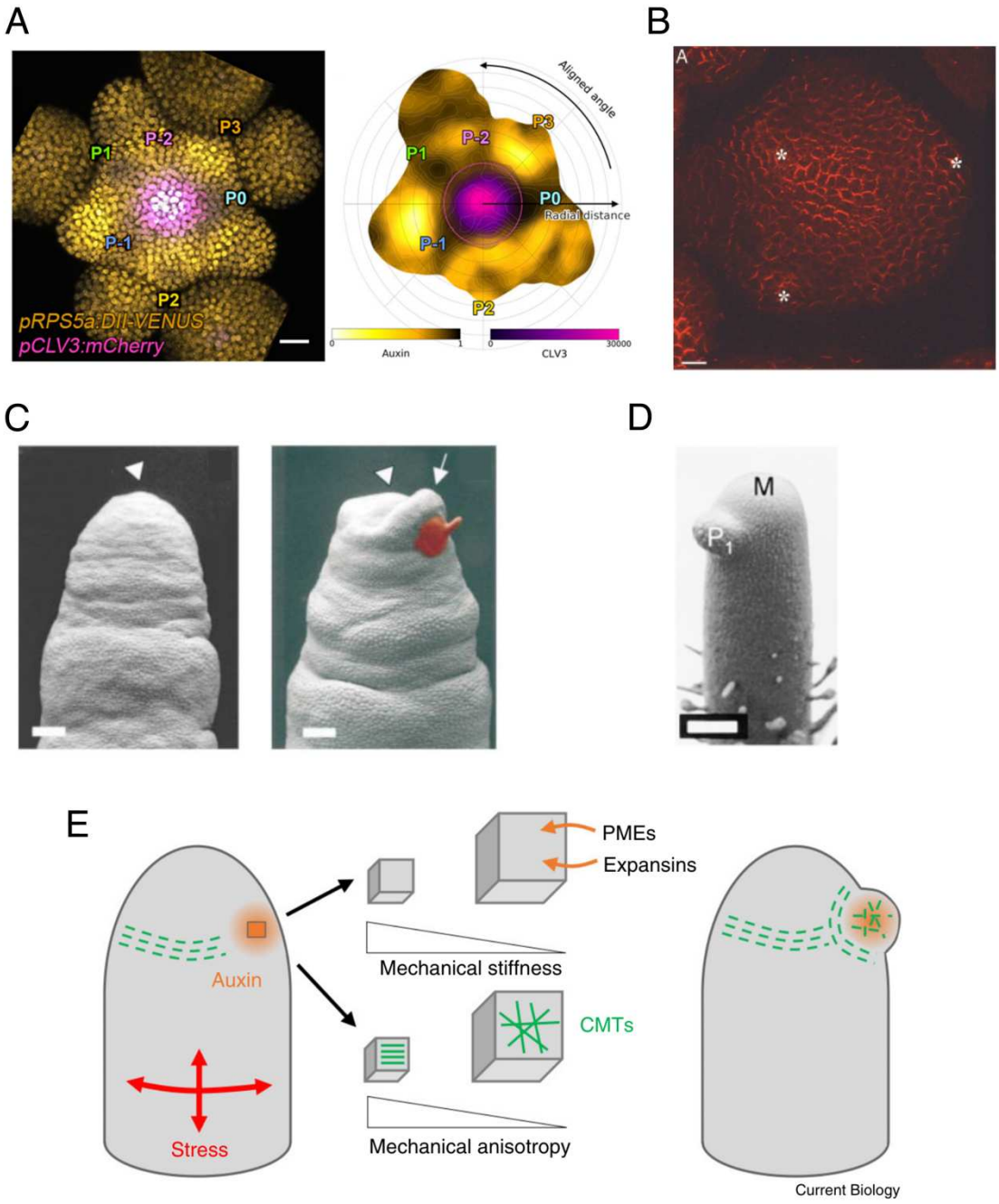

Figure I8: Auxin mediates organ initiation at the SAM of *Arabidopsis*. (A) (Adapted from Galvan-Ampudia *et al.*, 2020) Auxin distribution throughout the SAM, and accumulating at the next primordium initiation place. The auxin levels are visualized by DII-VENUS-N7 (yellow) and the central zone of the meristem by CLV3:mCherry (magenta) (left image). The schematic representation (right image) shows an accumulation of auxin at P-1. The scale bar is 20 µm. (B) (Adapted from Barbier de Reuille *et al.*, 2006) Immunolocalization of PIN1 (red) at the SAM. PIN1 are localized at the plasma membrane, and are polarized in most cells. The asterisks show the young organ primordia. PIN1 seem to converge towards young primordia in neighboring cells. The scale bar is 10 µm. (C-D) (Adapted from Reinhardt *et al.*, 2000). (C) Stems and SAMs (white arrowhead) of *pin1* mutants in control conditions (left image), or 38 hours after exogenous application of auxin (IAA) at the red spot (right image). After auxin application, a bulge starts to appear (white arrow). The scale bars are 100 µm. (D) NPA-grown stem and meristem (M), 3 days after transferring to NPA-free medium. A primordium initiation is visible (P1). The scale bar is 100 µm. (E) (Adapted from Trinh *et al.*, 2021) Auxin-mediated organ initiation acts through the activation of wall-relaxing factors (PMEs and expansins), leading to a decrease in mechanical stiffness, or through the disruption of microtubule (CMTs) organization, leading to a decrease in mechanical anisotropy.

3. Boundaries

The presence of polarity fields introduces the notion of molecular boundaries between the different domains. In the *Drosophila* wing, for example, dorso-ventral axiality is regulated by short-range signaling of dorsal and ventral cells. As a result, a specialized cell type emerges at the boundary, and appears as an organizer that keeps the organ pattern through morphogen generations (Meinhardt, 1983; Diaz-Benjumea and Cohen, 1993). In the *Arabidopsis* leaf, gene regulatory networks maintain axiality and determine boundaries (Manuela and Xu, 2020). The adaxial-abaxial polarity, for example, is maintained by HD-ZIP III transcription factors (adaxial identity), and KANADI and YABBY transcription factors (abaxial identity) (Manuela and Xu, 2020). *WOX1* and *PRS* are genes expressed at the boundary between the adaxial and the abaxial regions (Manuela and Xu, 2020).

On top of boundaries, organ margins are especially important in morphogenesis, as shapes can be defined by the form outlines. Leaf shape complexity, and serration levels, are genetically regulated by modulating growth at the leaf margin (Kierzkowski *et al.*, 2019; Figure I3A). Indeed, leaf shape emerges from specific inhibition of growth, tightly regulated in time and space (Bar and Ori, 2014). The leaf shape of *Cardamine hirsuta* and *Arabidopsis*, for example, comes from the specific patterning of *SHOOT MERISTEMLESS* (*STM*) and *REDUCED COMPLEXITY* (*RCO*) genes throughout the leaf margins, combined with specific auxin patterns, promoting or inhibiting growth, respectively (Kierzkowski *et al.*, 2019).

As mentioned earlier, the epidermis, which can be viewed as the margin layer between the inner tissues of an organism and the outside, is limiting for growth. First evidences come from the characterization of the brassinosteroid (BR) phytohormone signaling pathway in the epidermis (Szekeres *et al.*, 1996; Nakaya *et al.*, 2002), and mutations in BR signaling or biosynthesis results in dwarf mutants (Savaldi-Goldstein *et al.*, 2007). Specific expression of the mutated BR receptor or biosynthetic enzyme in the epidermis alone is sufficient to rescue the dwarf phenotypes (Savaldi-Goldstein *et al.*, 2007). Furthermore, the growth rate and mechanical strength of the epidermis is determinant for the growth of the whole organism. In a BR-deficient *Utricularia* mutant, the epidermis presents a reduced growth rate, resulting in increased internal tissue stress, and inducing the twisted internal tissue and dwarf phenotypes observed (Kelly-Bellow *et al.*, 2023). The importance of the epidermis in plant morphogenesis is also highlighted by the presence of epidermal-specific genes such as *ARABIDOPSIS THALIANA MERISTEM LAYER1* (*ATML1*) and *PROTODERMAL FACTOR* (*PDF*) (Nakamura *et al.*, 2006). *atml1-3* and *pdf2* double mutants result in embryonic arrest (Ogawa *et al.*, 2015). At the SAM, the epidermal layer appears as necessary for organ initiation, as its removal leads to organogenesis arrest in tomato, whereas organ formation continues after ablation of the central zone of the meristem (leading to the establishment of a new meristem center) (Reinhardt *et al.*, 2003).

IV. Cell wall

While the link between hormones and transcription factors provide the bases for the molecular control of morphogenesis, it only indirectly relates to geometry and mechanics. To get the nexus between geometry, mechanics and biochemistry, one needs to delve into the molecular mechanical effectors of cell shape changes. In plants, these are mainly the regulators of the cell wall (as shown in the Lockhart model, Chapter II2B of the Introduction).

The composition and size of the cell wall can vary between cell types and cell ages, and is decomposed in a primary cell wall (mainly present in young cells) and a secondary cell wall below the primary one (synthetized later). The secondary cell wall is synthesized by older and more specialized cells, and its composition can vary depending on the function of the cell (Zhong *et al.*, 2018). Furthermore, while growth is mainly mediated by the turgor pressure of the protoplast, the force it exerts on the walls is isotropic, and cannot explain oriented growth. It is the cell wall properties and composition (through mechanical anisotropy and polarity) that controls the orientation and rate of cell growth (Cosgrove, 2016).

The primary cell wall is mainly made of polysaccharides. Namely cellulose, hemicelluloses (mainly xyloglucans), and pectins (Figure I9A). It is considered as a gel-like matrix, with its cellulosic components being associated with load bearing, as cellulose stiffness (the most relevant property when studying growth since there is no breakage) is comparable to that of steel (Coen and Cosgrove, 2023).

1. Cellulose

Cellulose is a β-1,4 glucose polymer arranged in fibers, called cellulose microfibrils (Turner and Kumar, 2018). The main component of the cell wall is a network of these cellulose microfibrils, connected together by other molecular components (Heredia *et al.*, 1995). Cellulose is the main load-bearing component of the cell wall, notably through cellulose-cellulose associations, and other cellulose-matrix interactions (Rongpipi *et al.*, 2019; Chebli and Geitman, 2017). Cellulose microfibrils usually appear highly aligned, and give the direction of cellular expansion, by resisting the pressure exerted by the protoplast (Baskin, 2005; Figure I9B). As mentioned above, it is the sliding of cellulose microfibrils through creep and a transient relaxation of the cell wall that allows cellular expansion. This wall relaxation is mediated by expansins, proteins in the cell wall that catalyze its expansion, without apparent enzymatic activity (McQueen-Mason *et al.*, 1992; McQueen-Mason and Cosgrove, 1995). Cellulose synthesis is mediated by a protein complex called the cellulose synthase (CESA) complex (CSC) (Bringmann *et al.*, 2012; Schneider *et al.*, 2016). Mutations in this complex affect cellulose content and have a wide range of rather severe effects on plant development (Hu *et al.*, 2018), ranging from dwarfism (MacKinnon *et al.*, 2006; Fujita *et*

al., 2013) to embryo lethality (Beeckman *et al.*, 2002). More subtle modulations are possible with other cell wall mutants.

2. Hemicelluloses

Hemicelluloses compose another big family of cell wall polysaccharide. Xyloglucans are the main hemicelluloses present in the cell wall, and strongly bind to cellulose (McNeil *et al.*, 1984; Hayashi *et al.*, 1994; Figure I9A). However, they seem to have little impact on the mechanical properties of the cell wall. Indeed, *xxt1xxt2* mutants affected in xyloglucan biosynthesis, through mutations in the XYLOGLUGAN TRANSFERASE 1 and 2 genes, exhibit no significative changes in cell wall composition besides xyloglucan content (Zhao *et al.*, 2019). Nevertheless, cellulose microfibrils appear highly aligned in this mutant, suggesting that xyloglucans function as spacers between cellulose microfibrils (Xiao *et al.*, 2016). Although the stiffness of the cell walls is not affected, it is worth noting that *xxt1xxt2* presents around 22% less cellulose content than in the WT's walls (Zhao *et al.*, 2019). Phenotypically, *xxt1xxt2* has swollen and shorter root hairs, and flatter SAMs (Cavalier *et al.*, 2008; Zhao *et al.*, 2019). It has recently been proposed that xyloglucans are involved in small points in the cell wall that concentrate the resistance to tension. These small points are called mechanical hotspots, where cellulose microfibrils would be held close together by xyloglucan molecules, facilitating interactions between cellulose microfibrils, and highly increasing mechanical resistance in these points (Cosgrove, 2014; Cosgrove, 2018). Expansins are thought to target these mechanical hotspots and allow creep. *xxt1xxt2* mutants, that should not display these hotspots, display very little wall extension after exogenous application of expansins (Park and Cosgrove, 2012). One explanation is that, in these mutants, the pectin components of the cell wall compensate and hold a more important load-bearing role than in the wild type (Park and Cosgrove, 2012).

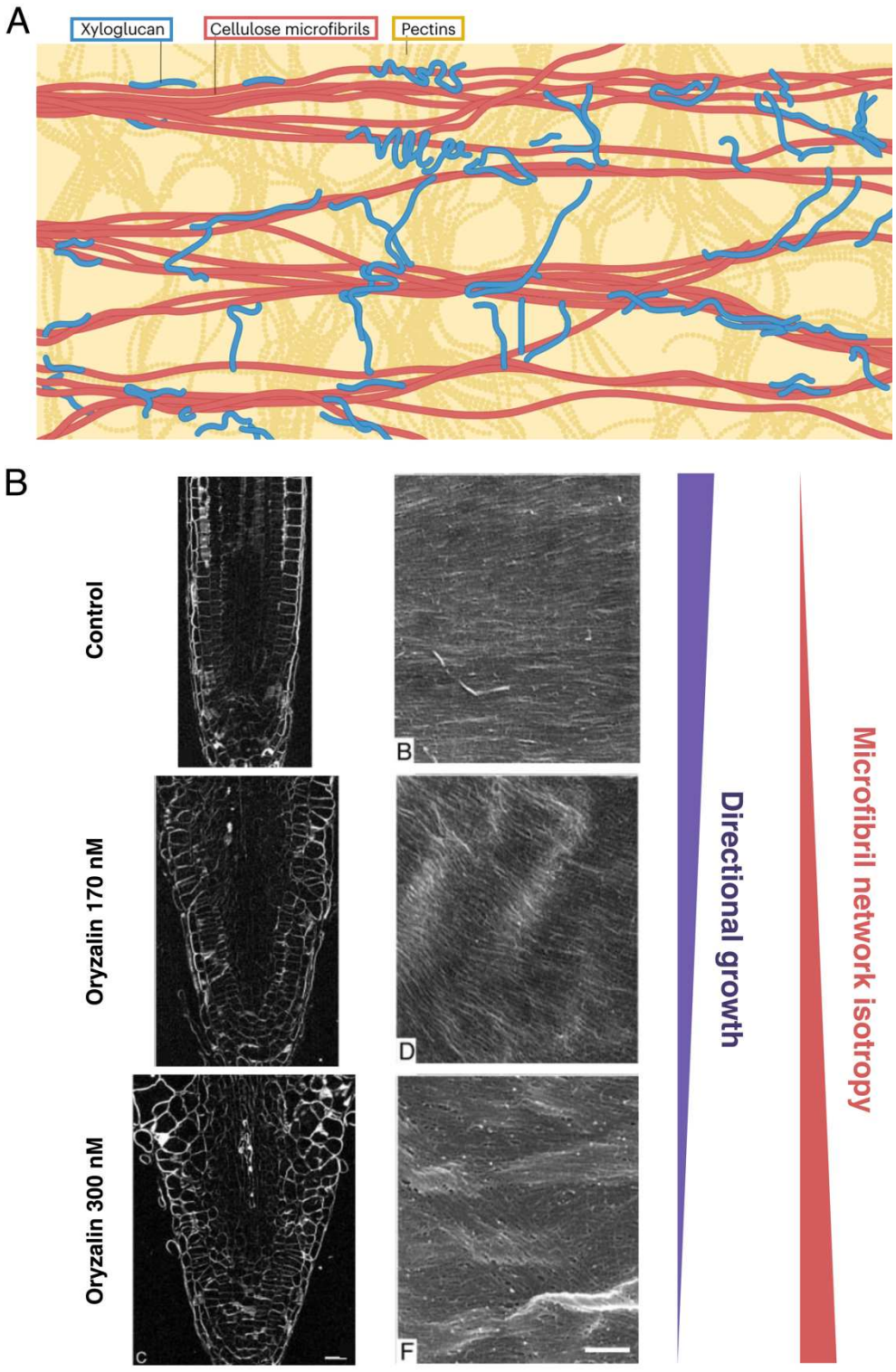

Figure I9: The plant cell wall and directional growth. (A) (Adapted from Cosgrove, 2024) Schematic representation of the plant cell wall composition and organization. Cellulose microfibrils form a lattice for the cell wall, and can interact together through contact sites. Xyloglucans can bind cellulose, tethering them together, or be trapped in cellulose bundles. Pectins form a network, embedding the cellulose and xyloglucan components. (B) (Adapted from Baskin *et al.*, 2004) Treatment of *Arabidopsis* root tips with oryzalin disrupts their growth, as well as their microfibril organizations (right images). Control roots present directional growth and highly aligned, anisotropic cellulose microfibrils. Mild treatment with oryzalin (170 nM) disrupts microfibril anisotropy and the consequent root growth. Stronger treatment with oryzalin (300 nM) further strengthens this phenotype. Scale bar for root images: 20 μm. Scale bar for microfibril images: 250 nm.

3. Pectins

Pectins, the last family of primary cell wall components, coat the cellulose microfibrils through loose bindings (Wang *et al.*, 2012; Wang *et al.*, 2015). They form a highly mobile hydrogel and are thought to regulate the cellulose-cellulose interactions (Zykwinska *et al.*, 2007). The modulation of cell wall properties is often associated with pectin modifications (Chebli *et al.*, 2012; Wang *et al.*, 2012; Pérez García *et al.*, 2011). More specifically, the level of esterification of homogalacturonans (HG, a type of pectins) appears as determinant for their interaction with cellulose, and therefore the resulting mechanical properties of the cell wall. While the level of methyl-esterification of HGs is undeniably associated with mechanical properties of the cell wall, it appears that their linking through calcium bonds is more relevant to stiffness than their methyl-esterification levels (Willats *et al.*, 2001; Wolf and Greiner, 2012; Bidhendi and Geitman, 2016). De-methyl-esterified pectins are more accessible for degradation by pectin lyases, thus making the walls softer (Wormit and Usadel, 2018). In the pollen tube, however, increased de-methyl-esterified pectins would lead to the formation of calcium cross-links and increase the wall stiffness (Wormit and Usadel, 2018). Newly synthetized HGs seem to be highly methyl-esterified in the trans-Golgi apparatus (Driouich *et al.*, 2012). *quasimodo1* and *quasimodo2* mutants are affected in pectin biosynthesis and display reduced cell adhesion (Bouton *et al.*, 2002; Mouille *et al.*, 2007). After their incorporation in the cell wall, pectin methyl-esterification status is regulated by PECTIN METHYLESTERASES (PMEs), that de-methyl-esterify pectins, which in turn can be inhibited by PME INHIBITORS (PMEIs). *pme35* mutants fail to de-methyl-esterify their HGs and display no mechanical support in their stems (Hongo *et al.*, 2012). In the ethanol-inducible *PMEI3* overexpressor line, pectins have a higher degree of methyl-esterification and, as a result, the cell walls are stiffer (Peaucelle *et al.*, 2011). Contrarily, the PME5 overexpressor line displays softer walls than the WT (Peaucelle *et al.*, 2011). Exogenous application of PME promotes organ growth, translating a softening of the cell wall (Armezzani *et al.*, 2018; Figure I8E).

The analysis of pectins at the SAM further confirms that cell wall stiffness is important for the initiation of organs (Peaucelle *et al.*, 2008). If the walls are too stiff, any deformation in the tissue is difficult to achieve. This can notably be reflected in the stiffness differences observed in the SAM regions, with the periphery (where new organs are generated) being softer than the center (Milani *et al.*, 2011; Sassi *et al.*, 2014). As mentioned above, auxin is the main hormone responsible for organ initiation. This is mainly mediated by the PIN-FORMED1 (PIN1) polar auxin transporter, that induces auxin accumulation at the organ initiation site (Figure I8A), and *pin1* mutations or NPA treatments result in completely inhibited primordia formation at the SAM (Reinhardt *et al.*, 2003; Reinhardt *et al.*, 2000). On the contrary, the exogenous application of the phytohormone auxin can induce the emergence of organs, and can rescue the abovementioned phenotype (Reinhardt *et al.*, 2000; Sassi *et al.*, 2014; Figures I8C and I8D). It has later been found that auxin activates cell wall remodeling enzymes, and that it is this wall remodeling that is responsible for the emergence of the organ (Murray *et al.*, 2012; Sassi and Vernoux, 2013). This is evidenced by the experiment discussed above of exogenous PME application (Armezzani *et al.*, 2018) in the SAM.

Other experiments made on roots converge towards the same conclusions. An auxin influx carrier called LAX3 is involved in lateral organ formation in the root, by regulating the spatial expression of cell-wall remodeling enzymes (Swarup *et al.*, 2008).

However, with the analysis of cell wall component, there is little insight in to how cell walls orient their components and modulate their mechanical anisotropy. Cellulose deposition can be self-organized, with the trajectory of CESA at the plasma membrane being constrained by the aligned cellulose microfibrils in the adjacent cell wall (Chan and Coen, 2020). Yet, how can this be modified? How can the cell walls dynamically change their mechanical anisotropy and/or rate of synthesis? This involves effectors at the cell cortex, and mainly the cytoskeleton.

4. The plasma membrane machinery behind cell wall synthesis

Hemicellulose, pectins and structural proteins are secreted by the cells through exocytosis (Ketelaar *et al.*, 2008). This pathway can thus modulate the rate of matrix synthesis. The mislocalization of RabA5c, a specific actor of the vesicular trafficking pathway, targeting vesicles at cell geometric edges, results in morphogenetic defects (Kirchhelle *et al.*, 2016). While the secretory pathway could affect the mechanical polarity of the cell, with exocytosis being more or less active in certain regions, it does not impact the mechanical anisotropy of the cell wall.

To understand how mechanical anisotropy is controlled in the cell wall, one needs to turn to the cytoskeleton. Cortical microtubules (CMTs, components of the cytoskeleton) have been found to guide CESA complexes along the plasma membrane, and therefore orchestrate cellulose microfibril organization and anisotropic cell growth (Paredez *et al.*, 2006; Cosgrove, 2024; Figures I10A and I10B). Interestingly, perturbation of microtubule organization alone can induce organ formation in *pin1* mutants (Sassi *et al.*, 2014; Figure I8E). On top of being generally guided by CMTs, CESA complexes have also been found to be guided by pre-existing cellulose microfibrils (Chan and Coen, 2020). This further shows how modulating wall properties can trigger organogenesis, and opens new questions of the role of the cytoskeleton in plant morphogenesis.

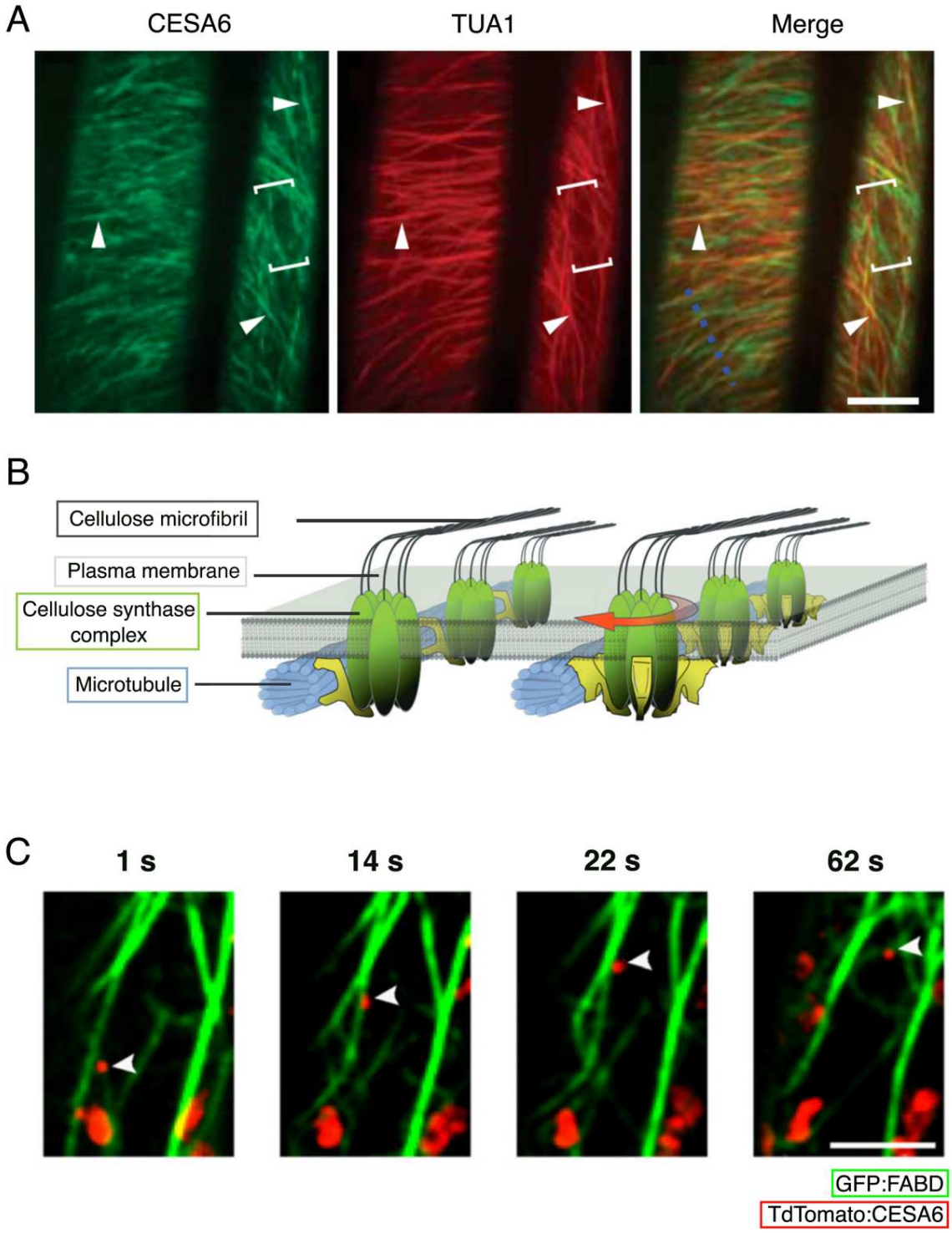

Figure I10: Cellulose deposition is under the control of the cytoskeleton. (A) (Adapted from Paredez *et al.*, 2006) Colocalization of CESA (green; YFP:CESA6) with microtubules (red; CFP:TUA1) in *Aradidopsis* etiolated hypocotyl cells. The images are averages of 30 frames, taken every 30 seconds, showing that the CESA particles travel along microtubules. The scale bar is 10 μm. (B) (Adapted from Bringmann *et al.*, 2012) Schematic representation of CESA complexes synthetizing cellulose microfibrils, generally guided by cortical microtubules. (C) (Adapted from Sampathkumar *et al.*, 2020) Tracking of a CESA particle (red; TdTomatoRFP:CESA6) overtime, in the subcortical region of an *Arabidopsis* hypocotyl cell. The fast movement of the CESA particle is mediated by actin filaments (green; GFP:FABD). The scale bar is 5 μm.

V. Cytoskeleton

The cytoskeleton is a network of protein polymers forming filaments, and insuring functions of structure maintenance and transport in the cell. On top of its structural and growth-related functions, the cytoskeleton is involved in cell division and therefore appears as a key actor of morphogenesis at the cell level. There are three main classes of cytoskeleton filaments in cells: actin, microtubules and intermediate filaments, insuring different functions and having different organizations depending on the organism (Frixione, 2000). In plants, microtubules ensure structural support of the membrane, a function given by actin in animal cells (Smith and Oppenheimer, 2005; Fletcher and Mullins, 2010). Intermediate filaments typically have functions related to tissue mechanics (Rölleke *et al.*, 2023), cell migration and organelle transport (Schwarz and Leube, 2023). While plant cells do not present intermediate filaments (Menzel, 1993), an analog has been found in *Allium cepa* (Ciska *et al.*, 2013). In this part, I will briefly detail some of what is known about the actin and microtubule cytoskeleton, mainly focusing on plants.

1. Actin

Actin filaments are essential components of the cytoskeleton. Actin is present as a monomer (G-actin), or organized in filaments (F-actin) (Gao and Nakamura, 2022). Actin filaments (AFs) are composed by two connected actin polymer strands, with a helical twist (Staiger and Blanchoin, 2006). They are dynamic structures, organized in a +/- polarity, with the plus-end known as the barbed end, and the minus-end as the pointed end (Yuan *et al.*, 2023; Figure I11). F-actin polymerization is an active process, and requires the hydrolysis of an ATP molecule to add a G-actin monomer at the barbed end of the filament (Gao and Nakamura, 2000; Figure I11). On the other hand, the pointed end of the filament is slow-growing, and rather undergoes slow depolymerization with the loss of ADP-actin molecules (Staiger and Blanchoin, 2006). Actin filaments are around 7 nm thick and polymerize at a rate of thousands of nanometers per second (Schneider and Persson, 2015).

The *de novo* formation of F-actin is referred to as actin nucleation. It can happen spontaneously from actin dimers or trimers, but this process is rather unlikely *in vivo* (Pollard *et al.*, 2000; Staiger and Blanchoin, 2006). Instead, it is facilitated by actin nucleator proteins such as formins, Spire or the Arp2/3 complexes (Wasteneys and Yang, 2004). In plants, the Arp2/3 complexes are thought to be involved in filament organization, and cell expansion (Deeks and Hussey, 2003). In animals, modulation of actin nucleation complex activity results in actin polymerization responses, a process that could be conserved in plants (Eden *et al.*, 2002; Le *et al.*, 2006; Djakovic *et al.*, 2006; Frank *et al.*, 2004; Ali and Kawashima, 2021).

In animals, muscle contraction is largely mediated by the force generated by actin and its motor protein myosin (Rayment *et al.*, 1993). More generally, cell motility involves acto-myosin activity at

the cell cortex (Salbreux *et al.*, 2012). However, when considering non-muscle actin, only two isoforms are present in vertebrates (Kabsch and Vandekerckhove, 1992).

Plant cells are not motile, and have comparatively less actin filaments at the cortex. Their cortical actin filaments, together with myosin motor proteins, are rather thought to contribute to cytoplasmic streaming (Tominaga *et al.*, 2013). Actin filaments in the cell are involved in vesicle trafficking, including the delivery of cell wall components (Peremyslov *et al.*, 2012).

Plants present a large actin gene family, with for instance 10 genes encoding for actin isoforms in *Arabidopsis* (McDowell *et al.*, 1996). Plant actins are classified as vegetative actin (ACT2, 7 and 8 in *Arabidopsis*) and reproductive actin (ACT1, 3, 4, 11 and 12 in *Arabidopsis*), depending on the tissues in which they are expressed (Kandasamy *et al.*, 2009). ACT5 and 9 are probably pseudogenes given their high degree of sequence divergence (McDowell *et al.*, 1996), and are typically not considered in actin studies. The vegetative and reproductive actins differ from 4 to 7% in their amino-acid sequence, which is similar or greater than the difference between cytoplasmic and muscle actins in animals (Kandasamy *et al.*, 2007). *actin2-7 actin7-4* (*act2act7*) double mutant is affected in vegetative actin content (Kandasamy *et al.*, 2009). In this mutant, very low levels of actin are detectable: around 16% of the WT's content in the shoot, and 25% of the WT's content in the roots. Developmental defects are noticeable, mainly dwarf plants and root hair development defects, consistent with defective wall component delivery (Kandasamy *et al.*, 2009).

The assembly as well as the density of the actin filament networks are modulated by actin-associated proteins (AAPs), and more particularly actin-binding proteins (ABPs) (Volkmann and Baluska, 1999). Interestingly, most of the actin in plants is found as monomers, with only 5-10% of the total actin content being filamentous in *Papaver rhoeas* or maize pollen, and 1-2% in tobacco suspension cells (Gibbon *et al.*, 1999; Snowman *et al.*, 2002; Wang *et al.*, 2005; Staiger and Blanchoin, 2006).

ABPs are highly diverse and interact with actin through a variety of modes, as reviewed in Gao and Nakamura (2022), or more specific to plants in García-González and van Gelderen (2021). Briefly, plant ABPs allow a fine-tuning of actin polymerization rates (through promoting polymerization or depolymerization), modulation of actin filaments dynamics through bundling, severing, or branching (Figure I11). Profilin, for example, binds G-actin and prevents their association for spontaneous nucleation and suppresses their assembly at the pointed end of AFs (Hussey *et al.*, 2006). Actin depolymerization factors (ADFs) or cofilin are ABPs that promote actin disassociation at the pointed end and have severing activities (Hussey *et al.*, 2006). They can also create new affinities for ADP-actin, which can result in the assembly of new filaments from the severed ones (Staiger and Blanchoin, 2006). Capping proteins are found at the barbed ends of AFs and control their polymerization dynamics (Huang *et al.*, 2003). Bundling of the AFs into thick cables is mediated by fimbrin and villin (Staiger and Blanchoin, 2006; Thomas *et al.*, 2009). Probably the most popular ABP is myosin, a motor protein used to generate force for vesicular or organellar transport in plants. However, other functions have been attributed to myosins, such as myosin

VIII and XI, involved in cell division purposes such as spindle formation, cell plate guidance and maturation (Reichelt *et al.*, 1999; Wu and Bezanilla, 2014; Huang *et al.*, 2024). Myosins also probably have a function in regulating the actin network dynamics (Park and Nebenführ, 2013).

Actin filaments are found throughout the whole cell cycle, but their aspect and functions vary depending on their localization or status. During interphase, filamentous actin is mainly found throughout the cytoplasm, and in high bundles in cytoplasmic streams (Palevitz *et al.*, 1974; Figure I12A). As mentioned above, the main role of actin filaments during interphase in plants is thought to ensure vesicular and organellar transport. They have been found to play a role in motility and dynamics of the endoplasmic reticulum (Ueda *et al.*, 2010), chloroplasts (Kadota *et al.*, 2009), mitochondria (Doniwa *et al.*, 2007) and the Golgi apparatus (Kim *et al.*, 2005; Akkerman *et al.*, 2001). Moreover, nuclear movements in plants are generally linked with the actin cytoskeleton. In growing root hairs, treatments with the actin polymerization inhibitory drugs Latrunculin B (Spector *et al.*, 1983) and Cytochalasin D (Brown and Spudich, 1979) affect nuclear migration towards the tip of the root hair cell. Microtubule stabilization (taxol, Schiff and Horwitz, 1980) or depolymerization (oryzalin, Cleary and Hardham, 1990) drugs, on the other hand, do not seem to affect nucleus movements (Chytilova *et al.*, 2000). Especially, actin is the driver of pre-mitotic nuclear migration in a wide variety of plant cells (Mineyuki and Palevitz, 1990; Kimata *et al.*, 2016; Vilches Barro *et al.*, 2019). Actin filaments also have a role in specialized cells, such as regulating the stomatal aperture (Higaki *et al.*, 2010), or even statoliths movements in roots during gravitropic responses (Nakamura *et al.*, 2011). Thinner and highly dynamic actin filaments are also present in the cortex of plants cells (Staiger *et al.*, 2009), and are marginally involved in cellulose deposition (as suggested in Gilliland *et al.*, 2002), notably by modulating the velocity of CESA complexes (Sampathkumar *et al.*, 2013; Figure I10C).

Regarding mechanical response, actin is the main mediator of adaptations to mechanical stresses in animals (Blanchoin *et al.*, 2014). They are also highly involved in maintaining cell integrity, and coordination of mobility (such as muscle contractions) (Pollard and Cooper, 2009). Actin filaments also reorganize in response to mechanical perturbations in plants. For instance, after a local ablation in the leaf epidermis of *Tradescantia albovittata*, inducing circumferential tensile stresses, cortical actin filaments become circumferential, following the new stress pattern (Goodbody and Lloyd, 1990; Figure I12C). However, this response has not been analyzed in full details, and would certainly deserve more investigation in the future.

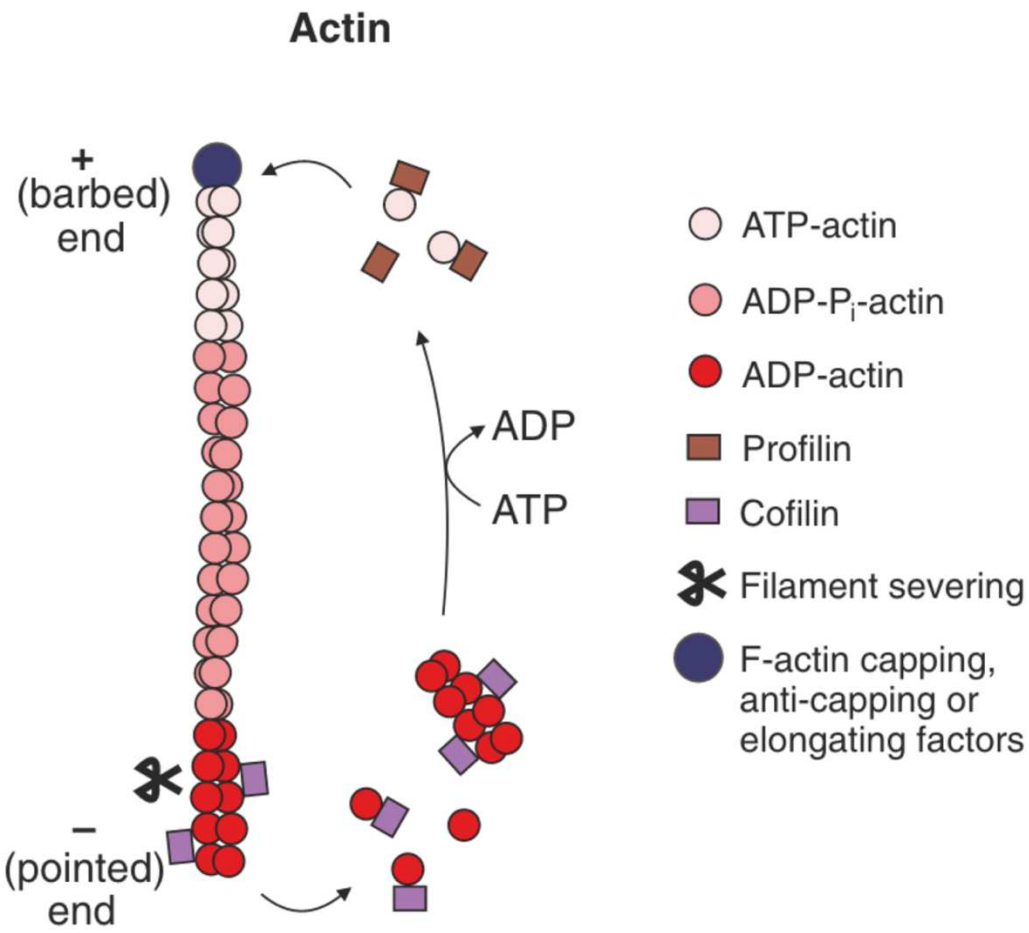

Figure I11: (Adapted from Coles *et al.*, 2015) Schematic representation of actin polymerization dynamics, and actin-associated proteins. The polymerization of actin at the barbed end requires ATP-actin, that is associated to profilin. Cofilin promotes the disassociation of actin at the pointed end. Capping proteins at the barbed end of the actin filament promote polymerization and control actin dynamics.

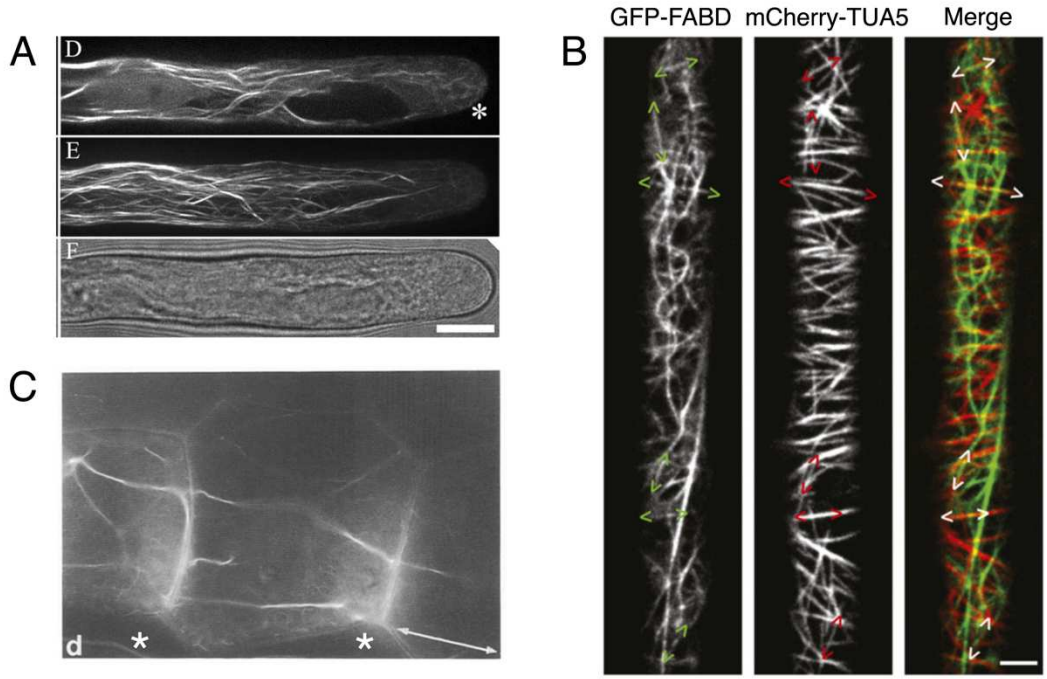

Figure I12: Actin localization in plant cells. (A) (Adapted from van der Honing *et al.*, 2011) Actin localization in root hairs, visualized using the Lifeact-mVenus fluorescent marker. The top image shows the midplane of a confocal stack. The middle image is a maximal Z-projection of the confocal Z stack, and the bottom image is a transmission image of the sample. The scale bar is 10 μm. (B) (Adapted from Sampathkumar *et al.*, 2011) Actin and microtubules co-localize in *Arabidopsis* hypocotyl cells. Actin was visualized using the GFP-FABD fluorescent marker, and microtubules using the mCherry-TUA5 fluorescent marker. The arrows show where both cytoskeletons co-localize. The scale bar is 5 μm. (C) (Adapted from Goodbody and Lloyd, 1990) Actin is responsive to wounding in *Tradescantia* leaf epidermal cells. Two days after wounding, actin filament strands align parallel to the wound (white arrow). The white asterisks show the localization of the ablation.

2. Microtubules

As plant cells lack intermediate filaments, microtubules (MTs) are the other essential component of their cytoskeleton. Microtubules are tubulin polymers, organized in 25 nm thick hollow tubes, giving the name "microtubules" (Slautterback, 1963; Ledbetter and Porter, 1963). These structures were first observed in plants, as they populate the plant cell cortex quite massively (Ledbetter and Porter, 1963). The building units of microtubules are heterodimers of α- and β-tubulin. These building units are stacked longitudinally to form a protofilament (Figure I13A). These protofilaments then associate together to form a microtubule (Hashimoto, 2015). A microtubule is typically formed by an arrangement of 13 protofilaments (Ledbetter and Porter, 1964), although this number can very, even within a given microtubule (Schaedel *et al.*, 2019). Microtubules are oriented in a plus-end (exposing β-tubulin) and a minus-end (exposing α-tubulin) polarity. The polymerization of microtubules is facilitated by GTP hydrolysis when the α subunit of the αβ-tubulin heterodimer binds to the β-tubulin- (plus-) end of the microtubule (Hashimoto, 2015). β-tubulin heads expose a GTP molecule, that is hydrolyzed into GDP after the addition of tubulin

to the microtubule (Figure I13A). For that reason, plus-ends grows approximately three times faster than minus-ends (Bergen *et al.*, 1980), even though the latter show constant slow depolymerization *in vivo* (Shaw *et al.*, 2003) if not anchored to a nucleation site. The plus-end of microtubules grows at a rate of hundreds of nanometers per second (Schneider and Persson, 2015; Erhardt and Shaw, 2006), that seems quite variable and dependent on tubulin concentration (Gildersleeve *et al.*, 1992; Desai and Mitchison, 1997; Gardner *et al.*, 2011). Similarly to actin, the polymerization at one end and the depolymerization at the other, giving the impression that the microtubule is "moving" across the cell, is called treadmilling (Mitchison and Kirschner, 1984).

Although MT dynamics was thought to be limited to its ends for the longest time, *in vitro* experiments showed that free tubulin could be incorporated in the lattice (Schaedel *et al.*, 2019; Figure I13B). Indeed, numerous lattice defects can be present in MTs, such as protofilament transitions (where the number of protofilaments vary within a single MT) or point defects (Romeiro Motta *et al.*, 2023). Schaedel *et al.* (2019) study shows that tubulin dimers assemble and disassemble along the lattice as well as the extremities, presenting the entire MT as a dynamic material. Additionally, they hypothesized that the incorporation of tubulin in lattice tears could be driven by the elastic stress associated with the tubulin dislocation, placing MTs as a mechanically responsive material (Schaedel *et al.*, 2019).

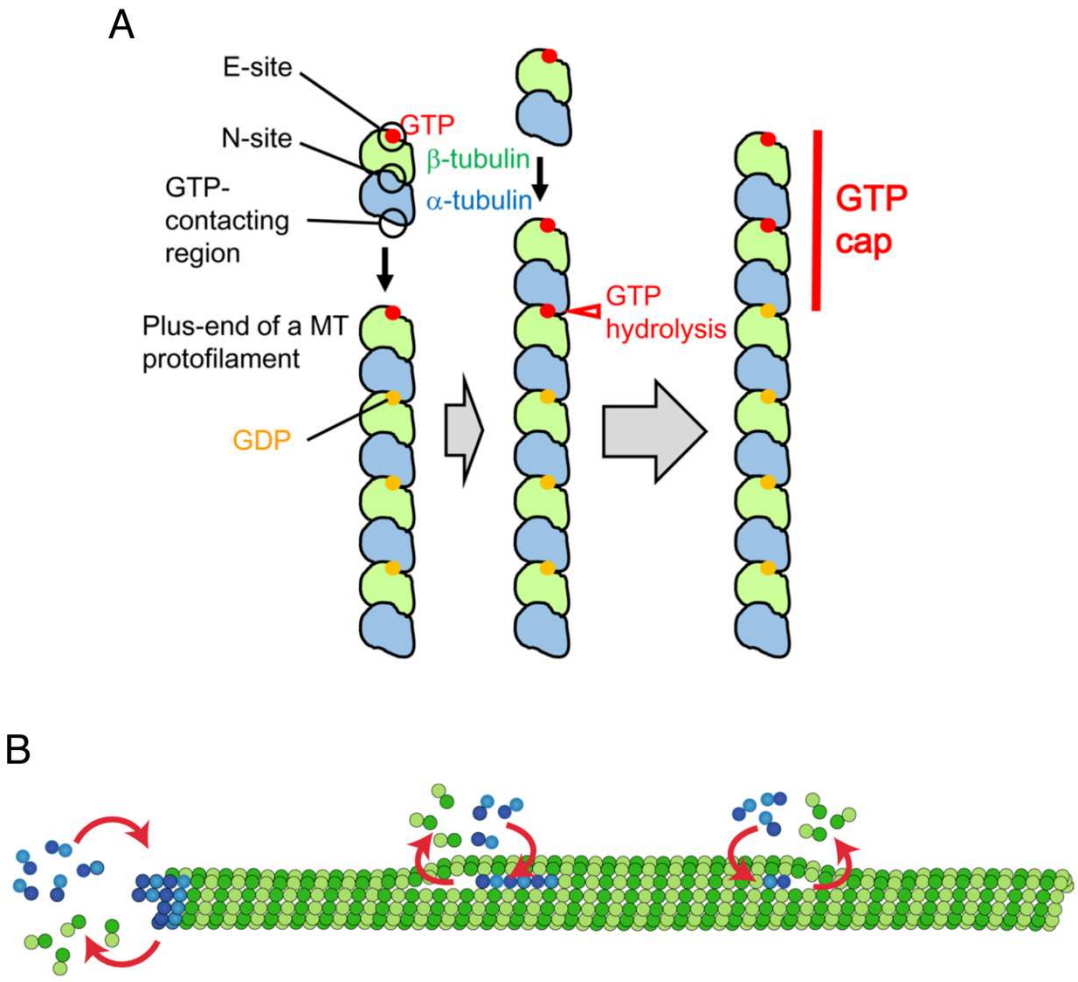

Figure I13: Schematic representation of microtubule polymerization. (A) (Adapted from Hashimoto, 2015) α- and β-tubulin dimers are added at the plus end of the microtubule, facilitated by GTP hydrolysis. This forms the GTP car at the plus end of microtubules. (B) (Adapted from Schaedel *et al.*, 2019) α- and β- tubulin dimers are incorporated at the plus end of the microtubule (as detailed in (A)), but also along its lattice where it presents defects. The green dots represent GDP-tubulin and the blue dots GTP-tubulin.

The *de novo* synthesis of microtubules is called microtubule nucleation. MT nucleation is mediated by another tubulin isoform, the γ-tubulin, and γ-tubulin complex proteins (GCPs), forming the γ-tubulin ring complex (γTuRC) (Kollman *et al.*, 2011; Hashimoto, 2015). γTuRC is a highly conserved mode of nucleation among higher eukaryotes (Zheng *et al.*, 1995). Nucleation is concentrated in regions called the microtubule organizing centers (MTOCs), typically anchoring the minus-ends of microtubules (Sulimenko *et al.*, 2017). In animals, the primary MTOC is the centrosome, an organelle that nucleates and organizes microtubules, but other nucleation sites are found in the cell such as the Golgi apparatus (Ori-McKenney *et al.*, 2012), the nuclear envelope (Bugnard *et al.*, 2005), and pre-existing microtubules (Sánchez-Huertas *et al.*, 2016). Plant cells lack centrosomes and present diffuse MTOC homolog proteins (Yi and Goshima, 2018). Yet, their microtubule arrays appear as highly organized (Yi and Goshima, 2018). In interphasic plant cells, microtubule nucleation is mainly initiated on existing microtubules at the cell cortex, in a process called MT-dependent MT nucleation (Murata *et al.*, 2005; Figure I14A). γTuRCs are recruited on the lattice of a microtubule, and the nascent microtubule is polymerizing at a precise angle of around 40° from the lattice MT (Murata *et al.*, 2005). The release of the new microtubule is then mediated by severing of the minus-end, or the depolymerization of the lattice MT (Nakamura *et al.*, 2010). At specific stages, such as before mitotic entry, γTuRC can be targeted at the nuclear surface, that acts as a nucleation point (Stoppin *et al.*, 1994; Canaday *et al.*, 2000; Erhardt *et al.*, 2002). More specifically, γ-tubulin accumulates during the G2 stage of the cell cycle of *Vicia faba* cells, and associates with pre-kinetochores before mitotic entry (Binarová *et al.*, 2000). The affinity of γ-tubulin for chromatin during G2 could give rise to spindle microtubules (during mitosis), forming ordered arrays later on (Kumagai and Hasezawa, 2001), even though spindle formation has also been proposed to arise from lateral interactions between microtubules (Smirnova and Bajer, 1992). Furthermore, targeted decrease of γ-tubulin levels in *Arabidopsis* roots does not prevent cellular progression through mitosis, but severely affects cytokinesis (latest phase of mitosis) (Binarová *et al.*, 2006).

Microtubules are highly dynamics structures, that constantly polymerize and depolymerize, and can interact together. Unlike animal cells' microtubules, that radiate from a centrosome with their plus-ends directed towards the plasma membrane, plant cells' microtubules are mainly located at the cell cortex. Cortical microtubules (CMTs) are confined to a roughly two-dimensional space, channeling and promoting their interactions (Ehrhardt and Shaw, 2006). This largely explains the highly organized arrays observed at the cortex of plant cells, through the emergent properties arising from their interactions in a constrained environment (Wasteneys and Ambrose, 2009). The outcome of these interactions highly depends on the angle at which a growing microtubule encounters another microtubule (Dixit and Cyr, 2004). More specifically, shallow-angle encounters (at less than 40°) promote the co-alignment of the growing microtubule on the pre-existing one, and consequent bundling, in a process called zippering (Dixit and Cyr, 2004; Figure I14B). On the other hand, steep-angle encounters tend to promote depolymerization of the colliding microtubule, in a process called catastrophe (Dixit and Cyr, 2004; Figure I14B). However, catastrophes are not systematic,

and the growing microtubule can be unaffected by the encounter, and continue its trajectory (Dixit and Cyr, 2004). The crossover point can then be severed, or not (Figure I14B). The alignment of microtubules in plant cells could result from these unique properties, as revealed by computational models. Indeed, simulations or probability-based studies reveal that the self-organization of MTs induce stable arrays, as observed in plants (Allard *et al.*, 2010; Tindemans *et al.*, 2010; Eren *et al.*, 2010; Hawkins *et al.*, 2010). Nevertheless, these studies differ in regarding zippering or catastrophes as the main driver of this self-organization (Deinum and Mulder, 2013).

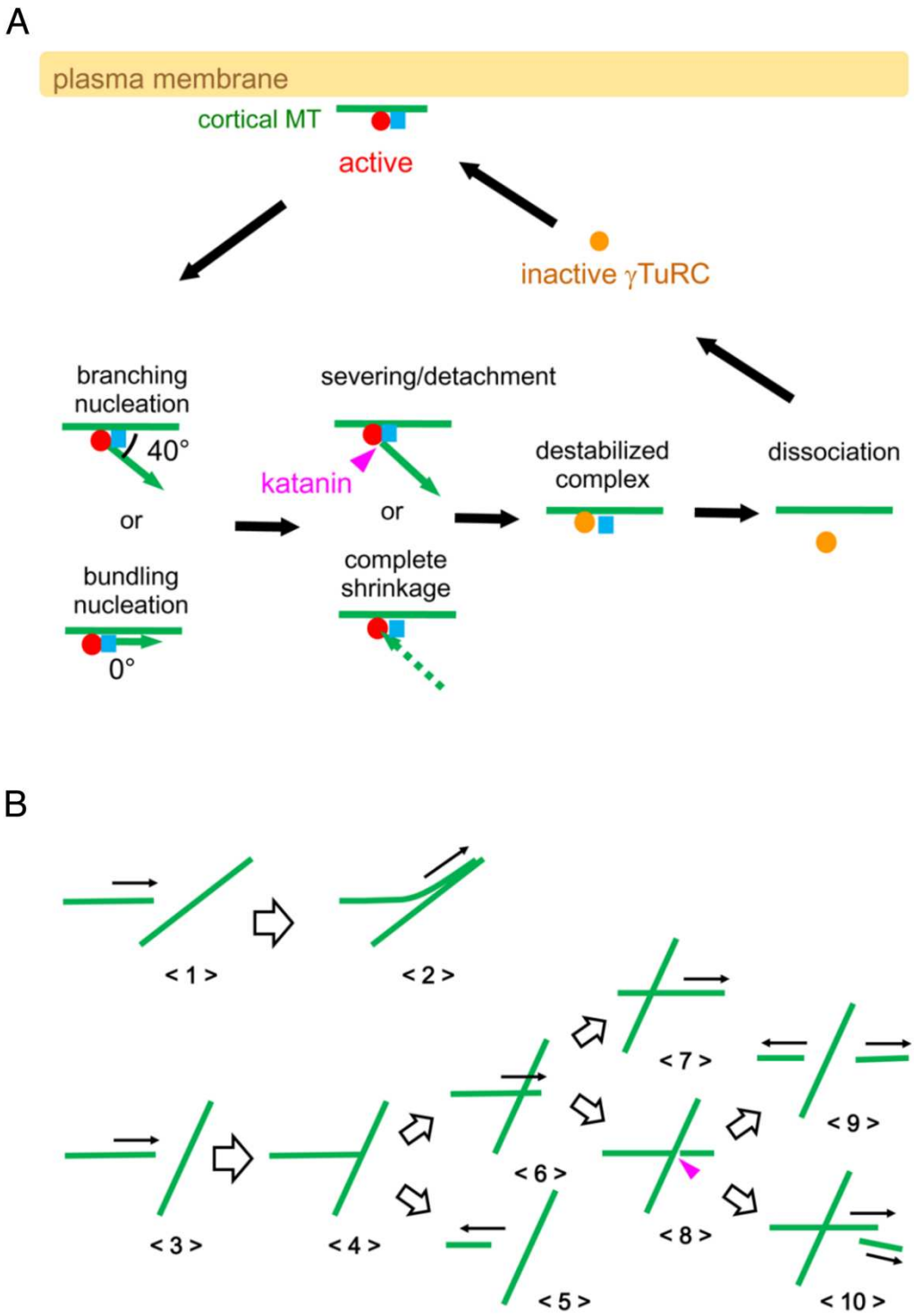

Figure I14: (Adapted from Hashimoto, 2015) Microtubule dynamics at the cortex of plant cells can mainly be explained by branched nucleation and microtubule interactions. (A) Schematic representation of MT-dependent MT nucleation. γTuRC (circle) is recruited along the lattice of an existing MT, and associates with activating factors (blue square). The new MT is initiated parallel to the existing one, or at 40° from it. Katanin then severs the new MT (at its minus end), destabilizing the γTuRC. (B) Schematic representation of different outcomes of MT-MT encounters. At shallow angles (1), the colliding MT changes direction to follow the pre-existing MT's, forming a bundle (2). At bigger angles (3), the colliding MT forms a crossover with the pre-existing one (4). It could continue its trajectory, unaffected (4,7) or can be severed (8) and depolymerize (9) or both generated plus-ends can grow (10). The colliding MT may also depolymerize upon wide-angled collision with the pre-existing one (5).

Microtubule catastrophes (the MT depolymerization from the plus end) can also happen spontaneously, from a loss of the GTP cap at the plus end (Mitchison and Kirschner, 1984; Howard and Hyman, 2009). Microtubules undergoing catastrophe seems a random process, but is dependent of MTs length and age (Gardner *et al.*, 2013). Interestingly, MTs undergoing catastrophe events can switch back to a polymerization state, in a process called microtubule rescue (Gardner *et al.*, 2013). *in vitro*, the occurrence of these events seems tubulin concentration-dependent (Walker *et al.*, 1988). Tension could be involved in MT rescue, as dynein-bound MTs (dynein is a motor protein, generating pulling forces) have stabilized plus ends *in vitro* (Laan *et al.*, 2012). Also, chromosome segregation generates stretching likely involved in kinetochore-attached MT rescue in yeast and animal cells (Akiyoshi *et al.*, 2010; Wan *et al.*, 2012). It is worth noting that microtubule growth can generate pushing forces, and that their shrinkage can generate pulling forces (Dogterom *et al.*, 2005; Grishchuk *et al.*, 2005). Nevertheless, MTs are also sensitive to mechanical forces. Microtubule bending, for example, induces tears in the lattice, and softens the MT as a consequence (Schaedel *et al.*, 2015). As mentioned above, MTs have the ability to self-repair these tears, from free tubulin being incorporated in the lattice at the damaged sites (Schaedel *et al.*, 2015). This repair process has also been seen to promote rescue (Aumeier *et al.*, 2016).

Microtubules properties are influenced by a wide range of microtubule-associated proteins (MAPs), specifically regulating various developmental processes (Buschmann and Lloyd, 2008).

- **MAP65**

MAP65 is a wide family of MAPs, which presents different functions. Some label interphasic structures, such as MAP65-1 and -2 labelling bundles of interphasic microtubules (Lucas *et al.*, 2011). Others label mitotic structures, such as MAP65-4 labelling forming spindles and kinetochore fibers (Fache *et al.*, 2010), and MAP65-3 being located in the middle of the central spindle, and at the phragmoplast midzone (Ho *et al.*, 2011).

- **End-binding 1 (EB1) and cytoplasmic linker-associated proteins (CLASPs)**

EB1 and CLASP are restricted to specific areas of the microtubule. EB1 proteins are a class of MAPs exclusively located at the plus-end of microtubules, binding to their GTP-hydrolysis area (Maurer *et al.*, 2012; Figure I15B). EB1 senses structural changes within the microtubule and can recruit other associated proteins accordingly (Maurer *et al.*, 2011). Among them, CLASPs, which are also located at the plus-end of microtubules (Ambrose *et al.*, 2007; Figure I15A). Furthermore, CLASPs are also found at the geometric edges of plant cells, and are thought to help microtubule stabilization and bending at sharp edges, and promote MT rescue (Ambrose *et* al., 2011; Al-Bassam and Chang, 2011; Figure I15C). They are believed to have a role in cell elongation, cell shape sensing and cell number regulation. *Arabidopsis clasp-1* mutants are dwarf, and present cell shape and elongation defects (Ambrose *et al.*, 2007). Recently, it was proposed that CLASP regulates

CMT response to larger mechanical stresses, by dampening their response at subcellular scales (Eng *et al.*, 2021).

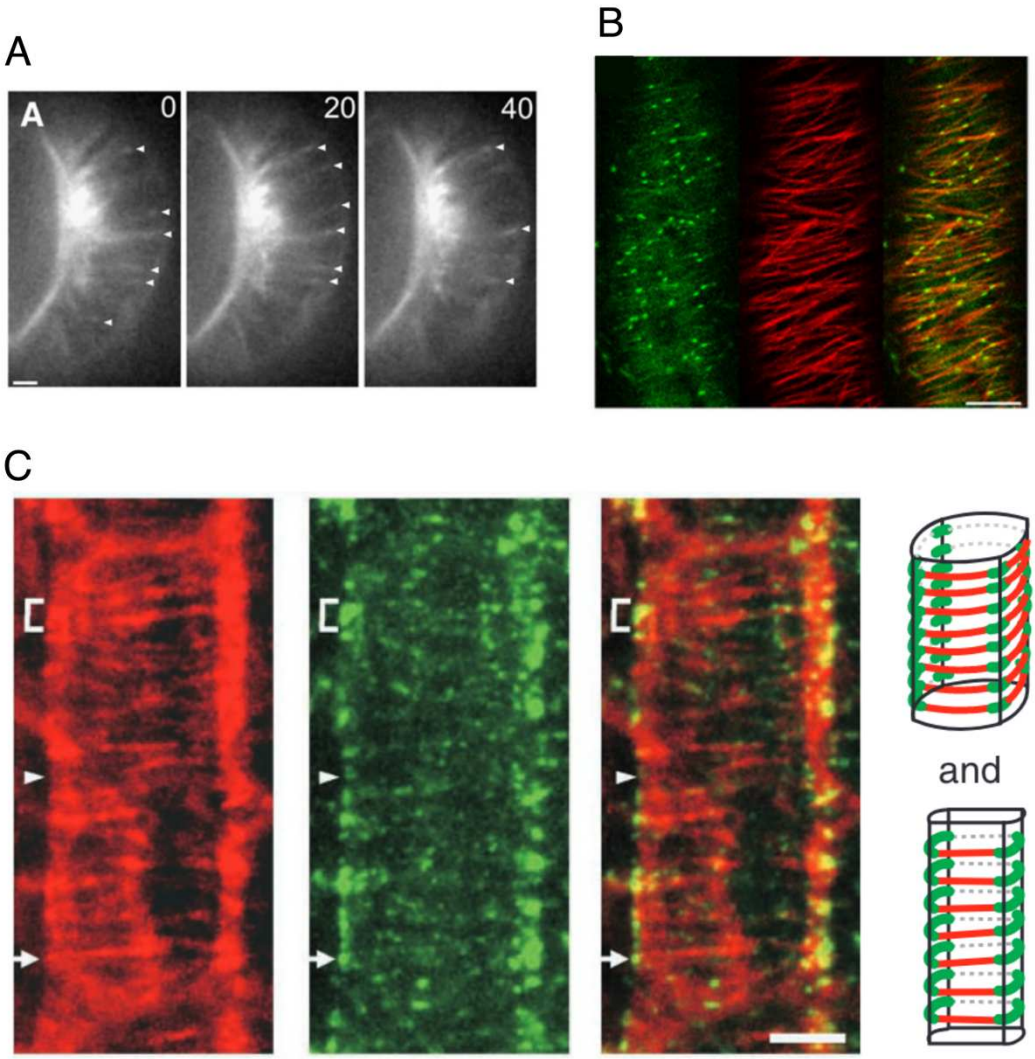

Figure I15: MAPs labelling the growing ends of MTs. (A) (Adapted from Ambrose *et al.*, 2007) Images showing GFP-CLASP signal in leaf guard cells. Images were taken every 20 seconds. There is an accumulation of CLASP at the plus-end of growing MTs. The scale bar is 5 µm. (B) (Adapted from Dhonukshe *et al.*, 2005) Images showing GFP-EB1 (green, left image), YFP-MAP4 (ref, middle image) signals, and both merged together (right image) in tobacco BY2 cells. EB1 localizes at the growing ends of MTs. The scale bar is 5 µm. (C) (Adapted from Ambrose *et al.*, 2011) Images showing RFP-TUB6 (red, left image), GFP-CLASP (green, middle image) signals, and both merged together (right image), in an elongating root cell. CLASP co-localizes with MTs, and enriched at the cell's geometric edges (schematic representations on the left). The scale bar is 5 µm.

- **SPIRAL (SPRs)**

SPR1 and SPR2, seem to control global CMT organization and orientation. *spr2* mutants display growth axis defects, with a right-hand helical organ growth. Overall, they show reduced growth anisotropy, due to a tilt in CMT organization (Furutani *et al.*, 2000; Buschmann *et al.*, 2004; Shoji *et*

al., 2004; Figure I16B). SPR2 accumulates at crossover sites, and at the minus-ends of newly formed microtubules at the cortex, and is thought to have a role in CMT branched nucleation and protection of the minus end against depolymerization (Fan *et al.*, 2018; Nakamura *et al.*, 2018; Figure I16A). On top of localizing to CMTs, SPR2 also is found at the minus end of spindle and phragmoplast (mitotic structures) MTs in *Physcomitrium patens* (Leong *et al.*, 2018). This protein also has a role in regulating MT severing. It has first been suggested to protect MTs from severing at crossover sites (Wightman *et al.*, 2013). On the contrary, it has later been proposed to promote their severing at crossovers (Nakamura *et al.*, 2018), a proposition that is supported by the recent discovery of a katanin-like domain (involved in severing) at the C terminus of SPIRAL2 (Bolhuis *et al.*, 2023). *spr2* mutants fail to properly reorganize their CMT arrays upon hypocotyl illumination (Figure I16C). SPR2 is involved in MT organization in response to mechanical stress, as *spr2* mutants exhibit enhanced response to tensile stress in sepals (Hervieux *et al.*, 2016) and in seeds (Bauer *et al.*, 2024), consistent with its reported increase in MT reorganization dynamics (Wightman *et al.*, 2013).

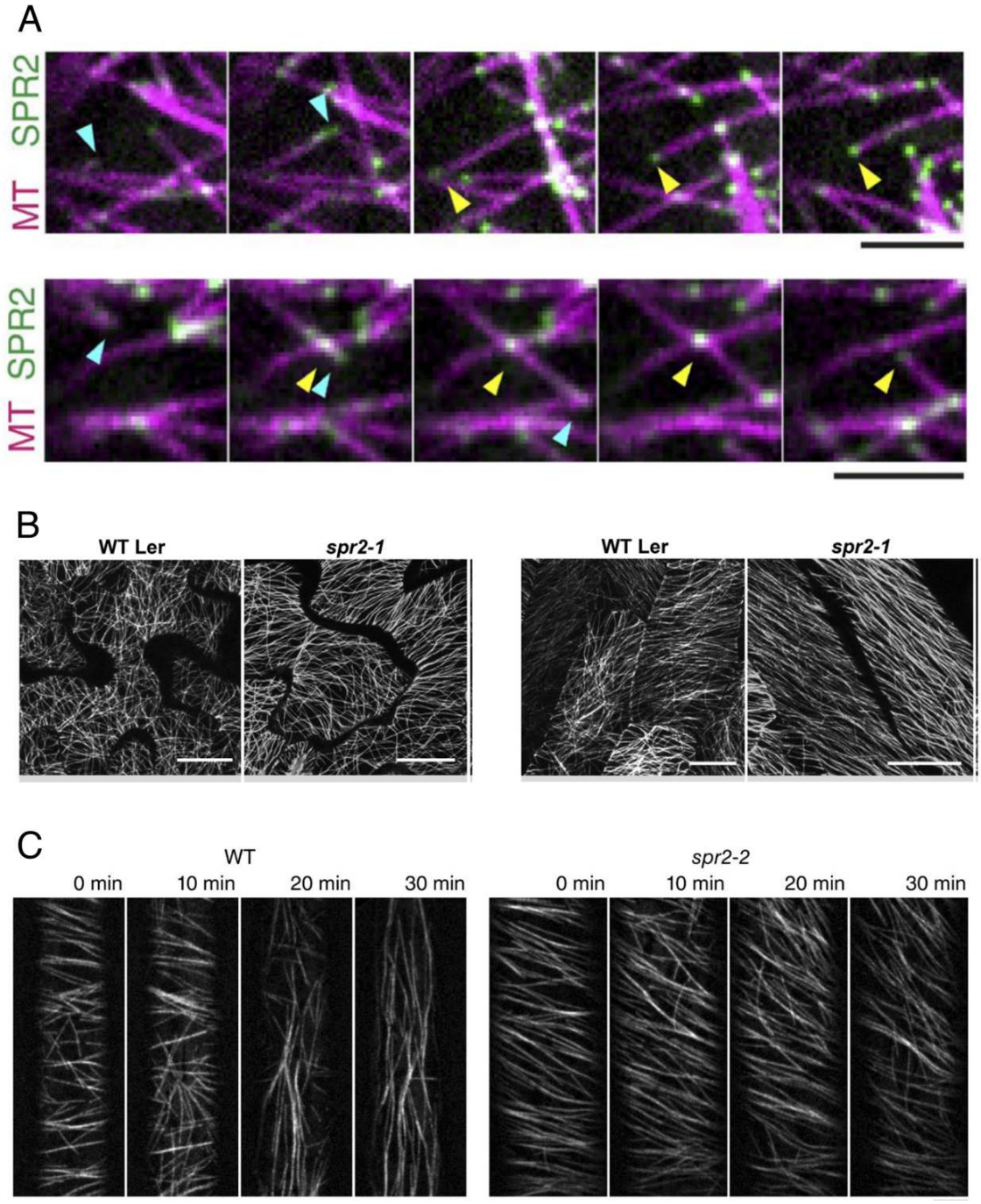

Figure I16: SPR2 as a regulator of microtubule dynamics and organization. (A) (Adapted from Nakamura *et al.*, 2018) Image showing localizations of SPR2-GFP (green) along microtubules (mCherry-TUA5, magenta). The top images show a MT nucleation event (plus end represented by the blue arrowhead and the minus end by the yellow arrowhead). SPR2 signal accumulates at the minus end of the new microtubule, after severing. The bottom images show the accumulation of SPR2 at the crossover site between two microtubules, and to a lesser extent, at the minus end of the severed microtubule. The scale bars are 3 μm. (B) (Adapted from Wightman *et al.*, 2013) Microtubule organizations in WT and *spr2-1* mutants in pavement cells (left images) and petioles (right images). In both organs, the MT arrays appear as more anisotropic in the *spr2-1* mutant compared to the WT. The scale bars are 20 μm. (C) (Adapted from Nakamura *et al.*, 2018). Time lapse images showing MT dynamics in WT and *spr2-1* etiolated hypocotyl cells, after illumination, using the mCherry-TUA5 fluorescent marker. WT cells udergo a reorientation of their MT arrays within 30 minutes. The *spr2-1* mutant, however, does fails to reorient its MT array within 30 minutes. The scale bar is 5 μm.

- **KATANIN (KTNs)**

KTNs are involved in MT dynamics through ATP-dependent severing (McNally and Vale, 1993; Burk and Ye, 2002; Stoppin-Mellet *et al.*, 2002). The overexpression of KTN results in shorter microtubules in *Arabidopsis* pavement cells (Stoppin-Mellet *et al.*, 2006). *ktn-1* mutants display slower MT dynamics and weaker ability to respond, notably, to tensile stress (Uyttewaal *et al.*, 2012; Zhang *et al.*, 2013; Figure I17C). Katanin is thought to cut at microtubule lattice defects, further showing how microtubule lattice dynamics contribute to the organization of MT arrays (Davis *et al.*, 2002). Furthermore, KTN is involved in the alignment, and reorganization of CMT arrays upon stimulation, notably by specifically severing at crossover sites (Wightman and Turner, 2007; Lindeboom *et al.*, 2013; Deinum *et al.*, 2017; Figures I17A and I17B). It is also required to generate new microtubules, and acts as an amplifier as the newly formed microtubules grow in alignment with the new organization of the array (Nakamura *et al.*, 2010; Lindeboom *et al.*, 2013). On top of regulating interphasic microtubule arrays, katanin also regulates mitotic ones. It has been reported that *ktn-1* mutants have trouble anchoring and narrowing their pre-prophase bands (PPBs, pre-mitotic structures) in petioles (Komis *et al.*, 2017), although not in roots of *Arabidopsis* (Panteris *et al.*, 2011). They also show slower progression through mitosis, due to their slower microtubule dynamics (Komis *et al.*, 2017). *ktn-1* mutants also fail to organize the mitotic spindles in a bipolar fashion, resulting in misoriented division planes (Panteris *et al.*, 2011).

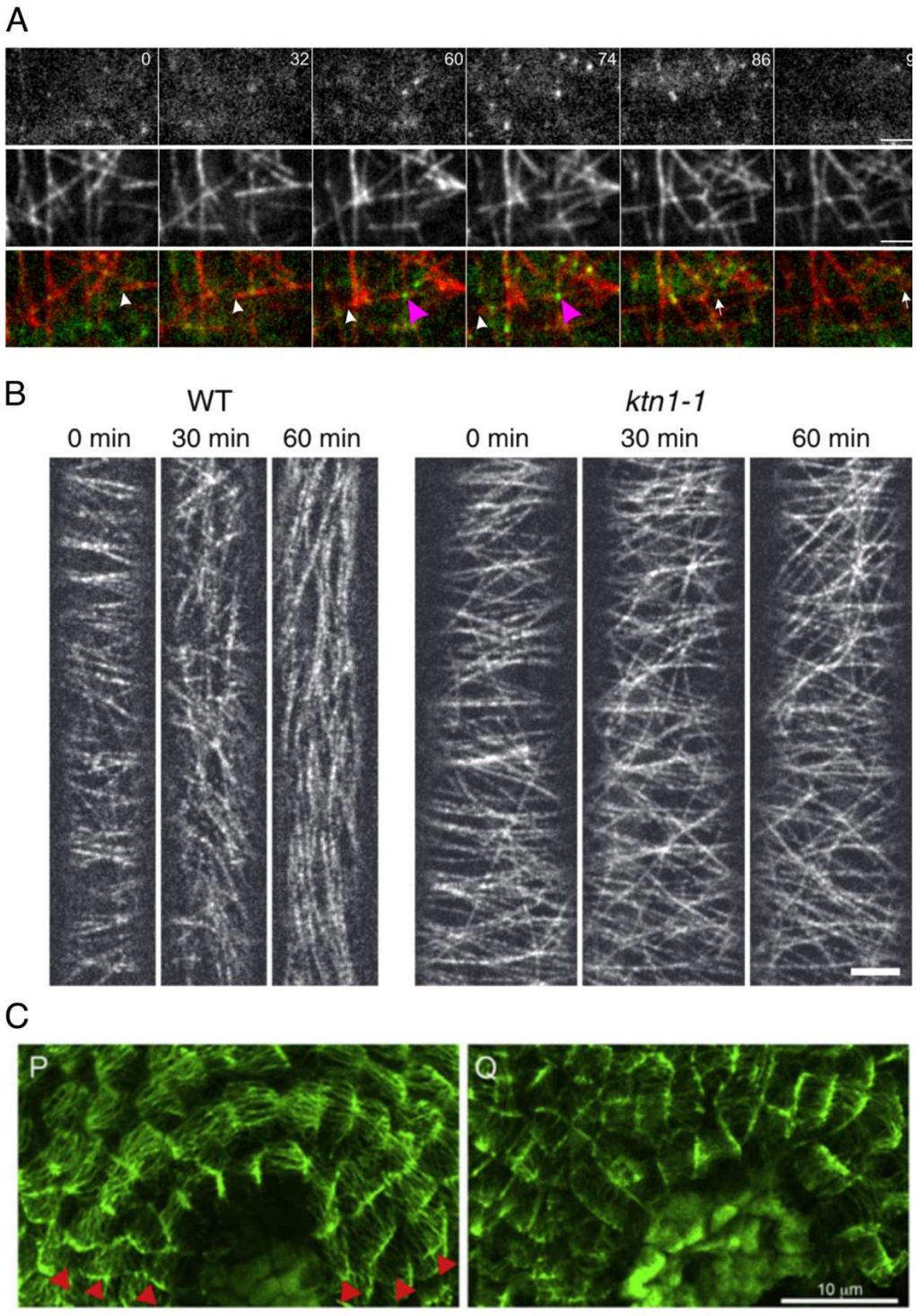

Figure I17: KTN as a severing protein, involved in MT dynamics. (A) (Adapted from Zhang *et al.*, 2013) Images showing KTN-GFP (green, top image) and RFP-TUB6 (red, middle image) signals, and both merged together (bottom image). KTN severs at crossover sites (magenta arrow head) when a growing microtubule (plus end represented by the white arrowhead) encounters another one. The white arrow tracks the depolymerizing MT after severing. The scale bars are 3 µm. (B) (Adapted from Lindeboom *et al.*, 2013). Time lapse images showing MT dynamics in WT and *ktn1-1* etiolated hypocotyl cells after illumination. WT cells udergo a reorientation of their MT arrays within 60 minutes. The *ktn1-1* mutant, however, does fails to completely reorient its MT array within 60 minutes. The scale bar is 5 µm. (C) (Adapted from Uyttewaal *et al.*, 2012) Signal of the GFP-MBD fluorescent microtubule marker in WT (right) and *ktn1* (left) SAMs after ablation. After wounding, WT microtubules reorient circumferentially around the wound. *ktn1* mutants do not present a strong circumferential bias after wounding. The scale bar is 10 µm.

- **Kinesins**

Kinesins are MT-associated motor proteins. They are typically moving towards the plus-ends of microtubules (Ali and Yang, 2020). Contrary to animals, plants genomes do not host dyneins, that travel towards the minus-ends of MTs in animal cells. Instead, a subclass of plant kinesins move towards the minus ends of MTs (Ali and Yang, 2020; Li *et al.*, 2021). Plant kinesins are mainly involved in cell division, controlling the expansion of the phragmoplast or spindle assembly (Oh *et al.*, 2012; Ambrose *et al.*, 2005; Ambrose and Cyr, 2007; Ali and Yang, 2020). They are also thought to be involved in organelle positioning, by fine-tuning the long-distance transport mediated by the actin-myosin complex (Cai and Cresti, 2012).

- **NIMA-related protein kinase 6 (NEK6)**

Never-in-mitosis A (NIMA) is a kinase that is involved in mitotic entry, and is the founder of the NEK family (Fry *et al.*, 2012). These proteins are highly conserved amongst eukaryotes, and are involved in mitosis-related functions, notably in spindle assembly (Quarmby and Mahjoub, 2005; Fry *et al.*, 2012). NIMA-protein kinase 6 (NEK6) is a kinase that phosphorylates β-tubulin and promotes the destabilization of microtubules (Takatani *et al.*, 2017). In plants, NEK6 localizes to discrete points along MTs, notably at branching points where it colocalizes with a γ-TuRC component, suggesting a possible relationship between NEK6 and MT nucleation (Motose *et al.*, 2008). In hypocotyls, NEK6 localizes to the shrinking plus and minus ends of MTs (Takatani *et al.*, 2017; Figure I18A). It has also been shown that *nek-6* mutants are affected in microtubule organization in the hypocotyl, where cells present unusual CMT organizations (basket or net-like) with curved microtubules, contrasting with the aligned parallel arrays observed in the WT (Takatani *et al.*, 2017). *nek-6* mutants also seem to be affected in CMT dynamics, and show an increased response to mechanical perturbations by hyper-aligning their CMT arrays (Takatani *et al.*, 2020; Figure I18B). *nek-6* mutants display epidermal cell morphological defects, likely mediated by microtubules, and higher growth deviations after touch or gravitropic stimulations (Sakai *et al.*, 2008; Takatani *et al.*, 2017; Takatani *et al.*, 2020). It was proposed that NEK6 may preferentially target MTs that are aligned with maximal tensile stress direction (Takatani *et al.*, 2020).

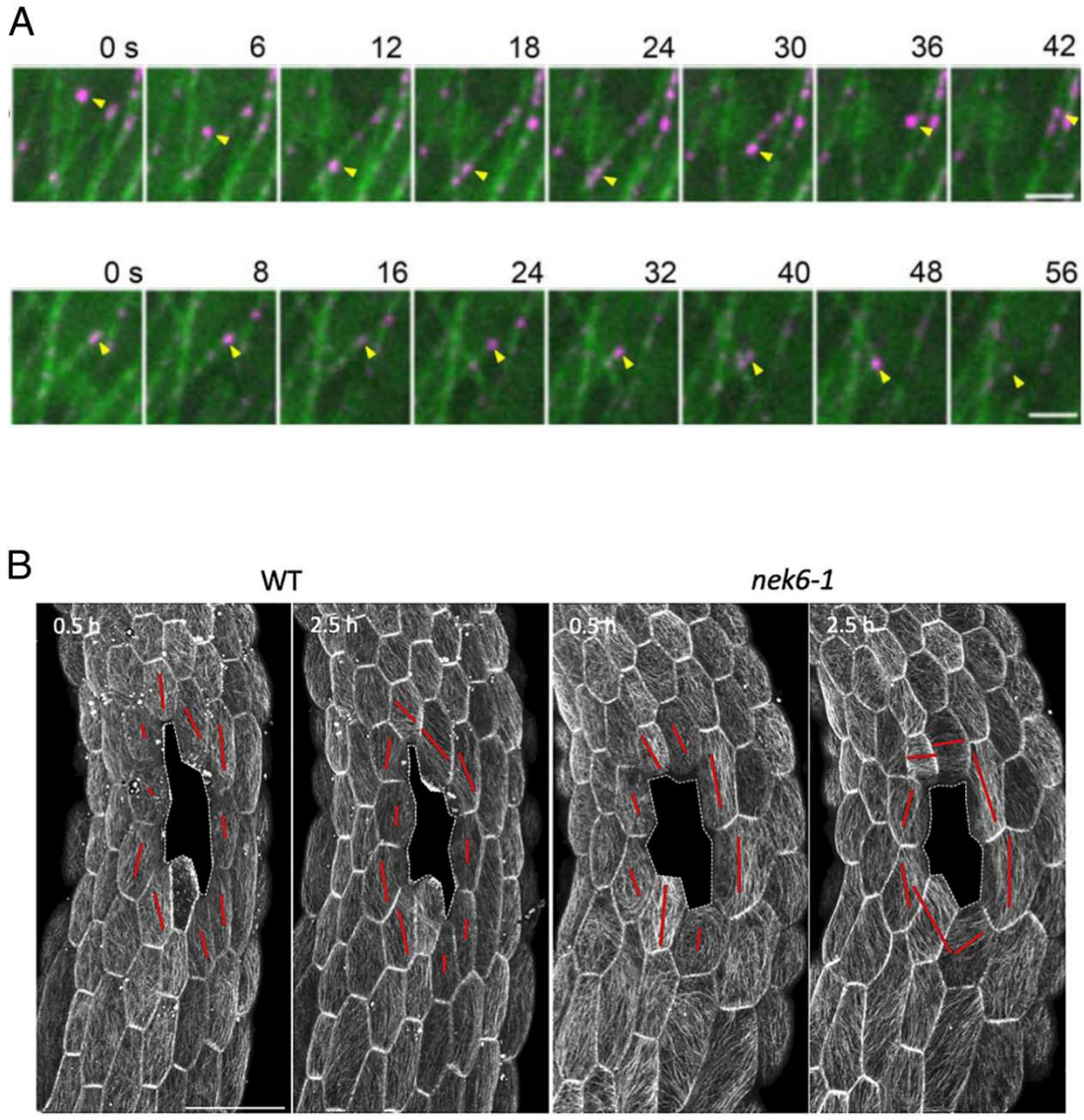

Figure I18: NEK6 localizes to MT shrinking ends, and is involved in mechanical response. (A) (Adapted from Takatani *et al.*, 2017) Images showing NEK6-GFP (magenta) and mCherry-TUB6 (green) signals. Arrowheads indicate the shrinking plus (top images) and minus (bottom images) ends of MTs, co-localizing with NEK6. The scale bars are 2 μm. (B) (Adapted from Takatani *et al.*, 2020) Microtubule organization in WT and *nek6-1* mutants' hypocotyls after cellular ablations. The red lines show the average orientations and anisotropy of the cells' MT arrays. The longer the line, the more anisotropic the arrays. *nek6-1* hypocotyls show a better circumferential alignment of their MTs around the wound than the WT, 2.5 hours after the ablation. The scale bar is 50 μm.

- **MT localization during interphase**

In interphasic plant cells, microtubules are present at the cortex, right under the plasma membrane in highly organized arrays (Paradez *et al.*, 2006), where they partially co-localize with cortical actin filaments (Sampathkumar *et al.*, 2011; Figure I12B). They are also present inside the cell, either diffusely or concentrated in cytoplasmic streams in bigger and highly vacuolated cells (Shimmen and Yokota, 2004). The latter class of microtubules are referred to as cytoplasmic/endoplasmic MTs or internal MTs (versus CMTs discussed above), even though all MTs are present in the

cytoplasm, technically. Interphasic internal MT function is ill-described, beyond their minor role in organelle positioning in cytoplasmic streams (Yamada *et al.*, 2017; Shimmen and Yokota, 2004). As mentioned above, CMTs, on the other hand, are known to guide the cellulose synthase complexes (Paredez *et al.*, 2006). In guiding these complexes, they therefore orient the cellulose microfibrils that will be synthetized, that in turn constrain cell growth (Braybrook and Jönson, 2016). Their direct involvement in the cell wall organization places CMTs in a central role when coordinating growth.

As stated previously, CMTs present highly organized arrays at epidermal cell cortex. What orients this array and how it acquires this parallel configuration is not a completely resolved question in plant biology (Paradez *et al.*, 2006). The main hypothesis nowadays is that tensile forces orient CMT arrays, although it has been proposed that CMTs are responsive to cellular polarity cues rather than tensile forces (Hush *et al.*, 1990). In the absence of a pulling force, CMTs tend to align following the flattest part of confined unpressurized protoplasts (without cortical tension), which is also their longest axis (Colin *et al.*, 2020; Durand-Smet *et al.*, 2020; Figure I19A). This could be easily explained by the high persistence length of microtubules that would channel such behavior (reduced bending is favored). Indeed, computer simulations showed that MTs consistently tend to align with the longest axis of a cell, and are highly sensitive to local curvature, but the anisotropy of the array can be overcome by external cues (Mirabet *et al.*, 2018). When the protoplast becomes pressurized by changing the medium osmolarity, CMTs tend to follow the shortest axis of the cell, coinciding with maximum curvature, but also with the maximal tensile stress orientation (Colin *et al.*, 2020; Figure I19B). In more physiological conditions, CMTs in pavement cells of *Arabidopsis* cotyledons also align with maximal tension (Sampathkumar *et al.*, 2014; Figure I19C). While CMT alignment with maximal tension is true at the cellular level, it is also true when considering tissue-derived tension. In SAMs, CMT arrays from cells at the boundary between the meristem and the organ primordium are highly anisotropic, following the predicted maximal tension (Hamant *et al.*, 2008; Figure I20B). In stem and hypocotyl epidermis, CMT arrays also follow the maximal tension patterns at the organ level (transverse for the stem, and longitudinal for the hypocotyl) (Verger *et al.*, 2018; Figure I20A). Furthermore, mechanical treatments reveal that CMTs are responsive to changes in mechanical stress patterns. Changing the osmolarity of the medium, or stretching or compressing hypocotyls change their global CMT array orientation bias (Hejnowicz *et al.*, 2000; Robinson and Kuhlmeier, 2018). CMTs also respond to local changes in stress patterns. Around developing trichomes, for example, they reorganize circumferentially around the trichome, following maximal tension (Hervieux *et al.*, 2017; Figure I20C). Local ablation of a cell, or a group of cells within the external tissue layer, changes the local tension pattern to be circumferential around the wound (Hamant *et al.*, 2008). Soon after the ablation treatments, CMTs reorganize circumferentially around the ablation site in wound-adjacent cells of SAMs (Figure I17C), cotyledons and hypocotyls (Hamant *et al.*, 2008; Sampathkumar *et al.*, 2014; Robinson and Kuhlmeier, 2018).

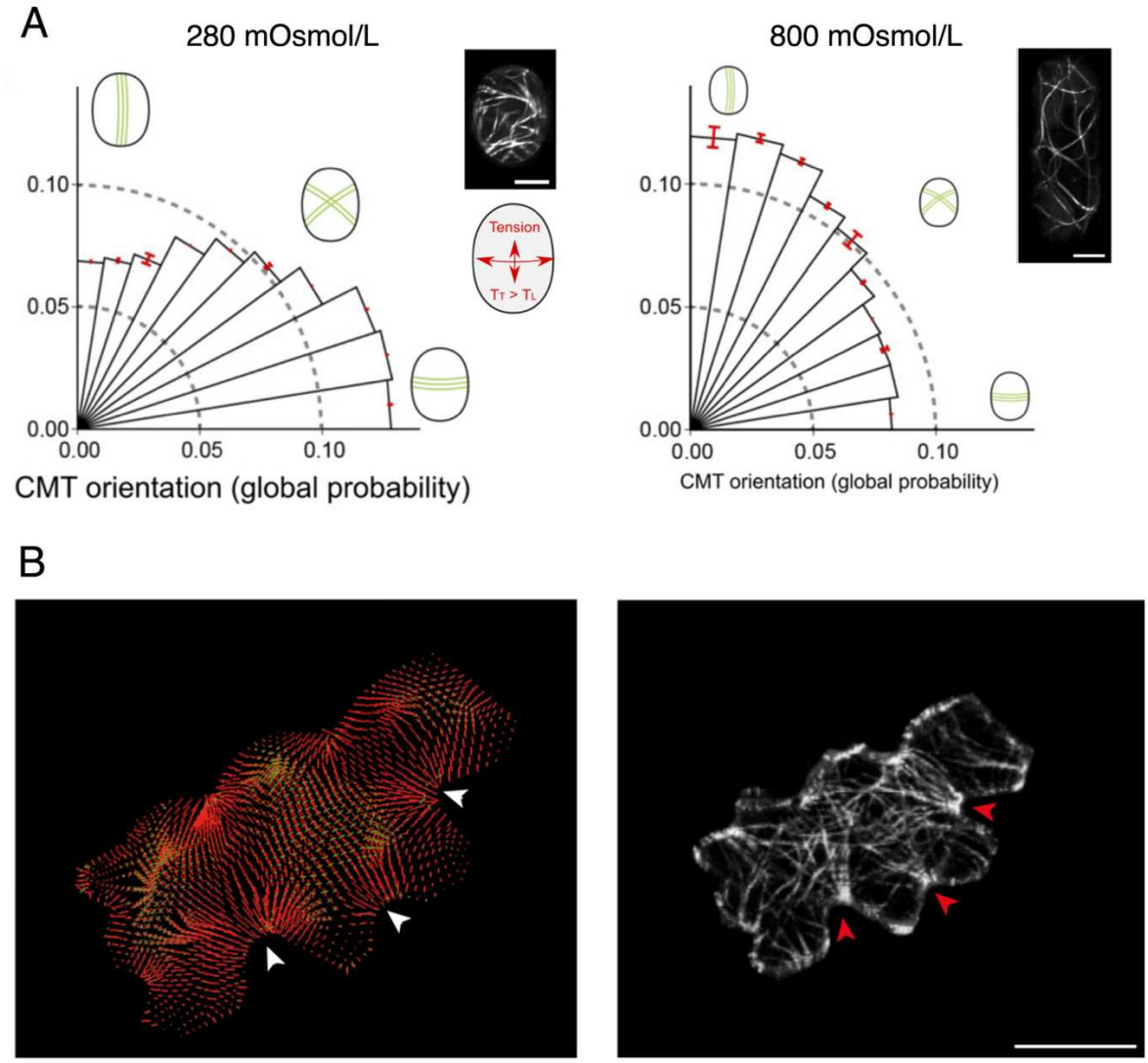

Figure I19: CMTs align with tension at the cellular scale. (A) (Adapted from Colin *et al.*, 2020) Histograms showing the probabilities of CMT orientations in confined oval protoplasts. The left histogram is the distribution for pressurized protoplasts, in a 280 mOsmol/L solution, and the left histogram for plasmolyzed protoplasts, in a 800 mOsmol/L solution. The images represent the GFP-MBD signal in protoplasts, showing their CMT organization. At low osmolarity, CMTs of the turgid protoplast align with maximal tension, transverse to the cell axis. At a higher osmolarity, the CMTs of the deflated protoplast tend to align along their longest axis. The scale bars are 5 μm. (B) (Adapted from Sampathkumar *et al.*, 2014). Mechanical modelling of pavement cells tension patterns shows highest force magnitude in the neck regions (white arrowheads). Microtubules (visualized by YFP-MBD) accumulate at the neck regions (red arrowheads) and show an overall organization similar to the model's tension vectors. The scale bar is 20 μm.

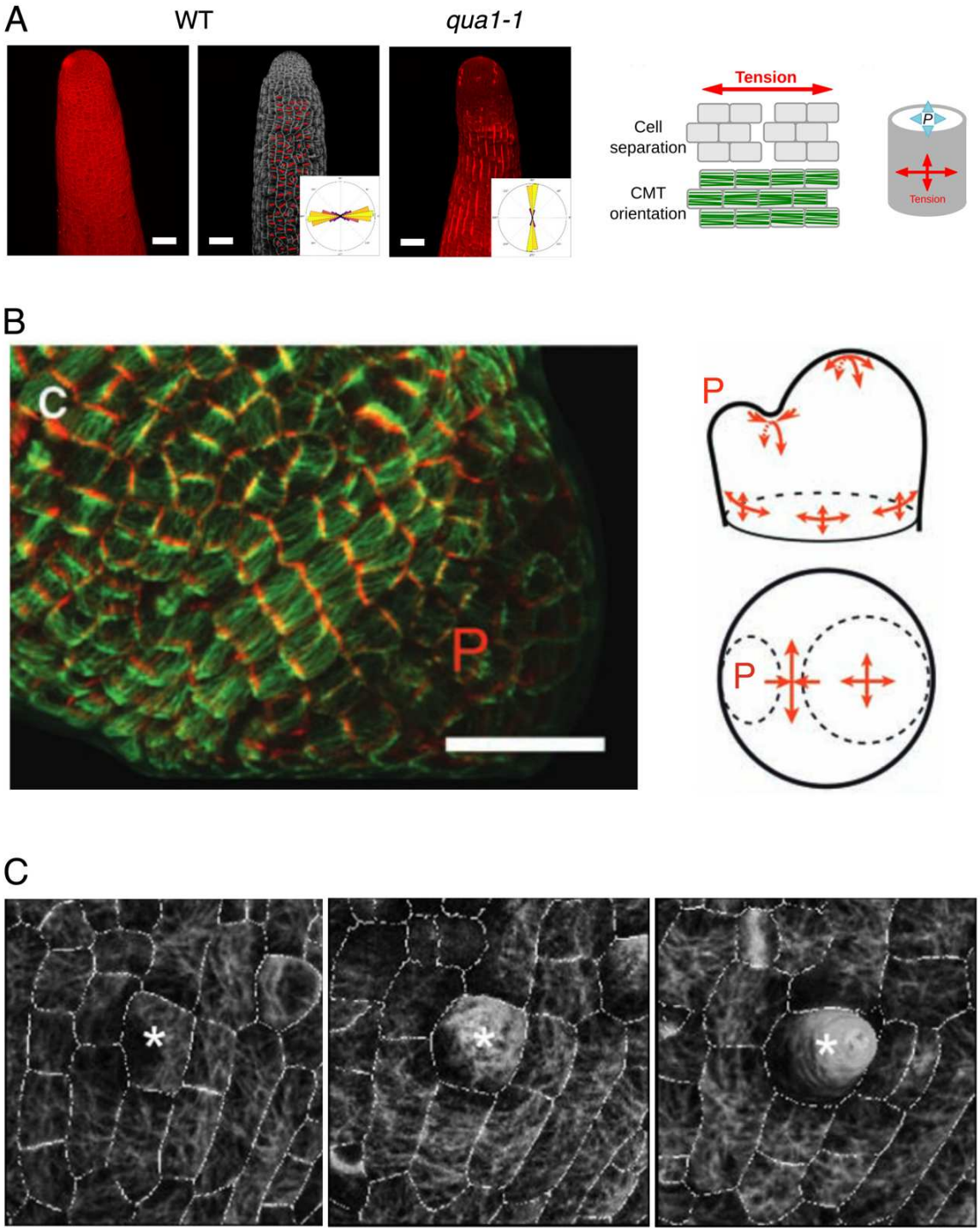

Figure I20: CMTs align with tension in tissues. (A) (Adapted from Verger *et al.*, 2018) Images of naked stems in the WT and *qua1-1* mutant. Red images show cell wall staining, and evidence the vertical cracks is *qua1-1*, confirming the transverse maximal tension. CMT arrays in WT cells (grey image) align transversally with the maximal tension orientation (red lines, showing their average orientation), as evidenced in the schematic drawing (right). The scale bars are 50 µm. (B) (Adapted from Hamant *et al.*, 2008). Image showing CMT organization (evidenced by GFP-MBD signal in green) at the boundary between the SAM and an organ primordium (P). CMTs align along the boundary axis, along the predicted maximal tension pattern (as shown in the drawing, left). The scale bar is 20 µm. (C) (Adapted from Hervieux *et al.*, 2016) CMT organization around a growing trichome (indicated by the star) in *Arabidopsis* sepals. During the phase of trichome's fast growth (middle image), CMTs organize circumferentially around the trichome. The scale bar is 20 µm.

If CMTs are responsive to stress, how they perceive the stress is largely unknown (Hamant *et al.*, 2019). Some MAPs have been shown to regulate MTs response to stress. *ktn-1* mutants, for example, fail to orient their CMT arrays in response to mechanical cues (Uyttewaal *et al.*, 2012; Figure I17C)). MTs aligning with tension are potentially destabilized by NEK6, as *nek-6* mutants are hyper-responsive to ablation treatments in *Arabidopsis* hypocotyls (Takatani *et al.*, 2020; Figure I18B). While many proteins modulate the response of CMTs to tension, in the corresponding mutants, CMTs still manage to align with maximal tension, ultimately. It has been proposed that the tensile forces are directly involved in MT polymerization and thus orients them (Hamant *et al.*, 2019). An alternative hypothesis is that CMTs are responsive to polarity cues in the cell, rather than to tensile forces (Hush *et al.*, 1990). The nexus between mechanical forces, microtubules and cellulose deposition gave rise to a model integrating a mechanical feedback loop as a driver of morphogenesis (Sampathkumar, 2020; Figure I21). In this model, tension would organize CMT arrays that guide cellulose deposition along the orientation of maximal tension, allowing mechanical resistance. The reinforcement of the cell wall at specific locations would constrain growth and change the mechanical stress pattern, thus reorienting CMTs (Hamant *et al.*, 2008; Sampathkumar, 2020; Figure I21).

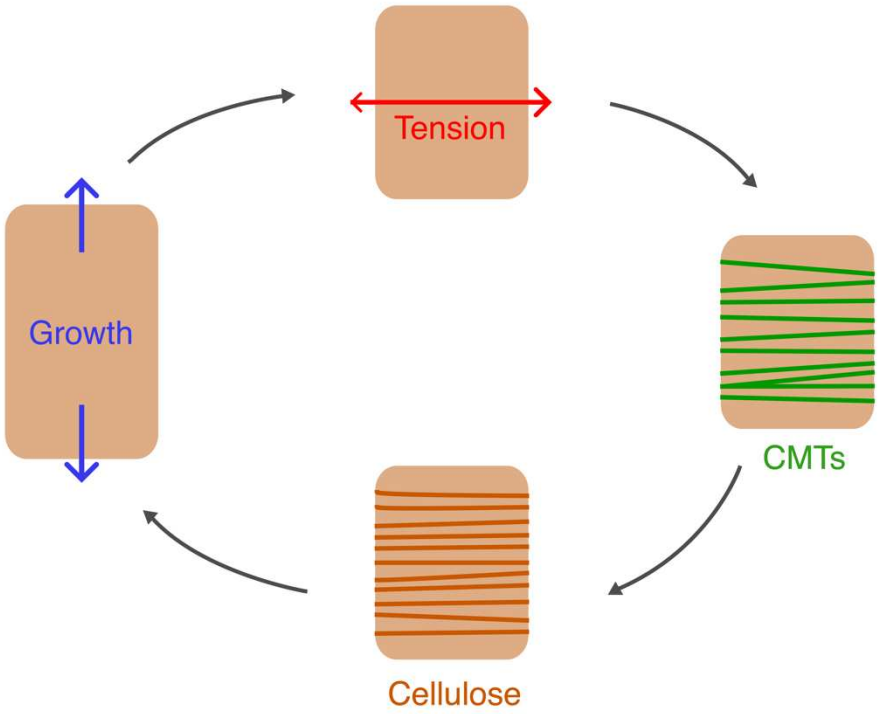

Figure I21: Schematic of the mechanical feedback loop model. CMT orientation follows that of maximal tension, driving the cellulose deposition along the maximal tension. The oriented cellulose microfibrils constrain growth, and induce anisotropic cellular growth, which in turn creates mechanical conflicts.

Beyond mechanical stress, MT organization is highly sensitive to other factors. As mentioned above, the phytohormone auxin influences the organization of the CMT arrays in the SAM (Sassi *et al.*, 2014). While auxin mediates a loosening of the cell wall affecting its mechanical properties probably reorganizing the MT array (Cosgrove, 2005; Nakayama *et al.*, 2012), it has also been shown to affect MTs through a transcriptional pathway (True and Shaw, 2020). Together with auxin, other phytohormones seem to impact MT organizations. Cytokinins, for example, induces orientation changes in MT arrays of root cells, but strikingly also modulate their dynamics in animal cells (Montesinos *et al.*, 2020). Brassinosteroids and ethylene have also been found to induce the reorientation of MT arrays in *Arabidopsis* (True and Shaw, 2020; Ma *et al.*, 2016; Wang *et al.*, 2018). MTs are also sensitive to environmental perturbations. Cold promotes their disassembly, and could be involved in signal sensing and cold resistance (Bartolo and Carter, 1991; Åström *et al.*, 1991; Pihakaski-Maunsbach and Puhakainen, 1995). Light has also been shown to affect the microtubule overall organization. In hypocotyls, the array switches from longitudinal to transverse orientations, leading to rapid cell elongation, upon illumination (Sambade *et al.*, 2012; Figures I16B and I17B).

VI. Mitosis and the cell cycle

So far, we discussed the role of growth and mechanics in morphogenesis, both at the organ and cellular scales. While morphogenesis is tightly correlated with growth rates and anisotropy at both levels, cell division and more specifically cell proliferation (symmetric divisions giving rise to two daughter cells with the same identity) is involved in organ formation (Fleming, 2006). At the SAM, for example, the peripheral zone has a mitotic index four to six times superior to that of the central zone (Laufs *et al.*, 1998). This regionalization can also be found in the root, where a correct domain restricted to cell division is necessary for correct root morphogenesis (Takatsuka and Umeda, 2014). Furthermore, fruit development is dependent on a developmental switch from cell division to cellular expansion (Ripoll *et al.*, 2019). Fruit shape differences between the *Arabidopsis* silique (near-cylindrical shape) and the *Capsella rubella* silicle (heart shape) also correlate with differences in division rounds and orientations (Eldridge *et al.*, 2016). Nevertheless, the specific role of cellular divisions in plant morphogenesis is debated. Mutants affected in cell proliferation do not present major morphogenetic defects, although are sometimes dwarf (Peng *et al.*, 1997; De Veylder *et al.*, 2001; Horiguchi *et al.*, 2005) or present mild defects in cell morphology (Schiessl *et al.*, 2014). Similarly, mutants affected in cell division orientation (which could appear as highly important in plants, as cells do not migrate), correctly produce organs (Traas *et al.*, 1995; Smith *et al.*, 1996; Schaefer *et al.*, 2017). These observations support the organismal theory, suggesting that plants should be considered as organisms chambered into cells rather than organized cellular aggregations (Kaplan, 1992; Fleming, 2006). From a mechanical standpoint, cell divisions could indeed be viewed as a consequence of growth rather than its driver: to resist forces, plant cells need to build new walls.

Nevertheless, just like animals, plant cells also undergo an undeniably extremely regulated mitotic cycle. The mitotic cycle is mainly divided between DNA replication (Synthesis or S-phase), and chromosome separation (Mitosis or M-phase) (Scofield *et al.*, 2014). These phases are separated by two Gap phases: 1 (G1), between mitosis and the S-phase, and 2 (G2) between the S-phase and mitosis (Scofield *et al.*, 2014). These different phases vary in duration and in function, and integrate various signals. In comparison with animals, plant cells often skip mitosis through endoreplication, explaining why plant cells are usually bigger than animal cells (Inzé and De Veylder, 2006).

A common consensus is that the cell cycle is unidirectional, with transitions driven by hysteresis (Coudreuse and Nurse, 2010; Sha *et al.*, 2002). In the following section, I will briefly detail the different cell cycle phases, mainly focusing on the checkpoints between G1/S and G2/M in plant cells, as these are the main potential arrest points of the cell cycle. The cellular division (chromosome separation and physical division) is referred to as mitosis, and is separated from the other phases, grouped and known as interphase.

1. Interphase

The main regulators of the cell cycle, and especially the transitioning between phases are the cyclin/cyclin-dependent kinase (CDK) complexes (Morgan, 1997; Lindqvist *et al.*, 2009). Plants present three main types of cyclins: A, B and D, involved in different phases of the cell cycle (Dewitte and Murray, 2003). Genes encoding for H-type cyclins have also been identified, although their involvement in the cell cycle remains poorly understood (Yamaguchi *et al.*, 2000). Associated to these cyclins are CDKs, which activate downstream pathways, and allow phase-specific gene expressions (Dewitte and Murray, 2003). Cyclins and CDKs exhibit oscillating expression patterns, that relate to the progression in the different phases. On top of presenting homologous CDKs to animals and fungi, land plants present other types of CDKs (such as CDKBs) (De Veylder and Beeckman, 2007). CDKB activities are only restricted to mitotic cells (from S- to M-phases), while CDKAs control phase transitions from G1 to S and from G2 to M (De Veylder and Beeckman, 2007; Figure I22). Playing with the expression of these proteins influences the duration of each cell cycle phase, adding evidence to their requirement for correct cell cycle progression (Iwakawa *et al.*, 2006; Cockcroft *et al.*, 2000; Dewitte *et al.*, 2002).

A. G1 phase

G1 is mainly referred to as the growth phase of the cell cycle, where most of the cellular processes happen. G1 is also associated with chromatin dynamics, in preparation for the genome duplication during the S phase (Sablowski and Gutirrez, 2022). Chromatin is decondensated to allow accessibility for the transcription machinery (Desvoyes *et al.*, 2014). This phase is also marked by

the assembly of pre-replications complexes (pre-RCs) that will later be used for DNA replication (Sanchez *et al.*, 2012; MacAlpine and Almouzni, 2013).

D-type cyclins appear as the key regulators of the G1 phase. Indeed, they are the central regulators of phosphorylation, through specific CDKs, of the RBR/E2F complex. Retinoblastoma (RB) in animals, and RB-related (RBR) in plants, are proteins that have a role in suppressing cell division, and in tumor suppression in humans (Scofield *et al.*, 2014). E2F, on the other hand, is a class of transcription factors (either activators (De Veylder *et al.*, 2002) or repressors (del Pozo *et al.*, 2006)) that promote cell cycle gene expression, notably necessary for the transition from G1 to S phases, and bind to RB(R) (Chellappan *et al.*, 1991; Figure I22). G1 progression into S phase is highly dependent on the activity of E2F, that is repressed when bound to RB(R) (Chellappan *et al.*, 1991; Scofield *et al.*, 2014). RB(R) phosphorylation, mediated D-type cyclins/CDKs complexes, induce the release of E2F transcription factors, leading to an activation of G1 progression genes (Boniotti and Gutirrez, 2001; Desvoyes *et al.*, 2006; Boudolf *et al.*, 2004; Figure I22). Therefore, low levels of CYCDs and some CDK inhibitors, especially Kip-RELATED proteins (KRPs) are needed to limit G1 progression (Menges *et al.*, 2006; Godínez-Palma *et al.*, 2017; Desvoyes and Gutirrez, 2020). In animals, CYCD acts as an external condition sensor for mitosis entry (Woo and Poon, 2003; Scofield *et al.*, 2014). Indeed, RB phosphorylation is mainly mediated by E-type cyclins, that are expressed when a threshold level of E2F activation is reached (through CYCD), inducing a feedforward activation loop (Scofield *et al.*, 2014). Plants lack E-type cyclins, and the subclass CYCD3 is thought to hold this function (Menges *et al.*, 2007).

B. S phase

The S-phase bears the genome replication function (MacAlpine and Almouzni, 2013). The pre-RCs assembly at the replication origins in the DNA during G1 initiate the formation of origin recognition complexes (ORCs) (Fragkos *et al.*, 2015). The replication of the genome and chromatin components is a tightly controlled process, that requires modification of the chromatin landscape (Fragkos *et al.*, 2015). During this phase, there is an increase in histone methylation and histone acetylation (Jasencakova *et al.*, 2001; Jasencakova *et al.*, 2003; Mayr *et al.*, 2003), and specific DNA methylation patterns, such as symmetric GC methylations that are transiently lost during the S phase in suspension cells (Borges *et al.*, 2021). The methylation of histones is important, notably, to recruit PCNA in HeLa cells (Yu *et al.*, 2012). Proliferating cell nuclear antigen (PCNA) is one of the key proteins involved in genome replication. PCNAs are highly conserved amongst eukaryotes, and ensure the correct binding and orientation of DNA polymerases, directly responsible for replication (Moldovan *et al.*, 2007; Strzalka and Ziemienowicz, 2011). During the S phase, PCNA1 is distributed in small foci scattered throughout the nucleus in yeast, human and plant cells, contrasting with its even localization during G1 and G2 (Meister *et al.*, 2007; Chagin *et al.*, 2010; Yokoyama *et al.*, 2016). On top of their involvements in genome replications, PCNAs regulate the

cell cycle progression, by binding to cyclin-CDK complexes or CDK inhibitors, and are involved in DNA repair (Maga and Hübscher, 2003; Strzalka and Ziemienowicz, 2011).

At this stage, some cells skip some of the G2, and mitotic steps to undergo the endocycle (a succession of G and S phases), either as part of their developmental program, or because of some detected damages in the DNA (Edgar *et al.*, 2014). Endocycling is mainly achieved by downregulation of the mitotic CDKs (Edgar *et al.*, 2014).

C. G2 phase

Once their genome is duplicated, cells transition from the S- onto the G2 phase. G2 is usually referred to as the "preparation for mitosis" stage of the cell cycle (Nurse and Bissett, 1981; Kousholt *et al.*, 2012). It is a checkpoint assessing if the genome has correctly been duplicated, to prevent any aberrations during division (De Schutter *et al.*, 2007; Kousholt *et al.*, 2012). It is also a point where the cell scans for any problems in genome integrity, and a system of chromatin repair is put in place (Culligan *et al.*, 2004). The transition between the G2 phase and mitosis (known as G2/M) is mediated by A- and B-type cyclins, and the associated CDK activity (De Veylder *et al.*, 2003; Weingartner *et al.*, 2003; Romeiro Motta *et al.*, 2021). The cyclin/CDK complexes required for mitotic onset are inhibited by specific proteins, notably Wee1 and Cell division cycle (CDC) proteins in most eukaryotes, through (de)phosphorylation (Nurse, 1990; Francis, 2011; Figure I22). In *Arabidopsis*, T-DNA insertion lines for both *WEE1* and *CDC25* show relatively WT-like phenotypes, suggesting functional redundancies (De Schutter *et al.*, 2007; Spadafora *et al.*, 2010; Francis, 2007). Although WEE1 transcripts are found in highly proliferative tissues of tomato fruits and *Arabidopsis* leaves (Sorrell *et al.*, 2002; Gonzalez *et al.*, 2007; Beemster *et al.*, 2005), it seems to be more involved in DNA damage response in plants (Kumar *et al.*, 2015). In plants, the CDK inhibitor family encoded by *SIAMESE* (*SIM*) and *SIM-RELATED* (*SMR*) genes is so far the widest accepted G2/M progression inhibitor (Kumar *et al.*, 2015), even though other mechanisms have been proposed (Boudolf *et al.*, 2006). Specific G2/M cyclin/CDK complexes control the activity of MYB transcription factors (Ito, 2005; Haga *et al.*, 2007; Chen *et al.*, 2017). MYB transcription factors are crucial for mitotic entry in plants as they control the expression of G2/M specific genes such as *KNOLLE*, required for cytokinesis (Lukowitz *et al.*, 1996; Assaad *et al.*, 1996). *myb3r1 myb3r4* double mutants display embryonic and post-embryonic developmental defects, and a significant decrease in G2/M-specific gene transcript levels (Haga *et al.*, 2011).

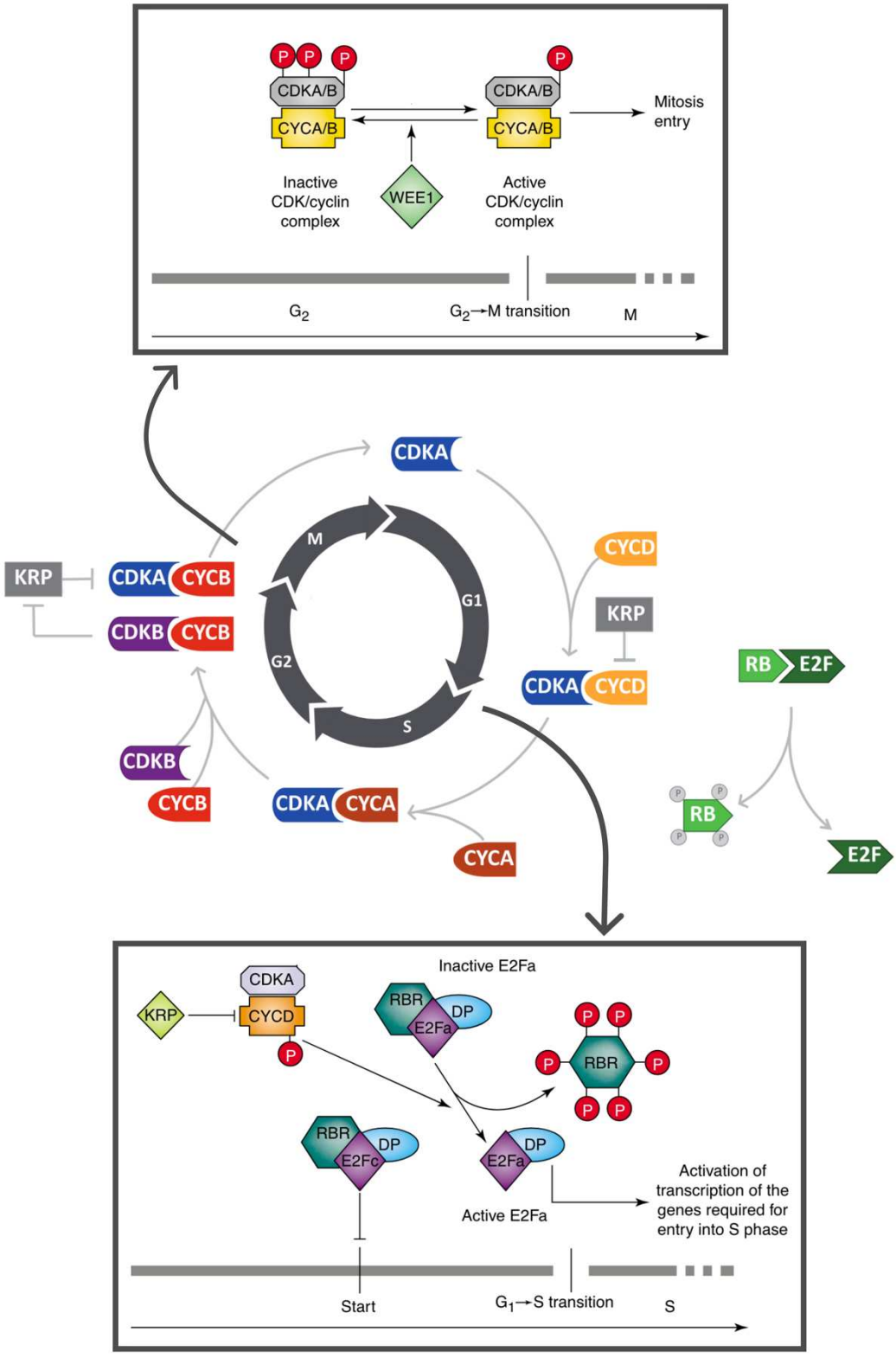

Figure I22: (Adapted from Scofield *et al.*, 2014 and Lloyd and Chan, 2006) Schematic representation of the molecular actors in the cell cycle. The framed boxes show detail on G2/M and G1/S transition controls.

2. Mitosis

The last phase of the cell cycle is mitosis. This is where the duplicated genome assembles into chromosomes, that are later separated at the poles of the mother cell (McIntosh, 2016). After chromosome separation, this mother cell is split in two daughter cells in a process called cytokinesis (McIntosh, 2016). Mitosis is divided in four main phases, that will briefly be detailed in this section.

Prophase is the first stage of mitosis. In early prophase, the nuclear envelope starts to break down, and the DNA starts to be condensed into chromosomes (Liu and Lee, 2022; Figure I23). At the same time, the spindle starts to assemble into the pro-spindle, around the nucleus (Lloyd and Chan, 2006). At late prophase/prometaphase, the nuclear envelope is gone and the chromosomes are fully condensed, and their kinetochores start to associate with spindle microtubules (Lloyd and Chan, 2006; Masoud *et al.*, 2013; Figure I23).

Metaphase is the next stage of mitosis, where the chromosomes are aligned in a plane called the metaphase plate (Masoud *et al.*, 2013). At this stage, microtubules from each spindle pole should be associated with the chromosomes' kinetochores (Figure I23). In order to assess the association between chromosomes and spindle microtubules, the cell undergoes a spindle checkpoint before proceeding to the next steps (Caillaud *et al.*, 2009).

Anaphase is the separation phase of the two sister chromatids to the opposing poles of the cells (Figure I23). This is mediated by the spindle, that pulls the kinetochore/microtubule complex to its opposite ends, combined with the disintegration of cohesins, proteins that hold the sister chromatids together (Higuchi and Uhlmann, 2005; Uhlmann *et al.*, 2000).

Telophase is the last phase of mitosis, and is marked by the disassembly of the spindle. At this stage, the chromosomes start to decondense, and the nuclear envelope starts to reform (Maddox *et al.*, 2000; Woodruff *et al.*, 2010; Figure I23). This stage overlaps with cytokinesis, which refers to the division of the cytoplasm between the two newly formed cells (Figure I23). The starting point of cytokinesis may even sometimes overlap with anaphase in some cells (Smertenko *et al.*, 2017; Pradillo *et al.*, 2019). It is mediated by the phragmoplast in plants, and the cleavage furrow in animals (Lloyd and Chan, 2006; Glotzer, 2001).

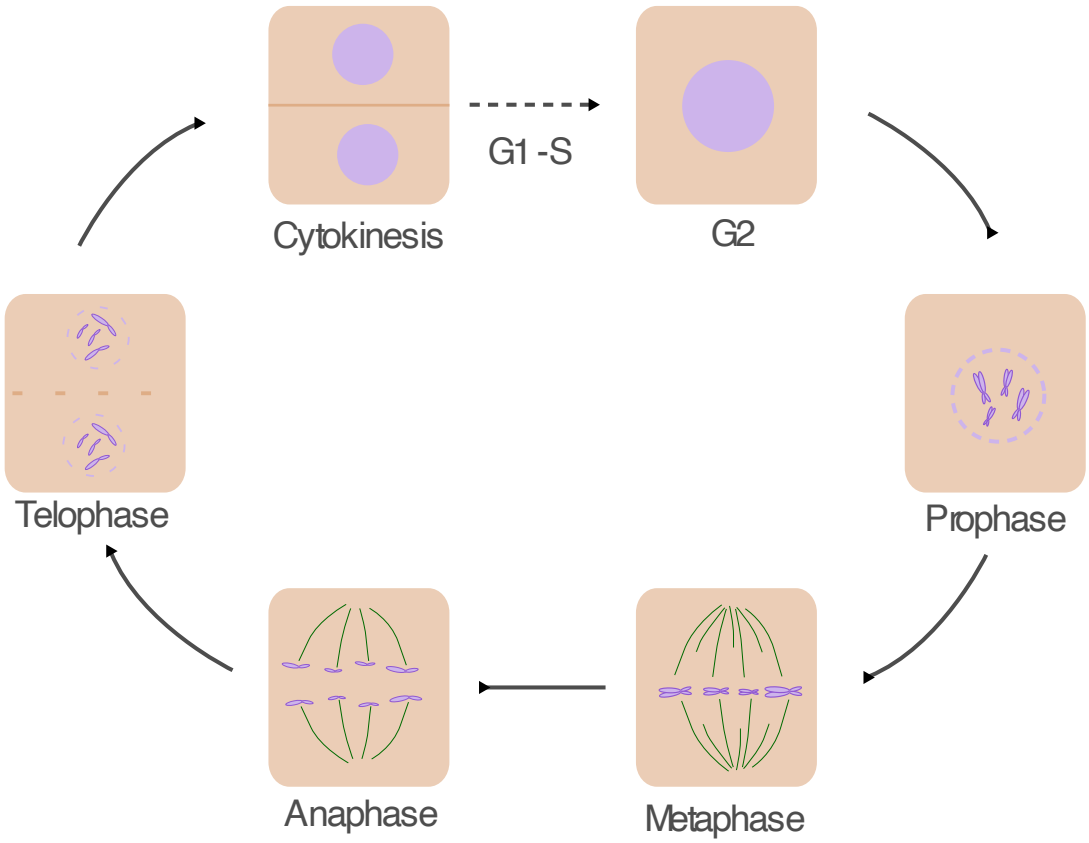

Figure I23: Schematic view of the mitotic cycle. At prophase, the nuclear envelope breaks down, and chromatin is condensed into chromosomes. During metaphase, these chromosomes become associated with spindle microtubules, that will pull them at opposing ends of the dividing cell during anaphase. In telophase, the nuclear envelopes start reforming around the separated chromosomes. The two daughter cells undergo physical separation during cytokinesis.

The cell's progression through the different phases of mitosis and interphase appears as an extremely controlled and sophisticated process (De Veylder *et al.*, 2007; Francis, 2007; Figure I22). Similarly to checkpoints that assess the cell's competence for transitioning between phases, signals are needed to inform the cell when to divide (Shimotohno *et al.*, 2021). Phytohormones have been found to directly influence the cell cycle, by modulating cyclins, CKDs and CKD inhibitors gene expression and protein activity (Dewitte and Murray, 2003; Shimotohno *et al.*, 2021). The circadian clock also appears as a regulator of the cell cycle through DNA replication modulation in higher plants (Farré, 2011; Greenwook and Locke, 2020; Fung-Uceda *et al.*, 2018; Johnson, 2010). The cell size has been proposed as a potential regulator of the cell cycle in *Arabisopsis*, in an intermediate rule between the cell reaching a critical size, and the cell adding a fixed size increment (Willis *et al.*, 2016; Jones *et al.*, 2017; Sablowski and Gutirrez, 2022; Pinto *et al.*, 2024). In cyanobacteria, cell division can be viewed as a cell size control mechanism, and seems controlled by the circadian clock (Martins *et al.*, 2018). DNA content is proposed to play a role in cell size assessment (D'Ario *et al.*, 2021). Moreover, and as will be discussed further below (Chapter VII of the Introduction),

the cytoskeleton undergoes deep changes in structure and function at different mitotic stages, under tight molecular control (Li *et al.*, 2015; Lian *et al.*, 2021).

While studies investigating the possible relationship between the cell cycle machinery and microtubule array modifications are scarce, some insights seem to indicate some links. Notably, some cell cycle proteins localize at the PPB (a mitotic structure appearing at the end of G2, discussed in Chapter VII1 of the Introduction), such as cyclins, CDKs and their inhibitors (Boruc *et al.*, 2010; Romeiro Motta *et al.*, 2022). Cell cycle-related proteins have been found to play a role in microtubule rearrangements and stabilization during mitosis in animals and plants (Charrasse *et al.*, 1998; Tournebize *et al.*, 2000; Ookata *et al.*, 1995). Similar functions could be relayed by cell cycle-related proteins for PPB microtubules organization before mitosis, although their targeting mechanisms remain unknown. MAP65-1, one of the MAP65 protein family, binds to microtubules in a cell-cycle dependent manner in plants (Smertenko *et al.*, 2006). It is mainly cortical in a subset of interphasic MTs and in the PPB, whereas it becomes mainly cytoplasmic during mitosis. Binding of the MAP65-1 protein to microtubules mainly promotes their bundling, and seems regulated by its phosphorylation status (Smertenko *et al.*, 2006). MAP65-1 phosphorylation is, at least partially, controlled by mitotic kinases such as Aurora kinases (Boruc *et al.*, 2017). CDC2 proteins are associated with G2/M transition control in animals and yeast (Nurse, 1990). In plants, CDC2 does not seem to control G2/M transitions, but associates with chromosomes, and also with MT mitotic structures (spindle and phragmoplast, discussed in Chapters I7B and I7C) (Hirt *et al.*, 1993; Stals *et al.*, 1997). Furthermore, the protein phosphatase PP2A controls mitosic kinase activity, and is also a subunit of a the TTP complex, which is key in regulating MTs, notably when transitioning towards mitotic functions (Ayaydin *et al.*, 2000; Spinner *et al.*, 2013; discussed in Chapter VII2 and VII3 of the Introduction). Last, endoreplication could also affect cell wall properties, and thus indirectly relate cell cycle and the cytoskeleton machinery (Bhosale *et al.*, 2019).

VII. Functions of the cytoskeleton in cell division

The cytoskeleton has a central role in cell division. All mitotic functions, between division plane and nuclear positioning, chromosome separation and cytokinesis, are ensured by cytoskeletal elements (Brown and Lemmon, 2001). Interestingly, plants have evolved specific cytoskeletal (and more specifically microtubule) systems, notably due to the fact that they are enclosed within a rigid cell wall (Brown and Lemmon, 2001). In this next section, I will discuss some of what is known for these unique structures.

1. The pre-prophase band (PPB)

The PPB has first been identified in wheat meristem cells by Pickett-Heaps and Northcote in 1966 (Pickett-Heaps and Northcote, 1966). They described it as "a band consisting of a large number of

microtubules", that formed a ring around the cell (Figure I24A). It is a structure that appears at the end of the G2 phase of the cell cycle, is plant specific and more especially land plant specific (Livanos and Müller, 2019). Interestingly, this band is positioned where the future division plane will be. It has later been found that, on top of CMTs forming a dense ring at the cell cortex, actin filaments were also present at the PPB (Palevitz, 1987; Kakimoto and Shibaoka, 1987; Panteris *et al.*, 2007). Actin seems to play a role in PPB narrowing (Mineyuki and Palevitz, 1990; Figure I25A). The formation of the PPB has not been extensively studied, notably in the dynamics of the CMTs. Some modeling has been put forward, proposing a spontaneous organization of a cortical ring structure through a differential spatio-temporal control of MT nucleation, coupled with dynamic interactions between MTs (Schneider *et al.*, 2021; Zumdieck *et al.*, 2005). Experimental evidence also proposed that the CMTs dynamics increases during the PPB formation stage, and that the PPB emerges from a "search and capture" mechanism of the microtubules (Vos *et al.*, 2004).

Several MAPs, including, on top of MAP65-1 (Boruc *et al.*, 2017), CLASP (Kirik *et al.*, 2008), KTN1 (Sasaki *et al.*, 2019) and the TON1-TRM-PP2A (TTP) complex (Spinner *et al.*, 2013; Dahiya and Bürstenbinder, 2023), localize at the PPB (Figure I24B). MAP65-1 is involved in CMT bundling at the PPB (Boruc *et al.*, 2017), KTN1 is thought to preferentially sever CMTs to correctly narrow and maintain PPB orientation (Komis *et al.*, 2017), while CLASP function at the PPB remains poorly understood (Kirik *et al.*, 2008). The TTP complex regulates many aspects of microtubule organization throughout the cell cycle, shares similarities with animal components localizing to centrioles and seems to be essential for the formation of the PPB (Spinner *et al.*, 2013). Indeed, mutations in all of the subunits of this complex leads to PPB-deficient plants. Mutations in the PP2A and TONNEAU1 components of the complex induce severe developmental defects, and aberrant division orientations (Camilleri *et al.*, 2002; Spinner *et al.*, 2013; Traas *et al.*, 1995; Azimzadeh *et al.*, 2008). In both of these mutants, interphasic CMT arrays appear as disorganized, indicating the role of the TTP complex in the control of interphase MTs. Indeed, several TONNEAU-RECUITING MOTIFs (TRMs) components of the TTP complex have a cell cycle-regulated expression pattern. The TRM 6, 7 and 8 isoforms, for example, are specifically expressed before mitosis entry. In the *trm678* triple mutant, interphasic CMT arrays (before mitosis) should therefore not be affected. While this mutant also displays a lack of PPB, plants seem to present only mild developmental defects (Schaefer *et al.*, 2017). The division planes are, however, more variable than the WT. More specifically, division planes in WT root tissues are rather stereotypical, oriented transversely from the root axis, with cells organized in files (Schaefer *et al.*, 2017). In *trm678*, the average orientation of the division angles in the root was similar to the WT's, but the variance between these angles was 2- to 3.2-fold higher (Schaefer *et al.*, 2017). This suggests that the PPB acts as a stabilizer for division plane orientation, and probably increases the robustness of plant development (Schaefer *et al.*, 2017).

The PPB, while being a cortical structure, is also connected to cytoplasmic microtubules that link it to the nucleus (Figure I28). These perinuclear/bridge MTs are thought to be essential for spindle bipolarity, and their accumulation could provide a tubulin reservoir for spindle formation

(Ambrose and Cyr, 2008; Masoud *et al.*, 2013). Moreover, tobacco BY-2 cells with an uneven distribution of these bridge microtubules around their nuclei display offset nuclei during mitosis (Ambrose and Cyr, 2008). Indeed, the PPB stage is thought to be linked with the pre-mitotic positioning of the nucleus. However, reports are not unanimous regarding this function. While some studies suggest that the nucleus location guides the PPB positioning (Bakhuizen *et al.*, 1985; Burgess, 1970), other studies relate nuclear migrations post-PPB (Pickett-Heaps, 1969; Granger and Cyr, 2001).

Indeed, the PPB is not necessary to complete divisions in land plants. Certain cell types of the moss *Physcomitrium patens* or suspension cells complete mitosis without the appearance of a PPB (Kosetsu *et al.*, 2017; Chan *et al.*, 2005). While the PPB has been well characterized and is undeniably linked with mitosis and division plane positioning, its specific role is still under debate. As mentioned above, it has been proposed to be involved in spindle polarity or in nuclear positioning. The most recent hypothesis, with the characterization of *trm678*, is that the PPB controls the robustness in division plane orientation (Schaefer *et al.*, 2017; Livanos and Müller, 2019).

The PPB is a marker of mitosis entry, and stays until nuclear envelope breakdown in prophase. After this stage, CMTs are completely absent in the cell, and actin filaments remains at the cortex, but slowly disappears from the PPB site to form the actin depleted zone (Liu ad Palevitz, 1992; Cleary *et al.*, 1992; Figures I25B and I25C). This zone is thought to limit the cytoplasmic streaming at the future division site and ensure proper insertion of the daughter wall (Sano *et al.*, 2005; Panteris, 2008).

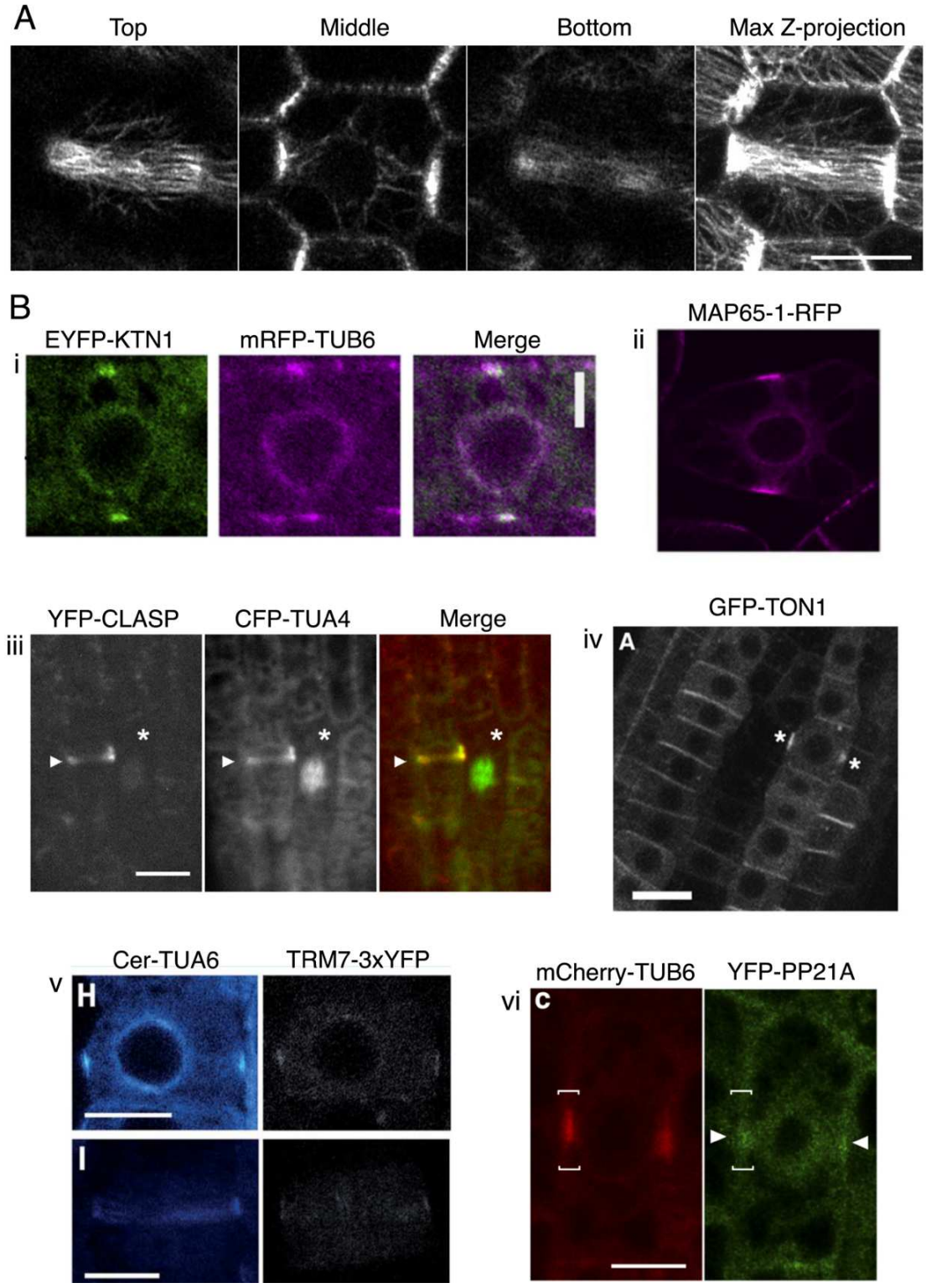

Figure I24: The PPB and its associated MAPs. (A) Image showing mCitrine-MBD signal, marking microtubules in a stem pre-mitotic cell. CMTs form a dense ring around the cell, as evidenced by the images at different focal planes of the confocal Z stack. The scale bar is 10 μm. (B) Different MAPs co-localizing with the PPB. (i) (Adapted from Sasaki *et al.*, 2019) KTN1 in mitotic root cells. The scale bar is 5 μm. (ii) (Adapted from Boruc *et al.*, 2017) MAP65-1 in tobacco BY2 cells. (iii) (Adapted from Kirik *et al.*, 2008) CLASP in mitotic hypocotyl cells. The scale bar is 10 μm. (iv) (Adapted from Azimzadeh *et al.*, 2008) TON1 in mitotic root tip cells. (v) (Adapted from Schaefer *et al.*, 2017) TRM7 in mitotic root cells. Top images are cross sections of the cell, and bottom images are surface views of the same cell. The scale bar is 10 μm. (vi) (Adapted from Spinner *et al.*, 2013) PP2A in root tip cells. The scale bar is 10 μm.

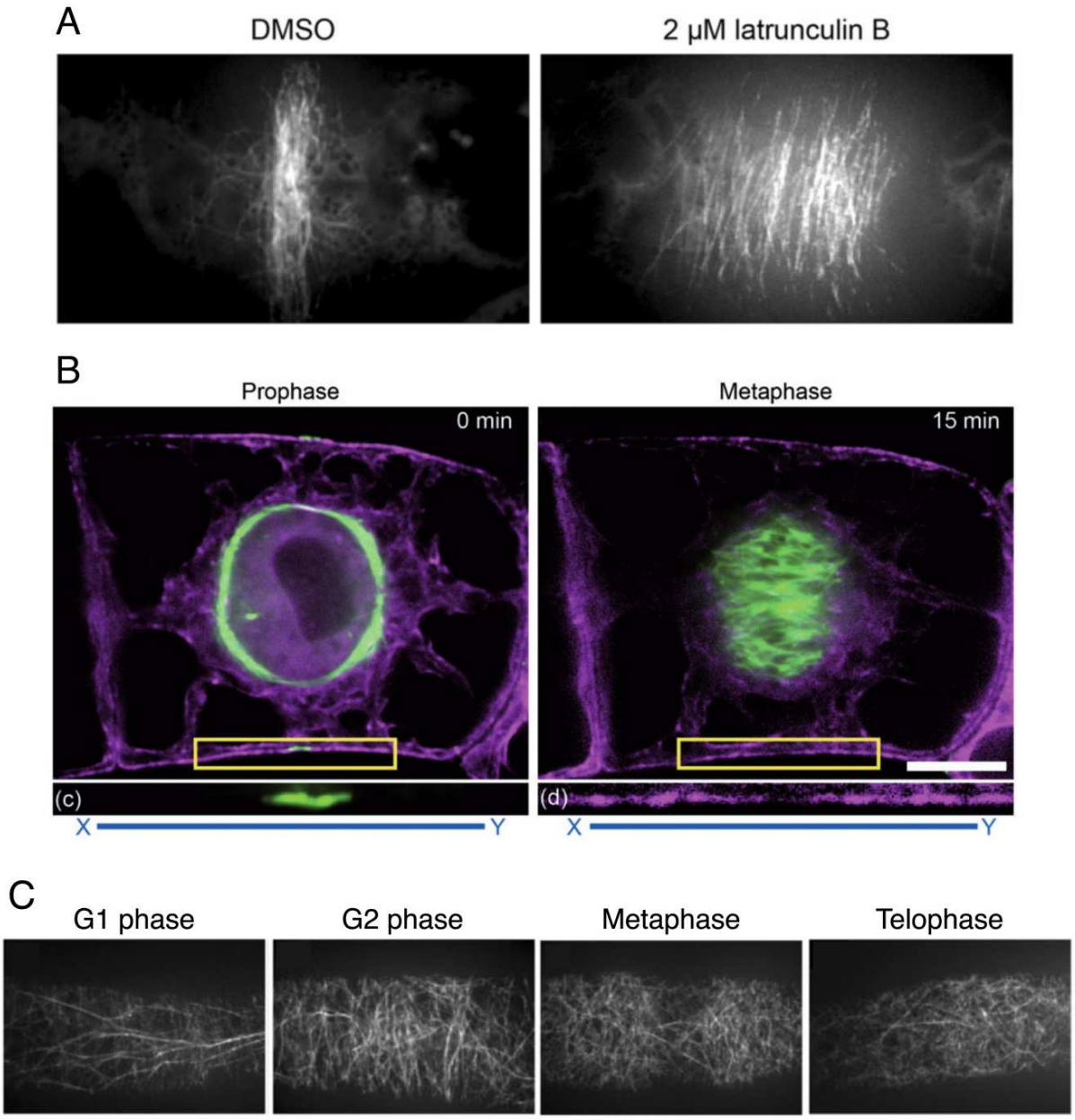

Figure I25: (Adapted from Kojo *et al.*, 2013) Involvement of actin in division plane positioning. (A) Microtubule visualization with the GFP-tubulin fluorescent marker in pre-mitotic tobacco BY2 cells, at the PPB stage. Cells were either treated with a control solution (DMSO, left) or with the actin polymerization inhibitor Lat B (right). Cells treated with Lat B exhibit much wider PPBs. (B) Visualization of both microtubules (YFP-tubulin, green) and actin (TdTomato-ABD2, magenta) in a mitotic tobacco BY2 cell. The top images are mid-plane sections through the cell, and the bottom images are magnifications of the yellow boxes. Actin is absent in methaphase from the former position of the PPB in prophase. The scale bar is 10 µm. (C) Actin filaments visualized with the GFP-ABD2 fluorescent marker in tobacco BY2 cells throughout the cell cycle. The actin depleted zone can be observed during metaphase.

2. Spindles

Spindles are microtubular structures that separate the sister chromatids after DNA duplication and condensation into chromosomes (Figure I27A). This separation process is also known as

karyokinesis. Unlike animal cells, plant spindle microtubules are not organized in condensed centrosomes, but rather present more or less diffuse "polar caps" (Yamada and Goshima, 2017). Kinesin proteins, associated to spindle MTs, generate force necessary for spindle assembly, structure and function (Ambrose and Cyr, 2007). Actin is also thought to be involved in chromosome separation, by pulling the chromatids at each pole of the dividing cell, thanks to the acto-myosin traction force (Staiger and Schliwa, 1987; Pickett-Heaps and Forer, 2009).

3. Phragmoplast

Cytokinesis is known as the step of physical separation of a mother cell in two daughter cells. This is the last mitotic step, and is differentially regulated between kingdoms (Guertin *et al.*, 2002). Indeed, as plant cells are surrounded by their rigid cell wall, any rapid deformation is impossible. Cytokinesis therefore does not occur by actin-mediated contraction, as in animals or fungi (Fededa and Gerlich, 2012; Bi, 2001; Figure I26). Instead, new wall and membrane material is deposited to partition the mother cell into two (Figure I26). This process could be assimilated as building a new wall in a room (Smith, 2001), and is mediated by the phragmoplast (Figure I27A), another plant-specific structure, which appeared early on in evolution with the Charales or stoneworts (Livanos and Müller, 2019). Non-plant species with walled cells also divide by the addition of new wall material at the division site, through different structures than the phragmoplast such as the septum in fungi and *Cylindrocapsa* or the cleavage furrow in *Chlamydomonas* (Verma, 2001; Roncero and Sánchez, 2010).

The phragmoplast can be viewed as a disk, or a circle, composed of microtubules and actin, expanding centrifugally as cytokinesis progresses (Murata *et al.*, 2013; Figures I26 and I27). The new wall being built is called the cell plate, is generated at the center of the cell and also expands centrifugally (Murata *et al.*, 2013). The phragmoplast localizes at the leading edge of the cell plate, bringing new material necessary for its expansion through vesicular trafficking, and follows it as it grows (Murata *et al.*, 2013).

The phragmoplast is therefore constantly evolving during cytokinesis, and requires to be highly dynamic. A lot of branched microtubule nucleation is happening during phragmoplast expansion, notably with the presence of augmin, that recruits γTuRC to pre-existing microtubules (Murata *et al.*, 2013; Hotta *et al.*, 2012). The dynamic expansion of the phragmoplast is, at least partially, mediated by KTN1 as the *ktn1-2* mutant's cytokinesis is significantly lower than the WT's (Komis *et al.*, 2017). While the phragmoplast needs to expand, the midzone needs to be conserved and stabilized. MAP65-3 and -4 cross-linking proteins ensure this function (Ho *et al.*, 2012; Kosetsu *et al.*, 2013; Li *et al.*, 2017; Müller *et al.*, 2004). Kinesin motor proteins are also involved in phragmoplast expansion. PHRAGMOPLAST ORIENTING KINESIN (POK) 1 and 2 are kinesin-12 proteins that interact with MAP65s and are involved in phragmoplast expansion

(Herrmann *et al.*, 2018) and correct attachment of the cell plate to the walls of the mother cell (Müller *et al.*, 2006).

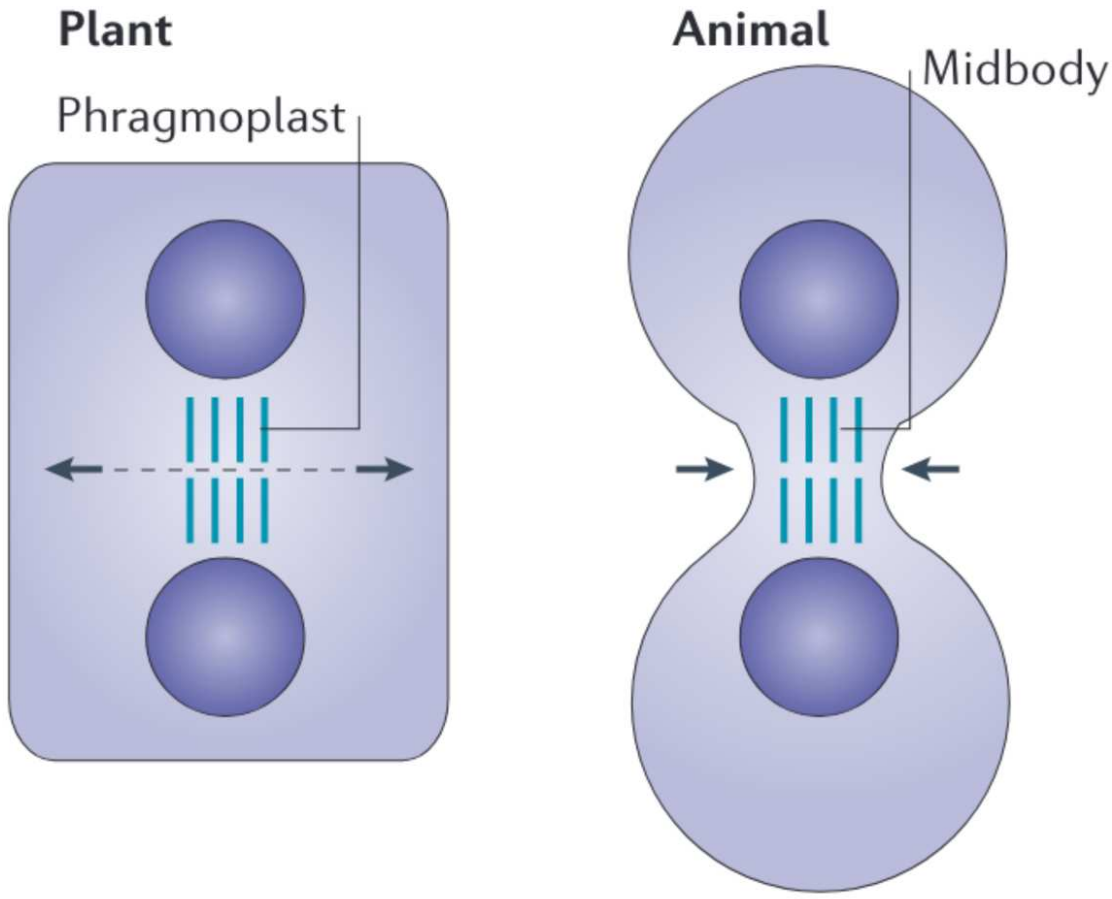

Figure I26: (Adapted from Lloyd and Chan, 2006) Illustration of the different modes of cytokinesis between plants and animals. In plants, it occurs through the deposition of new wall material, by centrifugal expansion of the phragmoplast. In animals, on the contrary, is occurs by the contraction of a ring, ultimately separating the two daughter cells.

The phragmoplast guidance and correct cell plate attachment is also ensured by the definition and maintenance of the cortical division zone (CDZ), formed notably by marks deposited at the PPB stage (Van Damme *et al.*, 2007). Amongst these marks, TANGLED (TAN), a CDZ protein that co-localizes with the PPB, is maintained at the future division site throughout mitosis (Dahiya and Bürstenbinder, 2023). TAN recruitment seems dependent on POK1 and 2, and microtubules, and *tan* mutants fail to correctly guide their phragmoplasts, showing aberrant division planes (Smith *et al.*, 1996; Walker *et al.*, 2007). The actin cytoskeleton probably also plays a role in anchoring the cell plate to the mother cell walls, as AFs have been seen at the junction between the phragmoplast and the CDZ, and actin-depolymerizing drugs produce tilted cell plate anchoring (Traas *et al.*, 1987;

Valster and Helper, 1997). Myosins also localize at the cortical division site, and at the newly formed cell plate, further suggesting that correct cell plate attachment is dependent on acto-myosin forces (Wu and Bezanilla, 2014; Molchan *et al.*, 2002; Reichelt *et al.*, 1999; Huang *et al.*, 2024).

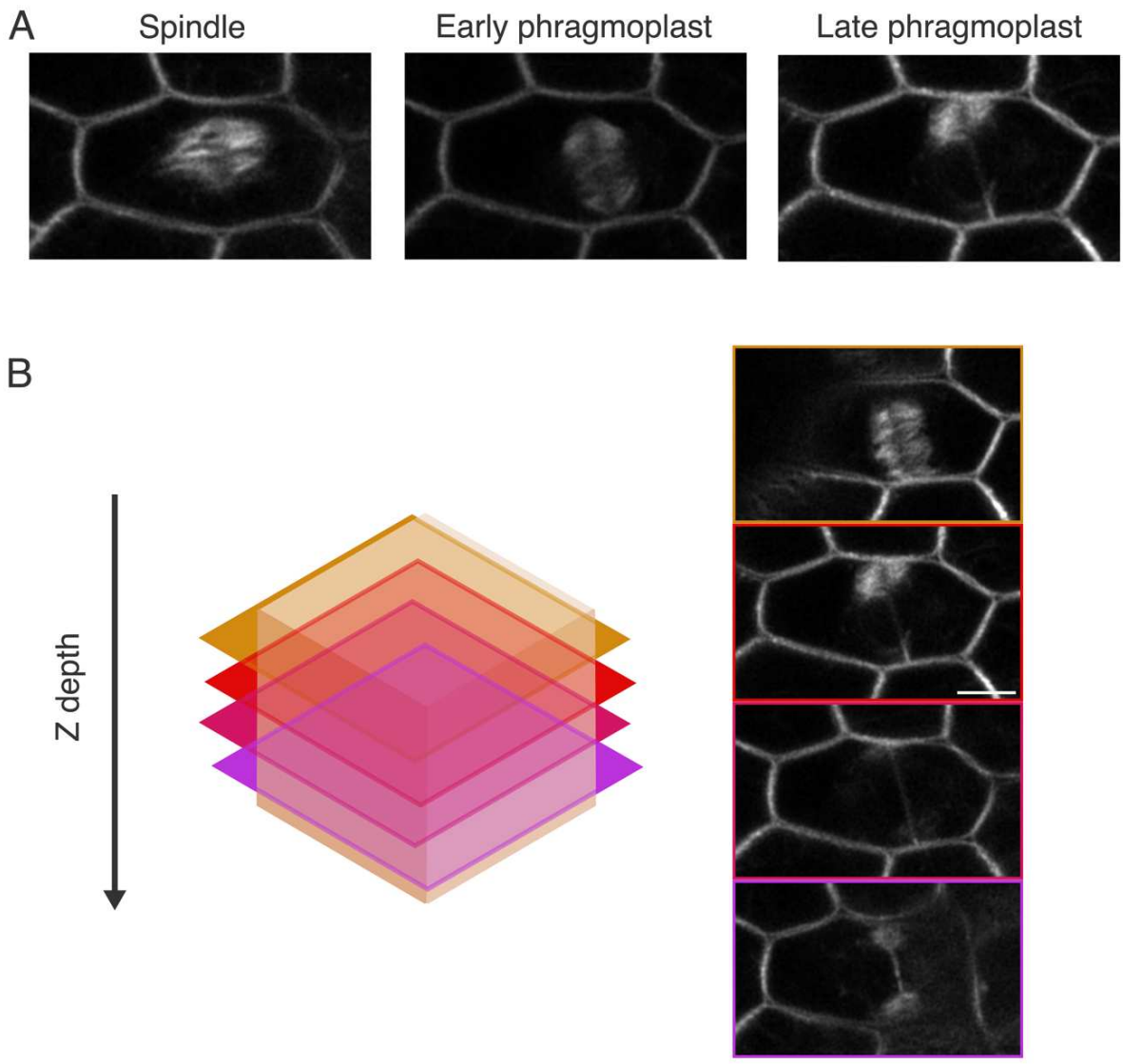

Figure I27: mCitrine-MBD signal, illustrating the MT mitotic structures in a dividing cell from a stem. In these images, the membrane is also visible. (A) The cell shows sequentially diffuse spindles (not organized through centrosomes) and a centrifugal expansion of the phragmoplast. The images are midplanes of a dividing cell. (B) Different planes from a confocal Z stack image illustrating the ring-like aspect of the phragmoplast, with the cell plate visible in the middle.

4. Changes in the cytoskeleton before mitosis

As the cell progresses through the mitotic cycle, it undergoes deep changes in its cytoskeletal structure and function (Figure I26). The cortical cytoskeleton is mainly relevant before mitotic entry, with the formation of the PPB, while the cytoplasmic cytoskeleton is the one mediating the mitotic steps of chromosome separation and wall deposition. Nevertheless, little is known about the transition phase of the cytoskeleton towards these (pre)mitotic organizations in plants. Overall, cytoplasmic microtubules seem to increase in density before the establishment of mitotic structures, both in cells that produce a PPB and in cells that do not (Figure I28). *Avena sativa* guard mother cells (GMCs), for example, present highly bundled radial MTs, that go deep in the cytoplasm and accumulate around the nucleus (Muilinax and Palevitz, 1989; Figure I29A) before PPB formation. Radial cytoplasmic MTs have also been observed preceding the formation of the PPB in *Zea mays* and *Lolium rigidum* GMCs (Galatis *et al.*, 1982; Cleary and Hardham, 1989). However, these cytoplasmic radiating MTs were not only observed during stomata development, but also in cytoplasmic strands of *Datura stramonium* epidermal cells (Flanders *et al.*, 1990; Figure I28B). These strands are under tension and help nucleus positioning by minimizing their length, and therefore placing the nucleus at the center of the cell (Goodbody *et al.*, 1991; Lloyd, 1991). At this stage, CMTs of *Datura stramonium* pre-mitotis cells are also arranged in a radial fashion (Figure I29B). Nevertheless, radiating pre-mitotic cytoplasmic MTs are not restricted to PPB-dependent divisions, as they are also found in megagametophytes of *Gingko biloba*, that do not present PPBs (Brown *et al.*, 2002; Figure I29C). In parallel, isolated plant nuclei are able to act as MTOCs, where MTs are generated in a radial fashion, reminiscent of what is observed *in vivo* (Mizuno, 1993; Stoppin *et al.*, 1994).

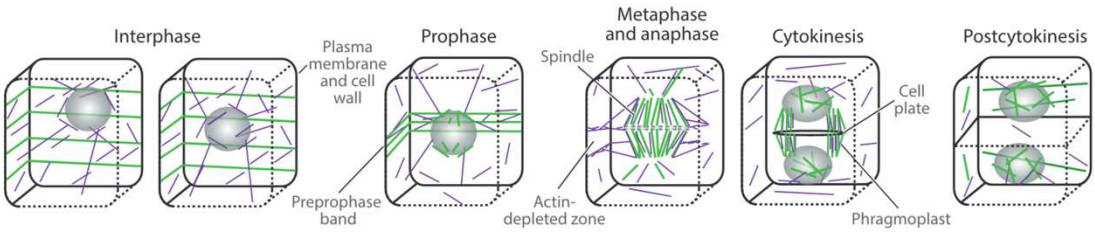

Figure I26: (Adapted from Livanos and Müller, 2019) Schematic view of the different microtubule structures throughout the cell cycle.

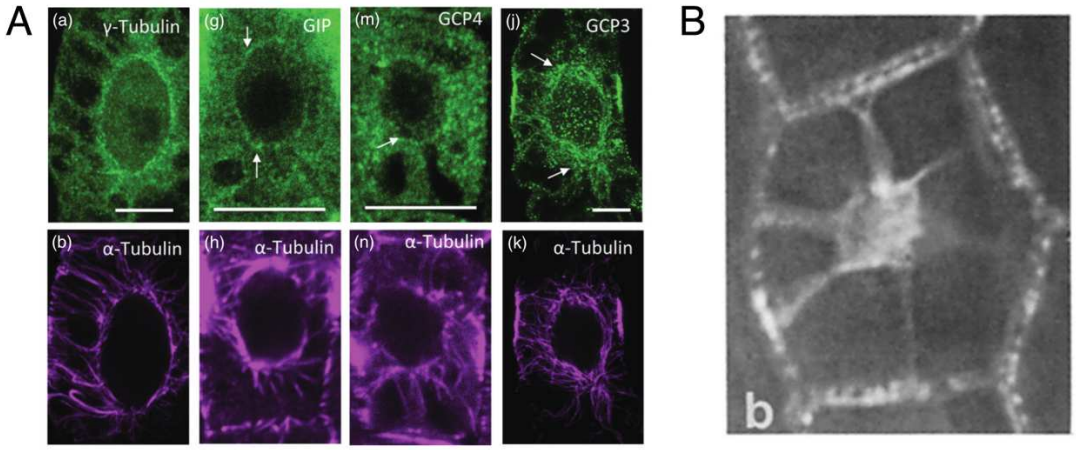

Figure I28: Cells show a pre-mitotic increase in cytoplasmic MTs, and perinuclear MT nucleation. (A) (Adapted from Masoud *et al.*, 2013) Labelling of members of the γTuRC, involved in MT nucleation, and microtubules (visualized with α-tubulin labelling). The images show mid-planes of pre-mitotic tobacco BY2 cells. The scale bars are 10 μm. (B) Mid-plane of a pre-mitotic *Datura stramonium* cell, visualizing MTs through immunostaining. We can observe thick cytoplasmic strands, containing MTs.

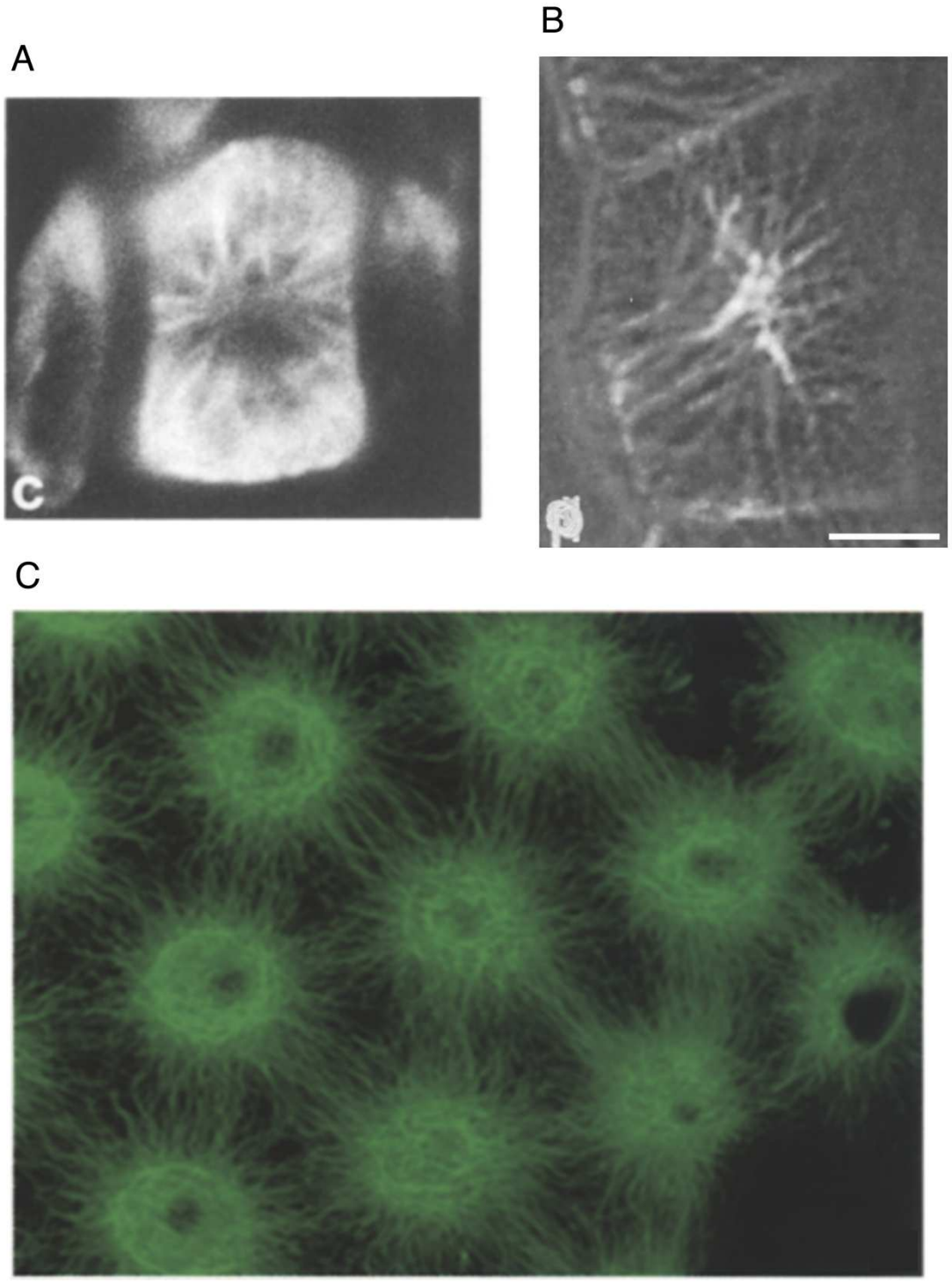

Figure I29: Radial MT arrays observed in various pre-mitotic cells. (A) (Adapted from Muilinax and Palevitz, 1989) Anti-tubulin staining showing a pre-mitotic GMC cell of *Avena sative* displaying cytoplasmic radial MTs and the interphasic microtubule band disappearing. (B) (Adapted from Flanders *et al.*, 1990) Maximal projections of the surface slices from a Z-stack image. The image show signal for anti-tubilin stainings performed in a pre-mitotic *Datura stramonium* cell. The CMTs appear as radial. The scale bar is 10 μm. (C) (Adapted from Brown and Lemmon, 2001) Immunostaining of microtubules in pre-mitotic *Gingko biloba* endosperm cells. The image show cytoplasmic MTs, radiating from the nucleus in a radial fashion.

Although not related to mitosis, the global changes in CMT array orientation in illuminated hypocotyls (Figures I16C and I17B) is preceded by a bipolarization of the CMTs, and a transient radial (or star) reorganization (Figures I30B and I30C), likely mediated by stable bundles of microtubules, serving as tracks for dynamic, growing ones (Chan *et al.*, 2007; Sambade *et al.*, 2012). Radial arrangements of CMTs are also found in other cell types, and often linked to growth. During root hair initiation, trichoblasts switch to tip growth, and present radial MTs at the growth site (Figure I30A), due to the radial stress pattern generated by a cell wall stiffening at the tip of the root hair, and a loosening around the tip (Krupinski *et al.*, 2016).

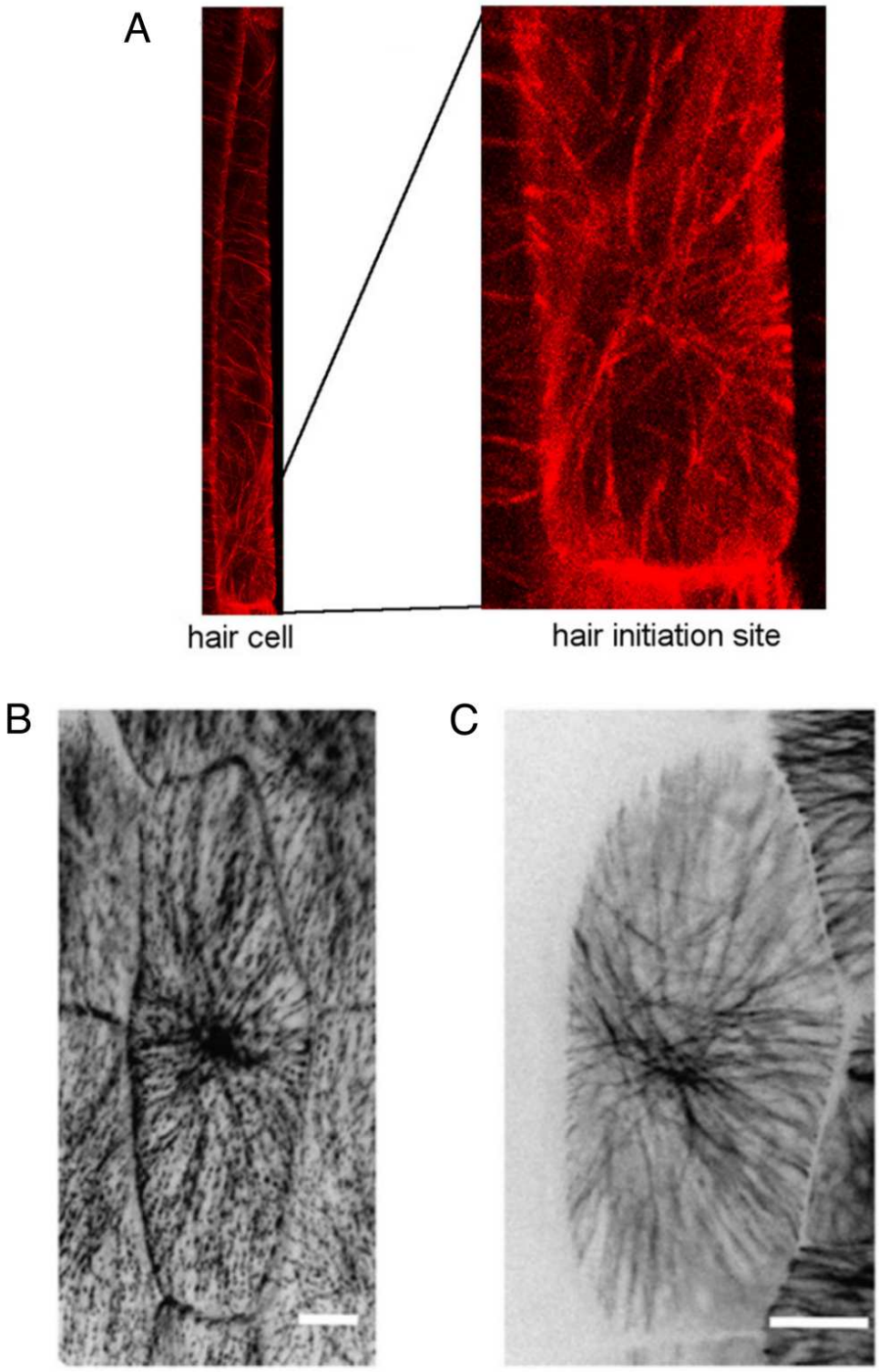

Figure I30: Examples of non-premitotic radial CMT arrays. (A) (Adapted from Krupinski *et al.*, 2016) Microtubules (visualized by RFP-TUB6) during root hair initiation in a trichoblast cell. At the hair initiation site (enlarged on the right image) CMTs form a radial pattern. (B and C) (Adapted from Sambade *et al.*, 2012) CMT arrays from hypocotyl cells at the onset of growth, upon illumination. Microtubules are visualized either by projection of time-lapse series of EB1a-GFP fluorescent signal (B, in the Ler ecotype) of with GFP-TUA fluorescent signal (C, in the Col-0 ecotype). At the onset of growth, the CMTs organize in a radial array. (B) The scale bar is 5 μm. (C) The scale bar is 10 μm.

VIII. Division plane orientation

Plant cells are embedded in their cell wall, which prevents them to deform and move. Cell division in plants is therefore achieved by the deposition of new wall and membrane material at the division plane. The coordination of the orientation of this plane is questionably of the utmost importance in plants since they prescribe division-based tissue growth.

Some rules have been proposed, most of them based on empirical observations, to predict the positioning of the future division plane. Most of the proposed division orientation rules rely on cell shape as the main parameter. In animal cells, the mitotic spindles often align with the longest plane of the cell, as stated by Hertwig's rule (Hertwig, 1893). As a result, the division plane results being perpendicular to the longest axis of the cell, even though some exceptions have been found, such as during zebrafish gastrulation (Gong *et al.*, 2004). Mirroring this rule, Hofmeister had proposed in 1863 that cells divide perpendicular to their axis of faster growth (Hofmeister, 1863). Other geometrical parameters have been proposed to orient the division plane positioning: Sachs proposition states that the division planes must be perpendicular to the walls of the mother cell, and create two daughter cells of equal size (Sachs, 1878; Figure I31). Another generally accepted rule is that division planes should go through the centroid of the cell (Lewis, 1926; Figure I31). Errera's rule, probably the most popular one, says that the division plane goes through one of the shortest planes of the cell (Errera, 1886). Even though most interpret it as "the shortest plane", it is in fact a stochastic rule, as evidenced by Besson and Dumais in 2011 (Besson and Dumais, 2011; Figures I32A and I32B). Indeed, the probability for a cell to divide following a given plane is proportional to its rank in being the shortest plane dividing the cell in two (Figure I32B). Even though the rules listed above have been put forward to describe symmetrical cell divisions, it has been proposed recently that for all divisions (symmetric and asymmetric) the division plane goes through, or very close to, the centroid of the cell and minimize its area, at least to some extent (Moukhtar *et al.*, 2019).

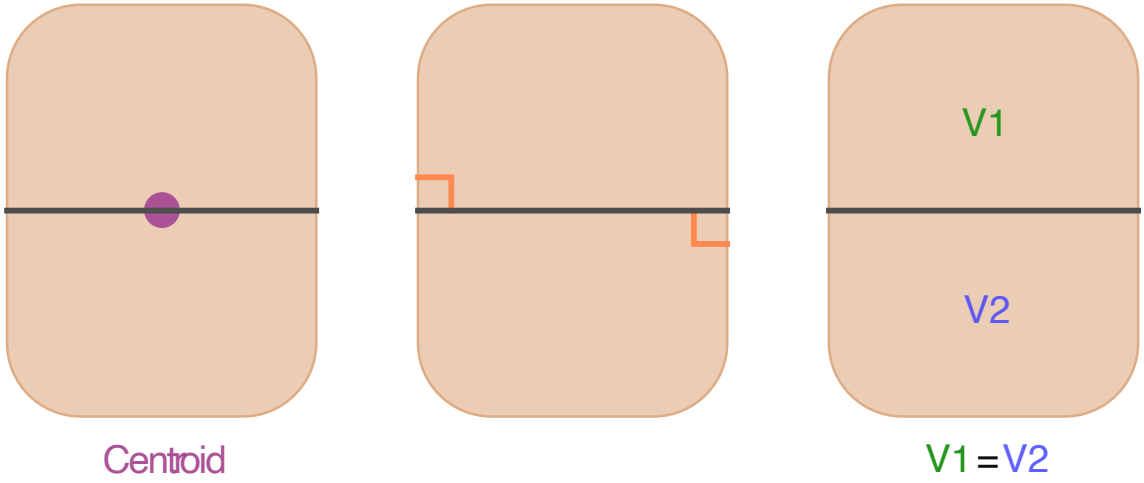

Figure I31: Schematic representation of purely geometric division rules. The division plane must go through the centroid of the cell (Lewis), be anchored at right angles from the mother walls (Sachs) and separate the daughter cells in two equal volumes (Sachs).

However, some observations regarding division plane positioning rather look at mechanical forces as being the main driver of orientation. Indeed, in line with Errera's rule, it has been proposed that cytoplasmic strands are under tension, and therefore seek to minimize their length (Figure I33). This implies that the path between the cortex and the nucleus is minimized, placing the nucleus at the center of the cell (Flanders *et al.*, 1990; Lloyd, 1991). Furthermore, division planes avoid the formation of four-way junctions (Lloyd, 1991). Indeed, three-way junctions are the most energetically stable form of attachment in a continuous tissue, and cell autonomous, passive mechanisms are widely accepted for four-way junction avoidance (Lloyd, 1991). On top of these observations, mechanical forces at the tissue level have been proposed to be central in orienting cell division planes. Indeed, some cell types in plants clearly do not follow Errera's rule, such as procambial cells in the vasculature (Fisher and Turner, 2007) or cells at boundaries between the SAM and an emerging primordium (Louveaux *et al.*, 2016; Figure I32C). In 1896, Kny proposed that division planes align with tension fields (Kny, 1896). This proposition has been formally observed in artichoke calli, where mechanical perturbations affect cell divisions (Yeoman and Brown, 1971). Furthermore, it has been observed that cell walls align with external forces in growing *Coleus* stems. The authors imposed clamps on the growing stems and observed that the cells walls of cells in phloem and cambium aligned transversely to the compression imposed by the clamps (Lintilhac and Vesecky, 1984). More recently, live experimental data has formalized that in *Arabidopsis* shoot apical meristems, the division planes align with the maximal tension orientation, especially at the boundary between the meristem and the growing organ, when tensile stress is high and very directional (Louveaux *et al.*, 2016; Figures I20B and I32C).

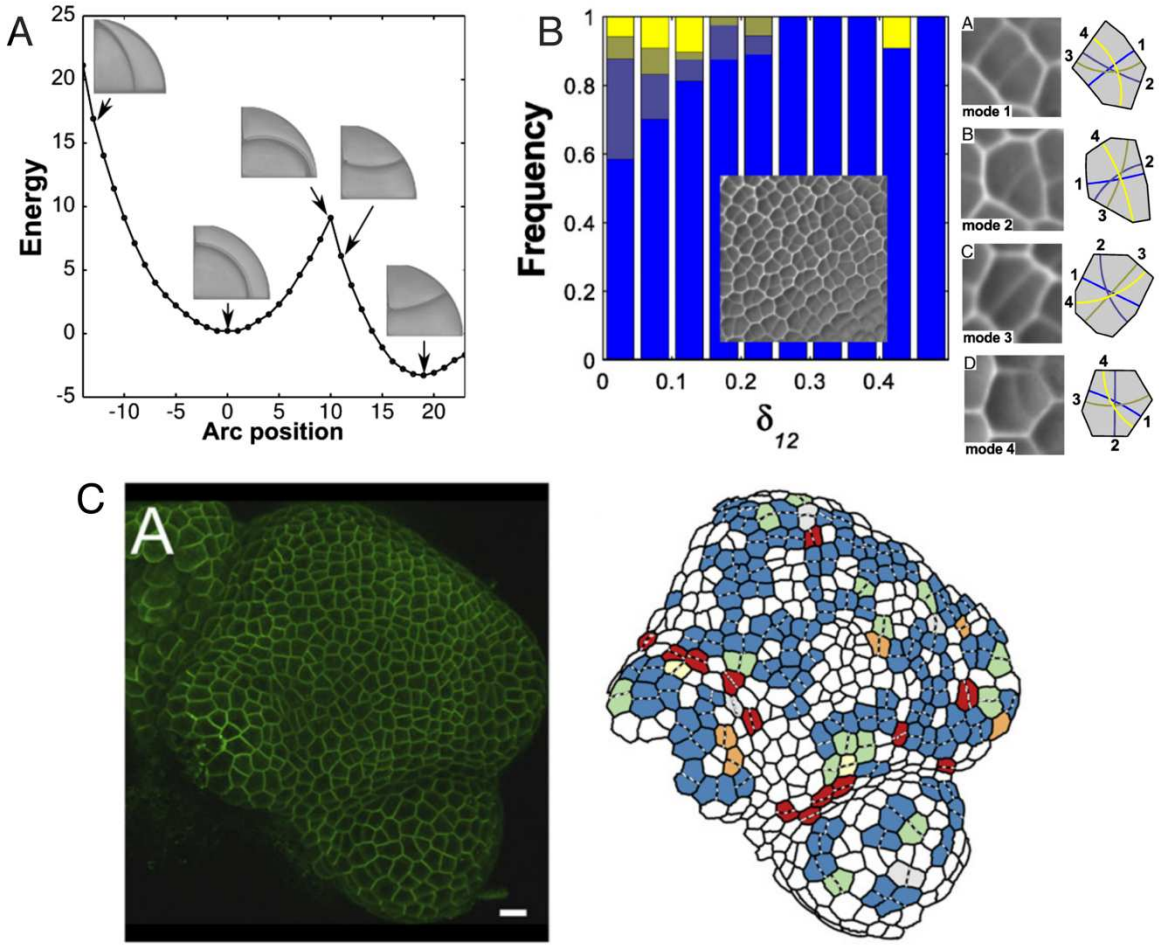

Figure I32: Tension drives division plane selection. (A and B) (Adapted from Besson and Dumais, 2011) (A) Quantification of the energy associated with different division plane configurations between two soap bubbles. The configurations showing local energy minima correspond to the division planes observed in glandular trichomes of *Dionaea muscipula*. (B) Data from division planes observed in *Microsorum punctatum* leaves. The colors correspond to the first, second, third or fourth shortest planes available for each cell (imaged on the right part), and the frequency of occurrence, as a function of the relative distance between the first and second shortest planes. The furthest the distance, the more likely the cell is to divide along its shortest plane. (C) (Adapted from Louveaux *et al.*, 2016) Cell wall staining of an *Arabidopsis* SAM (left) and identification of its recently divided cells (colored cells, right). The red cells divided following their longest plane, which correspond to the orientation of maximal tension, at the meristem boundaries. The scale bar is 10 μm.

However, cell shape parameters and mechanical parameters are not to be looked at as two independent parameters. Indeed, in pressurized oval, wall-less cells, the maximal tensile stress is modelled to be transverse to the longest axis of the cell (Colin *et al.*, 2020), corresponding to its shortest axis (Figures I7E). Flanders *et al.*'s study also proposes that nucleus positioning prior to mitosis is driven by cytoplasmic strands that are under tension, and are able to move, looking for the minimal path (Flanders *et al.*, 1990; Figure I33). Division plane positioning rules are therefore rather on a gradient, going from purely geometrical parameters to purely mechanical parameters. Depending on external, or internal, cues, the cell would adapt its division plane positioning within this spectrum (Figure I34). However, how the cell distinguishes intracellular, local and global tension fields is unknown.

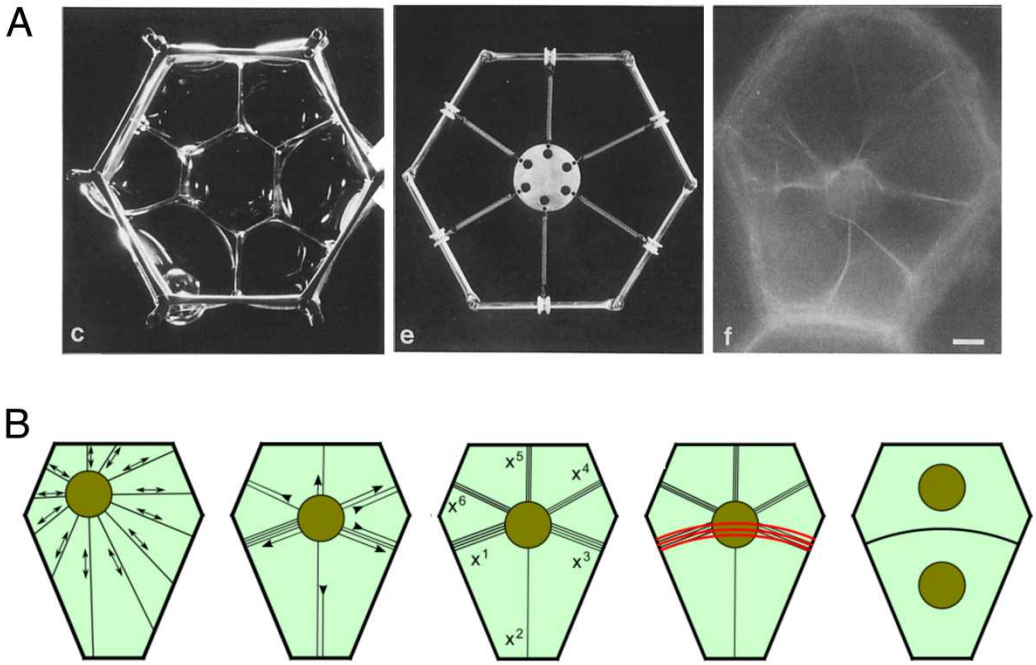

Figure I33: Pre-mitotic nucleus positioning, through cytoplasmic strands under tension. (A) (Adapted from Flanders *et al.*, 1990) Analog models for nuclear positioning through tension. Soap bubbles (left image) arrange by minimizing the surface tension, and the subsequent length of the planes separating them. Springs (middle) within a Teflon frame also tend to minimize follow their shortest path. In cells, these models hold true for cytoplasmic strands connected to the nucleus, that tend to follow their shortest path. The scale bar is 10 μm. (B) (Adapted from Besson and Dumais, 2011) Model proposed for division plane selection, driven by nuclear positioning through tension. Cytoplasmic strands linking the nucleus to the cellular walls will arrange to minimize their path, positioning the nucleus at the center of the future division plane.

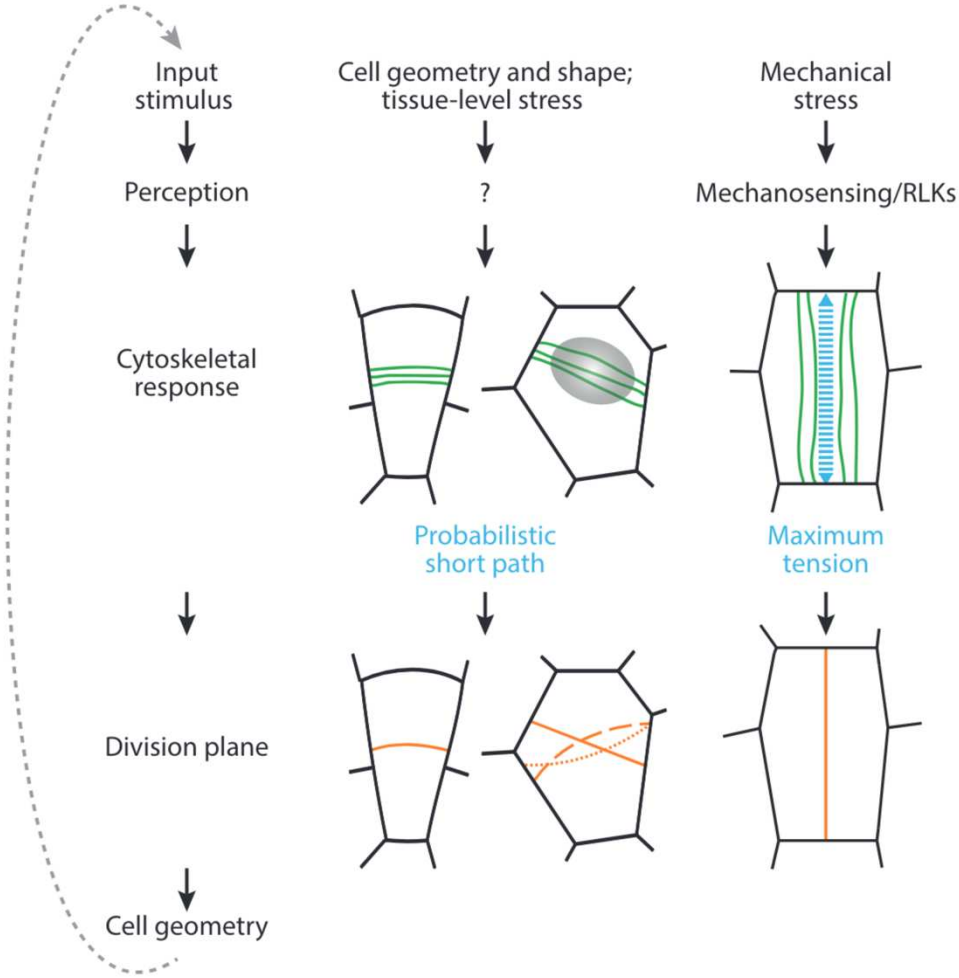

Figure I34: (Adapted from Livanos and Müller, 2019) Feedback loop integrating the different actors in division plane positioning. In absence of strong anisotropic mechanical stresses, the cell will divide following its probabilistic shortest path. However, in the presence of a strong and anisotropic stress, the cell will divide following this orientation, through a mechanosensing pathway leading to microtubule responses.

IX. Conclusions and questions of the PhD

While many questions regarding the cues orienting the cell division plane positioning, as well as the molecular regulators involved have been explored and provide valuable insights in the mitotic process, many remain. Notably, how these cues are being read and integrated by the cell is yet to be understood. The PPB appears as a potential integrator of the different rules orienting the division plane. Nevertheless, the PPB is already placed at the future division site at the end of G2. The integration of the different cues orienting it therefore happens before the complete maturation of the PPB: either during the maturation process or even before the transition towards the PPB stage. Hence, there must be a mechanism preceding the full PPB maturation integrating the different cell shape, tissular context and mechanical cues in order to properly orient division. CMTs are responsive to tension, and to cell shape cues (shown for example by their interaction with CLASP proteins), and appear as potential integrators for correct division plane positioning. The PPB being also highly dense in CMTs places them as central candidates for division plane orientation processes. As mentioned above, some cell types or organisms do not need a PPB to complete division, or correctly orient their division planes. These mechanisms could be common between plants, and be independent from PPB formation, or different strategies could have emerged separately to ensure this function.

Another question remaining is how CMTs switch between their interphasic function of guiding the cellulose deposition and therefore ensuring mechanical resistance for the cell, to PPB microtubules. Indeed, before the onset of mitosis, the cell becomes widely depopulated from cortical microtubules, and the PPB does not appear to have cellulose-related functions. In protoxylem, multiple dense rings of CMTs are found throughout the cell and could resemble PPBs (Wightman and Turner, 2008). These structures do impact cellulose deposition and explain protoxylem's multi-ring reinforcements (Wightman and Turner, 2008). Combined with the fact that these structures are not related to mitosis, one could argue that the PPB is not long-lasting enough to have an impact. Some PPB-less divisions such as in *Funaria* protonema, however, show a small deposition of cell wall at the future division site (Sawidis *et al.*, 1991). To my knowledge, no analysis of cell wall components deposition at the future division site has been conducted for higher plants, but could present an additional guide for the cell plate.

Although some evidence, and textbook drawings suggest that the PPB forms by a concentration of CMTs at the future division site, the dynamics of CMTs before the assembly of the PPB has not been studied in detail (Gunning and Sammut, 1990; Livanos and Müller, 2019; Figure I26). During leaf development, the average orientation of CMTs coincides with the orientation of the future division plane, further suggesting that the PPB forms by a concentration of interphasic CMTs (Zhang and Ambrose, 2022). Nevertheless, these observations do not hold true in every tissue, such as in GMCs of *Avena sativa*, that place their PPB at 90° from their interphasic microtubule band (Muilinax and Palevitz, 1989). Microtubule dynamics post-PPB have extensively been studied,

notably to describe their involvement in mitosis. However, pre-PPB CMT dynamics have not been described, in a context where tissue stress is stereotypical and stable (to prevent conflicting cues). Indeed, change in MT function during this particular transition stage (between cellulose deposition and PPB assembly) could be accompanied by a change in MT organization or dynamics. It has been proposed that ring configurations are spontaneously formed through MT interactions and a differential spatio-temporal control of nucleation at the cortex (Schneider *et al.*, 2021; Zumdieck *et al.*, 2005). It has also been suggested that the PPB emerges from an increase in dynamic instability of CMTs before mitosis, from a "search and capture" mechanism (Vos *et al.*, 2004).

We therefore proposed to follow pre-PPB CMT organization overtime. Our chosen model study was the *Arabidopsis* stem epidermis, and especially the area directly below the meristem. It is one of the few organs that present experimental confirmation of stable and stereotypical tensile stress pattern, while still displaying highly active cell divisions. Indeed, the vertical cracks in the *quasimodo1-1* stem confirm the transverse maximal stress orientation in stem epidermis (Verger *et al.*, 2018). We decided to follow the microtubules from the outermost cortex of the stems. On top of describing pre-PPB microtubule dynamics, we believe that the stem could reveal an excellent system to study cell division or mechanics-related questions *in vivo*. The imaging of the stem is extremely easy, as it required very little dissection, and can be imaged in its growth medium. Cells are also bigger than the SAM (that has classically been used to study morphogenesis), and the subsequent image resolution is increased. The stem presents a highly stable tension pattern, transverse throughout the whole stem, due to its rather cylindrical structure. This suppresses any biases that could arise regarding the localization of the sample within the organ.

Another remaining question is how cells could differentiate the global tension pattern derived from the tissue, from local tension patterns, or cellular tension patterns. This could also be related to the orientation of division, and could provide an explanation for the different parameter, either cell shape-derived, or tissue tension-derived. To investigate these questions further, cell shape needs to be uncoupled from global tissue stresses. Indeed, applying a stress, and subsequent deformation, to a tissue induces inevitable cell deformations. Different systems than the stem are needed: some to study purely cellular parameters separately from the tissue, and others to study purely tissue tension contributions, without considering cell shapes. For this, protoplasts and calli could be useful systems for placing cells in a different, non-physiological tissue context. Nevertheless, they are not optimized for mitosis research, even though they could reveal valuable insight into the mechanics and biochemistry behind cell division.

Results

I. Characterization of the radial step and its implications in cell division

This part describes the discovery of the "radial step" in *Arabidopsis* stems.

Contribution: In this project, I have conducted all of the experiments on the stems, with the experiments on NPA in collaboration with Shogo Takatani (co-first author in the publication, who made the initial observation). I have made all the measurements and all the figures. I also participated in the writing of the text.

Publication: This work is published in Proceedings of the National Academy of Sciences, USA, and unless indicated otherwise, the text in this chapter is identical to that of the article. More specifically, some figures and part of the text (part I5 of the Results on trichomes), have been modified (deleted or added) to better fit the thesis. The published version of the article has been added in the annexes.

1. A stereotypical radial CMT organization before cell division

To observe CMTs in dividing cells over time, we used plant lines expressing the MAP4 microtubule binding domain (MBD) fused to mCitrine and focused our analysis on dissected shoot apices, as previously described (Burian *et al.*, 2013), but here with higher spatial and temporal resolution (see Material and Methods).

In the Shoot Apical Meristem (SAM), as previously reported, we typically observed CMT alignment at the tissue scale, with a bias towards circumferential direction in the organogenetic (peripheral) zone, whereas no particular bias was observed in the central zone (Hamant *et al.*, 2008; Figure R3A). However, when considering individual cells over time, CMT behavior appeared much more variable. In particular, before cell division, we often observed cells with radial CMT orientations, as viewed from the top (Figure R3B; Figure R1A and R1B).

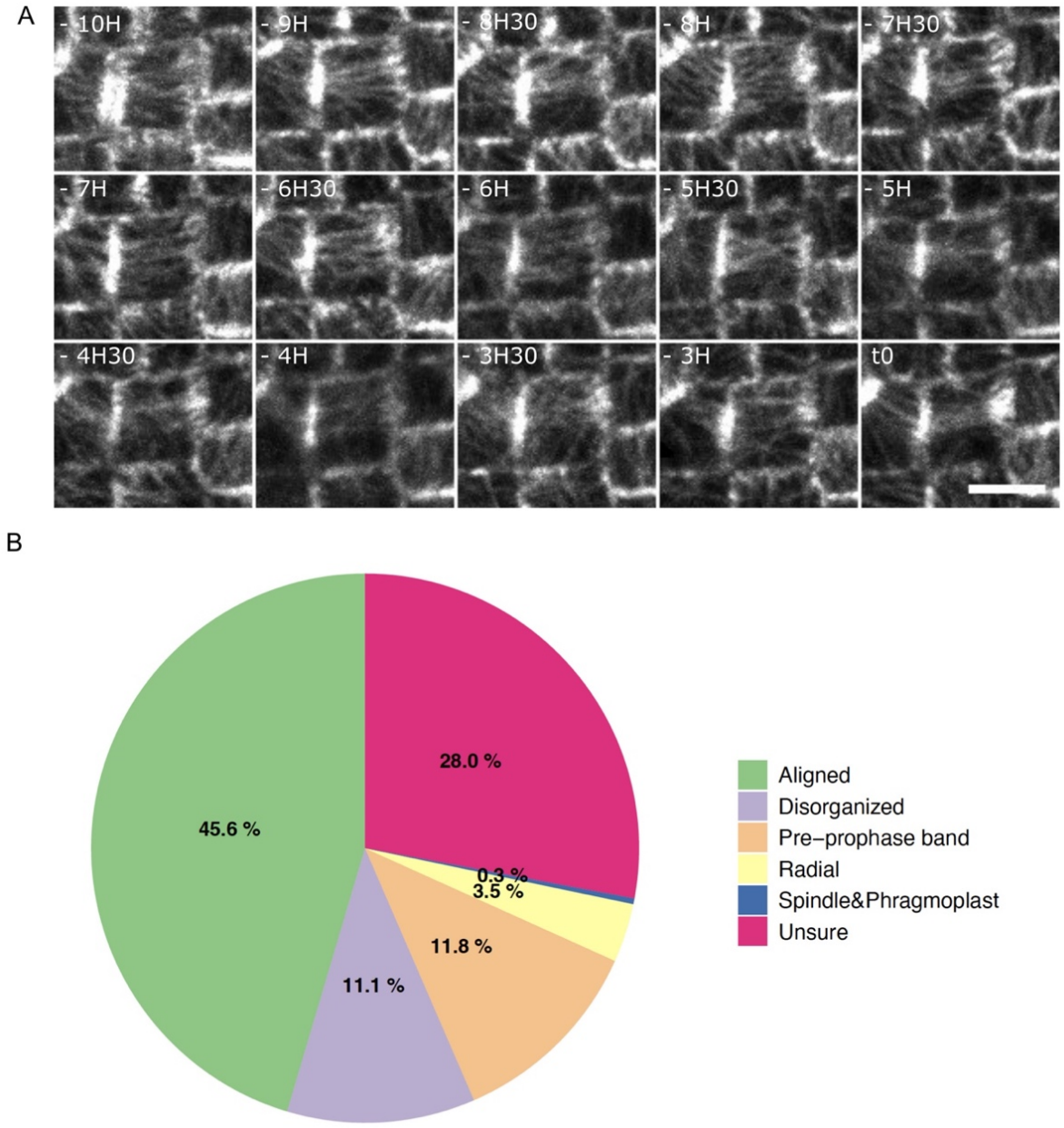

Figure R1: Radial array of CMTs in pre-mitotic cells at the shoot apical meristem. (A) Other example of a time lapse showing CMTs dynamics before the establishment of the PPB. From -10 hours to -6 hours, CMTs maintain a stable orientation. From -5h30 onwards, CMTs exhibit less consistent orientations, up to PPB formation. Images are SurfCut projections of the area between 0 and 4 µm of the surface of the *pPDF1::mCitrine-MBD* signal. Scale bar: 5 µm. The Brightness and Contrast parameters have been modified for a better visualization of the microtubules. (B) Pie chart representing the average percentages of the different organizations of CMT arrays in shoot apical meristems. Aligned reflect the directional organization, typically at interphase. PPB corresponds to the cells where a clear band of microtubules is observed. Radial shows the radial array we described above. Spindle/Phragmoplast corresponds to cells that are undergoing mitosis. Disorganized is when the array is visible, but all of the above categories are not suited to describe it, whereas unsure reflets cells where no clear classification could be made (either the resolution was too low or the image was blurry). These classifications were made qualitatively on a total of 4 shoot apical meristems, where only the central zone was observed.

To explore this further, we needed higher spatial resolution. This led us to analyze this behavior in the stem from *in vitro*-grown plants. We focused on the stem region immediately below the shoot apical meristem, a region of active cell division, where cells are 2 to 3-fold larger (Figure R3). Using cell-cell adhesion mutants, we previously demonstrated that the *Arabidopsis* stem exhibits a stereotypical and stable tensile stress pattern, with a maximum in the transverse orientation (Verger *et al.*, 2018). In this tissue, we confirmed the presence of a strong and global bias of CMTs, towards the circumferential orientation (Figure R2), parallel to the predicted maximal tensile stress (Verger *et al.*, 2018; Figure R3C). Again, when analyzing individual cells over time, we consistently observed a switch from the interphasic alignment of the MT array to a radial array before the formation of the PPB (Figure R3D). In order to increase the number of observable dividing cells, we analyzed cell division in stems from plants grown *in-vitro* on cytokinin-supplemented medium (ACM medium). This readily increased the number of dividing cells imaged in time-lapses: we observed 24 dividing cells on 2 independent stems on ACM medium, vs. 13 dividing cells on 4 independent stems on the growth Arabidopsis Medium (AM). A transient radial CMT behavior could be observed in all cases (Figure R3E). Note that this result was also confirmed when using a *pUBQ10::RFP-TUA6* marker line, albeit with lower spatial resolution (Figure R4A). From 5 time-lapse experiments with a time resolution of 1 hour, we estimated that this behavior preferentially occurred around 3 hours before cell division, lasts for about 2 hours, and is followed by the formation of the PPB (Figure R3D).

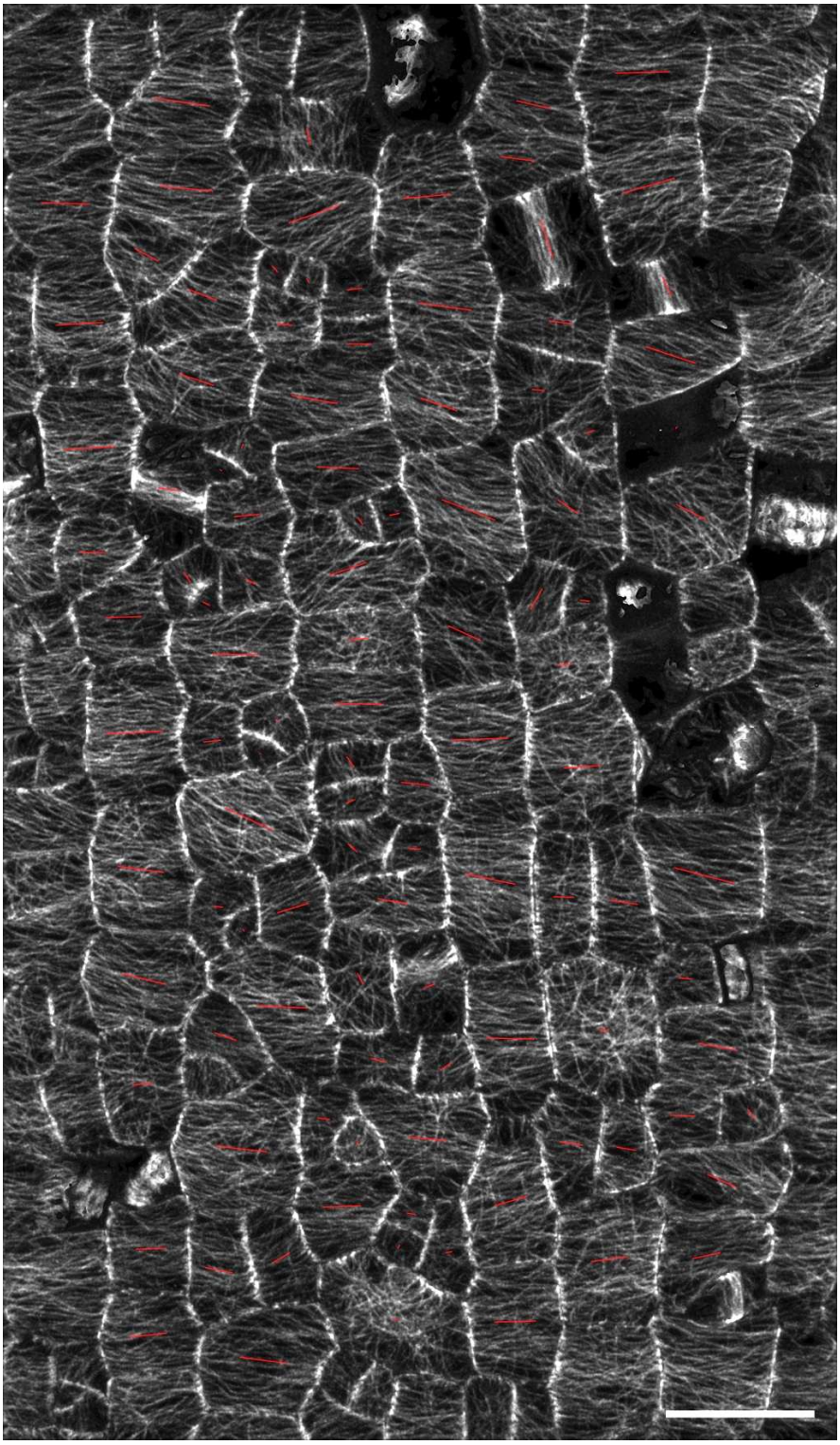

Figure R2: Average CMT orientations in an *Arabidopsis* stem. This image represents the projection of the *pPDF1::mCitrine*-MBD signal between 0 and 4 µm, using SurfCut. Cells were segmented manually, and the average orientation of CMTs was extracted and displayed, using an automated version of the FibrilTool plugin in Fiji (http://doi.org/10.5281/zenodo.2528872). The red lines represent the average orientation of CMTs. The length of the line corresponds to the anisotropy of the CMT arrays: the longer the line, the higher the anisotropy value. Most of the cells display transverse CMTs, following the predicted maximal tensile stress pattern. Scale bar: 20 µm. The Brightness&Contrast was modified for better visualization.

To go beyond these qualitative observations, we measured the distribution of orientations of the CMT arrays using the Directionality plugin in ImageJ for each time-lapse experiment. In all quantifications, time 0 corresponds to the closest timepoint preceding nuclear envelope breakdown, as inferred from the disruption of the PPB, and the initiation of the mitotic spindle. As expected, at t = -4 hours, we found a bias towards the transverse orientation (-2.8° at -4 hours; 1st quartile = -10.6°, 3rd quartile = 12.1°), which corresponds to the transverse axis of the stem (also the predicted maximal tensile stress direction) (Figure R3F, n=34 cells). From 1 hour before t=0 up to PPB formation, CMT arrays also exhibited an orientation bias, reflecting the PPB orientation (Figure R3F, n=37 cells). However, 3 to 2 hours before t=0, the bias was much weaker (-11.9 ° at -3 hours; 1st quartile = -65.7°, 3rd quartile = 20.2° ; -23.6° at -2 hours; 1st quartile = -90°, 3rd quartile = 5.1°) (Figure R3F, n=35 cells). To assess the statistical differences between CMT orientation distribution at each timepoints, we performed Kolmogorov-Smirnoff tests. We found differences to be statistically significant between -2 or -3 hours and earlier timepoints, meaning that the radial array of CMTs appear significantly different from previous interphasic CMT co-alignments (Figure R6). As a negative control, we also found no statistical differences between the distributions at -6 hours and -5 hours, or between the distributions at -3 hours and -2 hours, at a threshold of 0.05 (Figure R6).

Figure R3 (next page): A transient pre-PPB radial pattern of CMTs in the meristem and the stem. (A) Top view of the shoot apical meristem expressing the *pPDF1::mCitrine-MBD* marker. Red arrows indicate a predicted isotropic tensile stress pattern in the central zone. (B) Time-lapse of a pre-mitotic cell of the SAM, showing the CMT dynamics before the formation of the PPB, using the *pPDF1::mCitrine-MBD* marker line. CMT organization changes from co-aligned arrays (-10h to -7h30) to radial arrays (-7h to -6h) before the start of PPB maturation. (C) Side view of the stem expressing the *pPDF1::mCitrine-MBD* marker. Red arrows indicate the transverse direction of maximal tensile stress, as demonstrated in (17). (D, E) Time lapse of pre-mitotic cells in the stem, showing CMT dynamics before PPB formation, using the *pPDF1::mCitrine-MBD* marker line on the growth medium (AM, D) and cytokinin-supplemented medium (ACM, E). Note the presence of radial CMTs ca. 3 hours before cell division. (F) Distribution of CMT orientations overtime in cells from the stem. The angle scale varies between -90° and +90°, 0° being the transverse orientation to the stem axis. Each row represents the time before t=0 (last timepoint before the nuclear envelope breakdown). Each color-coded curve represents the results obtained for one cell. $n_{-6\ hrs} = 20$; $n_{-5\ hrs} = 25$; $n_{-4\ hrs} = 34$; $n_{-3\ hrs} = 35$; $n_{-2\ hrs} = 37$; $n_{-1\ hr} = 37$; $n_{t0} = 37$. (G) Schematic summary of the transition between the aligned, interphasic CMT array and the PPB array. The top panel illustrates the simplest scenario, and the bottom panel recapitulates the observations made with the time-lapse experiments. (H) Graphical representation of the evolution of the anisotropy values obtained with FibrilTool overtime (** p-value < 0.01, Tuckey test). $n_{-6\ hrs} = 21$; $n_{-5\ hrs} = 26$; $n_{-4\ hrs} = 35$; $n_{-3\ hrs} = 36$; $n_{-2\ hrs} = 38$; $n_{-1\ hr} = 38$; $n_{t0} = 39$. The cells used for analysis in (G, H) were from stems imaged on either AM or ACM media. For all images in this figure, SurfCut projections were used, projecting the mCitrine signal between 0 and 4 µm from the surface. The Brightness & Contrast parameters have been modified for a better visualization of CMTs. Scale bars: 10 µm (A, C) ; 5 µm (B, D, E).

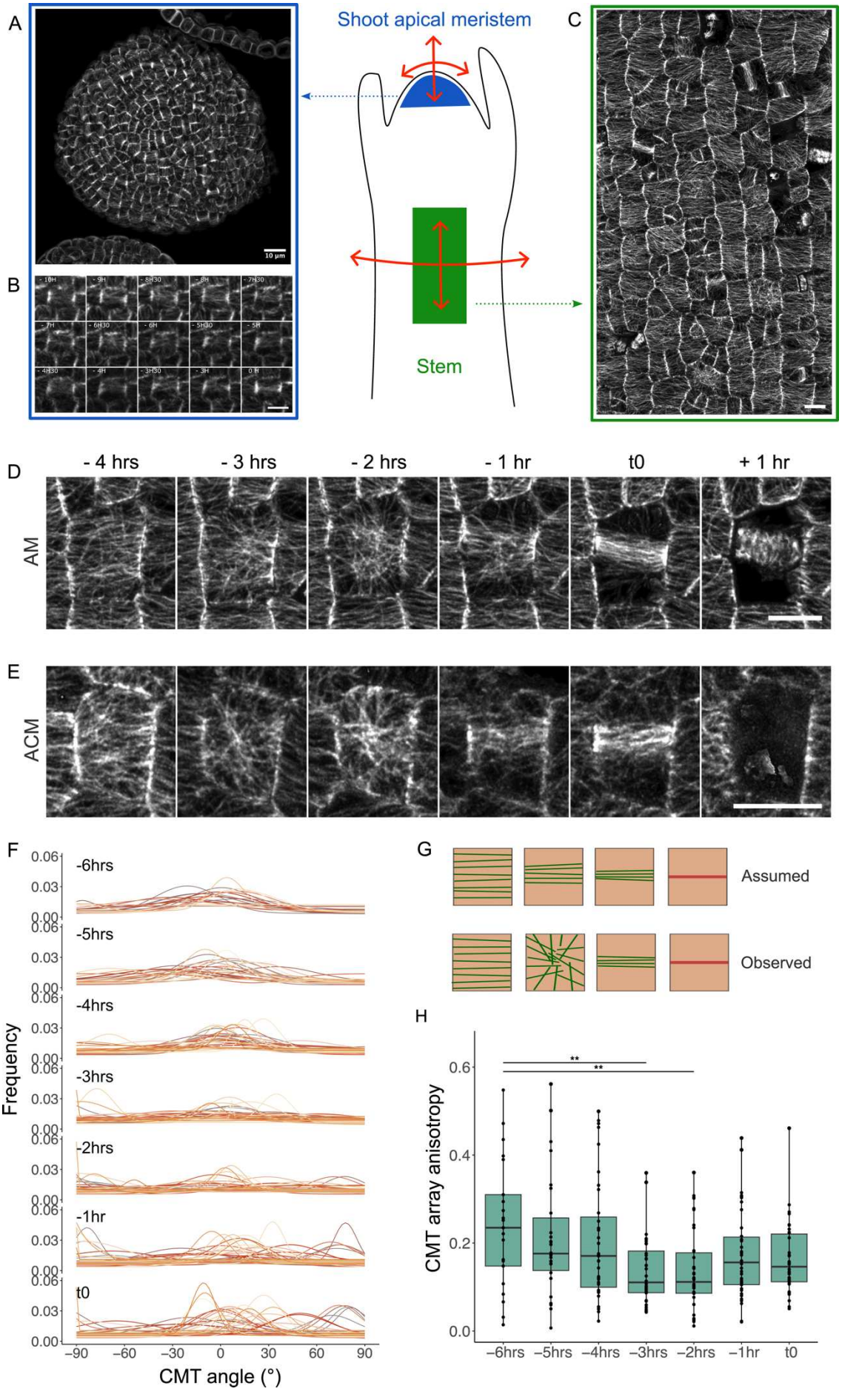
A
B
C
Shoot apical meristem
Stem
D
- 4 hrs
- 3 hrs
- 2 hrs
- 1 hr
t0
+ 1 hr
AM
E
ACM
F
-6hrs
-5hrs
-4hrs
-3hrs
-2hrs
-1hr
t0
Frequency
CMT angle (°)
G
Assumed
Observed
H
CMT array anisotropy
−6hrs
−5hrs
−4hrs
−3hrs
−2hrs
−1hr
t0

To confirm this observation, we used the FibrilTool plugin in ImageJ (Boudaoud *et al.*, 2014) to quantify the anisotropy of the CMT arrays in each cell and analyzed the anisotropy distribution per time point (Figure R4B). This analysis revealed a drop in the anisotropy value two to three hours before t=0 (Figure R3H, n=36 cells). Anisotropy then increased again from 1 hour before t=0 up to PPB maturation (Figure R3H, n=38 cells). Based on these quantifications, we established that, in the stem, the radial array starts ca. 3 hours before the PPB formation and lasts for ca. 2 hours until the start of the PPB maturation. This finding thus challenges the often assumed continuity between interphasic CMTs and PPB (Figure R3G). We propose to call this stage where CMTs form a radial pattern 3 hours before cell division, the "radial step".

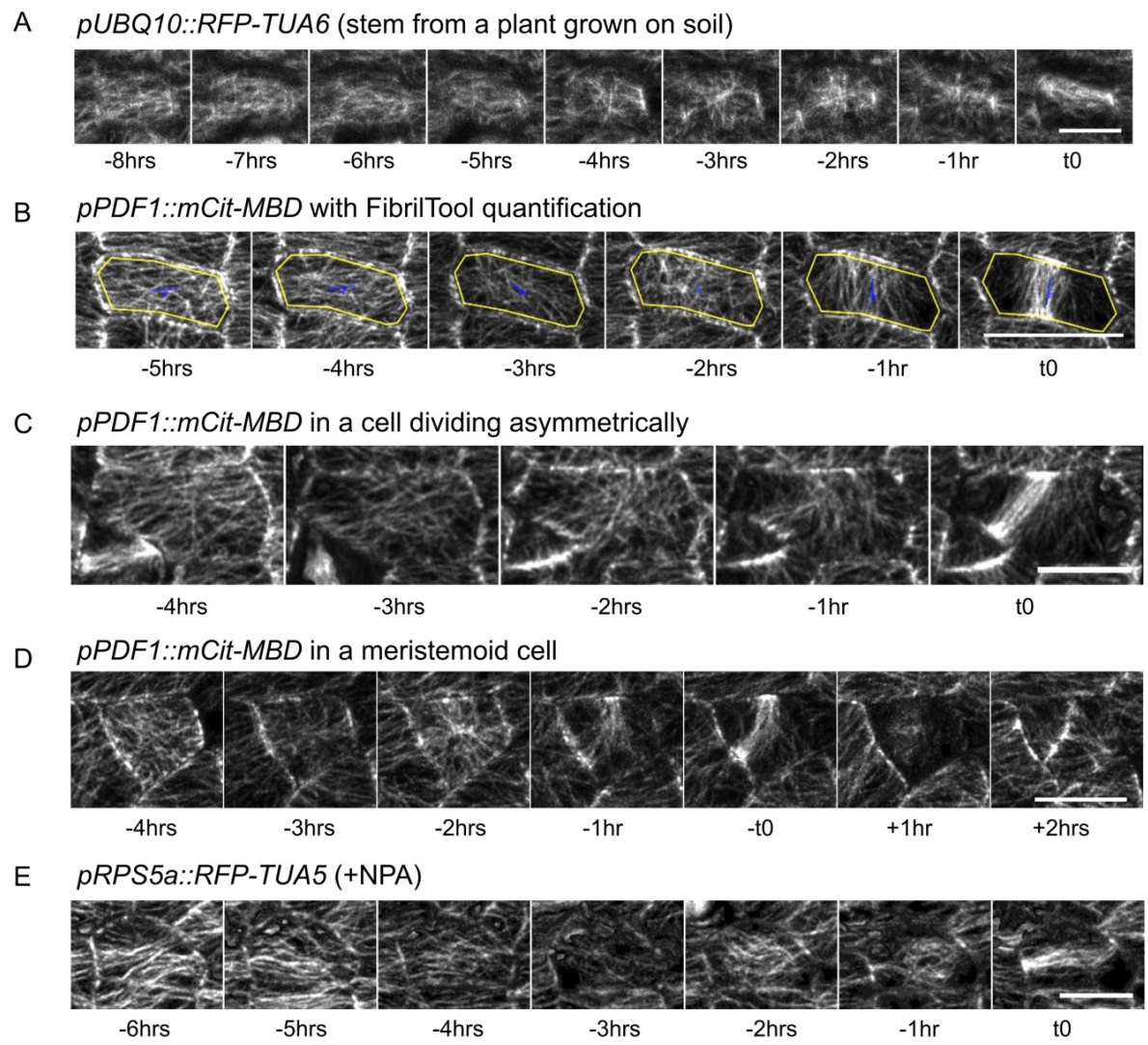

Figure R4: Additional evidence of radial CMTs before cell division. (A) CMT dynamics before cell division in stems, using the *pUBQ10::RFP-TUA6* marker line grown on soil. (B) Example of FibrilTool measurement: the yellow contour defines the region of interest from which the measurements are made. The blue line represents the anisotropy of the CMT arrays with its length, and the predominant orientation of the CMTs with its orientation. (C) Example of CMT dynamics in an asymmetrically dividing cell. (D) Example of CMT dynamics in a meristemoid cell (dividing asymmetrically). (E) CMT dynamics before cell division in stems, using the *pRPS5a::RFP-TUA5*, with NPA from germination on plants grown in vitro. All images reveal the fluorescent signal, and are SurfCut projections from 0 to 4 μm from the surface of the stem. Scale bars: 10 μm. The Brightness&Contrast was modified for better visualization.

2. The radial step can be uncoupled from cell shape and final division plane orientation

To assess whether the radial step relates to cell division plane orientation, we analyzed its behavior in cells of different shapes. In stem tissues, isodiametric cells tend to divide perpendicular to the stem axis (Figure R5B), whereas elongated cells tend to divide along the shortest plane (Figure R5C). Such difference could be related to cellular stress patterns, as inferred from the curvature of the outer wall: the shape of elongated cells prescribes transverse derived maximal tensile stress direction (Figure R5A), whereas the shape of isodiametric cells prescribes isotropic tensile stress direction (Louveaux *et al.*, 2016). Note that in contrast to the tensile stress pattern in the stem, which was experimentally validated (Verger *et al.*, 2018), this cell-shape-derived stress pattern is only predicted from a pressure vessel model of an epidermal cell (Louveaux *et al.*, 2016; Sampathkumar *et al.*, 2014). We thus explored whether the radial step may depend on differences in cell shape and/or related stress pattern.

Figure R5 (next page): The radial step occurs independently of cell shape or polar auxin transport. (A) Diagram representing the predicted tensile stress patterns for epidermal cells in stems. The cylindrical shape of the stem prescribes maximal tensile stress transverse to the stem axis. At cell scale, the minor axis of the cell is also the predicted tensile stress maximal direction. Depending on cell orientation, tissue stress and cell shape-derived stress are synergistic or antagonistic (B) Representative example of a cell expressing the *pPDF1::mCitrine-MBD* marker, with its major axis parallel to the stem axis. The cell forms a radial CMT organization before dividing perpendicular to the stem axis. (C) Representative example of a cell expressing the *pPDF1::mCitrine-MBD* marker, with its major axis perpendicular to the stem axis. The cell forms a radial CMT organization before dividing parallel to the stem axis. (D) Dotplot representing the orientation relative to the stem of the PPB or division planes of cells, in the stem in function of their aspect ratio (the ratio between the longest and the shortest axis of an ellipse fitted around the cell contours). The color code reflects the angle between the major axis of the cell and the stem axis. Light colors highlight cells with their longest axis along the stem axis, dark colors highlight cells with their longest axis transverse to the stem axis. (E) Same as (D), with normalized the data to fit a logistic regression (scale 0 to 1), using the glm function in R studio ($R^2 = 0.312$). (D, E) $n = 141$. (F) Time lapse showing pre-miotic cells in the stem expressing the *pPDF1::mCitrine-MBD* marker, with NPA from germination. (G) Same as (D), with NPA from germination. (H) Same as (E), with NPA from germination ($R^2 = 0.457$). (G, H) $n = 166$. (I) Same as Figure 1D, with NPA from germination. $n_{\text{-6 hrs}} = 29$; $n_{\text{-5 hrs}} = 30$; $n_{\text{-4 hrs}} = 41$; $n_{\text{-3 hrs}} = 45$; $n_{\text{-2 hrs}} = 45$; $n_{\text{-1 hr}} = 47$; $n_{t0} = 58$. (J) Distribution of CMT angles normal to the stem axis overtime from NPA-treated plants using the OrientationJ - vector field function in Fiji. $n_{\text{-6 hrs}} = 159$; $n_{\text{-5 hrs}} = 50$; $n_{\text{-4 hrs}} = 47$; $n_{\text{-3 hrs}} = 107$; $n_{\text{-2 hrs}} = 165$; $n_{\text{-1 hr}} = 228$; $n_{t0} = 244$. *p*-values from the result of a Kolmogorov-Smirnoff statistical test comparing the distribution of the data to a uniform distribution: $p_{\text{-6 hrs}} < 2.2e\text{-}16$; $p_{\text{-5 hrs}} < 2.2e\text{-}16$; $p_{\text{-4 hrs}} = 2e\text{-}10$; $p_{\text{-3 hrs}} = 1e\text{-}05$; $p_{\text{-2 hrs}} = 4e\text{-}09$; $p_{\text{-1 hr}} = 3e\text{-}14$; $p_{t0} < 2.2e\text{-}16$. (K) same as (J) but for cells with an aspect ratio below 0.6 (most elongated cells). $n_{\text{-6 hrs}} = 63$; $n_{\text{-5 hrs}} = 15$; $n_{\text{-4 hrs}} = 19$; $n_{\text{-3 hrs}} = 45$; $n_{\text{-2 hrs}} = 73$; $n_{\text{-1 hr}} = 93$; $n_{t0} = 101$. *p*-values from the result of a Kolmogorov-Smirnoff statistical test comparing the distribution of the data to a uniform distribution: $p_{\text{-6 hrs}} < 2.2e\text{-}16$; $p_{\text{-5 hrs}} = 3e\text{-}02$; $p_{\text{-4 hrs}} = 1e\text{-}02$; $p_{\text{-3 hrs}} = 2e\text{-}04$; $p_{\text{-2 hrs}} = 2e\text{-}11$; $p_{\text{-1 hrs}} = 1e\text{-}09$; $p_{t0} = 2e\text{-}13$. (L) same as (J) but for cells with an aspect ratio above 0.6 (most isodiametric cells). $n_{\text{-6 hrs}} = 96$; $n_{\text{-5 hrs}} = 35$; $n_{\text{-4 hrs}} = 28$; $n_{\text{-3 hrs}} = 62$; $n_{\text{-2 hrs}} = 92$; $n_{\text{-1 hr}} = 135$; $n_{t0} = 143$. *p*-values from the result of a Kolmogorov-Smirnoff statistical test comparing the distribution of the data to a uniform distribution: $p_{\text{-6 hrs}} < 2.2e\text{-}16$; $p_{\text{-5 hrs}} < 2.2e\text{-}16$; $p_{\text{-4 hrs}} = 2e\text{-}09$; $p_{\text{-3 hrs}} = 6e\text{-}03$; $p_{\text{-2 hrs}} = 8e\text{-}05$; $p_{\text{-1 hr}} < 2.2e\text{-}16$; $p_{t0} < 2.2e\text{-}16$. The cells used for analysis in (D, E) were from stems imaged on either AM or ACM media. The cells used for analysis in (G-L) were from stems imaged on ACM medium supplemented with NPA. All images are SurfCut projections between 0 to 4 µm from the surface of the mCitrine signal. Scale bars: 5 µm.

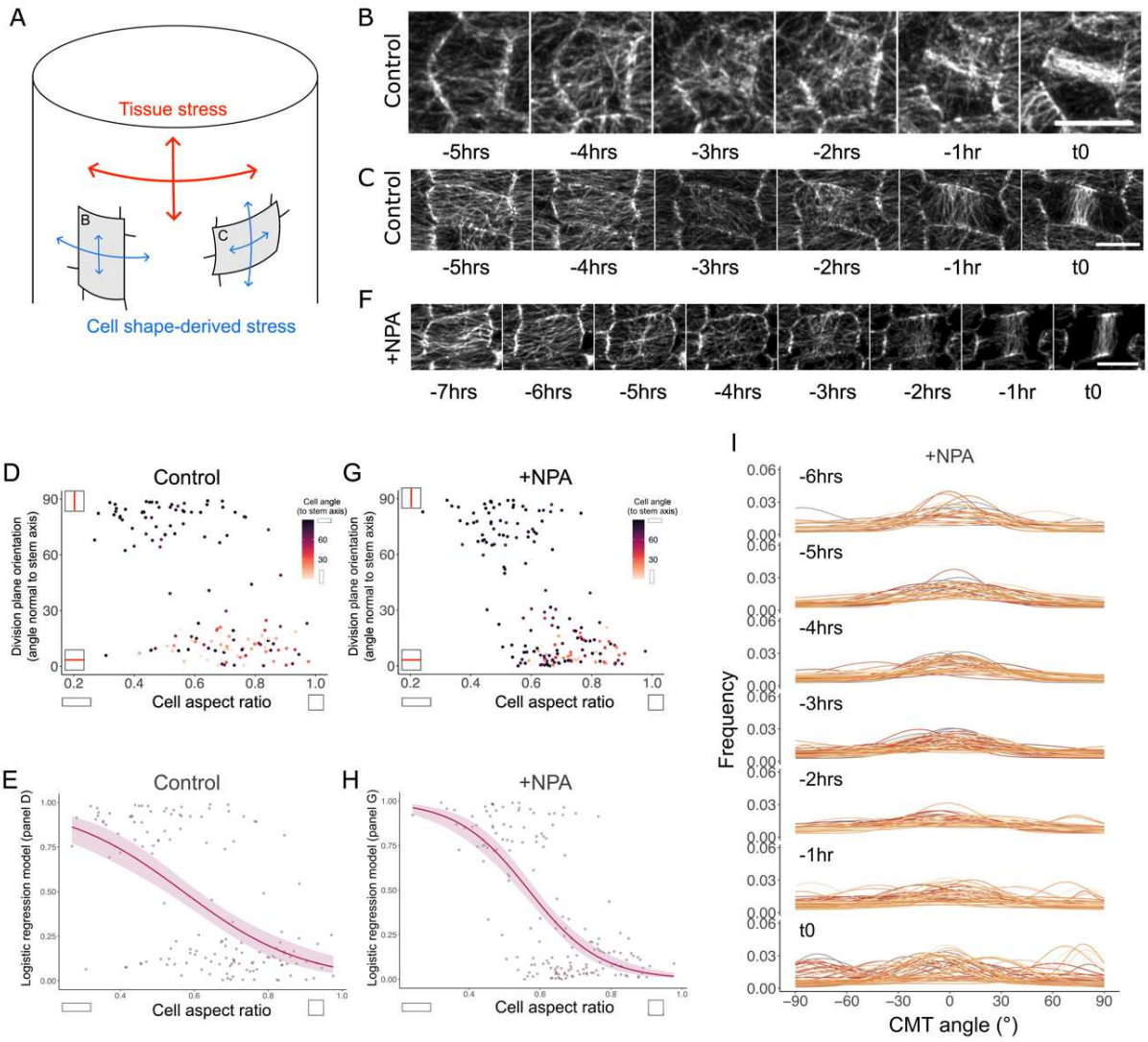
A
Tissue stress
B
C
Cell shape-derived stress
B
Control
-5hrs
-4hrs
-3hrs
-2hrs
-1hr
t0
C
Control
-5hrs
-4hrs
-3hrs
-2hrs
-1hr
t0
F
+NPA
-7hrs
-6hrs
-5hrs
-4hrs
-3hrs
-2hrs
-1hr
t0
D
Control
Division plane orientation (angle normal to stem axis)
Cell angle (to stem axis)
Cell aspect ratio
G
+NPA
Division plane orientation (angle normal to stem axis)
Cell angle (to stem axis)
Cell aspect ratio
I
+NPA
-6hrs
-5hrs
-4hrs
-3hrs
-2hrs
-1hr
t0
Frequency
CMT angle (°)
E
Control
Logistic regression model (panel D)
Cell aspect ratio
H
+NPA
Logistic regression model (panel G)
Cell aspect ratio
J
CMT angle normal to the stem axis (°)
-6hrs
-5hrs
-4hrs
-3hrs
-2hrs
-1hr
t0
K
CMT angle normal to the stem axis (°)
-6hrs
-5hrs
-4hrs
-3hrs
-2hrs
-1hr
t0
L
CMT angle normal to the stem axis (°)
-6hrs
-5hrs
-4hrs
-3hrs
-2hrs
-1hr
t0

To monitor this quantitatively, we calculated the cell aspect-ratio and plotted cell division orientation with respect to the stem axis, using either the PPB as a predictor of the future division plane, or the plasma membrane resulting from a division (Figure R5D, n=141 cells). This confirmed a dual behavior according to cell aspect ratio, at least for cells with an extreme aspect ratio. In particular, more isodiametric cells tend to display division planes perpendicular to the stem axis (i.e. parallel to predicted maximal tissue stress); whereas more elongated cells displayed division planes rather parallel to the stem axis (i.e. perpendicular to maximal tissue stress) (Figure R5D). In order to find the threshold value at which cells switch their behavior, we fitted a logistic regression using the binomial method of the generalized linear models in R (with a *p*-value of $3.40e^{-11}$). This method only partially fit the data ($R^2 = 0.312$), due to the bimodal distribution of division plane orientations and noise in division orientation in either group, but allowed us to successfully retrieve an inflection point at 0.6 (Figure R5E, see Material and methods). To monitor the orientation of division relative to the cell axis, we measured the orientation of the long axis of the cell relative to the axis of the stem. These measurements revealed that most anisotropically shaped cells were elongated transversely to the stem ("C cell" in Figure R5A, see Cell angle color code in Figure R5D), implying that their shortest axis, and thus the maximal tension derived from the cell shape, was orthogonal to the tissue-derived maximal tensile stress. Taking advantage of this dual behavior according to cell shape, we could confirm that in the stem, cells with an aspect ratio below 0.6 tend to divide following cell-shape-derived tension, respecting the local minima rule (Besson and Dumais, 2011). The ones with an aspect ratio above 0.6 (rounder cells) tend to divide following the tissue-derived maximal tensile stress, that is perpendicular to the stem axis. It is worth noting that the few cells with an aspect ration below 0.6 that were elongated along the stem axis divided perpendicularly to the stem, following both cell-derived and tissue-derived maximal tension.

Even though the conflict between maximal tension orientations derived from the cell shape or the tissue may affect the positioning of the division plane, the radial step was comparable in both types of cells, whether these were elongated (Figure R5B) or not (Figure R5C). We also confirmed this quantitatively with the Directionality measurements, by creating two data subsets: one for cells with a PPB oriented along the stem axis, and the other for cells with a PPB perpendicular to the stem axis. In both cases, the CMT array underwent the radial step (Figures R7A and R7B). To further confirm that the radial step appears independently of the final division plane orientation, we observed asymmetrically dividing cells in stems, and we could find a radial step again around 3 hours before cell division (Figure R4C and R4D).

A)

WT (Control)	**-6 hrs**	**-5 hrs**	**-4 hrs**	**-3 hrs**	**-2 hrs**	**-1 hr**	**t0**
-6 hrs	XXXXX	0.1646	$5.02e^{-06}$	$< 2.2e^{-16}$	$< 2.2e^{-16}$	$7.10e^{-04}$	$1.84e^{-11}$
-5 hrs	XXXXX	XXXXX	$8.00e^{-07}$	$< 2.2e^{-16}$	$< 2.2e^{-16}$	0.00591	$4.76e^{-10}$
-4 hrs	XXXXX	XXXXX	XXXXX	2.18e-13	$4.90e^{-10}$	2.15e-14	$< 2.2e^{-16}$
-3 hrs	XXXXX	XXXXX	XXXXX	XXXXX	0.3048	$< 2.2e^{-16}$	$< 2.2e^{-16}$
-2 hrs	XXXXX	XXXXX	XXXXX	XXXXX	XXXXX	$< 2.2e^{-16}$	$< 2.2e^{-16}$
-1 hr	XXXXX	XXXXX	XXXXX	XXXXX	XXXXX	XXXXX	$1.54e^{-05}$
0	XXXXX	XXXXX	XXXXX	XXXXX	XXXXX	XXXXX	XXXXX

B)

WT (+ NPA)	**-6 hrs**	**-5 hrs**	**-4 hrs**	**-3 hrs**	**-2 hrs**	**-1 hr**	**t0**
-6 hrs	XXXXX	0.1548	0.1552	$7.18e^{-05}$	$< 2.2e^{-16}$	$3.62e^{-04}$	$< 2.2e^{-16}$
-5 hrs	XXXXX	XXXXX	0.6853	$8.33e^{-04}$	$< 2.2e^{-16}$	0.005563	$< 2.2e^{-16}$
-4 hrs	XXXXX	XXXXX	XXXXX	$9.04e^{-05}$	$< 2.2e^{-16}$	$2.21e^{-04}$	$< 2.2e^{-16}$
-3 hrs	XXXXX	XXXXX	XXXXX	XXXXX	< 2.2e-16	0.763	$< 2.2e^{-16}$
-2 hrs	XXXXX	XXXXX	XXXXX	XXXXX	XXXXX	$< 2.2e^{-16}$	$< 2.2e^{-16}$
-1 hr	XXXXX	XXXXX	XXXXX	XXXXX	XXXXX	XXXXX	$< 2.2e^{-16}$
0	XXXXX	XXXXX	XXXXX	XXXXX	XXXXX	XXXXX	XXXXX

Figure R6: *p*-value results for Kolmogorov-Smirnoff tests, comparing the distributions of CMT orientations under control conditions (A), or NPA conditions (B), between the different timepoints. The dataset used for this test was the results obtained with the Directionality plugin in Fiji. The null hypothesis for the Kolmogorov-Smirnoff test is "There are no differences between the two distributions".

3. The radial step can be uncoupled from polar auxin transport

Our analysis so far shows that the radial step is independent of cell shape variability. Next, we investigated whether the radial step depends on larger polarizing cues. To do so, we impaired polar auxin transport using Naphtylphtalamic acid (NPA), as auxin has previously been shown to affect cell division rate in roots (Ai *et al.*, 2023) and plane orientation in embryos (Yoshida *et al.*, 2014). We grew plants on NPA-containing medium and, using the same *pPDF1::mCitrine-MBD* marker line, we observed the effect of NPA on CMT organization in stems. Note that the inhibition of flower formation on stems vastly facilitated the imaging and thus significantly increased sample size.

We observed the presence of the radial step before PPB formation in the presence of NPA as well (Figure R5F, n=58 cells). Note that the radial step could also be observed in the *pRPS5a::RFP-TUA5* marker line treated with NPA (Figure R4E). This demonstrates that the occurrence of the radial step is not dependent upon polar auxin transport. However, the duration of the radial step was longer with NPA (ca. 3 hours) than in its absence (ca. 2 hours) (Figure R5F and R5I, Figure R4E). While cells were usually more isodiametric on NPA than in absence of NPA, the division plane orientation followed a bimodal distribution (transverse or longitudinal) similar to untreated cells (Figure R5G and R5H, n=194 cells). We also fitted a logistic regression with the *glm* function in R to the data and found an inflection point at 0.6 as well (p-value $< 2.2e^{-16}$). The function fit the data better than in control conditions ($R^2 = 0.457$), probably due to the larger sample size. This suggests that the observation that cells tend to divide following the maximal tension derived either from their shape, or from the tissue is dependent on their aspect ratio, remains true in NPA conditions. When dividing the data in two subsets (one for cells with PPBs following the stem axis, and one for cells with PPBs normal to the stem axis), we could also conclude that occurrence of the radial step is independent of the final orientation of the PPB (Figure R7C and R7D).

Taking advantage of the larger sample size, we next analyzed CMT orientation with respect to the stem axis in NPA-treated plants, using the *OrientationJ* plugin in Fiji. CMTs were reliably perpendicular to the stem axis (i.e. parallel to predicted maximal tensile stress direction) before -3 hours (Figure R5J), and this trend was temporarily lost between -4 hours and -3 hours, with a more uniform distribution of CMT orientations reflecting the radial step (Figure R5J). We then repeated the same analysis for cells with an aspect-ratio below 0.6 (i.e. the most elongated cells, Figure R5K) and above 0.6 (i.e. the most isodiametric cells, Figure R5L). The conclusions were conserved, further confirming that the radial step is independent of cell shape and auxin transport. In the end, most of the elongated cells divided parallel to the stem axis (i.e. perpendicular to maximal tensile stress direction, Figure R5K), in contrast to most isodiametric cells, which divided perpendicular to the stem axis (i.e. parallel to maximal tensile stress direction, Figure R5L). This analysis further confirms that the presence radial step is not dependent on the final cell division plane orientation.

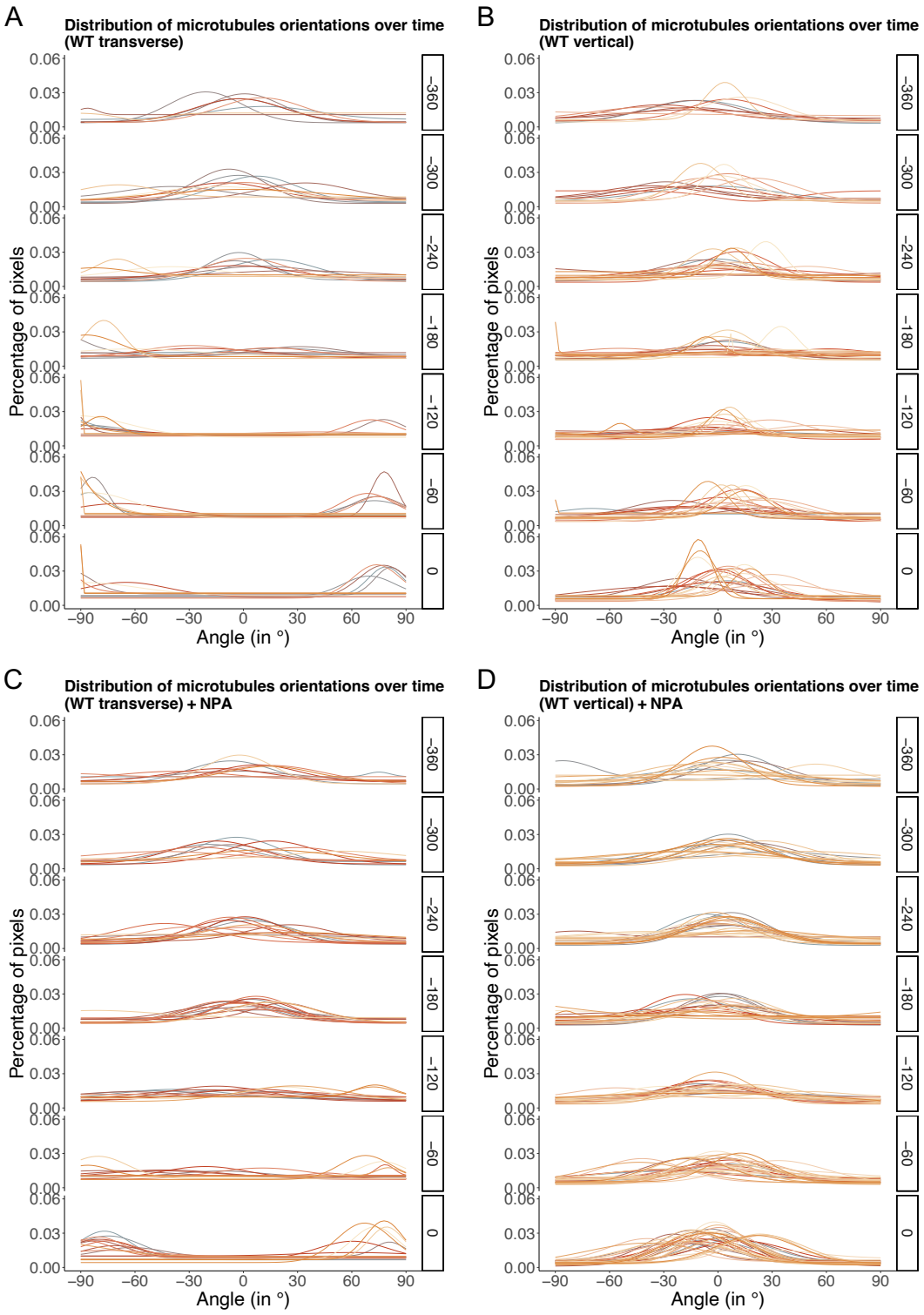

Figure R7: Evolution of CMT orientation over time in WT pre-mitotic cells from the stem, divided in four data subsets. (A-D) The angle scale varies between -90° and +90°, 0° being the transverse orientation to the stem axis. Each row represents the time before t=0 (last timepoint before the nuclear envelope breakdown). Each color-coded curve represents the results obtained for one cell. The dataset used is the same as the one used for Figures 1G and 2I. (A) Results obtained for cells that produce a preprophase band oriented along the stem axis (i.e. between -30° and 30°), grown on media without NPA. (B) Results obtained for cells that produce a preprophase band oriented transverse to the stem axis (i.e. between -60° and -90°, and between 60° and 90°), grown on media without NPA. (C) Similar to (A), for cells grown on NPA conditions. (D) Similar to (B), for cells grown on NPA conditions.

4. The radial step coincides with a pre-mitotic increase in cytoplasmic microtubules when this process is promoted

Because the radial step occurs independently of microtubule markers used, growth media or polar auxin transport, we hypothesized that its presence and timing of appearance is mainly controlled by intrinsic factor(s). In plants, and contrary to many eukaryotes, there is no microtubule organizing center (MTOC) and the formation of new microtubules is mostly distributed, and strongly relies on microtubule-dependent γ-tubulin recruitment and branched nucleation (Liu *et al.*, 1993; Joshi and Palevitz, 1996; Murata *et al.*, 2005). Consistently, γ-tubulin mutants display mitotic and interphasic microtubule defects (Pastuglia *et al.*, 2006). However, there is multiple evidence of microtubule nucleation specifically at the nuclear envelope (Mizuno, 1993; Stoppin *et al.*, 1994) at the end of the G2 phase, before and during PPB formation (Chumová *et al.*, 2019; Wick and Duniec, 1983; Liu *et al.*, 1993). This well-established behavior is generally thought to ensure a connection between the PPB and the nucleus (Wick and Duniec, 1983; Liu *et al.*, 1993), and to provide a population of peri-nuclear microtubules to complete mitotic tasks, such as spindle formation (Yamada and Goshima, 2017; Lee and Liu 2019). Here we investigated whether this behavior also occurs in the stem and whether it temporally correlates with the radial step.

To assess the cytoplasmic microtubule content, we analyzed the microtubule signal in XZ maximal projections, i.e. through anticlinal cell sections, and calculated the ratio between the endoplasmic signal and the cortical signal. As expected, we observed a gradual increase of the internal microtubule content as the cell reached the PPB stage, with an average increase between the first and the last timepoints of 162% (Figure R8A and R8B, Figure R9A). Cytoplasmic microtubules started to accumulate around 3 hours before cell division, i.e. coincident with the radial step.

Figure R8 (next page): The radial array of CMTs correlates with a pre-mitotic increase of internal microtubule content. (A-D) Evolution of cytoplasmic microtubules overtime in WT background (A) or in the trm678 mutant background (C). (A) Time-lapse images of pre-mitotic cells, the top panel being the cortical projection with SurfCut and the bottom panel an orthogonal projection through the cell. Cortex images are 8-bit, with the B&C range varying between 0 and 160, and orthogonal projections are 16-bit, with the B&C range varying between 0 and 1400. (B) Ratio between the average internal signal and the average of the cortical mCitrine-MBD signal over time. The colors correspond to qualitative classifications of cortical arrays (interphasic, radial step and PPB). Each line represents the kinetics for a given cell. $n_{WT, -6\ hrs} = 6$; $n_{WT, -5\ hrs} = 11$; $n_{WT, -4\ hrs} = 16$; $n_{WT, -3\ hrs} = 17$; $n_{WT, -2\ hrs} = 17$; $n_{WT, -1\ hr} = 17$; $n_{WT, t0} = 17$. (C) same as (A) but in the *trm678* mutant. (D) same as (B) but in the *trm678* mutant. $n_{trm678, -6\ hrs} = 6$; $n_{trm678, -5\ hrs} = 7$; $n_{trm678, -4\ hrs} = 7$; $n_{trm678, -3\ hrs} = 14$; $n_{trm678, -2\ hrs} = 15$; $n_{trm678, -1\ hr} = 17$; $n_{trm678, t0} = 19$. (E) Evolution of the ratio of mCitrine-MBD signal (internal/cortical) overtime in WT vs. *trm678*. (F) Evolution of CMT array anisotropy overtime, using the FibrilTool plugin in Fiji. Results from the WT are reproduced here from Figure 1H for ease of reading, to compare with *trm678*. $n_{trm678, -6\ hrs} = 9$; $n_{trm678, -5\ hrs} = 15$; $n_{trm678, -4\ hrs} = 14$; $n_{trm678, -3\ hrs} = 21$; $n_{trm678, -2\ hrs} = 26$; $n_{trm678, -1\ hr} = 28$; $n_{trm678, t0} = 29$. The cells used for analysis in (B, D-F) were from stems imaged on either AM or ACM media. Scale bars: 10 μm (surface projections), 5 μm (orthogonal projections).

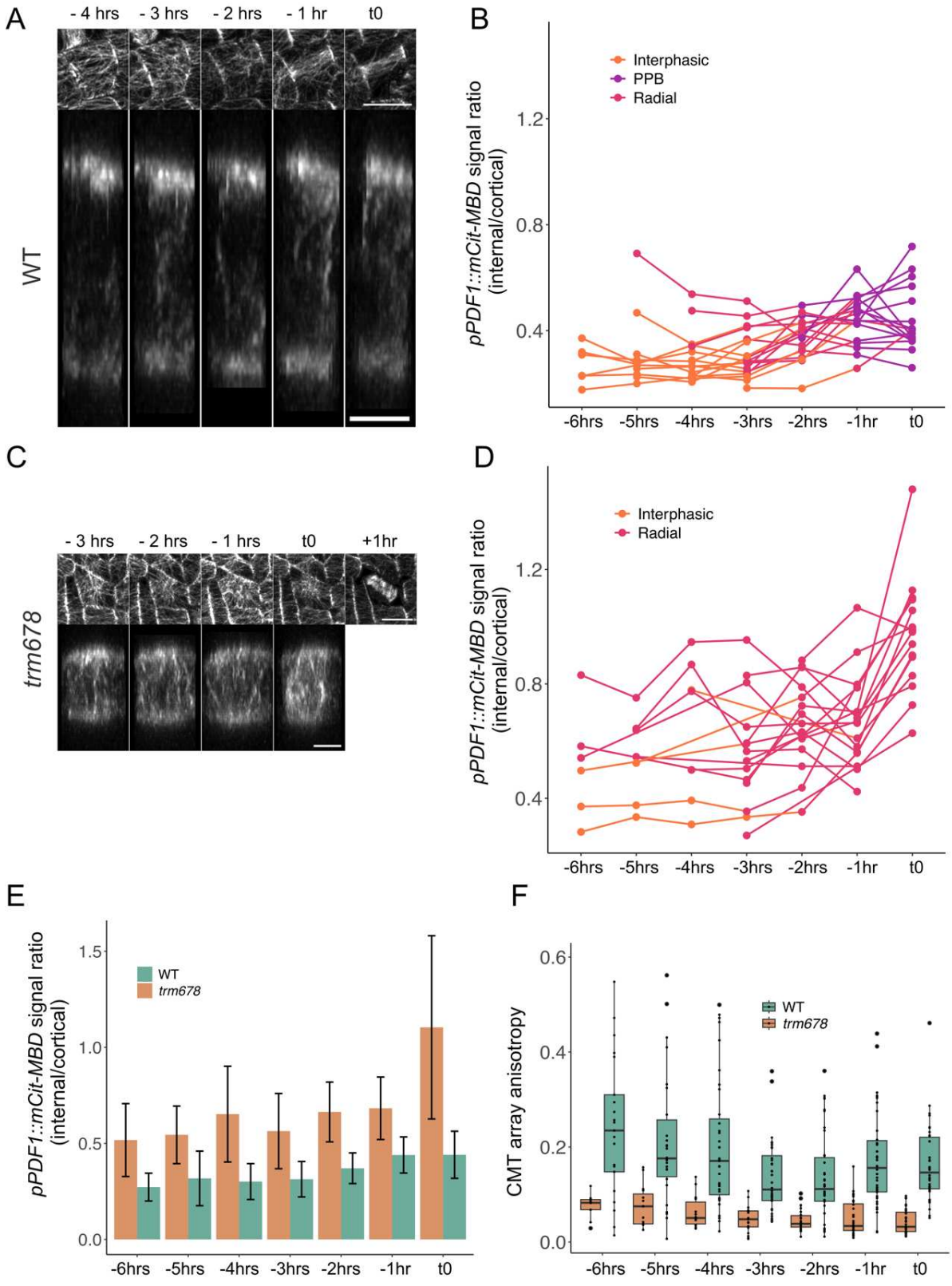
A
- 4 hrs
- 3 hrs
- 2 hrs
- 1 hr
t0
WT
B
Interphasic
PPB
Radial
pPDF1::mCit-MBD signal ratio (internal/cortical)
1.2
0.8
0.4
-6hrs
-5hrs
-4hrs
-3hrs
-2hrs
-1hr
t0
C
- 3 hrs
- 2 hrs
- 1 hrs
t0
+1hr
trm678
D
Interphasic
Radial
pPDF1::mCit-MBD signal ratio (internal/cortical)
1.2
0.8
0.4
-6hrs
-5hrs
-4hrs
-3hrs
-2hrs
-1hr
t0
E
pPDF1::mCit-MBD signal ratio (internal/cortical)
WT
trm678
1.5
1.0
0.5
0.0
-6hrs
-5hrs
-4hrs
-3hrs
-2hrs
-1hr
t0
F
CMT array anisotropy
WT
trm678
0.6
0.4
0.2
0.0
-6hrs
-5hrs
-4hrs
-3hrs
-2hrs
-1hr
t0

To test the connection between the radial step and cytoplasmic microtubule accumulation, we next investigated the radial step in a *trm678* mutant background, grown and imaged in control conditions, as described for the WT. This mutant, as other PPB-deficient mutants, displays a strong accumulation of perinuclear MTs before mitosis (Traas *et al.*, 1995; Schaefer *et al.*, 2017). The *fass* mutant exhibits a slight increase in microtubule nucleation (Kirik *et al.*, 2012), and this could be a feature of most TTP complex mutants, such as *trm678*, with some evidence pointing towards this hypothesis (Sawidis *et al.*, 1991; Traas *et al.*, 1995). Because *ton1* and *fass* mutants exhibit very disrupted interphasic microtubules (Traas *et al.*, 1995), this would hinder the analysis of more subtle changes in CMT behavior, and notably the radial step. Among these PPB-deficient mutants, *trm678* exhibit WT-like interphasic microtubules (Schaefer *et al.*, 2017; Figure R10A), allowing us to investigate the radial step behavior in that background.

The mitotic index was comparable in WT and *trm678* stems (1.56% +/- 1.04% in WT stems, and 2.00% +/- 1.21% in *trm678* stems). In the stem, the average duration of mitosis was roughly 50% longer in *trm678* (ca. 3 hours) than in the WT (ca. 2 hours, Figure R10B and R10C), even though the exact difference is difficult to assess due to our time resolution. As previously seen in the wild-type, we observed a radial step in *trm678* stems (Figure R8C, n = 29 cells). As expected for a PPB-deficient mutant, the division orientations in the *trm678* stems were noisier than in the WT (Figure R8C; Scott *et al.*, 2023), further confirming that the radial step appears independent of final cell division plane orientation. However, the radial step exhibited two unique features in *trm678*. First, it seemed visually clearer than in the WT (Figure R8C). To ascertain this, we measured the anisotropy of CMT arrays in the *trm678* mutant 3 hours before cell division and found it to be half that of the WT, consistent with the observation of a better-defined radial step (p-value = $6{,}05e^{-6}$ at -2 hours, TuckeyHSD test; Figure R8F). Second, the radial step appeared to last much longer than in the WT. The exact average duration of the radial step in *trm678* is difficult to estimate, because in most of our kinetics, the radial step lasted at least 6 hours, and we missed the full sequence (from interphasic CMTs to the radial step to mitosis) within a multi-hour kinetics (Figure R8C and Figure R10A). We could observe that switch only in exceptional cases, i.e. when the radial step was shorter (ca. 4 hours) before cell division (Figure R9B). In the *trm678* mutant, the internal microtubule signal was significantly higher than in the WT, as shown when following individual kinetics (Figure R8D, Figure R9) and when pooling measurements (a 213% increase between t = -6 hours and t = 0, p-value = $2.38e^{-4}$ for *trm678*, and a 162 % increase between t = -6 hours and t = 0, p-value = $1.13e^{-3}$ for the WT, Wilcoxon test, Figure R8E). We also measured the anisotropy of CMT array, using ImageJ FibrilTool, and observed reduced anisotropy in *trm678* on average, when compared to WT, consistent with the prolonged radial step in the mutant (Figure R8F). Since the radial step starts at t = -6 hours or earlier, the anisotropy remains low for the duration of the analyzed time-lapse. However, we could find aligned CMT arrays in the *trm678* mutant during interphase prior to the radial step, when its duration was exceptionally shorter (Figure R9B, R10A). This analysis further suggests that the transient radial organization of CMTs reflects the start of cytoplasmic microtubule accumulation before cell division.

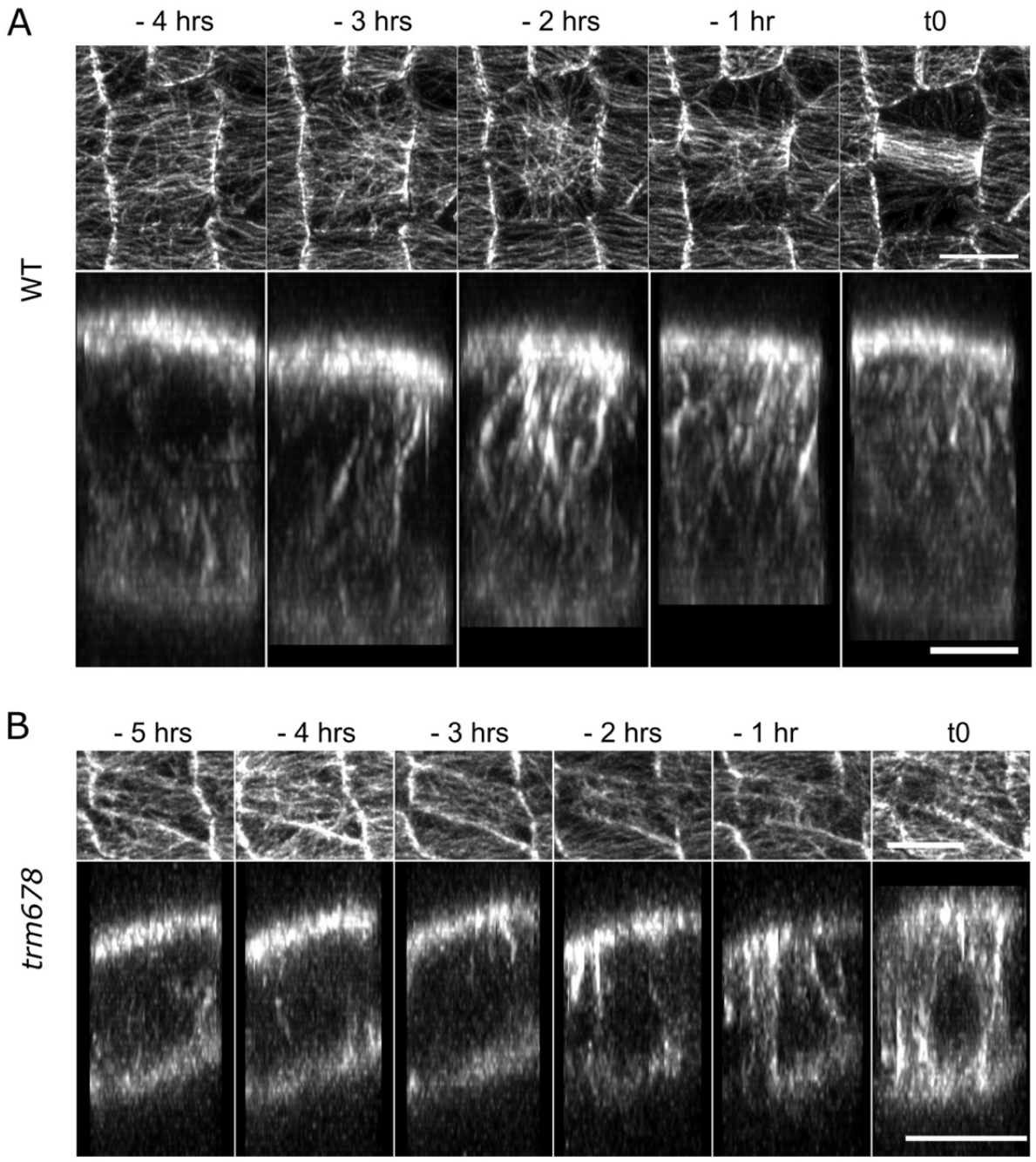

Figure R9: Other examples of the evolution of cytoplasmic microtubule content in pre-mitotic cells. (A) Time-lapse images of pre-mitotic cells, the top panel being the cortical projection with SurfCut and the bottom panel an orthogonal projection through the cell. Cortex images are 8-bit, with the B&C range varying between 0 and 160, and orthogonal projections are 16-bit, with the B&C range varying between 0 and 2600. (B) Same as (A) but in *trm678* mutant cell. Note that this is an exceptional case where the radial step is short in *trm678*, which allows the visualization of the full sequence: interphase - radial step - mitosis, further showing the correlation between radial step and perinuclear microtubule accumulation. Scale bars: 10 μm (surface projections), 5 μm (XZ orthogonal projections).

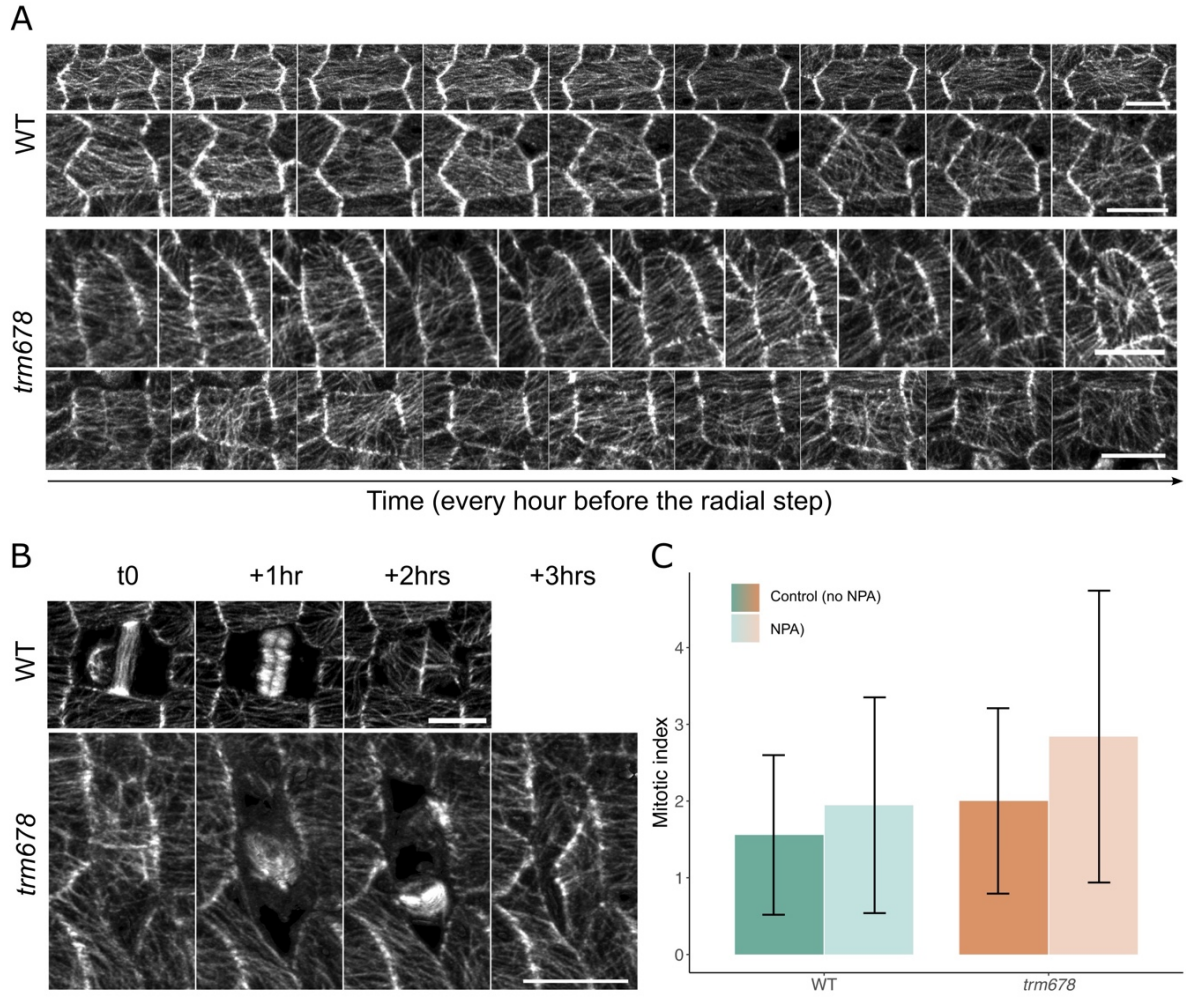

Figure R10: CMT dynamics and mitosis in WT and *trm678* (A) CMT dynamics before the radial step in the WT and *trm678*. Images were taken every hour. (B) CMT behavior during division in a representative WT cell (top panel) and a representative *trm678* cell (bottom panel). The images are SurfCut projections between 0 and 4 µm from the surface of the stem. (C) Mitotic indexes for cells in both genetic background and in control, or NPA conditions. The mitotic index corresponds to the ratio between mitotic cells (where we can observe spindle or phragmoplast structures) and the total number of cells in the image, and is displayed as a proxy for cell cycle duration. *trm678* cells have a slightly higher mitotic index than the WT, and the addition of NPA increases the mitotic index in both backgrounds. $n_{\text{WT, control}} = 12$; $n_{\text{WT, NPA}} = 5$; $n_{\textit{trm678}\text{, control}} = 16$; $n_{\textit{trm678}\text{, NPA}} = 9$. Scale bars: 10 µm. The Brightness&Contrast was modified for better visualization.

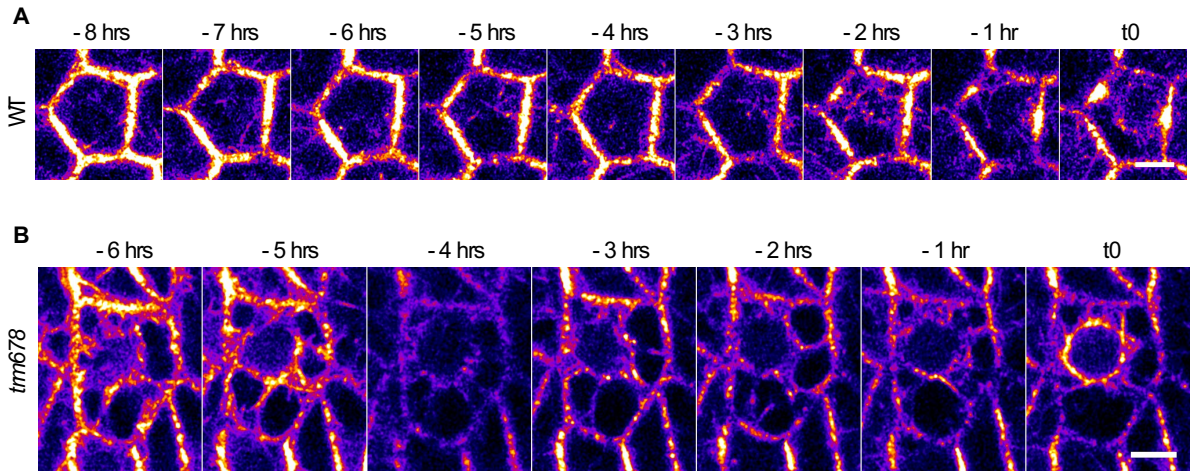

Figure R11: *pPDF1::mCitrine-MBD* signal at the equator of a cell from the stem overtime. (A,B) These images were made showing a single slice of the Z-stack in the middle of the cell. (A) WT cell: these 16-bit images are obtained using the fire Look-up table in Fiji, with the Brightness&Contrast values set between 0 and 1000. (B) *trm678* mutant cell: these 16-bit images are obtained using the fire Look-up table in Fiji, with the Brightness&Contrast values set between 0 and 3000. Scale bars: 5 μm.

5. The presence of the radial step is robust to mechanical perturbations

Altogether, the radial organization of CMTs coincides with increased cytoplasmic microtubule accumulation around the nucleus (Figure R11), which is even more pronounced in the absence of TRM6/7/8. This provides a scenario in which the radial step emerges from a destabilization of CMTs, either from increased connections between CMTs and the nucleus, or from competition between different sites of microtubule nucleation. This also suggests that the radial step reflects a transient disruption of CMT alignment with tensile stress at the outer periclinal wall. To further test that hypothesis, we next investigated whether the radial step is maintained, or not, when the local pattern of tensile stress changes artificially (around ablations) or physiologically (around developing trichomes).

It is well established that a local ablation in a tissue shifts the direction of maximal tensile stress to a circumferential orientation around the ablation site (Hamant *et al.*, 2008). We therefore performed manual ablations with a needle on stems, changing the tensile stress pattern from transverse to the stem axis, to circumferential around the wound site (Figure R13A). In the first few hours after the ablation, cell division was inhibited. However, 15 hours after the ablation, cell divisions reappeared. Importantly, the CMTs were still organized circumferentially around the ablation (Figure R12A, R13B), prompting us to conclude that the tensile stress pattern was still circumferential 15 hours after the ablation. We also observed that the division planes were oriented circumferentially around the ablation site, confirming similar findings previously reported for the shoot apical meristem (Louveaux *et al.*, 2016; Figure R12B). We also noticed that the PPBs were wider than in control conditions, and the formation of the pro-spindles started before the PPB started to depolymerize (Figure R14C and R14D).

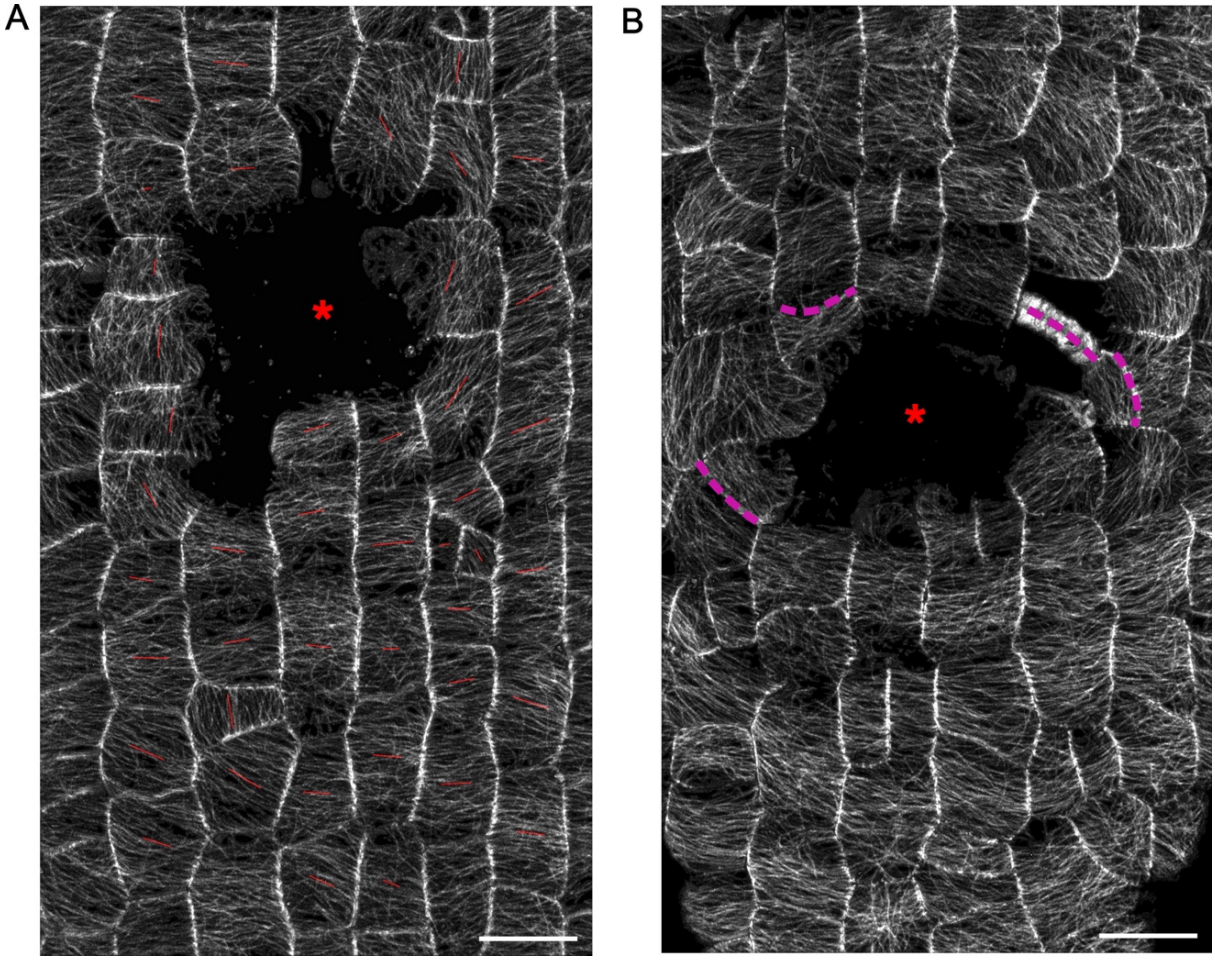

Figure R12: A circumferential tensile stress pattern at ablation sites affects CMT orientation and cell division plane orientations. (A) This image represents the projection of the *pPDF1::mCitrine*-MBD signal between 0 and 4 µm, using SurfCut. Cells were segmented manually, and the average orientation of CMTs was extracted and displayed, using an automated version of the FibrilTool plugin in Fiji (http://doi.org/10.5281/zenodo.2528872). The red lines represent the average orientation of CMTs per cell. The length of the line corresponds to the anisotropy of the CMT arrays per cell: the longer the line, the higher the anisotropy value. The red star represents the ablation site. The cells around the ablation display CMTs that are aligned circumferentially to the ablation site, following the predicted maximal tensile stress pattern induced by the ablation. The cells far from the ablation display CMTs aligned transversely to the stem, following the predicted maximal tension prescribed by the stem. (B) This image is a SurfCut projection, between 0 and 4 µm from the surface, of the *pPDF1::mCitrine-MBD* signal. An ablation was performed on this stem (red star), and this image corresponds to the last image of a time-lapse experiment, 25 hours after the ablation (the experiment started 15 hours after the ablation). The purple dotted lines highlight the recent division planes (during the time-lapse imaging). The circumferential division planes align with the predicted maximal tensile stress directions prescribed by the ablation. Scale bars: 20 µm. The B&C was modified for better visualization.

Following CMT dynamics in cells around the ablation site, we could observe a transient radial organization of the array before the formation of the preprophase band (Figure R13D). We measured the anisotropy over time and found, as in control conditions, a drop around 2 hours before t0 (with an average of 0.21 +/- 0.35 at t = -6 hours, and of 0.13 +/- 0.28 at t = -2 hours, Figure R13I). Note that this step lasted for a shorter duration than in control conditions (only one hour), since the anisotropy increased back at t = -1 hours to reach and average of 0.15 +/- 0.34, reflecting the formation of the PPB. The cytoplasmic microtubule content increased in pre-mitotic cells around the ablation site as well, coinciding with the presence of the radial step (Figure R13E). This shows that the radial step is robust to mechanical perturbations, consistent with a scenario in which the accumulation of cytoplasmic microtubules in late G2 disrupts the ability of CMTs to align with tensile stress.

Figure R13 (next page): The radial array of CMTs still occurs after modifying the mechanical environment of the cell. (A) Schematic representation of the tensile stress pattern after a local ablation (red star) in an epidermis under tension. The predicted stress is circumferential around the ablation and overrides the global tensile stress prescribed by the tissue. (B) Close-up of an ablation site in a WT stem expressing the *pPDF1::mCitrine-MBD* marker. Note the circumferential alignment of CMTs around the ablation site, following the predicted maximal tensile stress pattern. The image is the cortical projection obtained with SurfCut. (C) Same as (B) in the *trm678* mutant. (D) Time-lapse images of pre-mitotic cells around an ablation, the top panel being the cortical projection with SurfCut and the bottom panel an orthogonal projection through the cell. Cortex images are 8-bit, with the B&C range varying between 0 and 80, and orthogonal projections are 8-bit, with the B&C range varying between 0 and 50. (E) Ratio between the average internal signal and the average of the cortical mCitrine-MBD signal over time. The colors correspond to qualitative classifications of cortical arrays (interphasic, radial step and PPB). Each line represents the kinetics for a given cell. $n_{WT,\ -6\ hrs} = 15$; $n_{WT,\ -5\ hrs} = 16$; $n_{WT,\ -4\ hrs} = 18$; $n_{WT,\ -3\ hrs} = 19$; $n_{WT,\ -2\ hrs} = 19$; $n_{WT,\ -1\ hr} = 21$; $n_{WT,\ t0} = 21$. (F) Same as (D) but in *trm678* mutant cells around an ablation site. (G) Same as (E) but in *trm678* mutant cells around an ablation site. $n_{trm678,\ -6\ hrs} = 9$; $n_{trm678,\ -5\ hrs} = 10$; $n_{trm678,\ -4\ hrs} = 11$; $n_{trm678,\ -3\ hrs} = 11$; $n_{trm678,\ -2\ hrs} = 12$; $n_{trm678,\ -1\ hr} = 12$; $n_{trm678,\ t0} = 12$. (H) Evolution of the ratio of mCitrine-MBD signal (internal/cortical) overtime in WT vs. *trm678*, around ablations. (I) Evolution of CMT array anisotropy overtime, using the FibrilTool plugin in Fiji, in WT vs. *trm678*, around ablations. $n_{WT,\ -6\ hrs} = 15$; $n_{WT,\ -5\ hrs} = 16$; $n_{WT,\ -4\ hrs} = 18$; $n_{WT,\ -3\ hrs} = 19$; $n_{WT,\ -2\ hrs} = 19$; $n_{WT,\ -1\ hr} = 22$; $n_{WT,\ t0} = 22$; $n_{trm678,\ -6\ hrs} = 9$; $n_{trm678,\ -5\ hrs} = 10$; $n_{trm678,\ -4\ hrs} = 11$; $n_{trm678,\ -3\ hrs} = 11$; $n_{trm678,\ -2\ hrs} = 13$; $n_{trm678,\ -1\ hr} = 13$; $n_{trm678,\ t0} = 13$. The cells used for analysis in (E, G-I) were from stems imaged on either AM or ACM media. Scale bars: 20 μm (B, C), 10 μm (D, F, surface projections), 5 μm (D, F, orthogonal projections).

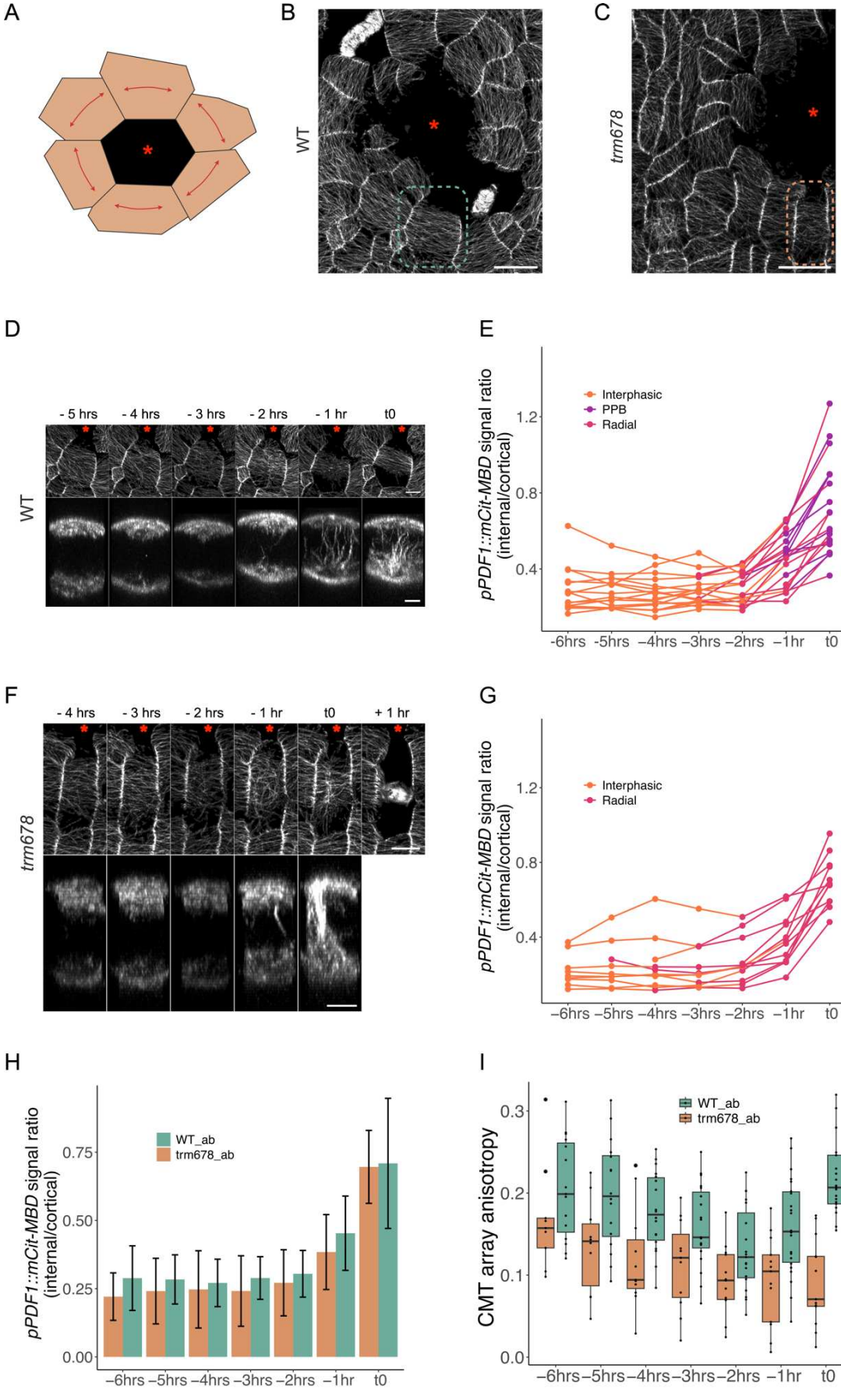
A
B
C
WT
trm678
D
E
- 5 hrs
- 4 hrs
- 3 hrs
- 2 hrs
- 1 hr
t0
WT
pPDF1::mCit-MBD signal ratio (internal/cortical)
Interphasic
PPB
Radial
1.2
0.8
0.4
-6hrs -5hrs -4hrs -3hrs -2hrs -1hr t0
F
G
- 4 hrs
- 3 hrs
- 2 hrs
- 1 hr
t0
+ 1 hr
trm678
pPDF1::mCit-MBD signal ratio (internal/cortical)
Interphasic
Radial
1.2
0.8
0.4
−6hrs −5hrs −4hrs −3hrs −2hrs −1hr t0
H
I
pPDF1::mCit-MBD signal ratio (internal/cortical)
WT_ab
trm678_ab
0.75
0.50
0.25
0.00
−6hrs −5hrs −4hrs −3hrs −2hrs −1hr t0
CMT array anisotropy
WT_ab
trm678_ab
0.3
0.2
0.1
0.0
−6hrs −5hrs −4hrs −3hrs −2hrs −1hr t0

To challenge this conclusion, we also performed the same ablation experiments on *trm678* mutant stems. CMTs in *trm678* responded to mechanical perturbations, as evidenced by their circumferential orientation around the ablation (Figure R13C). In this background, the radial step also appeared before mitosis, and lasted for a shorter duration than in *trm678* cells in control conditions (Figure R13F). We measured a drop in CMT array anisotropy 4 hours before t0 in dividing cells around the ablation (with an average of 0.17 +/- 0.07 at t = -6 hours, and of 0.12 +/- 0.06 at t = -4 hours, Figure R13I). Since there is no PPB in this genetic background, the anisotropy remained low until t0, as in non-ablated *trm678* stems (0.09 +/- 0.05). When looking at cytoplasmic microtubule content over time, we observed an increase as the cell progressed towards mitosis, consistent with the timing of the radial step emergence (Figure R13G). Note that in both *trm678* and WT genetic backgrounds, the increase in microtubule content before mitosis was more pronounced around ablations than under control conditions. When pooling the measurements, we could see a 315 % increase in cytoplasmic microtubule content between t = -6 hours and t = 0 (*p*-value = $6.80e^{-6}$, Wilcoxon test), while this increase was of 246 % in the WT background, around ablations (*p*-value = $1.34e^{-7}$, Wilcoxon test) (Figure R13H). While these minor deviations to microtubule behavior show that the cell behaves slightly differently next to an ablation site, the radial step still occurs independently of the genetic background, consistent with a transient blindness of CMTs to tensile stress caused by cytoplasmic microtubule accumulation.

Figure R14 (next page): The cytoplasmic microtubule content as the radial step appears in WT and *trm678*, with and without ablations. (A) Time-lapse images of pre-mitotic cells, the top panel being the cortical projection with SurfCut and the bottom panel an orthogonal projection through the cell, in WT cells around an ablation site (red star). Cortex images are 8-bit, with the B&C range varying between 0 and 80, and orthogonal projections are 8-bit, with the B&C range varying between 0 and 50. (B) Same as (A) but in *trm678* mutant cells, around an ablation site. (C) Maximal projection of the *pPDF1::mCitrine-MBD* signal of WT cells at t0, in PPB stage. (D) Same as (C) but in WT cells around an ablation site. Note that in cells around an ablation, the PPB seems slightly wider than in control conditions. Also, no pro-spindles are noticeable before the start of PPB depolymerization in control conditions, while pro-spindles start to form at this stage for cells around an ablation. Cells from (C, D) come from a single stem. (E) Correlation graph between the anisotropy value of the CMT arrays and the cytoplasmic microtubule content. For this graph, all the cells at all timepoints were used, except for WT cells at PPB stage. We can see that the higher the cytoplasmic microtubule content, the lower the anisotropy value. The slopes are $0.04x + 0.003$ for the WT (R^2 = 0.282), $0.03x + 0.07$ for the WT around ablations (R^2 = 0.259), $0.01 + 0.04$ for *trm678* (R^2 = 0.049), and $0.01 + 0.08$ for *trm678* around ablations (R^2 = 0.087), with x being the inverse of the ratio of cytoplasmic over cortical MBD signals. While the slopes between WT and *trm678* are slightly different, they are comparable between ablated and control conditions within a genetic background. This graph shows that the dynamics of the anisotropy of the CMT array correlates with the cytoplasmic microtubule content. $n_{WT,\ control} = 68$; $n_{WT,\ ablation} = 122$; $n_{trm678,\ control} = 87$; $n_{trm678,\ ablation} = 83$. Scale bars: 10 µm (A, B, surface projections), 5 µm (A, B, XZ orthogonal projections), 10 µm (C, D).

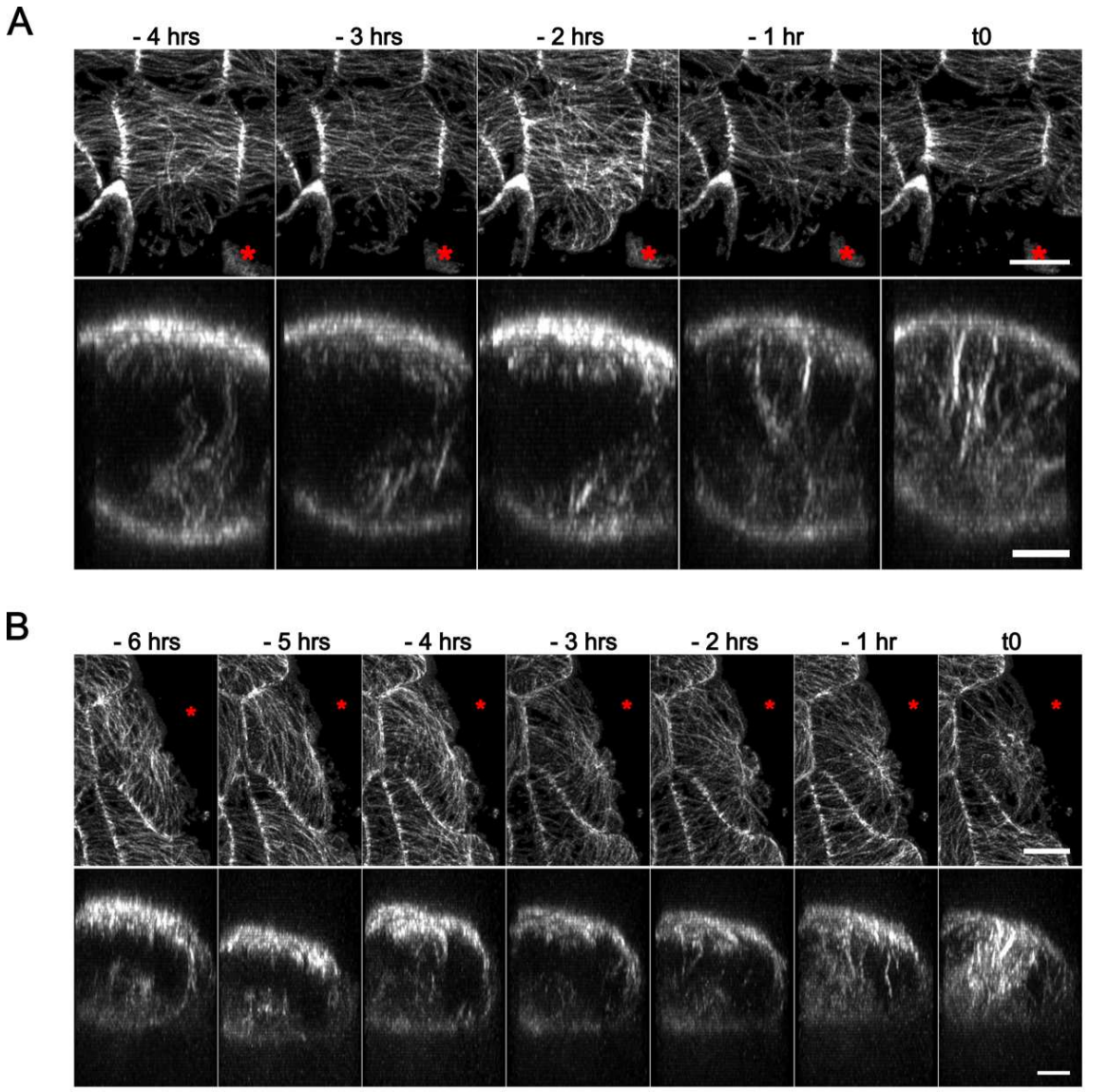
A
- 4 hrs
- 3 hrs
- 2 hrs
- 1 hr
t0
B
- 6 hrs
- 5 hrs
- 4 hrs
- 3 hrs
- 2 hrs
- 1 hr
t0
C
D
E
Anisotropy of the cortical MT array
in function of the internal MT content
WT
WT_ab
trm678
trm678_ab
Anisotropy
0.0
0.1
0.2
0.3
0.0
2.5
5.0
7.5
1/(Cytoplasmic MBD signal/Cortical MBD signal)

On top of modifying the stress pattern, ablations also introduce other artificial biochemical and electrochemical modifications. A perturbation of the local tension pattern is possible in physiological conditions with the formation of trichomes (Hervieux *et al.*, 2017). Indeed, trichome development proceeds in two steps: first, the fast growth of the trichome cell in the plane of the tissue, followed by an outgrowth perpendicular to the tissue plane. During the first step of development, the fast growth of the cell is predicted to induce a re-organization of the tension pattern, circumferential around the developing trichome in the epidermis. This is due mainly to the cell wall gluing cells to one another, imposing a stress on neighboring cells when there is differential growth (through osmotic and/or differential growth). *Arabidopsis* stems do develop trichomes. However, most trichomes had already achieved their full development in three-week old plants, when we performed our analysis. In plants grown on NPA supplemented media, the development of trichomes continued after three weeks. This was probably due to the lack of organ formation, and the possible modification of temporal or differentiation informations given to tissue cells.

In order to analyze pre-mitotic CMT dynamics in the presence of mechanical heterogeneities, we focused our analysis on dividing cells next to young trichome cells that had not yet buldge out of the stem plane. For the reason listed above, we used plants grown on NPA supplemented media, and followed CMTs over time. However, the data was limited, due to the limited number of situations in which a developing trichome is next to dividing cells. Trichomes were identified qualitatively by their cell shape, their rapid growth and their microtubule organization, which was different than for regular cells in the stem. Our first observation was that, in cells around developing trichomes, interphasic CMT arrays were oriented circumferentially around the trichome (Figure R15A), as described previously in sepals (Hervieux *et al.*, 2017). Secondly, the pre-prophase bands and the subsequent division planes were also mainly oriented circumferentially around the developing trichome, following the predicted tension pattern (Figure R15B). These observations are consistent with a scenario in which the fast growth from the first step of trichome development prescribes a circumferential tension pattern around the growing trichome in the stem. We could observe CMT dynamics in pre-mitotic cells around growing trichomes, and they appeared to undergo a radial re-organization before the formation of the PPB (Figure R15C). Due to the very low sample size, and gap in the time-lapse imaging, we could not draw conclusions on the duration this step. Furthermore, these observations were made in stems grown in NPA conditions, and it has been described that auxin regulates, on some level, MT dynamics (Chen *et al.*, 2014) and cell cycle progression (Perrot-Rechenmann, 2010). Nevertheless, with these words of caution in mind, our data suggests that the radial step, in the stem, occurs regardless of the tensile stress pattern in physiological conditions.

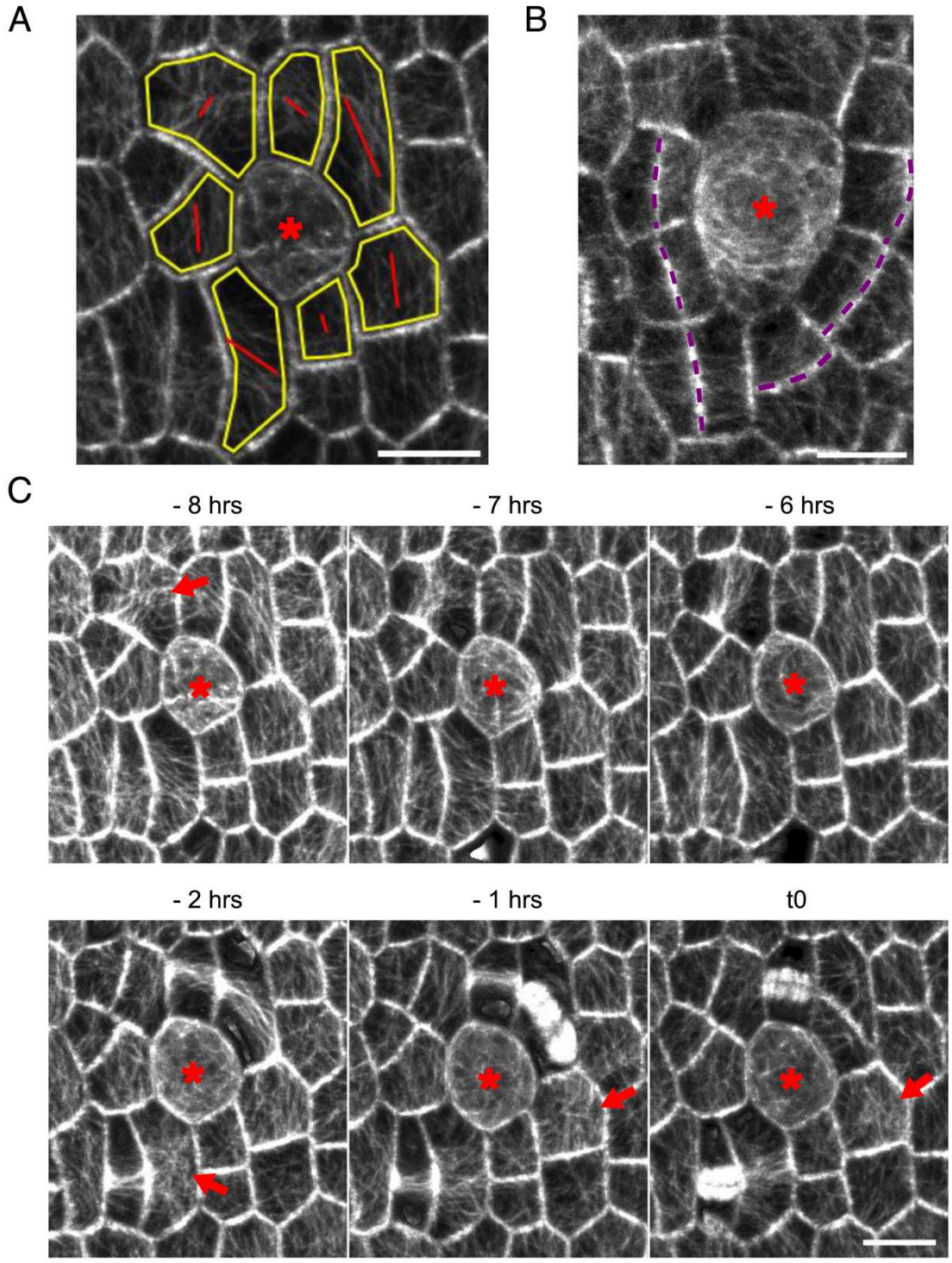

Figure R15: CMT behavior in cells around growing trichomes. (A) FibrilTool analysis interphasic CMT array orientations in cells surrounding a trichome. The yellow polygons are the regions of interest used for the measurements, and the red lines show the average orientation of the CMT arrays. CMTs are oriented circumferentially to the growing trichome. (B) Division plane orientations in cells surrounding a growing trichome. The purple dashed lines show the orientation of cells having divided during the time-lapse experiment. The division planes are oriented circumferentially to the trichome. (C) Time-lapse of pre-mitotic cells around a growing trichome cell from stems expressing the *pPDF1::mCitrine-MBD* microtubule marker. The red arrows show the cells undergoing the radial step (qualitatively). The plants were grown, and imaged on NPA-supplemented media. The images signal is a SurfCut projection of the mCitrine signal, from 0 to 4 µm from the surface. The red stars indicate the growing trichomes. The Brightness&Contrast parameters have been modified for better visualization. The scale bars are 10 µm.

6. Disruption in the balance between cortical and cytoplasmic microtubule accumulation in *trm678* increases the precision of cell division

While the radial step appears robust, reflecting a transient disruption of CMTs by cytoplasmic microtubules, one could wonder whether this reset sequence has a biological function. The identification of a step where cells become blind to their mechanical environment echoes data in Drosophila epithelia where cell rounding allow the cell to perceive its centroid, independently from adjacent cells influence, in order to define the degree of cell division symmetry (Stewart *et al.*, 2011; Chanet *et al.*, 2017). We wondered whether the radial step might have a comparable function in plants.

Note that the inner periclinal cortex also displays a radial reorganization of the CMT array before the formation of the PPB (Figure R16).

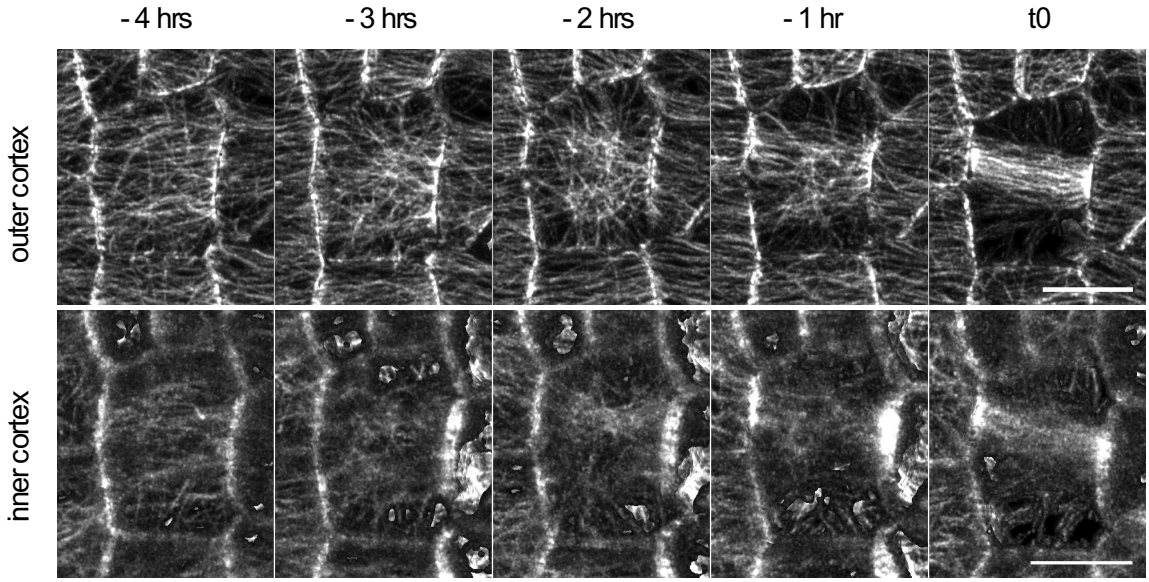

Figure R16: CMT dynamics of a pre-mitotic cell, displaying the signal from the periclinal outer (top) and inner (bottom) cortex. The images are SurfCut projections of the *pPDF1::mCitrine-MBD* signal between 0 and 4 μm, either starting from the top (top images) or bottom (bottom images) of the cell. The signal from the inner cortex is noisier due to the weaker signal, and the more difficult extraction of the tissue surface. Scale bars: 10 μm.

To address this question, we analyzed daughter cell volumes in WT and *trm678* stems, and plotted the volumes ratio for both genotypes. The mean ratios were comparable (1.30 +/- 0.26 in WT vs. 1.20 +/- 0.14 in *trm678*; Figure R17A). The means are higher than 1 because we measured the ratio between the larger daughter cell and the smaller one. Interestingly, while the averages were not significantly different (Wilcoxon test *p*-value = 0.253), the variances were significantly different (0.07 in WT and 0.02 in *trm678*, Fligner test *p*-value = 0.005): symmetry between daughter cells was 3.79 times less variable in *trm678* than in wild-type. This suggests that a longer and better-defined radial step correlates with more precise divisions, reducing the variability in daughter cell volume ratios.

Because the *trm678* has a prolonged radial step and a prolonged M phase (Figure R10B), we next checked whether increased precision is simply the result of a slower pre-mitotic stage. To do so, we performed the same analysis in NPA-treated WT plants, which exhibit slightly longer radial step and slightly longer mitosis than non-NPA treated plants. This did not affect the variance of daughter cell volumes (Figure R17A). When performing the same analysis on NPA-treated *trm678* stems, we instead observed a partial rescue: the variance in NPA-treated *trm678* stems was lower than NPA-treated WT stems, but higher than control *trm678* stems (Figure R17A). Thus, the precision in cell division does not correlate with a slower pre-mitosis and mitosis dynamics, but instead, with a longer and qualitatively more clear-cut radial step, in *trm678*.

Altogether, we propose that the accumulation of cytoplasmic microtubules near the nuclear envelope 3 hours before cell division in stems transiently disrupts the co-alignment of CMTs with tensile stress, forming a radial organization of CMTs, thus allowing the cell to control the precision of its division, by becoming less sensitive to external cues.

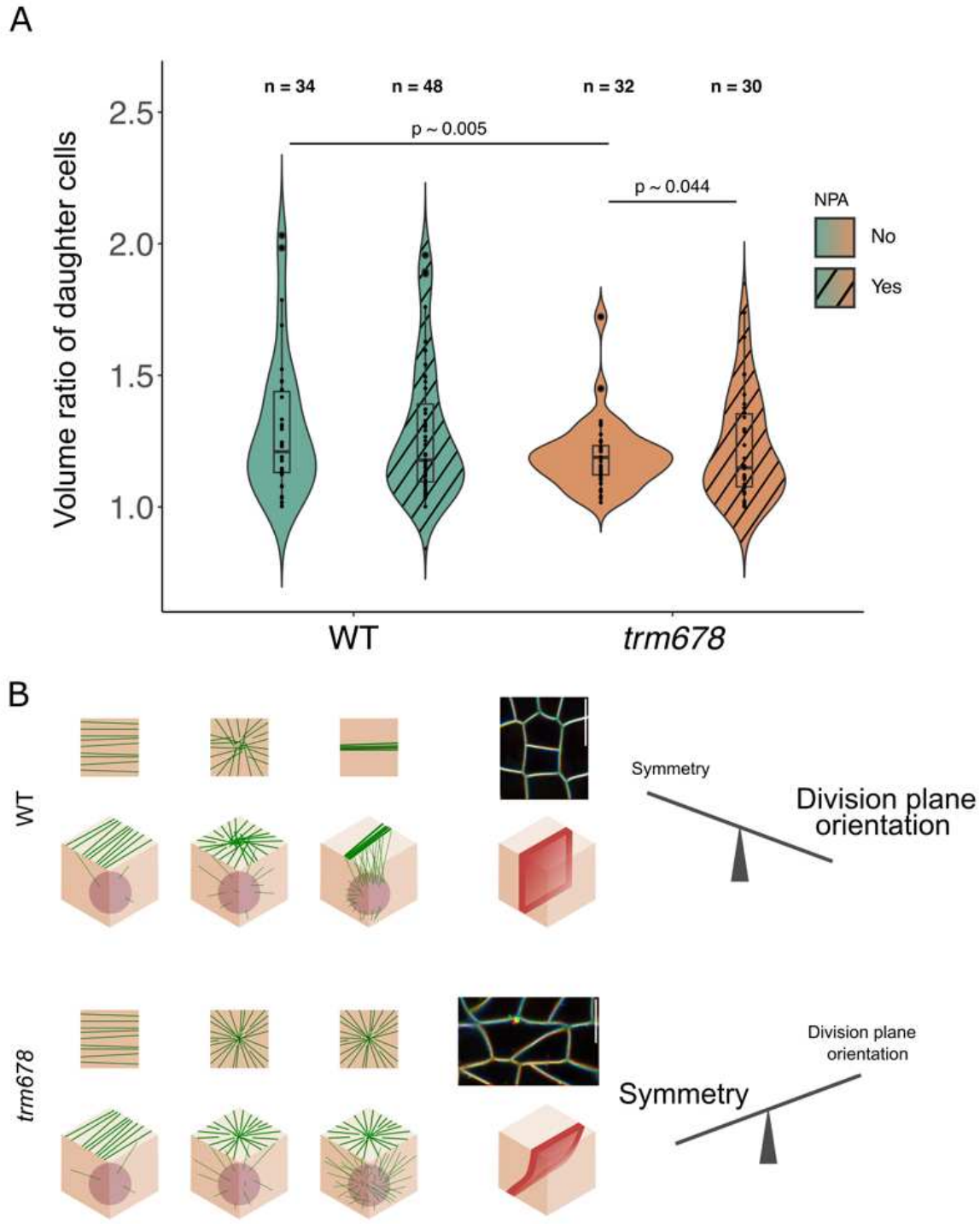

Figure R17: A model: the radial step could contribute to the precision of cell division symmetry. (A) Violin plot showing the distribution of the ratio between the volume of the two daughter cells in WT and *trm678* backgrounds, in both control and NPA conditions. The measurements were made using images from cells expressing *pUBQ10::Lti6b-TdTomato* membrane marker. The ratio is always calculated between the larger daughter cell and the smaller daughter cell. The *p*-values displayed are the ones obtained from the Fligner's statistical test using R studio. (B) Model: In the WT (top panel), a suboptimal radial step allows the cell to sense its own geometry to define cell division symmetry loosely, while the formation of the PPB defines robust division plane orientation; in the *trm678* mutant (bottom panel), a better-defined radial step improves the division precision (daughter cell volumes), to the detriment of division plane orientation robustness. Radial step and PPB reflect a trade-off in robustness (division precision vs. division plane orientation, respectively). Images: RGB projection of recently divided cells at different focal planes (red: top of the cell, green: middle of the cell, blue: bottom of the cell) in the WT (top cell) and *trm678* (bottom cell). Scale bars: 10 μm.

II. The radial step is robust to different conditions

Rationale: In the previous sections, I report that the transition from interphase to mitosis is marked by a re-arrangement of the CMTs where they become radially organized. This radial step has been found in pre-mitotic cells in the SAM and in the stem of *Arabidopsis thaliana*, and appeared robust to auxin transport perturbations and to local mechanical perturbations in the tissue (although its duration happens to be slightly variable). We propose that the radial re-arrangement of the CMT array results from the pre-mitotic cytoplasmic MT increase, leading to a transient mechanical shield of the cell from external cues, possibly to correctly position its division plane.

However, we do not know whether this radial step is present in other tissues, and in particular in cells with highly stereotyped division orientations. Indeed, the division rules present in the stem do not hold true in every tissue. In the root epidermis, for example, division plane orientations determine cell files and are, as well as cell shapes, highly stereotyped (Dolan *et al.*, 1993; Zhang *et al.*, 2016). In addition, roots are also exposed to other mechanical conditions than shoots, either external through their localization in the soil, or internal with their different tissue organization, possibly affecting their CMT organizations (Stöckle *et al.*, 2022; Mimault *et al.*, 2023; Hoermayer *et al.*, 2024). Although we analyzed CMT dynamics in different growth conditions and in *trm678* (see Chapter I of the Results), we also do not know to what extent the radial step would be robust to more global cellular and mechanical perturbations. I exposed dividing cells to different water availability conditions, and induced cell wall and microtubule perturbations through the use of mutants or drugs in the stem. I performed time-lapse imaging on pre-mitotic cells of developing lateral roots. I studied the pre-mitotic CMT dynamics and/or division symmetry in these different contexts, with the hope to disrupt the radial step and reveal its biological function. This part can thus be considered as a screen for candidate radial step mutants, as well as a stress test for radial step robustness. Some of the datasets from such a screen build on small sample sizes, and the conclusions should thus be considered as preliminary.

Contribution: In this part, I performed all experiments and subsequent analyses. The initial experiments with Latrunculin B and with the PCNA marker line were performed with Shogo Takatani.

1. The radial step is robust to tissue context

The radial step has been observed in pre-mitotic cells in SAM and stem epidermis of *Arabidopsis thaliana* (Figure R3A). To further study pre-PPB CMT dynamics in another tissue context, I decided to observe young lateral root epidermis. This tissue is easily observed due to the very small amount of root cap present, and shows highly active cell divisions (Figure R18A). On top of changing the system observed (root system vs. shoot system), cell divisions are highly stereotyped in root

epidermis (Dolan *et al.*, 1993; Zhang *et al.*, 2016), removing the possible wavering step of the cell between different division plane positions. I prepared samples as described previously (Kirchhelle *et al.*, 2016), and followed young lateral roots of around 10-day old plants expressing the *p35S::GFP-MBD* microtubule fluorescent marker.

Lateral roots seemed overall more sensitive to the confocal microscope laser than stems. Bleaching occurred quite quickly (after around 2.5 hours), and the microtubule signal was variable between samples, although largely weak. While roots cells are smaller than the ones in the stem, reducing the image resolution, microtubule arrays were still visible. Overall, I managed to obtain 3 lateral root samples out of 12 observed, spread over 3 different experiments. Interphase CMT arrays appeared organized, and aligned transversely to the root axis (Figure R18). Some root cap cells could be distinguished visually, and sometimes divided following the root axis while epidermal cells divided transversely. Mitosis was faster to complete in roots than in the stem. In the SAM, cell cycle duration seems linked with cell size (Jones *et al.*, 2017), and it could be reasonable to assume that the cell cycle is globally shorter in the roots than in the stems. In order to limit tissue bleaching by the laser while allowing a reasonable observation of CMT dynamics, I reduced the time resolution to one image every 25 minutes.

When analyzing individual pre-mitotic cells over time, I was able to observe a re-organization of the CMT array before the formation of the pre-prophase band (Figure R18B). Again, in this system the sample size is low, but qualitative analysis indicated that there is a radial step in lateral roots epidermal cells. The exact duration of this step is difficult to estimate with a time resolution of 25 minutes, but in the cells observed it lasted for around 50 minutes. I could see an increase in cytoplasmic microtubule signal intensity when the radial step appeared at the cortex (Figure R18B).

With these images, I could confirm that the radial step appears in another organ, even where there is a highly stereotyped division orientation, and where stresses are very different than in shoots. Using the root system could be a better system to study pre-PPB microtubules, even though it would need some optimization. Particularly, the reproducibility is very low, as signal quality varies a lot between samples, and even between lateral roots of a same plant. Also, even though a time resolution of 25 minutes seems like a good compromise between visualizing CMT dynamics and signal bleaching, having a line with a higher fluorescence could help having a more precise view on the radial step. As young lateral root cells seem to have faster cell cycles, and are very active in terms of cell divisions, experiments should be much faster. However, little is known on the mechanical stresses experienced by the lateral root epidermis (Galletti *et al.*, 2016).

Figure R18 (next page): The radial step is also present in pre-mitotic young lateral root cells. (A) This image represents the projection of the *p35S::GFP-MBD* signal between 0 and 4 µm, using SurfCut. Cells were segmented manually, and the average orientation of CMTs was extracted and displayed, using an automated version of the FibrilTool plugin in Fiji (http://doi.org/10.5281/zenodo.2528872). The red lines represent the average orientation of CMTs. The length of the line corresponds to the anisotropy of the CMT arrays: the longer the line, the higher the anisotropy value. Most of the cells display CMTs arrays transverse to the root axis. Scale bar: 20 µm. The Brightness&Contrast was modified for better visualization. (B) CMT dynamics of a pre-mitotic lateral root cell. The radial step is marked by a red dotted line. The top panel is a raw image from a SurfCut projection between 0 and 4 µm. The middle panel is the same image, with a Gaussian blur and a visual representation of the different pixel orientations. The hue of the image represents the different orientations. In these two panels, the Brightness&Contrast have been modified for better visualization. The bottom panel shows the middle plane of the Z-stack for the cells at each timepoints. In this last panel, the Brightness&Contrast has been set between 0 and 50. The scale bars are 10 µm.

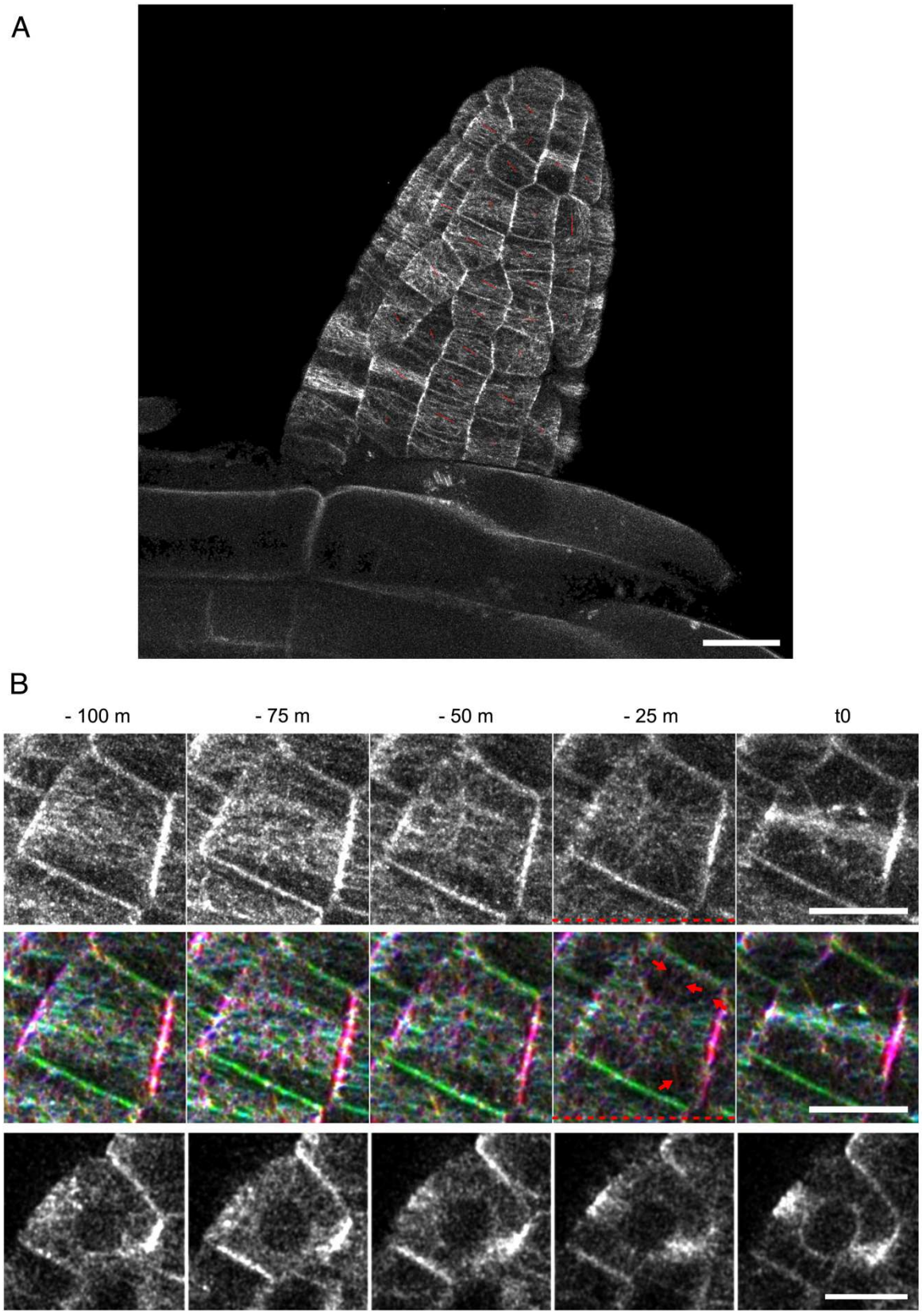
A
B
- 100 m
- 75 m
- 50 m
- 25 m
t0

2. The radial step is robust to different osmolarities

Next, I challenged the robustness of the radial step to new growth conditions. A simple way to modify tensile stress levels in plants is to grow them on different agar concentrations, modifying the matric potential (Verger *et al.*, 2018). Changing agar concentrations in the growth media changes the tension magnitude, influences cell growth, and also affects CMTs response to stress (Verger *et al.*, 2018; Sampathkumar *et al.*, 2014).

Pre-mitotic cells were observed in stems from plants grown and imaged on media with different agar concentrations. I used media with 0.8% agar to increase the water availability, and 2.5% agar to decrease the water availability. 1% agar concentration was the control condition, as all the characterization of the radial step had been made accordingly.

As expected, agar concentration in the medium affected the growth rate: plants grown on 0.8% agar bolted in around two and a half weeks, plants grown on 1% agar in about three weeks, and plants grown on 2.5% agar in about one month. This difference in growth was also reflected in the mitotic index, which was determined as the number of cells presenting spindles or phragmoplasts, divided by the total number of cells in the image frame (Figure R19A). At the time of the experiment, the mitotic index was of 1.56 +/- 1.04 for plants in 1% agar conditions, 3.24 +/- 1.27 in 0.8% agar and 0.86 +/- 0.86 in 2.5% agar. Only a significative difference between mitotic index has been found between 0.8% and 2.5% agar conditions, when comparing the means (p-value = 0.02, Tuckey's statistical test). I looked at 5 stems in 0.8% agar conditions over 3 experiments, and 4 stems in 2.5% agar conditions over 3 experiments.

In 0.8% agar conditions, CMTs tended to orient transversely to the stem, following the prescribed maximal tension pattern, and conserved this bias overtime. I could not observe obvious differences with dividing cells in stems grown and imaged on 1% agar. The CMT array re-organized radially before the formation of the PPB, around 3 hours before t0, lasting for around 2 hours, as in 1% agar conditions (Figure R19C). In 2.5% agar conditions, CMTs were overall transversely oriented at the beginning of the experiment, following the predicted maximal tension pattern. When observing pre-mitotic cells overtime, I could observe the presence of the radial step before the formation of the PPB. As the sample size was low, it is difficult to determine the exact duration of this step in 2.5% agar, but the radial step appeared around 3 hours before t0 (Figure R19C). Therefore, the temporality seemed unchanged from 1%, or 0.8% agar conditions. The presence and features of the radial step do not seem to depend on the water availability in the medium, or stable changes in the osmotic potential of the cells. Despite that, it is highly probable that changing the agar concentration in the medium affects other cellular parameters, such as cell cycle duration, microtubule dynamics or shape reading parameters.

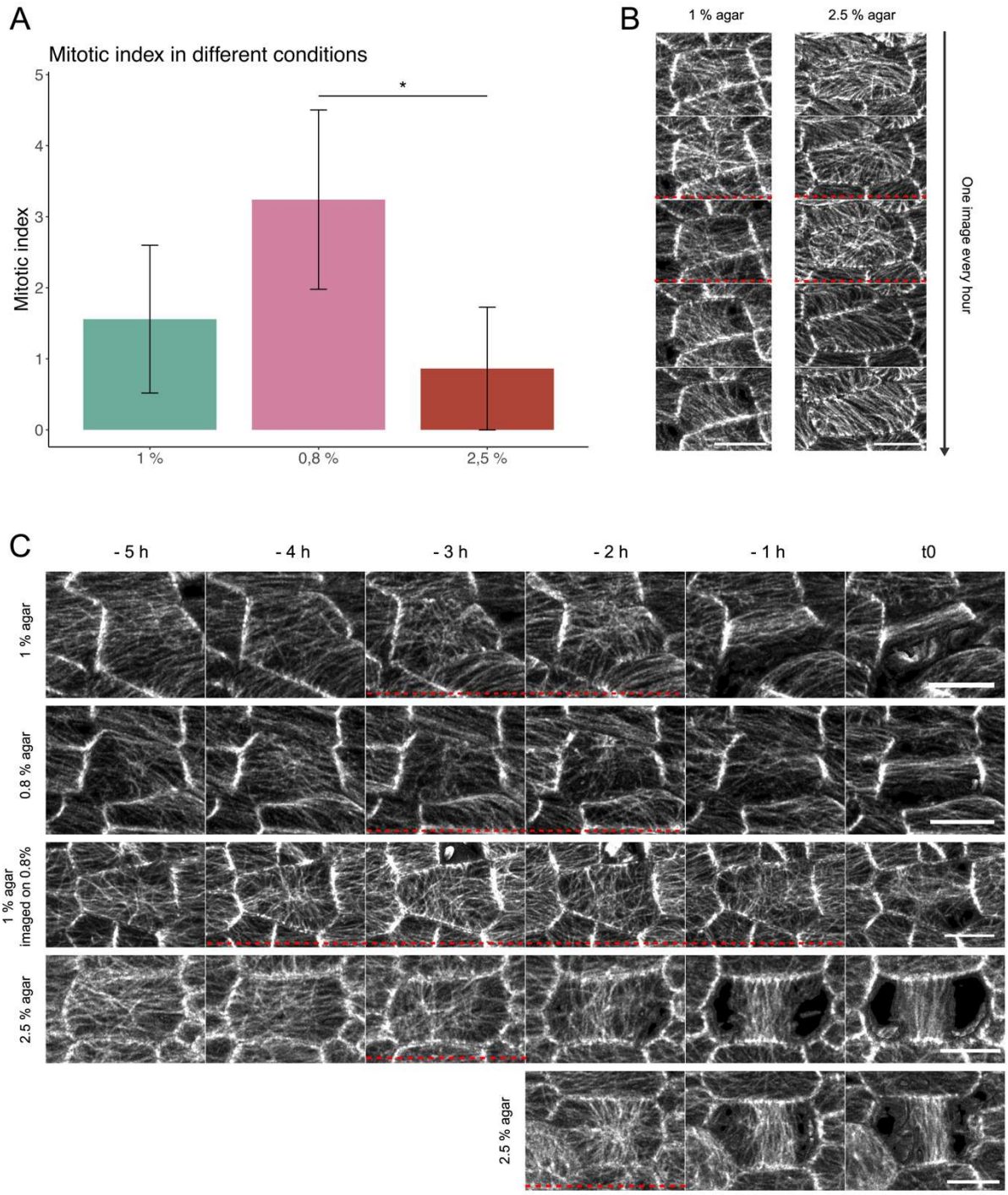

Figure R19: CMT dynamics in different agar concentrations. (A) Mitotic index in *Arabidopsis* stems grown and imaged on media with different agar concentrations. The mitotic index has been calculated as the number of cells presenting mitotic structures, divided by the total number of cells in the frame. The statistical tests performed were Tuckey's tests to compare the means. Number of frames analyzed: $n_{1\%\ agar} = 12$; $n_{0.8\%\ agar} = 5$; $n_{2.5\%\ agar} = 4$. (B) A radial CMT array precedes CMT orientation changes and not PPB formation. Time-lapse of CMTs from cells on 1% (left) or 2.5% (right) agar conditions changing their orientation over time. These cells undergo a radial array of CMTs before changing their orientation. (C) Pre-mitotic CMT dynamics in different agar conditions. From top to bottom: CMT dynamics from a cell grown and imaged on 1% agar; from a cell grown and imaged on 0.8% agar; from a cell grown on 1% agar, and imaged on 0.8% agar; from 2 cells grown and imaged on 2.5% agar. The radial step is marked by the red dotted lines. The images are SurfCut projections between 0 and 4 µm from the surface of the stem. Brightness&Contrast parameters have been adjusted for better visualization. The scale bars are 10 µm.

On top of unraveling the radial step, time-lapse imaging of pre-mitotic cells showed other interesting behaviors. Firstly, overall interphasic CMT array orientation sometimes changed over the course of the time-lapse. This change in global orientation was often preceded by a radial re-organization of the array. Qualitatively, it was difficult to distinguish the pre-rotary interphasic radial array from the pre-mitotic radial array (Figure R19B). Secondly, in 1% agar concentrations, I could observe cells at the PPB stage that went back to an interphasic microtubule array. This process did not involve a radial microtubule array, but rather appeared as a decondensation of PPB MTs (Figure 20B). Other unusual PPB behaviors appeared such as PPBs changing their preferential orientations, or cells blocked at the PPB stage for up to 8 hours (Figure 20B). This last phenomenon also occurs in SAMs.

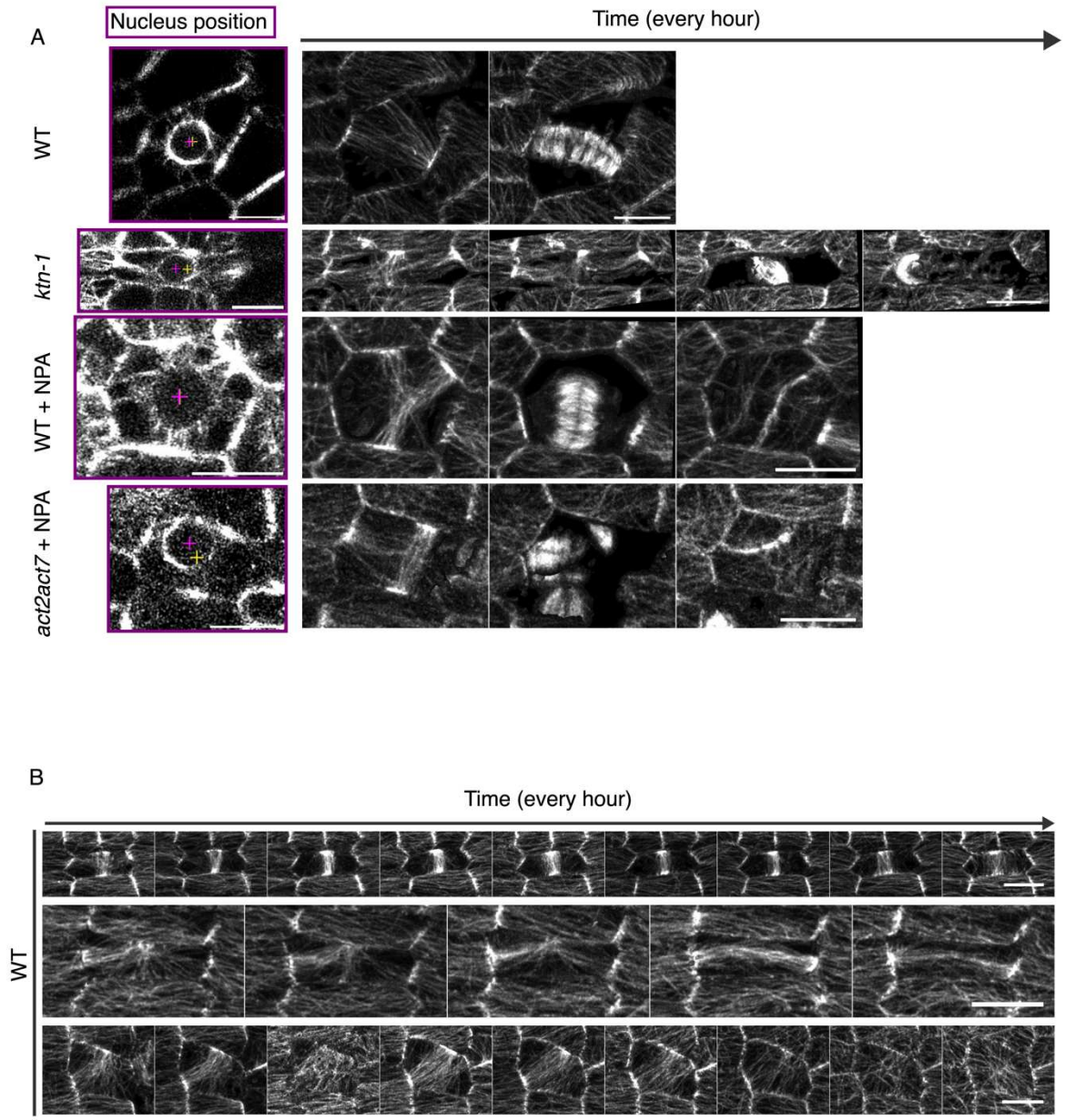

Figure R20: PPB defects observed in *Arabidopsis* stems in various conditions. (A) Split PPBs observed in different conditions. The left part of the panel shows a mid-plane of the cells Z-stacks, where the Brightness&Contrast has been set to visualize the nucleus. The yellow cross shows the centroid of the cell and the magenta cross shows the centroid of the nucleus. The right part of the panel shows the CMT dynamics during mitosis in these cells, as well as the final division plane adopted. (B) Abnormal behavior of PPB microtubules overtime. The top panel shows a stuck PPB. The middle panel shows a PPB apparently changing its preferential orientation overtime. The bottom panel shows a cell presenting a PPB that dissociate to go back to an interphasic array. The Brightness&Contrast parameters have been changed for better visualization. The images are SurfCut projections between 0 and 4 μm from the stem surface. The scale bars are 10 μm.

3. The volume partitioning between daughter cells is affected by pectin methylesterification

Another way to modify the stress pattern in plant tissues is to modify the cell walls (see Chapter IV of the Introduction). While affecting the cellulose deposition could weaken the cell wall rigidity and thus impact the tension magnitude, cellulose content modifications may have too many effects on plant development (Hu *et al.*, 2018). Moreover, preliminary experiments with the cellulose deposition inhibitor isoxaben were hard to interpret due to the changes in cell shapes.

More subtle modulations are possible with other cell wall mutants (part IV2 and IV3 of the Introduction). In the ethanol-inducible *p35S::PMEI5* overexpressor line, pectins have a higher degree of (native) methyl-esterification and, as a result, the cell walls appear stiffer (Peaucelle *et al.*, 2011). Note that the inducible construct is leaky in this line and an intermediate PMEI5 overexpressor phenotype appears even without the induction. In addition to pectins, alteration of cell wall stiffness can be achieved by targeting xyloglucans biosynthesis in the primary cell wall. Notably, the *xxt1xxt2* double mutants are affected in Xyloglucantransferases 1 and 2 and present reduced xyloglucan and cellulose content, as well as more methylesterified pectins (Zhao *et al.*, 2019). Thus, the *xxt1xxt2* and *p35S::PMEI5* backgrounds offer alternatives to study the radial step in a different mechanical context.

Ideally, we would analyze pre-mitotic CMT behavior in the *xxt1xxt2* double mutant and in the *p35S::PMEI5* overexpressor line (leaky/non-induced) in parallel to the control, to test whether the radial step is sensitive to such cell wall modifications. However, since the lines were not ready in time for analysis, I analyzed the precision of cell division symmetry as an indirect proxy for the radial step perturbation (see Chapter I6 of the Results; Figure R16A).

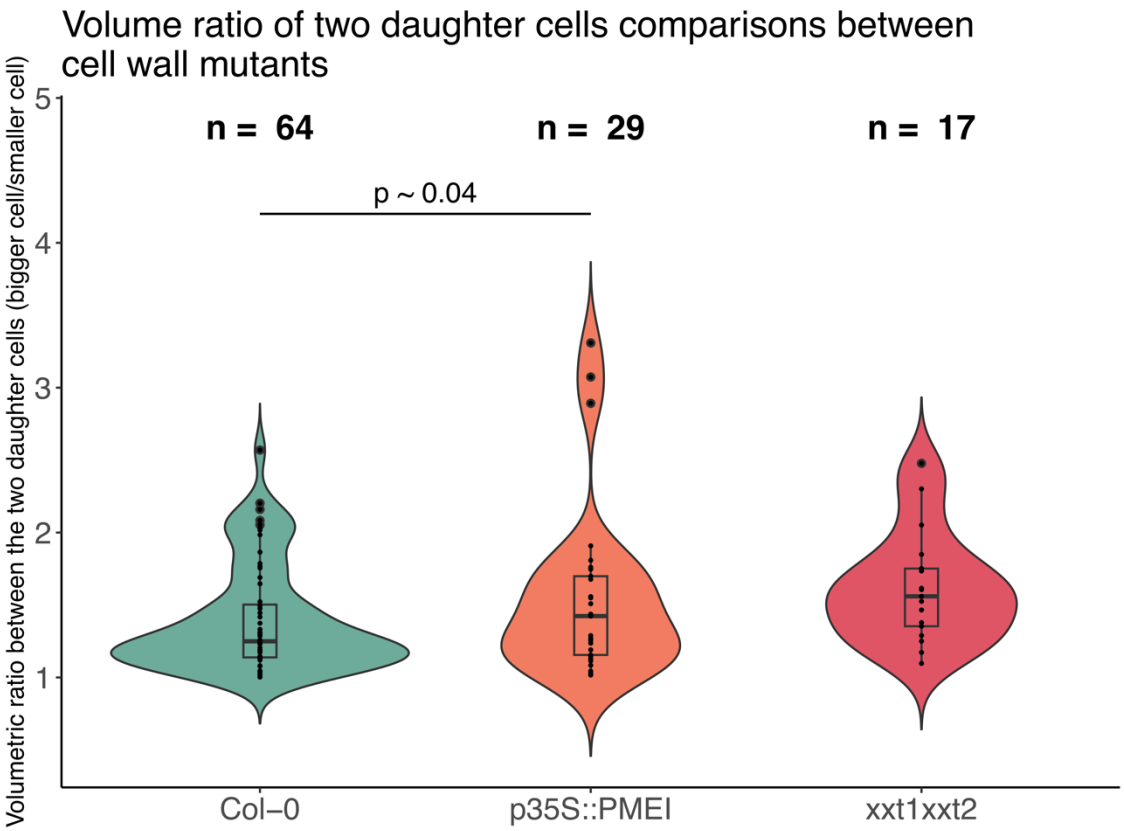

Figure R21: Violin plots representing the distribution of volume ratios between daughter cells in the *p35S::PMEI5* (marked as *p35S::PMEI*) and the *xxt1xxt2* cell wall mutants. The statistical tests performed were Fligner's test to compare the variances between values

- **Volume ratio between daughter cells**

In order to perform a volumetric segmentation and extract cell volumes, I stained either cell walls with the propidium iodide (PI, Sigma) dye, or with the plasma membrane with the FM4-64 (Life Technologies) dye. Using these dyes is a quick and effective way to visualize cell contours, without the need to stably express a fluorescent marker. Since, with the resolution of the microscope, cell wall and membrane structures seemed indistinguishable, I pooled the results together to increase the sample size. For *p35S::PMEI5*, I looked at 2 stems over 2 different experiments, stained with FM4-64, and 4 stems over 2 experiments stained with PI. For *xxt1xxt2*, I looked at 2 stems over 2 experiments, stained with FM4-64, and 5 stems over 2 experiments, stained with PI. Note that PI staining worked better than the FM4-64 staining in stems, which could be due to penetration differences through the presence of a cuticle, for example. I also used the images from the previous volume analysis (see Chapter I6 of the Results) of Col-0 plants expressing the *pUBQ$_{10}$::Lti6-TdTomato* membrane fluorescent marker in order to increase the sample size. I found an average volume ratio of 1.39 +/- 0.37 for the Col-0, of 1.62 +/- 0.38 for the *xxt1xxt2* mutant and of 1.56 +/- 0.59 for the *p35S::PMEI5* background (Figure R21). Despite this trend, no significative differences have been found between Col-0 and either of the mutants, when comparing the means, using the Wilcoxon test in RStudio. However, when performing the Fligner's test to compare the variances, *p35S::PMEI5* results showed statistical difference with the WT (*p*-value = 0.044, Fligner test), while *xxt1xxt2* did not appear statistically different when compared to the WT (*p*-value = 0.651, Fligner test). The interquartile range (IQR) gives an idea about the spread of the data. As *p35S::PMEI5*'s IQR is higher than the WT's (IQR_{WT} = 0.365, $IQR_{p35S::PMEI5}$ = 0.543, $IQR_{xxt1xxt2}$ = 0.398), I could confirm that variance in symmetry ratio between daughter cells is statistically higher than the WT's. *xxt1xxt2*, on the other hand, presents a similar IQR to the WT's. While the overall tissue topology seemed unaffected by the mutations in both backgrounds, I could find some instances of wavy division planes in the *p35S::PMEI5* mutant background (Figure R25).

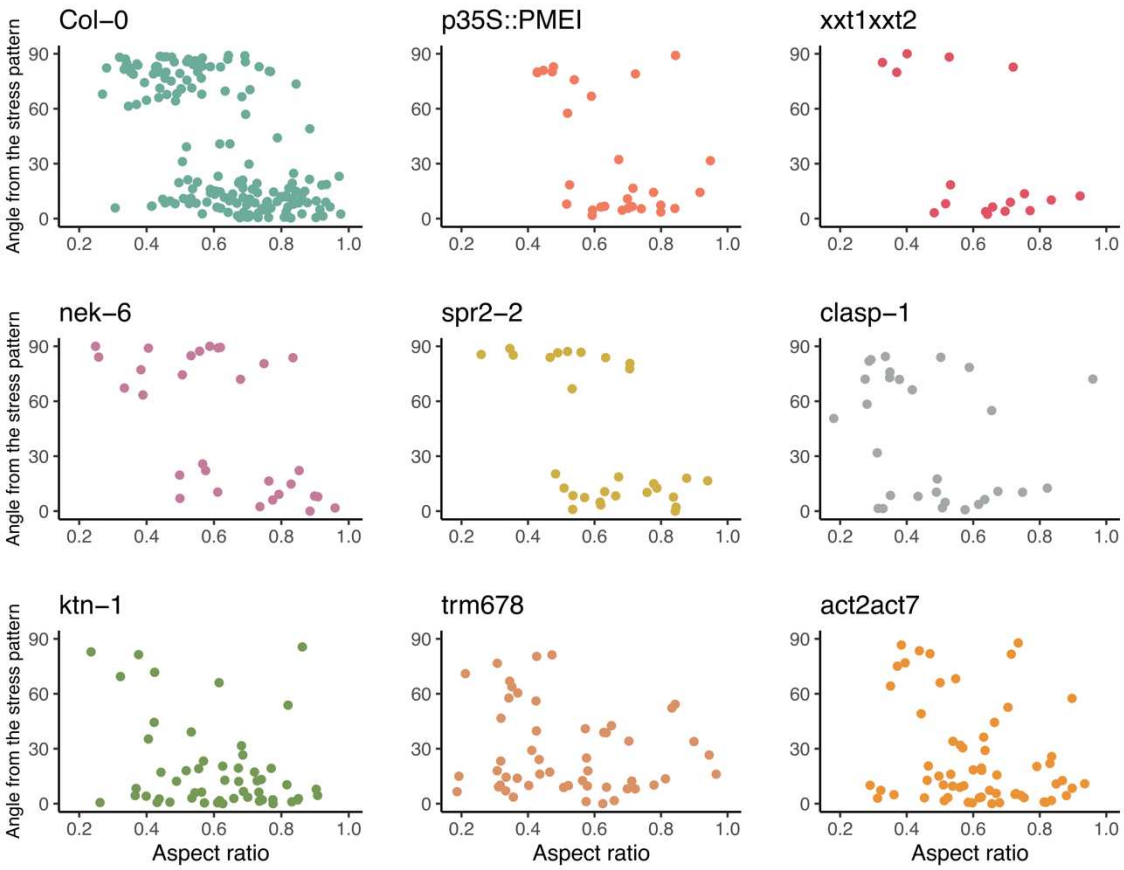

Figure R22: Division orientations of cells in the stem in different genetic backgrounds. The X-axis shows the aspect ratio of the cells, with 1 showing a completely round cell and 0 a completely flat cell. The Y-axis shows the angle of the PPB or the division plane from the maximal tension pattern. 0° therefore is following the tension pattern (transverse to the stem) and 90° transverse to the stress pattern (parallel to the stem axis). $n_{WT} = 171$; $n_{p35S::PMEI} = 29$; $n_{xxt1xxt2} = 17$; $n_{nek-6} = 30$; $n_{spr2-2} = 29$; $n_{clasp-1} = 29$; $n_{ktn-1} = 54$; $n_{trm678} = 52$; $n_{act2act7} = 61$

- **Division plane orientation analysis**

Next, I decided to measure the orientation of the division plane from recent divisions from the maximal tension pattern in the stem (transverse to the stem) in these cell wall mutants. Indeed, even though the radial step occurrence seems independent from cell shape (see Chapter I2 of the Results), cell wall modifications and subsequent global tension patterns alterations could impact the division rules in the stem. I used the addition of the two daughter cells as a proxy for the mother cell. As described above, WT cells tend to divide following their shortest plane when they have an aspect ratio below 0.6, and tend to divide following the maximal tissue tension when their aspect ratio is above 0.6 (see Chapter I2 of the Results). When plotting the division angles of *xxt1xxt2* and *p35S::PMEI5* as a function of the cells' aspect ratios, I could distinguish two populations of cells, as in the WT (Figure R22). As the sample size is low, I could not fit a logistic function to the data, to extract the exact aspect ratio threshold at which cells change division orientations, but I could qualitatively estimate it at 0.6 for both genetic backgrounds, as in the WT. *p35S::PMEI5* cells seemed to be rounder than WT cells, as I did not measure any cells with an aspect ratio below 0.4.

4. The radial step is robust to microtubule perturbations

Here, I investigated the possible role of MAPs regulating MT dynamics in the radial step. I focused on four candidates: KTN1, NEK6, SPR2 and CLASP (see Chapter V2 of the Introduction) through the use of mutants. Briefly, *ktn-1* exhibits slower microtubules dynamics, *nek-6* is affected in MT response to wounding, and touch and gravitropic responses. *spr2-2* is impacted in microtubule-dependent microtubule nucleation, as well as severing, and *clasp-1* is affected in microtubule bending at cell edges, and possibly cell shape sensing.

- **Volume ratio between daughter cells**

As previously, I first measured the volumetric ratio between the daughter cells of a recent division in the different mutant backgrounds affected in microtubule behaviors, as an indirect proxy for the radial step. Again, PI and FM4-64 stains were performed and their results were pooled together to increase the sample size (see Chapter II3 of the Results). The same Col-0 dataset as before was kept for comparison. For *ktn-1*, I looked at 3 stems over 2 different experiments, stained with FM4-64, and 2 stems over 2 different experiments, stained with PI. For *nek-6*, I looked at 1 stem stained with FM4-64, and 6 stems over 2 experiments, stained with PI. For *clasp-1*, I looked at 1 stem stained with FM4-64, and 5 stems over 2 experiments, stained with PI. For *spr2-2*, I looked at 4 stems over 2 experiments, stained with FM4-64.

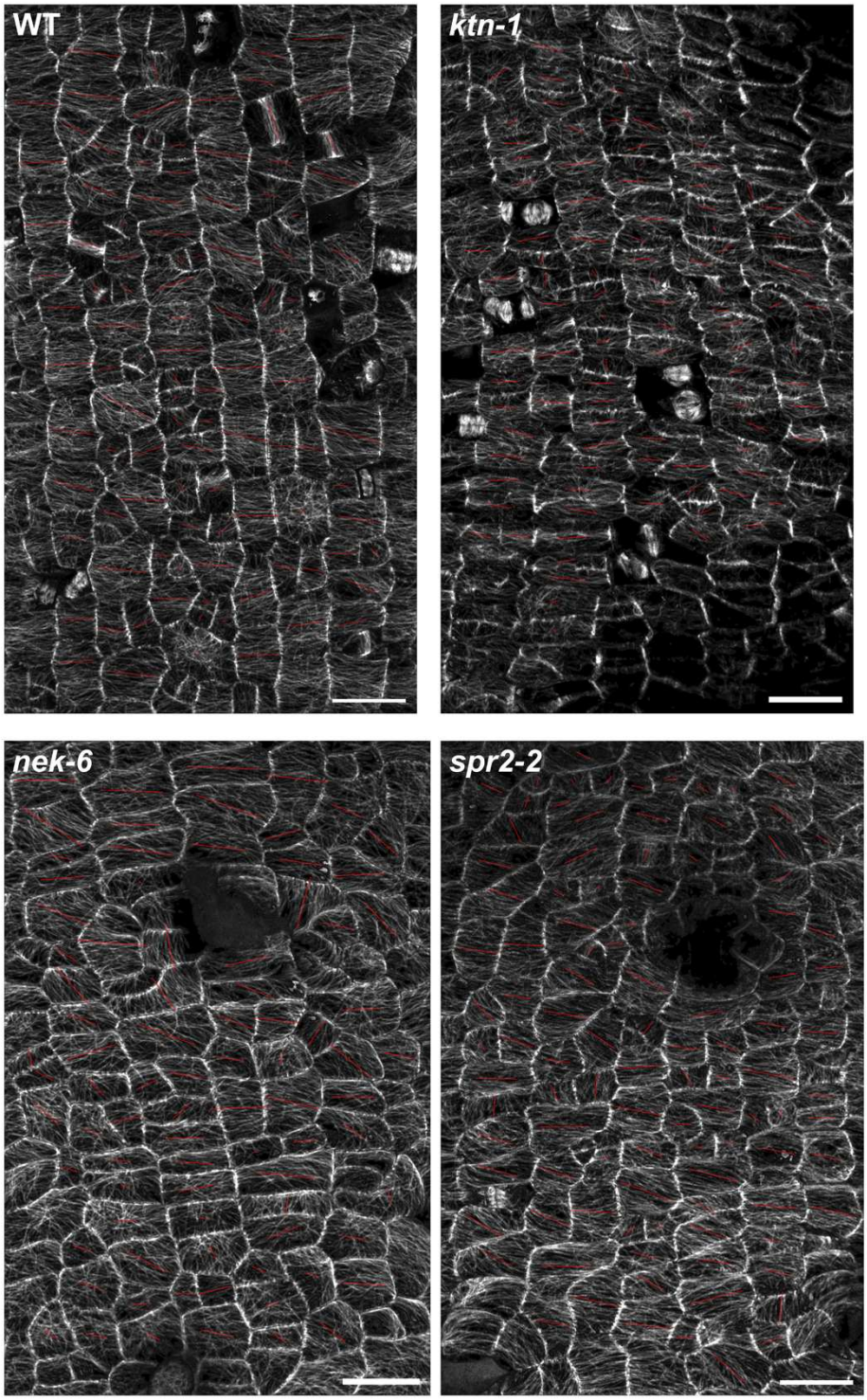

Figure R23: Average CMT orientation in stems of *ktn-1*, *nek-6*, and *spr2-2* microtubule mutants. These images are projections of the microtubule fluorescent signals between 0 and 4 μm, using SurfCut. Cells were segmented manually, and the average orientation of CMTs was extracted and displayed, using an automated version of the FibrilTool plugin in Fiji (http://doi.org/10.5281/zenodo.2528872). The red lines represent the average orientation of CMTs. The length of the line corresponds to the anisotropy of the CMT arrays: the longer the line, the higher the anisotropy value. In these different genetic backgrounds, most of the cells display transverse CMTs, following the predicted maximal tensile stress pattern, even though *ktn-1* microtubules seem thinner than in other backgrounds. The black holes in the images are trichomes that were not included in the imaging. Scale bar: 20 μm. The Brightness&Contrast was modified for better visualization.

I found an average volume ratio of 1.39 +/- 0.37 for the WT, 1.64 +/- 0.94 for *ktn-1*, 1.52 +/- 0.61 for *nek-6*, 1.50 +/- 0.38 for *spr2-2* and 1.40 +/- 0.61 for *clasp-1*. When comparing the means using the Wilcoxon test in RStudio, I found no statistically significant differences between the WT and any of the mutants (Figure R24C). On the other hand, I found a significative difference between the WT and *ktn-1* variances (*p*-value = 0.044, Fligner's test), but no significative differences between the WT and *nek-6* (*p*-value = 0.060, Fligner's test), nor between the WT and *spr2-2* (*p*-value = 0.540, Fligner's test) or between the WT and *clasp-1* (*p*-value = 0.902, Fligner's test). I also looked at the values dispersions with the IQR values (IQR_{WT} = 0.365, IQR_{ktn-1} = 0.495, IQR_{nek-6} = 0.618, IQR_{spr2-2} = 0.489, $IQR_{clasp-1}$ = 0.333). We can therefore conclude that the *ktn-1* mutant displays a higher variability in daughter cells volume ratios than the WT. Also, while their differences are not statistically significant, we can appreciate that the values are more spread for the *nek-6* and *spr2-2* mutants.

Figure R24 (next page): CMT dynamics and geometric symmetry in microtubule mutants. (A) CMT dynamics in pre-mitotic cells of *ktn-1*, *nek-6* and *spr2-2* microtubule mutants. Although not as clear as in the WT, we can observe a radial re-organization of the CMT array before the formation of the PPB. The radial step is marked by the red dotted lines. (B) Examples of *ktn-1* phragmoplast expansion dynamics, in comparison to the WT's. Phragmoplast expansion can be as dynamic as the WT's, or far slower, depending on the sample of *ktn-1*. The images are SurfCut projections between 0 and 4 μm. The Brightness&Contrast was modified for better visualization. The scale bars are 10 μm. (C) Same as R21, but for microtubule mutants.

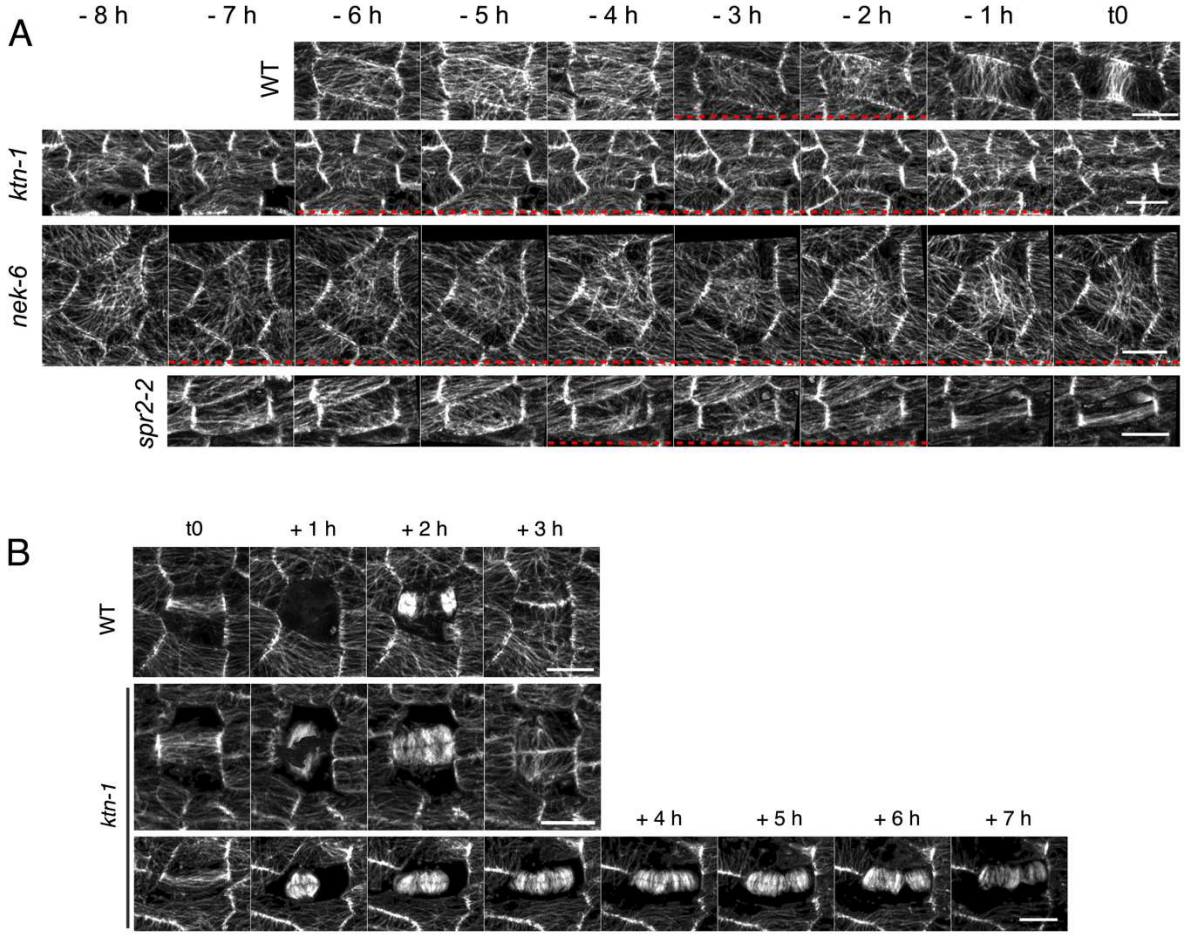
A
- 8 h
- 7 h
- 6 h
- 5 h
- 4 h
- 3 h
- 2 h
- 1 h
t0
WT
ktn-1
nek-6
spr2-2
B
t0
+ 1 h
+ 2 h
+ 3 h
+ 4 h
+ 5 h
+ 6 h
+ 7 h
WT
ktn-1
C
Volume ratio of two daughter cells comparisons between microtubule mutants
Volumetric ratio between the two daughter cells (bigger cell/smaller cell)
n = 64
n = 32
n = 28
n = 33
n = 29
n = 20
p ~ 0.04
p ~ 2.23e-4
0
2
4
6
8
Col-0
trm678
clasp-1
ktn-1
nek-6
spr2-2

- **Cortical microtubule dynamics in pre-mitotic cells**

I next looked at pre-mitotic CMT dynamics in these mutants. The *clasp-1* mutant expressing a stable fluorescent microtubule marker was not ready in time for the analysis, and was therefore not included. Nevertheless, I used the *pPDF1::mCitrine-MBD* microtubule fluorescent marker in the *ktn-1* and *nek-6* mutants, and the *p35S::GFP-MBD* fluorescent marker in the *spr2-2* background. I looked at microtubule dynamics in 6 stems over 3 experiments for *ktn-1*, 3 stems over 2 experiments for *nek-6* and 5 stems over 2 experiments for *spr2-2*. When analyzing overall microtubule orientation in the stems, I noticed that *nek-6* and *spr2-2* CMTs were presenting a transversal bias, as the WT, aligning with the prescribed maximal tension. This suggests that microtubules in these mutants are able to respond to tensile stress (Figure R23). In the *ktn-1* mutant background, while CMTs appeared thinner and visually not highly organized, I could still observe an overall bias towards the transverse axis of the stem. When observing individual pre-mitotic cells over time, I could observe a radial organization of the CMT arrays before the formation of the PPB in all three mutants (Figure R24A). Note that the sample size is low and that the variability between cells is not accounted for. Nevertheless, while the radial step did not appear as clearcut as in the WT, pre-PPB arrays differ from the average interphasic CMT array observed in the rest of the stem. Its duration also seemed affected in the *ktn-1* and *nek-6* mutants, when compared to the WT. In *nek-6*, the radial step qualitatively lasted for at least 8 hours, and in *ktn-1* for around 5 hours. The *spr2-2* mutant, on the other hand, displayed a relatively WT-like radial step, both in terms of aspect and duration. Even though further analysis is needed to confirm the presence of the radial step in all cells for each background, and determine its exact duration, these preliminary data strongly suggests that the radial step is present in *ktn-1*, *nek-6* and *spr2-2* mutant backgrounds. Yet, the duration and aspect of the radial step in *ktn-1* and *nek-6* mutants qualitatively differed from the WT both in aspect and duration (Figure R24A).

On top of revealing pre-mitotic CMT dynamics in these different mutants, time-lapse imaging of MTs showed other phenotypes, especially for the *ktn-1* mutant. Firstly, *ktn-1* mutants were highly sensitive to the confocal microscope laser exposure, and the signal bleached very quickly (around 3-4 hours for some samples), along with a visible degradation of the microtubule arrays. Secondly, phragmoplast expansion was highly reduced, some lasting for at least 8 hours (compared to around 1 hours in the WT, Figure R24B), and could result from the increased sensitivity of *ktn-1* microtubules to the laser. However, this dramatic observation had been made in only one sample, and could account for the variability among samples.

- **Pre-prophase band morphology analysis**

Moreover, one could wonder about the interdependence between the radial step and PPB morphology. While the presence of the PPB is not required for the presence of the radial step, as evidenced by the *trm678* mutant (see Chapter I4 of the Results), this rearrangement of CMTs could help in making the PPB ring, for example by a search and capture mechanism (Vos *et al.*, 2004).

Interestingly, *ktn-1* PPBs were maturing very slowly, and were sometimes very wide, and not organized as a clear band as in the WT. I measured mature PPBs' widths, from cells that underwent mitosis in the next timepoint in both WT and *ktn-1* cells. The PPBs middle points were 2.78 +/- 1.17 μm wide in the WT (n = 60) and 4.07 +/- 1.20 μm wide in the *ktn-1* mutant (n = 23), in average, which was statistically significant (*p*-value = $1.96e^{-4}$, Tuckey test in RStudio). The ratios between the two anchoring points of the PPB, when measuring the widest over the smallest, were of 1.28 +/- 0.34 for the WT, and of 1.36 +/- 0.28 for *ktn-1* mutants. While this indicates a slight broadening of the PPB at one side of *ktn-1* cells, when compared to the WT, these averages were not statistically different using Tuckey's test in RStudio (*p*-value = 0.72, Tuckey's test).

- **Division plane orientation analysis**

I took advantage of these MT-defective backgrounds to further test the interdependence between the radial step and the division plane orientation. I measured the orientation of either newly formed division planes, or the PPBs in *clasp-1*, *nek-6*, *ktn-1* and *spr2-2* mutant backgrounds, from the maximal tension pattern in the stem (transverse to the stem). I plotted this angle as a function of the aspect ratio of the cell, to see if we could observe the two populations of cells as in the WT (see Chapter I2 of the Results, Figure R22). As the sample size was low, I did not fit a logistic curve to the data, and was therefore not able to obtain a potential threshold separating the two populations, but qualitative analysis of the data was sufficient to give insights. In *nek-6* and *spr2-2* mutants, two populations of cells could be distinguished. Cells with a lower aspect ratio tended to divide at around 90° from the tension pattern (following the stem axis, and probably their shortest plane), while cells with a higher aspect ratio tended to divide at around 0° from the maximal tension orientation (transverse to the stem). Qualitatively, the threshold in aspect ratio separating the two populations seemed to be at around 0.6, as in the WT. In *clasp-1*, the same observations could be made. Interestingly, though, the threshold in aspect ratio separating the two populations seemed much lower than in the WT, *nek-6* or *spr2-2*, at around 0.4, suggesting that the division rules are slightly modified in this genetic background. In *ktn-1*, on the other hand, I could not distinguish different populations of cells, and most of the cells tended to divide following the maximal tension orientation. For reference, I plotted the division orientations as a function of the cell aspect ratio in the *trm678* PPB-deficient mutants that display a longer radial step, and a decreased variability in daughter cells volume ratios. In this genetic background, I could not find the two populations of cells as in the WT.

It is worth noting that I found some instances of aberrant divisions in *ktn-1*, *nek-6* and *clasp-1* mutants (Figure R25). More specifically, divisions were sometimes incomplete, wavy and I found some instances of oblique, periclinal divisions. Following CMT dynamics before and during mitosis of these aberrant divisions could be interesting for investigating the role of the radial step in correct mitosis preparation.

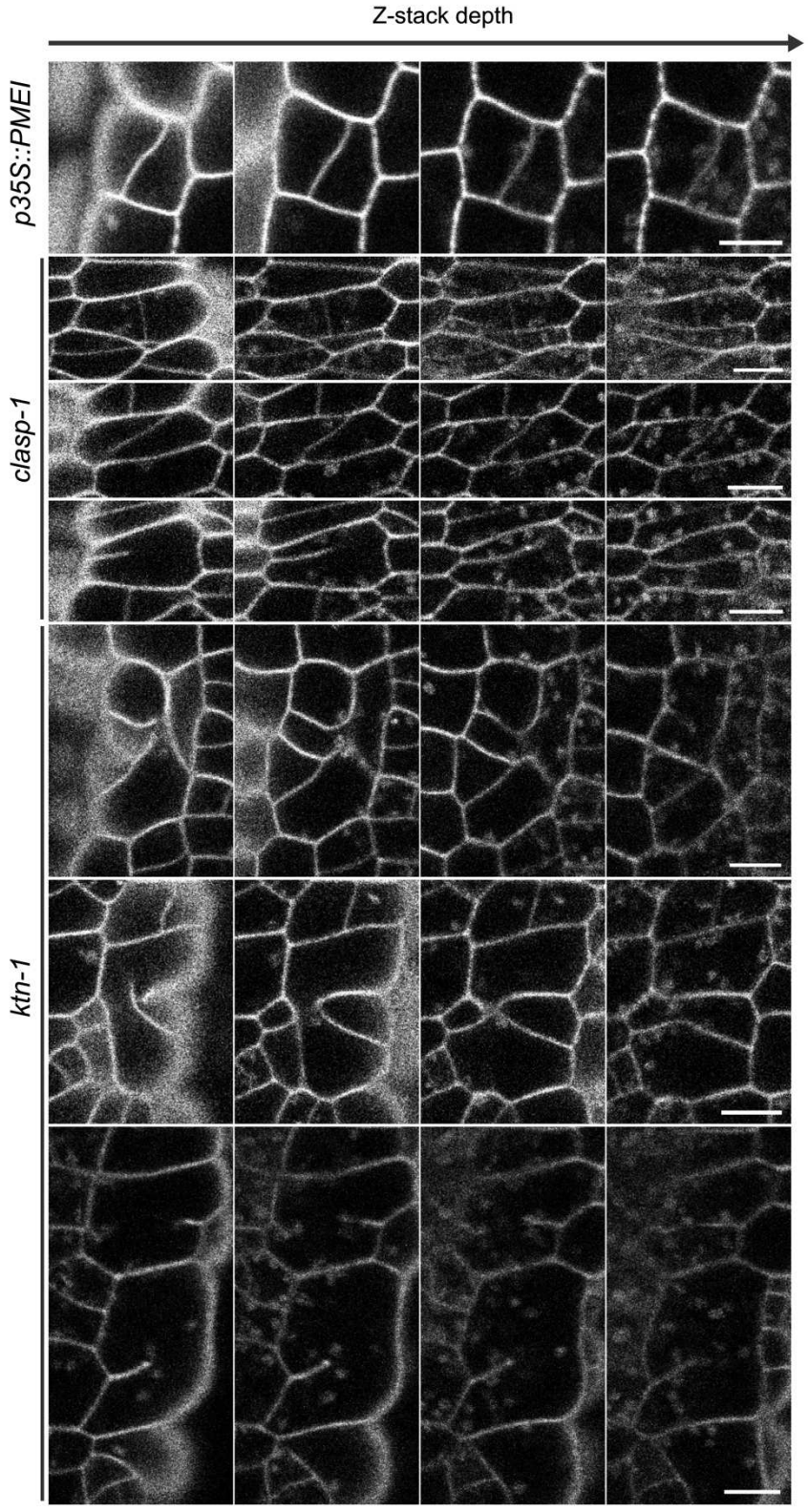
Z-stack depth
p35S::PMEI
clasp-1
ktn-1

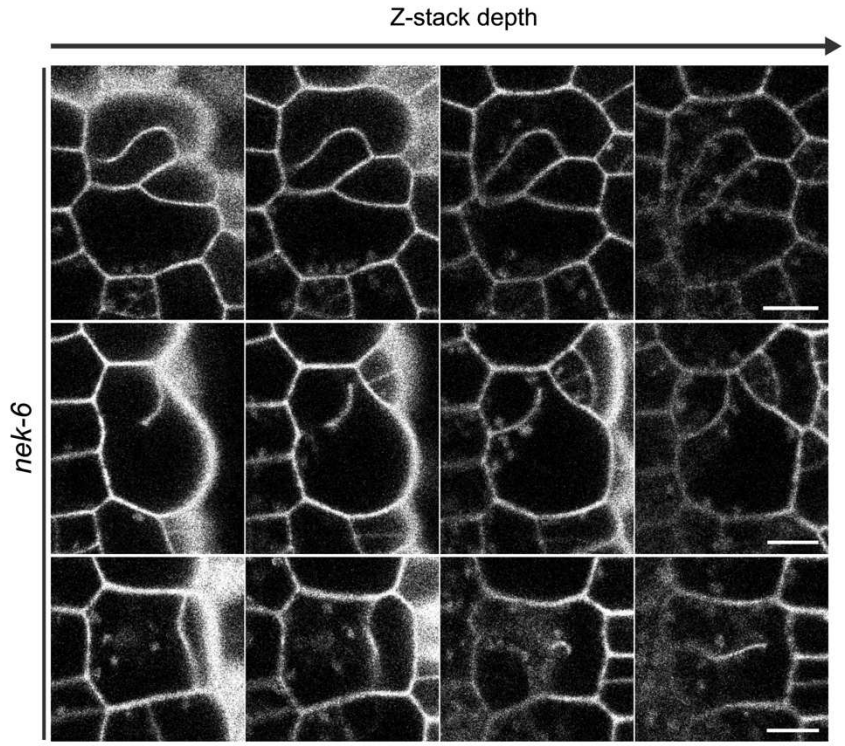

Figure R25: Examples of aberrant divisions in various mutant backgrounds. Each series of images for one cell are different focal planes of a Z-stack, illustrating best the defects in division planes. The images show the PI staining signal of cells from *Arabidopsis* stems in the different mutant backgrounds. The Brightness&Contrast parameters have been adjusted for better visualization. The scale bars are 10 μm.

5. The radial step is robust to actin perturbations

Because the radial step involves a structural change of the cytoskeleton, I next tested whether perturbations in actin filaments could affect the radial step. This notably builds on studies showing the interplay between both cytoskeletons (Sampathkumar *et al.*, 2011; Figure II12C). Furthermore, the actin cytoskeleton also plays a role in mitosis preparation with the nuclear movement and the formation of the PPB (Palevitz, 1987; Traas *et al.*, 1987; Kakimoto and Shibaoka, 1987), as well as during mitosis, with the polarization of actin at cell poles and the actin depleted zone (Lebecq *et al.*, 2022; Liu and Palevitz, 1992; Cleary *et al.*, 1992).

- **Volume ratio between daughter cells**

In order to explore the potential role of actin in the radial step, I used the *actin2-7 actin7-4* (*act2act7*) double mutant, which is affected in vegetative actin content and displays strong developmental defects (Kandasamy *et al.*, 2009; see Chapter V1 of the Introduction). As previously, I first measured the ratios in daughter cell volumes in the *act2act7* mutant background, as an indirect proxy for the radial step. After staining the stems with either PI or FM4-64, the results were pooled together to increase the sample size. The WT results taken for comparison were the same as above (see Chapter II3 and II4 of the Results). I analyzed 2 stems over one experiment, stained with FM4-64, and 4 stems over 2 experiments, stained with PI. The average volume ratios between daughter cells was of 1.39 +/- 0.37 for the WT and of 2.03 +/- 0.84 for the *act2act7* mutants (Figure R28B). The means were not significantly different, using the Wilcoxon test in RStudio (p-value = 0.06, Wilcoxon test). The variances, however, were significantly different using the Fligner's test in RStudio (p-value = $1.23e^{-5}$), as well as the distribution of the results (p-value = $4.42e^{-4}$). The IQR value was much higher for *act2act7* than for the WT (IQR_{WT} = 0.365, $IQR_{act2act7}$ = 1.25), indicating that the variance in *act2act7* daughter cells volume ratios is bigger than in the WT. To investigate further the role of actin in pre-PPB dynamics, I followed pre-mitotic cells of *act2act7* expressing the *p35S::GFP-MBD* microtubule marker (Marc *et al.*, 1998; Wang, 2022).

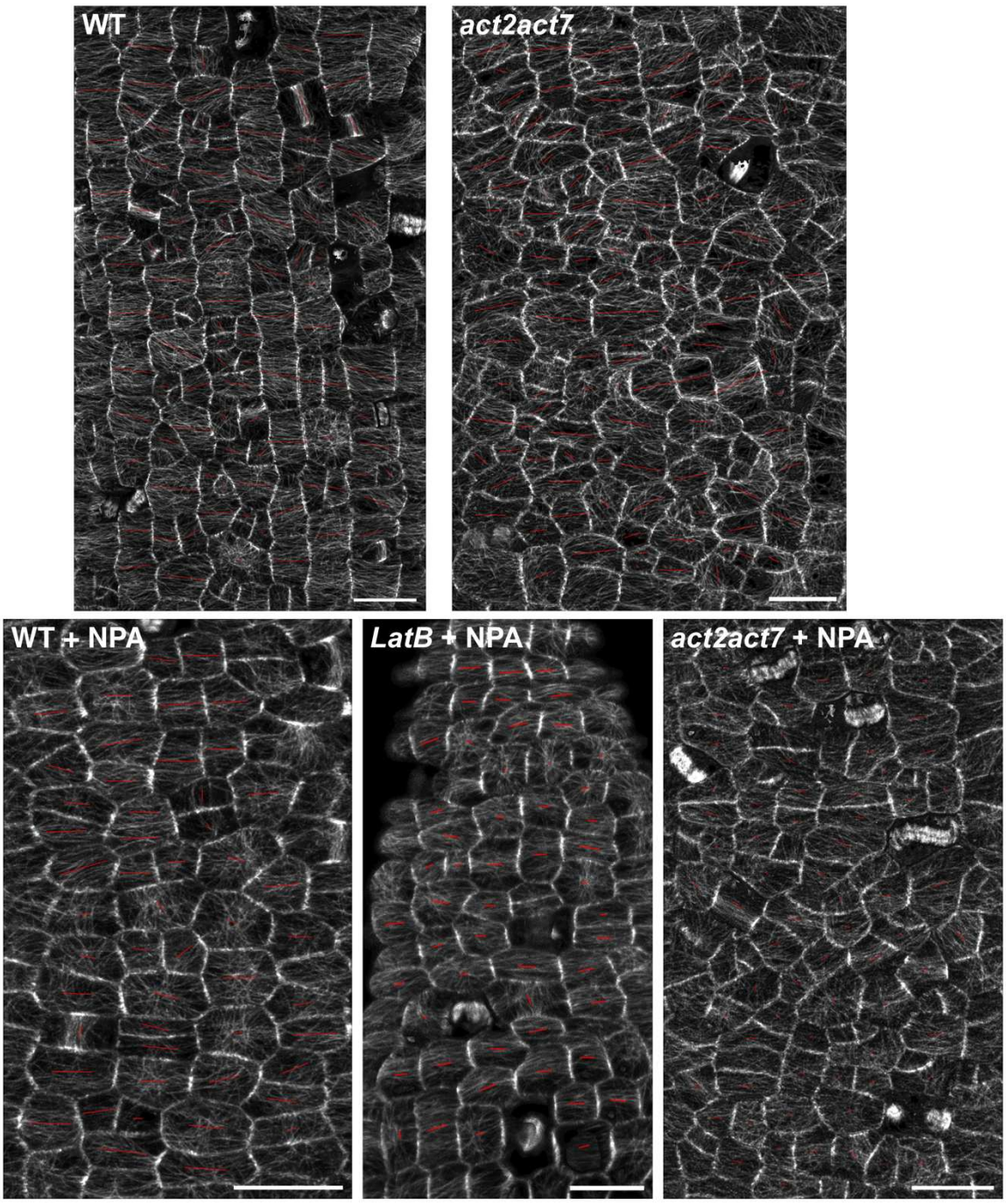

Figure R26: Average CMT orientation in stems subjected to actin perturbations. Same as Figure R23. Overall, we can observe a transverse bias in CMT array. *act2act7* mutants display arrays slightly tilted from the transverse orientation, probably due to their cell shapes.

- **Cortical microtubule dynamics in pre-mitotic cells**

The tissue topology in *act2act7* was different than the WT, notably with bulgy cells, as described previously in roots (Gilliland *et al.*, 2002). Indeed, actin has been correlated with cellulose synthase complexes mobility, and cell wall composition in *act2act7* stems is very likely altered (Sampathkumar *et al.*, 2013). I followed CMT dynamics in 4 stems of *act2act7* mutants over 2 different experiments. CMT orientations were overall transverse to the stem, suggesting that microtubules respond correctly to tension in this mutant (Figure R26). However, when looking at individual cells, the array was not perfectly transverse to the stem, as for most WT cells, which could be due to the differences in cell shapes, or in cell wall composition (Figure R26). Following pre-mitotic CMT dynamics over time, I could observe a radial step in *act2act7*, that qualitatively started around 3 hours before t0, and lasted for 2 hours, as in the WT background (Figure R28A). These results show that ACTIN2 and ACTIN7 are not required for the presence of the radial step. I also visualized microtubules in *act2act7* mutants grown and imaged on NPA-containing media. In these conditions, I imaged 13 stems over the course of 2 different experiments. The overall transverse bias in stems' CMT arrays was reduced compared to the control *act2act7* conditions, and the WT in NPA conditions (Figure R26). Nevertheless, individual pre-mitotic cells also underwent the radial step before forming their PPB. This step started around 3 hours before t0 and lasted for 2 hours, as in the WT in NPA conditions, and in control conditions (Figure R28A).

To further perturb the actin cytoskeleton, we applied a Latrunculin B (LatB) actin polymerization inhibitor (Spector *et al.*, 1983) treatment to stems in NPA conditions, two and a half hours before imaging. We imaged 5 stems over one experiment. The CMT arrays in the stem were highly biased towards the transverse orientation, and the tissue topology appeared WT-like (Figure R26). This suggests that the lack of transverse organization in the *act2act7* CMT arrays in NPA conditions were likely due to the cell shape or cell wall modifications induced by the mutation. Pre-mitotic cells also underwent the radial step before the formation of the PPB in stems treated with LatB and NPA (Figure R28A). The results were highly comparable to what was observed in NPA conditions, further indicating that actin is not required for the formation of the radial step.

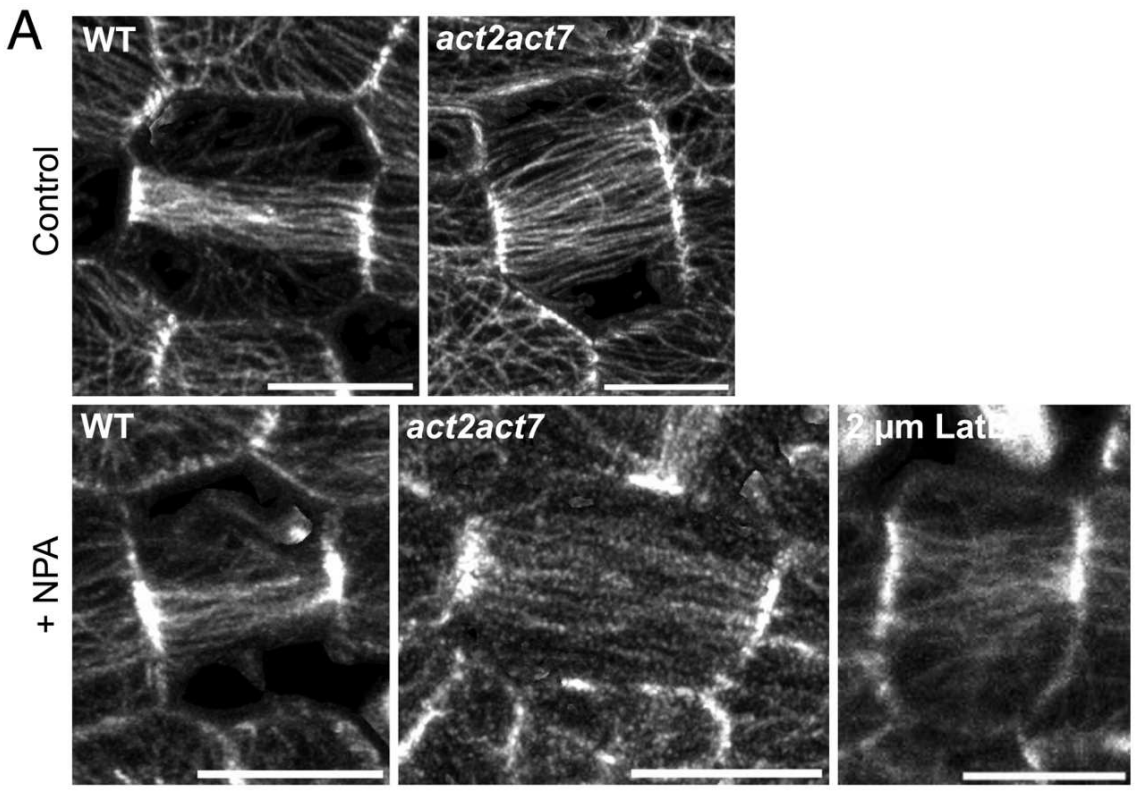

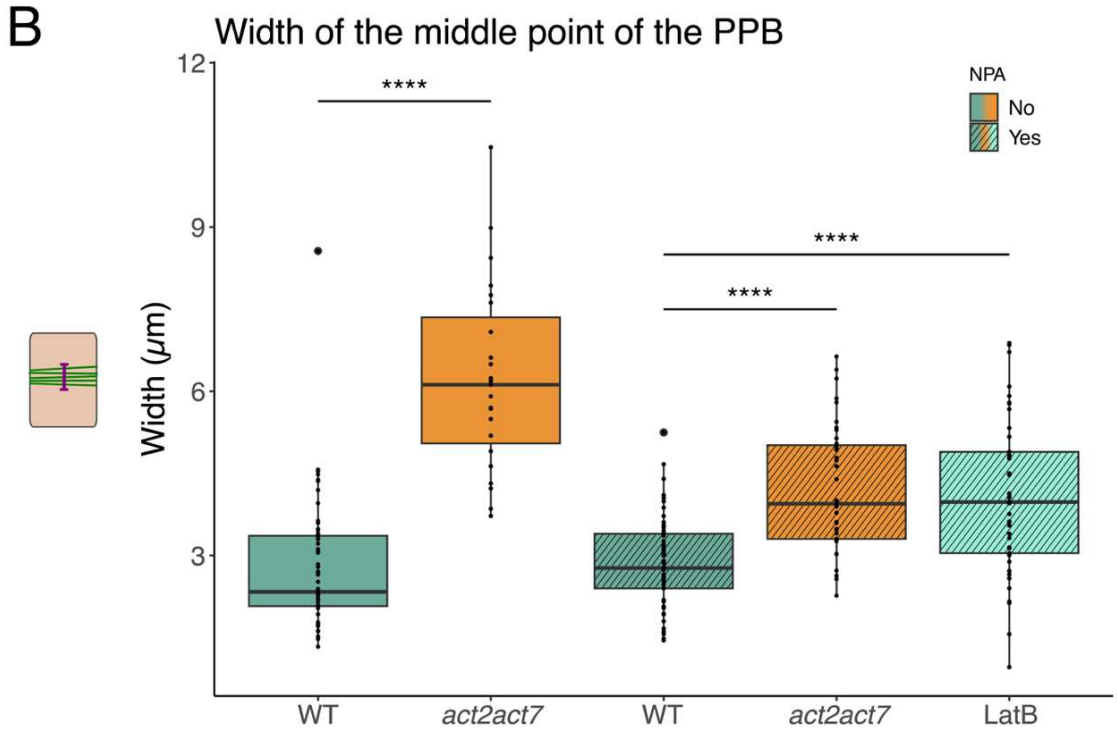

Figure R27: PPPs are wider when subjected to actin perturbations. (A) Mature PPBs in WT, *act2act7* backgrounds, and LatB treatment. The top panels display control conditions, and bottom panels show stems grown and imaged in NPA conditions. Images are SurfCut projections from 0 to 4 µm from the surface of the stem. The Brightness&Contrast parameters have been adjusted for better visualization. The scale bars are 10 µm. (B) Boxplot showing the average width of the middle of the PPB. (**** p-value < 1e^{-04}, Tuckey's Test). $n_{\text{WT, control}} = 60$; $n_{\textit{act2act7}, \text{control}} = 23$; $n_{\text{WT, NPA}} = 62$; $n_{\textit{act2act7}, \text{NPA}} = 39$; $n_{\text{LatB, NPA}} = 45$.

- **Pre-prophase band morphology analysis**

To further test the interdependence between the radial step and the PPB morphology, I took advantage of these actin perturbation conditions. Indeed, actin perturbations lead to enlarged PPBs (Mineyuki and Palevitz, 1990; Kojo *et al.*, 2013; Figure I25A). This was also reflected in our data when measuring PPB widths of pre-mitotic cells. To ensure the PPB was at its latest maturation point, I only selected cells that entered mitosis at the next timepoint (Figure R27A). In the WT background, PPBs were of 2.78 +/- 1.17 μm in control conditions, and of 2.88 +/- 0.83 μm in NPA conditions. In the *act2act7* mutants, PPBs were 6.24 +/- 1.71 μm in control conditions, and 4.24 +/- 1.14 μm in NPA conditions. PPBs from LatB treated cells were 4.06 +/- 1.40 μm in NPA conditions (Figure R27B). PPB width in the WT between control and NPA conditions were not statistically different, when comparing the means (p-value = 1.00, Tuckey's test in RStudio). However, PPB width between the WT and *act2act* were statistically different both in control conditions (*p*-value = $7.72e^{-14}$, Tuckey's test in RStudio) and in NPA conditions (*p*-value = $1.22e^{-6}$, Tuckey's test in RStudio). In the WT, between NPA and LatB + NPA treatments, average PPB widths were also statistically different (*p*-value = $1.52e^{-5}$, Tuckey's test in RStudio). The results above were obtained measuring the middle point of the PPB, but I also measured the width of both anchoring points, as viewed from the top in a surface projection. When measuring the ratios of both anchoring points (always dividing the bigger by the smaller one, for comparison purposes), I found 1.28 +/- 0.34 for the WT and 1.31 +/- 0.34 for *act2act7*, in control conditions. In NPA conditions, I found 1.25 +/- 0.24 for the WT, 1.30 +/- 0.24 for *act2act7* and 1.37 +/- 0.37 for LatB-treated cells. No statistical differences were found for the ratios in any of these conditions, when looking at the means. This indicates that there are no differences in PPB anchoring between the cell sides.

- **Division plane orientation analysis**

To further test the interdependence between the radial step and division plane orientations, and because *act2act7* tissue topology seemed affected in the stem, I decided to measure division plane orientations in this mutant background. I measured recent division planes, or PPB orientations in *act2act7* with respect to the maximal tension orientation in the stem (transverse to the stem). When plotting these angles as a function of the aspect ratio, I could not distinguish two populations of cells, as in the WT, and cells seemed to largely divide following the maximal tension pattern (Figure R22). This indicates that in the *act2act7* mutant background, division rules are changed with respect to WT cells. As the radial step still happens in *act2act7*, it gives us further evidence that this step happens regardless of the orientation of the future division plane, even though it could be involved in its positioning. It is worth mentioning that in this genetic background, the final division plane did not always follow the one prescribed by the PPB (Figure R28C). This could come from defects in the PPB establishment, in signaling properties from the actin cytoskeleton, or in phragmoplast expansion and guidance.

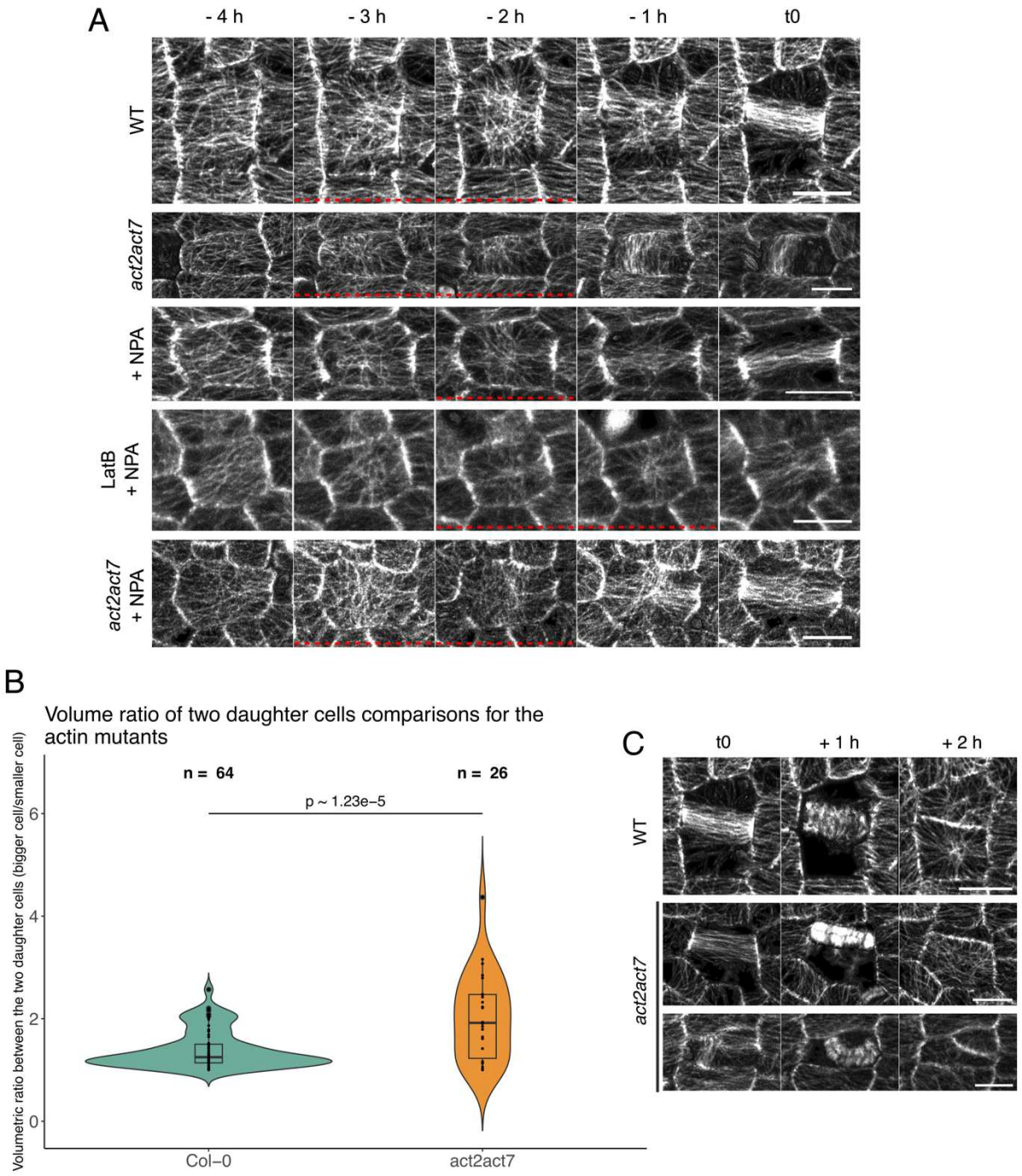

Figure R28: CMT dynamics and geometric symmetry with actin perturbations. (A) CMT dynamics in pre-mitotic cells of *act2act7* and LatB-treated cells in control and NPA conditions. We can observe a radial step before the formation of the PPB in all of these conditions. The radial step is marked by the red dotted lines. (B) Same as R21, but for the *act2act7* mutant. The radial step is marked by the red dotted lines. (C) Examples of dividing cells not following the prescribed PPB plane in the *act2act7* mutant. (A) and (C) are SurfCut projections between 0 and 4 μm from the stem surface. The B&C parameters have been adjusted for better visualization of the microtubules. The scale bars are 10 μm.

Overall, I could confirm that actin perturbations produce defects in PPB width and division plane positioning. The *act2act7* mutant also exhibits much more variability in daughter cell volume ratios then the WT. Nevertheless, actin perturbations from this mutant or from LatB treatments do not prevent the formation of the radial step. However, the correlation between the radial step and volume partitioning is difficult to make for *act2act7* as division defects are mainly visible during mitosis and after PPB formation. In this mutant, the division plane sometimes did not follow the prescribed PPB plane, likely due to a misalignment between the nucleus and the PPB (Figure R20A). One could wonder whether the nucleus is the main driver of PPB positioning, or if these two processes are independent, and how the radial step could potentially play a role in them.

6. Testing the interdependence between the radial step and nuclear movements

Pre-mitotic microtubule behavior may depend on a broader set of regulators. In particular, the positioning of the nucleus may have a key role. Cytoplasmic microtubules have been shown to be involved in pre-mitotic (Muroyama *et al.*, 2020) and post-mitotic (Yamada and Goshima, 2018) nuclear movements. Nevertheless, nuclear movements in plants are generally linked with the actin cytoskeleton (Chytilova *et al.*, 2000; Mineyuki and Palevitz, 1990; Kimata *et al.*, 2016; Vilches Barro *et al.*, 2019). Our analysis of the *act2act7* mutant and LatB treatment may suggest that nucleus movement is not required for radial step emergence (see Chapter II5 of the Results). Yet, given the increase of cytoplasmic microtubules at the radial step stage (see Chapter I4 of the Results), and the more variable ratio in daughter cell volume in the *act2act7* mutant, we decided to investigate nuclear movements in dividing cells from stems.

Figure R29 (next page): The radial step occurs during G2 and is loosely correlated with nuclear positioning at the centroid of the cell. (A) Adapted from Yokoyama *et al.* (2016). Scheme showing the localization of PCNA1 during different phases of the cell cycle. (B) Pre-mitotic cell expressing *pPDF1::mCitrine-MBD* (in green) and *pPCNA1::PCNA1-RFP* (in magenta), grown and imaged in NPA conditions. Microtubules are visualized through a SurfCut projection between 0 and 4 µm from the stem surface and the nucleus is visualized through a maximal projection of the Z-stack. The radial step is marked by a red dotted line, corresponding to a "whole" localization of PCNA1, and the G2 phase of the cell cycle. The B&C parameters have been adjusted for better visualization. The scale bar is 10 µm. (C) Average distance between the cell centroid and the nucleus centroid overtime. This distance has been calculated as $\frac{\sqrt{(xC-xN)^2+(yC-yN)^2}}{Cell\ area}$, with xC, yC, xN and yN being the XY coordinated of the cell centroid and nucleus centroid, respectively, as determined through Fiji. All of these measurements were made for cells in NPA conditions. $n_{-10\ hrs} = 4$; $n_{-9\ hrs} = 10$; $n_{-8\ hrs} = 17$; $n_{-7\ hrs} = 25$; $n_{-6\ hrs} = 27$; $n_{-5\ hrs} = 31$; $n_{-4\ hrs} = 32$; $n_{-3\ hrs} = 28$; $n_{-2\ hrs} = 33$; $n_{-1\ hr} = 34$; $n_{t0} = 35$. (D) Same data as (C), but represented according to qualitative assessment of the CMT array configurations. (p-value < $1e^{-03}$, Tuckey's test). $n_{Interphasic} = 130$; $n_{Radial} = 89$; $n_{PPB} = 57$.

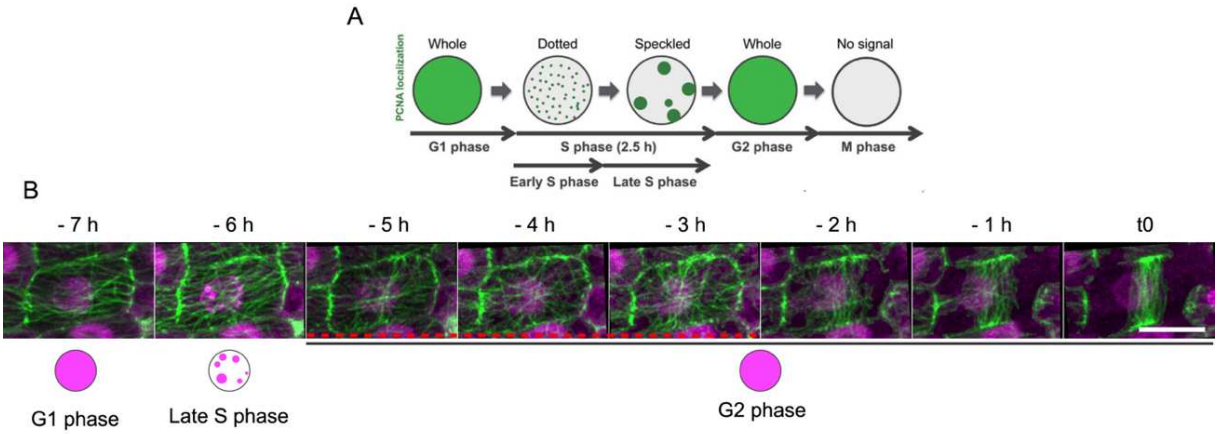
A
PCNA localization
Whole
Dotted
Speckled
Whole
No signal
G1 phase
S phase (2.5 h)
G2 phase
M phase
Early S phase
Late S phase
B
- 7 h
- 6 h
- 5 h
- 4 h
- 3 h
- 2 h
- 1 h
t0
G1 phase
Late S phase
G2 phase

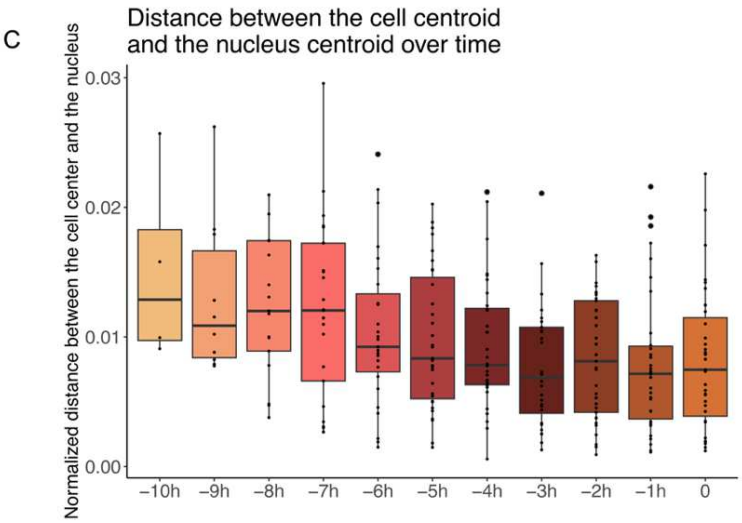
C
Distance between the cell centroid and the nucleus centroid over time
Normalized distance between the cell center and the nucleus
0.03
0.02
0.01
0.00
−10h
−9h
−8h
−7h
−6h
−5h
−4h
−3h
−2h
−1h
0

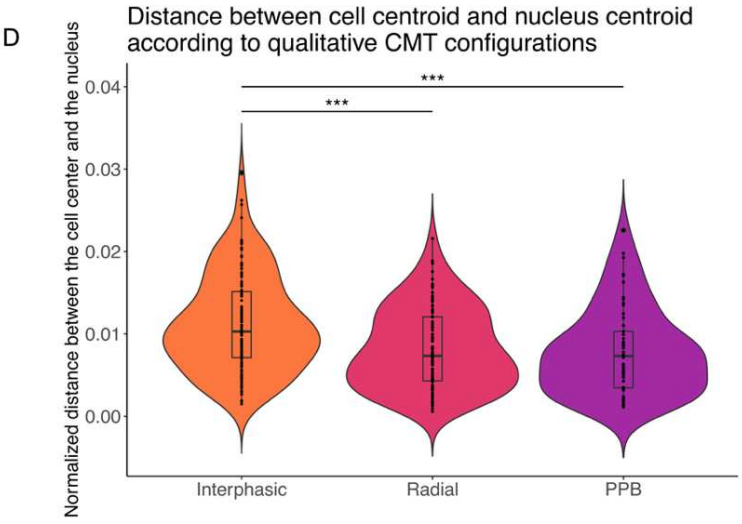
D
Distance between cell centroid and nucleus centroid according to qualitative CMT configurations
Normalized distance between the cell center and the nucleus
0.04
0.03
0.02
0.01
0.00
***
***
Interphasic
Radial
PPB

To investigate CMT dynamics in relation with nucleus movements over time, we performed time lapse experiments using plants expressing the *pPCNA1::PCNA1-RFP* fluorescent nucleus marker crossed with the *pPDF1::mCitrine-MBD* fluorescent microtubule marker. Proliferating Cell Nuclear Antigen (PCNA) is a protein involved in DNA replication, distributed throughout the nucleus in different patterns depending on the cell cycle phase (Yokoyama *et al.*, 2016; see Chapter VI1B of the Introduction). Whole patterns indicate cells either in G1 or G2 phases, dotted and speckled patterns show early and late S phases, respectively (Figure R29A). No signal is detected during mitosis. We performed our analysis on plants grown and imaged in NPA conditions, and imaged 11 stems over 2 separate experiments.

The first observation we made was that, qualitatively, the radial step seems to occur when the PCNA1 protein is distributed uniformly in the nucleus. Since the next step is mitosis, we can therefore confirm that the cell is in the G2 phase of the cell cycle (Figure R29B). This is expected as, if the radial step is indeed linked with preparation for mitosis, it would happen after DNA replication (during the S phase). To investigate nucleus movements over time, I measured the distance between the cell centroid and the nucleus centroid, in 2D. Overall, there seems to be a diminishment of this distance overtime, indicating that the nucleus moves closer to the cell center (Figure R29C), as it progresses through the cell cycle (average distance of 0.01 +/- 0.005 at -6 hrs, of 0.008 +/- 0.005 at t0). Tuckey's statistical test to compare the means revealed no statistical differences between any timepoints. Therefore, even if there is a gradual migration of the nucleus towards the cell center visually, it does not seem to happen at a specific time before mitosis. Nevertheless, if we group cells and timepoints by the qualitative aspect of their CMT array (interphasic when they are aligned, radial or PPB), we can observe differences in the distances between the cell center and the nucleus center (Figure R29D). Cells with interphasic CMT arrays showed distances between the nucleus centroid and the cell centroid of 0.011 +/- 0.006, cells in radial array configurations of 0.008 +/- 0.005 and cells in PPB of 0.008 +/- 0.005. When running a statistical test to compare the means between different qualitative CMT arrays, we found statistical differences between the cell centroid and nucleus centroid distances in interphasic versus radial cells and in interphasic versus PPB cells (p-value = $4.88e^{-4}$ for radial cells, p-values = $7.48e^{-4}$ for PPB cells, Tuckey's test). Whereas no statistical difference was found between cells in a radial array and PPB cells (p-value = 0.99, Tuckey's test). These results suggest that while there is no precise timepoint at which the nucleus starts migrating towards the center, cells undergoing the radial array seem to have their nucleus positioned at a position that is consistent with the one adopted at the PPB stage. This could be explained by the temporal variability of the radial step, and PPB maturation. Also, these movements (at least measured in 2D) were very subtle, surely due to the fact that in these cells, the nucleus occupies most of the cell (the area ratio between the nucleus and the cell was 0.19 +/- 0.05).

Nevertheless, links between the nucleus displacement and the PPB positioning are under debate (see Chapter VII1 of the Introduction). Even though nuclei positioning at the radial step stage and at the PPB stage are similar in stems, I found some instances of split PPBs. This observation of multiple, or split PPBs has been described in other systems, notably in tobacco cultured BY-2 cells (Granger and Cyr, 200; Yoneda *et al.*, 2005). In the stem, these PPBs were most of the time split in a Y-shaped structure, with one side being anchored at one point of the cell vertex (as seen in 2D), and the other side of the PPB got separated into two, that usually were anchored surrounding a tri-cellular junction (Figure R20A). With maturation, only one plane was retained and the cell division adopted the latter, likely due to the narrowing of the split PPB into a unique plane, that I could not see with the 1-hour time resolution. It is worth noting that I observed split PPBs in almost all the conditions tested in the stem (in the WT either in control, or in NPA-supplemented conditions, and in *act2act7* and *ktn-1* mutant backgrounds). These PPB structures seem to appear when the optimal division plane position goes through a tri-cellular junction, and the cell has to adapt it between two alternatives. In that case, the radial step would not be involved in division plane 4-way-junction avoidance, as it happens regardless of the PPB morphology (split or uniform). The presence of these split PPB structures shows that the division plane position is not final with the appearance of the PPB, and that the cell still integrates cues as the PPB matures.

While we could establish a correlation between the displacement of the nucleus towards the center of the cell, the increase in cytoplasmic microtubules and the radial array of CMTs, the time resolution is limiting to really tie these three processes together. The nucleus seems to be stabilized at its position during the G2 phase, suggesting that its localization in the cell is important at that stage (Mineyuki and Furuya, 1980). Increasing the cell size with respect to the nucleus size could help better visualize pre-mitotic nuclear movements, and precise the correlation between the radial step and nucleus positioning.

III. Development of new systems to study the contributions of the tissue context and integrity in pre-mitotic microtubule dynamics

While the *Arabidopsis* stem is a model system presenting numerous advantages to study mitotic phenomena *in planta*, some limitations are met when studying specific contributions of various parameters. Indeed, while global tissue tension can be changed to some extent, cell shape cannot be precisely manipulated. Also, as mentioned previously, cells are rather small, and the nucleus occupies most of the cell volume. In order to further investigate the function of the radial step in mitosis and pre-mitotic processes, we aimed to develop new systems to overcome the limitations presented by the stem. Notably, we tried following pre-mitotic CMT behaviors in dividing tobacco pavement cells, and visualize divisions in calli and protoplasts from *Arabidopsis*.

Contribution: In this part, I performed all the experiments. The part on tobacco infiltrations was made together with Camille Gauthier, who did an internship in our team, under my supervision.

1. Using the *Nicotiana benthamiana* pavement cells to study pre-mitotic nuclear movements

To investigate the organization of CMTs when nuclear movements occurred, we decided to take advantage of a system with bigger cells, where nuclear movements would be more striking: the *Nicotiana benthamiana* mesophyll pavement cells. Although these cells are already differentiated, division can be induced upon *Agrobacterium tumefaciens* infiltrations with *p35S::*At*CYCD3;1* plasmids (Wydro *et al.*, 2006; Xu *et al.*, 2020). We used the *p35S::AtCYCD3;1-Turquoise2* construct in order to visualize the nucleus, as well as induce cell divisions, in tobacco plants expressing the *p35S::GFP-TUA6* construct, to visualize microtubules (Gillespie *et al.*, 2002). As expected, we observed mitotic structures in leaves as early as 24h hours after the infiltration, depending on the leaf stage (see Camille Gauthier's internship report in Annexes). As GFP and Turquoise2 emission spectra overlap, we were able to visualize both microtubules and nuclei, limiting the tissue exposure to laser, and subsequent bleaching. While the infiltration method was technically easy and reproducible, the imaging of leaves was quite challenging. Indeed, the mitosis induction was more efficient in younger leaves (leaf 4-7), but they were highly crinkled, due to their age, as they flatten overtime. The leaf sample was therefore difficult to flatten and the resulting images were hard to analyze. Surface projections were subsequently not easy to extract, and most of the visualization was done using maximal Z-projections, or focusing on a single slice of the Z-stack. Consequently, CMTs from the top or the bottom cortex of the cell, and cytoplasmic microtubules were indistinguishable.

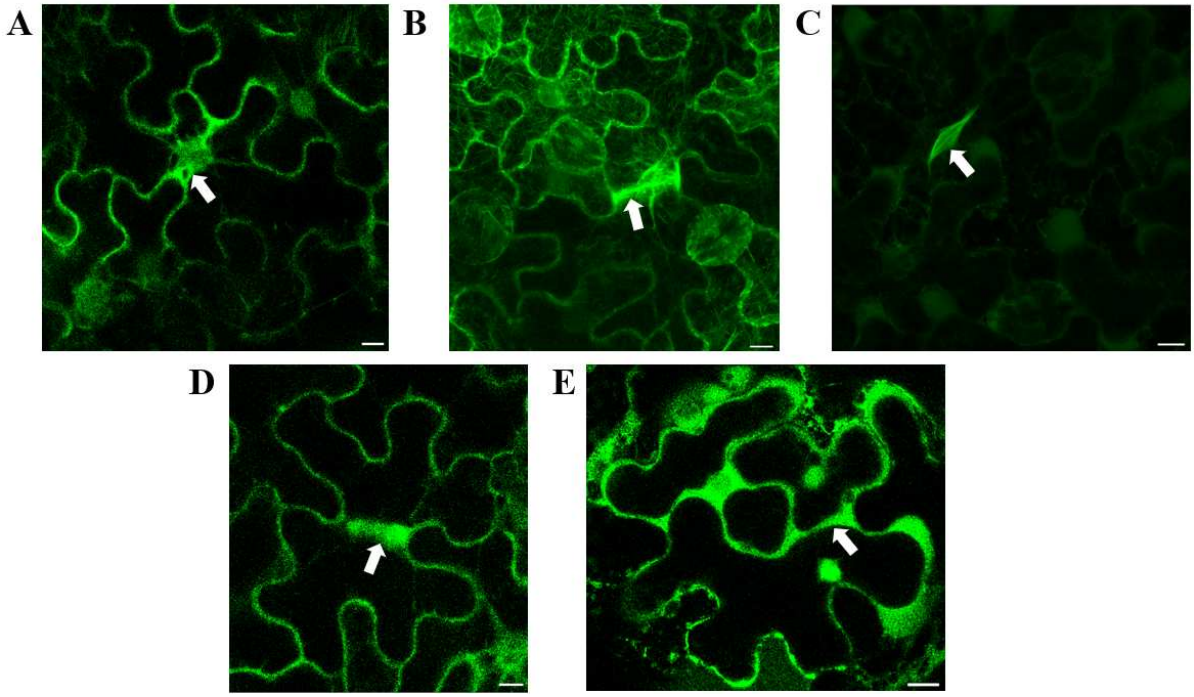

Figure R30: Adapted from Camille Gauthier's internship report. Infiltration of *N. benthamiana* leaves with *p35S::AtCYCD3;1-Turquoise2* effectively induces mitosis. The images show *P35S::TUA6-GFP* signal in tobacco leaves. Nuclei from infected cells can be visualized through the overlap between GFP and Turquoise2 spectra. (A-B) The arrows show PPB structures. (C) The arrow shows spindles. (D) The arrow shows a phragmoplast. (E) The arrow shows a division plane from recently divided cells. (A), (D) and (F) show a single focal plane from the Z-stack. (B) and (C) are maximal projections from the Z-stack. The Brightness&Contrast in these images has been adjusted from better visualization. The scale bars are 10 μm.

The mitotic structures we could observe (spindles and phragmoplasts) looked similar to the ones reported before (Xu *et al.*, 2020), and the ones we could observe in *Arabidopsis* stems (Figure R30). Interestingly, the non-mature pre-prophase bands were often wide, and split between different possible division planes (Figure R31C, right image). This observation is reminiscent of the split PPBs observed in *Arabidopsis* stems, suggesting that the PPB maturation process often presents this split stage (see Chapter II6 of the Results; Figure R20A). In *Nicotiana benthamiana* mesophyll cells, the planes prescribed by this structure did not necessarily go through the nucleus, which could indicate that while the nucleus moves towards the region of the future division plane, it does not directly predict where the pre-prophase band will form. Instead, various non-mature PPB rings formed, often between two neck regions of the cell, that could suggest an exploration step between different division planes. However, images of unique PPBs (not split) went through the nucleus (Figure R30A; Figure R31C, right image), suggesting that there is no major offset between the PPB position and the nucleus position. Static images also showed some instances of radially organized microtubules, as viewed from maximal Z projections (Figure R31C). It is difficult to establish whether this structure come from CMTs, or cytoplasmic stands radiating from the nucleus. Even though MT organization in pavement cells is far from the highly aligned CMT array observed in stems, it is somewhat stereotypical (Sampathkumar *et al.*, 2014). The radial MT structures were different than interphasic microtubule organization, either from cells infected or not (Figure R31C). Also, we found them only in a small population of CYCD3;1-expressing cells (2 out of around 30), suggesting that they may reflect a specific pre-mitotic stage, supported by the fact that the nucleus seemed in the center of these cells (in regions between two necks where cells usually divided). Nevertheless, the lack of dynamic images prevents linking this radial MT behavior to PPB formation. Dynamic images are also required to study nuclear movements before PPB formation, as well as the corresponding CMT organization.

To follow both CMT dynamics and nuclei movements, we tried time-lapse imaging over the course of 7 hours, with a time resolution of one hour, 24 hours after the infiltration with *p35S::CYCD3;1-Turquoise2*. CMT dynamics were observed using the *p35S::GFP-TUA6* construct. The GFP signal bleached very quickly, after one or two hours of imaging, and long time-lapses proved inefficient to follow microtubules, at least tagged by the *p35S::GFP-TUA6* construct (Figure R31A). Nuclei, on the other hand, were easier to follow over the time period as the Turquoise2 signal seemed more resistant to laser exposure. We were able to see quite drastic nuclei movements in some cells (Figure R31B). However, as the GFP signal weakened over time, linking these nuclei movements with any changes in the microtubule organization was not possible. Furthermore, to further confirm that these nuclei movements are due to CYCD3;1 expression-induced mitosis, we would need to visualize nuclear dynamics in cells not infected by *Agrobacterium*, through the expression of another nuclear fluorescent marker.

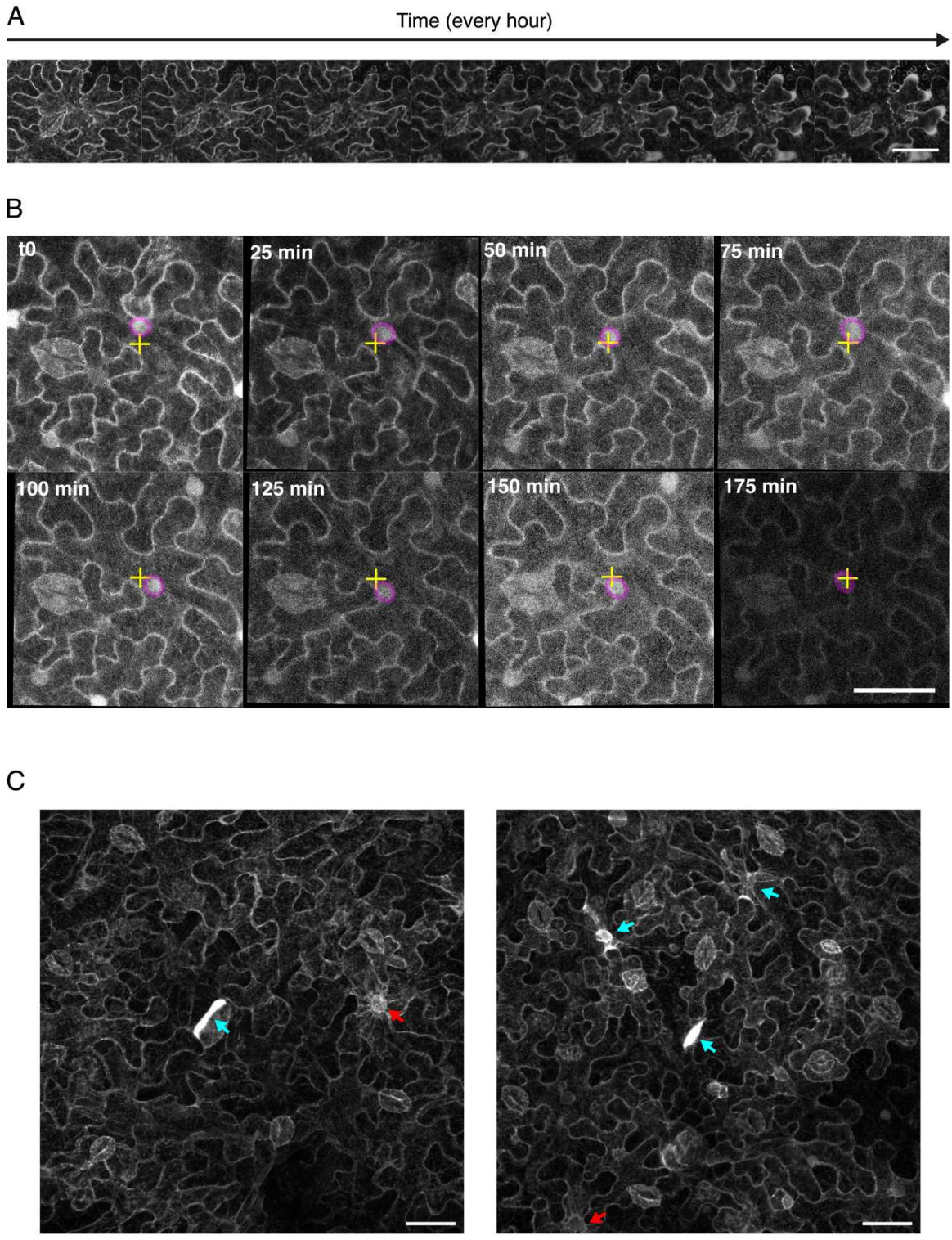

Figure R31: Preliminary data for potential pre-mitotic steps in infected *N. benthamiana* leaves. (A) Maximal Z-projections of the *p35S::TUA6-GFP* signal overtime. The GFP signal bleaches quickly, and we can the cell being stressed towards the end of the imaging. The image is 8-bits and B&C parameters have been set between 0 and 100. The scale bar is 20 μm. (B) Nuclear movements in an infected tobacco cell overtime. The yellow cross shows the centroid of the cell and the magenta circle marks the nucleus for better visualization. These images are maximal Z-projections. The scale bar is 20 μm. (C) Maximal projections of microtubules and nuclei, visualized through GFP signal detection. The blue arrows point to mitotic or pre-mitotic structures (PPBs, spindles or phragmoplast). The red arrows mark radial structures, as seen from the maximal projections. The B&C has been modified for better visualization of the images. The scale bars are 50 μm.

Overall, the *N. bethamiana* appeared as a potentially relevant alternative to study nucleus movements, as nuclei seem to undergo drastic and rapid migrations over time. The visualization of microtubule dynamics proved difficult in plants stably expressing a tubulin fluorescent marker, and transient expression of an MBD fluorescent marker through *Argobacterium* also yielded very weak signal. Therefore, a bright and laser-resistant microtubule fluorescent marker would be required to go further with this system. Another way could be to use sepal giant cells of *Arabidopsis* and forcing them to divide (Roeder *et al.*, 2010).

2. Impairment of the organization into a tissue, while keeping the multicellular context through the use of calli

Other systems, beyond the tissue context and its level of organization, are needed to study other parameters that may play a role in the establishment of the radial step. Calli are a mass of proliferating cells. Even though they have been shown to have a bias for root identity (Sugimoto *et al.*, 2010), and some level of organization and cell differentiation (Zhai and Xu, 2021), calli are often referred to as undifferentiated proliferating mass of cells. I wanted to investigate whether the radial step could also be present in such a perturbed context.

First, 2-week-old calli derived from either roots or leaves were analyzed. The calli were obtained by transferring a piece of tissue on a callus-inducing medium (see Material and Methods). Microtubules were visualized with the *p35S::GFP-MBD* fluorescent microtubule marker. In this system, imaging and subsequent image analysis were very challenging. Indeed, callus development is highly three-dimensional and the shapes of both the callus surface and the cells prevented a clear visualization of the outer layer of the callus.

No obvious supracellular organization of the CMT array was observed, consistent with the lack of structure of the callus (Figure R32). As image analysis was difficult, maximal Z-projections were made for microtubule visualization, and not surface projections. As a result, the differentiation between the outermost cells of the callus and the underlying ones was challenging. Nevertheless, I tried some time-lapse imaging with a time resolution of one hour. I was able to observe some mitotic structures in the calli, such as pre-prophase bands, spindles and phragmoplasts (Figure R33). As mentioned before, the maximal Z projections prevented distinguishing between cells from the outer layer of inner layers. I was not able to clearly observe any pre-mitotic changes in CMT array organization. More generally, I could not follow CMT dynamics for one particular cell, due to the visualization issues.

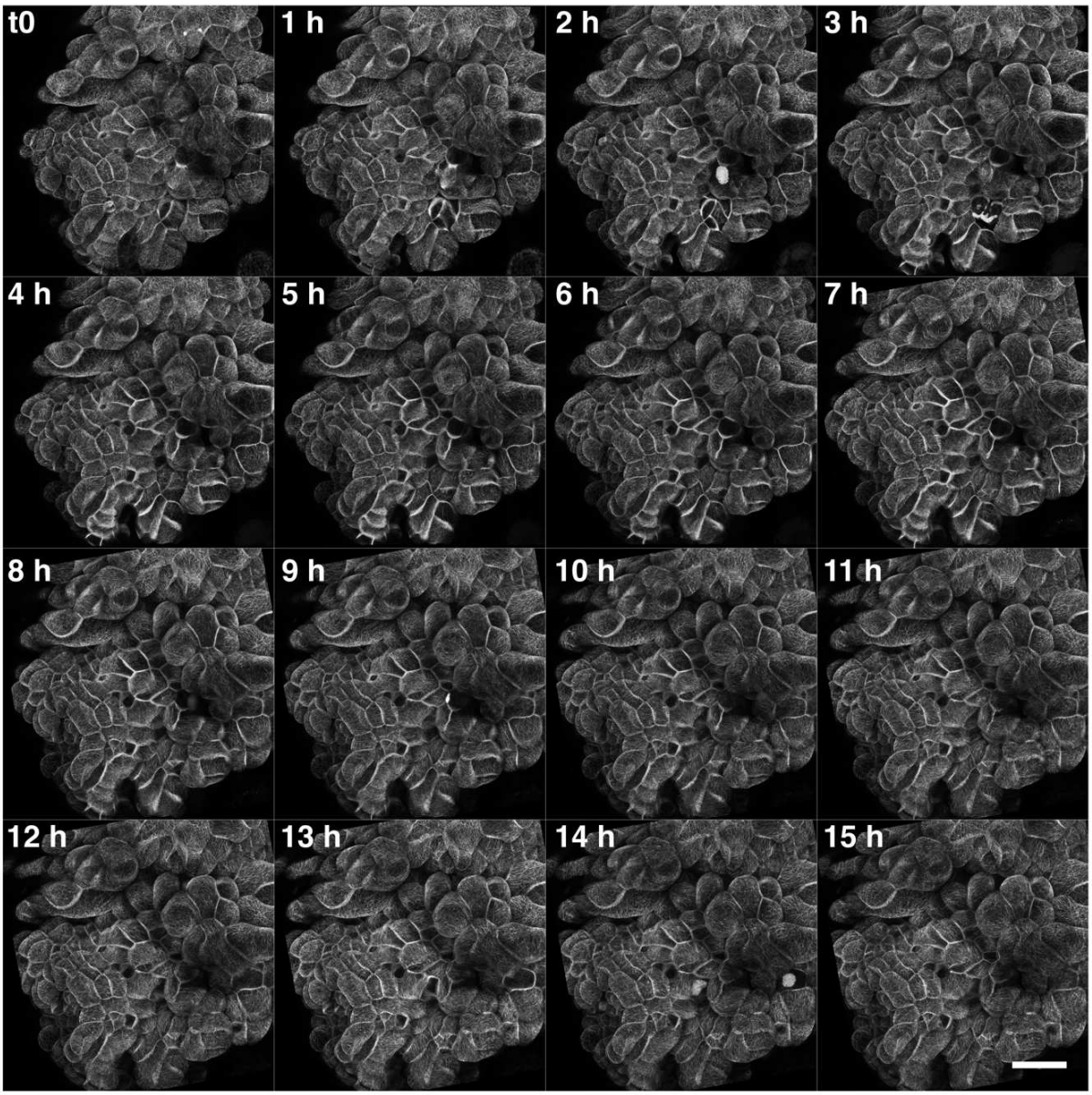

Figure R32: Microtubule dynamics in a 2-week-old callus. These images are maximal Z-projections of the *p35S::GFP-MBD* signal. The Brightness&Contrast parameters have been modified for better visualization. The scale bar is 20 μm.

Even though no clear conclusions could be made on the radial step in calli, visualization of microtubules in these structures led to other interesting observations. Firstly, the orientations of the divisions were not predictable, as in epidermal cells, as they could occur periclinally (Figure R33B) or anticlinally (Figure R33A) even in outermost cells. This suggests that epidermal identity is not acquired for the outermost cells of the callus. The aspect of the PPBs was also different than in physiological tissues. Indeed, they seemed much narrower, split (which was sometimes the case in physiological tissues) and we found one occurrence of a cell displaying two PPBs at two distinct positions in the cell (Figure R33A). The anomalies in division plane orientations or PPB morphology could come from the hormonal supplementation of the medium, to induce the callus formation, affecting the cytoskeleton, cell identity and growth, the lack of tissular organization or the resulting mechanical patterns.

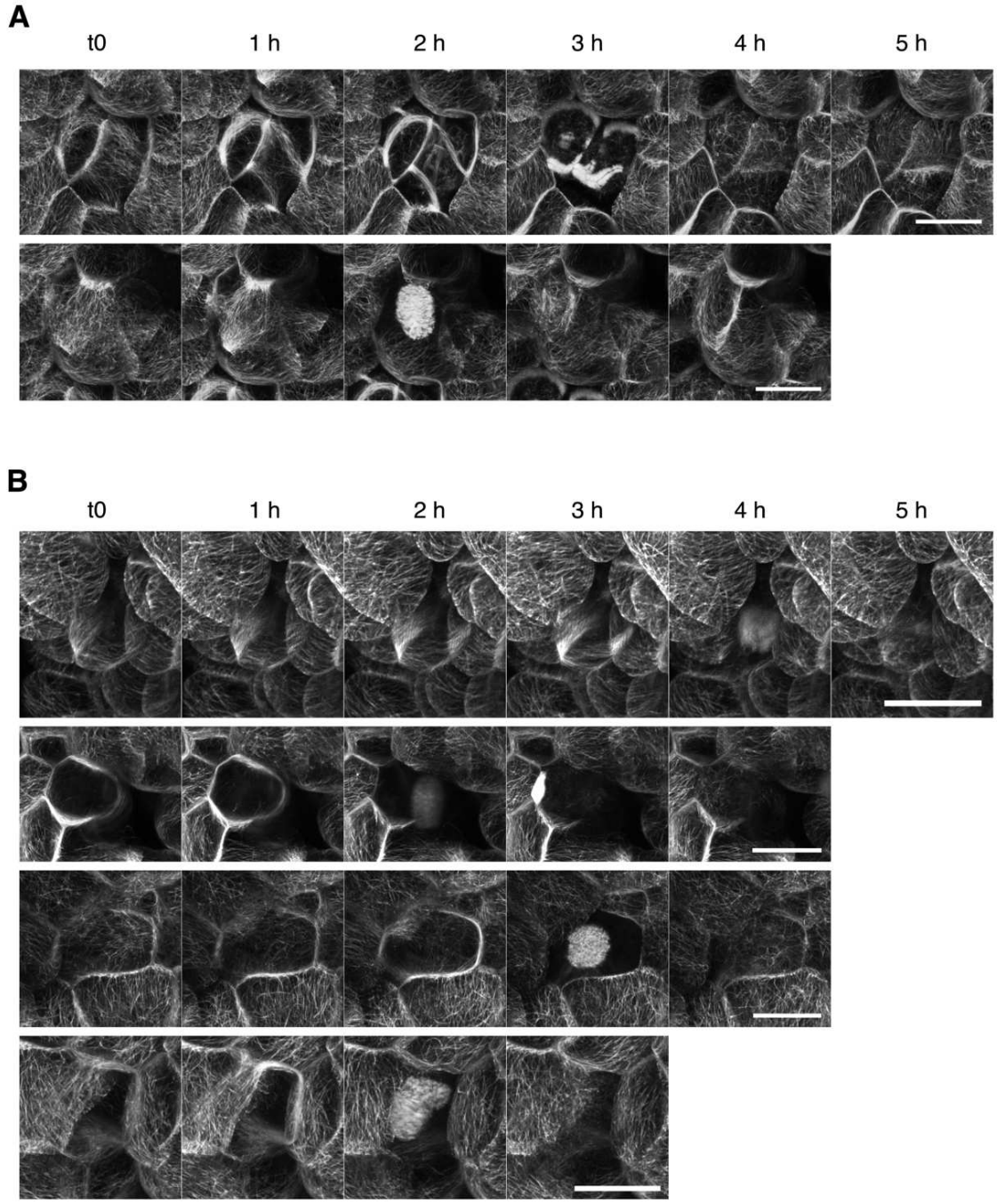

Figure R33: Crops of dividing cells from the callus displayed in Figure R32. The cells have been divided in anticlinal divisions (A) and periclinal divisions (B). We can observe some split or double PPBs in the top panel of (A). Overall, we can appreciate that the division plane does not always follow the prescribed PPB plane in some of these cells. The B&C has been adjusted for better visualization. The scale bars are 20 μm.

Callus formation typically starts from a wound site (Ikeuchi *et al.*, 2013). To overcome image visualization issues and image younger and much smaller structures, I tried imaging the callus formation directly on cut leaves or roots, at the cutting site, 3 days after transferring onto callus-inducing medium. Although it indeed decreased the Z-length of the acquisition, callus-precursor cells turned out to be also difficult to image and, surprisingly, did not seem to divide during our acquisition time. Moreover, the microtubule array seemed scarce, at least visualized with *p35S::GFP-MBD*. This was true for root calli precursors as well as leaf calli precursor (Figure R34).

As a last trial to decrease the size of the samples, I tried generating microcalli from 2 weeks-old calli. I did a few attempts through vortexing a callus in some liquid medium, and transferring the solution to a solid callus medium for a day before observation. While this method did not kill the calli, it was not effective in detaching some cells from the structure. I then tried to gently press the callus between two glass slides before transferring it to liquid medium, under rotation, overnight before observation. On the contrary, this method effectively detached some microcalli from the structure, but the cells were dead. Therefore, an optimization for microcallus isolation is required. It is worth noting that microcalli are often found in cell suspensions of *Arabidopsis thaliana* (Leboeuf *et al.*, 2004).

Following the CMT dynamics in pre-mitotic 2-week-old calli cells was difficult, as the visualization of the images was made through maximal Z-projections. Despite this technical difficulty, no pre-mitotic cells could be observed during our time-lapse experiments, except from one that divided periclinally so pre-PPB microtubules were difficult to observe. There was no supra-cellular organization of the interphasic CMT array, although some level of alignment was visible in some cells. We could not draw any conclusions regarding the presence or the aspect of the radial step in the callus model system. Nevertheless, if optimized for microtubule visualization and time-lapse imaging, it could be helpful in revealing some functional relevance of the radial step. Especially for applying different types of external stresses (with the use of the MicroVice to compress organs (Fal *et al.*, 2021) for example), drugs or changes in culture medium.

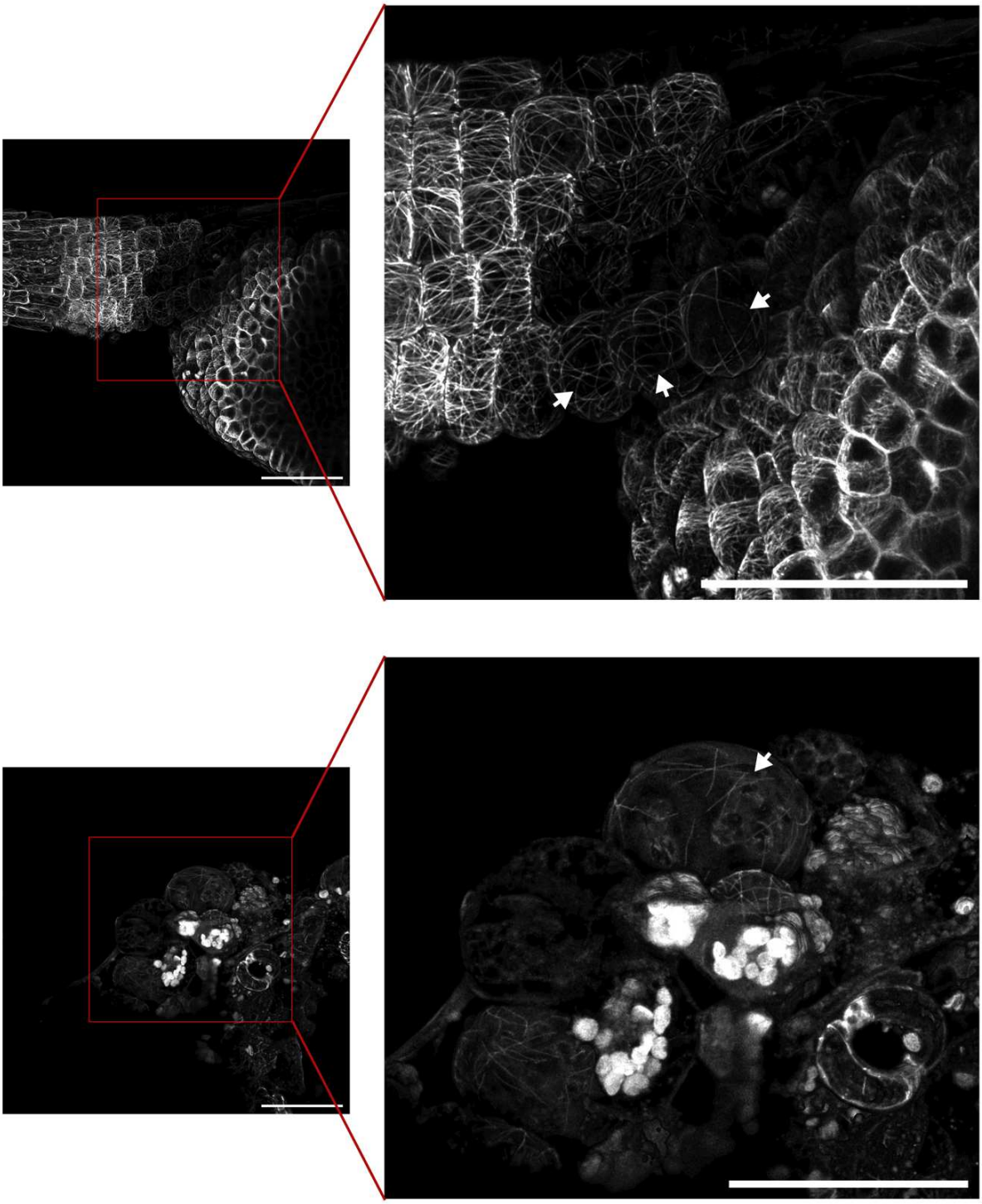

Figure R34: Callus initiation from root (top) or leaf (bottom) cuttings, 3 days after transfer on callus inducing medium. The signal is a SurfCut projection of *p35S::GFP-MBD* signal from 0 to 4 μm from the top of the structures. The white arrows point to the callus initiation cells. The Brightness&Contrast has been adjusted for better visualization. The scale bars are 50 μm.

3. Get rid of the tissular context, and study the cell shape contribution to the radial step through the use of protoplasts

In order to specifically study the contribution of cell shape in affecting the radial step, I next attempted to extract the cell from the tissue context. While conclusions on links between the radial step and pre-mitotic nuclear movements are hard to draw, we cannot exclude that it could be a way for the cell to acquire information on its shape. I therefore decided to use *Arabidopsis* protoplasts as a model system. Protoplasts are plant single cells, deprived from a cell wall. With the development of microfluidic or microfabricated devices in plant biology, manipulation of protoplasts has become increasingly popular, and allow very fine control of cellular parameters, notably cell shape. Particularly, time-lapse imaging (Sakai *et al.*, 2019) and shape manipulation (Colin *et al.*, 2020; Durand-Smet *et al.*, 2020; Thorand, 2018) of protoplasts gave promising results. The theoretical advantage, with protoplasts, is that by getting rid of the tissue context, they could help study the contribution of tissue-derived tension, neighboring cells, and purely the cell shape in pre-mitotic CMT dynamics.

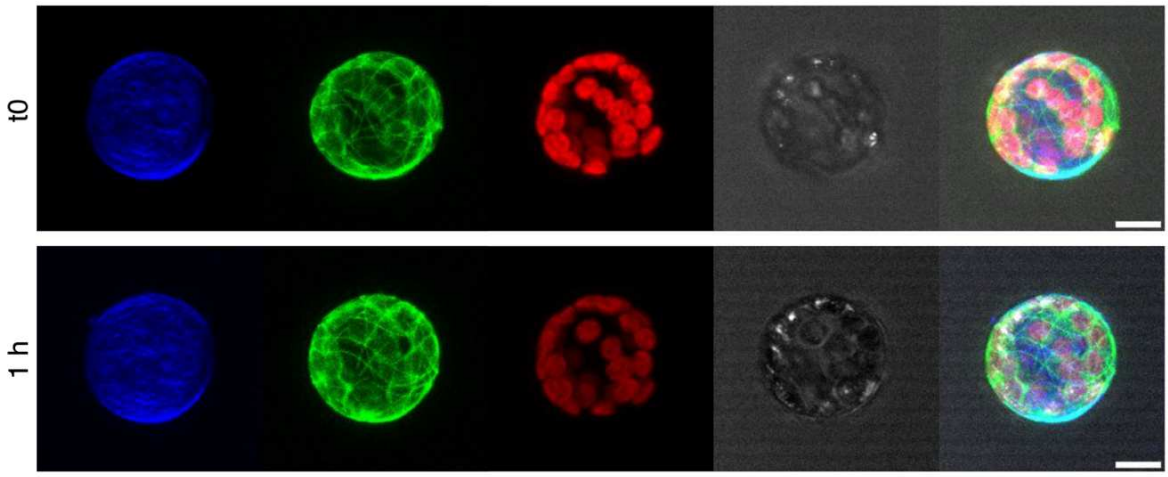

Figure R35: Protoplasts regenerate their cell wall 1 day after isolation, and can be imaged over time. The color channels represent from left to right: cellulose (through Calcofluor staining), microtubules (through the *pUBQ$_{10}$::GFP-MBD* signal), chloroplast autofluorescence, the transmission image, and the merge. After 1 hour of imaging, the protoplast does not seem affected. We can observe a heterogeneous distribution of cellulose around the protoplast, that seems to be dynamic as it gets more homogeneous after 1 hour. These images are maximal Z-projections The Brightness&Contrast parameters have been adjusted for better visualization. The scale bars are 10 μm.

I used *Arabidopsis* protoplasts, generated from enzymatic digestion of the cell walls of plantlets. I decided to work with the areal parts of the plantlets, as they have been described to be the easiest to protoplast (Chupeau *et al.*, 2013). The goal was then to regenerate the protoplasts' cell walls, and observe their first division. In the literature, there are a lot of protocols describing protoplast regeneration, suggesting that the reproducibility of these protocols is rather low. Nevertheless, the process is always an enzymatic digestion of plants, followed by gentle centrifugations, and some culture conditions. I tried a few protocols from the literature, detailed in the annex. I modified some parameters to try and adapt these protocols to our laboratory. I used *in vitro* grown plants, or plants grown on soil, I tried modifying the digestion time, the enzyme concentration, or the digestion conditions (light/dark and temperature). I also tried different culture conditions in terms of light/dark, temperature, protoplast density, petri dish material, and still or shaken conditions. Note that all of these protocols were made in liquid culture condition, to fit the aim to manipulate the protoplasts shapes.

Figure R36 (next page): Size distributions of protoplasts several days after isolation, in two separate experiments (A) and (B). (A) Plants used for protoplasting in were 10 days old. $n_{T0} = 61$; $n_{T24h} = 21$; $n_{T48h} = 15$; $n_{T72h} = 7$; $n_{T96h} = 20$. The table details de density and viability measured, as well as the average and standard deviation for the diameter, for each day. (B) Plants used for protoplasting were 18 days old $n_{T0} = 77$; $n_{T24h} = 38$; $n_{T48h} = 20$. The table details de density and viability measured, as well as the average and standard deviation for the diameter, for each day.

A

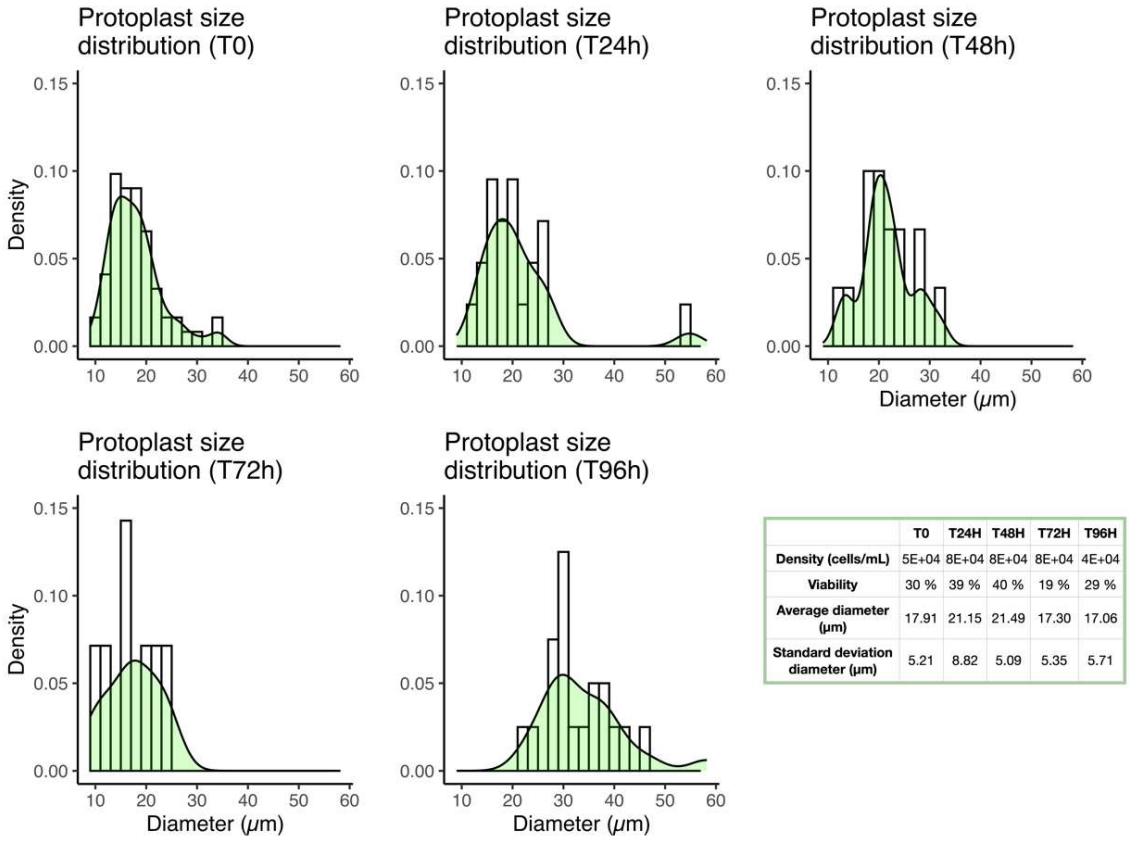

	T0	T24H	T48H	T72H	T96H
Density (cells/mL)	5E+04	8E+04	8E+04	8E+04	4E+04
Viability	30 %	39 %	40 %	19 %	29 %
Average diameter (μm)	17.91	21.15	21.49	17.30	17.06
Standard deviation diameter (μm)	5.21	8.82	5.09	5.35	5.71

B

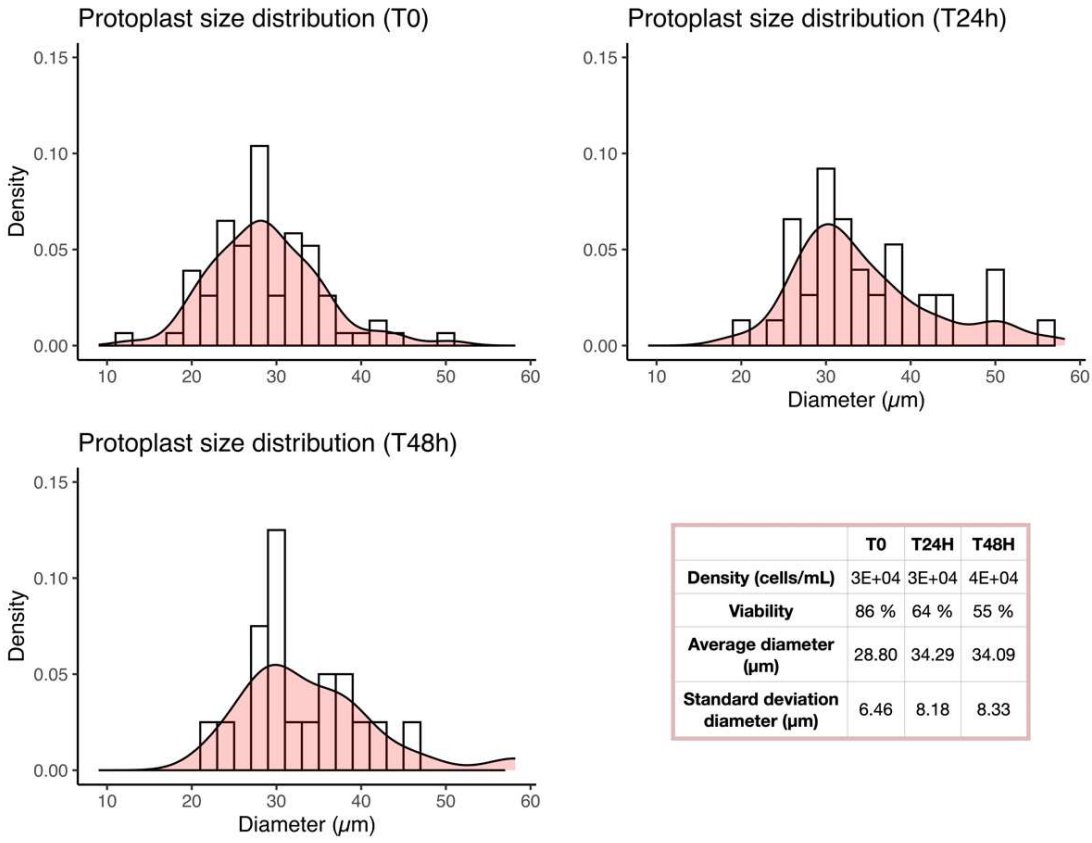

	T0	T24H	T48H
Density (cells/mL)	3E+04	3E+04	4E+04
Viability	86 %	64 %	55 %
Average diameter (μm)	28.80	34.29	34.09
Standard deviation diameter (μm)	6.46	8.18	8.33

The protocol yielding the best viability, for the longest time was Xuan and Menzcel liquid medium (Xuan and Menzcel, 1979), detailed in the material and methods (Figure R36). While protoplasts regenerated their cell walls after 48 hours in these conditions (Figure R35), no divisions were observed, even after 5 days of protoplast culture. What I found, however, is that on top of cell wall regeneration, cultured protoplasts developed and bulged into sub-protoplasts (Figure R37). Sub-protoplasts have been reported in the literature, and are thought to arise from high osmotica concentrations (Bradley, 1983). Cell wall regeneration in protoplasts seems to be quite heterogeneous (Tagawa *et al.*, 2019). It has been observed that the buds form after cell wall regeneration, and could occur due to a weakening in the cell wall and an increase in the cell's osmotic pressure (Bawa and Torrey, 1971). It has also been reported that some of the protoplasts creating these buds could be containing multiple nuclei (Bawa and Torrey, 1971), depending on the size of the subprotoplasts (Kroh and Knuiman, 1988) but I did not visualize nuclei. I could find several forms of sub-protoplasts: ones that presented a small bulge in comparison to the bigger part of the cell; ones that bulged in two equal parts; and sub-protoplasts that formed many bulges, either in two dimensions, or in many directions (Figure R37). I managed to follow the formation of one of these bulges (Figure R38A), and their retraction (Figure R38B). Despite these observations, I did not observe any cell divisions, as the separation between different bulges was not evidenced by the calcofluor white staining indicating that cell wall was not separating the two subparts of the protoplast.

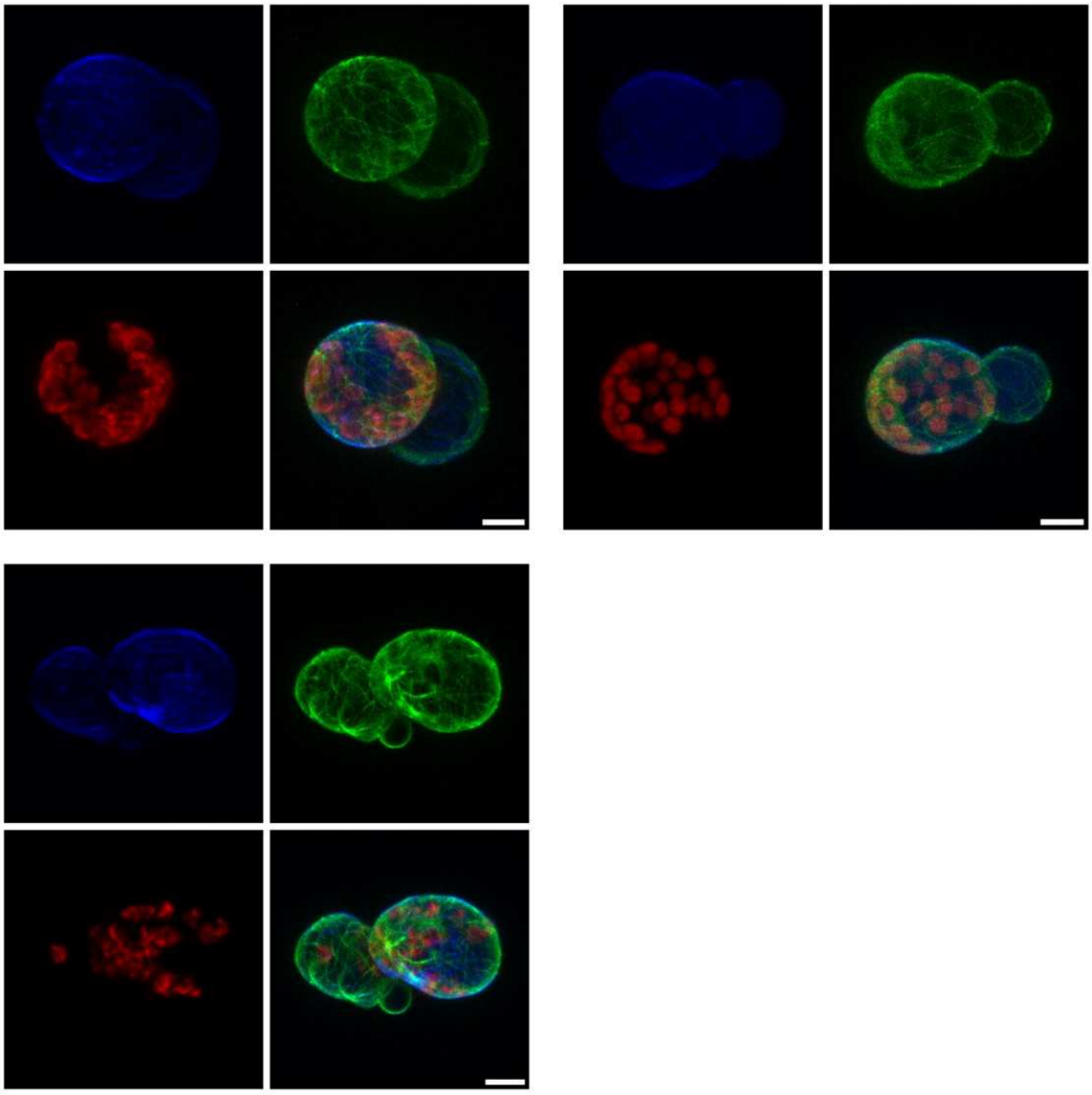

Figure R37: The subprotoplasts can adopt different shapes and aspects. From left to right, and top to bottom, we can observe subprotoplasts being partitioned in two equal volumes, one small buldge on the side of a cell, or a multitude of subprotoplasts in 3D. These images are maximal Z-projections. The blue channel represents cellulose (through Calcofluor staining), the green channel shows the microtubule signal (through the *pUBQ$_{10}$::GFP-MBD* fluorescent marker), the red channel shows the chloroplasts. Some of these protoplasts were dying, and images are shows for illustration purposes. The Brightness&Contrast parameters have been adjusted for better visualization. The scale bars are 10 μm.

Interestingly, I noticed one instance of a developing bud in an *Arabidopsis* protoplast over the course of one hour (Figure R38A). I noticed that there was an accumulation of MTs around the area where the bulge arises. This is reminiscent of the actin organization before the outgrowth of subprotoplasts from *Nicotiana tabacum* pollen tubes (Rutten and Derksen, 1990). Cellulose also seems to be directly synthetized after the formation of the bud (Figure R38B).

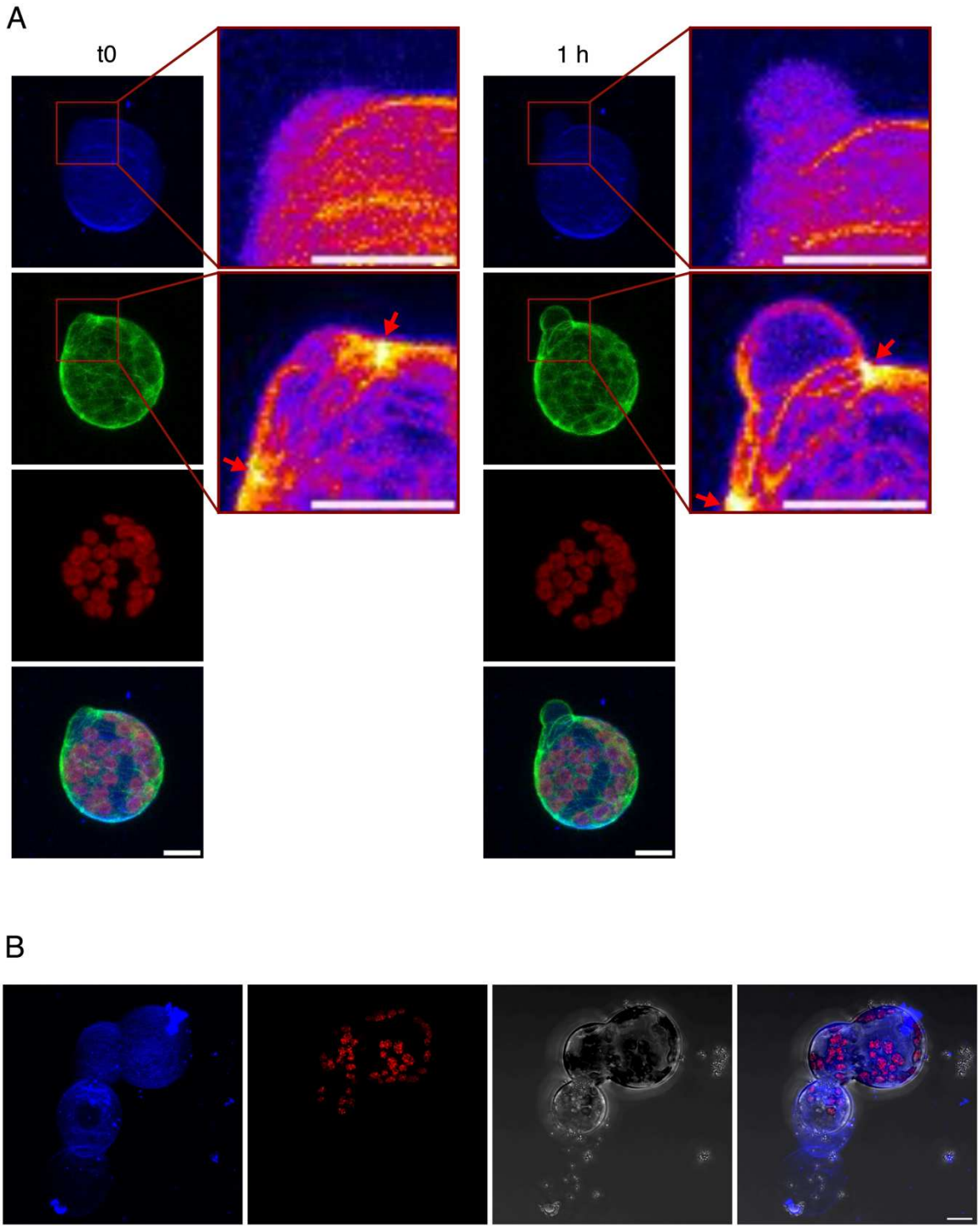

Figure R38: Subprotoplasts structures seem dynamic. (A) Visualization of the formation of a buldge on the side of a protoplast in one hour. The image magnifications show the cellulose and microtubule channels with the "fire" look-up table in Fiji to better represent differences in intensity. The red arrows show an accumulation of microtubules on either side of the buldging site. (B) Example of a subprotoplast that seem to have retracted from when the cellulose was first synthetized. For (A) and (B) the blue channel represents cellulose (through Calcofluor staining), the green channel shows the microtubule signal (through the *pUBQ*$_{10}$*::GFP-MBD* fluorescent marker), the red channel shows the chloroplasts. The protoplast in (B) was dying, and images are shows for illustration purposes. These images are maximal Z-projections.The Brightness&Contrast parameters have been adjusted for better visualization. The scale bars are 10 μm.

To constrain protoplasts in given shapes, I used a system confining protoplasts in microfabricated wells, developed in our laboratory (Colin *et al.*, 2020; Figure R39A). I managed to confine the protoplasts in given shapes (Figure R39B). However, their viability in the wells was very low, and culturing them in this system over several days proved ineffective.

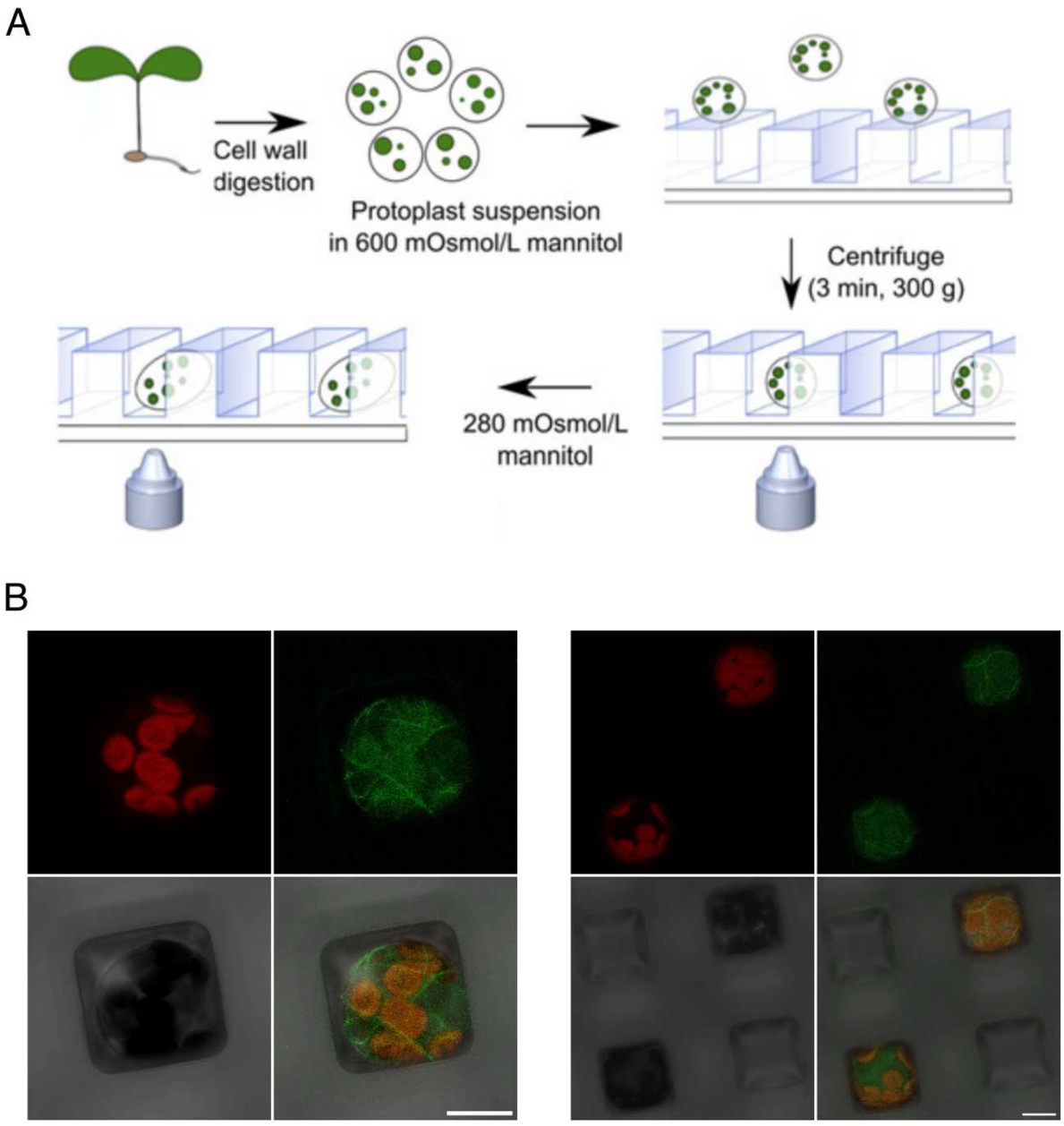

Figure R39: Illustration of protoplasts confined in microfabricated wells. (A) Adapted from Colin *et al.* (2020), showing a schematic representation of the method to embed the protoplasts in the wells. (B) Images of confined protoplasts in 20 µm x 20 µm wells. The green channel shows the microtubule signal (through the *pUBQ$_{10}$::GFP-MBD* fluorescent marker), the red channel shows the chloroplasts. The Brightness&Contrast parameters have been adjusted for better visualization. The scale bars are 10 µm.

To follow CMT dynamics over time, we decided to implement Sakai *et al.* (2020) microfluidic chip, consisting of trapping protoplasts, and provide them a continuous flow of liquid medium (Figure R40A). This technique, developed for *Physcomitrium patens*, enabled the authors to regenerate full moss plants from a single protoplast. After measuring the distribution of *Arabidopsis* protoplasts sizes in our population (Figure R36), I decided to use traps 45 µm in diameters and 70 µm in height. Unlike in what has been published, I provided the medium through a syringe pump with a flow of 1 µL/min. I could effectively trap protoplasts in the device (Figure R40B), and follow them over time (Figure R40C), but they seemed to rapidly decline, and I could keep them alive for a maximum of 3 days in the microfluidic system. It is worth noting that I moved the setup many times to transport it from the microscope to the growth chamber and vice versa. This movement could also decrease the viability of the protoplasts.

Overall, it was very difficult if not impossible to obtain protoplast divisions. Particularly, protoplasts seem very sensitive to a wide variety of parameters (such as atmospheric pressure, light, temperature, movement, density, etc.). I think a fine-tuning of the protocols' parameters are necessary for each laboratory in order to optimize the culture conditions and observe divisions. The fact that I consistently obtained subprotoplasts seems to indicate that the osmolarity of the medium was not optimal for the protoplasts. Also, protoplast culture in liquid conditions seem stressful and most successful protocols for plant regeneration from protoplasts immobilize them in a thin alginate layer (Luo and Koop, 1997; Chupeau *et al.*, 2013; Dovzhenko *et al.*, 2003). Even though the shape modulation methods tested require protoplasts to be in a liquid medium, it could be worth trying the sodium alginate methods. Notably, an old method developed by Lynch and Lintilhac in 1997 successfully allowed to apply mechanical stresses, and visualize divisions in tobacco protoplasts embedded in an agarose gel (Lynch and Lintilhac, 1997).

Figure R40: Illustration of protoplasts trapped in a microfluidic system. (A) Adapted from Sakai *et al.* (2019) showing the microfluidic chip in (a) and a magnification on the traps in (b-d). The scale bars are 500 µm in (b), and 40 µm in (c) and (d). (B) Images of subprotoplasts, 3 days after isolation and trapping in the chip. The protoplasts are dying, indicating that cultures over three days in this device is difficult with our isolation protocol or culture medium. (C) Time-lapse of a trapped protoplast. This system can be used to follow cells overtime with a rather high time resolution. The green channel shows the microtubule signal (through the *pUBQ$_{10}$::GFP-MBD* fluorescent marker), the red channel shows the chloroplasts, and the grey channel shows the transmission images. The Brightness&Contrast parameters have been adjusted for better visualization. The scale bars are 10 µm.

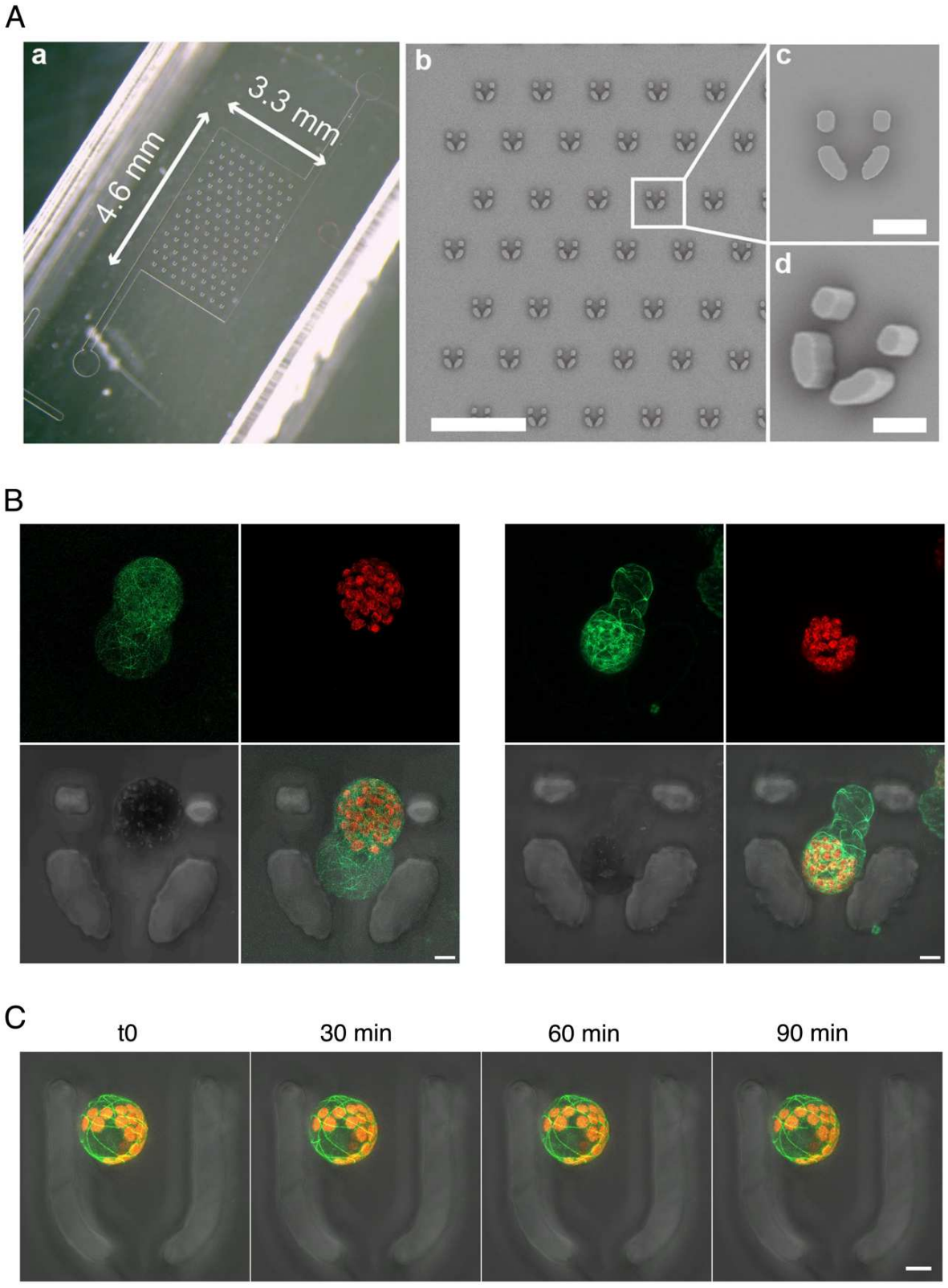
A
a
3.3 mm
4.6 mm
b
c
d
B
C
t0
30 min
60 min
90 min

Discussion

We identified a pre-PPB step in the *Arabidopsis* stem, where CMTs lose their interphasic organization (highly aligned following tissue tension) and become radially organized. We named this step the "radial step". This section aims to sum up the characterization of the radial step, and propose a functional relevance in preparation for mitosis.

I. A transient radial cortical microtubule array primes cell division in *Arabidopsis*

This part of the discussion is the same to the one published in Proceedings of the National Academy of Sciences, USA, except some modifications that have been made to better fit the rest of the text.

Our results are consistent with a sequential model in which the progressive accumulation of cytoplasmic microtubules during the G2 phase would disrupt CMT alignment with tensile stress to allow the cell to sense its own geometry for a short time window and to ensure the precision of cell division (Figure R17B). This "radial step" could also help the cell to acquire information on other key cell division parameters, such as centroid position (Moukhtar *et al.*, 2019). After this transitory stage, CMTs would resume their alignment either with the short axis of the cell when cells are elongated (Errera's rule, also matching cell-shape derived maximum of tensile stress) or with tissue stress, when cells are isodiametric, to control the final division plane orientation. Identifying conditions in which the radial step is absent will be necessary to challenge this model.

1. The transient CMT organization before mitosis as an exception to the CMT alignment with tensile stress

So far, the alignment of CMTs with maximal tensile stress has been verified in most plant tissues (Hamant *et al.*, 2019; Trinh *et al.*, 2021), and suffers only a few exceptions. Although this needs to be formally investigated, most of these exceptions could be explained by invoking differences in stress levels. For instance, one could propose that a drop in turgor pressure in hypocotyls switching from dark to light could explain the rapid growth arrest and associated switch in CMT orientation (Lindeboom *et al.*, 2013). Similarly, the progressive reinforcement of cell walls during differentiation, and thus reduction in stress level, could explain the loss of CMT co-alignment in leaf epidermis (Zhao *et al.*, 2020). This notably builds on recent investigations in protoplasts that are confined in microwells: in this case, CMTs are transverse, aligned with the shortest axis of an elongated cells, which is also a local maximum of stress, following Laplace-Young law (Colin *et al.*, 2020). However, when they are placed in a hyperosmotic medium, i.e. when tension decreases, CMTs switch to the long axis of the cell: they follow the flattest part of the protoplast contour, which is also the minimum of bending energy (Colin *et al.*, 2020; Durand-Smet *et al.*, 2020).

To our knowledge, the only undisputable exception of CMTs alignment with tensile stress is thus provided in this work, in the sense that during the timeframe of the radial step, the global pattern of tension should not change: 3 hours before cell division, cells in stems exhibit a radial organization of their CMT arrays. This cannot be explained by a change in tissue stress pattern, as adjacent cells usually exhibit CMTs that are aligned with predicted tissue stress direction. A change in cell wall properties would be too slow to affect the CMTs so transiently. When the tensile stress is changed around ablations in the tissue, the radial step is affected (shorter duration), but is still present. Although we cannot exclude the possibility that turgor level would transiently change 3 hours before cell division, this would be unlikely to cause a radial CMT organization. As shown in the protoplast experiments, following a drop of turgor pressure, CMTs would align with the long axis of the cell, and would not make a radial pattern.

2. The radial CMT step could be present in other species

Our time-lapse analyses shed a new light on past reports on guard mother cells (GMCs). In particular, to quote Yoshinobu Mineyuki in 1999 (Mineyuki, 1999), notably building on studies by Muilinax and Palevitz in 1989 (Muilinax and Palevity, 1989), “graminean GMCs have "interphase microtubule bands" that orient perpendicular to PPBs. This transverse interphase microtubule band precedes a radial microtubule array, which is then replaced by a PPB prior to the longitudinal cell division”. These past reports together with our analysis suggest that the radial step is not a guard mother cell exception, but more likely the rule. Whereas long-term tracking of dividing cells with microtubule markers and at high enough resolution are still rare in the literature, we could find examples of *Datura stramonium* pre-mitotic cells, presenting thick cytoplasmics MTs in the phragmosome, with a CMT pattern reminiscent of what we observed in *Arabidopsis* (Flanders *et al.*, 1990). Observing pre-mitotic CMT dynamics in other species would inform us on its conservation.

3. A trade-off in precision between division plane orientation and division precision

The idea of a competition between internal and cortical microtubules is not totally new. Indeed, cytoplasmic microtubules have major impacts on cortical array in non-dividing cells (Ambrose and Wasteneys, 2014). Cytoplasmic microtubules can generate an isotropic array overriding the pre-existing microtubule array through the tethering function of CLASP (Le and Ambrose, 2018). Because pre-mitotic cytoplasmic microtubules are prominent in late G2 phase, it could cause great impact on cortical microtubule array. Cytoplasmic microtubules are likely to play a primary role in division precision. There is ample literature showing how tension within cytoplasmic microtubules may act as a sensor of cell geometry (Flanders *et al.*, 1990). A search and capture mechanism for instance would depend on the length of microtubules, and thus on cell width. Our results support

that scenario, also suggesting that the accumulation of cytoplasmic microtubules before cell division does not only serve as a reservoir of microtubules to prepare mitosis, but it would also contribute to the precision of cell division, possibly by making the cell more self-centered on its nucleus and less sensitive to external cues. In this scenario, the radial array at the cortex would not necessarily be the main player in geometry perception.

Yet, one could explore ways in which CMTs contribute to geometry sensing in synergy with cytoplasmic microtubules. The recent work by Muroyama et al. (Muroyama *et al.*, 2023) might be inspiring. They showed that CMTs at the cell contour are biased by BASL for asymmetric division. They had previously shown the importance of microtubules for nuclear positioning before cell division (Muroyama *et al.*, 2020). Therefore, the radial step might be important for even CMT distribution at the cell contour to allow nuclear position and control the robustness of division symmetry. In that scenario, the radial step would open a window in which the cell tends towards "perfect" symmetry until it is overridden by other cortical signals such as BASL, mechanical stress or the formation of the PPB, later on. Note that the radial step is also present in cells dividing asymmetrically, thus these other cortical cues may also affect the radial step, this time to secure asymmetric division. In other words, although our analysis suggests that the radial step reflects the precision of division, it does not seem to determine the degree of symmetry. It could, for example, be a probing step ensuring volume availability, assessing the nucleus position, or even contribute to pre-mitotic nuclear migration.

In conditions of high mechanical stress, such as around ablation sites, we observed that the radial step appears for a shorter time, and the increase in cytoplasmic microtubules was more pronounced and in a shorter time window. A disruption in the CMT array organization through cytoplasmic microtubule accumulation might be difficult to maintain when aligned CMTs are needed to respond to reinforce the cell wall along maximal tensile stress directions. Knowing when the experiment was performed, relative to the time of ablation, and when cell division reactivates around the ablation could help identifying when CMTs recover their mitotic functions. We also cannot exclude that the cell cycle regulation could be modified around ablations.

II. The radial step is robust to various perturbations

1. The radial CMT step is unaffected by global changes in mechanical patterns

On top of being robust to different cell identities and ablations, or the presence of trichomes in the stem, the presence of the radial step is not abolished when changing the global tension intensity in the stem by modifying the water availability in the medium (with differential agar concentrations). In confined protoplasts, a drop in turgor pressure induces MTs to align along the longest axis in protoplasts (Colin *et al.*, 2020). Even though cells in stems epidermis are embedded in a tissue, and present a cell wall (unlike wall-less protoplasts), which could affect MTs, it seems

that minor changes in cell geometry are also not required to induce the radial step, since differences in osmolarity did not affect the radial step. One may however be cautious here, as it is possible that the epidermis retains some osmotic stability, through water exchange with inner cells. In fact, Verger *et al.* (2018) showed that turgor pressure in the epidermis remains constant after hyperosmotic treatment, while wall tension decreases, most likely through intercellular water movements. More generally, it is worth mentioning that we described the radial step only for epidermal cells in the stem. The epidermis has particular characteristics in *Arabidopsis*, as it is the tissue layer under tension, it typically presents exclusively anticlinal divisions, and is protected by a cuticle on its outer cortex. Studying pre-mitotic CMT dynamics in inner layers of organs could inform us on its layer-specificity.

Changing the composition of the cell wall also affects its properties. In plants, cell wall integrity regulates, to some extent, cell cycle progression (Gigli-Bisceglia *et al.*, 2018). Links between endoreduplication and cell wall composition have also been found (Bhosale *et al.*, 2019). However, how plant cell cycles react to more stable changes in the cell wall remains elusive.

My results show that that a higher level of methyl-esterified pectins in the cell wall produces a higher variability in daughter cells volume ratios. Affecting the xyloglucan content, however, does not seem to impact division symmetry. While cell wall composition could directly have an effect on the cell division, it is also possible that the differences in mechanical stress experienced by the cell that could drive the differences observed in volume symmetry. Indeed, more methyl-esterified pectins in the cell wall stiffens it (although debated), while xyloglucan content modifications do not seem to majorly affect its mechanical properties (Peaucelle *et al.*, 2011; Cavalier *et al.*, 2008). Stiffer walls could prevent an effective potential mechanical shielding step, when preparing for mitosis. The apparent conservation of the division rules in the stem for both cell wall mutants tested suggest that division symmetry is independent of overall division plane orientation. To investigate the presence of the radial step and the behavior of CMTs in these backgrounds, further time-lapse analyses are required, using microtubule fluorescent markers.

Consistent with the radial step being robust to different cell wall composition or mechanical status, the radial step was also observed in various organs, like the root. In these other organs, it is however often more difficult to relate the radial step and the tissue stress pattern, as it is usually only inferred, but not demonstrated experimentally. Although the lateral root epidermis lacks clear investigation on the tensile stress patterns it experiences, this further confirms that the radial step is a robust structure.

2. The radial step is robust to cytoskeletal perturbations

If external perturbations did not affect the radial step, we wondered whether internal perturbations, such as microtubule modifications, would. Microtubule perturbations, through the use of various

MAP mutants did not prevent the formation of the radial step. This suggests that the pre-mitotic radial re-arrangement of CMTs is not dependent on any of the proteins tested (KTN-1, NEK-6, SPR2-2). Yet, we cannot exclude dependence on other proteins. For instance, nucleation points or polarity cues changes before mitosis could also have a direct impact on CMT organization. Rho-of-plants (ROP) signaling orders MTs and establishes cell polarity in *Arabidopsis* (ROP6; Fu *et al.*, 2009) and the spatial orientation of division in *Marchantia polymorpha* (Rong *et al.*, 2021). Members of the linker of the nucleoskeleton and cytoskeleton (LINC) complexes have been shown to be involved in organizing microtubule nucleation and cell division plane establishment (Tatout *et al.*, 2014; Ashraf *et al.*, 2022).

Little is known about the interdependence between cytoplasmic and cortical MTs organizations, although a continuity between nucleus-initiated and cortical MTs has been shown (Ambrose and Wasteneys, 2014). Many of these unknown actors could help us decipher the effectors of the radial step. Furthermore, MT organizing centers at the nucleus are important for organizing the CMT array (Ambrose and Wasteneys, 2014). Manipulating the expression of MT nucleation complex components is needed to investigate how the cytoplasmic microtubule array organizes the cortical one, even though it induces severe developmental defects and can even be lethal (Pastuglia *et al.*, 2006; Batzenschlager *et al.*, 2013; Janski *et al.*, 2012; Nakamura *et al.*, 2012).

Depletion of ACTIN 2 and 7 did not impair radial step formation either. Although the *act2act7* mutant suffers from various developmental phenotypes, the interphasic CMT array of its stems looks unaffected (responds to tension and has a WT-like aspect). Even though interactions between the microtubular and the actin cytoskeleton have been shown in plants (Sampathkumar *et al.*, 2011; Schneider and Persson, 2015), the radial step formation is unaffected in actin-depleted conditions. Visualizing the actin cytoskeleton dynamics could further unravel its potential links with the radial step.

Except for *trm678*, all of the cytoskeleton mutants I investigated produced a PPB, and the division plane aberrations are likely induced during mitosis/cytokinesis. Moreover, only *act2act7* and *ktn-1* have daughter cell volumetric ratios more variable than the WT. This could be explained by CDZ signaling defects for *act2act7*, or phragmoplast expansion defects for *ktn-1*. Nucleus positioning also seems affected, as well as overall division plane orientation rules in stems of both of these mutants. Therefore, these observations are not necessarily in contradiction with the radial step as a reset mechanism to ensure proper volume partitioning between daughter cells. Rather, the volume partitioning defects observed could result from destabilization or slower dynamics of the mitotic machinery, as shown for the *ktn-1* mutant (Komis *et al.*, 2017).

3. Radial step duration and phenotype display some degree of variability

Even though the presence of the radial step was not impaired in any of the conditions tested, some phenotypic variability of the radial step could be detected. Namely, the duration of this step, as well as its aspect could vary between genotypes and conditions. *trm678* mutants display longer and more clear-cut radial steps. Polar auxin transport defects, *nek-6* and *ktn-1* mutations induce longer radial steps. *ktn-1*'s radial step also appears less clear-cut than the WT's. Perhaps the presence of the radial step is not as relevant as its characteristics for its function. Also, its exact duration was difficult to estimate, even in control conditions, due to our limitation in time resolution, as well as the intercellular variability. The PPB maturation duration was not extremely consistent, for example. An increased time resolution could help draw correlations between the duration of the radial step and the volume ratio between daughter cells. Better tools would be helpful to describe the radial step's phenotypes (for example to analyze how clear-cut it is), and relate them to their possible function in the cell. It is also worth mentioning that the one-hour time resolution could prevent observing subtler differences in the radial step duration (between cells or between genetic backgrounds).

4. Interdependence between the radial step and PPB morphology

One could also wonder about the involvement of the radial step as a priming element for the formation of the PPB. As evidenced by the *trm678* mutant, which does not produce a PPB but still presents a radial step, the formation of the PPB is not necessary for the emergence of the radial step. Nevertheless, it is possible that PPB morphology could result from the radial step. Indeed, as evidenced by the split PPBs observed in a non-negligible population of cells from all genotypes, maturation of the PPB seems to occur in sequences. It is possible that the radial step produces isotropic CMT strands, that will be stabilized at favorable planes, and will narrow into one unique plane right before mitosis, going in the sense of a "search and capture mechanism" for PPB establishment (Vos *et al.*, 2004). However, both *act2act7* mutants and *ktn-1* mutants display defects in PPB morphology while still presenting a radial step, albeit altered in *ktn-1*. Nevertheless, one cannot confidently decorrelate the radial step from PPB formation, as these mutants could present their defects only during PPB establishment. Indeed, both *ktn-1* mutations and actin perturbation induce defects in PPB anchoring (Komis *et al.*, 2017; Kojo *et al.*, 2013). The less clear-cut aspect of the radial step in *ktn-1* mutant background could correlate with the defects in PPB anchoring it presents.

Interestingly, the split PPBs observed in the stem seemed to separate around an existing tri-cellular junction. Division planes usually avoid these tri-cellular junctions, as four-way junctions are highly unstable, energetically (Sinnott and Bloch, 1941; Flanders *et al.*, 1990). Previous analysis in roots revealed that the cell plate attaches at a fixed distance from a tricellular junction (Lebecq, 2023). It could be interesting to measure the distances of these split PPBs from the tri-cellular junction they surround, in order to investigate if this distance is consistent, and whether it varies from the ones

observed in roots. Early stages of PPB maturation could therefore hold a tri-cellular junction avoidance function.

Furthermore, my results seem to fuel the debate about the interdependence between nucleus and PPB positioning (Panteris *et al.*, 2006; Dhonukshe *et al.*, 2005; Bouchez *et al.*, 2024). In artificially dividing tobacco mesophyll cells, the PPB location does not necessarily match the nucleus position, at early stages of PPB formation. In some cases, early PPBs are not split but rather seem to localize at two different planes, one of which does not go through the nucleus (Figure R31C, right image). The lack of dynamic images prevents concluding on which of these planes will mature into the final PPB: the one that goes through the nucleus, or the one that does not, in which case the nucleus must migrate after the initiation of the PPB. In the *act2act7* mutants, some instances of split PPBs do not prescribe the following division plane position, due to a misplacement of the nucleus (Figure R20A). This shows that the continuity between PPB, nucleus and division plane positions is not obvious, and that the positioning of the PPB, at least in the early stages of its maturation, is not dependent on nucleus positioning.

III. The radial step as a reset stage

In this section, I will detail some hypotheses, supported by my results, on the function of the radial step. I will also propose future experimental procedures to validate these hypotheses.

1. The radial CMT step as a mechanical reset mechanism

Our observations go against a common assumption that PPB orientation usually follows that of CMT during interphase. We instead identified a reset stage where CMTs become disorganized for a duration of ca. 2 hour and at a well-defined time window (3 hours before cell division). The radial step reflects a stage during which CMTs switch from their role in guiding the deposition of cellulose microfibrils, to their role in controlling cell division. Other cortical microtubule arrays have been shown to have links with cell division (typically, the PPB, and cortical-telophase microtubules (Lucas, 2021; Bellinger *et al.*, 2023)), further suggesting that close to mitosis, there is a change in CMTs function. Based on the temporal correlation between cytoplasmic microtubule enrichment during the G2 phase and on the prolongation and better-definition of the radial step when cytoplasmic microtubule accumulation is promoted (in *trm678*), we propose that the radial step is a period during which increased cytoplasmic microtubule accumulation disrupts the CMT self-organization, thereby making the CMT network transiently blind to external mechanical cues. There have been many studies to identify mechanosensors at all scales (Hamant and Haswell, 2017), but few studies have investigated mechanisms in which cell factors instead become blind to mechanical stress. We believe that the radial step belongs to this category.

2. A transient mechanical shield for pre-mitotic nuclear positioning?

The position of the nucleus, at the radial step stage, is comparable to the position of the nucleus at the PPB stage. Both of these positions differ from the one observed during interphase, where the nucleus is slightly offset from the cell's centroid. While dynamic images of nuclear migration do not indicate a clear timepoint at which the nucleus moves towards the cell centroid, its final positioning looks correlated with the radial step. As mentioned previously, the timeframe of the radial step is variable between cells (both in appearance and duration), which could explain the lack of correlation found when averaging dynamic images. Indeed, the duration of PPB maturation can be quite variable between cells. Normalizing the times by other parameters (to define the t0) than nuclear envelope breakdown/PPB disassembly, such as POK1 polarization at the PPB (Lipka *et al.*, 2014) could help reduce the variability observed and draw clearer conclusions on timely parameters of the radial step.

To properly acquire spatial information from its own geometry, the cell must temporarily ignore external perturbations (from its neighbors, from the tissue). The nucleus position, which appears as a good integrator for geometric information, is highly sensitive to mechanical stimulations (Qu and Sun, 2007). Proper nucleus positioning in relation to cell geometry must therefore be achieved in a mechanically-neutral environment. As mentioned previously, BASL protein polarity has been shown to drive nucleus positioning in stomata precursor cells (asymmetric divisions) (Muroyama *et al.*, 2020). Since the radial step happens in these types of divisions (Figure R4D), the polar distribution of BASL in these cells could be a polarity cue organizing the cortical cytoskeleton. Nevertheless, the mechanism behind the radial step emergence is likely the same in symmetrically and asymmetrically dividing cells (in terms of identity).

While it is largely unknown how mechanical signals are perceived by plant cells, the CMTs both reflect the cell's response to cortical cues, and may even be involved in mechanotransduction (Hamant *et al.*, 2019). A transient loss of this response, reflected in an isotropic CMT reorganization (the radial step), could momentarily reflect loss of CMT response to tissue stress, and could also disturb mechanotransduction in the cell, downstream of CMTs. Perturbing the balance between cytoplasmic and cortical MTs, through nucleation complex proteins overexpression for example, would reveal if nucleation point changes could be involved in mechanical shielding. Nevertheless, little is known on how plant cells would react to an "overnucleation" of microtubules.

3. A more general mechanism for CMT reorganization?

Transient radial CMT arrays have also been observed in non-mitotic cells. In hypocotyls, radial organizations precede global orientation changes of CMTs in response to light (Sambade *et al.*, 2012). In stems, we observed non-mitotic radial arrays in both 1% and 2.5% agar conditions (Figure

R19B). These organizations appeared before a global change in CMT orientation (usually from transverse to longitudinal). Qualitatively, it is hard to distinguish pre-mitotic and non-pre-mitotic radial arrays. Interestingly, all of them appear before a change in the CMT configuration, either linked to mitosis (with the appearance of the PPB) or not, potentially placing the radial step as a marker of CMT arrangement changes, rather than it being linked to a particular step in the cell cycle. It would be interesting to investigate whether such changes also involve transient cytoplasmic microtubule accumulation, or other mechanism.

The radial steps could also reflect a checkpoint step, where the cell explores its suitability to undergo mitosis. In that sense, we observed that some cells exhibiting a PPB went back to an interphasic CMT array. This challenges the textbook view of the cell cycle as being an irreversible process and questions the PPB as a mitotic onset marker. Furthermore, cells undergoing endoreduplication do not present PPBs, as endocycles are exclusively composed of G and S phases (Breuer *et al.*, 2010). Conversely, when a radial organization of CMTs is observed in non-dividing cells, it might be possible that these cells are at G2 stage before an endoreduplication step (a cycle where mitosis is skipped and move from G2 to G1). This hypothesis would require further investigation.

4. The radial step is uncorrelated from final division plane positioning

Our experiments show consistently that the radial step seems uncoupled from final division plane positioning. The root epidermis presents stereotyped divisions, where an "exploration" step would not be required, and still undergoes the radial step. Cells in stems have a bimodal distribution of their division orientation, and present the radial step in all cases. *ktn-1*, *act2act* and *trm678*, which do not present this bimodal rule in their stems also undergo the radial step. We therefore cannot relate it to any particular mode of division. Furthermore, the division plane orientation is decorrelated from division symmetry. *p35S::PMEI* cells present altered daughter cells symmetry, but correct division plane orientation. On the contrary, *clasp-1* cells presents correct daughter cells symmetry but slightly altered division plane orientations (that could reflect an impairment in cell shape reading). The lack of CMT dynamics in these genetic backgrounds prevent from drawing conclusions on the involvement of the radial step in these parameters.

ktn-1 and *trm678* cells both present altered division symmetry and division plane orientation. *ktn-1* cells have a less clear-cut radial step than the WT and have a more variable daughter cell volume ratio. On the contrary, *trm678* has a more clear-cut radial step and less variability in daughter cell volume ratio than the WT. Both of these mutants present a radial step longer than the WT. This strengthens the idea that the aspect of the radial step (i.e. how clear-cut it is) as being more important than its duration when defining the symmetry between daughter cells. Measuring the anisotropy of cells undergoing the radial step in *ktn-1* would give a quantitative idea on how "clear-cut" it is.

IV. Concluding remarks and perspectives on the study of the radial step

While the description of the radial step and the preliminary exploration of its function have been performed during my project, many questions remain. Indeed, while many studies investigate pre-mitotic stages of the cell cycle, most of them focus on the functional role of the PPB and the recruitment of CDZ markers (Dahiya and Bürstenbinder, 2023). The study of pre-PPB steps remains largely unexplored, likely due to the absence of a clear marker of the transition towards the PPB.

By unraveling the radial step, we identified a transition stage towards the PPB. Studying the dynamics of nucleation complexes appears as a key next step to confirm the involvement of cortical/cytoplasmic MTs balance in cytoskeletal organization. Overall, the radial step seems robust to local changes in tension patterns, as evidenced by the dividing cells around developing trichomes, and around ablations. Therefore, it reinforces the idea that the radial step could indeed be a pre-mitotic mechanical reset stage for the cell.

We also highlighted the stem as an excellent model system to study cell divisions, and more generally as one that should be considered in future studies. Nevertheless, these experiments have been performed in small cells, still embedded in tissues, and other tools are required to specifically study different contributions to the pre-mitotic radial step of microtubules. Artificial induction of cell divisions in tobacco mesophyll cells revealed a good alternative to study pre-mitotic nuclear migrations and PPB maturation. Optimization and troubleshooting steps are, however, required to obtain resistant microtubule fluorescence, easy image analysis and reproducible results.

Calli would also appear as theoretically relevant systems to investigate the contribution of tissue integrity to the radial step, and could also be coupled to microfluidics techniques for drug application/medium modification, and mechanical stress treatments. The experiments I conducted revealed that the optimization of the callus system is not as straightforward, especially for image analysis. Obtaining microcalli could reduce the volume of the specimen and facilitate the imaging. While mechanical shaking did not prove effective to obtain viable microcalli, partial enzymatic digestion of the cell walls could be a promising alternative.

Lastly, protoplasts were considered for exploring the contribution of neighboring cells and cell shape to the radial step. While protoplasts are widely used for molecular biology studies (Ryu *et al.*, 2019; Giacomello, 2021), or transformations through regeneration of plants (Yoo *et al.*, 2007), developmental studies reveal more challenging. The main limit is managing to make the protoplasts divide. A lot of optimization would be necessary to carry out this project. Notably, using a different source for the protoplasts, such as *Arabidopsis* roots, calli, or a different model species, could help this process. It has also been reported that protoplasts cultivated on solid media using sodium

alginate increases their regeneration ability (Jeong *et al.*, 2021; Pati *et al.*, 2005). However, with the trapping and confining methods I have tried, liquid protoplast culture is required. While some protocols exist to solubilize sodium alginate (Draget *et al.*, 1996), I have doubts on the protoplast survival to these methods.

To go one step further, the proposed function of the radial step could echo the cell rounding step function in *Drosophila* epithelia. In animals, a pre-mitotic reset is marked by the cell rounding before spindle formation, accompanied by a stiffening of the cell's cortex and an increase in its surface tension (Taubenberger *et al.*, 2020). The function of this step is proposed to help spindle positioning, and to generate space in order to divide (Taubenberger *et al.*, 2020). Upon disruption of cell rounding through myosin motor inactivation, *Drosophila* epithelial cells remain packed as they divide, and their division plane follows cell geometry instead of tissue stress (Chanet *et al.*, 2017). Even though the mechanical properties of a plant tissue are different than that of an animal due to the presence of cell walls, our analysis of cell division plane orientation according to cell aspect ratio also fits the idea that a threshold of stress, either prescribed by cell shape or tissue shape, determines the final orientation of division plane. Interestingly, in our study, we could explore the consequence of a prolonged radial step, and we found an increase in cell division volume precision. One might thus wonder whether a prolonged cell rounding in *Drosophila* would also increase the precision of cell division.

Material and methods

1. Plant material and growth conditions

All *Arabidopsis thaliana* lines were in the Col-0 ecotype, and are detailed in Table MM1.

Lines used	References
Col-0 x *pPDF1::mCitrine-MBD*	Armezzani *et al.*, 2018
Col-0 x *pUBQ10::Lti6-TdTomato*	Melnyk *et al.*, 2015
Col-0 x *pRPS5a::RFP-TUA5*	Prusicki *et al.*, 2019
Col-0 x *pUBQ10::RFP-TUA6*	Van Damme *et al.*, 2004
Col-0 x *p35S::GFP-MBD*	Hamant *et al.*, 2008
Col-0 x *pPCNA1::PCNA1-RFP* x *pPDF1::mCitrine-MBD*	Yokoyama *et al.*, 2016
trm678 x *pPDF1 ::mCitrine-MBD*	Schaefer *et al.*, 2017
trm678 x *pUBQ10::Lti6-TdTomato*	Schaefer *et al.*, 2017
p35S::PMEI	Lionetti *et al.*, 2007
xxt1xxt2	Cavalier *et al.*, 2008
ktn-1 x *pPDF1::mCitrine-MBD*	Chen *et al.*, 2014
nek-6 x *pPDF1::mCitrine-MBD*	Motose *et al.*, 2008
spr2-2 x *p35S::GFP-MBD*	Shoji *et al.*, 2004
act2act7 x *p35S::GFP-MBD*	Gilliland *et al.*, 2002
clasp-1	Ambrose *et al.*, 2007

Table MM1: Description of all of the *Arabidopsis* genetic backgrounds used for the analysis

- **SAM imaging (Chapter I1 of the Results, I did not perform the experiments)**

For SAM imaging, *Arabidopsis* wild-type lines were sown on soil and grown in climatic chambers under short-day conditions (8-h light/16-h dark) for 6 weeks and then grown under long-day conditions (16-h light/8-h dark regime) for 4 weeks.

- **Stem imaging**

For stem imaging, seeds were sterilized using a sterilization solution (88 mg/mL sodium dichloroisocyanurate and 90% ethanol). 50 to 300 µL of seeds were first incubated in 1 mL of the sterilization solution for 6 minutes, and then washed twice with 96% ethanol and left to dry. Seeds were sown on solid Arabidopsis medium (11.82 g/L Arabidopsis medium (Duschefa, a custom-

made medium for the lab, recipe in the Table MM2), 2 mM $Ca(NO3)2\ 4H2O$, pH 5.8 KOH (10 M), 10 g/L granulated agar (Merck)). In NPA conditions, this medium was supplemented with 10 μm of naphthylphthalamic acid (NPA). The seeds were left for stratification for 2 days at 4°C in the dark, and plants were grown for around 3 weeks in long day conditions (16-h light/8-h dark) at 20°C, until the first flower buds developed.

It is worth noting that, while the cell division is very active at the tip of the stem, imaging conditions can inhibit division and affect microtubule dynamics. This happened in both Arabidopsis and ACM media. We noticed that the winter season is usually more prone to induce slow division rates.

Arabidopsis medium	
Formula	**mg/mL**
$CoCl_2.6H_2O$	0.0025
$CuSO_4.5H_2O$	0.13
Ferric Ammonium Citrate	50
NaCl	0.58
H_3BO_3	4.33
$MnCl_2.4H_2O$	2.77
$Na_2MoO_4.2H_2O$	0.05
$ZnSO_4.7H_2O$	0.29
KH_2PO_4	340.25
KNO_3	500.5
$MgSO_4.7H_2O$	246.5
Myo-Inositol	100
Nicotinic Acid	1
Pyridoxine HCl	1
Thiamine HCl	1
Ca-Panthotenate	1
Biotine	0.01
Sucrose	10000
MES	700

Table MM2: Composition of the *Arabidopsis* medium

- **Lateral root imaging**

For lateral root imaging, after sterilization, the seeds were sown on 1.1 g/L Murashige and Skoog medium with vitamins (Duschefa), 10 g/L sucrose, pH 5.7 (KOH), 15 g/L bacto-agar (BD). The seeds were left for stratification for 2 days at 4°C in the dark, and plants were grown for 7 to 10 days, until small lateral roots were observed.

- **Tobacco leaf imaging**

For *Nicotiana benthamiana* leaf imaging, seeds of plants expressing the *p35S::GFP-TUA6* fluorescent microtubule marker (Gillespie *et al.*, 2002) were sown on soil, and grown at 21°C, in long day conditions (16-h light/8-h dark regime) under a plastic cap to prevent dehydration. Single plantlets were transplanted to individual pots after one week, and were grown for 3 weeks before the experiment.

2. Callus initiation and imaging

For callus initiation, small cuts of roots or leaves of *Arabidopsis* plants expressing the *p35S::GFP-MBD* microtubule fluorescent marker were deposited on solid callus induction medium (4.3 g/L Murashige and Skoog basal salt mixture (Sigma), 20 g/L sucrose (Sigma), 10 mg/L myo-inositol, 100 µg/L nicotinic acid, 1 mg/L thiamine-HCl, 100 µg/L pyridoxine-HCl, 400 µg/L glycine, 0.46 µM kinetin, 2.25 µM 2,4-D, 10 g/L phytagel (Sigma), pH 5.7 (KOH)). The liquid callus medium was identical, without the addition of phytagel. The petri dishes were then kept in the growth chamber in long days conditions (16h light/8h dark) at 20°C.
Callus precursor cells were imaged at the cutting sites, 3 days after transfer onto callus induction medium (Figure R34). Otherwise, the formed calli were maintained by transferring a small piece of callus on new solid callus induction medium every 3 weeks.
Calli were imaged using the LSM980 – Airyscan 2 upright microscope, using a 20x water immersion lens (NA: 1.0, see section below).

3. SAM dissection and imaging

Dissected apices were embedded in ACM culture medium (2.2 g/L Murashige and Skoog medium without vitamins (Duschefa), 10 g/L sucrose, pH 5.8 KOH (10 M), 8 g/L agarose) supplemented with 1x Morel and Wetmore vitamins and 570 nmol/L trans-zeatin (12.5 µl of 1mg/mL of stock solution in 100ml of ACM medium), and maintained under long-day conditions (16-h light/8-h dark regime, 21°C) as described in Hamant *et al.* (2008). Dissected shoot apices were imaged with a Leica SP8 upright confocal microscope (Figures R1A, R31, and R3B). Confocal z-stacks were acquired (every 30 min for 10 hours) at a resolution of 0.09 × 0.09 × 0.2 µm per voxel using a HC FLUOTAR L 25x/0.95 N.A. water immersion objective. The confocal scan speed was no more than 7, and line averaging was set to 2.

4. Stem preparation and imaging

Arabidopsis stems from *in vitro* plants with a few unopened flower buds were selected. For easier dissection, we selected stems that were ca.1.5 cm long. Then, the organs impairing a correct imaging were dissected (cauline leaves and flower buds). The imaging medium was either the same as the growth medium (Arabidopsis Medium, AM), or Apex Culture Medium (ACM). In the NPA conditions, the ACM medium was supplemented with 10 µm of naphthylphthalamic acid (NPA). The plants with prepared stems were transferred to an imaging medium and fixed in the medium by placing the roots and leaves inside the agar, exposing the area of interest. In ablation conditions, the ablation was made manually, using a small needle and gently poking the stem. The plate containing the samples was placed in the growth chamber for one day (15 to 20 hours) before the experiment. Figure MM1 illustrates the different steps of stem preparation.

For membrane stainings, a drop of FM4-64 (around 10-20 µL) at 1 mg/mL was deposited in the area of the stem of interest, and left for 30 minutes before rincing twice with water. For propidium idodide (PI) stainings, a drop of PI at 1 mg/mL was deposited in the area of interest of the stem, and left for 20 minutes before rinsing twice with water. All of the stainings were made just before the imaging experiments.

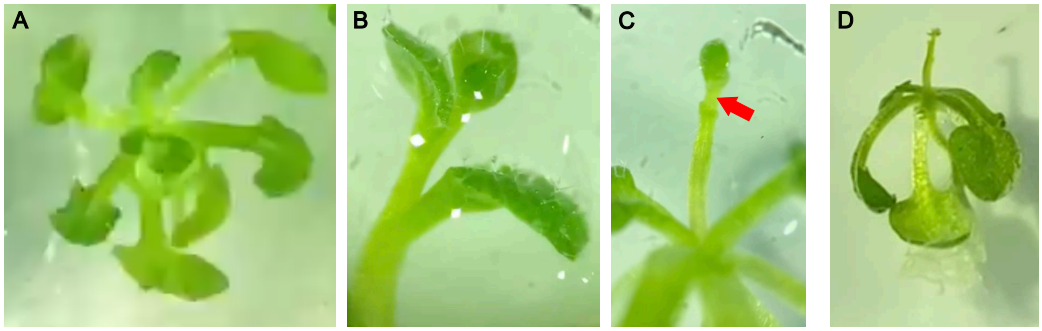

Figure MM1: Step-by-step representation of the stem sample preparation (left to right). First, select a seedling with a stem of around 1.5 cm in length and with a few unopened flower buds (A). The area of interest (the stem portion under the meristem) is often covered by a few organs (B). These organs are dissected out in order to expose the area of interest (red arrow) (C). Finally, insert the roots and a few leaves inside the agar to fix the sample, while leaving the area of interest on top of the agar for it to be accessible to the microscope (D).

Images were acquired with the SP8 confocal microscope (Leica), the LSM980 – Airyscan 2 confocal microscopes (Zeiss), upright or inverted, or with the LSM800 inverted confocal microscope (Zeiss).

- **SP8 microscope**

The images for Figure R4A, R15, and the Latrunculin B experiments in Chapter II of the Results, as well as for the production of the measurements of Figures R5D-E, R5G-H, R5J-2L were

acquired using the SP8 confocal microscope (Leica). The samples were imaged using a x25 water-immersion lens (NA = 0.95), with the resonant scanner switched off, to obtain better resolution. 8-bit images were taken in 1024x512 μm/pixels format, with the XY-resolution of 0.152 μm/pix and Z-stack slices of 0.500 μm. Images were acquired with a scanning speed of 1000 and averaged 4 times. The mCitrine signal was imaged using the the 514 nm laser (0.5% intensity) and a HyD 1 detector between 518 nm and 549 nm.

- **LSM980 – Airyscan 2 inverted microscope**

Some of the images used for Figures R5D-R5G, R5E-R5H, R5J-R5L acquired using the LSM980 – Airyscan 2 inverted confocal microscope (Zeiss). All the samples were imaged under the C-Apochromat x40 water immersion lens (NA: 1.2), and were kept under immersion during the whole experiment by placing a droplet of water directly on the objective. The rest of the parameters are the same as described above.
Protoplasts in the microfluidic traps (Figure R40) were imaged using the same microscope with the classical confocal mode (without airyscan detection), using a 63x oil immersion lens (NA: 1.4).

- **LSM980 – Airyscan 2 upright microscope**

The images for all figures of Chapters I and III of the Results, except Figures R1, R3A-B, R4A, R15, and the Lat B experiments, were acquired using the LSM980 – Airyscan 2 upright confocal microscope (Zeiss). All the stems for microtubule dynamics experiments were made using the airyscan mode of the microscope, imaged under the W Plan-Apochromat 20x water immersion lens (NA: 1.0), and were kept under immersion during the whole experiment. For this, the size of the image needed to be optimized for the Airyscan module, which resulted in a pixel size of around 0.065 μm x 0.065 μm. The Z resolution was always 0.500 μm. The pixel time could vary between experiments, but the scanning was always bidirectional and averaged twice by frame. Airyscan parameters are detailed in Figure S12B. The results for Figures R5D, R5G, R5E, R5H, R5J-L were made using images from the three microscopes.

The stems stained with FM4-64 or PI were imaged using the classical confocal mode of the microscope (without airyscan detection). Images were made using the same 20x water immersion lens (NA: 1.0), with a size of 788 x 1352 pixels, and an XY resolution 0.16 μm/pixel and Z resolution of 0.500 μm.

- **LSM800 inverted microscope**

Figures R35 and R37 were acquired with the LSM800 inverted confocal microscope (Zeiss). The samples were imaged using a 63x oil immersion lens (NA: 1.4). 8-bit images were taken in 397 x 397 pixels format, with the resolution of 0.27 μm/pixel and Z-stack slices of 0.500 μm.

Fluorescent protein	mCitrine	TdTomato/RFP	GFP
Laser (λ, power)	514 nm, 0.1 %	561 nm, 0.1 %	488 nm, 0.1 %
Main Beam Splitter	445/514/561/639	488/561	488/639
Secondary Beam Splitter	SP 615	SP 615	SP 615
Emission Filters for the Airyscan detector	BP 420-480 + BP 495-550	Plate (transmission 100%)	BP 495-555 + LP 660

Figure MM3: Airyscan detection parameters for *Arabidopsis* stem, protoplast, calli and root imaging.

Fluorescent protein	FM4-64	PI
Laser (λ, power)	514 nm, 0.1 %	561 nm, 0.2 %
Main Beam Splitter	514/639	445/561
Secondary Beam Splitter	Plate	Plate
Detection band	605 nm – 730 nm	579 nm – 704 nm

Figure MM4: GaAsP PMT detection parameters for *Arabidopsis* stem imaging.

5. Lateral root sample preparation and imaging

The lateral root samples were prepared as detailed in Kirchhelle *et al.* (2016). Briefly, a chamber was cut in Carolina gel (Blades Biological) spread across a microscopy slide (Rogo-Sampaic) using glass spacers. A thin strip of root growth medium was placed in the chamber, where up to 4 root samples could be placed. Finally, the mount was immerged in perfluorodecalin (Sigma), and covered with a large coverslip. The samples were left in the growth chamber 4 to 12 hours before observation.

The samples were imaged every 25 minutes for up to 3 hours using the LSM980 – Airyscan 2 upright confocal microscope (Zeiss), with the Airyscan confocal mode and a x20 water-immersion lens (NA = 1). Images were taken in 212.13 µm x 212.13 µm (3904 x 3904 pixels) format, with Z-stack slices of 1 µm. For the detection parameters, see Table MM4.

6. Image processing

All the processing of the images was done on the Fiji (ImageJ) software.

The LSM980 images were processed using the Airyscan Processing program in the Zeiss software, with the "All Images (2D)" program and the Auto Filter. They were then converted from the Carl

Zeiss Image format (.czi) to Tagged Image Format File (.tiff) format, using a slightly modified version of the lifRxiv program (https://github.com/sverger/lifRxiv).

The SP8 images were converted from Leica Image File Format (.liff) to Tagged Image Format File (.tiff) format, using the lifRxiv program.

The image stacks were then processed using the SurfCut program (Erguvan *et al.*, 2019) projecting the upper signal from the top slices (between 0 and 4 µm of the epidermis). The SurfCut projections coming from the same sample at different time points were then assembled into stacks. We selected the cells that divided or exhibited a PPB by the end of the time frame of the experiment.

7. Division plane orientation analysis

Cells of interest, showing either a PPB or a recent division, were identified. The longest and shortest axis were measured by manually drawing a region of interest to the cell's contours, and extracting the fitted ellipse using Fiji. The aspect ratio was then obtained by dividing the shortest plane by the longest plane of this fitted ellipse.

The orientation of the division plane, or the PPB, was also measured manually using the Fiji software. The orientations were normalized to keep the results between 0° and 90°, with the 0° orientation being horizontal.

The division angles were all divided by 90, to get a dataset between 0 and 1, in order to perform the logistic regression. The regression was made with the "glm" fit in R, with the "quasi-binomial" family to account for the dispersion of the data, and the "logit" link. To assess the goodness of the fit, we calculated the R-squared value using the null deviance, and the residual deviance given by the glm function, as followed:

$$R^2 = 1 - \left(\frac{Residual\ deviance}{Null\ deviance}\right)$$

To find an approximation of the inflection point of the fitted curve, we acknowledged that the "logit" link uses the following regression:

$$\log\left(\frac{p}{1-p}\right) = ax + b$$

With p being the probability of the response being 1, a being the slope, and b the intercept.
We therefore calculated x with p set at 0.5, and a and b being the result of the "glm" fit.

8. Cortical microtubule orientation analysis

We manually drew rectangles in the center of the cortex, avoiding the edges (to prevent biases in the measurements) on SurfCut projections, for the cells of interest. To measure the local orientations of microtubules overtime, we used the Directionality function in Fiji, using the "Local gradient orientation" method. The output of this program is a distribution of the pixel orientations between -90° and 90° (with 0° being the vertical orientation), as well as a gaussian fit to the data. We plotted the gaussian fit, for each cell at each timepoint.

We used the OrientationJ package's "vector field" function in Fiji (http://bigwww.epfl.ch/demo/orientation/) as another way of measuring CMT orientation (Figure R5J-L). For this, we wrote a homemade macro allowing to extract the vectors inside the region of interest. Briefly, we defined the ROI manually and blacken it. We then extract the coordinates of the vectors inside this blackened area by setting a threshold on the energy value given by the "vector field" output. Once these coordinates are saved, we run the "vector field" on the unchanged image and retain the orientation of the vectors of interest. To test the differences in the distribution of these vectors' orientations overtime, we ran the Klomogorov-Smirnoff test in RStudio (null hypothesis: the samples follow a given distribution). With this test, we compared the distribution of the data at each timepoint with a uniform sequence, generated with RStudio.

To measure the anisotropy of the microtubule arrays, we used the SurfCut images, and delimited the region of interest by hand, following the cell contour, but excluding the anticlinal cortex to avoid any bias. We ran the FibrilTool plugin (Boudaoud *et al.*, 2014) in Fiji to extract the anisotropy. To test the differences between the different genetic background and the different timepoints, we ran the Tukey Honestly Significant Difference (HSD) test in RStudio (null hypothesis: the means of the tested groups are equal).

9. Cytoplasmic microtubule content analysis

To analyze the cytoplasmic microtubule, we used Z-stacks of images from lines expressing *pPDF1::mCitrine-MBD*. To project the cytoplasmic microtubule signal, we used the reslice function in Fiji, with "Output spacing" set at 0.5 µm, starting at the top. We then made a maximal projection of the reslice output to obtain the cytoplasmic microtubule signal. The region of interest for the reslice projection was determined by hand, by being careful of excluding the anticlinal cortex of the cell to only project the internal signal.

The outer periclinal cortex, as well as the inside of the cell were marked by hand, and the average signal was measured using Fiji. For each cell, at each timepoint, the ratio between the internal signal and the cortical signal was plotted, to be able to compare all the measurements, and balance the

photobleaching that the samples experienced overtime. We tested the differences in these values between the different genetic backgrounds and between each timepoint using the Tukey-Kramer test in RStudio.

10. Volume measurements

Membrane marker images obtained with the Airyscan mode of the microscope were resized to obtain a voxel size with a X of around 250 μm. The images were then processed using the MorphoGraphX software (Barbier de Reuille *et al.*, 2015). First, images were blurred using the Gaussian blur stack function, and then the segmentation was made using the ITK Watershed Auto Seeded function, and the parameters were fine-tuned to obtain a suitable 3D segmentation. A mesh was then applied using the Marching Cube 3D function, and the volumes were extracted with the Cell Analysis 3D function.

Recent divisions were spotted by eye, as newer membranes separating two daughter cells are straight, anchored at 90° from the edges and are thinner than older membranes. The ratio between the two volumes was then always measured by dividing the bigger daughter cell's volume by the smaller ones. To compare the averages of the ratios, we performed Wilcoxon's statistical test in RStudio. To compare the variances, we used Fligner's test in RStudio.

11. Tobacco leaf infiltration

Nicotiana benthamiana infiltration was performed as described in Doumane and Caillaud (2020), and is shortly detailed below.

- ***Agrobacterium tumefaciens*** **culture and preparation**

Agrobacterium strain GV3101/C58 (resistant to rifampicin) expressing *p35S::*At*CYCD3;1-Turquoise2* (Xu *et al.*, 2020) were cultured on Yeast Extract Broth (YEB) medium (5 g/L beef extract (Sigma), 1 g/L yeast extract (Meridis), 5 g/L peptone (BD), 5 g/L sucrose, pH 7.2 (NaOH), 14 g/L agar (Merck)) supplemented with RGS (50 μg/mL rifampicin, 20 μg/mL gentamicin, 250 μg/mL spectinomycin) for 2 to 3 days at 29°C, and then kept at 4°C. The day before the infiltration, a scoop of the colonies was suspended in liquid Lysogeny Broth (LB) medium (10 g/L peptone (BD), 5 g/L yeast extract (Meridis), 86 μM NaCl), spread on a YEB + RGS plate, and incubated at 29°C overnight. The bacteria were then collected, suspended in infiltration solution (10 mM $MgCl_2$, 10 mM Tris-HCl pH 7.5), and properly diluted to reach an OD_{600} of 1.

- **Leaf agroinfiltration**

Using a needleless syringe, inject between 200 and 300 µL of the *Agrobacterium* suspension in the abaxial side of *Nicotiana benthamiana* leaves 4 to 7, expressing the *p35S::TUA6-GFP* microtubule fluorescent marker (Gillespie *et al.*, 2002). The plants were brought back to the growth chamber 24 to 54 hours before imaging.

- **Sample preparation and imaging**

A piece of agro-infiltrated leaves was cut and placed abaxial-side-up on a drop of water in a glass slide. Another drop of water was added before covering with a coverslip.
The samples were imaged every hour for up to 7 hours using the LSM980 – Airyscan 2 upright confocal microscope (Zeiss), using the Airyscan confocal mode and a x20 water-immersion lens (NA = 1.0). Images were taken in 212.13 µm x 212.13 µm (3904 x 3904 pixels) format, with Z-stack slices of 1 µm.

Fluorescent protein	Turquoise2	GFP
Laser (λ, power)	445 nm, 0.2 %	488 nm, 0.1 %
Main Beam Splitter	445/561	488/639
Secondary Beam Splitter	SP 550	SP 615
Emission Filters for the Airyscan detector	Plate (transmission 100%)	BP 495-555 + LP 660

Figure MM5: Airyscan detection parameters for tobacco leaf imaging.

Annexes

PROTOPLAST PROTOCOLS

Protocols followed for protoplast isolation and culture:

PROTOCOL 1:

Cell wall regeneration medium 1: Gamborg's B5 basal medium with minimal organics (3.2 g/L), Glucose 1 M, Mannitol 0.25 M, NAA 1 μM, pH 5.8 (KOH). Filter sterilized.
Enzymatic solution: Cellulysine (17 mg/mL), Cellulase (17 mg/mL), Pectolyase (0.4 mg/mL), BSA (3.5 mg/mL). Dilute in cell wall regeneration medium and filter sterilize.

Place the areal parts of around 5 20-day-old plants in 2 mL of the enzymatic solution.
Rotate at 15 rpm for 2 hours
Centrifuge for 5 minutes at 1000 rpm and discard the supernatant
Rince with cell wall regeneration medium and centrifuge at 1000 rpm for 5 minutes twice. Pipette very gently as the protoplasts are very fragile at this stage.
Determine the density of protoplasts with a Malassez cell, and resuspend with the according volume of cell wall regeneration solution to obtain $4e10^6$ protoplasts/mL.
Culture the protoplasts at 25°C in continuous light, under constant agitation (at 10 rpm).

PROTOCOL 2:

Solution A: $CaCl_2$ (2 mM), $MgCl_2$ (2 mM), MES (10 mM), pH 5,5 (KOH), Mannitol 0.6M. Autoclave.
Solution A+Enzymes: Same as the enzymatic solution in protocol 1, diluted in solution A.
Cell wall regeneration medium 2: Gamborg's B5 medium with minimal organics (3.2 g/L), Trehalose 0.4 M, Glucose 0.05 M, NAA 1 μM, pH 5.7 (NaOH or HCl). Filter sterilize.

Place the areal parts of 50-100 of 10-day-old seedlings in 15 mL of solution A+Enzymes
Rotate at 15 rpm for 4 hours at 21°C
Filter the solution through a 100 μm nylon mesh, and then a 40 μm nylon mesh
Centrifuge 2 minutes at 100 g to collect the protoplasts
Discard the supernatant and wash in 1 mL of solution A with another centrifugation for 2 minutes at 100 g
Discard the supernatant and resuspend in 5 mL of cell wall regeneration solution
Culture the protoplasts in a large petri dish at 22°C in continuous light

Cell wall regeneration medium 3 (Adapted from Dovzhenko *et al.*, 2003): Gamborg's B5 medium with minimal organics (3.2 g/L), Glucose 0.4 M, Dicamba (2 mg/L), BAP (0.15 mg/mL),

$MgSO_4.7H_2O$ (746 mg/L), $CaCl_2.2H_2O$ (450 mg/L), L-glutamine (50 mg/L), Casein hydrolysate (50 mg/L), Coconut water (20 mL/L), NAA (0.5 mg/L), MES (10 mM)

Cell wall regeneration medium 4 (Adapted from Xuan and Menzcel, 1979; Damm and Willmitzer, 1988): Gamborg's B5 medium with minimal organics (3.2 g/L), Glucose (0.4 M), $CaCl_2$ (1 g/L), 2,4-D (0.3 mg/L), BAP (0.15 mg/L)

PROTOCOL 4:

Place 50-100 7-day-old plantlets in 10 mL of solution A+1/2 Enzymes (Cellulysine (8.5 mg/mL), Cellulase (8.5 mg/mL), Pectolyase (0.2 mg/mL)) in a petri dish.
Digest the plants in the dark at room temperature for 4 hours[1]
Slowly move the petri dish to release the protoplasts
Filter through a 100 µm, and a 40 µm mesh, and centrifuge at 1000 rpm for 4 minutes[2]
Discard the supernatant and wash in 10 mL of cell wall regeneration solution[3] and centrifuge again at 1000 rpm for 4 minutes
Discard the supernatant and count protoplast density with a Malassez cell, and resuspend to obtain $2e10^5$ protoplasts/mL[4]
Culture the protoplasts in a large petri dish at 20°C in the dark[5]

[1] I tried also digesting overnight, in continuous light, and under rotation, at 4°C or at 20 °C

[2] I tried with various ramps of acceleration and deceleration. The deceleration seemed the most important to keep protoplast integrity during the centrifugation steps.

[3] I tried with cell wall regeneration solutions 2, 3 and 4

[4] I tried different densities of protoplasts

[5] I tried culturing the protoplasts in the dark or in continuous light, keeping the petri dish still, or shaken

GAUTHIER Camille Année 2022/2023

Mémoire UE « Découverte de la recherche »

Titre : Dynamique des microtubules et du noyau avant la mitose dans les feuilles de *Nicotiana benthamiana*

Adresse du laboratoire d'accueil : 46 allée d'Italie, 69364 LYON Cedex 07 FRANCE
UMR 5667 Laboratoire de Reproduction et Développement des Plantes – ENS Lyon
Equipe Mécanotransduction et Développement

Maître de stage : Christophe TREHIN
Encadrante : Isaty MELOGNO

Remerciements

Je tiens à remercier toutes les personnes qui ont contribué au bon déroulement de mon stage et qui m'ont aidé lors de la rédaction de mon rapport.

Je voudrais dans un premier temps remercier l'ensemble du RDP, et en particulier tous les membres de l'équipe Mécanotransduction et Développement qui m'ont accueillie chaleureusement avec enthousiasme et qui m'ont conseillée durant mon stage.

Je remercie Christophe TREHIN, mon tuteur de stage, pour sa disponibilité et ses conseils judicieux, qui ont contribué à alimenter ma réflexion et ont su répondre à mes interrogations.

Et enfin, je remercie également Isaty MELOGNO, pour sa patience, pour m'avoir accompagnée tout au long de ces semaines et pour toute sa bonne humeur qui a contribué à rendre ce stage d'autant plus enrichissant.

Sommaire :

Table des tableaux et des figures :

Tables des abréviations :

MTC : microtubules corticaux

PPB : Bande de pré-prophase

TUA6 : Tubuline alpha 6

CYCD3.1 : Cycline D3.1

1. Introduction

Les plantes produisent des organes de différentes formes et tailles. Cette diversité repose principalement sur la croissance qui, à l'échelle du tissu, dépend de l'expansion cellulaire et de la division cellulaire. Cette croissance génère des patrons de contraintes mécaniques à l'échelle du tissu ou de l'organe (Trinh et al. 2021). Par ailleurs, l'existence d'une paroi cellulaire rigide autorise une pression de turgescence intracellulaire importante entrainant un gonflement des cellules et donc un stress mécanique (Trinh et al. 2021). Ainsi, dans un tissu en développement, chaque cellule est soumise à des tensions/signaux mécaniques issus des propriétés des cellules elles-mêmes (liées à leurs géométries) et du tissu dans lequel elles se trouvent.

La division cellulaire, et notamment son orientation, est particulièrement importante au cours du développement chez les plantes car les cellules ne migrent pas. L'orientation de la division cellulaire détermine ainsi la position des cellules filles et donc l'axe de croissance des organes. Plusieurs modèles sont proposés pour prédire l'orientation du plan de division. Les premiers prennent en compte la géométrie cellulaire et prédisent que le plan de division passe par le centroïde (assimilé au centre dans le cas des cellules, Lewis, 1923) et suit le plan le plus court (loi déterministe, Errera, 1888) ou l'un des plans les plus courts (loi probabiliste, Besson et Dumais 2011). D'autres prennent en compte les propriété mécaniques à l'échelle du tissu et prédisent que le plan de division peut, dans certains cas, suivre la tension maximale du tissu, même si ce n'est pas le plan le plus court (Louveaux et al., 2016). Ces deux règles peuvent coexister mais comment la cellule sait-elle laquelle elle doit suivre ?

Pour répondre à cette question, mon équipe d'accueil suit la dynamique des microtubules corticaux (MTC) puisqu'ils s'alignent selon la tension maximale pendant l'interphase ("lecture" de la tension tissulaire, Hamant et al., 2019) et se réorganisent en un anneau appelé bande de pré-prophase (PPB), qui va déterminer la position du futur plan de division, juste avant la mitose (Rasmussen et al., 2013). Ainsi, dans les tiges d'*Arabidopsis thaliana*, il a été observé que les MTC adoptent une structure radiale avant la formation de la PPB. Cette structure est différente de l'organisation interphasique, et différente de la structure annulaire observée avant l'entrée en mitose. Une hypothèse possible de la fonction de cette étape appelée « radial » de par son aspect, serait de positionner le noyau au bon endroit avant la division. Néanmoins, dans les tiges d'Arabidopsis, les cellules sont très petites et le noyau occupe la majorité de cet espace. En outre, cette structure radiale n'a été observée que sur des tissus en croissance.

L'objectif du stage est d'observer la dynamique des MTC pendant la transition interphase/PPB, dans un système très différent : les feuilles matures de *Nicotiana benthamiana*. Pour induire des divisions actives dans ces cellules différenciées, je me suis basée sur des recherches antérieures qui ont établi que l'induction d'une cycline de type D (*At*CYCD3.1), activant et ciblant les kinases cycline-dépendantes (CDK), favorise l'entrée en division (Xu et al. 2020). J'ai donc utilisé la méthode d'infiltration de *Nicotiana benthamiana* par *Agrobacterium tumefaciens* pour transitoirement exprimer la cycline D3.1 dans les feuilles de tabac. Ainsi, que se passe-t-il

lorsque l'on induit la division dans ces cellules qui sont grandes (plus facile de suivre les mouvements du noyau), présentent une forme de puzzle (géométrie particulière), présentent un patron de tension mécanique caractéristique (tension maximale aux necks, Sapala et al., 2018) et sont dans un état initialement différencié ? Nous pouvons donc énoncer les objectifs suivants : (i) Rendre compte du taux d'induction de la division cellulaire afin d'optimiser le protocole. (ii) Mettre en évidence les différentes étapes de pré division et division afin d'identifier une phase « radial » d'orientation des MTC dans ce système. (iii) Mettre en évidence une potentielle dynamique du noyau avant la formation de la PPB.

2. Matériel et méthodes

2.1 Matériel végétal et bactérien

L'infiltration a été réalisée avec la souche d'*Agrobacterium* (C58/GV3101) contenant la séquence codante du gène *AtCYCD3.1* d'Arabidopsis fusionné à la séquence codante de la protéine fluorescente Turquoise, le tout sous contrôle du promoteur constitutif *p35S* (p35S::*At*CYCD3.1-Turquoise2, Xu et al., 2020). Les bactéries ont été cultivées sur un milieu YEB (Annexe 1) + RGS (rifampicine, gentamicine, spectinomycine), à une température d'incubation de 29°C, pendant 2 à 3 jours puis conservées à 4°C. 1 jour avant l'agroinfiltration, les bactéries sont diluées dans 300 µl de milieu LB (FISHER) pour être étalées. Les bactéries de la moitié d'une boîte de pétri ont été collectées et mises en suspension dans 5 mL de solution d'infiltration ($MgCL_2$ 10 mM et TrisHCl 10 mM), à une DO600 de 1,0 (figure 1).
L'infiltration a été réalisée sur des plants de tabac (*Nicotiana benthamiana*) transgéniques exprimant la protéine fusion p35S::TUA6-GFP (Gillespie et al. 2002). TUA6 correspond à l'α-tubulin et permet de visualiser les MTC. Les plants ont été cultivés pendant 3 à 4 semaines, après repiquage en terre, dans une chambre de culture de jours longs (photopériode 16h/8h), à température constante de 22°C.

2.2 Agroinfiltration

Entre 0,2 et 0,3 mL de suspension agrobactérienne a été infiltrée sur le côté abaxial des trois plus jeunes stades foliaires, grâce à une seringue en plastique de 1 mL, en appliquant une légère pression. 3 plants ont été infiltrés chaque semaine (figure 1).
Après infiltration, les plantes ont été laissées à température ambiante pendant 5h avant d'être remise en chambre de culture à 22°C jusqu'à observation par microscopie confocale.

2.3 Microscopie confocale

Les disques foliaires infiltrés de 6 mm de diamètre ont été montés entre lame et lamelle dans du milieu ACM (Annexe 2).

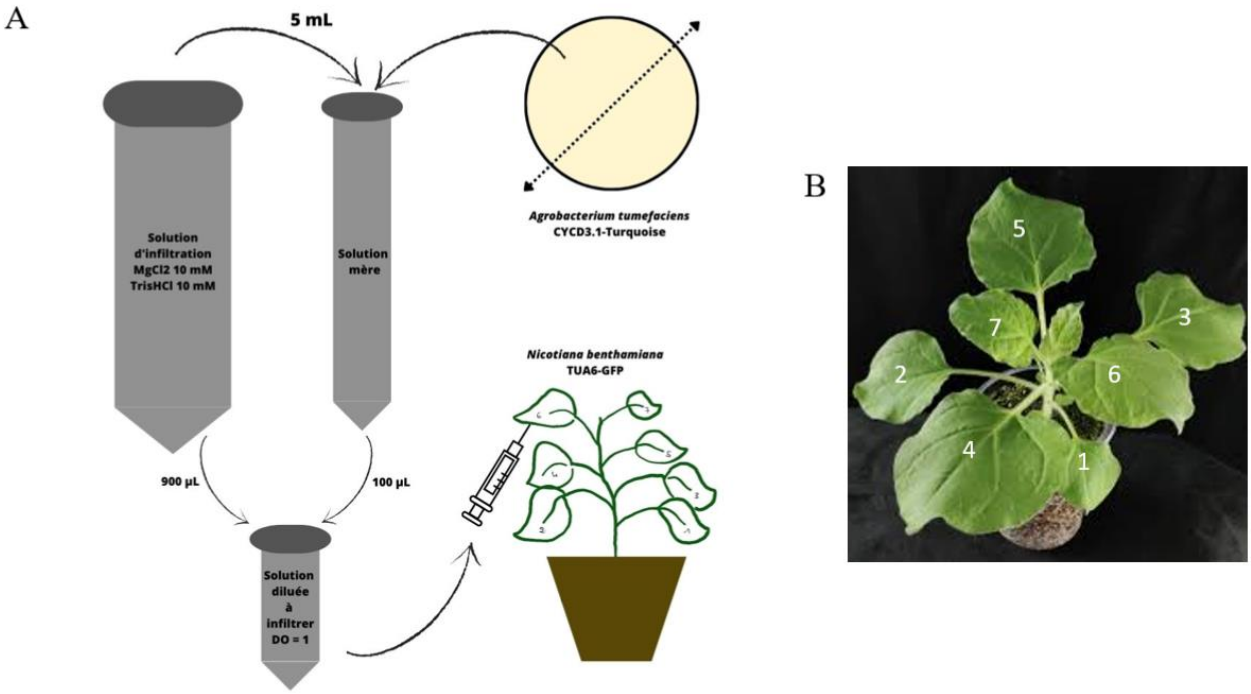

Figure 1 : Schéma récapitulatif du protocole d'infiltration.
A) Préparation de la solution à infiltrer. B) photo indiquant les différents stades foliaires, de 1 (le plus ancien) à 7 (le plus jeune).

Des échantillons ont été prélevés 24h après l'infiltration, et imagés jusqu'à 50h après montage pour évaluer la survie des tissus. Des échantillons ont été prélevés 48h après infiltration et imagés durant les 7h consécutives pour suivre la dynamique des MTC.
L'imagerie confocale a été réalisée à l'aide d'un microscope Zeiss LSM 980 AiryScan2. L'acquisition des images a été réalisée grâce à un objectif à immersion à eau x20 (ouverture numérique de 1.0). Les protéines GFP et Turquoise ont été excitées à l'aide d'un laser à 488 nm et 445 nm, respectivement, et la fluorescence a été capturée à 495-550 nm et 380-480 nm, respectivement.
La taille des images lors de l'acquisition était de 212,13 µm x 212,13 µm (3904 x 3904 pixels) et le pas entre deux plans en Z était de 1 µm.

2.4 Analyse d'images

Toutes les analyses d'images ont été réalisées avec le logiciel ImageJ (Schindelin et al., 2012). Les images du canal Turquoise, permettant de visualiser la cycline *At*CYCD3.1, ont été traitées avec un programme qui réalise une projection maximale de tous les plans confocaux (Annexe 3). Les images du canal GFP, permettant de visualiser les MTC, ont été traitées avec un programme qui réalise une projection de surface entre 0 et 4 µm (SurfCut) afin d'observer exclusivement les microtubules corticaux (Erguvan et al., 2019).
Les graphiques présentés ont été réalisés avec le logiciel RStudio (RStudio Team., 2015)

3. Résultats

3.1 L'infiltration permet d'exprimer *At*CYCD3.1 dans un grand nombre de cellules de feuille

Le premier objectif de cette étude a été de vérifier que le protocole d'agroinfiltration fonctionne efficacement dans nos conditions expérimentales et de tester la viabilité des échantillons après montage entre lame et lamelle. Pour cela, des comptages ont été réalisés sur plusieurs stades foliaires (figure 2) et à plusieurs points de temps (figure 3), afin d'obtenir le ratio suivant : $\frac{nombre\ de\ cellules\ exprimant\ AtCYCD3.1}{nombre\ de\ cellules\ totales}$.

On observe tout d'abord que visuellement, l'efficacité de transformation semble dépendre du stade de développement de la feuille infiltrée (figure 2A-D). Les comptages montrent qu'une feuille au stade 4 présente un ratio moyen de 0,22 tandis qu'une feuille de stade 6 possède un ratio moyen de 0,64 (figure 2E). Ainsi, plus la feuille infiltrée est jeune, plus l'efficacité de transformation est forte (ratio élevé).
Visuellement, on observe que l'efficacité de transformation semble également dépendre du temps post-infiltration (figure 3A-B). Les comptages montrent en effet que pour une feuille de stade 6 imagée 24 heures après infiltration, le ratio moyen est de 0,46, que cette même feuille imagée 48 heures après infiltration il est de 0,71, et à 54 heures après infiltration il est de 0,88 (figure 3C). Ainsi, plus on image longtemps après l'infiltration, plus l'efficacité de transformation est élevée, sans atteindre de plateau.

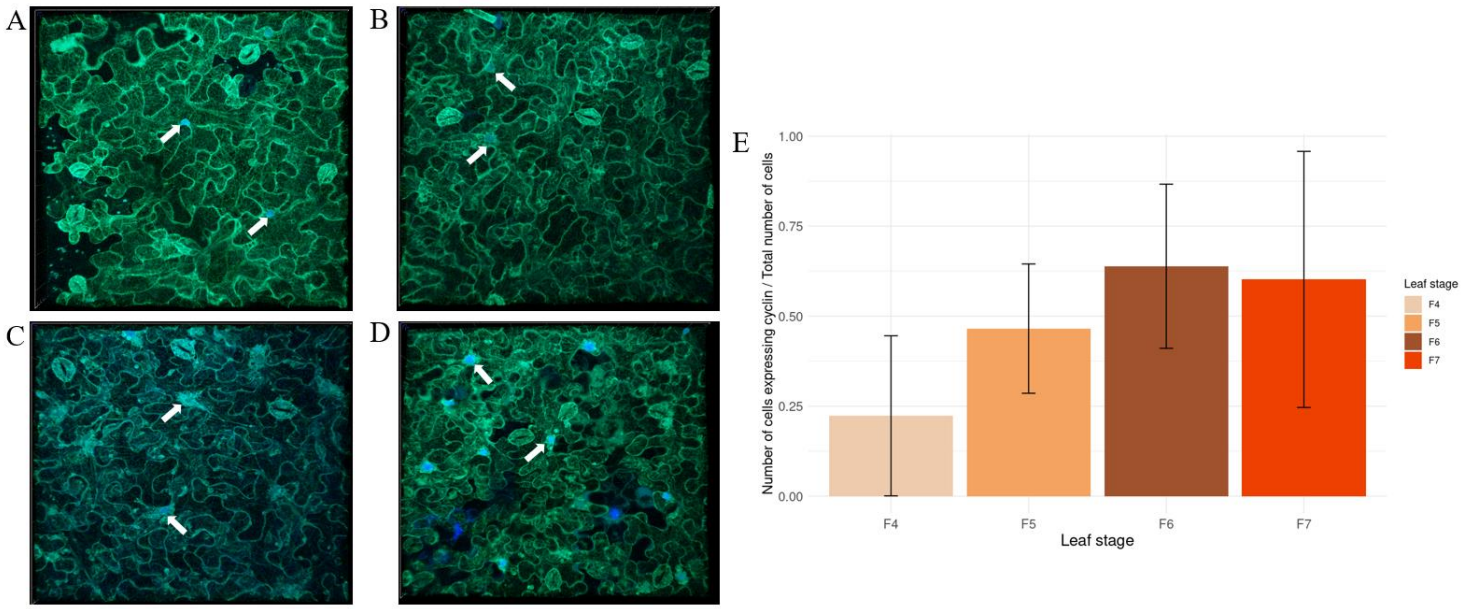

Figure 2 : Efficacité de l'infiltration en fonction du stade foliaire infiltré.
A-D) Images représentant des cellules de feuille 54h après infiltration pour les stades 4 (A) stade 5 (B), stade 6 (C) et stade 7 (D). Les zones bleues correspondent à l'expression de *At*CYCD3.1 dans les noyaux (flèches blanches). E) Comptages montrant en ordonnée, la moyenne du nombre de cellules exprimant *At*CYCD3.1/nombre de cellules totales et en abscisse : stade foliaire infiltré

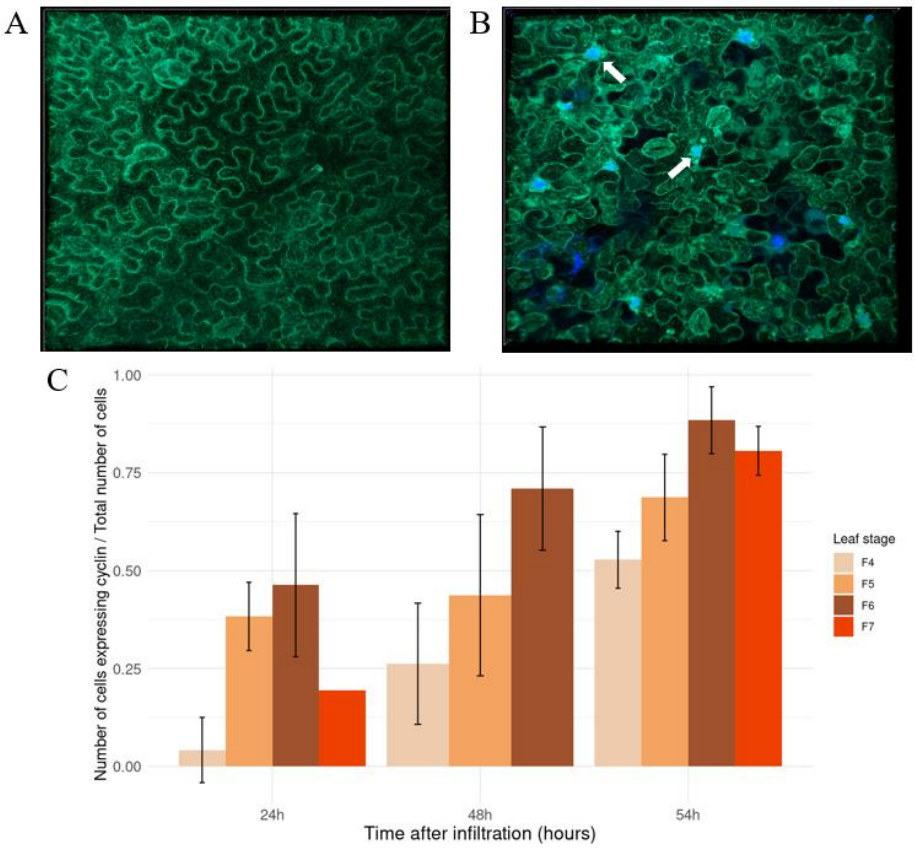

Figure 3 : Efficacité de l'infiltration en fonction du temps après infiltration.
A-B) Images représentant des cellules de feuille de stade 7, 24h après infiltration (A) et 54h après infiltration (B). Les zones bleues correspondent à l'expression de *At*CYCD3.1 dans les noyaux (flèches blanches). C) Comptages pour différents stades foliaires, montrant en ordonnée, la moyenne du nombre de cellules exprimant *At*CYCD3.1/nombre de cellules totales et en abscisse, le temps après infiltration en heures.

Un des objectifs de cette étude était également de s'assurer que les échantillons prélevés et montés entre lame et lamelles puissent survivre au-delà de 48h. Les résultats présentés sur les figures 2 et 3 montrent qu'après plus de 50h entre lame et lamelle, les échantillons sont toujours viables : les cellules présentent une forme homogène et attendue, le signal GFP est clair et intègre. Des figures de division (voir paragraphe 3.2) confirment ce résultat.
Ces observations permettent par la suite d'optimiser les conditions afin de pouvoir se concentrer sur les observations liées à l'orientation de la division cellulaire.

3.2 L'expression d'*At*CYCD3.1 induit la division cellulaire dans les cellules de feuille

L'objectif ici était de vérifier que le système inductible utilisé induit bien des divisions cellulaires dans les feuilles matures de *Nicotiana benthamiana*.
La figure 4 montre plusieurs structures caractéristiques de la mitose. En particulier, on distingue des anneaux de pré-prophase (PPB, figure 4A et B), des fuseaux mitotiques (figure 4C), des phragmoplastes (figure 4D) ainsi que des cellules filles venant de se diviser (figure 4E). Ces figures de mitose ont pu être observées sur différents échantillons indépendants mais au minimum 45 heures après infiltration.

3.3 L'observation confocale n'a pas permis de mettre en évidence d'étape « radial »

Le système d'infiltration étant fonctionnel, j'ai tenté de suivre la dynamique des MTC dans les cellules de feuille de tabac juste avant la formation de la PPB pour tester l'existence d'une potentielle structure radiale, similaire à celle observée dans l'équipe d'accueil sur des tiges d'Arabidopsis.
Pour cela, j'ai imagé des feuilles, 48 heures après transformation, pendant 7 heures consécutives : la figure 5 présente des résultats représentatifs d'un réplicat, obtenus sur 5 réplicats. Le signal des MTC a pu être clairement observé durant les 4-5 premières heures d'imagerie (figure 5 T0 à T4). En revanche, au-delà, le signal TUA6-GFP s'atténue fortement et ne nous permet plus de distinguer l'orientation des MTC. Aucune structure radiale précédant la mitose n'a pu être mise en évidence durant cette étude.

3.4 Les noyaux sont dynamiques dans les cellules épidermiques

Une des questions du projet concerne le positionnement du noyau dans les cellules, un éventuel déplacement de celui-ci, le lien entre sa position et celle de la PPB et la potentielle relation entre l'étape « radiale » et la position du noyau. J'ai donc utilisé le fait que la *At*CYCD3.1 soit fusionnée à la protéine Turquoise pour suivre la dynamique du noyau juste avant la mitose.
On observe en effet une dynamique des noyaux pendant toute la durée d'acquisition (figure 6A et B). Les noyaux semblent systématiquement se placer entre deux necks. Malheureusement, la durée d'acquisition n'a pas permis d'observer de mitoses à la suite de ces déplacements. Ces

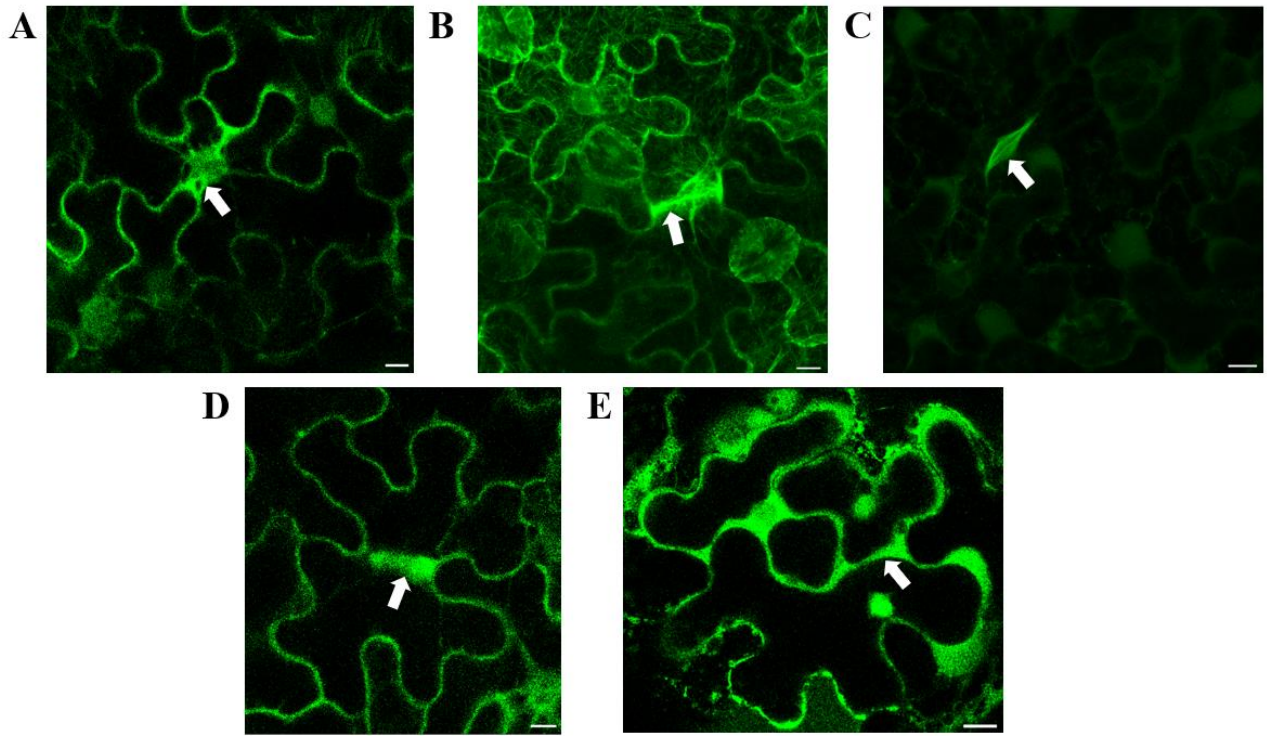

Figure 4 : Observations des différentes structures de mitose dans différents échantillons.
Les MTC sont visualisés grâce au signal de la protéine rapporteur GFP fusionnée à TUA6 (p35S::TUA6-GFP).
A-B) bandes de pré-prophase (PPB, flèche blanche). C) fuseaux mitotiques (flèche blanche). D) phragmoplaste (flèche blanche). E) cellules filles venant de se diviser (flèche blanche = nouvelle paroi). Echelle = 10 µm.

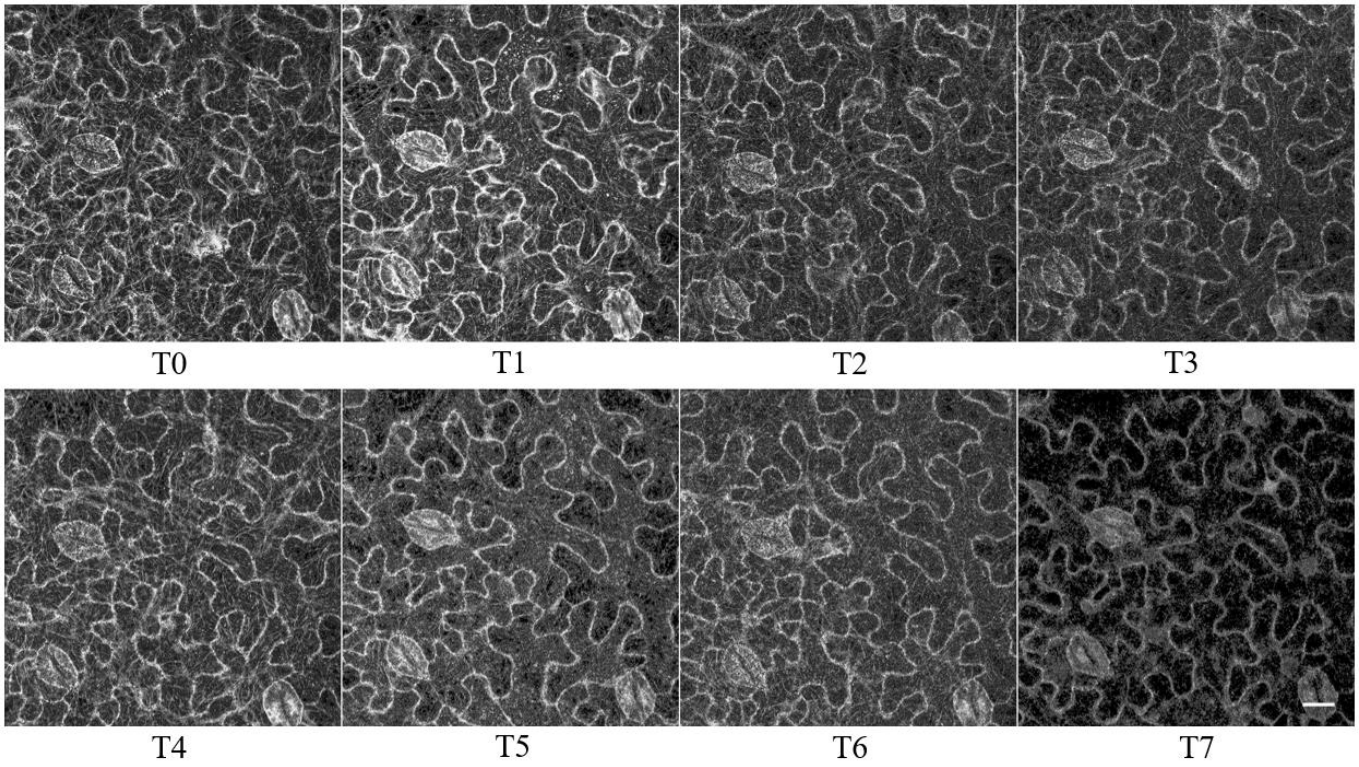

Figure 5 : Timelapse du suivi de la dynamique des MTC sur une feuille de stade 6.
Les MTC sont visualisés grâce au signal de la protéine rapporteur GFP fusionnée à la protéine Tua6 (p35S::TUA6-GFP).
Les points de temps ont été réalisés toutes les heures, de 0 à 7 heures. Echelle = 20 µm

observations ne nous permettent donc pas de conclure quant à un lien entre la dynamique des noyaux et la position de l'anneau de pré-prophase qui marque le début de la mitose.

4. Discussion et conclusion

D'après les résultats présentés, les feuilles néoformées présentent un taux d'expression de la cycline plus important que les feuilles plus âgées, ce qui nous indique que l'efficacité de l'agroinfiltration est dépendant de l'âge de la feuille. Il a également été montré que le taux d'expression de la cycline est dépendant du temps après infiltration. Cependant, nous n'avons pas échantillonné au-delà de 54 heures après infiltration, donc nous ignorons si un plateau est atteint par la suite ou non.

Dans un second temps, l'efficacité de l'agroinfiltration a été montré par l'observation de différentes structures de divisions.

Le système *Nicotiana benthamiana* présente différents intérêts pour l'étude de l'orientation du plan de division. Les cellules de l'épiderme des feuilles ont un patron de stress assez caractéristique (Sapala et al. 2018), et il est intéressant d'essayer de comprendre comment celui-ci pourrait influencer l'orientation de la division cellulaire. De plus, la taille des cellules permet de visualiser plus aisément les mouvements du noyau, contrairement aux cellules de tiges chez *Arabidopsis thaliana*. Les résultats obtenus au cours de ce stage ont permis de montrer que le système inductible de division cellulaire dans les cellules déjà différentiées de feuilles fonctionne très bien comme rapporté précédemment (Xu et al., 2020). Néanmoins, celle-ci ont seulement été observées indépendamment les unes des autres, et jamais au sein d'un suivi d'une seule cellule par timelapse.

La dynamique des MTC, juste avant la formation de la bande de pré-prophase, n'a malheureusement pas pu être déterminée. D'une part à cause de la durée des timelapses qui n'a pas permis de visualiser des mitoses à l'issue de ceux-ci. D'autre part à cause du signal qui diminue fortement au cours de l'acquisition et qui rend les MTC non-distinguables. Pour y remédier et limiter le photobleaching, il sera proposé de diminuer la puissance des lasers, diminuer le temps d'acquisition et/ou de n'utiliser qu'un seul canal d'excitation puisque les canaux d'excitation de *At*CYCD3.1-Turquoise et de TUA6-GFP se recoupent. En outre, on pourra utiliser une lignée de tabac exprimant un marqueur de tubuline réputé moins sensible, comme la GFP-MDB (Malivert et al. 2021), à la place de la TUA6-GFP. Ces modifications pourront, peut-être, permettre de répondre à quelques questions comme : quel est le comportement des MTC lorsque les cellules se divisent ? Y a-t-il un stade radial ? Ce stade touche t'il l'entièreté des MTC ou seulement ceux à proximité de la zone de division ?

Nous pouvons noter qu'aucune structure ressemblant à la structure radiale des tiges d'Arabidopsis n'a été observée dans les feuilles de tabac. Néanmoins, comme les MTC interphasiques sont beaucoup moins anisotropiques dans les feuilles que dans les tiges, nous ne pouvons pas exclure un changement des MTC avant la mise en place de la PPB.

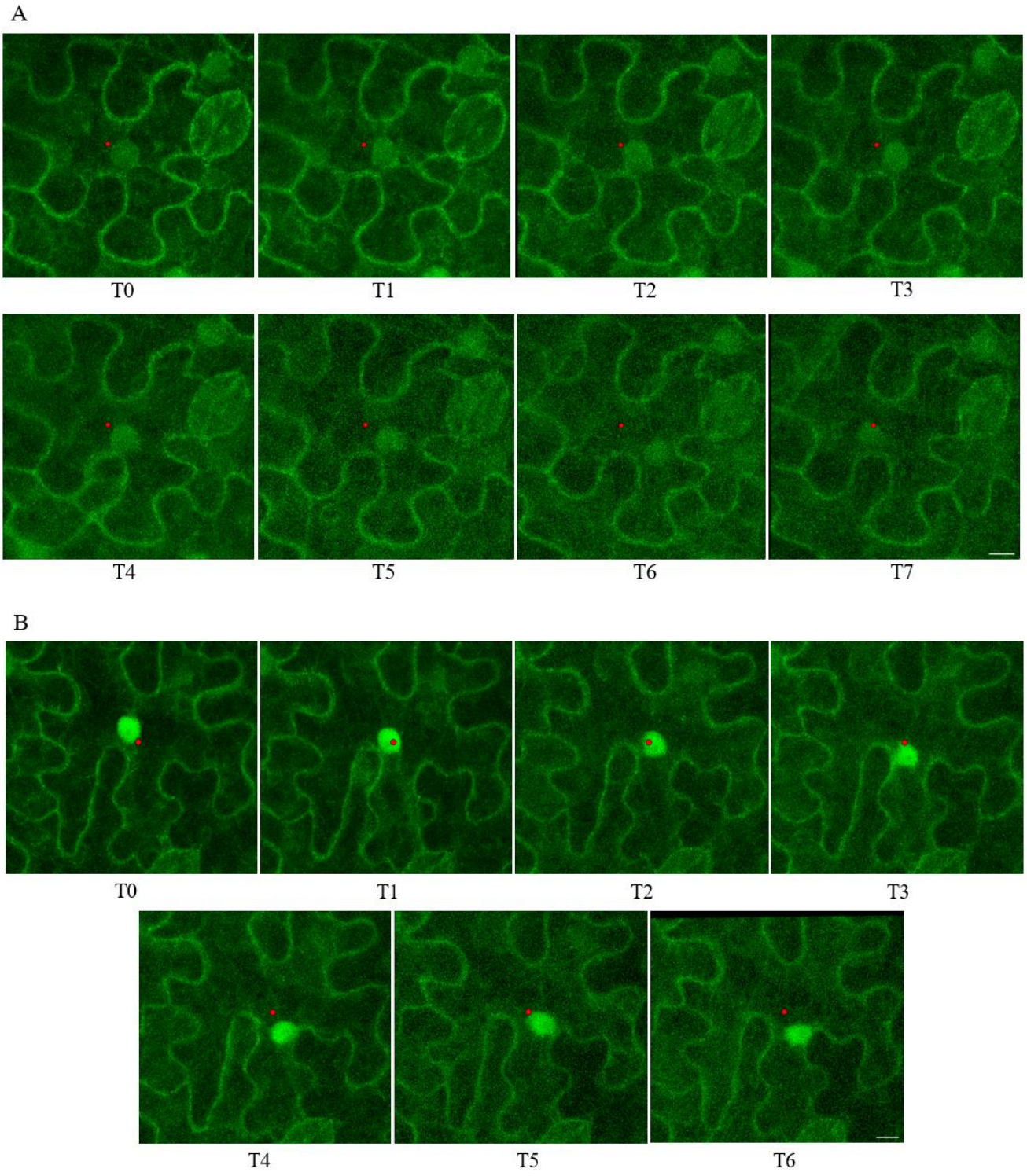

Figure 5 : Timelapse du suivi de la dynamique des noyaux sur une feuille de stade 6 (échelle = 10 µm).
Les noyaux sont visualisés grâce au signal de la protéine rapporteur p35S::AtCYCD3.1-Turquoise2.
Les points rouges représentent le centroïde de la cellule, servant de repères de déplacement.
A et B représentent deux cellules différentes dans une même feuille.
Les points de temps ont été réalisés toutes les heures, de 0 à 6 ou 7h.
Echelle = 10 µm

Une dynamique des noyaux a par contre été observée. Les résultats ont montré que les noyaux avaient effectivement un déplacement, qui, de façon intéressante, se situe toujours entre deux necks. Or on a également vu que les bandes de pré-prophases se localisaient à chaque fois entre deux necks. On pourrait émettre l'hypothèse qu'en effet, les noyaux se déplacent à l'endroit où le plan de division va se mettre en place. Néanmoins, pour la même raison que précédemment, nous ne pouvons conclure à ce sujet, n'ayant pas eu de mitose à la fin des timelapses. Dans un premier temps, il reste cependant à tester si ce mouvement est spécifique de l'activation du cycle cellulaire via l'injection de CYCD3.1. Pour répondre à cette question, il faudra transformer les cellules avec un marquer du noyau qui n'induit pas la division cellulaire et comparer les mouvements du noyau. Ensuite, plusieurs perspectives s'offrent à nous à la suite de ces observations sur la dynamique des noyaux. Premièrement, nous pourrions nous demander ce qui dirige le noyau. En effet, même si aucune étape radiale n'a pu être identifiée, la structuration des microtubules durant l'interphase pourrait être à l'origine du déplacement du noyau. Nous pouvons également nous demander si le déplacement du noyau a un lien avec la règle que la cellule va suivre pour se diviser. Dans des séances d'imageries ultérieures, nous avons proposé d'étudier la position de la nouvelle paroi chez des cellules venant de se diviser. Des analyses seront réalisées afin de regarder si les cellules se divisent en deux volumes égaux, au niveau du centroïde, ou d'une toute autre manière.

Bibliographie

Besson, Sébastien, et Jacques Dumais. 2011. « Universal Rule for the Symmetric Division of Plant Cells ». *Proceedings of the National Academy of Sciences* 108 (15): 6294-99. https://doi.org/10.1073/pnas.1011866108.

Erguvan, Özer, Marion Louveaux, Olivier Hamant, et Stéphane Verger. 2019. « ImageJ SurfCut: A User-Friendly Pipeline for High-Throughput Extraction of Cell Contours from 3D Image Stacks ». *BMC Biology* 17 (1): 38. https://doi.org/10.1186/s12915-019-0657-1.

Errera, L. 1888. *Über Zellformen und Seifenblasen.* Vol. 34: 395–398. German. Botanisches Centralblatt.

Gillespie, Trudi, Petra Boevink, Sophie Haupt, Alison G. Roberts, Rachel Toth, Tracy Valentine, Sean Chapman, et Karl J. Oparka. 2002. « Functional Analysis of a DNA-Shuffled Movement Protein Reveals That Microtubules Are Dispensable for the Cell-to-Cell Movement of *Tobacco Mosaic Virus* ». *The Plant Cell* 14 (6): 1207-22. https://doi.org/10.1105/tpc.002303.

Hamant, Olivier, Daisuke Inoue, David Bouchez, Jacques Dumais, et Eric Mjolsness. 2019. « Are Microtubules Tension Sensors? » *Nature Communications* 10 (1): 2360. https://doi.org/10.1038/s41467-019-10207-y.

Lewis, Frederic T. 1923. « The Typical Shape of Polyhedral Cells in Vegetable Parenchyma and the Restoration of That Shape Following Cell Division ». *Proceedings of the American Academy of Arts and Sciences* 58 (15): 537. https://doi.org/10.2307/20026027.

Louveaux, Marion, Jean-Daniel Julien, Vincent Mirabet, Arezki Boudaoud, et Olivier Hamant. 2016. « Cell Division Plane Orientation Based on Tensile Stress in *Arabidopsis Thaliana* ». *Proceedings of the National Academy of Sciences* 113 (30). https://doi.org/10.1073/pnas.1600677113.

Malivert, Alice, Özer Erguvan, Antoine Chevallier, Antoine Dehem, Rodrigue Friaud, Mengying Liu, Marjolaine Martin, Théophile Peyraud, Olivier Hamant, et Stéphane Verger. 2021. « FERONIA and Microtubules Independently Contribute to Mechanical Integrity in the Arabidopsis Shoot ». Édité par Mark Estelle. *PLOS Biology* 19 (11): e3001454. https://doi.org/10.1371/journal.pbio.3001454.

Rasmussen, Carolyn G., Amanda J. Wright, et Sabine Müller. 2013. « The Role of the Cytoskeleton and Associated Proteins in Determination of the Plant Cell Division Plane ». *The Plant Journal* 75 (2): 258-69. https://doi.org/10.1111/tpj.12177.

Sapala, Aleksandra, Adam Runions, Anne-Lise Routier-Kierzkowska, Mainak Das Gupta, Lilan Hong, Hugo Hofhuis, Stéphane Verger, et al. 2018. « Why Plants Make Puzzle Cells, and How Their Shape Emerges ». *ELife* 7 (février): e32794. https://doi.org/10.7554/eLife.32794.

Schindelin, Johannes, Ignacio Arganda-Carreras, Erwin Frise, Verena Kaynig, Mark Longair, Tobias Pietzsch, Stephan Preibisch, et al. 2012. « Fiji: An Open-Source Platform for Biological-Image Analysis ». *Nature Methods* 9 (7): 676-82. https://doi.org/10.1038/nmeth.2019.

Trinh, Duy-Chi, Juan Alonso-Serra, Mariko Asaoka, Leia Colin, Matthieu Cortes, Alice Malivert, Shogo Takatani, et al. 2021. « How Mechanical Forces Shape Plant Organs ». *Current Biology* 31 (3): R143-59. https://doi.org/10.1016/j.cub.2020.12.001.

Xu, Jie, Yuh-Ru Julie Lee, et Bo Liu. 2020. « Establishment of a Mitotic Model System by Transient Expression of the D-type Cyclin in Differentiated Leaf Cells of Tobacco (*Nicotiana Benthamiana*) ». *New Phytologist* 226 (4): 1213-20. https://doi.org/10.1111/nph.16309.

Annexes

Annexe 1 : Milieu YEB + RGS (antibiotiques)

	For 1 L
Beef extract	5 g/L
Yeast extract	1 g/L
Peptone	5 g/L
Sucrose	5 g/L
NaOH	→ pH 7.2
Agar	14 g/L

Antibiotiques :

- Rifampicine : 50 µg/mL
- Gentamycine : 20 µg/mL
- Spectinomycine : 250 µg/mL

Annexe 2 : Milieu ACM

	For 1 L
MS medium without vitamins (Duschefa)	2,2 g/L
Sucrose	10 g/L
KOH (10M)	→ pH 5,8
H2O	→ 1 L
Agarose (not agar-agar)	8 g/L

Autoclave

Add vitamins and hormones (previously filtered at 22µm under the hood):

When the medium is at 55°C, add 1 mL/L of vitamins (50 mL of milliq water with 5 g myo-inositol; 0,05 g nicotinic acid; 0,05 g pyridonine hydrochloride (vitamin B6); 0,5 g thiamine hydrochloride; 0,1 g glucine)
Also add 555 nM of N6-Benzyladenine (BAP), or 62,5 µL of a 1mg/mL stock solution (first dissolve in a small volume of NaOH 1M, then adjust to the right volume)

Annexe 3 : Script du programme de projection maximale

```
//////Autrice: Isaty MELOGNO/////////////////////////////////////////////////////////////
//////Date: 14 octobre 2022/////////////////////////////////////////////////////////////
//////But du programme: Faire des projections Z maximales en batch//////////////////
//////Entrée: Sélectionner un dossier////////////////////////////////////////////////////
//////Sortie: Sauvegarde les projections dans un dossier nommé "max_proj" à créer///
////////////////////////////////////////////////////////////////////////////////////////


//Choose the directory containing your images//
dir = getDirectory("Choose a directory")
setBatchMode(true);
list = getFileList(dir);

//Treat each image one after the other//
for (FileInd=0; FileInd<list.length; FileInd++){
    FileName = list[FileInd];
    path = dir+FileName;
    newName=replace(FileName, ".tif", "");

        //Open the Z-stack image//
    run("Bio-Formats", "open=["+path+"] color_mode=Default open_all_series rois_import=[ROI manager] view=Hyperstack stack_order=XYCZT use_virtual_stack");
    run("Z Project...", "projection=[Max Intensity]");
    saveAs("Tiff", dir + File.separator + "max_proj" + File.separator + newName + "_MAX_PROJ");
    close();

        print("Done with", FileName,"!");
};
print("Done with this folder!!!");
```

Gauthier Camille
Master Biologie Végétale- Université Claude Bernard, Lyon 1.

Titre : Dynamique des microtubules et du noyau avant la mitose dans les feuilles de *Nicotiana benthamiana*

Résumé :

Des mesures du taux d'expression de *AtCYD3.1* et des observations de structures de mitoses ont permis de déterminer l'efficacité de l'agroinfiltration dans des feuilles différenciées de *Nicotiana benthamiana* et d'optimiser le protocole mis en place pour observer la dynamique des microtubules corticaux avant l'entrée en mitose.

L'orientation des microtubules corticaux avec la construction TUA6-GFP a pu être observée durant les premières heures d'imagerie mais n'a pas permis de mettre en évidence une structure radiale précédent la formation de la bande de pré-prophase.

Parallèlement, le signal *AtCYCD3.1*-Turquoise2 a permis de visualiser la dynamique des positionnements des noyaux au sein des cellules épidermiques. Cette dynamique n'a pu être mise en lien avec la localisation de la bande de pré-prophase par la suite mais elle a pu être quantifiée de manière plus précise au vu de ce système.

Mots-clés : *mitoses, agroinfiltration, microtubules corticaux, imagerie, bande de pré-prophase, dynamique*

Laboratoire d'accueil : UMR 5667 Laboratoire de Reproduction et Développement des Plantes.
Equipe Mécanotransduction et Développement

Maître de stage : Christophe TREHIN
Encadrante : Isaty MELOGNO

PNAS RESEARCH ARTICLE | PLANT BIOLOGY

A transient radial cortical microtubule array primes cell division in *Arabidopsis*

Isaty Melogno[a,1], Shogo Takatani[a,b,1], Paula Llanos[c], Coralie Goncalves[d], Chie Kodera[d], Marjolaine Martin[a], Claire Lionnet[a], Magalie Uyttewaal[d], Martine Pastuglia[d], Christophe Trehin[a], David Bouchez[d], Jacques Dumais[c], and Olivier Hamant[a,2]

Edited by Dominique Bergmann, Stanford University, Stanford, CA; received November 21, 2023; accepted May 23, 2024

Although the formation of new walls during plant cell division tends to follow maximal tensile stress direction, analyses of individual cells over time reveal a much more variable behavior. The origin of such variability as well as the exact role of interphasic microtubule behavior before cell division have remained mysterious so far. To approach this question, we took advantage of the *Arabidopsis* stem, where the tensile stress pattern is both highly anisotropic and stable. Although cortical microtubules (CMTs) generally align with maximal tensile stress, we detected a specific time window, ca. 3 h before cell division, where cells form a radial pattern of CMTs. This microtubule array organization preceded preprophase band (PPB) formation, a transient CMT array predicting the position of the future division plane. It was observed under different growth conditions and was not related to cell geometry or polar auxin transport. Interestingly, this cortical radial pattern correlated with the well-documented increase of cytoplasmic microtubule accumulation before cell division. This radial organization was prolonged in cells of the *trm678* mutant, where CMTs are unable to form a PPB. Whereas division plane orientation in *trm678* is noisier, we found that cell division symmetry was in contrast less variable between daughter cells. We propose that this "radial step" reflects a trade-off in robustness for two essential cell division attributes: symmetry and orientation. This involves a "reset" stage in G2, where an increased cytoplasmic microtubule accumulation transiently disrupts CMT alignment with tissue stress.

cell division | microtubules | mechanical stress | cell geometry | robustness

Significance

In all kingdoms of life, cells divide according to their own geometry as well as external cues. We identified a transient stage in plant cells, where part of the division machinery becomes blind to mechanical forces originating from the tissue. Using quantitative imaging and mutant analysis, we propose that this premitotic stage allows cells to take their own geometry into account and increase the precision of the ensuing division.

Cell division is first and foremost a geometric question: cells generally divide along a given division plane orientation, and more or less symmetrically, as defined by the relative volume of the resulting daughter cells. How mitosis operates is now well described in all kingdoms (1). However, we lack a clear understanding of how the cell division machinery achieves precision (i.e., reducing the variance in symmetric division) despite broad variation in cell shapes and division rates.

In *Drosophila* epithelia, cell division symmetry does not occur by default, but instead involves an active process. A "reset" stage is observed, where cells become round. This premitotic cell rounding has been proposed to allow cells to identify their centroid, thus triggering more symmetric divisions, independently of extracellular cues (2). Conversely, disruption of cell rounding in myosin motor mutants puts more weight on premitotic cell geometry, through the maintenance of cell packing, thus biasing division plane orientation (3). Whether this also affects the precision of cell division symmetry remains unknown.

In plants, the presence of stiff cell walls mechanically prevents any cell deformation before mitosis. However, in late G2, the periphery of plant cells becomes largely depopulated of cortical microtubules (CMTs), and a dense ring forms, named the preprophase band (PPB). This transient premitotic structure precisely predicts the position of the future division plane, established at cytokinesis. Since its discovery, the PPB was thought to be an essential attribute of cell division in most plant tissues (4), until specific PPB-less mutants were obtained and shown to have only mild developmental defects, at least under controlled conditions (5, 6). Furthermore, the PPB contributes to the robustness of division plane orientation, independently of division symmetry (in the geometrical sense), since both symmetrically and asymmetrically dividing cells produce a PPB. Strongly asymmetric divisions, as in meristemoid cells, involve polarity cues that are inherited from interphase (7). However, this does not apply to most plant tissues, where cells divide symmetrically. How plant cells control the symmetry of division and its robustness is mostly unknown.

During interphase, the parallel alignment of CMTs has been shown to regulate the deposition of cellulose microfibrils in the wall (8). With few exceptions, the PPB, formed in G2 prior to mitosis, adopts the same orientation as the former interphasic cortical array (9). In addition, CMTs have also been found to align with maximal tensile stress in

Author affiliations: [a]Laboratoire de Reproduction et Développement des Plantes, Université de Lyon, Ecole Normale Supérieure de Lyon, Université Claude Bernard Lyon 1, Institut national de recherche pour l'agriculture, l'alimentation et l'environnement (INRAE), CNRS, 69364 Lyon Cedex 07, France; [b]Department of Biological Science, Graduate School of Science, Nagoya University, Nagoya 464-8602, Japan; [c]Faculty of Engineering and Sciences, Universidad Adolfo Ibáñez, Viña del Mar 2520000, Chile; and [d]Université Paris-Saclay, INRAE, AgroParisTech, Institute Jean-Pierre Bourgin for Plant Sciences (IJPB), Versailles 78000, France

Author contributions: I.M., S.T., C.T., J.D., and O.H. designed research; I.M., S.T., C.G., C.K., M.M., and M.U. performed research; I.M., S.T., P.L., C.L., M.P., C.T., and D.B. contributed new reagents/analytic tools; I.M., S.T., and C.L. analyzed data; M.P., C.T., J.D., and D.B. supervision; O.H. supervision and funding acquisition; and I.M., S.T., C.T., and O.H. wrote the paper.

The authors declare no competing interest.

This article is a PNAS Direct Submission.

[1]I.M. and S.T. contributed equally to this work.

[2]To whom correspondence may be addressed. Email: olivier.hamant@ens-lyon.fr.

This article contains supporting information online at https://www.pnas.org/lookup/suppl/doi:10.1073/pnas.2320470121/-/DCSupplemental.

Published July 11, 2024.

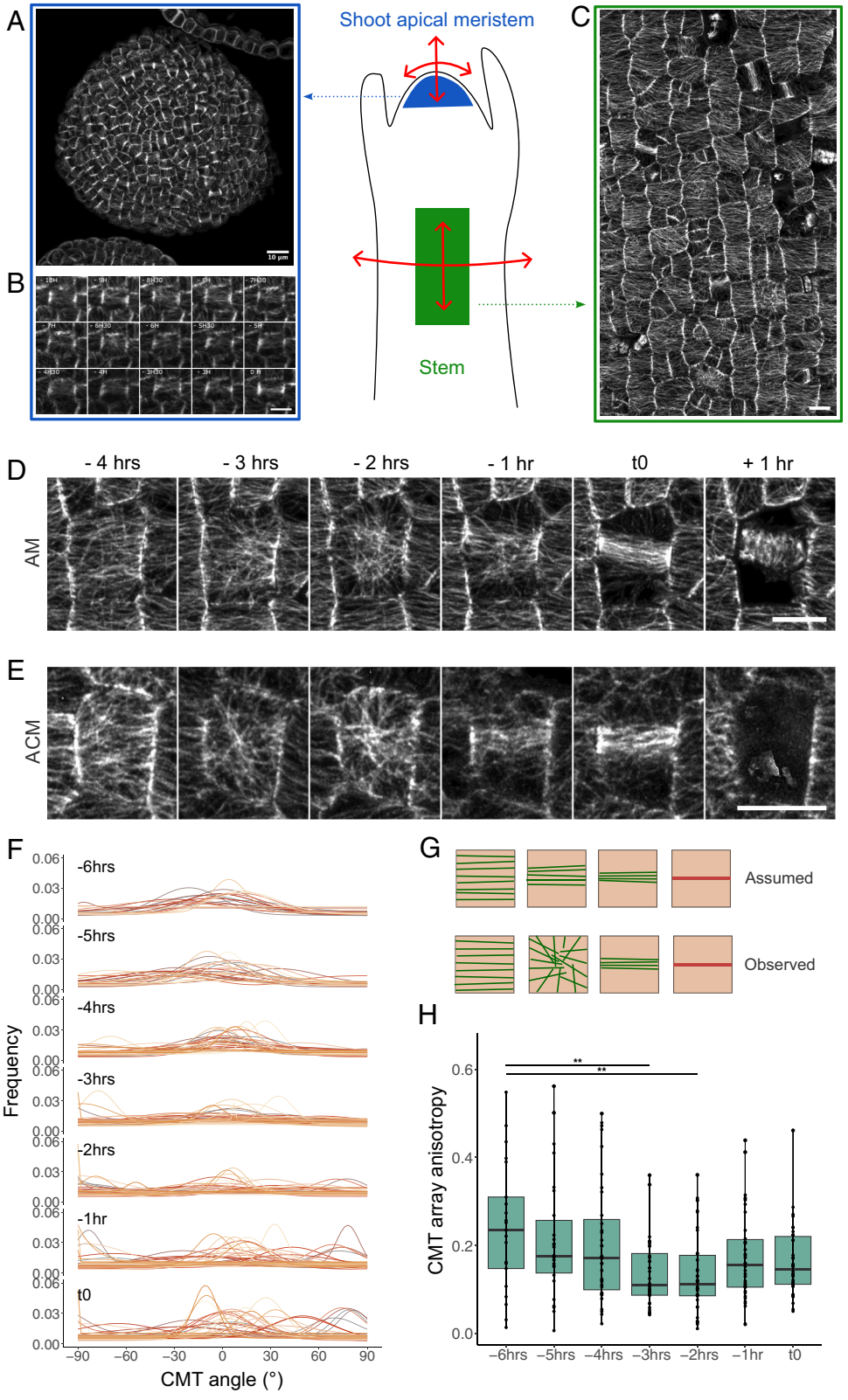

Fig. 1. A transient pre-PPB radial pattern of CMTs in the meristem and the stem. (*A*) Top view of the SAM expressing the *pPDF1::mCitrine-MBD* marker. Red arrows indicate a predicted isotropic tensile stress pattern in the central zone. (*B*) Time-lapse of a premitotic cell of the SAM, showing the CMT dynamics before the formation of the PPB, using the *pPDF1::mCitrine-MBD* marker line. CMT organization changes from coaligned arrays (−10 h to −7 h 30) to radial arrays (−7 h to −6 h) before the start of PPB maturation. (*C*) Side view of the stem expressing the *pPDF1::mCitrine-MBD* marker. Red arrows indicate the transverse direction of maximal tensile stress, as demonstrated in ref. 17. (*D* and *E*) Time lapse of premitotic cells in the stem, showing CMT dynamics before PPB formation, using the *pPDF1::mCitrine-MBD* marker line on the growth medium (AM, *D*) and cytokinin-supplemented medium (ACM, *E*). Note the presence of radial CMTs ca. 3 h before cell division. (*F*) Distribution of CMT orientations overtime in cells from the stem. The angle scale varies between −90° and +90°, 0° being the transverse orientation to the stem axis. Each row represents the time before t = 0 (last timepoint before the nuclear envelope breakdown). Each color-coded curve represents the results obtained for one cell. $n_{-6\,h}$ = 20; $n_{-5\,h}$ = 25; $n_{-4\,h}$ = 34; $n_{-3\,h}$ = 35; $n_{-2\,h}$ = 37; $n_{-1\,h}$ = 37; n_{t0} = 37. (*G*) Schematic summary of the transition between the aligned, interphasic CMT array and the PPB array. The *Top* panel illustrates the simplest scenario, and the *Bottom* panel recapitulates the observations made with the time-lapse experiments. (*H*) Graphical representation of the evolution of the anisotropy values obtained with FibrilTool overtime (**P*-value < 0.01, Tukey test). $n_{-6\,h}$ = 21; $n_{-5\,h}$ = 26; $n_{-4\,h}$ = 35; $n_{-3\,h}$ = 36; $n_{-2\,h}$ = 38; $n_{-1\,h}$ = 38; n_{t0} = 39. The cells used for analysis in (*G* and *H*) were from stems imaged on either AM or ACM media. For all images in this figure, SurfCut projections were used, projecting the mCitrine signal between 0 and 4 μm from the surface. The Brightness & Contrast parameters have been modified for a better visualization of CMTs. [Scale bars, 10 μm (*A* and *C*); 5 μm (*B*, *D*, and *E*).]

different organs and under different experimental conditions (10). Because of the coalignment between interphasic CMTs, PPB, and division plane over time, division planes are also often aligned with maximal tensile stress (11). This provides a scenario in which plant cells and tissues would resist tensile stress, through cellulose-dependent wall reinforcement during interphase and new cell wall formation at mitosis, all parallel to maximal tensile stress orientation.

However, this scenario suffers from a number of empirical and conceptual issues. In particular, CMTs are not always coaligned during interphase. For instance, basket/star configurations have been reported in hypocotyl cells (12). Besides, CMT array orientation is not necessarily homogeneous within a cell, and can change over time, for instance displaying global rotations (13), consistent with cellulose deposition dynamics too (14). Whether such behaviors can be reconciled with a response

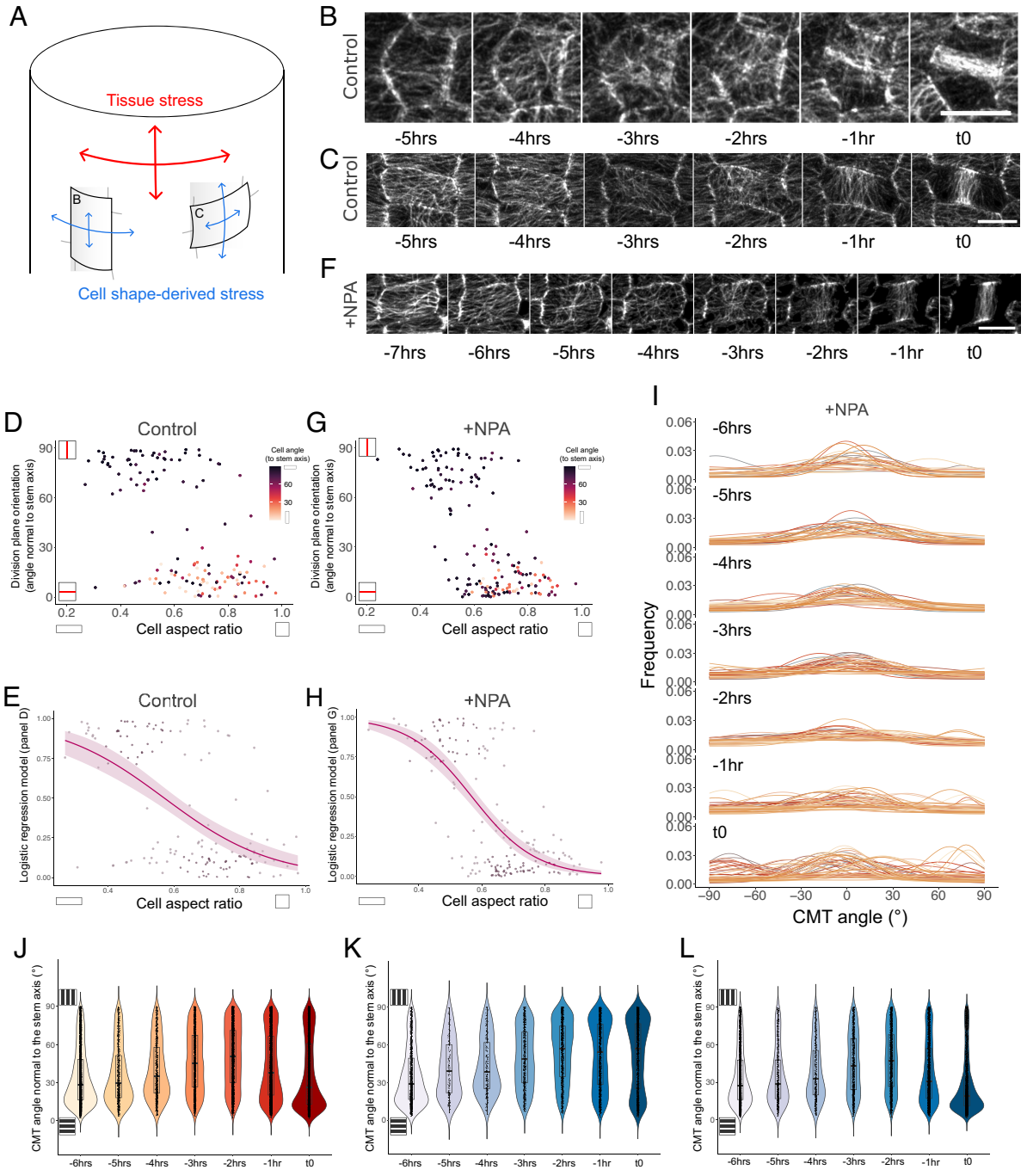

Fig. 2. The radial step occurs independently of cell shape or polar auxin transport. (*A*) Diagram representing the predicted tensile stress patterns for epidermal cells in stems. The cylindrical shape of the stem prescribes maximal tensile stress transverse to the stem axis. At cell scale, the minor axis of the cell is also the predicted tensile stress maximal direction. Depending on cell orientation, tissue stress and cell shape-derived stress are synergistic or antagonistic (*B*) Representative example of a cell expressing the *pPDF1::mCitrine-MBD* marker, with its major axis parallel to the stem axis. The cell forms a radial CMT organization before dividing perpendicular to the stem axis. (*C*) Representative example of a cell expressing the *pPDF1::mCitrine-MBD* marker, with its major axis perpendicular to the stem axis. The cell forms a radial CMT organization before dividing parallel to the stem axis. (*D*) Dotplot representing the orientation relative to the stem of the PPB or division planes of cells, in the stem in function of their aspect ratio (the ratio between the longest and the shortest axis of an ellipse fitted around the cell contours). The color code reflects the angle between the major axis of the cell and the stem axis. Light colors highlight cells with their longest axis along the stem axis, dark colors highlight cells with their longest axis transverse to the stem axis. (*E*) Same as (*D*), with normalized the data to fit a logistic regression (scale 0 to 1), using the glm function in R studio (R^2 = 0.312). (*D* and *E*) *n* = 141. (*F*) Time lapse showing premiotic cells in the stem expressing the *pPDF1::mCitrine-MBD* marker, with NPA from germination. (*G*) Same as (*D*), with NPA from germination. (*H*) Same as (*E*), with NPA from germination (R^2 = 0.457). (*G* and *H*) n = 166. (*I*) Same as Fig. 1*D*, with NPA from germination. $n_{-6\,h}$ = 29; $n_{-5\,h}$ = 30; $n_{-4\,h}$ = 41; $n_{-3\,h}$ = 45; $n_{-2\,h}$ = 45; $n_{-1\,h}$ = 47; n_{t0} = 58. (*J*) Distribution of CMT angles normal to the stem axis overtime from NPA-treated plants using the OrientationJ-vector field function in Fiji. $n_{-6\,h}$ = 159; $n_{-5\,h}$ = 50; $n_{-4\,h}$ = 47; $n_{-3\,h}$ = 107; $n_{-2\,h}$ = 165; $n_{-1\,h}$ = 228; n_{t0} = 244. *P*-values from the result of a Kolmogorov–Smirnov statistical test comparing the distribution of the data to a uniform distribution: $P_{-6\,h} < 2.2e^{-16}$; $P_{-5\,h} < 2.2e^{-16}$; $P_{-4\,h} = 2e^{-10}$; $P_{-3\,h} = 1e^{-05}$; $P_{-2\,h} = 4e^{-09}$; $P_{-1\,h} = 3e^{-14}$; $P_{t0} < 2.2e^{-16}$. (*K*) same as (*J*) but for cells with an aspect ratio below 0.6 (most elongated cells). $n_{-6\,h}$ = 63; $n_{-5\,h}$ = 15; $n_{-4\,h}$ = 19; $n_{-3\,h}$ = 45; $n_{-2\,h}$ = 73; $n_{-1\,h}$ = 93; n_{t0} = 101. *P*-values from the result of a Kolmogorov–Smirnov statistical test comparing the distribution of the data to a uniform distribution: $P_{-6\,h} < 2.2e^{-16}$; $P_{-5\,h} = 3e^{-02}$; $P_{-4\,h} = 1e^{-02}$; $P_{-3\,h} = 2e^{-04}$; $P_{-2\,h} = 2e^{-11}$; $P_{-1\,h} = 1e^{-09}$; $P_{t0} = 2e^{-13}$. (*L*) same as (*J*) but for cells with an aspect ratio above 0.6 (most isodiametric cells). $n_{-6\,h}$ = 96; $n_{-5\,h}$ = 35; $n_{-4\,h}$ = 28; $n_{-3\,h}$ = 62; $n_{-2\,h}$ = 92; $n_{-1\,h}$ = 135; n_{t0} = 143. *P*-values from the result of a Kolmogorov–Smirnov statistical test comparing the distribution of the data to a uniform distribution: $P_{-6\,h} < 2.2e^{-16}$; $P_{-5\,h} < 2.2e^{-16}$; $P_{-4\,h} = 2e^{-09}$; $P_{-3\,h} = 6e^{-03}$; $P_{-2\,h} = 8e^{-05}$; $P_{-1\,h} < 2.2e^{-16}$; $P_{t0} < 2.2e^{-16}$. The cells used for analysis in (*D* and *E*) were from stems imaged on either AM or ACM media. The cells used for analysis in (*G*–*L*) were from stems imaged on ACM medium supplemented with NPA. All images are SurfCut projections between 0 to 4 μm from the surface of the mCitrine signal. (Scale bar, 5 μm.)

to tensile stress and the control of cell division remains to be investigated.

Here, using the *Arabidopsis* stem as a model system, and taking advantage of its stereotypical tissue stress pattern, we identified a transient radial CMT organization that appears prior to PPB formation, and that diverges from alignment with tissue stress. We propose that this stage is analogous to the mitotic cell rounding step in *Drosophila* epithelia where, in preparation to mitosis, cells sense their own geometry rather than tissue-related cues.

Results

A Stereotypical Radial CMT Organization Before Cell Division. To observe CMTs in dividing cells over time, we used plant lines expressing the MAP4 microtubule-binding domain (MBD) fused to mCitrine and focused our analysis on dissected shoot apices, as previously described (15), but here with higher spatial and temporal resolution (*Materials and Methods*).

In the Shoot Apical Meristem (SAM), as previously reported, we typically observed CMT alignment at the tissue scale, with a bias toward circumferential direction in the organogenetic (peripheral) zone, whereas no particular bias was observed in the central zone (Fig. 1*A*) (16). However, when considering individual cells over time, CMT behavior appeared much more variable. In particular, before cell division, we often observed cells with radial CMT orientations, as viewed from the top (Fig. 1*B* and *SI Appendix*, Fig. S1 *A* and *B*).

To explore this further, we needed higher spatial resolution. This led us to analyze this behavior in the stem from in vitro-grown plants. We focused on the stem region immediately below the SAM, a region of active cell division, where cells are two- to three-fold larger (Fig. 1*C*). Using cell–cell adhesion mutants, we previously demonstrated that the *Arabidopsis* stem exhibits a stereotypical and stable tensile stress pattern, with a maximum in the transverse orientation (17). In this tissue, we confirmed the presence of a strong and global bias of CMTs, toward the circumferential orientation (*SI Appendix*, Fig. S2), parallel to the predicted maximal tensile stress (Fig. 1*C*) (17). Again, when analyzing individual cells over time, we consistently observed a switch from the interphasic alignment of the MT array to a radial array before the formation of the PPB (Fig. 1*D*). In order to increase the number of observable dividing cells, we analyzed cell division in stems from plants grown in vitro on cytokinin-supplemented medium (ACM medium). This readily increased the number of dividing cells imaged in time-lapses: we observed 24 dividing cells on two independent stems on ACM medium, vs. 13 dividing cells on four independent stems on the growth *Arabidopsis* medium (AM). A transient radial CMT behavior could be observed in all cases (Fig. 1*E*). Note that this result was also confirmed when using a *pUBQ10::RFP-TUA6* marker line, albeit with lower spatial resolution (*SI Appendix*, Fig. S3*A*). From five time-lapse experiments with a time resolution of 1 h, we estimated that this behavior preferentially occurred around 3 h before cell division, lasts for about 2 h, and is followed by the formation of the PPB (Fig. 1*D*).

To go beyond these qualitative observations, we measured the distribution of orientations of the CMT arrays using the Directionality plugin in ImageJ for each time-lapse experiment. In all quantifications, time 0 corresponds to the closest timepoint preceding nuclear envelope breakdown, as inferred from the disruption of the PPB, and the initiation of the mitotic spindle. As expected, at t = −4 h, we found a bias toward the transverse orientation (−2.8° at −4 h; 1st quartile = −10.6°, 3rd quartile = 12.1°), which corresponds to the transverse axis of the stem (also the predicted maximal tensile stress direction) (Fig. 1*F*, n = 34 cells). From 1 h before t = 0 up to PPB formation, CMT arrays also exhibited an orientation bias, reflecting the PPB orientation (Fig. 1*F*, n = 37 cells). However, 3 to 2 h before t = 0, the bias was much weaker (−11.9° at −3 h; 1st quartile = −65.7°, 3rd quartile = 20.2°; −23.6° at −2 h; 1st quartile = −90°, 3rd quartile = 5.1°) (Fig. 1*F*, n = 35 cells). To assess the statistical differences between CMT orientation distribution at each timepoints, we performed Kolmogorov–Smirnov tests. We found differences to be statistically significant between −2 or −3 h and earlier timepoints, meaning that the radial array of CMTs appears significantly different from previous interphasic CMT coalignments (*SI Appendix*, Fig. S4). As a negative control, we also found no statistical differences between the distributions at −6 h and −5 h, or between the distributions at −3 h and −2 h, at a threshold of 0.05 (*SI Appendix*, Fig. S4).

To confirm this observation, we used the FibrilTool plugin in ImageJ (18) to quantify the anisotropy of the CMT arrays in each cell and analyzed the anisotropy distribution per time point (*SI Appendix*, Fig. S3*B*). This analysis revealed a drop in the anisotropy value 2 to 3 h before t = 0 (Fig. 1*H*, n = 36 cells). Anisotropy then increased again from 1 h before t = 0 up to PPB maturation (Fig. 1*H*, n = 38 cells). Based on these quantifications, we established that, in the stem, the radial array starts ca. 3 h before the PPB formation and lasts for ca. 2 h until the start of the PPB maturation. This finding thus challenges the often-assumed continuity between interphasic CMTs and PPB (Fig. 1*G*). We propose to call this stage where CMTs form a radial pattern 3 h before cell division, the "radial step."

The Radial Step Can be Uncoupled from Cell Shape and Final Division Plane Orientation. To assess whether the radial step relates to cell division plane orientation, we analyzed its behavior in cells of different shapes. In stem tissues, isodiametric cells tend to divide perpendicular to the stem axis (Fig. 2*B*), whereas elongated cells tend to divide along the shortest plane (Fig. 2*C*). Such difference could be related to cellular stress patterns, as inferred from the curvature of the outer wall: the shape of elongated cells prescribes transverse derived maximal tensile stress direction (Fig. 2*A*), whereas the shape of isodiametric cells prescribes isotropic tensile stress direction (11). Note that in contrast to the tensile stress pattern in the stem, which was experimentally validated (17), this cell-shape-derived stress pattern is only predicted from a pressure vessel model of an epidermal cell (11, 19). We thus explored whether the radial step may depend on differences in cell shape and/or related stress pattern.

To monitor this quantitatively, we calculated the cell aspect-ratio and plotted cell division orientation with respect to the stem axis, using either the PPB as a predictor of the future division plane, or the plasma membrane resulting from a division (Fig. 2*D*, n = 141 cells). This confirmed a dual behavior according to cell aspect ratio, at least for cells with an extreme aspect ratio. In particular, more isodiametric cells tend to display division planes perpendicular to the stem axis (i.e., parallel to predicted maximal tissue stress); whereas more elongated cells displayed division planes rather parallel to the stem axis (i.e., perpendicular to maximal tissue stress) (Fig. 2*D*). In order to find the threshold value at which cells switch their behavior, we fitted a logistic regression using the binomial method of the generalized linear models in R (with a *P*-value of $3.40e^{-11}$). This method only partially fit the data (R^2 = 0.312), due to the bimodal distribution of division plane orientations and noise in division orientation in either group, but allowed us to successfully retrieve an inflection point at 0.6 (Fig. 2*E*; *Materials and Methods*). To monitor the orientation of division relative to the cell axis, we measured the orientation of the long axis of the cell relative to the axis of the stem. These measurements revealed that most anisotropically shaped cells were

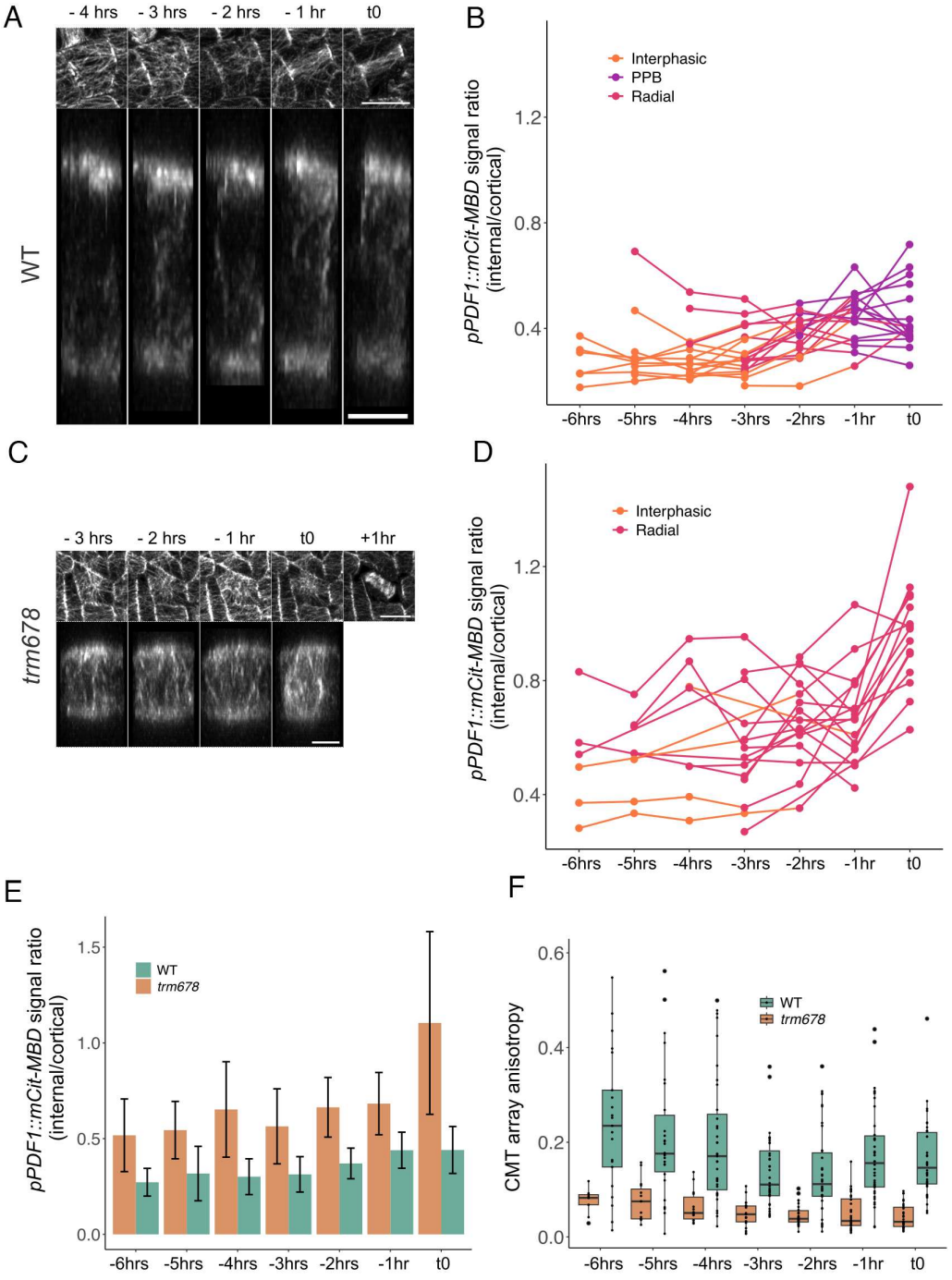

Fig. 3. The radial array of CMTs correlates with a premitotic increase of internal microtubule content. (*A*–*D*) Evolution of cytoplasmic microtubules overtime in WT background (*A*) or in the *trm678* mutant background (*C*). (*A*) Time-lapse images of premitotic cells, the *Top* panel being the cortical projection with SurfCut and the *Bottom* panel an orthogonal projection through the cell. Cortex images are 8-bit, with the B&C range varying between 0 and 160, and orthogonal projections are 16-bit, with the B&C range varying between 0 and 1,400. (*B*) Ratio between the average internal signal and the average of the cortical mCitrine-MBD signal over time. The colors correspond to qualitative classifications of cortical arrays (interphasic, radial step, and PPB). Each line represents the kinetics for a given cell. $n_{WT,\ -6\ h} = 6$; $n_{WT,\ -5\ h} = 11$; $n_{WT,\ -4\ h} = 16$; $n_{WT,\ -3\ h} = 17$; $n_{WT,\ -2\ h} = 17$; $n_{WT,\ -1\ h} = 17$; $n_{WT,\ t0} = 17$. (*C*) same as (*A*) but in the *trm678* mutant. (*D*) same as (*B*) but in the *trm678* mutant. $n_{trm678,\ -6\ h} = 6$; $n_{trm678,\ -5\ h} = 7$; $n_{trm678,\ -4\ h} = 7$; $n_{trm678,\ -3\ h} = 14$; $n_{trm678,\ -2\ h} = 15$; $n_{trm678,\ -1\ h} = 17$; $n_{trm678,\ t0} = 19$. (*E*) Evolution of the ratio of mCitrine-MBD signal (internal/cortical) overtime in WT vs. *trm678*. (*F*) Evolution of CMT array anisotropy overtime, using the FibrilTool plugin in Fiji. Results from the WT are reproduced here from Fig. 1*H* for ease of reading, to compare with *trm678*. $n_{trm678,\ -6\ h} = 9$; $n_{trm678,\ -5\ h} = 15$; $n_{trm678,\ -4\ h} = 14$; $n_{trm678,\ -3\ h} = 21$; $n_{trm678,\ -2\ h} = 26$; $n_{trm678,\ -1\ h} = 28$; $n_{trm678,\ t0} = 29$. The cells used for analysis in (*B* and *D*–*F*) were from stems imaged on either AM or ACM media. [Scale bars, 10 µm (surface projections) and 5 µm (orthogonal projections).]

elongated transversely to the stem ("C cell" in Fig. 2*A*; see cell angle color code in Fig. 2*D*), implying that their shortest axis, and thus the maximal tension derived from the cell shape, was orthogonal to the tissue-derived maximal tensile stress. Taking advantage of this dual behavior according to cell shape, we could confirm that in the stem, cells with an aspect ratio below 0.6 tend to divide following cell-shape-derived tension, respecting the local minima rule (20). The ones with an aspect ratio above 0.6 (rounder cells) tend to divide following the tissue-derived maximal tensile stress, that is perpendicular to the stem axis.

Even though the conflict between maximal tension orientations derived from the cell shape or the tissue may affect the positioning

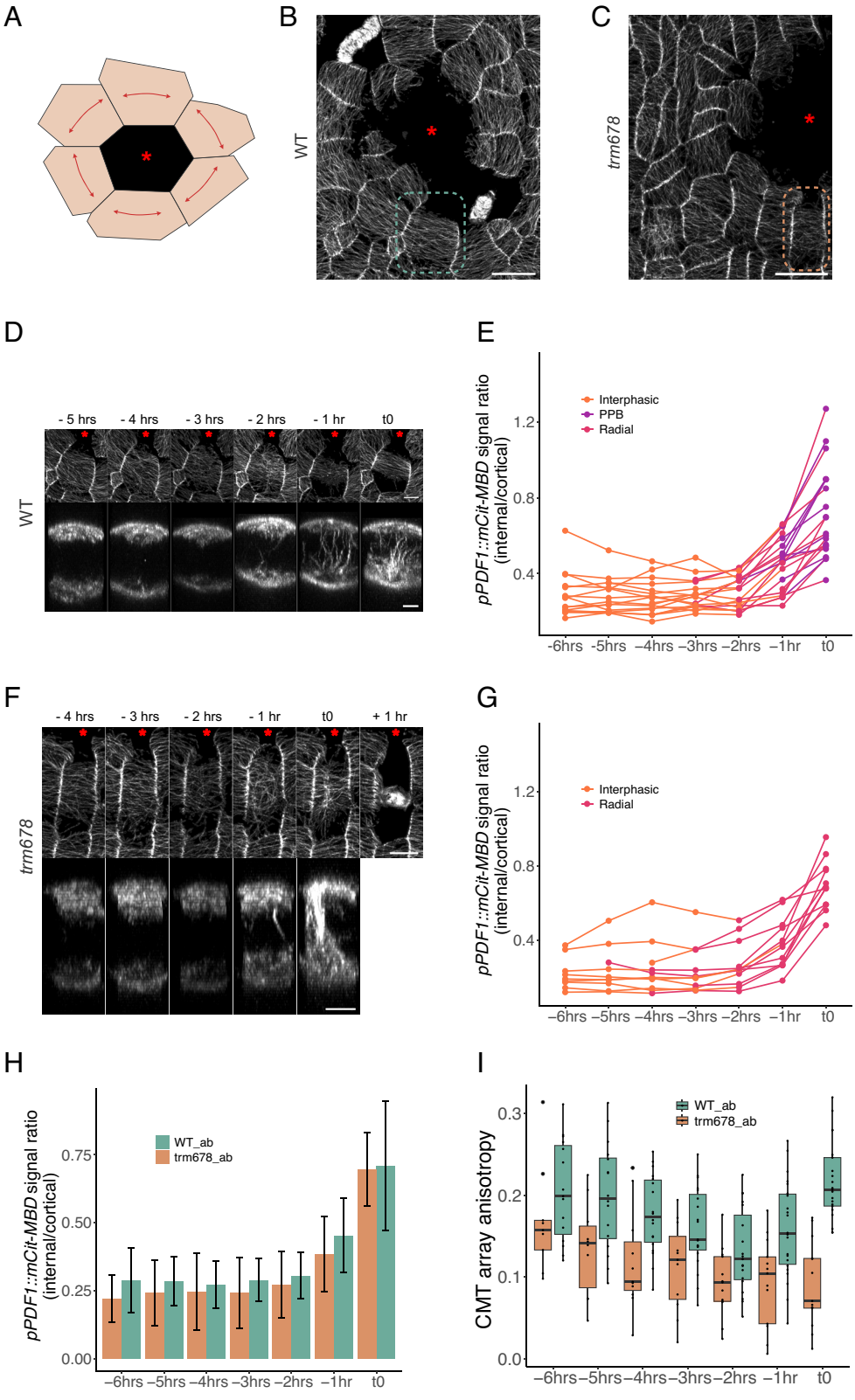

Fig. 4. The radial array of CMTs still occurs after modifying the mechanical environment of the cell. (*A*) Schematic representation of the tensile stress pattern after a local ablation (red star) in an epidermis under tension. The predicted stress is circumferential around the ablation and overrides the global tensile stress prescribed by the tissue. (*B*) Close-up of an ablation site in a WT stem expressing the *pPDF1::mCitrine-MBD* marker. Note the circumferential alignment of CMTs around the ablation site, following the predicted maximal tensile stress pattern. The image is the cortical projection obtained with SurfCut. (*C*) Same as (*B*) in the *trm678* mutant. (*D*) Time-lapse images of premitotic cells around an ablation, the *Top* panel being the cortical projection with SurfCut and the *Bottom* panel an orthogonal projection through the cell. Cortex images are 8-bit, with the B&C range varying between 0 and 80, and orthogonal projections are 8-bit, with the B&C range varying between 0 and 50. (*E*) Ratio between the average internal signal and the average of the cortical mCitrine-MBD signal over time. The colors correspond to qualitative classifications of cortical arrays (interphasic, radial step, and PPB). Each line represents the kinetics for a given cell. $n_{WT,\ -6\,h}$ = 15; $n_{WT,\ -5\,h}$ = 16; $n_{WT,\ -4\,h}$ = 18; $n_{WT,\ -3\,h}$ = 19; $n_{WT,\ -2\,h}$ = 19; $n_{WT,\ -1\,h}$ = 21; $n_{WT,\ t0}$ = 21. (*F*) Same as (*D*) but in *trm678* mutant cells around an ablation site. (*G*) Same as (*E*) but in *trm678* mutant cells around an ablation site. $n_{trm678,\ -6\,h}$ = 9; $n_{trm678,\ -5\,h}$ = 10; $n_{trm678,\ -4\,h}$ = 11; $n_{trm678,\ -3\,h}$ = 11; $n_{trm678,\ -2\,h}$ = 12; $n_{trm678,\ -1\,h}$ = 12; $n_{trm678,\ t0}$ = 12. (*H*) Evolution of the ratio of mCitrine-MBD signal (internal/cortical) overtime in WT vs. *trm678*, around ablations. (*I*) Evolution of CMT array anisotropy overtime, using the FibrilTool plugin in Fiji, in WT vs. *trm678*, around ablations. $n_{WT,\ -6\,h}$ = 15; $n_{WT,\ -5\,h}$ = 16; $n_{WT,\ -4\,h}$ = 18; $n_{WT,\ -3\,h}$ = 19; $n_{WT,\ -2\,h}$ = 19; $n_{WT,\ -1\,h}$ = 22; $n_{WT,\ t0}$ = 22; $n_{trm678,\ -6\,h}$ = 9; $n_{trm678,\ -5\,h}$ = 10; $n_{trm678,\ -4\,h}$ = 11; $n_{trm678,\ -3\,h}$ = 11; $n_{trm678,\ -2\,h}$ = 13; $n_{trm678,\ -1\,h}$ = 13; $n_{trm678,\ t0}$ = 13. The cells used for analysis in (*E* and *G*–*I*) were from stems imaged on either AM or ACM media. [Scale bars, 20 μm (*B* and *C*), 10 μm (*D* and *F*, surface projections), and 5 μm (*D* and *F*, orthogonal projections).]

of the division plane, the radial step was comparable in both types of cells, whether these were elongated (Fig. 2*B*) or not (Fig. 2*C*). We also confirmed this quantitatively with the Directionality measurements, by creating two data subsets: one for cells with a PPB oriented along the stem axis and the other for cells with a PPB perpendicular to the stem axis. In both cases, the CMT array underwent the radial step (*SI Appendix*, Fig. S5 *A* and *B*). To further confirm that the radial step appears independently of the final division plane orientation, we observed asymmetrically dividing cells in stems, and we could find a radial step again around 3 h before cell division (*SI Appendix*, Fig. S3 *C* and *D*).

The Radial Step Can be Uncoupled from Polar Auxin Transport. Our analysis so far shows that the radial step is independent of cell shape variability. Next, we investigated whether the radial step depends on larger polarizing cues. To do so, we impaired polar

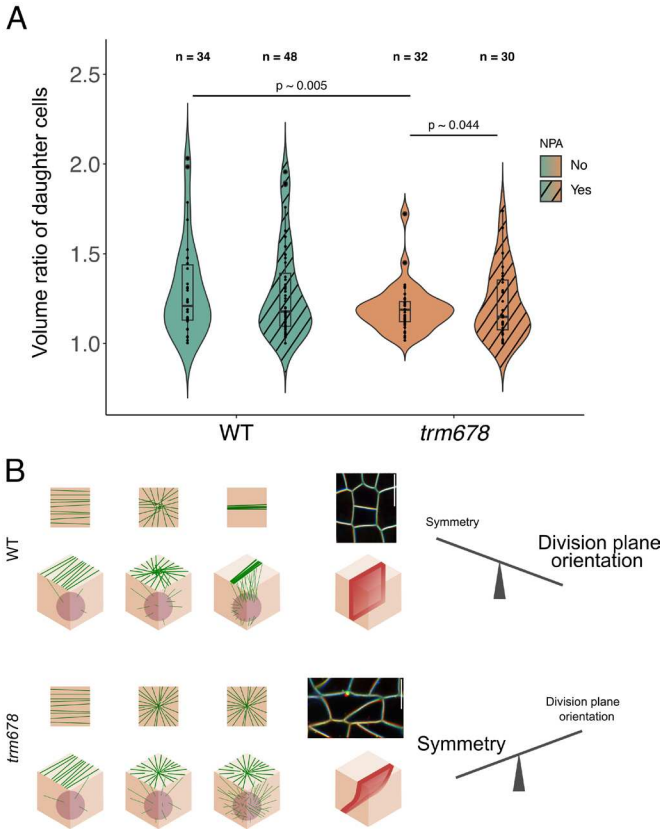

Fig. 5. A model: the radial step could contribute to the predictability of cell division symmetry. (*A*) Violin plot showing the distribution of the ratio between the volume of the two daughter cells in WT and *trm678* backgrounds, in both control and NPA conditions. The measurements were made using images from cells expressing *pUBQ10::Lti6b-TdTomato* membrane marker. The ratio is always calculated between the larger daughter cell and the smaller daughter cell. The *p*-values displayed are the ones obtained from the Fligner's statistical test using R studio. (*B*) Model: in the WT (*Top* panel), a suboptimal radial step allows the cell to sense its own geometry to define cell division symmetry loosely, while the formation of the PPB defines robust division plane orientation; in the *trm678* mutant (*Bottom* panel), a better-defined radial step improves the division precision (daughter cell volumes), to the detriment of division plane orientation robustness. Radial step and PPB reflect a trade-off in robustness (division precision vs. division plane orientation, respectively). Images: RGB projection of recently divided cells at different focal planes (red: top of the cell, green: middle of the cell, blue: bottom of the cell) in the WT (top cell) and *trm678* (bottom cell). (Scale bar, 10 µm.)

auxin transport using naphthylphthalamic acid (NPA), as auxin has previously been shown to affect cell division rate in roots (21) and plane orientation in embryos (22). We grew plants on NPA-containing medium and, using the same *pPDF1::mCitrine-MBD* marker line, we observed the effect of NPA on CMT organization in stems. Note that the inhibition of flower formation on stems vastly facilitated the imaging and thus significantly increased sample size.

We observed the presence of the radial step before PPB formation in the presence of NPA as well (Fig. 2*F*, n = 58 cells). Note that the radial step could also be observed in the *pRPS5a::RFP-TUA5* marker line treated with NPA (*SI Appendix*, Fig. S3*E*). This demonstrates that the occurrence of the radial step is not dependent upon polar auxin transport. However, the duration of the radial step was longer with NPA (ca. 3 h) than in its absence (ca. 2 h) (Fig. 2 *F* and *I* and *SI Appendix*, Fig. S3*E*). While cells were usually more isodiametric on NPA than in absence of NPA, the division plane orientation followed a bimodal distribution (transverse or longitudinal) similar to untreated cells (Fig. 2 *G* and *H*, n = 194 cells). We also fitted a logistic regression with the *glm* function in R to the data and found an inflection point at 0.6 as well (*P*-value < $2.2e^{-16}$). The function fit the data better than in control conditions (R^2 = 0.457), probably due to the larger sample size. This suggests that the observation that cells tend to divide following the maximal tension derived either from their shape, or from the tissue is dependent on their aspect ratio, remains true in NPA conditions. When dividing the data in two subsets (one for cells with PPBs following the stem axis, and one for cells with PPBs normal to the stem axis), we could also conclude that occurrence of the radial step is independent of the final orientation of the PPB (*SI Appendix*, Fig. S5 *C* and *D*).

Taking advantage of the larger sample size, we next analyzed CMT orientation with respect to the stem axis in NPA-treated plants, using the *OrientationJ* plugin in Fiji. CMTs were reliably perpendicular to the stem axis (i.e., parallel to predicted maximal tensile stress direction) before −3 h (Fig. 2*J*), and this trend was temporarily lost between −4 and −3 h, with a more uniform distribution of CMT orientations reflecting the radial step (Fig. 2*J*). We then repeated the same analysis for cells with an aspect-ratio below 0.6 (i.e., the most elongated cells, Fig. 2*K*) and above 0.6 (i.e., the most isodiametric cells, Fig. 2*L*). The conclusions were conserved, further confirming that the radial step is independent of cell shape and auxin transport. In the end, most of the elongated cells divided parallel to the stem axis (i.e., perpendicular to maximal tensile stress direction, Fig. 2*K*), in contrast to most isodiametric cells, which divided perpendicular to the stem axis (i.e., parallel to maximal tensile stress direction, Fig. 2*L*). This analysis further confirms that the presence of the radial step is not dependent on the final cell division plane orientation.

The Radial Step Coincides with the Premitotic Increase in Cytoplasmic Microtubule Content and Is Prolonged When This Process Is Promoted. Because the radial step occurs independently of microtubule markers used, growth media, or polar auxin transport, we hypothesized that its presence and timing of appearance are mainly controlled by intrinsic factor(s). In plants, and contrary to many eukaryotes, there is no microtubule organizing center (MTOC) and the formation of new microtubules is mostly distributed, and strongly relies on microtubule-dependent γ-tubulin recruitment and branched nucleation (23–25). Consistently, γ-tubulin mutants display mitotic and interphasic microtubule defects (26). However, there are multiple pieces of evidence of microtubule nucleation specifically at the nuclear envelope (27, 28) at the end of the G2 phase, before and during PPB formation (9, 23, 29). This well-established behavior is generally thought to ensure a connection between the PPB and the nucleus (9, 23), and to provide a population of perinuclear microtubules to complete mitotic tasks, such as spindle formation (30, 31). Here, we investigated whether this behavior also occurs in the stem and whether it temporally correlates with the radial step.

To assess the cytoplasmic microtubule content, we analyzed the microtubule signal in XZ maximal projections, i.e., through anticlinal cell sections, and calculated the ratio between the endoplasmic signal and the cortical signal. As expected, we observed a gradual increase of the internal microtubule content as the cell reached the PPB stage, with an average increase between the first and the last timepoints of 162% (Fig. 3 *A* and *B* and *SI Appendix*, Fig. S7*A*). Cytoplasmic microtubules started to accumulate around 3 h before cell division, i.e., coincident with the radial step.

To test the connection between the radial step and cytoplasmic microtubule accumulation, we next investigated the radial step in a *trm678* mutant background, grown and imaged in control conditions, as described for the WT. This mutant, as other PPB-deficient mutants, displays a strong accumulation of perinuclear MTs before

mitosis (5, 6). The *fass* mutant exhibits a slight increase in microtubule nucleation (32), and this could be a feature of most TTP complex mutants, such as *trm678*, with some evidence pointing toward this hypothesis (4, 5). Because *ton1* and *fass* mutants exhibit very disrupted interphasic microtubules (5), this would hinder the analysis of more subtle changes in CMT behavior, and notably the radial step. Among these PPB-deficient mutants, *trm678* exhibits WT-like interphasic microtubules (6) (*SI Appendix*, Fig. S6*A*), allowing us to investigate the radial step behavior in that background.

The mitotic index was comparable in WT and *trm678* stems (1.56% ± 1.04% in WT stems, and 2.00% ± 1.21% in *trm678* stems). In the stem, the average duration of mitosis was roughly 50% longer in *trm678* (ca. 3 h) than in the WT (ca. 2 h, *SI Appendix*, Fig. S6 *B* and *C*), even though the exact difference is difficult to assess due to our time resolution. As previously seen in the wild-type, we observed a radial step in *trm678* stems (Fig. 3*C*, n = 29 cells). As expected for a PPB-deficient mutant, the division orientations in the *trm678* stems were noisier than in the WT (Fig. 3*C*) (33), further confirming that the radial step appears independent of final cell division plane orientation. However, the radial step exhibited two unique features in *trm678*. First, it seemed visually clearer than in the WT (Fig. 3*C*). To ascertain this, we measured the anisotropy of CMT arrays in the *trm678* mutant 3 h before cell division and found it to be half that of the WT, consistent with the observation of a better-defined radial step (*P*-value = $6.05e^{-6}$ at −2 h, Tukey HSD test; Fig. 3*F*). Second, the radial step appeared to last much longer than in the WT. The exact average duration of the radial step in *trm678* is difficult to estimate, because in most of our kinetics, the radial step lasted at least 6 h, and we missed the full sequence (from interphasic CMTs to the radial step to mitosis) within a multihour kinetics (Fig. 3*C* and *SI Appendix*, Fig. S6*A*). We could observe that switch only in exceptional cases, i.e., when the radial step was shorter (ca. 4 h) before cell division (*SI Appendix*, Fig. S7*B*). In the *trm678* mutant, the internal microtubule signal was significantly higher than in the WT, as shown when following individual kinetics (Fig. 3*D* and *SI Appendix*, Fig. S7) and when pooling measurements (a 213% increase between t = −6 h and t = 0, *P*-value = $2.38e^{-4}$ for *trm678*, and a 162% increase between t = −6 h and t = 0, *P*-value = $1.13e^{-3}$ for the WT, Wilcoxon test, Fig. 3*E*). We also measured the anisotropy of CMT array, using ImageJ FibrilTool, and observed reduced anisotropy in *trm678* on average, when compared to WT, consistent with the prolonged radial step in the mutant (Fig. 3*F*). Since the radial step starts at t = −6 h or earlier, the anisotropy remains low for the duration of the analyzed time-lapse. However, we could find aligned CMT arrays in the *trm678* mutant during interphase prior to the radial step, when its duration was exceptionally shorter (*SI Appendix*, Fig. S6*A*). This analysis further suggests that the transient radial organization of CMTs reflects the start of cytoplasmic microtubule accumulation before cell division.

The Presence of the Radial Step Is Robust to Mechanical Perturbations. Altogether, the radial organization of CMTs coincides with increased cytoplasmic microtubule accumulation around the nucleus (*SI Appendix*, Fig. S8), which is even more pronounced in the absence of TRM6/7/8. This provides a scenario in which the radial step emerges from a destabilization of CMTs, either from increased connections between CMTs and the nucleus, or from competition between different sites of microtubule nucleation. This also suggests that the radial step reflects a transient disruption of CMT alignment with tensile stress at the outer periclinal wall. To further test that hypothesis, we next investigated whether the radial step is maintained, or not, when the local pattern of tensile stress changes.

It is well established that local ablations in a tissue shifts the direction of maximal tensile stress to a circumferential orientation around the ablation site (16). We therefore performed manual ablations with a needle on stems, changing the tensile stress pattern from transverse to the stem axis, to circumferential around the wound site (Fig. 4*A*). In the first few hours after the ablation, cell division was inhibited. However, 15 h after the ablation, cell divisions reappeared. Importantly, the CMTs were still organized circumferentially around the ablation (Fig. 4*B* and *SI Appendix*, Fig. S9*A*), prompting us to conclude that the tensile stress pattern was still circumferential 15 h after the ablation. We also observed that the division planes were oriented circumferentially around the ablation site, confirming similar findings previously reported for the SAM (11) (*SI Appendix*, Fig. S9*B*). We also noticed that the PPBs were wider than in control conditions, and the formation of the prospindles started before the PPB started to depolymerize (*SI Appendix*, Fig. S10 *C* and *D*).

Following CMT dynamics in cells around the ablation site, we could observe a transient radial organization of the array before the formation of the PPB (Fig. 4*D*). We measured the anisotropy overtime and found, as in control conditions, a drop around 2 h before t0 (with an average of 0.21 ± 0.35 at t = −6 h, and of 0.13 ± 0.28 at t = −2 h, Fig. 4*I*). Note that this step lasted for a shorter duration than in control conditions (only 1 h), since the anisotropy increased back at t = −1 h to reach and average of 0.15 ± 0.34, reflecting the formation of the PPB. The cytoplasmic microtubule content increased in premitotic cells around the ablation site as well, coinciding with the presence of the radial step (Fig. 4*E*). This shows that the radial step is robust to mechanical perturbations, consistent with a scenario in which the accumulation of cytoplasmic microtubules in late G2 disrupts the ability of CMTs to align with tensile stress.

To challenge this conclusion, we also performed the same ablation experiments on *trm678* mutant stems. CMTs in *trm678* responded to mechanical perturbations, as evidenced by their circumferential orientation around the ablation (Fig. 4*C*). In this background, the radial step also appeared before mitosis, and lasted for a shorter duration than in *trm678* cells in control conditions (Fig. 4*F*). We measured a drop in CMT array anisotropy 4 h before t0 in dividing cells around the ablation (with an average of 0.17 ± 0.07 at t = −6 h, and of 0.12 ± 0.06 at t = −4 h, Fig. 4*I*). Since there is no PPB in this genetic background, the anisotropy remained low until t0, as in nonablated *trm678* stems (0.09 ± 0.05). When looking at cytoplasmic microtubule content over time, we observed an increase as the cell progressed toward mitosis, consistent with the timing of the radial step emergence (Fig. 4*G*). Note that in both *trm678* and WT genetic backgrounds, the increase in microtubule content before mitosis was more pronounced around ablations than under control conditions. When pooling the measurements, we could see a 315 % increase in cytoplasmic microtubule content between t = −6 h and t = 0 (*P*-value = $6.80e^{-6}$, Wilcoxon test), while this increase was of 246 % in the WT background, around ablations (*P*-value = $1.34e^{-7}$, Wilcoxon test) (Fig. 4*H*). While these minor deviations to microtubule behavior show that the cell behaves slightly differently next to an ablation site, the radial step still occurs independently of the genetic background, consistent with a transient blindness of CMTs to tensile stress caused by cytoplasmic microtubule accumulation.

Disruption in the Balance between Cortical and Cytoplasmic Microtubule Accumulation in *trm678* Increases the Precision of Cell Division. While the radial step appears robust, reflecting a transient disruption of CMTs by cytoplasmic microtubules, one

could wonder whether this reset sequence has a biological function. The identification of a step where cells become blind to their mechanical environment echoes data in *Drosophila* epithelia where cell rounding allows the cell to perceive its centroid, independently from adjacent cells' influence, in order to define the degree of cell division symmetry (2, 3). We wondered whether the radial step might have a comparable function in plants.

Note that the inner periclinal cortex also displays a radial reorganization of the CMT array before the formation of the PPB (*SI Appendix*, Fig. S11).

To address this question, we analyzed daughter cell volumes in WT and *trm678* stems, and plotted the volume ratio for both genotypes. The mean ratios were comparable (1.30 ± 0.26 in WT vs. 1.20 ± 0.14 in *trm678*; Fig. 5*A*). The means are higher than 1 because we measured the ratio between the larger daughter cell and the smaller one. Interestingly, while the averages were not significantly different (Wilcoxon test *P*-value = 0.253), the variances were significantly different (0.07 in WT and 0.02 in *trm678*, Fligner test *P*-value = 0.005): symmetry between daughter cells was 3.79 times less variable in *trm678* than in wild-type. This suggests that a longer and better-defined radial step correlates with more predictable divisions, reducing the variability in daughter cell volume ratios.

Because the *trm678* has a prolonged radial step and a prolonged M phase (*SI Appendix*, Fig. S6*B*), we next checked whether increased predictability is simply the result of a slower premitotic stage. To do so, we performed the same analysis in NPA-treated WT plants, which exhibit slightly longer radial step and slightly longer mitosis than non-NPA-treated plants. This did not affect the variance of daughter cell volumes (Fig. 5*A*). When performing the same analysis on NPA-treated *trm678* stems, we instead observed a partial rescue: the variance in NPA-treated *trm678* stems was lower than NPA-treated WT stems, but higher than control *trm678* stems (Fig. 5*A*). Thus, the predictability in cell division does not correlate with a slower premitosis and mitosis dynamics, but instead, with a longer and qualitatively more clear-cut radial step, in *trm678*.

Altogether, we propose that the accumulation of cytoplasmic microtubules near the nuclear envelope 3 h before cell division in stems transiently disrupts the coalignment of CMTs with tensile stress, forming a radial organization of CMTs, thus allowing the cell to control the robustness of its division, by becoming less sensitive to external cues.

Discussion

Altogether, our results are consistent with a sequential model in which the progressive accumulation of cytoplasmic microtubules during the G2 phase would disrupt CMT alignment with tensile stress to allow the cell to sense its own geometry for a short time window and to ensure the precision of cell division (Fig. 5*B*). This radial step could also help the cell to acquire information on other key cell division parameters, such as centroid position (34). After this transitory stage, CMTs would resume their alignment either with the short axis of the cell when cells are elongated (Errera's rule, also matching cell-shape derived maximum of tensile stress) or with tissue stress, when cells are isodiametric, to control the final division plane orientation. Identifying conditions in which the radial step is absent will be necessary to test this model.

The Transient CMT Organization Before Mitosis as an Exception to the CMT Alignment with Tensile Stress. So far, the alignment of CMTs with maximal tensile stress has been verified in most plant tissues (10, 35), and suffers only a few exceptions. Although this needs to be formally investigated, most of these exceptions could be explained by invoking differences in stress levels. For instance, one could propose that a drop in turgor pressure in hypocotyls switching from dark to light could explain the rapid growth arrest and associated switch in CMT orientation (36). Similarly, the progressive reinforcement of cell walls during differentiation, and thus reduction in stress level, could explain the loss of CMT coalignment in leaf epidermis (37). This notably builds on recent investigations in protoplasts that are confined in microwells: In this case, CMTs are transverse, aligned with the shortest axis of an elongated cell, which is also a local maximum of stress, following Laplace–Young law (38). However, when they are placed in a hyperosmotic medium, i.e., when tension decreases, CMTs switch to the long axis of the cell: they follow the flattest part of the protoplast contour, which is also the minimum of bending energy (38, 39).

To our knowledge, the only undisputable exception of CMTs alignment with tensile stress is thus provided in this work, in the sense that during the timeframe of the radial step, the global pattern of tension should not change: 3 h before cell division, cells in stems exhibit a radial organization of their CMT arrays. This cannot be explained by a change in tissue stress pattern, as adjacent cells usually exhibit CMTs that are aligned with predicted tissue stress direction. A change in cell wall properties would be too slow to affect the CMTs so transiently. When the tensile stress is changed around ablations in the tissue, the radial step is affected (shorter duration), but is still present. Although we cannot exclude the possibility that turgor level would transiently change 3 h before cell division, this would be unlikely to cause a radial CMT organization. As shown in the protoplast experiments, following a drop of turgor pressure, CMTs would align with the long axis of the cell, and would not make a radial pattern.

The Radial CMT Step as a Reset Mechanism. Our observation goes against a common assumption that PPB orientation usually follows that of CMT during interphase. We instead identified a reset stage where CMTs become disorganized for a duration of ca. 2 h and at a well-defined time window (3 h before cell division). The radial step reflects a stage during which CMTs switch from their role in guiding the deposition of cellulose microfibrils, to their role in controlling cell division. Other CMT arrays have been shown to have links with cell division [typically, the PPB, and cortical-telophase microtubules (40, 41)], further suggesting that close to mitosis, there is a change in CMTs function. Based on the temporal correlation between cytoplasmic microtubule enrichment during the G2 phase and on the prolongation and better definition of the radial step when cytoplasmic microtubule accumulation is promoted (in *trm678*), we propose that the radial step is a period during which increased cytoplasmic microtubule accumulation disrupts the CMT self-organization, thereby making the CMT network transiently blind to external mechanical cues.

Our time-lapse analyses shed light on past reports on guard mother cells (GMCs). In particular, to quote Mineyuki (42), notably building on studies by Mullinax and Palevitz (43), "graminean GMCs have 'interphase microtubule bands' that orient perpendicular to PPBs. This transverse interphase microtubule band precedes a radial microtubule array, which is then replaced by a PPB prior to the longitudinal cell division." These past reports together with our analysis suggest that the radial step is not a guard mother cell exception, but more likely the rule.

To go one step further, the radial step in plant cells could serve the same function as the cell rounding step in *Drosophila* epithelia. Upon disruption of cell rounding through myosin motor inactivation,

Drosophila epithelial cells remain packed as they divide, and their division plane follows cell geometry instead of tissue stress (3). Even though the mechanical properties of a plant tissue are different than that of an animal due to the presence of cell walls, our analysis of cell division plane orientation according to cell aspect ratio also fits the idea that a threshold of stress, either prescribed by cell shape or tissue shape, determines the final orientation of division plane. Interestingly, in our study, we could explore the consequence of a prolonged radial step, and we found an increase in cell division volume precision. One might thus wonder whether a prolonged cell rounding in *Drosophila* would also increase the precision of cell division.

A Trade-Off in Precision between Division Plane Orientation and Division Precision. The idea of a competition between internal and cortical microtubules is not totally new. Indeed, cytoplasmic microtubules have major impacts on cortical array in nondividing cells (44). Cytoplasmic microtubules can generate an isotropic array overriding the preexisting microtubule array through the tethering function of CLASP (45). Because premitotic cytoplasmic microtubules are prominent in late G2 phase, it could cause great impact on CMT array. Cytoplasmic microtubules are likely to play a primary role in division precision. There is ample literature showing how tension within cytoplasmic microtubules may act as a sensor of cell geometry (46). A search and capture mechanism for instance would depend on the length of microtubules, and thus on cell width. Our results support that scenario, also suggesting that the accumulation of cytoplasmic microtubules before cell division does not only serve as a reservoir of microtubules to prepare mitosis, but it would also contribute to the precision of cell division, possibly by making the cell more self-centered on its nucleus and less sensitive to external cues. In this scenario, the radial array at the cortex would not necessarily be the main player in geometry perception.

Yet, one could explore ways in which CMTs contribute to geometry sensing in synergy with cytoplasmic microtubules. The recent work by Muroyama et al. (47) might be inspiring. They showed that CMTs at cell contour are biased by BASL for asymmetric division. They had previously shown the importance of microtubules for nuclear positioning before cell division (48). Therefore, the radial step might be important for even CMT distribution at cell contour to allow nuclear position and control the robustness of division symmetry. In that scenario, the radial step would open a window in which the cell tends toward "perfect" symmetry until it is overridden by other cortical signals such as BASL, mechanical stress, or the formation of the PPB, later on. Note that the radial step is also present in cells dividing asymmetrically, thus these other cortical cues may also affect the radial step, this time to secure asymmetric division. In other words, although our analysis suggests that the radial step reflects the robustness of division, it does not seem to determine the degree of symmetry.

In conditions of high mechanical stress, such as around ablation sites, we observed that the radial step appears for a shorter time, and the increase in cytoplasmic microtubules was more pronounced and in a shorter time window. A disruption in the CMT array organization through cytoplasmic microtubule accumulation might be difficult to maintain when aligned CMTs are needed to reinforce the cell wall along maximal tensile stress directions. We also cannot exclude that the cell cycle regulation could be modified around ablations.

We showed that the radial step is robust to different cell shapes, cell identity (SAM, stem, meristemoids), mechanical perturbations (local ablations), and growth conditions [AM and apex culture medium (ACM), with or without NPA], where cortical and cytoplasmic microtubule behavior is likely to vary. Such robustness may emerge from a more fundamental parameter: the conflict between cytoplasmic and CMTs. Whereas long-term tracking of dividing cells with microtubule markers and at high enough resolution is still rare in the literature, we could find examples of *Datura stramonium* cells with a transient pattern reminiscent of what we observed in *Arabidopsis* (46). We thus propose that the radial step reflects the sequential control of cell division, where division precision precedes division plane robustness. We can speculate that the radial step is an integral part of the preparation for mitosis and therefore could be extended to other tissues and cell types. This sequence also suggests that division precision is more variable than division plane orientation (as its control is temporally more distant from mitosis), possibly because a small error in division precision has less implications than a small error in division plane orientation, at least from a mechanical point of view.

Materials and Methods

Detailed protocols are available in *SI Appendix*.

Plant Material and Growth Conditions. All *Arabidopsis thaliana* lines [wild type, *trm678* (6), *pPDF1::mCitrine-MBD* (49), *pUBQ10::Lti6-TdTomato* (50), *pRPS5a::RFP-TUA5, pUBQ10::RFP-TUA6]* were in the Col-0 ecotype. Growth conditions for SAM imaging were as described in ref. 51. Growth conditions for stem imaging, with or without 10 μM of NPA, were as described in ref. 16.

Stem Preparation and Imaging. *Arabidopsis* stems from in vitro plants with a few unopened flower buds were selected. For easier dissection, we selected stems that were ca.1.5 cm long. Then, the organs impairing a correct imaging were dissected (cauline leaves and flower buds). The plants with prepared stems were transferred to an imaging medium (AM or ACM) and fixed in the medium by placing the roots and leaves inside the agar, exposing the area of interest. Ablation was made manually, using a small needle and gently poking the stem. The plate containing the samples was placed in the growth chamber for 1 d (15 to 20 h) before the experiment (*SI Appendix*, Fig. S12*A*).

The images for all figures were acquired using the LSM980–Airyscan 2 confocal microscope (Zeiss) or SP8 confocal microscope (Leica) equipped with a water immersion lens.

Image Processing. The LSM980 images were processed using the Airyscan Processing program in Zeiss software, with the "All Images (2D)" program and the Auto Filter. The image stacks were then processed using the SurfCut program (52) projecting the upper signal from the top slices (between 0 and 4 μm of the epidermis). All the processing of the images was done on the Fiji (ImageJ) software.

Division Plane Orientation Analysis. Cells of interest, showing either a PPB or a recent division, were identified. The longest and shortest axes were measured by manually drawing a region of interest to the cell's contours, and extracting the fitted ellipse using Fiji. The aspect ratio was then obtained by dividing the shortest plane by the longest plane of this fitted ellipse. The orientation of the division plane, or the PPB, was also measured manually using Fiji software. The orientations were normalized to keep the results between 0° and 90°, with the 0° orientation being horizontal.

CMT Orientation Analysis. To measure the local orientations of microtubules overtime, we used the Directionality function in Fiji, using the "Local gradient orientation" method. We also used the OrientationJ package's "vector field" function in Fiji (http://bigwww.epfl.ch/demo/orientation/) as another way of measuring CMT orientation (Fig. 2 *J*, *K*, and *L*). To measure the anisotropy of the microtubule arrays, we used the SurfCut images and ran the FibrilTool plugin (18) in Fiji to extract the anisotropy in ROIs. To test the differences between the different genetic background and the different timepoints, we ran the Tukey–Kramer test in RStudio.

Cytoplasmic Microtubule Content Analysis. To analyze the cytoplasmic microtubule, we used Z-stacks of images from lines expressing *pPDF1::mCitrine-MBD*. To project the cytoplasmic microtubule signal, we used the reslice function in Fiji,

with "Output spacing" set at 0.5 μm, starting at the top. We then made a maximal projection of the reslice output to obtain the cytoplasmic microtubule signal. The region of interest for the reslice projection was determined by hand, by being careful of excluding the anticlinal cortex of the cell to only project the internal signal. The outer periclinal cortex as well as the inside of the cell were marked by hand, and the average signal was measured using Fiji. For each cell, at each timepoint, the ratio between the internal signal and the cortical signal (next to the outer wall) was plotted, and we tested the differences in these values using the Tukey–Kramer test in RStudio.

Volume Measurements. Membrane marker images were processed using MorphoGraphX software (53). Recent divisions were spotted by eye, as newer walls separating two daughter cells are straight, anchored at 90° from the edges and are thinner than older walls. The ratio between the two volumes was then measured by dividing the bigger daughter cell's volume by the smaller one's. For statistical tests, we first performed a Wilcoxon test in RStudio, comparing the averages of the ratios with respect to the NPA conditions (with or without NPA), for each genetic background (WT and *trm678*). As there was not a statistically significant difference between the averages, with a threshold of 0.05, and due to the aspect of the data, we performed a Fligner's test in RStudio that focuses on the variances. The *P*-values are displayed in Fig. 5*A*.

Data, Materials, and Software Availability. Original image stacks have been deposited in Figshare (54). Other study data are included in the article and/or *SI Appendix*.

ACKNOWLEDGMENTS. We thank the MechanoDevo team at the RDP (Reproduction et Développement des Plantes) lab for insightful discussion, and Platim for help with imaging. This work was supported by a Human Frontier Science Program Long-Term-Fellowship (LT000891/2018-L to S.T.), by the European Research Council (ERC-2021-AdG-101019515 "Musix" to O.H.) and by Human Frontier Science Program Grant RGP0023/2018. This work was also supported by the AgreenSkills+ fellowship program, which has received funding from the European Union's Seventh FrameworkProgram under Grant Agreement FP7-609398 (AgreenSkills+ contract to ST). This work has benefited from the support of IJPB's Plant Observatory technological platforms. The IJPB (Institut Jean-Pierre Bourgin) benefits from the support of Saclay Plant Sciences-SPS (ANR-17-EUR-0007). J.D. and P.L. acknowledge support from Fondecyt 1211568.

1. B. Alberts, *Molecular Biology of the Cell* (W. W. Norton & Company, ed. 7, 2022).
2. M. P. Stewart *et al.*, Hydrostatic pressure and the actomyosin cortex drive mitotic cell rounding. *Nature* **469**, 226–230 (2011).
3. S. Chanet, R. Sharan, Z. Khan, A. C. Martin, Myosin 2-induced mitotic rounding enables columnar epithelial cells to interpret cortical spindle positioning cues. *Curr. Biol.* **27**, 3350–3358.e3 (2017).
4. T. Sawidis, H. Quader, M. Bopp, E. Schnepf, Presence and absence of the preprophase band of microtubules in moss protonemata: A clue to understanding its function? *Protoplasma* **163**, 156–161 (1991).
5. J. Traas *et al.*, Normal differentiation patterns in plants lacking microtubular preprophase bands. *Nature* **375**, 676–677 (1995).
6. E. Schaefer *et al.*, The preprophase band of microtubules controls the robustness of division orientation in plants. *Science* **356**, 186–189 (2017).
7. A. Muroyama, D. Bergmann, Plant cell polarity: Creating diversity from inside the box. *Annu. Rev. Cell Dev. Biol.* **35**, 309–336 (2019).
8. A. R. Paredez, C. R. Somerville, D. W. Ehrhardt, Visualization of cellulose synthase demonstrates functional association with microtubules. *Science* **312**, 1491–1495 (2006).
9. S. M. Wick, J. Duniec, Immunofluorescence microscopy of tubulin and microtubule arrays in plant cells. II. Transition between the pre-prophase band and the mitotic spindle. *Protoplasma* **122**, 45–55 (1984).
10. D.-C. Trinh *et al.*, How mechanical forces shape plant organs. *Curr. Biol.* **31**, R143–R159 (2021).
11. M. Louveaux, J.-D. Julien, V. Mirabet, A. Boudaoud, O. Hamant, Cell division plane orientation based on tensile stress in *Arabidopsis thaliana*. *Proc. Natl. Acad. Sci. U.S.A.* **113**, E4294–4303 (2016).
12. L. Vineyard, A. Elliott, S. Dhingra, J. R. Lucas, S. L. Shaw, Progressive transverse microtubule array organization in hormone-induced *Arabidopsis* hypocotyl cells. *Plant Cell* **25**, 662–676 (2013).
13. J. Chan, G. Calder, S. Fox, C. Lloyd, Cortical microtubule arrays undergo rotary movements in *Arabidopsis* hypocotyl epidermal cells. *Nat. Cell Biol.* **9**, 171–175 (2007).
14. J. Chan *et al.*, The rotation of cellulose synthase trajectories is microtubule dependent and influences the texture of epidermal cell walls in *Arabidopsis* hypocotyls. *J. Cell Sci.* **123**, 3490–3495 (2010).
15. A. Burian *et al.*, A correlative microscopy approach relates microtubule behaviour, local organ geometry, and cell growth at the *Arabidopsis* shoot apical meristem. *J. Exp. Bot.* **64**, 5753–5767 (2013).
16. O. Hamant *et al.*, Developmental patterning by mechanical signals in *Arabidopsis*. *Science* **322**, 1650–1655 (2008).
17. S. Verger, Y. Long, A. Boudaoud, O. Hamant, A tension–adhesion feedback loop in plant epidermis. *eLife* **7**, e34460 (2018).
18. A. Boudaoud *et al.*, FibrilTool, an ImageJ plug-in to quantify fibrillar structures in raw microscopy images. *Nat. Protoc.* **9**, 457–463 (2014).
19. A. Sampathkumar *et al.*, Subcellular and supracellular mechanical stress prescribes cytoskeleton behavior in *Arabidopsis* cotyledon pavement cells. *eLife* **3**, e01967 (2014).
20. S. Besson, J. Dumais, Universal rule for the symmetric division of plant cells. *Proc. Natl. Acad. Sci. U.S.A.* **108**, 6294–6299 (2011).
21. H. Ai *et al.*, Auxin-dependent regulation of cell division rates governs root thermomorphogenesis. *EMBO J.* **42**, e111926 (2023).
22. S. Yoshida *et al.*, Genetic control of plant development by overriding a geometric division rule. *Dev. Cell* **29**, 75–87 (2014).
23. B. Liu, J. Marc, H. C. Joshi, B. A. Palevitz, A γ-tubulin-related protein associated with the microtubule arrays of higher plants in a cell cycle-dependent manner. *J. Cell Sci.* **104**, 1217–1228 (1993).
24. H. C. Joshi, B. A. Palevitz, γ-Tubulin and microtubule organization in plants. *Trends Cell Biol.* **6**, 41–44 (1996).
25. T. Murata *et al.*, Microtubule-dependent microtubule nucleation based on recruitment of γ-tubulin in higher plants. *Nat. Cell Biol.* **7**, 961–968 (2005).
26. M. Pastuglia *et al.*, γ-Tubulin is essential for microtubule organization and development in *Arabidopsis*. *Plant Cell* **18**, 1412–1425 (2006).
27. K. Mizuno, Microtubule-nucleation sites on nuclei of higher plant cells. *Protoplasma* **173**, 77–85 (1993).
28. V. Stoppin, Isolated plant nuclei nucleate microtubule assembly: The nuclear surface in higher plants has centrosome-like activity. *Plant Cell Online* **6**, 1099–1106 (1994).
29. J. Chumová, H. Kourová, L. Trögelová, P. Halada, P. Binarová, Microtubular and nuclear functions of γ-tubulin: Are they LINCed? *Cells* **8**, 259 (2019).
30. M. Yamada, G. Goshima, Mitotic spindle assembly in land plants: Molecules and mechanisms. *Biology* **6**, 6 (2017).
31. Y. J. Lee, B. Liu, Microtubule nucleation for the assembly of acentrosomal microtubule arrays in plant cells. *New Phytol.* **222**, 1705–1718 (2019).
32. A. Kirik, D. W. Ehrhardt, V. Kirik, TONNEAU2/FASS regulates the geometry of microtubule nucleation and cortical array organization in interphase *Arabidopsis* cells. *Plant Cell* **24**, 1158–1170 (2012).
33. C. B. Scott *et al.*, Graph metric learning quantifies morphological differences between two genotypes of shoot apical meristem cells in *Arabidopsis*. *Silico Plants* **5**, diad001 (2023).
34. J. Moukhtar *et al.*, Cell geometry determines symmetric and asymmetric division plane selection in *Arabidopsis* early embryos. *PLoS Comput. Biol.* **15**, e1006771 (2019).
35. O. Hamant, D. Inoue, D. Bouchez, J. Dumais, E. Mjolsness, Are microtubules tension sensors? *Nat. Commun.* **10**, 2360 (2019).
36. J. J. Lindeboom *et al.*, A mechanism for reorientation of cortical microtubule arrays driven by microtubule severing. *Science* **342**, 1245533 (2013).
37. F. Zhao *et al.*, Microtubule-mediated wall anisotropy contributes to leaf blade flattening. *Curr. Biol.* **30**, 3972–3985.e6 (2020).
38. L. Colin *et al.*, Cortical tension overrides geometrical cues to orient microtubules in confined protoplasts. *Proc. Natl. Acad. Sci. U.S.A.* **117**, 32731–32738 (2020).
39. P. Durand-Smet, T. A. Spelman, E. M. Meyerowitz, H. Jönsson, Cytoskeletal organization in isolated plant cells under geometry control. *Proc. Natl. Acad. Sci. U.S.A.* **117**, 17399–17408 (2020).
40. J. R. Lucas, Appearance of microtubules at the cytokinesis to interphase transition in *Arabidopsis thaliana*. *Cytoskeleton* **78**, 361–371 (2021).
41. M. A. Bellinger *et al.*, Cortical microtubules contribute to division plane positioning during telophase in maize. *Plant Cell* **35**, 1496–1512 (2023).
42. Y. Mineyuki, "The preprophase band of microtubules: Its function as a cytokinetic apparatus in higher plants" in *International Review of Cytology*, K. W. Jeon, Ed. (Elsevier, 1999), pp. 1–49.
43. J. B. Mullinax, B. A. Palevitz, Microtubule reorganization accompanying preprophase band formation in guard mother cells of *Avena sativa* L. *Protoplasma* **149**, 89–94 (1989).
44. C. Ambrose, G. O. Wasteneys, Microtubule initiation from the nuclear surface controls cortical microtubule growth polarity and orientation in *Arabidopsis thaliana*. *Plant Cell Physiol.* **55**, 1636–1645 (2014).
45. P. Y. Le, C. Ambrose, CLASP promotes stable tethering of endoplasmic microtubules to the cell cortex to maintain cytoplasmic stability in *Arabidopsis* meristematic cells. *PLoS ONE* **13**, e0198521 (2018).
46. D. J. Flanders, D. J. Rawlins, P. J. Shaw, C. W. Lloyd, Nucleus–associated microtubules help determine the division plane of plant epidermal cells: Avoidance of four-way junctions and the role of cell geometry. *J. Cell Biol.* **110**, 1111–1122 (1990).
47. A. Muroyama, Y. Gong, K. S. Hartman, D. C. Bergmann, Cortical polarity ensures its own asymmetric inheritance in the stomatal lineage to pattern the leaf surface. *Science* **381**, 54–59 (2023).
48. A. Muroyama, Y. Gong, D. C. Bergmann, Opposing, polarity-driven nuclear migrations underpin asymmetric divisions to pattern *Arabidopsis* stomata. *Curr. Biol.* **30**, 4467–4475.e4 (2020).
49. A. Armezzani *et al.*, Transcriptional induction of cell wall remodelling genes is coupled to microtubule-driven growth isotropy at the shoot apex in *Arabidopsis*. *Development* **145**, dev162255 (2018).
50. C. W. Melnyk, C. Schuster, O. Leyser, E. M. Meyerowitz, A developmental framework for graft formation and vascular reconnection in *Arabidopsis thaliana*. *Curr. Biol.* **25**, 1306–1318 (2015).
51. O. Hamant, P. Das, A. Burian, "Time-lapse imaging of developing shoot meristems using a confocal laser scanning microscope" in *Plant Cell Morphogenesis, Methods in Molecular Biology*, F. Cvrčková, V. Žárský, Eds. (Springer, New York, NY, 2019), pp. 257–268.
52. Ö. Erguvan, M. Louveaux, O. Hamant, S. Verger, ImageJ SurfCut: A user-friendly pipeline for high-throughput extraction of cell contours from 3D image stacks. *BMC Biol.* **17**, 38 (2019).
53. P. Barbier de Reuille *et al.*, MorphoGraphX: A platform for quantifying morphogenesis in 4D. *eLife* **4**, 05864 (2015).
54. I. Melogno *et al.*, Data from "A transient radial cortical microtubule array primes cell division in Arabidopsis." Figshare. https://dx.doi.org/10.6084/m9.figshare.26124994. Deposited 28 June 2024.

A transient radial cortical microtubule array primes cell division in Arabidopsis

Isaty Melogno[1*], Shogo Takatani[1,2*], Paula Llanos[3], Coralie Goncalves[4], Chie Kodera[4], Marjolaine Martin[1], Claire Lionnet[1], Magalie Uyttewaal[4], Martine Pastuglia[4], Christophe Trehin[1], David Bouchez[4], Jacques Dumais[3], Olivier Hamant[1,+]

Supplementary Information

Detailed material and methods

Plant material and growth conditions

All *Arabidopsis thaliana* lines were in the Col-0 ecotype. Wild-type Col-0 and the *trm678* triple mutant(1) were transformed using the dipping floral method(2). Transgenic lines were expressing a microtubule marker (*pPDF1::mCitrine-MBD*(3)*)* and/or a plasma membrane marker (*pUBQ10::Lti6-TdTomato*(4)). As controls, we also used plants expressing the *pRPS5a::RFP-TUA5* tubulin marker, and plants expressing the *pUBQ10::RFP-TUA6* tubulin marker.

For SAM imaging, *Arabidopsis* Wild-type and *trm678* mutant lines were sown on soil and grown in climatic chambers under short-day conditions (8-h light/16-h dark) for 6 weeks and then grown under long-day conditions (16-h light/8-h dark regime) for 4 weeks. Dissected apices were embedded in ACM culture medium (2.2 g/L Murashige and Skoog medium without vitamins (Duschefa), 10 g/L sucrose, pH 5.8 KOH (10 M), 8 g/L agarose) supplemented with 1x Morel and Wetmore vitamins and 570 nmol/L trans-zeatin (12.5 µL of 1 mg/mL of stock solution in 100 mL of ACM medium), and maintained under long-day conditions (16-h light/8-h dark regime, 21°C) as described in (5).

For stem imaging, seeds were sterilized using a sterilization solution (88 mg/mL sodium dichloroisocyanurate and 90% ethanol). 50 to 300 µL of seeds were first incubated in 1 mL of the sterilization solution for 6 minutes, and then washed twice with 96% ethanol and left to dry. Seeds were sown on solid Arabidopsis medium (11.82 g/L Arabidopsis medium (Duschefa, a custom-made medium for the lab, see Supplementary Table 1 below), 2 mM $Ca(NO_3)_2$ $4H_2O$, pH 5.8 KOH (10 M), 10 g/L granulated agar (Merck)). In NPA conditions, this medium was

supplemented with 10 µM of naphthylphthalamic acid (NPA). The seeds were left for stratification for 2 days at 4°C in the dark, and plants were grown for around 3 weeks in long day conditions (16h light/8h dark) at 20°C, until the first flower buds developed.

Supplementary Table 1. Detail of the composition of the Arabidopsis medium.

Arabidopsis medium	
Formula	**mg/mL**
$CoCl_2.6H_2O$	0.0025
$CuSO_4.5H_2O$	0.13
Ferric Ammonium Citrate	50
NaCl	0.58
H_3BO_3	4.33
$MnCl_2.4H_2O$	2.77
$Na_2MoO_4.2H_2O$	0.05
$ZnSO_4.7H_2O$	0.29
KH_2PO_4	340.25
KNO_3	500.5
$MgSO_4.7H_2O$	246.5
Myo-Inositol	100
Nicotinic Acid	1
Pyridoxine HCl	1
Thiamine HCl	1
Ca-Panthotenate	1
Biotine	0.01
Sucrose	10000
MES	700

It is worth noting that, while the cell division is very active at the tip of the stem, imaging conditions can inhibit division and affect microtubule dynamics. This happened in both Arabidopsis and ACM media. We noticed that the winter season is usually more prone to induce slow division rates.

SAM dissection and imaging

Dissected shoot apices were imaged with a Leica SP8 upright confocal microscope (Figures 1A, 1B, and S1A). Confocal z-stacks were acquired (every 30 min for 10 hours) at a resolution of 0.09 × 0.09 × 0.2 µm per voxel using a HC FLUOTAR L 25x/0.95 N.A. water immersion objective. The confocal scan speed was no more than 7, and line averaging was set to 2.

Stem preparation and imaging

Arabidopsis stems from *in vitro* plants with a few unopened flower buds were selected. For easier dissection, we selected stems that were ca.1.5 cm long. Then, the organs impairing a correct imaging were dissected (cauline leaves and flower buds). The imaging medium was either the same as the growth medium (Arabidopsis Medium, AM), or Apex Culture Medium (ACM). In the NPA conditions, the ACM medium was supplemented with 10 µm of naphthylphthalamic acid (NPA). The plants with prepared stems were transferred to an imaging medium and fixed in the medium by placing the roots and leaves inside the agar, exposing the area of interest. In ablation conditions, the ablation was made manually, using a small needle and gently poking the stem. The plate containing the samples was placed in the growth chamber for one day (15 to 20 hours) before the experiment. Figure S12A illustrates the different steps of stem preparation.

The images for all figures, except Figures 1A, 1B, S1A and S3A, were acquired using the LSM980 – Airyscan 2 upright confocal microscope (Zeiss). All the samples were imaged under the W Plan-Apochromat x20 water immersion lens (NA: 1.0), and were kept under immersion during the whole experiment. All images were made using the airyscan mode of the microscope. For this, the size of the image needed to be optimized for the Airyscan module, which resulted in a pixel size of around 0.065 µm x 0.065 µm. The Z resolution was always 0.500 µm. The pixel time could vary between experiments, but the scanning was always bidirectional and averaged twice by frame. Airyscan parameters are detailed in Figure S12B.

Some of the images used for Figures 2D-2G, 2H, 2I acquired using the LSM980 – Airyscan 2 inverted confocal microscope (Zeiss). All the samples were imaged under the C-Apochromat x40 water immersion lens (NA: 1.2), and were kept under immersion during the whole experiment by placing a droplet of water directly on the objective. The rest of the parameters are the same as described above.

The images for Figure S3A, as well as for the production of the measurements of Figures 2D-E, 2G-H, 2J-2L were acquired using the SP8 confocal microscope (Leica). The samples were imaged using a x25 water-immersion lens (NA = 0.95), with the resonant scanner switched off, to obtain better resolution. 8-bit images were taken in 1024x512 µm/pixels format, with the XY-resolution of 0.152 µm/pix and Z-stack slices of 0.500 µm. Images were acquired with a

scanning speed of 1000 and averaged 4 times. The mCitrine signal was imaged using the the 514 nm laser (0.5% intensity) and a HyD 1 detector between 518 nm and 549 nm. The results for Figures 2D, 2G, 2E, 2H were made using images from the three microscopes.

Image processing

All the processing of the images was done on the Fiji (ImageJ) software.

The LSM980 images were processed using the Airyscan Processing program in the Zeiss software, with the "All Images (2D)" program and the Auto Filter. They were then converted from the Carl Zeiss Image format (.czi) to Tagged Image Format File (.tiff) format, using a slightly modified version of the lifRxiv program (https://github.com/sverger/lifRxiv).

The SP8 images were converted from Leica Image File Format (.liff) to Tagged Image Format File (.tiff) format, using the lifRxiv program.

The image stacks were then processed using the SurfCut program(6) projecting the upper signal from the top slices (between 0 and 4 µm of the epidermis). The SurfCut projections coming from the same sample at different time points were then assembled into stacks. We selected the cells that divided or exhibited a PPB by the end of the time frame of the experiment.

Division plane orientation analysis

Cells of interest, showing either a PPB or a recent division, were identified. The longest and shortest axis were measured by manually drawing a region of interest to the cell's contours, and extracting the fitted ellipse using Fiji. The aspect ratio was then obtained by dividing the shortest plane by the longest plane of this fitted ellipse.

The orientation of the division plane, or the PPB, was also measured manually using the Fiji software. The orientations were normalized to keep the results between 0° and 90°, with the 0° orientation being horizontal.

The division angles were all divided by 90, to get a dataset between 0 and 1, in order to perform the logistic regression. The regression was made with the "glm" fit in R, with the "quasi-binomial" family to account for the dispersion of the data, and the "logit" link. To assess the

goodness of the fit, we calculated the R-squared value using the null deviance, and the residual deviance given by the glm function, as followed:

$$R^2 = 1 - \left(\frac{Residual\ deviance}{Null\ deviance}\right)$$

To find an approximation of the inflection point of the fitted curve, we acknowledged that the "logit" link uses the following regression:

$$\log\left(\frac{p}{1-p}\right) = ax + b$$

With *p* being the probability of the response being 1, *a* being the slope, and *b* the intercept. We therefore calculated *x* with p set at 0.5, and *a* and *b* being the result of the "glm" fit.

Cortical microtubule orientation analysis

We manually drew rectangles in the center of the cortex, avoiding the edges (to prevent biases in the measurements) on SurfCut projections, for the cells of interest. To measure the local orientations of microtubules overtime, we used the Directionality function in Fiji, using the "Local gradient orientation" method. The output of this program is a distribution of the pixel orientations between -90° and 90° (with 0° being the vertical orientation), as well as a gaussian fit to the data. We plotted the gaussian fit, for each cell at each timepoint.

We used the OrientationJ package's "vector field" function in Fiji (http://bigwww.epfl.ch/demo/orientation/) as another way of measuring CMT orientation (Figure 2J, 2K, 2L). For this, we wrote a homemade macro allowing to extract the vectors inside the region of interest. Briefly, we defined the ROI manually and blacken it. We then extract the coordinates of the vectors inside this blackened area by setting a threshold on the energy value given by the "vector field" output. Once these coordinates are saved, we run the "vector field" on the unchanged image and retain the orientation of the vectors of interest. To test the differences in the distribution of these vectors' orientations overtime, we ran the Klomogorov-Smirnoff test in RStudio. With this test, we compared the distribution of the data at each timepoint with a uniform sequence, generated with RStudio.

To measure the anisotropy of the microtubule arrays, we used the SurfCut images, and delimited the region of interest by hand, following the cell contour, but excluding the anticlinal cortex to avoid any bias. We ran the FibrilTool plugin(7) in Fiji to extract the anisotropy. To test the differences between the different genetic background and the different timepoints, we ran the Tukey-Kramer test in RStudio.

Cytoplasmic microtubule content analysis

To analyze the cytoplasmic microtubule, we used Z-stacks of images from lines expressing *pPDF1::mCitrine-MBD*. To project the cytoplasmic microtubule signal, we used the reslice function in Fiji, with "Output spacing" set at 0.5 µm, starting at the top. We then made a maximal projection of the reslice output to obtain the cytoplasmic microtubule signal. The region of interest for the reslice projection was determined by hand, by being careful of excluding the anticlinal cortex of the cell to only project the internal signal.

The outer periclinal cortex, as well as the inside of the cell were marked by hand, and the average signal was measured using Fiji. For each cell, at each timepoint, the ratio between the internal signal and the cortical signal was plotted, to be able to compare all the measurements, and balance the photobleaching that the samples experienced overtime. We tested the differences in these values between the different genetic backgrounds and between each timepoint using the Tukey-Kramer test in RStudio.

Volume measurements

Membrane marker images were resized to obtain a voxel size with a X of around 250 µm. The images were then processed using the MorphoGraphX software(8). First, images were blurred using the Gaussian blur stack function, and then the segmentation was made using the ITK Watershed Auto Seeded function, and the parameters were fine-tuned to obtain a suitable 3D segmentation. A mesh was then applied using the Marching Cube 3D function, and the volumes were extracted with the Cell Analysis 3D function.

Recent divisions were spotted by eye, as newer walls separating two daughter cells are straight, anchored at 90° from the edges and are thinner than older walls. The ratio between the two volumes was then always measured by dividing the bigger daughter cell's volume by the

smaller one's. For statistical tests, we first performed a Wilcoxon test in RStudio, comparing the averages of the ratios with respect to the NPA conditions (with or without NPA), for each genetic background (WT and *trm678*). As there was not a statistically significant difference between the averages, with a threshold of 0.05, and due to the aspect of the data, we performed a Fligner's test in RStudio that focuses on the variances. The *p*-values are displayed on Figure 5A.

Supplementary references

1. **E. Schaefer, *et al.*, The preprophase band of microtubules controls the robustness of division orientation in plants. *Science* 356, 186–189 (2017).**

2. **S. J. Clough, A. F. Bent, Floral dip: a simplified method forAgrobacterium-mediated transformation ofArabidopsis thaliana: Floral dip transformation of Arabidopsis. *Plant J.* 16, 735–743 (1998).**

3. **A. Armezzani, *et al.*, Transcriptional induction of cell wall remodelling genes is coupled to microtubule-driven growth isotropy at the shoot apex in Arabidopsis. *Dev. Camb. Engl.* 145 (2018).**

4. **C. W. Melnyk, C. Schuster, O. Leyser, E. M. Meyerowitz, A Developmental Framework for Graft Formation and Vascular Reconnection in Arabidopsis thaliana. *Curr. Biol.* 25, 1306–1318 (2015).**

5. **O. Hamant, P. Das, A. Burian, "Time-Lapse Imaging of Developing Shoot Meristems Using A Confocal Laser Scanning Microscope" in *Plant Cell Morphogenesis*, Methods in Molecular Biology., F. Cvrčková, V. Žárský, Eds. (Springer New York, 2019), pp. 257–268.**

6. **Ö. Erguvan, M. Louveaux, O. Hamant, S. Verger, ImageJ SurfCut: a user-friendly pipeline for high-throughput extraction of cell contours from 3D image stacks. *BMC Biol.* 17, 38 (2019).**

7. **A. Boudaoud, *et al.*, FibrilTool, an ImageJ plug-in to quantify fibrillar structures in raw microscopy images. *Nat. Protoc.* 9, 457–463 (2014).**

8. **P. Barbier de Reuille, *et al.*, MorphoGraphX: A platform for quantifying morphogenesis in 4D. *eLife* 4, 05864 (2015).**

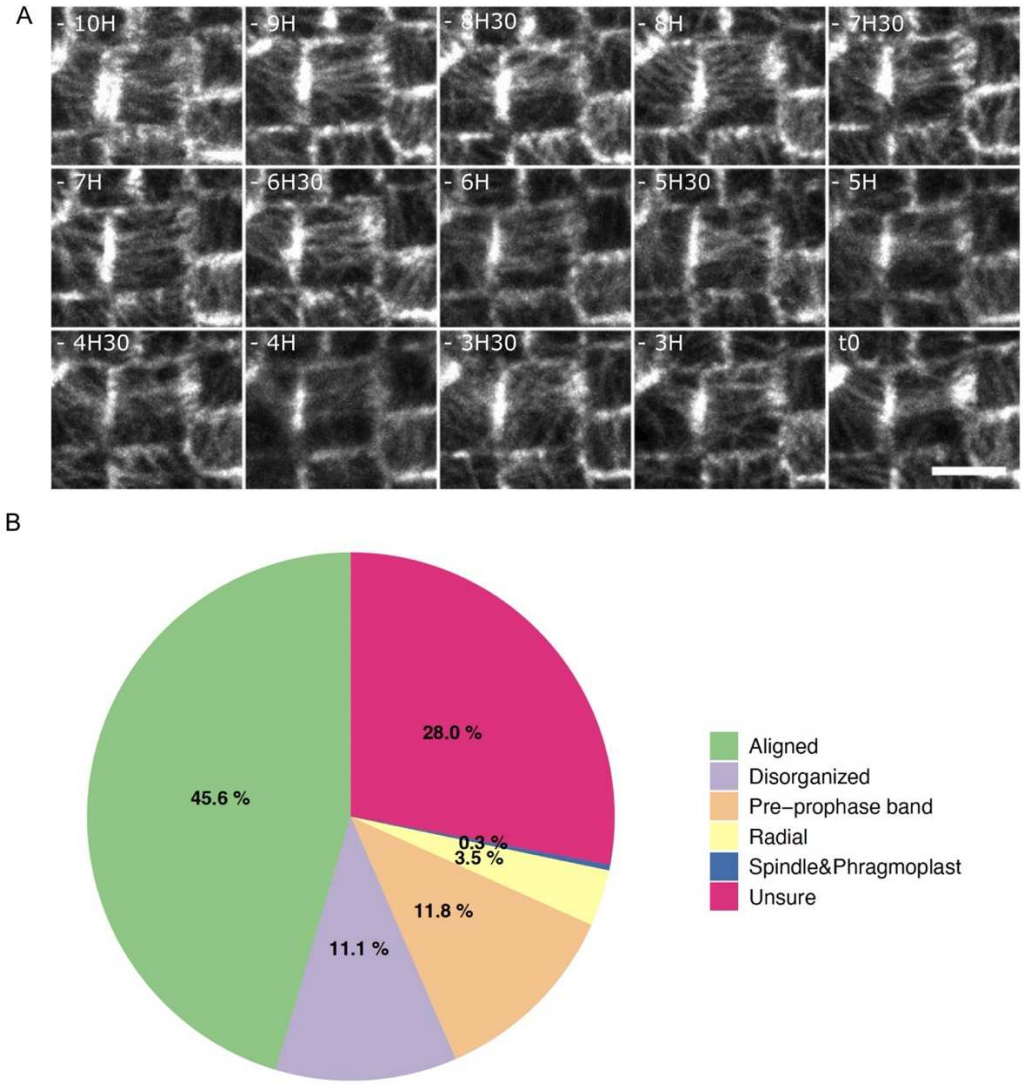

Figure S1. Radial array of CMTs in pre-mitotic cells at the shoot apical meristem
(A) Other example of a time lapse showing cortical microtubules dynamics before the establishment of the PPB. From -10 hours to -6 hours, CMTs maintain a stable orientation. From -5h30 onwards, CMTs exhibit less consistent orientations, up to PPB formation. Images are SurfCut projections of the area between 0 and 4 µm of the surface of the *pPDF1::mCit-MBD* signal. Scale bar: 5 µm. The Brightness and Contrast parameters have been modified for a better visualization of the microtubules. (B) Pie chart representing the average percentages of the different organizations of CMT arrays in shoot apical meristems. Aligned reflect the directional organization, typically at interphase. PPB corresponds to the cells where a clear band of microtubules is observed. Radial shows the radial array we described above. Spindle/Phragmoplast corresponds to cells that are undergoing mitosis. Disorganized is when the array is visible, but all of the above categories are not suited to describe it, whereas unsure reflets cells where no clear classification could be made (either the resolution was too low or the image was blurry). These classifications were made qualitatively on a total of 4 shoot apical meristems, where only the central zone was observed.

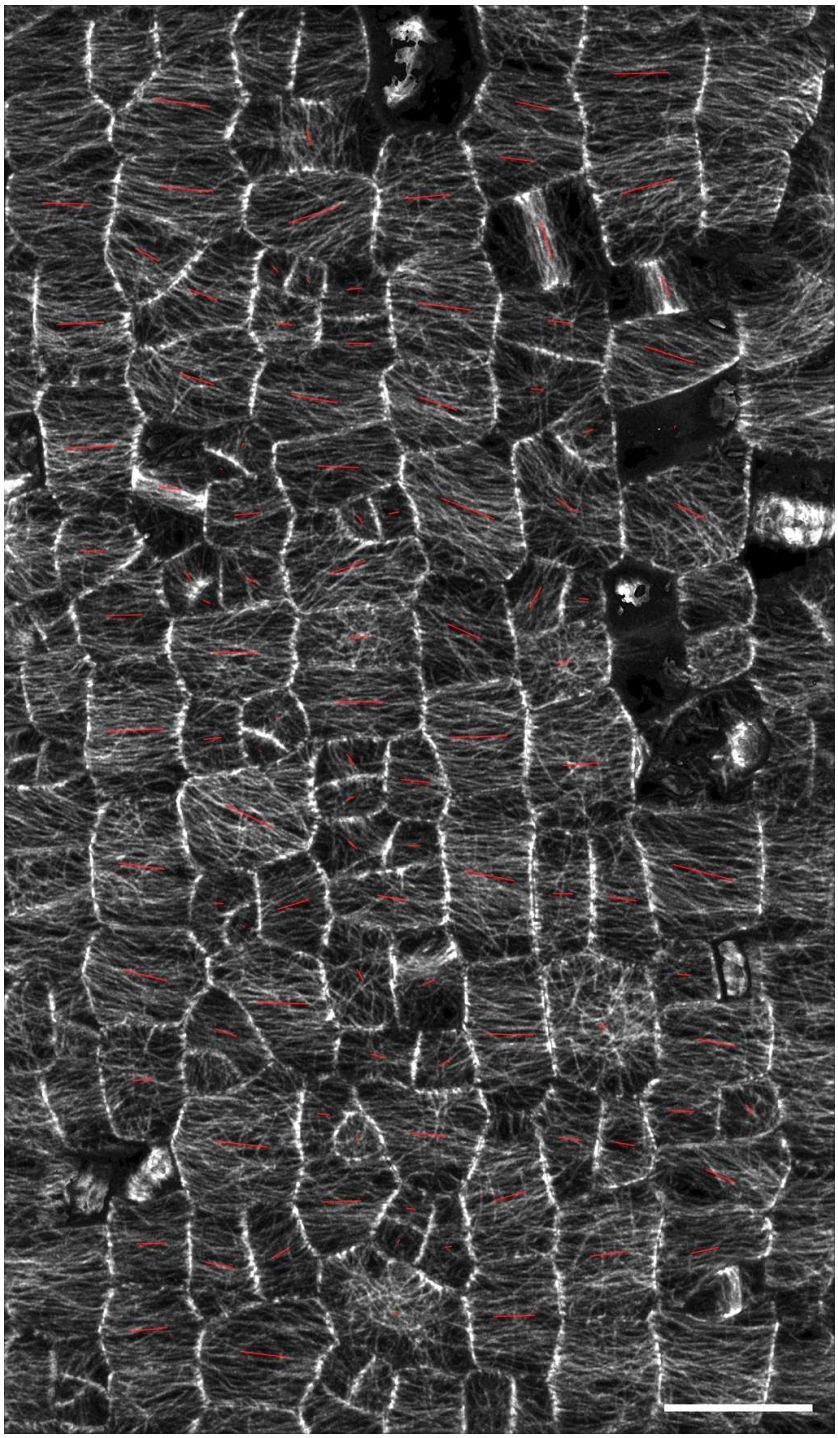

Figure S2. Average CMT orientations in an *Arabidopsis* stem.
This image represents the projection of the *pPDF1::mCitrine*-MBD signal between 0 and 4 µm, using SurfCut. Cells were segmented manually, and the average orientation of CMTs was extracted and displayed, using an automated version of the FibrilTool plugin in Fiji (http://doi.org/10.5281/zenodo.2528872). The red lines represent the average orientation of CMTs. The length of the line corresponds to the anisotropy of the CMT arrays: the longer the line, the higher the anisotropy value. Most of the cells display transverse cortical microtubules, following the predicted maximal tensile stress pattern. Scale bar: 20 µm. The Brightness&Contrast was modified for better visualization.

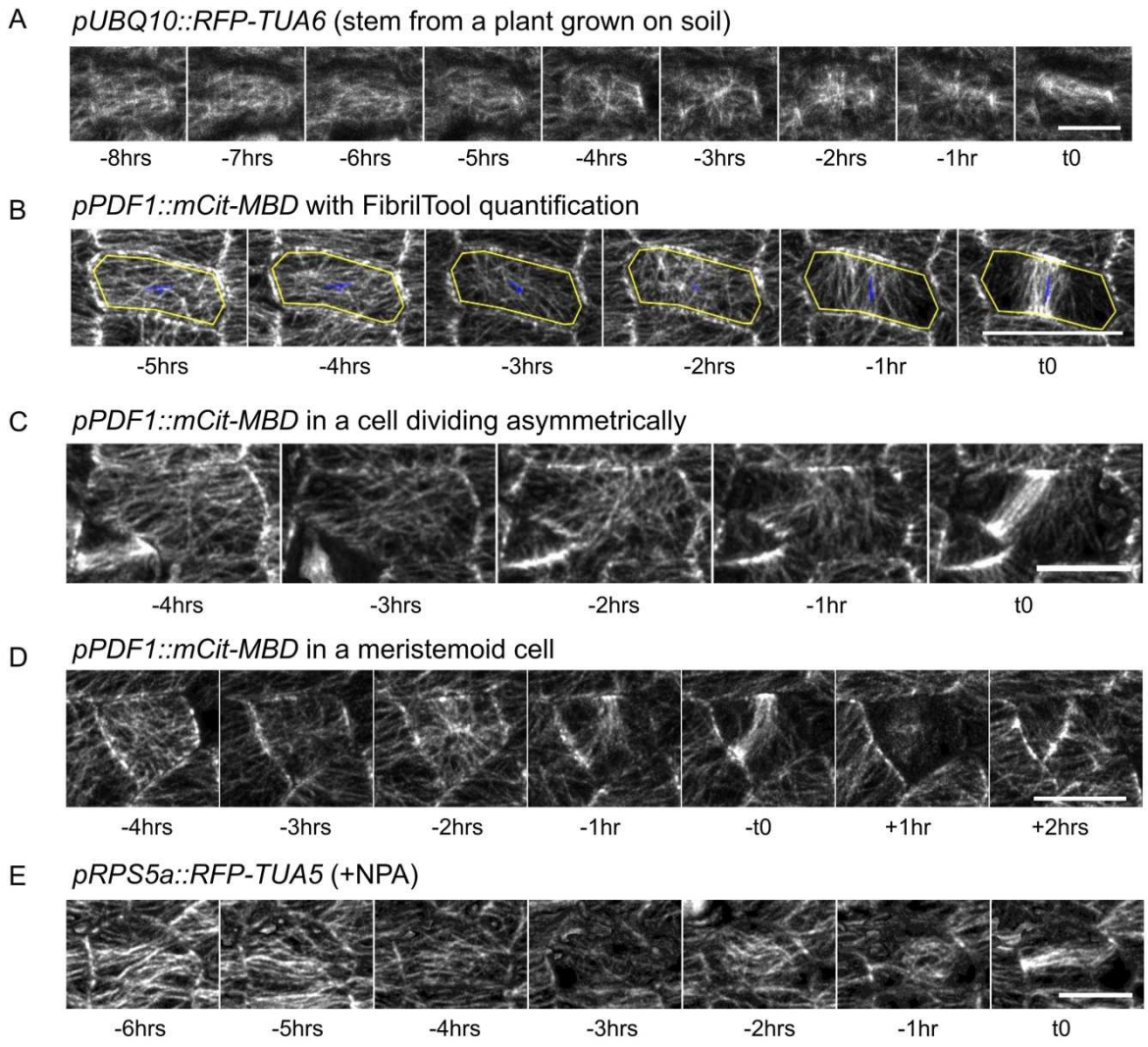

Figure S3. Additional evidence of radial CMTs before cell division

(A) CMT dynamics before cell division in stems, using the *pUBQ10::RFP-TUA6* marker line grown on soil. (B) Example of FibrilTool measurement: the yellow contour defines the region of interest from which the measurements are made. The blue line represents the anisotropy of the CMT arrays with its length, and the predominant orientation of the CMTs with its orientation. (C) Example of CMT dynamics in an asymmetrically dividing cell. (D) Example of CMT dynamics in a meristemoid cell (dividing asymmetrically). (E) CMT dynamics before cell division in stems, using the *pRPS5a::RFP-TUA5*, with NPA from germination on plants grown in vitro. All images reveal the fluorescent signal, and are SurfCut projections from 0 to 4 µm from the surface of the stem. Scale bars: 10 µm. The Brightness&Contrast was modified for better visualization.

A)

WT (Control)	-6 hrs	-5 hrs	-4 hrs	-3 hrs	-2 hrs	-1 hr	t0
-6 hrs	XXXXX	0.1646	$5.02e^{-06}$	$< 2.2e^{-16}$	$< 2.2e^{-16}$	$7.10e^{-04}$	$1.84e^{-11}$
-5 hrs	XXXXX	XXXXX	$8.00e^{-07}$	$< 2.2e^{-16}$	$< 2.2e^{-16}$	0.00591	$4.76e^{-10}$
-4 hrs	XXXXX	XXXXX	XXXXX	2.18e-13	$4.90e^{-10}$	2.15e-14	$< 2.2e^{-16}$
-3 hrs	XXXXX	XXXXX	XXXXX	XXXXX	0.3048	$< 2.2e^{-16}$	$< 2.2e^{-16}$
-2 hrs	XXXXX	XXXXX	XXXXX	XXXXX	XXXXX	$< 2.2e^{-16}$	$< 2.2e^{-16}$
-1 hr	XXXXX	XXXXX	XXXXX	XXXXX	XXXXX	XXXXX	$1.54e^{-05}$
0	XXXXX	XXXXX	XXXXX	XXXXX	XXXXX	XXXXX	XXXXX

B)

WT (+ NPA)	-6 hrs	-5 hrs	-4 hrs	-3 hrs	-2 hrs	-1 hr	t0
-6 hrs	XXXXX	0.1548	0.1552	$7.18e^{-05}$	$< 2.2e^{-16}$	$3.62e^{-04}$	$< 2.2e^{-16}$
-5 hrs	XXXXX	XXXXX	0.6853	$8.33e^{-04}$	$< 2.2e^{-16}$	0.005563	$< 2.2e^{-16}$
-4 hrs	XXXXX	XXXXX	XXXXX	$9.04e^{-05}$	$< 2.2e^{-16}$	$2.21e^{-04}$	$< 2.2e^{-16}$
-3 hrs	XXXXX	XXXXX	XXXXX	XXXXX	< 2.2e-16	0.763	$< 2.2e^{-16}$
-2 hrs	XXXXX	XXXXX	XXXXX	XXXXX	XXXXX	$< 2.2e^{-16}$	$< 2.2e^{-16}$
-1 hr	XXXXX	XXXXX	XXXXX	XXXXX	XXXXX	XXXXX	$< 2.2e^{-16}$
0	XXXXX	XXXXX	XXXXX	XXXXX	XXXXX	XXXXX	XXXXX

Figure S4. *p*-value results for Kolmogorov-Smirnoff tests, comparing the distributions of CMT orientations under control conditions (A), or NPA conditions (B), between the different timepoints. The dataset used for this test was the results obtained with the Directionality plugin in Fiji. The null hypothesis for the Kolmogorov-Smirnoff test is "There are no differences between the two distributions".

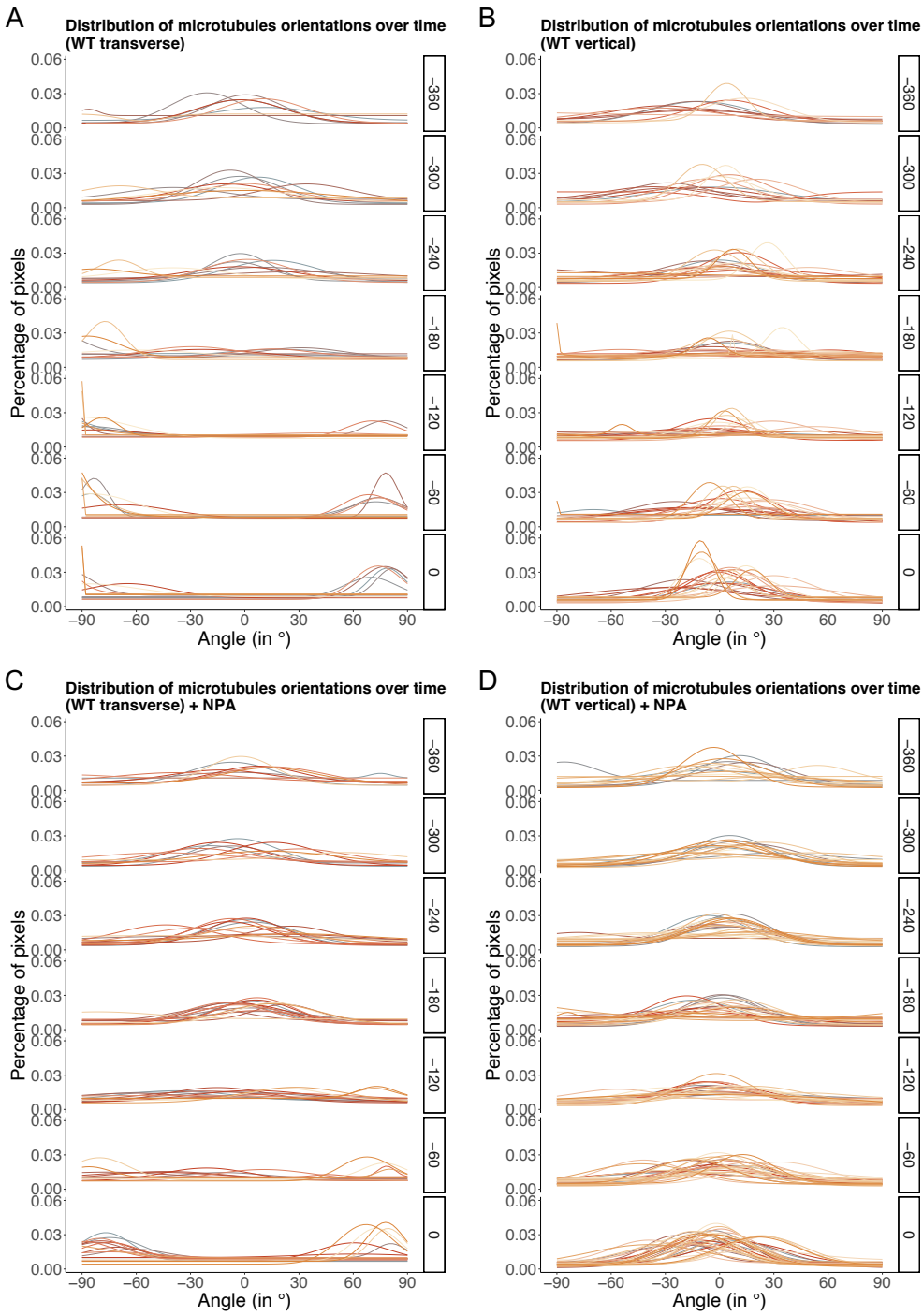

Figure S5. Evolution of CMT orientation over time in WT pre-mitotic cells from the stem, divided in four data subsets.

(A-D) The angle scale varies between -90° and +90°, 0° being the transverse orientation to the stem axis. Each row represents the time before t=0 (last timepoint before the nuclear envelope breakdown). Each color-coded curve represents the results obtained for one cell. The dataset used is the same as the one used for Figures 1G and 2I. (A) Results obtained for cells that produce a preprophase band oriented along the stem axis (i.e. between -30° and 30°), grown on media without NPA. (B) Results obtained for cells that produce a preprophase band oriented transverse to the stem axis (i.e. between -60° and -90°, and between 60° and 90°), grown on media without NPA. (C) Similar to (A), for cells grown on NPA conditions. (D) Similar to (B), for cells grown on NPA conditions.

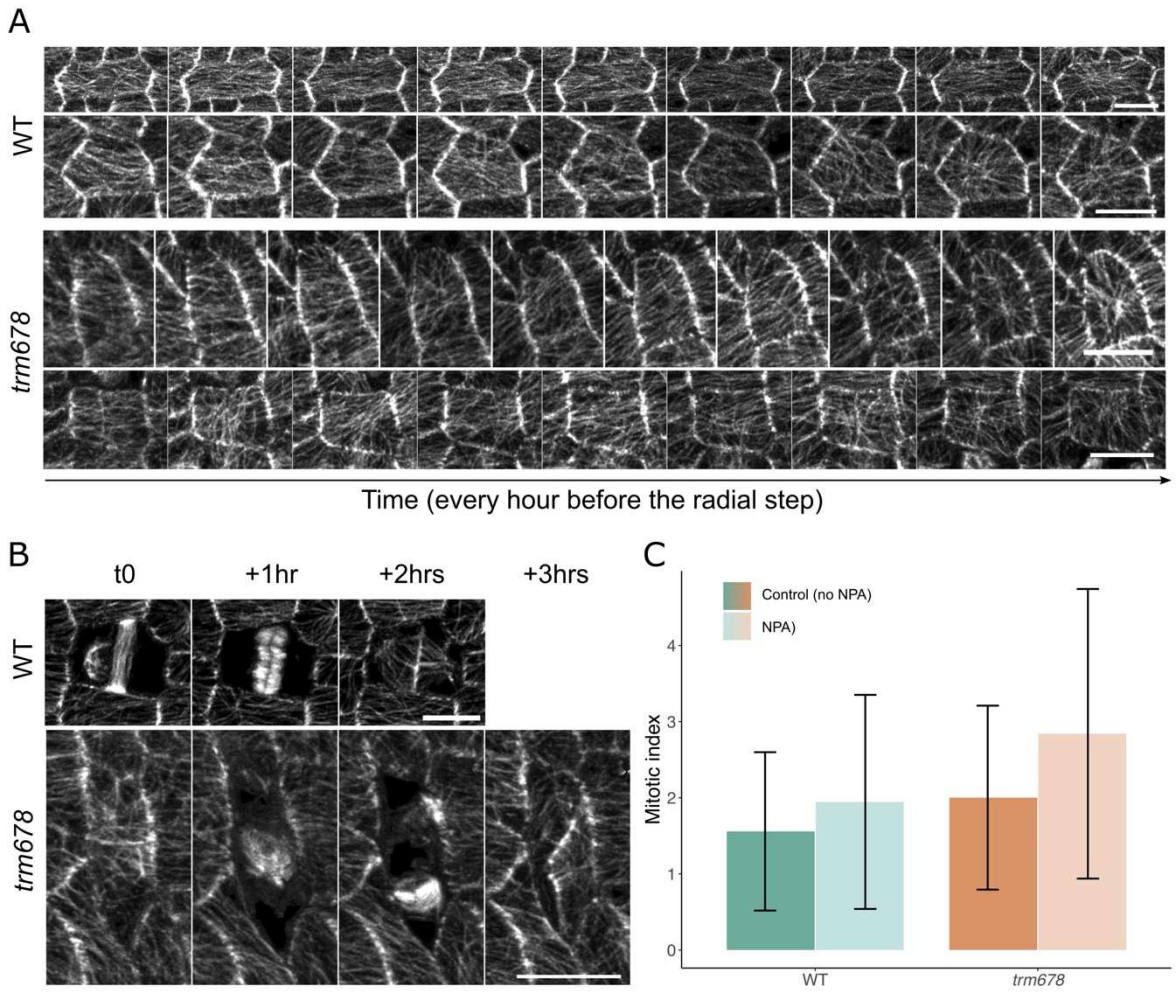

Figure S6. CMT dynamics and mitosis in WT and *trm678*

(A) CMT dynamics before the radial step in the WT and *trm678*. Images were taken every hour. (B) CMT behavior during division in a representative WT cell (top panel) and a representative *trm678* cell (bottom panel). The images are SurfCut projections between 0 and 4 µm from the surface of the stem. (C) Mitotic indexes for cells in both genetic background and in control, or NPA conditions. The mitotic index corresponds to the ratio between mitotic cells (where we can observe spindle or phragmoplast structures) and the total number of cells in the image. *trm678* cells have a slightly higher mitotic index than the WT, and the addition of NPA increases the mitotic index in both backgrounds. $n_{WT,\ control} = 12$; $n_{WT,\ NPA} = 5$; $n_{trm678,\ control} = 16$; $n_{trm678,\ NPA} = 9$. Scale bars: 10 µm. The Brightness&Contrast was modified for better visualization.

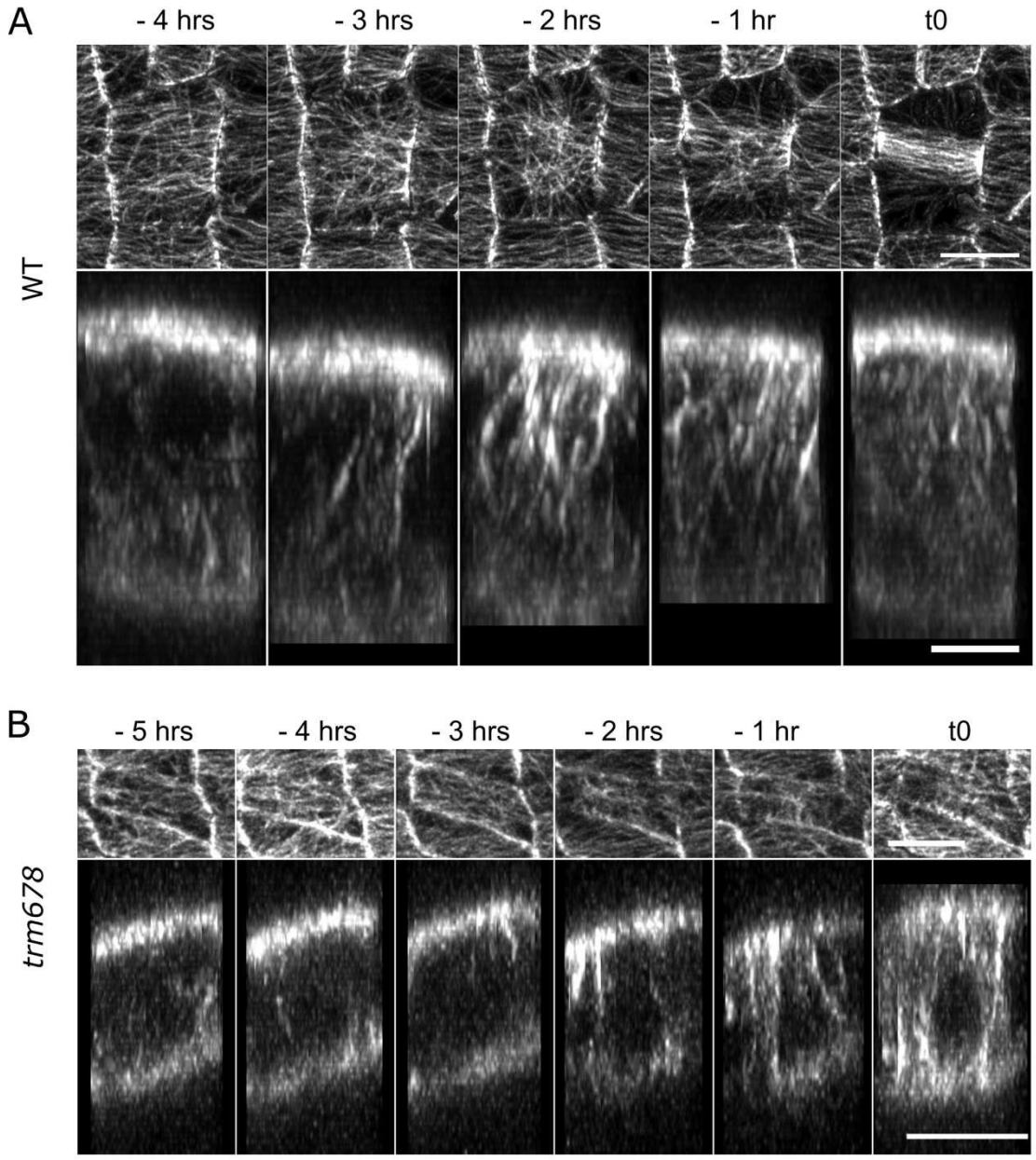

Figure S7. Other examples of the evolution of cytoplasmic microtubule content in pre-mitotic cells.

(A) Time-lapse images of pre-mitotic cells, the top panel being the cortical projection with SurfCut and the bottom panel an orthogonal projection through the cell. Cortex images are 8-bit, with the B&C range varying between 0 and 160, and orthogonal projections are 16-bit, with the B&C range varying between 0 and 2600. (B) Same as (A) but in *trm678* mutant cell. Note that this is an exceptional case where the radial step is short in *trm678*, which allows the visualization of the full sequence: interphase - radial step - mitosis, further showing the correlation between radial step and perinuclear microtubule accumulation. Scale bars: 10 µm (surface projections), 5 µm (XZ orthogonal projections).

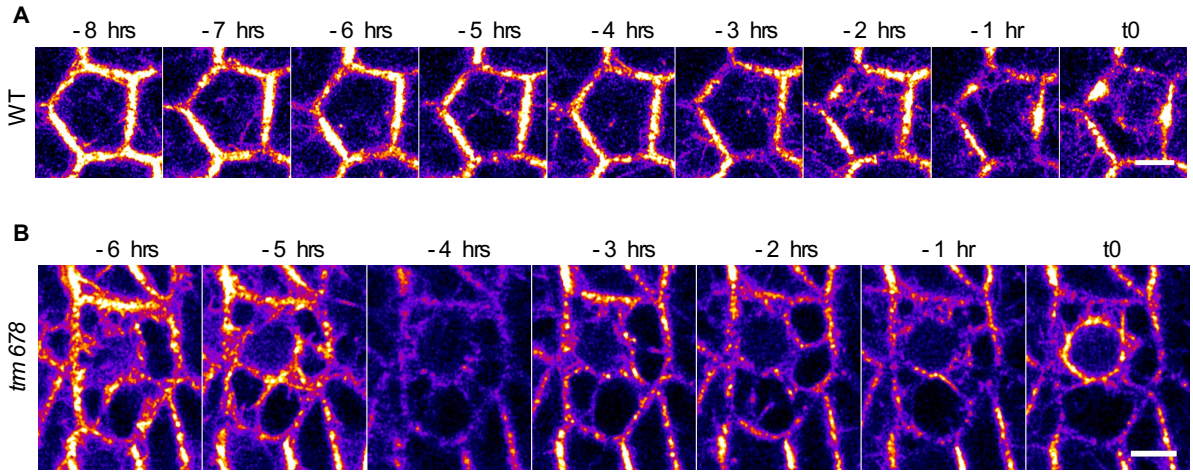

Figure S8. *pPDF1::mCitrine-MBD* signal at the equator of a cell from the stem overtime. (A,B) These images were made showing a single slice of the Z-stack in the middle of the cell. (A) WT cell: these 16-bit images are obtained using the fire Look-up table in Fiji, with the Brightness&Contrast values set between 0 and 1000. (B) *trm678* mutant cell: these 16-bit images are obtained using the fire Look-up table in Fiji, with the Brightness&Contrast values set between 0 and 3000. Scale bars: 5 µm.

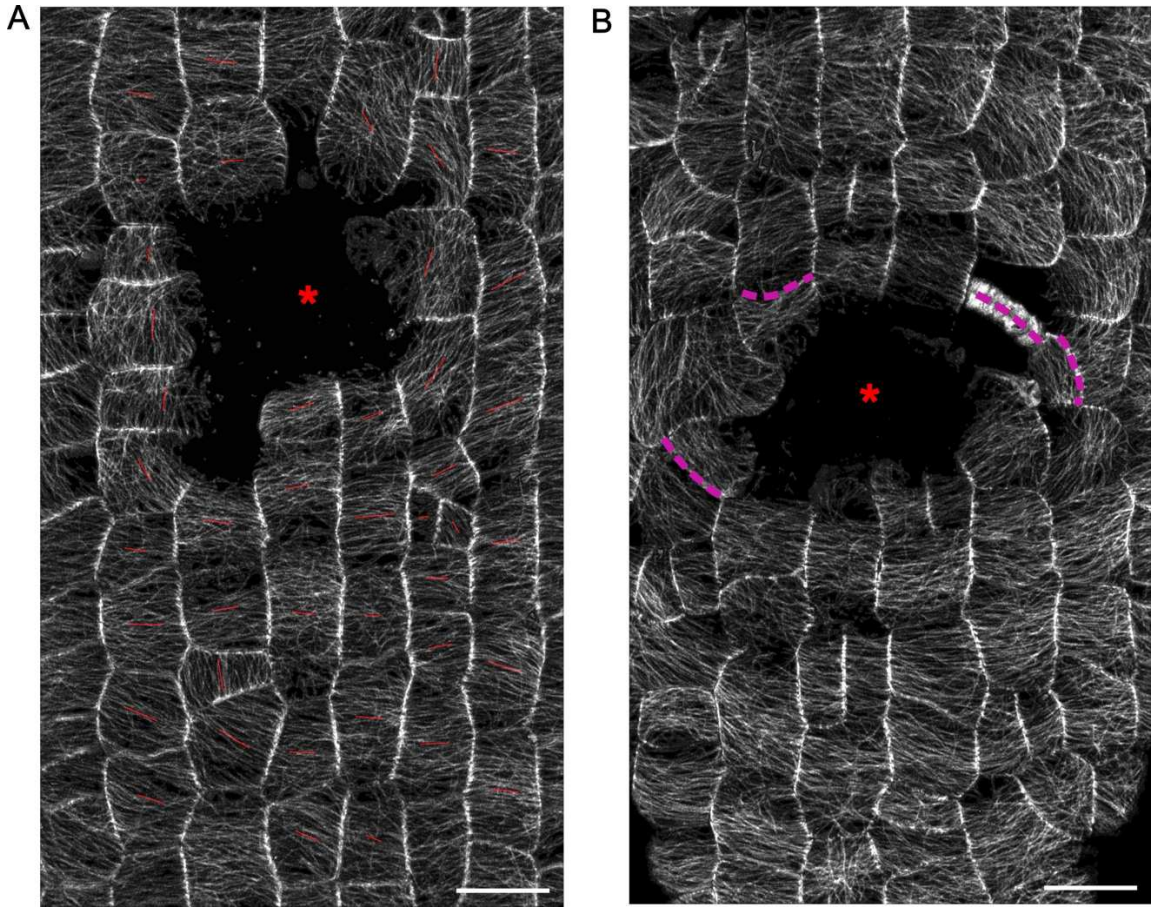

Figure S9. A circumferential tensile stress pattern at ablation sites affect CMT orientation and cell division plane orientations.
(A) This image represents the projection of the *pPDF1::mCitrine*-MBD signal between 0 and 4 µm, using SurfCut. Cells were segmented manually, and the average orientation of CMTs was extracted and displayed, using an automated version of the FibrilTool plugin in Fiji (http://doi.org/10.5281/zenodo.2528872). The red lines represent the average orientation of CMTs per cell. The length of the line corresponds to the anisotropy of the CMT arrays per cell: the longer the line, the higher the anisotropy value. The red star represents the ablation site. The cells around the ablation display CMTs that are aligned circumferentially to the ablation site, following the predicted maximal tensile stress pattern induced by the ablation. The cells far from the ablation display cortical microtubules aligned transversely to the stem, following the predicted maximal tension prescribed by the stem. (B) This image is a SurfCut projection, between 0 and 4 µm from the surface, of the *pPDF1::mCitrine-MBD* signal. An ablation was performed on this stem (red star), and this image corresponds to the last image of a time-lapse experiment, 25 hours after the ablation (the experiment started 15 hours after the ablation). The purple dotted lines highlight the recent division planes (during the time-lapse imaging). The circumferential division planes align with the predicted maximal tensile stress directions prescribed by the ablation. Scale bars: 20 µm. The B&C was modified for better visualization.

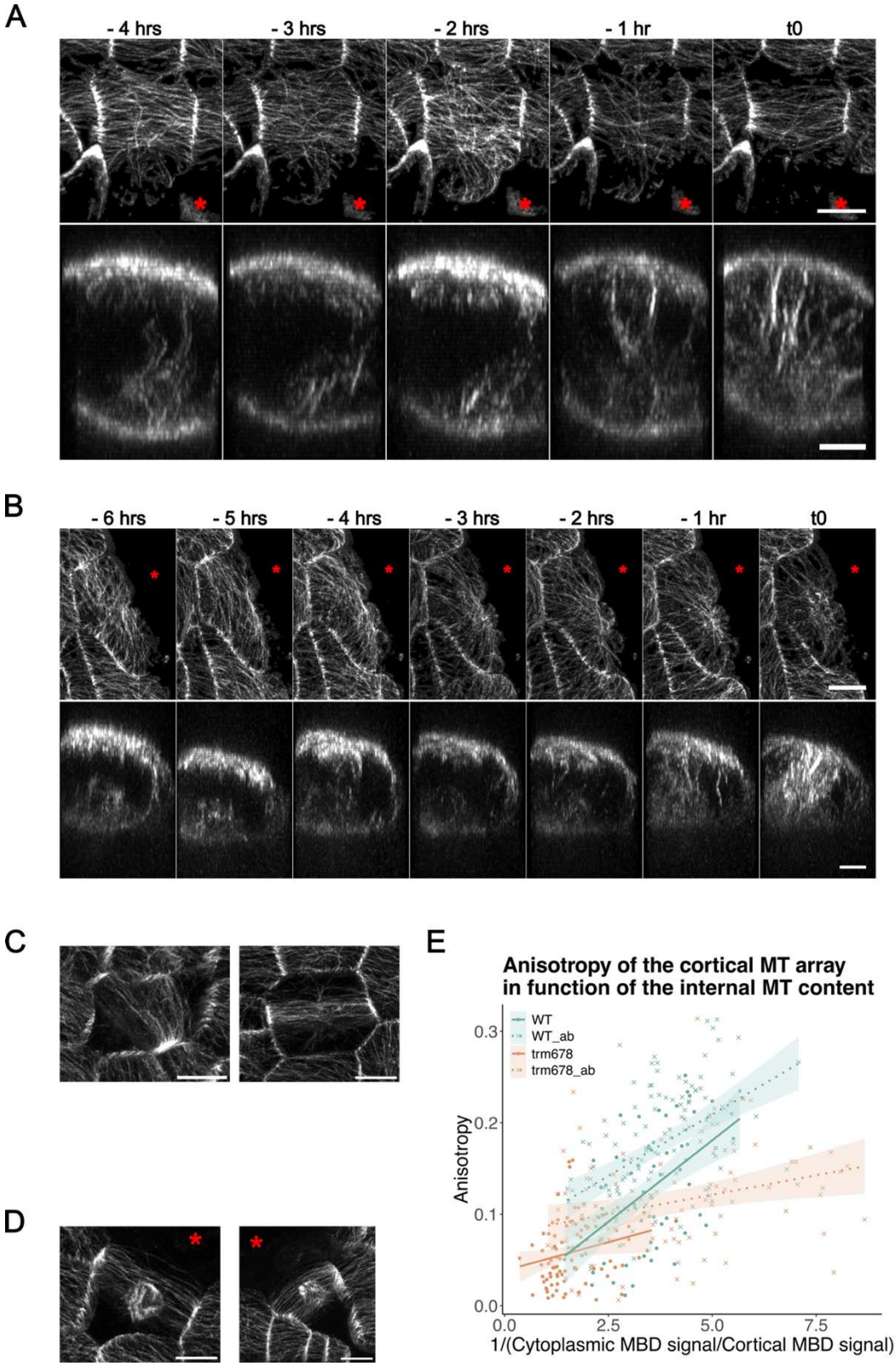

Figure S10. The cytoplasmic microtubule content as the radial step appears in WT and *trm678*, with and without ablations

(A) Time-lapse images of pre-mitotic cells, the top panel being the cortical projection with SurfCut and the bottom panel an orthogonal projection through the cell, in WT cells around an ablation site (red star). Cortex images are 8-bit, with the B&C range varying between 0 and 80, and orthogonal projections are 8-bit, with the B&C range varying between 0 and 50. (B) Same as (A) but in *trm678* mutant cells, around an ablation site. (C) Maximal projection of the *pPDF1::mCitrine-MBD* signal of WT cells at t0, in PPB stage. (D) Same as (C) but in WT cells around an ablation site. Note that in cells around an ablation, the PPB seems slightly wider than in control conditions. Also, no pro-spindles are noticeable before the start of PPB depolymerization in control conditions, while pro-spindles start to form at this stage for cells around an ablation. Cells from (C, D) come from a single stem. (E) Correlation graph between the anisotropy value of the CMT arrays and the cytoplasmic microtubule content. For this graph, all the cells at all timepoints were used, except for WT cells at PPB stage. We can see that the higher the cytoplasmic microtubule content, the lower the anisotropy value. The slopes are $0.04x + 0.003$ for the WT, $0.03x + 0.07$ for the WT around ablations, $0.01 + 0.04$ for *trm678*, and $0.01 + 0.08$ for *trm678* around ablations, with x being the inverse of the ratio of cytoplasmic over cortical MBD signals. While the slopes between WT and *trm678* are slightly different, they are comparable between ablated and control conditions within a genetic background. This graph shows that the dynamics of the anisotropy of the CMT array correlates with the cytoplasmic microtubule content. $n_{\text{WT, control}} = 68$; $n_{\text{WT, ablation}} = 122$; $n_{trm678, \text{control}} = 87$; $n_{trm678, \text{ablation}} = 83$. Scale bars: 10 µm (A, B, surface projections), 5 µm (A, B, XZ orthogonal projections), 10 µm (C, D).

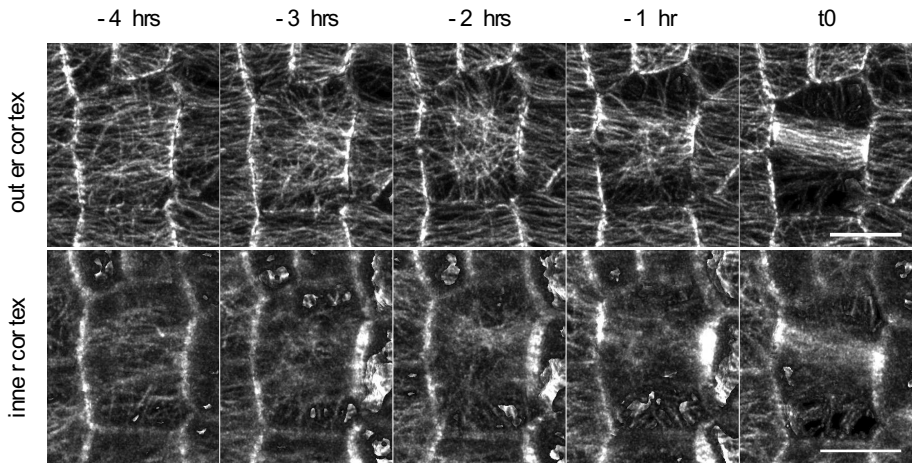

Figure S11. Cortical microtubule dynamics of a pre-mitotic cell, displaying the signal from the periclinal outer (top) and inner (bottom) cortex. The images are SurfCut projections of the *pPDF1::mCitrine-MBD* signal between 0 and 4 µm, either starting from the top (top images) or bottom (bottom images) of the cell. The signal from the inner cortex is noisier due to the weaker signal, and the more difficult extraction of the tissue surface. Scale bars: 10 µm.

A

B

	mCitrine	TdTomato
Laser (λ, power)	514 nm, 0.10 %	561 nm, 0.10 %
Main Beam Splitter	MBS 445/514/561/639	MBS 488/561
Secondary Beam Splitter	SBS SP 615	SBS SP 615
Emission Filters for the Airyscan detector	BP 420-480 + BP 495-550	Plate (transmission 100%)

Figure S12. Protocols: additional data

(A) Step-by-step representation of the stem sample preparation (left to right). First, select a seedling with a stem of around 1.5 cm in length and with a few unopened flower buds. The area of interest (the stem portion under the meristem) is often covered by a few organs. These organs are dissected out in order to expose the area of interest (red arrow). Finally, insert the roots and a few leaves inside the agar to fix the sample, while leaving the area of interest on top of the agar for it to be accessible to the microscope. (B) Airyscan detection parameters.

References

Abas L, Kolb M, Stadlmann J, Janacek D, Lukic K, Schwechheimer C, Sazanov L, Mach L, Friml J, and Hammes U. Naphthylphthalamic acid associates with and inhibits PIN auxin transporters. PNAS. 2021. https://doi.org/10.1073/pnas.2020857118

Ai H, Bellstaedt J, Bartusch KS, Eschen-Lippold L, Babben S, Balcke GU, Tissier A, Hause B, Andersen TG, Delker C, et al. Auxin-dependent regulation of cell division rates governs root thermomorphogenesis. The EMBO Journal. 2023:**42**(11):e111926. https://doi.org/10.15252/embj.2022111926

Akiyoshi B, Sarangapani KK, Powers AF, Nelson CR, Reichow SL, Arellano-Santoyo H, Gonen T, Ranish JA, Asbury CL, and Biggins S. Tension directly stabilizes reconstituted kinetochore-microtubule attachments. Nature. 2010:**468**(7323):576–579. https://doi.org/10.1038/nature09594

Akkerman M, Overdijk EJR, Schel JHN, Emons AMC, and Ketelaar T. Golgi Body Motility in the Plant Cell Cortex Correlates with Actin Cytoskeleton Organization. Plant and Cell Physiology. 2011:**52**(10):1844–1855. https://doi.org/10.1093/pcp/pcr122

Al-Bassam J and Chang F. Regulation of Microtubule Dynamics by TOG-domain proteins XMAP215/Dis1 and CLASP. Trends Cell Biol. 2011:**21**(10):604–614. https://doi.org/10.1016/j.tcb.2011.06.007

Ali I and Yang W-C. The functions of kinesin and kinesin-related proteins in eukaryotes. Cell Adhesion & Migration. 2020:**14**(1):139–152. https://doi.org/10.1080/19336918.2020.1810939

Ali MF and Kawashima T. Formins control dynamics of F-actin in the central cell of Arabidopsis thaliana. Plant Signaling & Behavior. 2021:**16**(8):1920192. https://doi.org/10.1080/15592324.2021.1920192

Ali O, Cheddadi I, Landrein B, and Long Y. Revisiting the relationship between turgor pressure and plant cell growth. New Phytologist. 2023:**238**(1):62–69. https://doi.org/10.1111/nph.18683

Ali S, Khan N, and Xie L. Molecular and Hormonal Regulation of Leaf Morphogenesis in Arabidopsis. IJMS. 2020:**21**(14):5132. https://doi.org/10.3390/ijms21145132

Allard JF, Wasteneys GO, and Cytrynbaum EN. Mechanisms of Self-Organization of Cortical Microtubules in Plants Revealed by Computational Simulations. MBoC. 2010:**21**(2):278–286. https://doi.org/10.1091/mbc.e09-07-0579

Alonso-Serra J, Shi X, Peaucelle A, Rastas P, Bourdon M, Immanen J, Takahashi J, Koivula H, Eswaran G, Muranen S, et al. ELIMÄKI Locus Is Required for Vertical Proprioceptive Response in Birch Trees. Current Biology. 2020:**30**(4):589-599.e5. https://doi.org/10.1016/j.cub.2019.12.016

Ambrose C, Allard JF, Cytrynbaum EN, and Wasteneys GO. A CLASP-modulated cell edge barrier mechanism drives cell-wide cortical microtubule organization in Arabidopsis. Nat Commun. 2011:**2**(1):430. https://doi.org/10.1038/ncomms1444

Ambrose C and Wasteneys GO. Microtubule Initiation from the Nuclear Surface Controls Cortical Microtubule Growth Polarity and Orientation in Arabidopsis thaliana. Plant and Cell Physiology. 2014a:**55**(9):1636–1645. https://doi.org/10.1093/pcp/pcu094

Ambrose C and Wasteneys GO. Microtubule Initiation from the Nuclear Surface Controls Cortical Microtubule Growth Polarity and Orientation in Arabidopsis thaliana. Plant and Cell Physiology. 2014b:**55**(9):1636–1645. https://doi.org/10.1093/pcp/pcu094

Ambrose JC and Cyr R. The Kinesin ATK5 Functions in Early Spindle Assembly in Arabidopsis. Plant Cell. 2007:**19**(1):226–236. https://doi.org/10.1105/tpc.106.047613

Ambrose JC and Cyr R. Mitotic Spindle Organization by the Preprophase Band. Molecular Plant. 2008:**1**(6):950–960. https://doi.org/10.1093/mp/ssn054

Ambrose JC, Li W, Marcus A, Ma H, and Cyr R. A Minus-End–directed Kinesin with Plus-End Tracking Protein Activity Is Involved in Spindle Morphogenesis. MBoC. 2005:**16**(4):1584–1592. https://doi.org/10.1091/mbc.e04-10-0935

Ambrose JC, Shoji T, Kotzer AM, Pighin JA, and Wasteneys GO. The Arabidopsis CLASP Gene Encodes a Microtubule-Associated Protein Involved in Cell Expansion and Division. Plant Cell. 2007:**19**(9):2763–2775. https://doi.org/10.1105/tpc.107.053777

Anten NPR and Schieving F. The Role of Wood Mass Density and Mechanical Constraints in the Economy of Tree Architecture. The American Naturalist. 2010:**175**(2):250–260. https://doi.org/10.1086/649581

Armezzani A, Abad U, Ali O, Robin AA, Vachez L, Larrieu A, Mellerowicz EJ, Taconnat L, Battu V, Stanislas T, et al. Transcriptional induction of cell wall remodelling genes is coupled to microtubule-driven growth isotropy at the shoot apex in Arabidopsis. Development. 2018:dev.162255. https://doi.org/10.1242/dev.162255

Ashraf MA, Liu L, and Facette MR. An outer nuclear membrane protein promotes a polarized nuclear position and the future division plane during asymmetric cell division. 2022.

Assaad FF, Mayer U, Wanner G, and Jürgens G. The KEULE gene is involved in cytokinesis in Arabidopsis. Mol Gen Genet. 1996:**253**(3):267–277. https://doi.org/10.1007/PL00008594

Åström H, Virtanen I, and Raudaskoski M. Cold-stability in the pollen tube cytoskeleton. Protoplasma. 1991:**160**(2–3):99–107. https://doi.org/10.1007/BF01539961

Aumeier C, Schaedel L, Gaillard J, John K, Blanchoin L, and Théry M. Self-repair promotes microtubule rescue. Nat Cell Biol. 2016:**18**(10):1054–1064. https://doi.org/10.1038/ncb3406

Ayaydin F, Vissi E, Mészáros T, Miskolczi P, Kovács I, Fehér A, Dombrádi V, Erdödi F, Gergely P, and Dudits D. Inhibition of serine/threonine-specific protein phosphatases causes premature activation of cdc2MsF kinase at G2/M transition and early mitotic microtubule organisation in alfalfa. The Plant Journal. 2000:**23**(1):85–96. https://doi.org/10.1046/j.1365-313x.2000.00798.x

Azimzadeh J, Nacry P, Christodoulidou A, Drevensek S, Camilleri C, Amiour N, Parcy F, Pastuglia M, and Bouchez D. Arabidopsis TONNEAU1 Proteins Are Essential for Preprophase Band Formation and Interact with Centrin. Plant Cell. 2008:**20**(8):2146–2159. https://doi.org/10.1105/tpc.107.056812

Bakhuizen R, Van Spronsen PC, Sluiman-den Hertog FAJ, Venverloo CJ, and Goosen-de Roo L. Nuclear envelope radiating microtubules in plant cells during interphase mitosis transition. Protoplasma. 1985a:**128**(1):43–51. https://doi.org/10.1007/BF01273234

Bakhuizen R, Van Spronsen PC, Sluiman-den Hertog FAJ, Venverloo CJ, and Goosen-de Roo L. Nuclear envelope radiating microtubules in plant cells during interphase mitosis transition. Protoplasma. 1985b:**128**(1):43–51. https://doi.org/10.1007/BF01273234

Balduzzi M, Binder BM, Bucksch A, Chang C, Hong L, Iyer-Pascuzzi AS, Pradal C, and Sparks EE. Reshaping Plant Biology: Qualitative and Quantitative Descriptors for Plant Morphology. Front Plant Sci. 2017:**08**. https://doi.org/10.3389/fpls.2017.00117

Bar M and Ori N. Leaf development and morphogenesis. Development. 2014:**141**(22):4219–4230. https://doi.org/10.1242/dev.106195

Barbier de Reuille P, Bohn-Courseau I, Ljung K, Morin H, Carraro N, Godin C, and Traas J. Computer simulations reveal properties of the cell-cell signaling network at the shoot apex in Arabidopsis. 2006. https://doi.org/10.1073/pnas.0510130103

Barbier De Reuille P, Routier-Kierzkowska A-L, Kierzkowski D, Bassel GW, Schüpbach T, Tauriello G, Bajpai N, Strauss S, Weber A, Kiss A, et al. MorphoGraphX: A platform for quantifying morphogenesis in 4D. eLife. 2015:**4**:e05864. https://doi.org/10.7554/eLife.05864

Bartolo ME and Carter JV. Microtubules in Mesophyll Cells of Nonacclimated and Cold-Acclimated Spinach 1. Plant Physiol. 1991:**97**(1):175–181.

Baskin TI. ANISOTROPIC EXPANSION OF THE PLANT CELL WALL. Annu Rev Cell Dev Biol. 2005:**21**(1):203–222. https://doi.org/10.1146/annurev.cellbio.20.082503.103053

Baskin TI, Beemster GTS, Judy-March JE, and Marga F. Disorganization of Cortical Microtubules Stimulates Tangential Expansion and Reduces the Uniformity of Cellulose Microfibril Alignment among Cells in the Root of Arabidopsis. Plant Physiol. 2004:**135**(4):2279–2290. https://doi.org/10.1104/pp.104.040493

Bastien R, Bohr T, Moulia B, and Douady S. Unifying model of shoot gravitropism reveals proprioception as a central feature of posture control in plants. Proc Natl Acad Sci USA. 2013:**110**(2):755–760. https://doi.org/10.1073/pnas.1214301109

Batzenschlager M, Masoud K, Janski N, Houlné G, Herzog E, Evrard J-L, Baumberger N, Erhardt M, Nominé Y, Kieffer B, et al. The GIP gamma-tubulin complex-associated proteins are involved in nuclear architecture in Arabidopsis thaliana. Front Plant Sci. 2013:**4**. https://doi.org/10.3389/fpls.2013.00480

Bauer A, Ali O, Bied C, Bœuf S, Bovio S, Delattre A, Ingram G, Golz JF, and Landrein B. Spatiotemporally distinct responses to mechanical forces shape the developing seed of Arabidopsis. EMBO J. 2024:**43**(13):2733–2758. https://doi.org/10.1038/s44318-024-00138-w

Bawa SB and Torrey JG. "Budding" and Nuclear Division in Cultured Protoplasts of Corn, Convolvulus, and Onion. Botanical Gazette. 1971:**132**(3):240–245.

Beauzamy L, Louveaux M, Hamant O, and Boudaoud A. Mechanically, the Shoot Apical Meristem of Arabidopsis Behaves like a Shell Inflated by a Pressure of About 1 MPa. Front Plant Sci. 2015:**6**. https://doi.org/10.3389/fpls.2015.01038

Beeckman T, Przemeck GKH, Stamatiou G, Lau R, Terryn N, De Rycke R, Inzé D, and Berleth T. Genetic Complexity of Cellulose Synthase A Gene Function in Arabidopsis

Embryogenesis. Plant Physiology. 2002:**130**(4):1883–1893. https://doi.org/10.1104/pp.102.010603

Beemster GTS, De Veylder L, Vercruysse S, West G, Rombaut D, Van Hummelen P, Galichet A, Gruissem W, Inzé D, and Vuylsteke M. Genome-Wide Analysis of Gene Expression Profiles Associated with Cell Cycle Transitions in Growing Organs of Arabidopsis. Plant Physiol. 2005:**138**(2):734–743. https://doi.org/10.1104/pp.104.053884

Bellinger MA, Uyehara AN, Allsman L, Martinez P, McCarthy MC, and Rasmussen CG. Cortical microtubules contribute to division plane positioning during telophase in maize. The Plant Cell. 2023:**35**(5):1496–1512. https://doi.org/10.1093/plcell/koad033

Benková E, Ivanchenko MG, Friml J, Shishkova S, and Dubrovsky JG. A morphogenetic trigger: is there an emerging concept in plant developmental biology? Trends in Plant Science. 2009:**14**(4):189–193. https://doi.org/10.1016/j.tplants.2009.01.006

Bergen L, Kuriyama R, and Borisy G. Polarity of microtubules nucleated by centrosomes and chromosomes of Chinese hamster ovary cells in vitro. The Journal of Cell Biology. 1980:**84**(1):151–159. https://doi.org/10.1083/jcb.84.1.151

Bertels J and Beemster GTS. *leafkin* —An R package for automated kinematic data analysis of monocot leaves. Quant Plant Bio. 2020:**1**:e2. https://doi.org/10.1017/qpb.2020.3

Besson S and Dumais J. Universal rule for the symmetric division of plant cells. Proceedings of the National Academy of Sciences. 2011:**108**(15):6294–6299. https://doi.org/10.1073/pnas.1011866108

Bhalerao RP and Bennett MJ. The case for morphogens in plants. Nat Cell Biol. 2003:**5**(11):939–943. https://doi.org/10.1038/ncb1103-939

Bhosale R, Maere S, and De Veylder L. Endoreplication as a potential driver of cell wall modifications. Current Opinion in Plant Biology. 2019:**51**:58–65. https://doi.org/10.1016/j.pbi.2019.04.003

Bi E. Cytokinesis in Budding Yeast: the Relationship between Actomyosin Ring Function and Septum Formation.

Bidhendi AJ and Geitmann A. Relating the mechanics of the primary plant cell wall to morphogenesis. EXBOTJ. 2016:**67**(2):449–461. https://doi.org/10.1093/jxb/erv535

Bidhendi AJ and Geitmann A. Methods to quantify primary plant cell wall mechanics. Journal of Experimental Botany. 2019:**70**(14):3615–3648. https://doi.org/10.1093/jxb/erz281

Binarová P, Cenklová V, Hause B, Kubátová E, Lysák M, Doležel J, Bögre L, and Dráber P. Nuclear γ-Tubulin during Acentriolar Plant Mitosis. Plant Cell. 2000:**12**(3):433–442.

Binarová P, Cenklová V, Procházková J, Doskočilová A, Volc J, Vrlík M, and Bögre L. γ-Tubulin Is Essential for Acentrosomal Microtubule Nucleation and Coordination of Late Mitotic Events in Arabidopsis. Plant Cell. 2006:**18**(5):1199–1212. https://doi.org/10.1105/tpc.105.038364

Blancaflor EB and Hasenstein KH. Growth and Microtubule Orientation of Zea mays Roots Subjected to Osmotic Stress. International Journal of Plant Sciences. 1995:**156**(6):774–783.

Blanchard GB, Kabla AJ, Schultz NL, Butler LC, Sanson B, Gorfinkiel N, Mahadevan L, and Adams RJ. Tissue tectonics: morphogenetic strain rates, cell shape change and intercalation. Nat Methods. 2009:**6**(6):458–464. https://doi.org/10.1038/nmeth.1327

Blanchoin L, Boujemaa-Paterski R, Sykes C, and Plastino J. Actin Dynamics, Architecture, and Mechanics in Cell Motility. Physiological Reviews. 2014:**94**(1):235–263. https://doi.org/10.1152/physrev.00018.2013

Bolhuis DL, Dixit R, and Slep KC. Crystal structure of the Arabidopsis SPIRAL2 C-terminal domain reveals a p80-Katanin-like domain. PLoS ONE. 2023:**18**(12):e0290024. https://doi.org/10.1371/journal.pone.0290024

Boniotti MB and Gutierrez C. A cell-cycle-regulated kinase activity phosphorylates plant retinoblastoma protein and contains, in Arabidopsis, a CDKA/cyclin D complex. The Plant Journal. 2001:**28**(3):341–350. https://doi.org/10.1046/j.1365-313X.2001.01160.x

Borges F, Donoghue MTA, LeBlanc C, Wear EE, Tanurdžić M, Berube B, Brooks A, Thompson WF, Hanley-Bowdoin L, and Martienssen RA. Loss of Small-RNA-Directed DNA Methylation in the Plant Cell Cycle Promotes Germline Reprogramming and Somaclonal Variation. Current Biology. 2021:**31**(3):591-600.e4. https://doi.org/10.1016/j.cub.2020.10.098

Boruc J, Mylle E, Duda M, De Clercq R, Rombauts S, Geelen D, Hilson P, Inzeů D, Van Damme D, and Russinova E. Systematic Localization of the Arabidopsis Core Cell Cycle Proteins Reveals Novel Cell Division Complexes. Plant Physiology. 2010:**152**(2):553–565. https://doi.org/10.1104/pp.109.148643

Boruc J, Weimer AK, Stoppin-Mellet V, Mylle E, Kosetsu K, Cedeño C, Jaquinod M, Njo M, De Milde L, Tompa P, et al. Phosphorylation of MAP65-1 by Arabidopsis Aurora Kinases Is Required for Efficient Cell Cycle Progression. Plant Physiol. 2017:**173**(1):582–599. https://doi.org/10.1104/pp.16.01602

Bouchez D, Uyttewaal M, and Pastuglia M. Spatiotemporal regulation of plant cell division. Current Opinion in Plant Biology. 2024:**79**:102530. https://doi.org/10.1016/j.pbi.2024.102530

Boudaoud A, Burian A, Borowska-Wykręt D, Uyttewaal M, Wrzalik R, Kwiatkowska D, and Hamant O. FibrilTool, an ImageJ plug-in to quantify fibrillar structures in raw microscopy images. Nat Protoc. 2014:**9**(2):457–463. https://doi.org/10.1038/nprot.2014.024

Boudolf V, Inze D, and Deveylder L. What if higher plants lack a CDC25 phosphatase? Trends in Plant Science. 2006:**11**(10):474–479. https://doi.org/10.1016/j.tplants.2006.08.009

Boudolf V, Vlieghe K, Beemster GTS, Magyar Z, Acosta JAT, Maes S, Van Der Schueren E, Inzé D, and De Veylder L. The Plant-Specific Cyclin-Dependent Kinase CDKB1;1 and Transcription Factor E2Fa-DPa Control the Balance of Mitotically Dividing and Endoreduplicating Cells in Arabidopsis. Plant Cell. 2004:**16**(10):2683–2692. https://doi.org/10.1105/tpc.104.024398

Bouton S, Leboeuf E, Mouille G, Leydecker M-T, Talbotec J, Granier F, Lahaye M, Höfte H, and Truong H-N. QUASIMODO1 Encodes a Putative Membrane-Bound Glycosyltransferase Required for Normal Pectin Synthesis and Cell Adhesion in Arabidopsis. Plant Cell. 2002:**14**(10):2577–2590. https://doi.org/10.1105/tpc.004259

Braam J. In touch: plant responses to mechanical stimuli. New Phytologist. 2005:**165**(2):373–389. https://doi.org/10.1111/j.1469-8137.2004.01263.x

Bradley PM. The production of higher plant subprotoplasts. Plant Mol Biol Rep. 1983:**1**(3):117–123. https://doi.org/10.1007/BF02668624

Brandizzi F and Wasteneys GO. Cytoskeleton-dependent endomembrane organization in plant cells: an emerging role for microtubules. The Plant Journal. 2013:**75**(2):339–349. https://doi.org/10.1111/tpj.12227

Braybrook SA and Jönsson H. Shifting foundations: the mechanical cell wall and development. Current Opinion in Plant Biology. 2016:**29**:115–120. https://doi.org/10.1016/j.pbi.2015.12.009

Breuer C, Ishida T, and Sugimoto K. Developmental control of endocycles and cell growth in plants. Current Opinion in Plant Biology. 2010:**13**(6):654–660. https://doi.org/10.1016/j.pbi.2010.10.006

Bringmann M, Landrein B, Schudoma C, Hamant O, Hauser M-T, and Persson S. Cracking the elusive alignment hypothesis: the microtubule–cellulose synthase nexus unraveled. Trends in Plant Science. 2012:**17**(11):666–674. https://doi.org/10.1016/j.tplants.2012.06.003

Brown R, B. L, and H. N. The microtubule cycle during successive mitotic waves in the syncytial female gametophyte of ginkgo. Journal of Plant Research. 2002:**115**(6):491–494. https://doi.org/10.1007/s10265-002-0056-4

Brown RC and Lemmon BE. The cytoskeleton and spatial control of cytokinesis in the plant life cycle. Protoplasma. 2001:**215**(1–4):35–49. https://doi.org/10.1007/BF01280302

Brown S and Spudich J. Cytochalasin inhibits the rate of elongation of actin filament fragments. The Journal of Cell Biology. 1979:**83**(3):657–662. https://doi.org/10.1083/jcb.83.3.657

Bugnard E, Zaal KJM, and Ralston E. Reorganization of microtubule nucleation during muscle differentiation. Cell Motility. 2005:**60**(1):1–13. https://doi.org/10.1002/cm.20042

Burda I, Martin AC, Roeder AHK, and Collins MA. The dynamics and biophysics of shape formation: Common themes in plant and animal morphogenesis. Developmental Cell. 2023:**58**(24):2850–2866. https://doi.org/10.1016/j.devcel.2023.11.003

Burgess J. Interactions between microtubules and the nuclear envelope during mitosis in a fern. Protoplasma. 1970:**71**(1–2):77–89. https://doi.org/10.1007/BF01294304

Burian A, Ludynia M, Uyttewaal M, Traas J, Boudaoud A, Hamant O, and Kwiatkowska D. A correlative microscopy approach relates microtubule behaviour, local organ geometry, and cell growth at the Arabidopsis shoot apical meristem. Journal of Experimental Botany. 2013:**64**(18):5753–5767. https://doi.org/10.1093/jxb/ert352

Burk DH and Ye Z-H. Alteration of Oriented Deposition of Cellulose Microfibrils by Mutation of a Katanin-Like Microtubule-Severing Protein. Plant Cell. 2002:**14**(9):2145–2160. https://doi.org/10.1105/tpc.003947

Burr DB, Robling AG, and Turner CH. Effects of biomechanical stress on bones in animals. Bone.

Buschmann H, Fabri CO, Hauptmann M, Hutzler P, Laux T, Lloyd CW, and Schäffner AR. Helical Growth of the Arabidopsis Mutant tortifolia1 Reveals a Plant-Specific Microtubule-Associated Protein. Current Biology. 2004:**14**(16):1515–1521. https://doi.org/10.1016/j.cub.2004.08.033

Buschmann H, Green P, Sambade A, Doonan JH, and Lloyd CW. Cytoskeletal dynamics in interphase, mitosis and cytokinesis analysed through Agrobacterium-mediated transient transformation of tobacco BY-2 cells. New Phytologist. 2011:**190**(1):258–267. https://doi.org/10.1111/j.1469-8137.2010.03587.x

Buschmann H and Lloyd CW. Arabidopsis Mutants and the Network of Microtubule-Associated Functions. Molecular Plant. 2008:**1**(6):888–898. https://doi.org/10.1093/mp/ssn060

Cai G and Cresti M. Are kinesins required for organelle trafficking in plant cells? Front Plant Sci. 2012:**3**. https://doi.org/10.3389/fpls.2012.00170

Caillaud M-C, Paganelli L, Lecomte P, Deslandes L, Quentin M, Pecrix Y, Le Bris M, Marfaing N, Abad P, and Favery B. Spindle Assembly Checkpoint Protein Dynamics Reveal Conserved and Unsuspected Roles in Plant Cell Division. PLoS ONE. 2009:**4**(8):e6757. https://doi.org/10.1371/journal.pone.0006757

Camilleri C, Azimzadeh J, Pastuglia M, Bellini C, Grandjean O, and Bouchez D. The Arabidopsis TONNEAU2 Gene Encodes a Putative Novel Protein Phosphatase 2A Regulatory Subunit Essential for the Control of the Cortical Cytoskeleton. Plant Cell. 2002:**14**(4):833–845. https://doi.org/10.1105/tpc.010402

Canaday J, Stoppin-Mellet V, Mutterer J, Lambert A-M, and Schmit A-C. Higher plant cells: Gamma-tubulin and microtubule nucleation in the absence of centrosomes. Microscopy Research and Technique. 2000:**49**(5):487–495. https://doi.org/10.1002/(SICI)1097-0029(20000601)49:5<487::AID-JEMT11>3.0.CO;2-I

Carter R, Sánchez-Corrales YE, Hartley M, Grieneisen VA, and Marée AFM. Pavement cells and the topology puzzle. Development. 2017:dev.157073. https://doi.org/10.1242/dev.157073

Cavalier DM, Lerouxel O, Neumetzler L, Yamauchi K, Reinecke A, Freshour G, Zabotina OA, Hahn MG, Burgert I, Pauly M, et al. Disrupting Two *Arabidopsis thaliana* Xylosyltransferase Genes Results in Plants Deficient in Xyloglucan, a Major Primary Cell Wall Component. The Plant Cell. 2008:**20**(6):1519–1537. https://doi.org/10.1105/tpc.108.059873

Chagin VO, Stear JH, and Cardoso MC. Organization of DNA Replication. Cold Spring Harbor Perspectives in Biology. 2010:**2**(4):a000737–a000737. https://doi.org/10.1101/cshperspect.a000737

Chan J, Calder G, Fox S, and Lloyd C. Localization of the Microtubule End Binding Protein EB1 Reveals Alternative Pathways of Spindle Development in Arabidopsis Suspension Cells. Plant Cell. 2005:**17**(6):1737–1748. https://doi.org/10.1105/tpc.105.032615

Chan J, Calder G, Fox S, and Lloyd C. Cortical microtubule arrays undergo rotary movements in Arabidopsis hypocotyl epidermal cells. Nat Cell Biol. 2007:**9**(2):171–175. https://doi.org/10.1038/ncb1533

Chan J and Coen E. Interaction between Autonomous and Microtubule Guidance Systems Controls Cellulose Synthase Trajectories. Current Biology. 2020:**30**(5):941-947.e2. https://doi.org/10.1016/j.cub.2019.12.066

Chanet S, Sharan R, Khan Z, and Martin AC. Myosin 2-Induced Mitotic Rounding Enables Columnar Epithelial Cells to Interpret Cortical Spindle Positioning Cues. Current Biology. 2017:**27**(21):3350-3358.e3. https://doi.org/10.1016/j.cub.2017.09.039

Charrasse S, MM S, Gauthier-Rouviere C, Ango F, Cassimeris L, Gard D, and Larroque C. The TOGp protein is a new human microtubule-associated protein homologous to the Xenopus XMAP215. Journal of cell science. 1998:**111 (Pt 10)**:1371–83. https://doi.org/10.1242/jcs.111.10.1371

Chebli Y and Geitmann A. Cellular growth in plants requires regulation of cell wall biochemistry. Current Opinion in Cell Biology. 2017:**44**:28–35. https://doi.org/10.1016/j.ceb.2017.01.002

Chebli Y, Kaneda M, Zerzour R, and Geitmann A. The Cell Wall of the Arabidopsis Pollen Tube—Spatial Distribution, Recycling, and Network Formation of Polysaccharides. Plant Physiology. 2012:**160**(4):1940–1955. https://doi.org/10.1104/pp.112.199729

Chellappan SP, Hiebert S, Mudryj M, Horowitz JM, and Nevins JR. The E2F transcription factor is a cellular target for the RB protein. Cell. 1991:**65**(6):1053–1061. https://doi.org/10.1016/0092-8674(91)90557-F

Chen J, Chen X, Zhang Q, Zhang Y, Ou X, An L, Feng H, and Zhao Z. A cold-induced pectin methyl-esterase inhibitor gene contributes negatively to freezing tolerance but positively to salt tolerance in Arabidopsis. Journal of Plant Physiology. 2018:**222**:67–78. https://doi.org/10.1016/j.jplph.2018.01.003

Chen P, Takatsuka H, Takahashi N, Kurata R, Fukao Y, Kobayashi K, Ito M, and Umeda M. Arabidopsis R1R2R3-Myb proteins are essential for inhibiting cell division in response to DNA damage. Nat Commun. 2017:**8**(1):635. https://doi.org/10.1038/s41467-017-00676-4

Chen X, Grandont L, Li H, Hauschild R, Paque S, Abuzeineh A, Rakusová H, Benkova E, Perrot-Rechenmann C, and Friml J. Inhibition of cell expansion by rapid ABP1-mediated auxin effect on microtubules. Nature. 2014:**516**(7529):90–93. https://doi.org/10.1038/nature13889

Chumová J, Kourová H, Trögelová L, Halada P, and Binarová P. Microtubular and Nuclear Functions of γ-Tubulin: Are They LINCed? Cells. 2019:**8**(3):259. https://doi.org/10.3390/cells8030259

Chupeau M-C, Granier F, Pichon O, Renou J-P, Gaudin V, and Chupeau Y. Characterization of the Early Events Leading to Totipotency in an *Arabidopsis* Protoplast Liquid Culture by Temporal Transcript Profiling. The Plant Cell. 2013:**25**(7):2444–2463. https://doi.org/10.1105/tpc.113.109538

Chytilova E, Macas J, Sliwinska E, Rafelski SM, Lambert GM, and Galbraith DW. Nuclear Dynamics in *Arabidopsis thaliana*. MBoC. 2000:**11**(8):2733–2741. https://doi.org/10.1091/mbc.11.8.2733

Ciska M, Masuda K, and Moreno Díaz De La Espina S. Lamin-like analogues in plants: the characterization of NMCP1 in Allium cepa. Journal of Experimental Botany. 2013:**64**(6):1553–1564. https://doi.org/10.1093/jxb/ert020

Cleary AL, Gunning BES, Wasteneys GO, and Hepler PK. Microtubule and F-actin dynamics at the division site in living *Tradescantia* stamen hair cells. Journal of Cell Science. 1992:**103**(4):977–988. https://doi.org/10.1242/jcs.103.4.977

Cleary AL and Hardham AR. Reinstatement of Microtubule Arrays from Cortical Nucleating Sites in Stomatal Complexes of Lolium rigidum Following Depolymerization of Microtubules by Oryzalin and High Pressure. Plant and Cell Physiology. 1990. https://doi.org/10.1093/oxfordjournals.pcp.a078004

Cockcroft CE, Den Boer BGW, Healy JMS, and Murray JAH. Cyclin D control of growth rate in plants. Nature. 2000:**405**(6786):575–579. https://doi.org/10.1038/35014621

Coen E and Cosgrove DJ. The mechanics of plant morphogenesis. Science. 2023:**379**(6631):eade8055. https://doi.org/10.1126/science.ade8055

Coen E, Kennaway R, and Whitewoods C. On genes and form. Development. 2017:**144**(23):4203–4213. https://doi.org/10.1242/dev.151910

Coen E, Rolland-Lagan A-G, Matthews M, Bangham JA, and Prusinkiewicz P. The genetics of geometry. 2004. https://www.pnas.org/doi/epdf/10.1073/pnas.0306308101. Retrieved July 5, 2024

Coles CH and Bradke F. Coordinating Neuronal Actin–Microtubule Dynamics. Current Biology. 2015:**25**(15):R677–R691. https://doi.org/10.1016/j.cub.2015.06.020

Colin L, Chevallier A, Tsugawa S, Gacon F, Godin C, Viasnoff V, Saunders TE, and Hamant O. Cortical tension overrides geometrical cues to orient microtubules in confined protoplasts. Proc Natl Acad Sci USA. 2020:**117**(51):32731–32738. https://doi.org/10.1073/pnas.2008895117

Cosgrove DJ. Wall extensibility: its nature, measurement and relationship to plant cell growth. New Phytologist. 1993:**124**(1):1–23. https://doi.org/10.1111/j.1469-8137.1993.tb03795.x

Cosgrove DJ. Growth of the plant cell wall. Nat Rev Mol Cell Biol. 2005:**6**(11):850–861. https://doi.org/10.1038/nrm1746

Cosgrove DJ. Re-constructing our models of cellulose and primary cell wall assembly. Curr Opin Plant Biol. 2014:**22**:122–131. https://doi.org/10.1016/j.pbi.2014.11.001

Cosgrove DJ. Catalysts of plant cell wall loosening. F1000Res. 2016:**5**:119. https://doi.org/10.12688/f1000research.7180.1

Cosgrove DJ. Diffuse Growth of Plant Cell Walls. Plant Physiol. 2018:**176**(1):16–27. https://doi.org/10.1104/pp.17.01541

Cosgrove DJ. Structure and growth of plant cell walls. Nat Rev Mol Cell Biol. 2024:**25**(5):340–358. https://doi.org/10.1038/s41580-023-00691-y

Coudreuse D and Nurse P. Driving the cell cycle with a minimal CDK control network. Nature. 2010:**468**(7327):1074–1079. https://doi.org/10.1038/nature09543

Culligan K, Tissier A, and Britt A. ATR Regulates a G2-Phase Cell-Cycle Checkpoint in Arabidopsis thaliana. Plant Cell. 2004:**16**(5):1091–1104. https://doi.org/10.1105/tpc.018903

Dahiya P and Bürstenbinder K. The making of a ring: Assembly and regulation of microtubule-associated proteins during preprophase band formation and division plane set-up. Current Opinion in Plant Biology. 2023:**73**:102366. https://doi.org/10.1016/j.pbi.2023.102366

Damm B and Willmitzer L. Regeneration of fertile plants from protoplasts of different Arabidopsis thaliana genotypes. Molec Gen Genet. 1988:**213**(1):15–20. https://doi.org/10.1007/BF00333392

Dantas M, Lima JT, and Ferreira JG. Nucleus-Cytoskeleton Crosstalk During Mitotic Entry. Front Cell Dev Biol. 2021:**9**:649899. https://doi.org/10.3389/fcell.2021.649899

D'Ario M, Tavares R, Schiessl K, Desvoyes B, Gutierrez C, Howard M, and Sablowski R. Cell size controlled in plants using DNA content as an internal scale. Science. 2021:**372**(6547):1176–1181. https://doi.org/10.1126/science.abb4348

Davis LJ, Odde DJ, Block SM, and Gross SP. The Importance of Lattice Defects in Katanin-Mediated Microtubule Severing in Vitro. Biophysical Journal. 2002:**82**(6):2916–2927. https://doi.org/10.1016/S0006-3495(02)75632-4

De Schutter K, Joubès J, Cools T, Verkest A, Corellou F, Babiychuk E, Van Der Schueren E, Beeckman T, Kushnir S, Inzé D, et al. *Arabidopsis* WEE1 Kinase Controls Cell Cycle Arrest in Response to Activation of the DNA Integrity Checkpoint. The Plant Cell. 2007:**19**(1):211–225. https://doi.org/10.1105/tpc.106.045047

De Veylder L and Beeckman T. The ins and outs of the plant cell cycle. Nature reviews Molecular cell biology. 2007:**8**:655–65. https://doi.org/10.1038/nrm2227

De Veylder L, Beeckman T, Beemster GTS, De Almeida Engler J, Ormenese S, Maes S, Naudts M, Van Der Schueren E, Jacqmard A, Engler G, et al. Control of proliferation, endoreduplication and differentiation by the *Arabidopsis* E2Fa-DPa transcription factor. The EMBO Journal. 2002:**21**(6):1360–1368. https://doi.org/10.1093/emboj/21.6.1360

De Veylder L, Beeckman T, Beemster GTS, Krols L, Terras F, Landrieu I, Van Der Schueren E, Maes S, Naudts M, and Inzé D. Functional Analysis of Cyclin-Dependent Kinase Inhibitors of Arabidopsis. Plant Cell. 2001:**13**(7):1653–1668. https://doi.org/10.1105/TPC.010087

De Veylder L, Joubès J, and Inzé D. Plant cell cycle transitions. Current Opinion in Plant Biology. 2003:**6**(6):536–543. https://doi.org/10.1016/j.pbi.2003.09.001

Deeks MJ and Hussey PJ. Arp2/3 and 'The Shape of things to come.' Current Opinion in Plant Biology. 2003:**6**(6):561–567. https://doi.org/10.1016/j.pbi.2003.09.013

Deinum EE and Mulder BM. Modelling the role of microtubules in plant cell morphology. Current Opinion in Plant Biology. 2013:**16**(6):688–692. https://doi.org/10.1016/j.pbi.2013.10.001

Deinum EE, Tindemans SH, Lindeboom JJ, and Mulder BM. How selective severing by katanin promotes order in the plant cortical microtubule array. Proc Natl Acad Sci USA. 2017:**114**(27):6942–6947. https://doi.org/10.1073/pnas.1702650114

Desai A and Mitchison TJ. MICROTUBULE POLYMERIZATION DYNAMICS. Annu Rev Cell Dev Biol. 1997:**13**(1):83–117. https://doi.org/10.1146/annurev.cellbio.13.1.83

Desvoyes B, FernÃ¡ndez-Marcos M, Sequeira-Mendes J, Otero S, Vergara Z, and Gutierrez C. Looking at plant cell cycle from the chromatin window. Front Plant Sci. 2014:**5**. https://doi.org/10.3389/fpls.2014.00369

Desvoyes B and Gutierrez C. Roles of plant retinoblastoma protein: cell cycle and beyond. The EMBO Journal. 2020:**39**(19):e105802. https://doi.org/10.15252/embj.2020105802

Desvoyes B, Ramirez-Parra E, Xie Q, Chua N-H, and Gutierrez C. Cell Type-Specific Role of the Retinoblastoma/E2F Pathway during Arabidopsis Leaf Development. Plant Physiol. 2006:**140**(1):67–80. https://doi.org/10.1104/pp.105.071027

Dewitte W and Murray JAH. The Plant Cell Cycle. Annu Rev Plant Biol. 2003:**54**(1):235–264. https://doi.org/10.1146/annurev.arplant.54.031902.134836

Dewitte W, Riou-Khamlichi C, Scofield S, Healy JMS, Jacqmard A, Kilby NJ, and Murray JAH. Altered Cell Cycle Distribution, Hyperplasia, and Inhibited Differentiation in Arabidopsis Caused by the D-Type Cyclin CYCD3. Plant Cell. 2003:**15**(1):79–92. https://doi.org/10.1105/tpc.004838

Dhonukshe P, Mathur J, Hülskamp M, and Gadella TW. Microtubule plus-ends reveal essential links between intracellular polarization and localized modulation of endocytosis during division-plane establishment in plant cells. BMC Biol. 2005:**3**(1):11. https://doi.org/10.1186/1741-7007-3-11

Diaz-Benjumea F. Interaction between dorsal and ventral cells in the imaginal disc directs wing development in Drosophila. Cell. 1993:**75**(4):741–752. https://doi.org/10.1016/0092-8674(93)90494-B

Dixit R and Cyr R. Encounters between Dynamic Cortical Microtubules Promote Ordering of the Cortical Array through Angle-Dependent Modifications of Microtubule Behavior. Plant Cell. 2004:**16**(12):3274–3284. https://doi.org/10.1105/tpc.104.026930

Djakovic S, Dyachok J, Burke M, Frank MJ, and Smith LG. BRICK1/HSPC300 functions with SCAR and the ARP2/3 complex to regulate epidermal cell shape in *Arabidopsis*. Development. 2006:**133**(6):1091–1100. https://doi.org/10.1242/dev.02280

Dogterom M, Kerssemakers JW, Romet-Lemonne G, and Janson ME. Force generation by dynamic microtubules. Current Opinion in Cell Biology. 2005:**17**(1):67–74. https://doi.org/10.1016/j.ceb.2004.12.011

Dolan L, Janmaat K, Willemsen VA, Linstead P, Poethig S, Roberts K, and Scheres B. Cellular organisation of the Arabidopsis thaliana root. Development (Cambridge, England). 1993:**119**:71–84. https://doi.org/10.1242/dev.119.1.71

Doniwa Y, Arimura S, and Tsutsumi N. Mitochondria use actin filaments as rails for fast translocation in Arabidopsis and tobacco cells. Plant Biotechnology. 2007a:**24**(5):441–447. https://doi.org/10.5511/plantbiotechnology.24.441

Doniwa Y, Arimura S, and Tsutsumi N. Mitochondria use actin filaments as rails for fast translocation in Arabidopsis and tobacco cells. Plant Biotechnology. 2007b:**24**(5):441–447. https://doi.org/10.5511/plantbiotechnology.24.441

Doumane M and Caillaud M-C. Assessing Extrinsic Membrane Protein Dependency to PI4P Using a Plasma Membrane to Endosome Relocalization Transient Assay in Nicotiana benthamiana. . In. Plant Endosomes, MS Otegui, ed, Methods in Molecular Biology. (Springer US: New York, NY), pp. 95–108. https://doi.org/10.1007/978-1-0716-0767-1_9

Dovzhenko A, Dal Bosco C, Meurer J, and Koop HU. Efficient regeneration from cotyledon protoplasts in Arabidopsis thaliana. Protoplasma. 2003:**222**(1–2):107–111. https://doi.org/10.1007/s00709-003-0011-9

Draget KI, Skjåk-Bræk G, Christensen BE, Gåserød O, and Smidsrød O. Swelling and partial solubilization of alginic acid gel beads in acidic buffer. Carbohydrate Polymers. 1996:**29**(3):209–215. https://doi.org/10.1016/0144-8617(96)00029-X

Drasdo D. Buckling Instabilities of One-Layered Growing Tissues. Phys Rev Lett. 2000:**84**(18):4244–4247. https://doi.org/10.1103/PhysRevLett.84.4244

Drevensek S, Goussot M, Duroc Y, Christodoulidou A, Steyaert S, Schaefer E, Duvernois E, Grandjean O, Vantard M, Bouchez D, et al. The Arabidopsis TRM1–TON1 Interaction Reveals a Recruitment Network Common to Plant Cortical Microtubule Arrays and Eukaryotic Centrosomes[C][W]. Plant Cell. 2012:**24**(1):178–191. https://doi.org/10.1105/tpc.111.089748

Driouich A, Follet-Gueye M-L, Bernard S, Kousar S, Chevalier L, Vicré-Gibouin M, and Lerouxel O. Golgi-Mediated Synthesis and Secretion of Matrix Polysaccharides of the Primary Cell Wall of Higher Plants. Front Plant Sci. 2012:**3**. https://doi.org/10.3389/fpls.2012.00079

Dumais J. Can mechanics control pattern formation in plants? Current Opinion in Plant Biology. 2007:**10**(1):58–62. https://doi.org/10.1016/j.pbi.2006.11.014

Dumais J and Kwiatkowska D. Analysis of surface growth in shoot apices. The Plant Journal. 2002:**31**(2):229–241. https://doi.org/10.1046/j.1365-313X.2001.01350.x

Dumais J and Steele CR. New Evidence for the Role of Mechanical Forces in the Shoot Apical Meristem. J Plant Growth Regul. 2000:**19**(1):7–18. https://doi.org/10.1007/s003440000003

Durand-Smet P, Spelman TA, Meyerowitz EM, and Jönsson H. Cytoskeletal organization in isolated plant cells under geometry control. Proc Natl Acad Sci USA. 2020:**117**(29):17399–17408. https://doi.org/10.1073/pnas.2003184117

Echevin E, Le Gloanec C, Skowrońska N, Routier-Kierzkowska A-L, Burian A, and Kierzkowski D. Growth and biomechanics of shoot organs. Journal of Experimental Botany. 2019:**70**(14):3573–3585. https://doi.org/10.1093/jxb/erz205

Eden S, Rohatgi R, Podtelejnikov AV, Mann M, and Kirschner MW. Mechanism of regulation of WAVE1-induced actin nucleation by Rac1 and Nck. Nature. 2002:**418**(6899):790–793. https://doi.org/10.1038/nature00859

Edgar BA, Zielke N, and Gutierrez C. Endocycles: a recurrent evolutionary innovation for post-mitotic cell growth. Nat Rev Mol Cell Biol. 2014:**15**(3):197–210. https://doi.org/10.1038/nrm3756

Ehrhardt DW and Shaw SL. MICROTUBULE DYNAMICS AND ORGANIZATION IN THE PLANT CORTICAL ARRAY. Annu Rev Plant Biol. 2006:**57**(1):859–875. https://doi.org/10.1146/annurev.arplant.57.032905.105329

Eldridge T, Łangowski Ł, Stacey N, Jantzen F, Moubayidin L, Sicard A, Southam P, Kennaway R, Lenhard M, Coen ES, et al. Fruit shape diversity in the Brassicaceae is generated by varying patterns of anisotropy. Development. 2016:**143**(18):3394–3406. https://doi.org/10.1242/dev.135327

Eloy C. Leonardo's Rule, Self-Similarity, and Wind-Induced Stresses in Trees. Phys Rev Lett. 2011:**107**(25):258101. https://doi.org/10.1103/PhysRevLett.107.258101

Eng RC, Schneider R, Matz TW, Carter R, Ehrhardt DW, Jönsson H, Nikoloski Z, and Sampathkumar A. KATANIN and CLASP function at different spatial scales to mediate microtubule response to mechanical stress in Arabidopsis cotyledons. Current Biology. 2021:**31**(15):3262-3274.e6. https://doi.org/10.1016/j.cub.2021.05.019

Entchev EV, Schwabedissen A, and González-Gaitán M. Gradient Formation of the TGF-β Homolog Dpp. 2000.

Eren EC, Dixit R, and Gautam N. A Three-Dimensional Computer Simulation Model Reveals the Mechanisms for Self-Organization of Plant Cortical Microtubules into Oblique Arrays. MBoC. 2010:**21**(15):2674–2684. https://doi.org/10.1091/mbc.e10-02-0136

Erguvan Ö, Louveaux M, Hamant O, and Verger S. ImageJ SurfCut: a user-friendly pipeline for high-throughput extraction of cell contours from 3D image stacks. BMC Biol. 2019:**17**(1):38. https://doi.org/10.1186/s12915-019-0657-1

Erhardt M, Stoppin-Mellet V, Campagne S, Canaday J, Mutterer J, Fabian T, Sauter M, Muller T, Peter C, Lambert A-M, et al. The plant Spc98p homologue colocalizes with γ-tubulin at microtubule nucleation sites and is required for microtubule nucleation. Journal of Cell Science. 2002:**115**(11):2423–2431. https://doi.org/10.1242/jcs.115.11.2423

Errera L. Sur une condition fondamentale d'équilibre des cellules vivantes. Annales de la Société belge de microscopie (1876). 1886:**13**(1):12–16.

Fache V, Gaillard J, Van Damme D, Geelen D, Neumann E, Stoppin-Mellet V, and Vantard M. *Arabidopsis* Kinetochore Fiber-Associated MAP65-4 Cross-Links Microtubules and Promotes Microtubule Bundle Elongation. The Plant Cell. 2010:**22**(11):3804–3815. https://doi.org/10.1105/tpc.110.080606

Fal K, Korsbo N, Alonso-Serra J, Teles J, Liu M, Refahi Y, Chabouté M-E, Jönsson H, and Hamant O. Tissue folding at the organ–meristem boundary results in nuclear compression and chromatin compaction. 2021. https://www.pnas.org/doi/10.1073/pnas.2017859118. Retrieved April 8, 2024

Fan Y, Burkart GM, and Dixit R. The Arabidopsis SPIRAL2 Protein Targets and Stabilizes Microtubule Minus Ends. Current Biology. 2018:**28**(6):987-994.e3. https://doi.org/10.1016/j.cub.2018.02.014

Farré EM. The regulation of plant growth by the circadian clock. Plant Biology. 2012:**14**(3):401–410. https://doi.org/10.1111/j.1438-8677.2011.00548.x

Fededa JP and Gerlich DW. Molecular control of animal cell cytokinesis. Nat Cell Biol. 2012:**14**(5):440–447. https://doi.org/10.1038/ncb2482

Feraru E and Friml J. PIN Polar Targeting. Plant Physiol. 2008:**147**(4):1553–1559. https://doi.org/10.1104/pp.108.121756

Finegan TM, Na D, Cammarota C, Skeeters AV, Nádasi TJ, Dawney NS, Fletcher AG, Oakes PW, and Bergstralh DT. Tissue tension and not interphase cell shape determines cell division orientation in the *Drosophila* follicular epithelium. EMBO J. 2019:**38**(3). https://doi.org/10.15252/embj.2018100072

Fisher K and Turner S. PXY, a Receptor-like Kinase Essential for Maintaining Polarity during Plant Vascular-Tissue Development. Current Biology. 2007:**17**(12):1061–1066. https://doi.org/10.1016/j.cub.2007.05.049

Flanders DJ, Rawlins DJ, Shaw PJ, and Lloyd CW. Nucleus-associated microtubules help determine the division plane of plant epidermal cells: avoidance of four-way junctions and the role of cell geometry. The Journal of cell biology. 1990:**110**(4):1111–1122. https://doi.org/10.1083/jcb.110.4.1111

Fleming AJ. The co-ordination of cell division, differentiation and morphogenesis in the shoot apical meristem: a perspective. Journal of Experimental Botany. 2006:**57**(1):25–32. https://doi.org/10.1093/jxb/eri268

Fleming AJ, McQueen-Mason S, Mandel T, and Kuhlemeier C. Induction of Leaf Primordia by the Cell Wall Protein Expansin. Science. 1997:**276**(5317):1415–1418. https://doi.org/10.1126/science.276.5317.1415

Fletcher DA and Mullins RD. Cell mechanics and the cytoskeleton. Nature. 2010:**463**(7280):485–492. https://doi.org/10.1038/nature08908

Fragkos M, Ganier O, Coulombe P, and Mechali M. DNA replication origin activation in space and time. Nature reviews Molecular cell biology. 2015:**16**:360–74. https://doi.org/10.1038/nrm4002

Francis D. The plant cell cycle − 15 years on. New Phytologist. 2007:**174**(2):261–278. https://doi.org/10.1111/j.1469-8137.2007.02038.x

Frank M, Egile C, Dyachok J, Djakovic S, Nolasco M, Li R, and Smith LG. Activation of Arp2/3 complex-dependent actin polymerization by plant proteins distantly related to Scar/WAVE. PNAS. 2004. https://doi.org/10.1073/pnas.0407392101

Frey N, Klotz J, and Nick P. A kinesin with calponin-homology domain is involved in premitotic nuclear migration. Journal of Experimental Botany. 2010:**61**(12):3423–3437. https://doi.org/10.1093/jxb/erq164

Frixione E. Recurring views on the structure and function of the cytoskeleton: A 300-Year Epic. Cell Motility. 2000:**46**(2):73–94. https://doi.org/10.1002/1097-0169(200006)46:2<73::AID-CM1>3.0.CO;2-0

Fry AM, O'Regan L, Sabir SR, and Bayliss R. Cell cycle regulation by the NEK family of protein kinases. Journal of Cell Science. 2012:jcs.111195. https://doi.org/10.1242/jcs.111195

Fu Y, Xu T, Zhu L, Wen M, and Yang Z. A ROP GTPase Signaling Pathway Controls Cortical Microtubule Ordering and Cell Expansion in Arabidopsis. Current Biology. 2009:**19**(21):1827–1832. https://doi.org/10.1016/j.cub.2009.08.052

Fujita M, Himmelspach R, Ward J, Whittington A, Hasenbein N, Liu C, Truong TT, Galway ME, Mansfield SD, Hocart CH, et al. The *anisotropy1* D604N Mutation in the Arabidopsis Cellulose Synthase1 Catalytic Domain Reduces Cell Wall Crystallinity and the Velocity of Cellulose Synthase Complexes. Plant Physiology. 2013:**162**(1):74–85. https://doi.org/10.1104/pp.112.211565

Fung-Uceda J, Lee K, Seo PJ, Polyn S, De Veylder L, and Mas P. The Circadian Clock Sets the Time of DNA Replication Licensing to Regulate Growth in Arabidopsis. Developmental Cell. 2018:**45**(1):101-113.e4. https://doi.org/10.1016/j.devcel.2018.02.022

Furutani I, Watanabe Y, Prieto R, Masukawa M, Suzuki K, Naoi K, Thitamadee S, Shikanai T, and Hashimoto T. The SPIRAL genes are required for directional control of cell elongation in Arabidopsis thaliana. Development (Cambridge, England). 2000:**127**:4443–53. https://doi.org/10.1242/dev.127.20.4443

Galatis B, Apostolakos P, Katsaros Chr, and Loukari H. Pre-prophase Microtubule Band and Local Wall Thickening in Guard Cell Mother Cells of Some Leguminosae. Annals of Botany. 1982:**50**(6):779–791. https://doi.org/10.1093/oxfordjournals.aob.a086422

Galletti R, Verger S, Hamant O, and Ingram GC. Developing a 'thick skin': a paradoxical role for mechanical tension in maintaining epidermal integrity? Development. 2016:**143**(18):3249–3258. https://doi.org/10.1242/dev.132837

Galvan-Ampudia CS, Cerutti G, Legrand J, Brunoud G, Martin-Arevalillo R, Azais R, Bayle V, Moussu S, Wenzl C, Jaillais Y, et al. Temporal integration of auxin information for the regulation of patterning. eLife. 2020:**9**:e55832. https://doi.org/10.7554/eLife.55832

Gälweiler L, Guan C, Müller A, Wisman E, Mendgen K, Yephremov A, and Palme K. Regulation of Polar Auxin Transport by AtPIN1 in *Arabidopsis* Vascular Tissue. Science. 1998:**282**(5397):2226–2230. https://doi.org/10.1126/science.282.5397.2226

Gao J and Nakamura F. Actin-Associated Proteins and Small Molecules Targeting the Actin Cytoskeleton. IJMS. 2022:**23**(4):2118. https://doi.org/10.3390/ijms23042118

García-González J and Van Gelderen K. Bundling up the Role of the Actin Cytoskeleton in Primary Root Growth. Front Plant Sci. 2021:**12**:777119. https://doi.org/10.3389/fpls.2021.777119

Gardner MK, Charlebois BD, Jánosi IM, Howard J, Hunt AJ, and Odde DJ. Rapid Microtubule Self-Assembly Kinetics. Cell. 2011:**146**(4):582–592. https://doi.org/10.1016/j.cell.2011.06.053

Gardner MK, Zanic M, and Howard J. Microtubule Catastrophe and Rescue. Curr Opin Cell Biol. 2013:**25**(1):14–22. https://doi.org/10.1016/j.ceb.2012.09.006

Giacomello S. A new era for plant science: spatial single-cell transcriptomics. Current Opinion in Plant Biology. 2021:**60**:102041. https://doi.org/10.1016/j.pbi.2021.102041

Gibbon BC, Kovar DR, and Staiger CJ. Latrunculin B has different effects on pollen germination and tube growth. Plant Cell. 1999:**11**(12):2349–2363.

Gigli-Bisceglia N, Engelsdorf T, Strnad M, Vaahtera L, Khan GA, Jamoune A, Alipanah L, Novák O, Persson S, Hejatko J, et al. Cell wall integrity modulates *Arabidopsis thaliana* cell

cycle gene expression in a cytokinin- and nitrate reductase-dependent manner. Development. 2018:dev.166678. https://doi.org/10.1242/dev.166678

Gildersleeve RF, Cross AR, Cullen KE, Fagen AP, and Williams RC. Microtubules grow and shorten at intrinsically variable rates. Journal of Biological Chemistry. 1992:**267**(12):7995–8006. https://doi.org/10.1016/S0021-9258(18)42399-X

Gillespie T, Boevink P, Haupt S, Roberts AG, Toth R, Valentine T, Chapman S, and Oparka KJ. Functional Analysis of a DNA-Shuffled Movement Protein Reveals That Microtubules Are Dispensable for the Cell-to-Cell Movement of Tobacco mosaic virus. Plant Cell. 2002:**14**(6):1207–1222. https://doi.org/10.1105/tpc.002303

Gilliland LU, Kandasamy MK, Pawloski LC, and Meagher RB. Both Vegetative and Reproductive Actin Isovariants Complement the Stunted Root Hair Phenotype of the Arabidopsis act2-1 Mutation. Plant Physiol. 2002:**130**(4):2199–2209. https://doi.org/10.1104/pp.014068

Gjorevski N and Nelson CM. The mechanics of development: Models and methods for tissue morphogenesis. Birth Defects Research Part C: Embryo Today: Reviews. 2010:**90**(3):193–202. https://doi.org/10.1002/bdrc.20185

Glotzer M. Animal Cell Cytokinesis. Annu Rev Cell Dev Biol. 2001:**17**(1):351–386. https://doi.org/10.1146/annurev.cellbio.17.1.351

Godínez-Palma SK, Rosas-Bringas FR, Rosas-Bringas OG, García-Ramírez E, Zamora-Zaragoza J, and Vázquez-Ramos JM. Two maize Kip-related proteins differentially interact with, inhibit and are phosphorylated by cyclin D–cyclin-dependent kinase complexes. Journal of Experimental Botany. 2017:**68**(7):1585–1597. https://doi.org/10.1093/jxb/erx054

Gong Y, Mo C, and Fraser SE. Planar cell polarity signalling controls cell division orientation during zebrafish gastrulation. Nature. 2004:**430**(7000):689–693. https://doi.org/10.1038/nature02796

Gonzalez N, Gévaudant F, Hernould M, Chevalier C, and Mouras A. The cell cycle-associated protein kinase WEE1 regulates cell size in relation to endoreduplication in developing tomato fruit. The Plant Journal. 2007:**51**(4):642–655. https://doi.org/10.1111/j.1365-313X.2007.03167.x

Goodbody KC and Lloyd CW. Actin filaments line up acrossTradescantia epidermal cells, anticipating wound-induced divison planes. Protoplasma. 1990:**157**(1–3):92–101. https://doi.org/10.1007/BF01322641

Goodbody KC, Venverloo CJ, and Lloyd CW. Laser microsurgery demonstrates that cytoplasm ic strands anchoring the nucleus across the vacuoie of premitotic plant cells are under tension. Implications for division plane alignment. 1991.

Gould KS and Lord EM. A kinematic analysis of tepal growth in Lilium longiflorum. Planta. 1989:**177**(1):66–73. https://doi.org/10.1007/BF00392155

Granger CL and Cyr RJ. Use of abnormal preprophase bands to decipher division plane determination. Journal of Cell Science. 2001:**114**(3):599–607. https://doi.org/10.1242/jcs.114.3.599

Greenwood M and Locke JC. The circadian clock coordinates plant development through specificity at the tissue and cellular level. Current Opinion in Plant Biology. 2020:**53**:65–72. https://doi.org/10.1016/j.pbi.2019.09.004

Grishchuk EL, Molodtsov MI, Ataullakhanov FI, and McIntosh JR. Force production by disassembling microtubules. Nature. 2005:**438**(7066):384–388. https://doi.org/10.1038/nature04132

Guertin DA, Trautmann S, and McCollum D. Cytokinesis in Eukaryotes. Microbiol Mol Biol Rev. 2002:**66**(2):155–178. https://doi.org/10.1128/MMBR.66.2.155-178.2002

Gunning B and Sammut M. Rearrangements of Microtubules Involved in Establishing Cell Division Planes Start Immediately after DNA Synthesis and Are Completed just before Mitosis. Plant Cell. 1990:**2**(12):1273–1282.

Guo N, Hawkins C, and Nathans J. Frizzled6 controls hair patterning in mice. PNAS. 2004.

Gurdon J, Harger P, Mitchell A, and Lemaire P. Activin signaling and response to a morphogen gradient. Nature. 1994:**371**:487–92. https://doi.org/10.1038/371487a0

Haga N, Kato K, Murase M, Araki S, Kubo M, Demura T, Suzuki K, Müller I, Voss U, Jürgens G, et al. R1R2R3-MYB proteins positively regulate cytokinesis through activation of KNOLLE transcription in Arabidopsis thaliana. Development (Cambridge, England). 2007:**134**:1101–10. https://doi.org/10.1242/dev.02801

Haga N, Kobayashi K, Suzuki T, Maeo K, Kubo M, Ohtani M, Mitsuda N, Demura T, Nakamura K, Jürgens G, et al. Mutations in MYB3R1 and MYB3R4 Cause Pleiotropic Developmental Defects and Preferential Down-Regulation of Multiple G2/M-Specific Genes in Arabidopsis1[C][W]. Plant Physiol. 2011:**157**(2):706–717. https://doi.org/10.1104/pp.111.180836

Hamant O and Haswell ES. Life behind the wall: sensing mechanical cues in plants. BMC Biol. 2017:**15**(1):59. https://doi.org/10.1186/s12915-017-0403-5

Hamant O, Heisler MG, Jönsson H, Krupinski P, Uyttewaal M, Bokov P, Corson F, Sahlin P, Boudaoud A, Meyerowitz EM, et al. Developmental Patterning by Mechanical Signals in *Arabidopsis*. Science. 2008:**322**(5908):1650–1655. https://doi.org/10.1126/science.1165594

Hamant O, Inoue D, Bouchez D, Dumais J, and Mjolsness E. Are microtubules tension sensors? Nat Commun. 2019:**10**(1):2360. https://doi.org/10.1038/s41467-019-10207-y

Hamant O and Moulia B. How do plants read their own shapes? New Phytologist. 2016:**212**(2):333–337. https://doi.org/10.1111/nph.14143

Hannezo E, Prost J, and Joanny J-F. Instabilities of Monolayered Epithelia: Shape and Structure of Villi and Crypts. Phys Rev Lett. 2011:**107**(7):078104. https://doi.org/10.1103/PhysRevLett.107.078104

Hashimoto T. Microtubules in Plants. Arabidopsis Book. 2015:**13**:e0179. https://doi.org/10.1199/tab.0179

Hawkins RJ, Tindemans SH, and Mulder BM. Model for the orientational ordering of the plant microtubule cortical array. Phys Rev E. 2010:**82**(1):011911. https://doi.org/10.1103/PhysRevE.82.011911

Hayashi T and Carthew RW. Surface mechanics mediate pattern formation in the developing retina. Nature. 2004:**431**(7009):647–652. https://doi.org/10.1038/nature02952

Hayashi T, Ogawa K, and Mitsuishi Y. Characterization of the adsorption of Xyloglucan to Cellulose. Plant and Cell Physiology. 1994:**35**(8):1199–1205. https://doi.org/10.1093/oxfordjournals.pcp.a078714

Heemskerk I, Lecuit T, and LeGoff L. Dynamic clonal analysis based on chronic *in vivo* imaging allows multiscale quantification of growth in the *Drosophila* wing disc. Development. 2014:**141**(11):2339–2348. https://doi.org/10.1242/dev.109264

Heidstra R and Sabatini S. Plant and animal stem cells: Similar yet different. Nature reviews Molecular cell biology. 2014:**15**:301–12. https://doi.org/10.1038/nrm3790

Heisler MG, Hamant O, Krupinski P, Uyttewaal M, Ohno C, Jönsson H, Traas J, and Meyerowitz EM. Alignment between PIN1 Polarity and Microtubule Orientation in the Shoot Apical Meristem Reveals a Tight Coupling between Morphogenesis and Auxin Transport. PLoS Biol. 2010:**8**(10):e1000516. https://doi.org/10.1371/journal.pbio.1000516

Hejnowicz Z, Rusin A, and Rusin T. Tensile Tissue Stress Affects the Orientation of Cortical Microtubules in the Epidermis of Sunflower Hypocotyl. J Plant Growth Regul. 2000:**19**(1):31–44. https://doi.org/10.1007/s003440000005

Heredia A, Jim□nez A, and Guill□n R. Composition of plant cell walls. Z Lebensm Unters Forch. 1995:**200**(1):24–31. https://doi.org/10.1007/BF01192903

Hernández-Hernández V, Rueda D, Caballero L, Alvarez-Buylla ER, and BenÃtez M. Mechanical forces as information: an integrated approach to plant and animal development. Front Plant Sci. 2014:**5**. https://doi.org/10.3389/fpls.2014.00265

Herrmann A, Livanos P, Lipka E, Gadeyne A, Hauser M, Van Damme D, and Müller S. Dual localized kinesin-12 POK 2 plays multiple roles during cell division and interacts with MAP 65-3. EMBO Reports. 2018:**19**(9):e46085. https://doi.org/10.15252/embr.201846085

Hertwig O. Ueber den Werth der ersten Furchungszellen ftir die Organbildung des Embryo.

Hervieux N, Dumond M, Sapala A, Routier-Kierzkowska A-L, Kierzkowski D, Roeder AHK, Smith RS, Boudaoud A, and Hamant O. A Mechanical Feedback Restricts Sepal Growth and Shape in Arabidopsis. Current Biology. 2016:**26**(8):1019–1028. https://doi.org/10.1016/j.cub.2016.03.004

Hervieux N, Tsugawa S, Fruleux A, Dumond M, Routier-Kierzkowska A-L, Komatsuzaki T, Boudaoud A, Larkin JC, Smith RS, Li C-B, et al. Mechanical Shielding of Rapidly Growing Cells Buffers Growth Heterogeneity and Contributes to Organ Shape Reproducibility. Current Biology. 2017:**27**(22):3468-3479.e4. https://doi.org/10.1016/j.cub.2017.10.033

Heyn ANJ. The physiology of cell elongation. Bot Rev. 1940:**6**(10):515–574. https://doi.org/10.1007/BF02879296

Higaki T, Kutsuna N, Sano T, Kondo N, and Hasezawa S. Quantification and cluster analysis of actin cytoskeletal structures in plant cells: role of actin bundling in stomatal movement during diurnal cycles in Arabidopsis guard cells. The Plant Journal. 2010:**61**(1):156–165. https://doi.org/10.1111/j.1365-313X.2009.04032.x

Higuchi T and Uhlmann F. Stabilization of microtubule dynamics at anaphase onset promotes chromosome segregation. Nature. 2005:**433**(7022):171–176. https://doi.org/10.1038/nature03240

Hirt H, Páy A, Bögre L, Meskiene I, and Heberle-Bors E. cdc2MsB, a cognate cdc2 gene from alfalfa, complements the G1/S but not the G2/M transition of budding yeast cdc28 mutants. The Plant Journal. 1993:**4**(1):61–69. https://doi.org/10.1046/j.1365-313X.1993.04010061.x

Ho C-MK, Hotta T, Guo F, Roberson RW, Lee Y-RJ, and Liu B. Interaction of Antiparallel Microtubules in the Phragmoplast Is Mediated by the Microtubule-Associated Protein MAP65-3 in Arabidopsis[W]. Plant Cell. 2011:**23**(8):2909–2923. https://doi.org/10.1105/tpc.110.078204

Hoermayer L, Montesinos JC, Trozzi N, Spona L, Yoshida S, Marhava P, Caballero-Mancebo S, Benková E, Heisenberg C-P, Dagdas Y, et al. Mechanical forces in plant tissue matrix orient cell divisions via microtubule stabilization. Developmental Cell. 2024:**59**(10):1333-1344.e4. https://doi.org/10.1016/j.devcel.2024.03.009

Hofmeister W. Hofmeister W (1863) Zusatze und berichtigungen zu den 1851 veröffentlichen untersuchungen der entwicklung höherer kryptogamen. Jahrbucher für Wissenschaft und Botanik 3: 259–293.

Hofmeister W. Über die beugungen saftreicher pflanzenteile nach erschütterung Botanik.

Hongo S, Sato K, Yokoyama R, and Nishitani K. Demethylesterification of the Primary Wall by PECTIN METHYLESTERASE35 Provides Mechanical Support to the Arabidopsis Stem[W]. Plant Cell. 2012:**24**(6):2624–2634. https://doi.org/10.1105/tpc.112.099325

van der Honing HS, van Bezouwen LS, Emons AMC, and Ketelaar T. High expression of Lifeact in Arabidopsis thaliana reduces dynamic reorganization of actin filaments but does not affect plant development. Cytoskeleton. 2011:**68**(10):578–587. https://doi.org/10.1002/cm.20534

Horiguchi G, Kim G-T, and Tsukaya H. The transcription factor AtGRF5 and the transcription coactivator AN3 regulate cell proliferation in leaf primordia of Arabidopsis thaliana. The Plant Journal. 2005:**43**(1):68–78. https://doi.org/10.1111/j.1365-313X.2005.02429.x

Hotta T, Kong Z, Ho C-MK, Zeng CJT, Horio T, Fong S, Vuong T, Lee Y-RJ, and Liu B. Characterization of the Arabidopsis Augmin Complex Uncovers Its Critical Function in the Assembly of the Acentrosomal Spindle and Phragmoplast Microtubule Arrays[W]. Plant Cell. 2012:**24**(4):1494–1509. https://doi.org/10.1105/tpc.112.096610

Howard J and Hyman AA. Growth, fluctuation and switching at microtubule plus ends. Nat Rev Mol Cell Biol. 2009:**10**(8):569–574. https://doi.org/10.1038/nrm2713

Hu H, Zhang R, Tao Z, Li X, Li Y, Huang J, Li X, Han X, Feng S, Zhang G, et al. Cellulose Synthase Mutants Distinctively Affect Cell Growth and Cell Wall Integrity for Plant Biomass Production in Arabidopsis. Plant and Cell Physiology. 2018:**59**(6):1144–1157. https://doi.org/10.1093/pcp/pcy050

Huang CH, Peng FL, Lee Y-RJ, and Liu B. The microtubular preprophase band recruits Myosin XI to the cortical division site to guide phragmoplast expansion during plant cytokinesis. Developmental Cell. 2024:S1534580724003332. https://doi.org/10.1016/j.devcel.2024.05.015

Huang S, Blanchoin L, Kovar DR, and Staiger CJ. Arabidopsis Capping Protein (AtCP) Is a Heterodimer That Regulates Assembly at the Barbed Ends of Actin Filaments. Journal of Biological Chemistry. 2003:**278**(45):44832–44842. https://doi.org/10.1074/jbc.M306670200

Hülskamp M. Trichomes. Current Biology. 2019:**29**(8):R273–R274. https://doi.org/10.1016/j.cub.2019.02.010

Hush J, Hawes C, and Overall R. Interphase microtubule re-orientation predicts a new cell polarity in wounded pea roots. Journal of Cell Science. 1990:**96**:47–61. https://doi.org/10.1242/jcs.96.1.47

Hussey PJ, Ketelaar T, and Deeks MJ. CONTROL OF THE ACTIN CYTOSKELETON IN PLANT CELL GROWTH. Annu Rev Plant Biol. 2006:**57**(1):109–125. https://doi.org/10.1146/annurev.arplant.57.032905.105206

Ikeuchi M, Sugimoto K, and Iwase A. Plant Callus: Mechanisms of Induction and Repression. Plant Cell. 2013:**25**(9):3159–3173. https://doi.org/10.1105/tpc.113.116053

Inzé D and De Veylder L. Cell Cycle Regulation in Plant Development. Annu Rev Genet. 2006:**40**(1):77–105. https://doi.org/10.1146/annurev.genet.40.110405.090431

Ito M. Conservation and diversification of three-repeat Myb transcription factors in plants. J Plant Res. 2005:**118**(1):61–69. https://doi.org/10.1007/s10265-005-0192-8

Iwakawa H, Shinmyo A, and Sekine M. Arabidopsis CDKA;1, a cdc2 homologue, controls proliferation of generative cells in male gametogenesis. The Plant Journal. 2006:**45**(5):819–831. https://doi.org/10.1111/j.1365-313X.2005.02643.x

Jaffe MJ and Forbes S. Thigmomorphogenesis: the effect of mechanical perturbation on plants. Plant Growth Regul. 1993:**12**(3):313–324. https://doi.org/10.1007/BF00027213

Janski N, Masoud K, Batzenschlager M, Herzog E, Evrard J-L, Houlné G, Bourge M, Chabouté M-E, and Schmit A-C. The GCP3-Interacting Proteins GIP1 and GIP2 Are Required for γ-Tubulin Complex Protein Localization, Spindle Integrity, and Chromosomal Stability[C][W]. Plant Cell. 2012:**24**(3):1171–1187. https://doi.org/10.1105/tpc.111.094904

Jasencakova Z, Meister A, and Schubert I. Chromatin organization and its relation to replication and histone acetylation during the cell cycle in barley. Chromosoma. 2001:**110**(2):83–92. https://doi.org/10.1007/s004120100132

Jasencakova Z, Soppe WJJ, Meister A, Gernand D, Turner BM, and Schubert I. Histone modifications in Arabidopsis– high methylation of H3 lysine 9 is dispensable for constitutive heterochromatin. The Plant Journal. 2003:**33**(3):471–480. https://doi.org/10.1046/j.1365-313X.2003.01638.x

Jeong YY, Lee H-Y, Kim SW, Noh Y-S, and Seo PJ. Optimization of protoplast regeneration in the model plant Arabidopsis thaliana. Plant Methods. 2021:**17**(1):21. https://doi.org/10.1186/s13007-021-00720-x

Johnson CH. Circadian clocks and cell division: What's the pacemaker? Cell Cycle. 2010:**9**(19):3864–3873. https://doi.org/10.4161/cc.9.19.13205

Jones A, Forero-Vargas M, Withers SP, Smith RS, Traas J, Dewitte W, and Murray JAH. Cell-size dependent progression of the cell cycle creates homeostasis and flexibility of plant cell size. Nat Commun. 2017:**8**(1):15060. https://doi.org/10.1038/ncomms15060

Jordan BM and Dumais J. Biomechanics of Plant Cell Growth. . In. Encyclopedia of Life Sciences. (Wiley). https://doi.org/10.1002/9780470015902.a0022336

Joshi H and Palevitz BA. γ-Tubulin and microtubule organization in plants. Trends Cell Biol. 1996. https://doi.org/10.1016/0962-8924(96)81008-7

Kabsch W and Vandekerckhove J. Structure and Function of Actin. Annual Review of Biophysics. 1992:**21**(Volume 21, 1992):49–76. https://doi.org/10.1146/annurev.bb.21.060192.000405

Kadota A, Yamada N, Suetsugu N, Hirose M, Saito C, Shoda K, Ichikawa S, Kagawa T, Nakano A, and Wada M. Short actin-based mechanism for light-directed chloroplast movement in *Arabidopsis*. Proc Natl Acad Sci USA. 2009:**106**(31):13106–13111. https://doi.org/10.1073/pnas.0906250106

Kakimoto T and Shibaoka H. Actin filaments and microtubules in the preprophase band and phragmoplast of tobacco cells. Protoplasma. 1987:**140**(2–3):151–156. https://doi.org/10.1007/BF01273724

Kandasamy MK, Burgos-Rivera B, McKinney EC, Ruzicka DR, and Meagher RB. Class-Specific Interaction of Profilin and ADF Isovariants with Actin in the Regulation of Plant Development. Plant Cell. 2007:**19**(10):3111–3126. https://doi.org/10.1105/tpc.107.052621

Kandasamy MK, McKinney EC, and Meagher RB. A Single Vegetative Actin Isovariant Overexpressed under the Control of Multiple Regulatory Sequences Is Sufficient for Normal *Arabidopsis* Development. The Plant Cell. 2009:**21**(3):701–718. https://doi.org/10.1105/tpc.108.061960

Kaplan DR. The Relationship of Cells to Organisms in Plants: Problem and Implications of an Organismal Perspective. International Journal of Plant Sciences. 1992:**153**(3):S28–S37.

Keller R. Shaping the Vertebrate Body Plan by Polarized Embryonic Cell Movements. Science. 2002:**298**(5600):1950–1954. https://doi.org/10.1126/science.1079478

Kelly-Bellow R, Lee K, Kennaway R, Barclay E, Whibley A, Bushell C, Spooner J, Yu M, Brett P, Kular B, et al. Brassinosteroid coordinates cell layer interactions in plants via cell wall and tissue mechanics. Science. 2023. https://doi.org/10.1126/science.adf0752

Ketelaar T, Galway ME, Mulder BM, and Emons AMC. Rates of exocytosis and endocytosis in *Arabidopsis* root hairs and pollen tubes. Journal of Microscopy. 2008:**231**(2):265–273. https://doi.org/10.1111/j.1365-2818.2008.02031.x

Kheibarshekan Asl L, Dhondt S, Boudolf V, Beemster GTS, Beeckman T, Inzé D, Govaerts W, and De Veylder L. Model-Based Analysis of Arabidopsis Leaf Epidermal Cells Reveals Distinct Division and Expansion Patterns for Pavement and Guard Cells. Plant Physiology. 2011:**156**(4):2172–2183. https://doi.org/10.1104/pp.111.181180

Kidner C and Timmermans M. Mixing and matching pathways in leaf polarity. Current Opinion in Plant Biology. 2007:**10**(1):13–20. https://doi.org/10.1016/j.pbi.2006.11.013

Kierzkowski D, Runions A, Vuolo F, Strauss S, Lymbouridou R, Routier-Kierzkowska A-L, Wilson-Sánchez D, Jenke H, Galinha C, Mosca G, et al. A Growth-Based Framework for Leaf Shape Development and Diversity. Cell. 2019:**177**(6):1405-1418.e17. https://doi.org/10.1016/j.cell.2019.05.011

Kim H, Park M, Kim SJ, and Hwang I. Actin Filaments Play a Critical Role in Vacuolar Trafficking at the Golgi Complex in Plant Cells. Plant Cell. 2005:**17**(3):888–902. https://doi.org/10.1105/tpc.104.028829

Kimata Y, Kato T, Higaki T, Kurihara D, Yamada T, Segami S, Morita MT, Maeshima M, Hasezawa S, Higashiyama T, et al. Polar vacuolar distribution is essential for accurate asymmetric division of *Arabidopsis* zygotes. Proc Natl Acad Sci USA. 2019:**116**(6):2338–2343. https://doi.org/10.1073/pnas.1814160116

Kirchhelle C, Chow C-M, Foucart C, Neto H, Stierhof Y-D, Kalde M, Walton C, Fricker M, Smith RS, Jérusalem A, et al. The Specification of Geometric Edges by a Plant Rab GTPase Is an Essential Cell-Patterning Principle During Organogenesis in Arabidopsis. Developmental Cell. 2016:**36**(4):386–400. https://doi.org/10.1016/j.devcel.2016.01.020

Kirik A, Ehrhardt DW, and Kirik V. TONNEAU2/FASS Regulates the Geometry of Microtubule Nucleation and Cortical Array Organization in Interphase Arabidopsis Cells[C][W]. Plant Cell. 2012:**24**(3):1158–1170. https://doi.org/10.1105/tpc.111.094367

Kirik V, Herrmann U, Parupalli C, Sedbrook J, Ehrhardt D, and Hülskamp M. CLASP localizes in two discrete patterns on cortical microtubules and is required for cell morphogenesis and cell division in Arabidopsis. Journal of cell science. 2008:**120**:4416–25. https://doi.org/10.1242/jcs.024950

Klingenberg C. Evolution and development of shape: Integrating quantitative approaches. Nature reviews Genetics. 2010:**11**:623–35. https://doi.org/10.1038/nrg2829

Klingenberg CP. Morphometrics and the role of the phenotype in studies of the evolution of developmental mechanisms. Gene. 2002:**287**(1–2):3–10. https://doi.org/10.1016/S0378-1119(01)00867-8

Kny L. Über den Einfluß von Zug und Druck auf die Richtung der Scheidewände in sich teilenden Pflanzenzellen. Ber Deutsch Bot Gesell 14:378–391.

Koch G, Sillet SC, Jennings GW, and Davis S. The limits of tree height. Nature. 2004:**428**.

Kojo KH, Higaki T, Kutsuna N, Yoshida Y, Yasuhara H, and Hasezawa S. Roles of Cortical Actin Microfilament Patterning in Division Plane Orientation in Plants. Plant and Cell Physiology. 2013:**54**(9):1491–1503. https://doi.org/10.1093/pcp/pct093

Kollman JM, Merdes A, Mourey L, and Agard DA. Microtubule nucleation by γ-tubulin complexes. Nat Rev Mol Cell Biol. 2011:**12**(11):709–721. https://doi.org/10.1038/nrm3209

Komis G, Luptovčiak I, Ovečka M, Samakovli D, Šamajová O, and Šamaj J. Katanin Effects on Dynamics of Cortical Microtubules and Mitotic Arrays in Arabidopsis thaliana Revealed by Advanced Live-Cell Imaging. Front Plant Sci. 2017:**8**:866. https://doi.org/10.3389/fpls.2017.00866

Kosetsu K, de Keijzer J, Janson ME, and Goshima G. MICROTUBULE-ASSOCIATED PROTEIN65 Is Essential for Maintenance of Phragmoplast Bipolarity and Formation of the Cell Plate in Physcomitrella patens[C][W]. Plant Cell. 2013:**25**(11):4479–4492. https://doi.org/10.1105/tpc.113.117432

Kouhen M, Dimitrova A, Scippa GS, and Trupiano D. The Course of Mechanical Stress: Types, Perception, and Plant Response. Biology. 2023:**12**(2):217. https://doi.org/10.3390/biology12020217

Kousholt AN, Menzel T, and Sørensen CS. Pathways for Genome Integrity in G2 Phase of the Cell Cycle. Biomolecules. 2012:**2**(4):579–607. https://doi.org/10.3390/biom2040579

Kraus G. Die Gewebespannung des Stammes und ihre Folgen (Gebauer-Schwetschke).

Kroh M and Knuiman B. Development of subprotoplasts from in vitro-grown tobacco pollen tubes. Sexual Plant Reprod. 1988:**1**(2). https://doi.org/10.1007/BF00189269

Krupinski P, Bozorg B, Larsson A, Pietra S, Grebe M, and Jönsson H. A Model Analysis of Mechanisms for Radial Microtubular Patterns at Root Hair Initiation Sites. Front Plant Sci. 2016:**7**. https://doi.org/10.3389/fpls.2016.01560

Kumagai F and Hasezawa S. Dynamic Organization of Microtubules and Microfilaments during Cell Cycle Progression in Higher Plant Cells. Plant Biology. 2001:**3**(1):4–16. https://doi.org/10.1055/s-2001-11749

Kumar N, Harashima H, Kalve S, Bramsiepe J, Wang K, Sizani BL, Bertrand LL, Johnson MC, Faulk C, Dale R, et al. Functional Conservation in the SIAMESE-RELATED Family of Cyclin-Dependent Kinase Inhibitors in Land Plants. Plant Cell. 2015:**27**(11):3065–3080. https://doi.org/10.1105/tpc.15.00489

Kutschera U and Niklas KJ. The epidermal-growth-control theory of stem elongation: An old and a new perspective. Journal of Plant Physiology. 2007:**164**(11):1395–1409. https://doi.org/10.1016/j.jplph.2007.08.002

Laan L, Pavin N, Husson J, Romet-Lemonne G, van Duijn M, López MP, Vale RD, Jülicher F, Reck-Peterson SL, and Dogterom M. Cortical Dynein Controls Microtubule Dynamics to Generate Pulling Forces that Position Microtubule Asters. Cell. 2012:**148**(3):502–514. https://doi.org/10.1016/j.cell.2012.01.007

Laufs P, Grandjean O, Jonak C, Kiêu K, and Traas J. Cellular parameters of the shoot apical meristem in Arabidopsis. Plant Cell. 1998:**10**(8):1375–1390.

Le J, Mallery EL, Zhang C, Brankle S, and Szymanski DB. Arabidopsis BRICK1/HSPC300 Is an Essential WAVE-Complex Subunit that Selectively Stabilizes the Arp2/3 Activator SCAR2. Current Biology. 2006:**16**(9):895–901. https://doi.org/10.1016/j.cub.2006.03.061

Le PY and Ambrose C. CLASP promotes stable tethering of endoplasmic microtubules to the cell cortex to maintain cytoplasmic stability in Arabidopsis meristematic cells. PLoS ONE. 2018:**13**(6):e0198521. https://doi.org/10.1371/journal.pone.0198521

Lease HM and Wolf BO. Exoskeletal chitin scales isometrically with body size in terrestrial insects. Journal of Morphology. 2010:**271**(6):759–768. https://doi.org/10.1002/jmor.10835

Lebecq A. Interplay between the phosphoinositides and the plant cytoskeleton dring plant cytokinesis in Arabidopsis thaliana.

Lebecq A, Fangain A, Boussaroque A, and Caillaud M-C. Dynamic apico-basal enrichment of the F-actin during cytokinesis in Arabidopsis cells embedded in their tissues. Quant Plant Bio. 2022:**3**:e4. https://doi.org/10.1017/qpb.2022.1

Leboeuf E. Physico-chemical characteristics of cell walls from Arabidopsis thaliana microcalli showing different adhesion strengths. Journal of Experimental Botany. 2004:**55**(405):2087–2097. https://doi.org/10.1093/jxb/erh225

Ledbetter MC and Porter KR. A "MICROTUBULE" IN PLANT CELL FINE STRUCTURE. The Journal of Cell Biology. 1963:**19**(1):239–250. https://doi.org/10.1083/jcb.19.1.239

Lee KJI, Bushell C, Koide Y, Fozard JA, Piao C, Yu M, Newman J, Whitewoods C, Avondo J, Kennaway R, et al. Shaping of a three-dimensional carnivorous trap through modulation of a planar growth mechanism. PLoS Biol. 2019:**17**(10):e3000427. https://doi.org/10.1371/journal.pbio.3000427

Lee Y-RJ and Liu B. Microtubule nucleation for the assembly of acentrosomal microtubule arrays in plant cells. New Phytologist. 2019:**222**(4):1705–1718. https://doi.org/10.1111/nph.15705

LeGoff L and Lecuit T. Mechanical Forces and Growth in Animal Tissues. Cold Spring Harb Perspect Biol. 2016:**8**(3):a019232. https://doi.org/10.1101/cshperspect.a019232

Leong SY, Yamada M, Yanagisawa N, and Goshima G. SPIRAL2 Stabilises Endoplasmic Microtubule Minus Ends in the Moss *Physcomitrella patens*. Cell Struct Funct. 2018:**43**(1):53–60. https://doi.org/10.1247/csf.18001

Levesque-Tremblay G, Pelloux J, Braybrook SA, and Müller K. Tuning of pectin methylesterification: consequences for cell wall biomechanics and development. Planta. 2015:**242**(4):791–811. https://doi.org/10.1007/s00425-015-2358-5

Lewis FT. The effect of cell division on the shape and size of hexagonal cells. Anat Rec. 1926:**33**(5):331–355. https://doi.org/10.1002/ar.1090330502

Li H, Sun B, Sasabe M, Deng X, Machida Y, Lin H, Julie Lee Y-R, and Liu B. Arabidopsis MAP65-4 plays a role in phragmoplast microtubule organization and marks the cortical cell division site. New Phytologist. 2017:**215**(1):187–201. https://doi.org/10.1111/nph.14532

Li S, Sun T, and Ren H. The functions of the cytoskeleton and associated proteins during mitosis and cytokinesis in plant cells. Front Plant Sci. 2015:**6**. https://doi.org/10.3389/fpls.2015.00282

Li Y, Deng Z, Kamisugi Y, Chen Z, Wang J, Han X, Wei Y, He H, Terzaghi W, Cove DJ, et al. A minus-end directed kinesin motor directs gravitropism in Physcomitrella patens. Nat Commun. 2021:**12**(1):4470. https://doi.org/10.1038/s41467-021-24546-2

Li Y, Kučera O, Cuvelier D, Rutkowski DM, Deygas M, Rai D, Pavlovič T, Vicente FN, Piel M, Giannone G, et al. Compressive forces stabilize microtubules in living cells. Nat Mater. 2023:**22**(7):913–924. https://doi.org/10.1038/s41563-023-01578-1

Lian N, Wang X, Jing Y, and Lin J. Regulation of cytoskeleton-associated protein activities: Linking cellular signals to plant cytoskeletal function. Journal of Integrative Plant Biology. 2021:**63**(1):241–250. https://doi.org/10.1111/jipb.13046

Lindeboom JJ, Nakamura M, Hibbel A, Shundyak K, Gutierrez R, Ketelaar T, Emons AMC, Mulder BM, Kirik V, and Ehrhardt DW. A Mechanism for Reorientation of Cortical Microtubule Arrays Driven by Microtubule Severing. Science. 2013:**342**(6163):1245533. https://doi.org/10.1126/science.1245533

Lindqvist A, Rodríguez-Bravo V, and Medema RH. The decision to enter mitosis: feedback and redundancy in the mitotic entry network. Journal of Cell Biology. 2009:**185**(2):193–202. https://doi.org/10.1083/jcb.200812045

Lintilhac PM and Vesecky TB. Mechanical Stress and Cell Wall Orientation in Plants. II. The Application of Controlled Directional Stress to Growing Plants; with a Discussion on the Nature of the Wound Reaction. 10.

Lionetti V, Raiola A, Camardella L, Giovane A, Obel N, Pauly M, Favaron F, Cervone F, and Bellincampi D. Overexpression of Pectin Methylesterase Inhibitors in Arabidopsis Restricts Fungal Infection by Botrytis cinerea. Plant Physiol. 2007:**143**(4):1871–1880. https://doi.org/10.1104/pp.106.090803

Lipka E, Gadeyne A, Stöckle D, Zimmermann S, De Jaeger G, Ehrhardt DW, Kirik V, Van Damme D, and Müller S. The Phragmoplast-Orienting Kinesin-12 Class Proteins Translate the Positional Information of the Preprophase Band to Establish the Cortical Division Zone in Arabidopsis thaliana[C][W]. Plant Cell. 2014:**26**(6):2617–2632. https://doi.org/10.1105/tpc.114.124933

Liu B and Lee Y-RJ. Spindle Assembly and Mitosis in Plants. 2022.

Liu B, Marc J, Joshi H, and Palevitz B. A gamma-tubulin-related protein associated with the microtubule arrays of higher plants in a cell cycle-dependent manner. Journal of cell science. 1993:**104 (Pt 4)**:1217–28. https://doi.org/10.1242/jcs.104.4.1217

Liu B and Palevitz BA. Organization of cortical microfilaments in dividing root cells. Cell Motil Cytoskeleton. 1992:**23**(4):252–264. https://doi.org/10.1002/cm.970230405

Liu Z, Jia L, Mao Y, and He Y. Classification and quantification of leaf curvature. Journal of Experimental Botany. 2010:**61**(10):2757–2767. https://doi.org/10.1093/jxb/erq111

Livanos P and Müller S. Division Plane Establishment and Cytokinesis. Annu Rev Plant Biol. 2019:**70**(1):239–267. https://doi.org/10.1146/annurev-arplant-050718-100444

Lloyd C and Chan J. Not so divided: the common basis of plant and animal cell division. Nat Rev Mol Cell Biol. 2006:**7**(2):147–152. https://doi.org/10.1038/nrm1831

Lloyd CW. How does the cytoskeleton read the laws of geometry in aligning the division plane of plant cells? Development. 1991:**113**(Supplement_1):55–65. https://doi.org/10.1242/dev.113.Supplement_1.55

Lockhart JA. An analysis of irreversible plant cell elongation. Journal of Theoretical Biology. 1965:**8**(2):264–275. https://doi.org/10.1016/0022-5193(65)90077-9

Logé G, Peñaloza L, and Guintcheva G. On the Impossibility of Sustainable Development without Culture The Gaze of Art and Perspectives on a Cultural Approach to Marketing. 2010.

Louveaux M, Julien J-D, Mirabet V, Boudaoud A, and Hamant O. Cell division plane orientation based on tensile stress in *Arabidopsis thaliana*. Proc Natl Acad Sci USA. 2016:**113**(30):E4294–E4303. https://doi.org/10.1073/pnas.1600677113

Lucas JR. Appearance of microtubules at the cytokinesis to interphase transition in *Arabidopsis thaliana*. Cytoskeleton. 2021:**78**(7):361–371. https://doi.org/10.1002/cm.21689

Lucas JR, Courtney S, Hassfurder M, Dhingra S, Bryant A, and Shaw SL. Microtubule-Associated Proteins MAP65-1 and MAP65-2 Positively Regulate Axial Cell Growth in Etiolated Arabidopsis Hypocotyls[W]. Plant Cell. 2011:**23**(5):1889–1903. https://doi.org/10.1105/tpc.111.084970

Lukowitz W, Mayer U, and Jürgens G. Cytokinesis in the Arabidopsis Embryo Involves the Syntaxin-Related KNOLLE Gene Product. Cell. 1996:**84**(1):61–71. https://doi.org/10.1016/S0092-8674(00)80993-9

Luo Y and Koop H-U. Somatic embryogenesis in cultured immature zygotic embryos and leaf protoplasts of Arabidopsis thaliana ecotypes. Planta. 1997:**202**(3):387–396. https://doi.org/10.1007/s004250050141

Lynch TM and Lintilhac PM. Mechanical Signals in Plant Development: A New Method for Single Cell Studies. Developmental Biology. 1997:**181**(2):246–256. https://doi.org/10.1006/dbio.1996.8462

Ma Q, Sun J, and Mao T. Microtubule bundling plays a role in ethylene-mediated cortical microtubule reorientation in etiolated hypocotyls. Journal of Cell Science. 2016:jcs.184408. https://doi.org/10.1242/jcs.184408

MacAlpine DM and Almouzni G. Chromatin and DNA Replication. Cold Spring Harbor Perspectives in Biology. 2013:**5**(8):a010207–a010207. https://doi.org/10.1101/cshperspect.a010207

Macefield VG. Recording and quantifying sympathetic outflow to muscle and skin in humans: methods, caveats and challenges. Clin Auton Res. 2021:**31**(1):59–75. https://doi.org/10.1007/s10286-020-00700-6

MacKinnon IM, Šturcová A, Sugimoto-Shirasu K, His I, McCann MC, and Jarvis MC. Cell-wall structure and anisotropy in procuste, a cellulose synthase mutant of Arabidopsis thaliana. Planta. 2006:**224**(2):438–448. https://doi.org/10.1007/s00425-005-0208-6

Maddox PS, Bloom KS, and Salmon ED. The polarity and dynamics of microtubule assembly in the budding yeast Saccharomyces cerevisiae. Nat Cell Biol. 2000:**2**(1):36–41. https://doi.org/10.1038/71357

Maeda S, Gunji S, Hanai K, Hirano T, Kazama Y, Ohbayashi I, Abe T, Sawa S, Tsukaya H, and Ferjani A. The Conflict Between Cell Proliferation and Expansion Primarily Affects Stem Organogenesis in Arabidopsis. Plant and Cell Physiology. 2014:**55**(11):1994–2007. https://doi.org/10.1093/pcp/pcu131

Maga G and Hübscher U. Proliferating cell nuclear antigen (PCNA): a dancer with many partners. Journal of Cell Science. 2003:**116**(15):3051–3060. https://doi.org/10.1242/jcs.00653

Manuela D and Xu M. Patterning a Leaf by Establishing Polarities. Front Plant Sci. 2020:**11**:568730. https://doi.org/10.3389/fpls.2020.568730

Marc J, Granger C, Brincat J, Fisher D, Kao T, McCubbin A, and Cyr R. A GFP-MAP4 reporter gene for visualizing cortical microtubule rearrangements in living epidermal cells. Plant Cell. 1998:**10**(11):1927–1940.

Martins BMC, Tooke AK, Thomas P, and Locke JCW. Cell size control driven by the circadian clock and environment in cyanobacteria. Proc Natl Acad Sci USA. 2018:**115**(48). https://doi.org/10.1073/pnas.1811309115

Masoud K, Herzog E, Chabouté M-E, and Schmit A-C. Microtubule nucleation and establishment of the mitotic spindle in vascular plant cells. The Plant Journal. 2013:**75**(2):245–257. https://doi.org/10.1111/tpj.12179

Massa GD and Gilroy S. Touch modulates gravity sensing to regulate the growth of primary roots of Arabidopsis thaliana. The Plant Journal. 2003:**33**(3):435–445. https://doi.org/10.1046/j.1365-313X.2003.01637.x

Mathur J, Spielhofer P, Kost B, and Chua NH. The actin cytoskeleton is required to elaborate and maintain spatial patterning during trichome cell morphogenesis in Arabidopsis thaliana. Development (Cambridge, England). 2000:**126**:5559–68. https://doi.org/10.1242/dev.126.24.5559

Maurer SP, Bieling P, Cope J, Hoenger A, and Surrey T. GTPγS microtubules mimic the growing microtubule end structure recognized by end-binding proteins (EBs). Proc Natl Acad Sci USA. 2011:**108**(10):3988–3993. https://doi.org/10.1073/pnas.1014758108

Maurer SP, Fourniol FJ, Bohner G, Moores CA, and Surrey T. EBs Recognize a Nucleotide-Dependent Structural Cap at Growing Microtubule Ends. Cell. 2012:**149**(2):371–382. https://doi.org/10.1016/j.cell.2012.02.049

Mayr C, Jasencakova Z, Meister A, Schubert I, and Zink D. Comparative analysis of the functional genome architecture of animal andplant cell nuclei. 2003.

McConnell J and Barton M. McConnell, J. R. & Barton, M. K. Leaf polarity and meristem formation in Arabidopsis. Development 125, 2935-2942. Development (Cambridge, England). 1998:**125**:2935–42.

McDowell JM, Huang S, McKinney EC, An YQ, and Meagher RB. Structure and Evolution of the Actin Gene Family in Arabidopsis Thaliana. Genetics. 1996:**142**(2):587–602.

McIntosh JR. Mitosis. Cold Spring Harb Perspect Biol. 2016:**8**(9):a023218. https://doi.org/10.1101/cshperspect.a023218

McNally FJ and Vale RD. Identification of katanin, an ATPase that severs and disassembles stable microtubules. Cell. 1993:**75**(3):419–429. https://doi.org/10.1016/0092-8674(93)90377-3

McNeil M, Darvill A, Fry S, and Albersheim P. Structure and Function of the Primary Cell Walls of Plants. Annual review of biochemistry. 1984:**53**:625–63. https://doi.org/10.1146/annurev.bi.53.070184.003205

McQueen-Mason S and Cosgrove DJ. Disruption of hydrogen bonding between plant cell wall polymers by proteins that induce wall extension. Proc Natl Acad Sci U S A. 1994:**91**(14):6574–6578.

McQueen-Mason S, Durachko DM, and Cosgrove DJ. Two endogenous proteins that induce cell wall extension in plants. Plant Cell. 1992:**4**(11):1425–1433. https://doi.org/10.1105/tpc.4.11.1425

McQueen-Mason SJ and Cosgrove DJ. Expansin mode of action on cell walls. Analysis of wall hydrolysis, stress relaxation, and binding. Plant Physiol. 1995:**107**(1):87–100.

Meinhardt H. A boundary model for pattern formation in vertebrate limbs. Development. 1983:**76**(1):115–137. https://doi.org/10.1242/dev.76.1.115

Meister P, Taddei A, Ponti A, Baldacci G, and Gasser SM. Replication foci dynamics: replication patterns are modulated by S-phase checkpoint kinases in fission yeast. EMBO J. 2007:**26**(5):1315–1326. https://doi.org/10.1038/sj.emboj.7601538

Melnyk CW, Schuster C, Leyser O, and Meyerowitz EM. A Developmental Framework for Graft Formation and Vascular Reconnection in Arabidopsis thaliana. Current Biology. 2015:**25**(10):1306–1318. https://doi.org/10.1016/j.cub.2015.03.032

Menges M, Pavesi G, Morandini P, Bögre L, and Murray JAH. Genomic Organization and Evolutionary Conservation of Plant D-Type Cyclins. Plant Physiol. 2007:**145**(4):1558–1576. https://doi.org/10.1104/pp.107.104901

Menges M, Samland AK, Planchais S, and Murray JAH. The D-Type Cyclin CYCD3;1 Is Limiting for the G1-to-S-Phase Transition in Arabidopsis. Plant Cell. 2006:**18**(4):893–906. https://doi.org/10.1105/tpc.105.039636

Menzel D. Chasing Coiled Coils: Intermediate Filaments in Plants. Botanica Acta. 1993:**106**(4):294–300. https://doi.org/10.1111/j.1438-8677.1993.tb00751.x

Milani P, Gholamirad M, Traas J, Arnéodo A, Boudaoud A, Argoul F, and Hamant O. In vivo analysis of local wall stiffness at the shoot apical meristem in Arabidopsis using atomic force microscopy. The Plant Journal. 2011:**67**(6):1116–1123. https://doi.org/10.1111/j.1365-313X.2011.04649.x

Milinkovitch MC, Manukyan L, Debry A, Di-Poï N, Martin S, Singh D, Lambert D, and Zwicker M. Crocodile Head Scales Are Not Developmental Units But Emerge from Physical Cracking. Science. 2013:**339**(6115):78–81. https://doi.org/10.1126/science.1226265

Mimault M, Ptashnyk M, and Dupuy LX. Particle-based model shows complex rearrangement of tissue mechanical properties are needed for roots to grow in hard soil. PLoS Comput Biol. 2023:**19**(3):e1010916. https://doi.org/10.1371/journal.pcbi.1010916

Mineyuki Y. The Preprophase Band of Microtubules: Its Function as a Cytokinetic Apparatus in Higher Plants. . In. International Review of Cytology. (Elsevier), pp. 1–49. https://doi.org/10.1016/S0074-7696(08)62415-8

Mineyuki Y and Furuya M. Effect of Centrifugation on the Development and Timing of Premitotic Positioning of the Nucleus in Adiantum Protonemata. Development, Growth & Differentiation. 1980:**22**(6):867–874. https://doi.org/10.1111/j.1440-169X.1980.00867.x

Mineyuki Y and Palevitz BA. Relationship between preprophase band organization, F-actin and the division site in *Allium*: Fluorescence and morphometric studies on cytochalasin-treated cells. Journal of Cell Science. 1990:**97**(2):283–295. https://doi.org/10.1242/jcs.97.2.283

Mirabet V, Das P, Boudaoud A, and Hamant O. The Role of Mechanical Forces in Plant Morphogenesis. Annu Rev Plant Biol. 2011:**62**(1):365–385. https://doi.org/10.1146/annurev-arplant-042110-103852

Mirabet V, Krupinski P, Hamant O, Meyerowitz EM, Jönsson H, and Boudaoud A. The self-organization of plant microtubules inside the cell volume yields their cortical localization, stable alignment, and sensitivity to external cues. PLoS Comput Biol. 2018:**14**(2):e1006011. https://doi.org/10.1371/journal.pcbi.1006011

Mitchison T and Kirschner M. Dynamic instability of microtubule growth. Nature. 1984:**312**(5991):237–242. https://doi.org/10.1038/312237a0

Mizuno K. Microtubule-nucleation sites on nuclei of higher plant cells. Protoplasma. 1993:**173**(1–2):77–85. https://doi.org/10.1007/BF01378864

Molchan T, Valster A, and Hepler P. Actomyosin promotes cell plate alignment and late lateral expansion in Tradescantia stamen hair cells. Planta. 2002:**214**(5):683–693. https://doi.org/10.1007/s004250100672

Moldovan G-L, Pfander B, and Jentsch S. PCNA, the Maestro of the Replication Fork. Cell. 2007:**129**(4):665–679. https://doi.org/10.1016/j.cell.2007.05.003

Möller B, Poeschl Y, Plötner R, and Bürstenbinder K. PaCeQuant: A Tool for High-Throughput Quantification of Pavement Cell Shape Characteristics. Plant Physiol. 2017:**175**(3):998–1017. https://doi.org/10.1104/pp.17.00961

Montesinos JC, Abuzeineh A, Kopf A, Juanes-Garcia A, Ötvös K, Petrášek J, Sixt M, and Benková E. Phytohormone cytokinin guides microtubule dynamics during cell progression from proliferative to differentiated stage. The EMBO Journal. 2020:**39**(17):e104238. https://doi.org/10.15252/embj.2019104238

Morey-Holton ER. The impact of gravity on life. . In. Evolution on Planet Earth. (Elsevier), pp. 143–159. https://doi.org/10.1016/B978-012598655-7/50036-7

Morgan DO. CYCLIN-DEPENDENT KINASES: Engines, Clocks, and Microprocessors. Annu Rev Cell Dev Biol. 1997:**13**(1):261–291. https://doi.org/10.1146/annurev.cellbio.13.1.261

Motose H, Tominaga R, Wada T, Sugiyama M, and Watanabe Y. A NIMA-related protein kinase suppresses ectopic outgrowth of epidermal cells through its kinase activity and the association with microtubules. The Plant Journal. 2008:**54**(5):829–844. https://doi.org/10.1111/j.1365-313X.2008.03445.x

Mouille G, Ralet M-C, Cavelier C, Eland C, Effroy D, Hématy K, McCartney L, Truong HN, Gaudon V, Thibault J-F, et al. Homogalacturonan synthesis in Arabidopsis thaliana

requires a Golgi-localized protein with a putative methyltransferase domain. The Plant Journal. 2007:**50**(4):605–614. https://doi.org/10.1111/j.1365-313X.2007.03086.x

Moukhtar J, Trubuil A, Belcram K, Legland D, Khadir Z, Urbain A, Palauqui J-C, and Andrey P. Cell geometry determines symmetric and asymmetric division plane selection in Arabidopsis early embryos. PLoS Comput Biol. 2019:**15**(2):e1006771. https://doi.org/10.1371/journal.pcbi.1006771

Moulia B, Coutand C, and Lenne C. Posture control and skeletal mechanical acclimation in terrestrial plants: implications for mechanical modeling of plant architecture. American Journal of Botany. 2006:**93**(10):1477–1489. https://doi.org/10.3732/ajb.93.10.1477

Moulia B and Fournier M. The power and control of gravitropic movements in plants: a biomechanical and systems biology view. Journal of Experimental Botany. 2009:**60**(2):461–486. https://doi.org/10.1093/jxb/ern341

Muilinax JB and Palevitz BA. Microtubule reorganization accompanying preprophase band formation in guard mother cells of Arena sativa L.

Müller S, Han S, and Smith LG. Two Kinesins Are Involved in the Spatial Control of Cytokinesis in Arabidopsis thaliana. Current Biology. 2006:**16**(9):888–894. https://doi.org/10.1016/j.cub.2006.03.034

Müller S, Smertenko A, Wagner V, Heinrich M, Hussey PJ, and Hauser M-T. The Plant Microtubule-Associated Protein AtMAP65-3/PLE Is Essential for Cytokinetic Phragmoplast Function. Current Biology. 2004:**14**(5):412–417. https://doi.org/10.1016/j.cub.2004.02.032

Murata T, Sano T, Sasabe M, Nonaka S, Higashiyama T, Hasezawa S, Machida Y, and Hasebe M. Mechanism of microtubule array expansion in the cytokinetic phragmoplast. Nat Commun. 2013:**4**(1):1967. https://doi.org/10.1038/ncomms2967

Murata T, Sonobe S, Baskin TI, Hyodo S, Hasezawa S, Nagata T, Horio T, and Hasebe M. Microtubule-dependent microtubule nucleation based on recruitment of γ-tubulin in higher plants. Nat Cell Biol. 2005:**7**(10):961–968. https://doi.org/10.1038/ncb1306

Muroyama A, Gong Y, and Bergmann DC. Opposing, Polarity-Driven Nuclear Migrations Underpin Asymmetric Divisions to Pattern Arabidopsis Stomata. Current Biology. 2020:**30**(22):4467-4475.e4. https://doi.org/10.1016/j.cub.2020.08.100

Muroyama A, Gong Y, Hartman KS, and Bergmann DC. Cortical polarity ensures its own asymmetric inheritance in the stomatal lineage to pattern the leaf surface. Science. 2023.

Murray JAH, Jones A, Godin C, and Traas J. Systems Analysis of Shoot Apical Meristem Growth and Development: Integrating Hormonal and Mechanical Signaling. Plant Cell. 2012:**24**(10):3907–3919. https://doi.org/10.1105/tpc.112.102194

Myers DC, Sepich DS, and Solnica-Krezel L. Convergence and extension in vertebrate gastrulae: cell movements according to or in search of identity? Trends in Genetics. 2002:**18**(9):447–455. https://doi.org/10.1016/S0168-9525(02)02725-7

Nakamura M, Ehrhardt DW, and Hashimoto T. Microtubule and katanin-dependent dynamics of microtubule nucleation complexes in the acentrosomal Arabidopsis cortical array. Nat Cell Biol. 2010:**12**(11):1064–1070. https://doi.org/10.1038/ncb2110

Nakamura M, Katsumata H, Abe M, Yabe N, Komeda Y, Yamamoto KT, and Takahashi T. Characterization of the Class IV Homeodomain-Leucine Zipper Gene Family in Arabidopsis. Plant Physiol. 2006:**141**(4):1363–1375. https://doi.org/10.1104/pp.106.077388

Nakamura M, Lindeboom JJ, Saltini M, Mulder BM, and Ehrhardt DW. SPR2 protects minus ends to promote severing and reorientation of plant cortical microtubule arrays. Journal of Cell Biology. 2018:**217**(3):915–927. https://doi.org/10.1083/jcb.201708130

Nakamura M, Naoi K, Shoji T, and Hashimoto T. Low Concentrations of Propyzamide and Oryzalin Alter Microtubule Dynamics in Arabidopsis Epidermal Cells. Plant and Cell Physiology. 2004:**45**(9):1330–1334. https://doi.org/10.1093/pcp/pch300

Nakamura M, Toyota M, Tasaka M, and Morita MT. An *Arabidopsis* E3 Ligase, SHOOT GRAVITROPISM9, Modulates the Interaction between Statoliths and F-Actin in Gravity Sensing. The Plant Cell. 2011:**23**(5):1830–1848. https://doi.org/10.1105/tpc.110.079442

Nakamura M, Yagi N, Kato T, Fujita S, Kawashima N, Ehrhardt DW, and Hashimoto T. Arabidopsis GCP3-interacting protein 1/MOZART 1 is an integral component of the γ-tubulin-containing microtubule nucleating complex. The Plant Journal. 2012:**71**(2):216–225. https://doi.org/10.1111/j.1365-313X.2012.04988.x

Nakaya M, Tsukaya H, Murakami N, and Kato M. Brassinosteroids Control the Proliferation of Leaf Cells of Arabidopsis thaliana. Plant and Cell Physiology. 2002:**43**(2):239–244. https://doi.org/10.1093/pcp/pcf024

Nakayama N, Smith RS, Mandel T, Robinson S, Kimura S, Boudaoud A, and Kuhlemeier C. Mechanical Regulation of Auxin-Mediated Growth. Current Biology. 2012:**22**(16):1468–1476. https://doi.org/10.1016/j.cub.2012.06.050

Nath U, Crawford BCW, Carpenter R, and Coen E. Genetic Control of Surface Curvature. Science. 2003:**299**(5611):1404–1407. https://doi.org/10.1126/science.1079354

Niklas KJ. The influence of gravity and wind on land plant evolution. Review of Palaeobotany and Palynology. 1998:**102**(1–2):1–14. https://doi.org/10.1016/S0034-6667(98)00011-6

Nowlan NC, Sharpe J, Roddy KA, Prendergast PJ, and Murphy P. Mechanobiology of embryonic skeletal development: Insights from animal models. Birth Defects Research Part C: Embryo Today: Reviews. 2010:**90**(3):203–213. https://doi.org/10.1002/bdrc.20184

Nurse P. Universal control mechanism regulating onset of M-phase. Nature. 1990:**344**(6266):503–508. https://doi.org/10.1038/344503a0

Nurse P and Bissett Y. Gene required in G1 for commitment to cell cycle and in G2 for control of mitosis in fission yeast. Nature. 1981:**292**(5823):558–560. https://doi.org/10.1038/292558a0

Oakenfull EA, Riou-Khamlichi C, and Murray AH. Plant D–type cyclins and the control of G1 progression. Phil Trans R Soc Lond B. 2002:**357**(1422):749–760. https://doi.org/10.1098/rstb.2002.1085

Ogawa E, Yamada Y, Sezaki N, Kosaka S, Kondo H, Kamata N, Abe M, Komeda Y, and Takahashi T. ATML1 and PDF2 Play a Redundant and Essential Role in Arabidopsis Embryo Development. Plant and Cell Physiology. 2015:**56**(6):1183–1192. https://doi.org/10.1093/pcp/pcv045

Oh SA, Allen T, Kim GJ, Sidorova A, Borg M, Park SK, and Twell D. Arabidopsis Fused kinase and the Kinesin-12 subfamily constitute a signalling module required for phragmoplast expansion. The Plant Journal. 2012:**72**(2):308–319. https://doi.org/10.1111/j.1365-313X.2012.05077.x

Ookata K, Hisanaga S, Bulinski JC, Murofushi H, Aizawa H, Itoh TJ, and Kishimoto T. Cyclin B Interaction with Microtubule-associated Protein 4 (MAP4) Targets p34edaKinase to Micrombules and Is a Potential Regulator of M-phase Microtubule Dynamics. The Journal of Cell Biology. 1995:**128**.

Ori-McKenney KM, Jan LY, and Jan Y-N. Golgi Outposts Shape Dendrite Morphology by Functioning as Sites of Acentrosomal Microtubule Nucleation in Neurons. Neuron. 2012:**76**(5):921–930. https://doi.org/10.1016/j.neuron.2012.10.008

Osterfield M, Du X, Schüpbach T, Wieschaus E, and Shvartsman SY. Three-Dimensional Epithelial Morphogenesis in the Developing Drosophila Egg. Developmental Cell. 2013:**24**(4):400–410. https://doi.org/10.1016/j.devcel.2013.01.017

Otegui M and Staehelin LA. Cytokinesis in flowering plants: more than one way to divide a cell. Current Opinion in Plant Biology. 2000:**3**(6):493–502. https://doi.org/10.1016/S1369-5266(00)00119-9

Palevitz BA. Actin in the preprophase band of Allium cepa. The Journal of cell biology. 1987:**104**(6):1515–1519. https://doi.org/10.1083/jcb.104.6.1515

Palevitz BA, Ash JF, and Hepler PK. Actin in the Green Alga, *Nitella*. Proc Natl Acad Sci USA. 1974:**71**(2):363–366. https://doi.org/10.1073/pnas.71.2.363

Paluch E and Heisenberg C-P. Biology and Physics of Cell Shape Changes in Development. Current Biology. 2009:**19**(17):R790–R799. https://doi.org/10.1016/j.cub.2009.07.029

Panteris E. Cortical actin filaments at the division site of mitotic plant cells: a reconsideration of the 'actin-depleted zone.' New Phytologist. 2008:**179**(2):334–341. https://doi.org/10.1111/j.1469-8137.2008.02474.x

Panteris E, Adamakis I-DS, Voulgari G, and Papadopoulou G. A role for katanin in plant cell division: Microtubule organization in dividing root cells of fra2 and lue1Arabidopsis thaliana mutants. Cytoskeleton. 2011:**68**(7):401–413. https://doi.org/10.1002/cm.20522

Panteris E, Apostolakos P, and Galatis B. Cytoskeletal asymmetry in Zea mays subsidiary cell mother cells: A monopolar prophase microtubule half-spindle anchors the nucleus to its polar position. Cell Motility. 2006:**63**(11):696–709. https://doi.org/10.1002/cm.20155

Panteris E, Galatis B, Quader H, and Apostolakos P. Cortical actin filament organization in developing and functioning stomatal complexes of Zea mays and Triticum turgidum. Cell Motility. 2007:**64**(7):531–548. https://doi.org/10.1002/cm.20203

Paradez A, Wright A, and Ehrhardt DW. Microtubule cortical array organization and plant cell morphogenesis. Current Opinion in Plant Biology. 2006:**9**(6):571–578. https://doi.org/10.1016/j.pbi.2006.09.005

Paredez AR, Somerville CR, and Ehrhardt DW. Visualization of Cellulose Synthase Demonstrates Functional Association with Microtubules. Science. 2006:**312**(5779):1491–1495. https://doi.org/10.1126/science.1126551

Park E and Nebenführ A. Myosin XIK of Arabidopsis thaliana Accumulates at the Root Hair Tip and Is Required for Fast Root Hair Growth. PLoS ONE. 2013:**8**(10):e76745. https://doi.org/10.1371/journal.pone.0076745

Park YB and Cosgrove DJ. Changes in Cell Wall Biomechanical Properties in the Xyloglucan-Deficient xxt1/xxt2 Mutant of Arabidopsis1[W][OA]. Plant Physiol. 2012:**158**(1):465–475. https://doi.org/10.1104/pp.111.189779

Pastuglia M, Azimzadeh J, Goussot M, Camilleri C, Belcram K, Evrard J-L, Schmit A-C, Guerche P, and Bouchez D. γ-Tubulin Is Essential for Microtubule Organization and Development in Arabidopsis. Plant Cell. 2006:**18**(6):1412–1425. https://doi.org/10.1105/tpc.105.039644

Pati PK, Sharma M, and Ahuja PS. Extra thin alginate film: an efficient technique for protoplast culture. Protoplasma. 2005:**226**(3–4):217–221. https://doi.org/10.1007/s00709-005-0096-4

Peaucelle A, Braybrook SA, Le Guillou L, Bron E, Kuhlemeier C, and Höfte H. Pectin-Induced Changes in Cell Wall Mechanics Underlie Organ Initiation in Arabidopsis. Current Biology. 2011:**21**(20):1720–1726. https://doi.org/10.1016/j.cub.2011.08.057

Peaucelle A, Louvet R, Johansen JN, Höfte H, Laufs P, Pelloux J, and Mouille G. Arabidopsis Phyllotaxis Is Controlled by the Methyl-Esterification Status of Cell-Wall Pectins. Current Biology. 2008:**18**(24):1943–1948. https://doi.org/10.1016/j.cub.2008.10.065

Peng J, Carol P, Richards DE, King KE, Cowling RJ, Murphy GP, and Harberd NP. The *Arabidopsis GAI* gene defines a signaling pathway that negatively regulates gibberellin responses. Genes Dev. 1997:**11**(23):3194–3205. https://doi.org/10.1101/gad.11.23.3194

Peremyslov VV, Klocko AL, Fowler JE, and Dolja VV. Arabidopsis Myosin XI-K Localizes to the Motile Endomembrane Vesicles Associated with F-actin. Front Plant Sci. 2012:**3**. https://doi.org/10.3389/fpls.2012.00184

Pérez García M, Zhang Y, Hayes J, Salazar A, Zabotina OA, and Hong M. Structure and Interactions of Plant Cell-Wall Polysaccharides by Two- and Three-Dimensional Magic-Angle-Spinning Solid-State NMR. Biochemistry. 2011:**50**(6):989–1000. https://doi.org/10.1021/bi101795q

Perrot-Rechenmann C. Cellular Responses to Auxin: Division versus Expansion. Cold Spring Harbor Perspectives in Biology. 2010:**2**(5):a001446–a001446. https://doi.org/10.1101/cshperspect.a001446

Peters WS and Tomos AD. The History of Tissue Tension.

Pickett-Heaps J and Forer A. Mitosis: spindle evolution and the matrix model. Protoplasma. 2009:**235**(1–4):91–99. https://doi.org/10.1007/s00709-009-0030-2

Pickett-Heaps JD. Preprophase microtubule bands in some abnormal mitotic cells of wheat. Journal of Cell Science. 1969:**4**(2):397–420. https://doi.org/10.1242/jcs.4.2.397

Pickett-Heaps JD and Northcote DH. Organization of microtubules and endoplasmic reticulum during mitosis and cytokinesis in wheat meristems. Journal of Cell Science. 1966:**1**(1):109–120. https://doi.org/10.1242/jcs.1.1.109

Pihakaski-Maunsbach K and Puhakainen T. Effect of cold exposure on cortical microtubules of rye (Secale cereale) as observed by immunocytochemistry. Physiologia Plantarum. 1995:**93**(3):563–571. https://doi.org/10.1111/j.1399-3054.1995.tb06859.x

Pinto SC, Stojilković B, Zhang X, and Sablowski R. Plant cell size: Links to cell cycle, differentiation and ploidy. Current Opinion in Plant Biology. 2024:**78**:102527. https://doi.org/10.1016/j.pbi.2024.102527

Plavcová L, Gallenmüller F, Morris H, Khatamirad M, Jansen S, and Speck T. Mechanical properties and structure–function trade-offs in secondary xylem of young roots and stems. Journal of Experimental Botany. 2019:**70**(14):3679–3691. https://doi.org/10.1093/jxb/erz286

Pollard TD, Blanchoin L, and Mullins RD. Molecular Mechanisms Controlling Actin Filament Dynamics in Nonmuscle Cells. Annu Rev Biophys Biomol Struct. 2000:**29**(1):545–576. https://doi.org/10.1146/annurev.biophys.29.1.545

Pollard TD and Cooper JA. Actin, a Central Player in Cell Shape and Movement. Science. 2009:**326**(5957):1208–1212. https://doi.org/10.1126/science.1175862

del Pozo JC, Diaz-Trivino S, Cisneros N, and Gutierrez C. The Balance between Cell Division and Endoreplication Depends on E2FC-DPB, Transcription Factors Regulated by the Ubiquitin-SCFSKP2A Pathway in Arabidopsis. Plant Cell. 2006:**18**(9):2224–2235. https://doi.org/10.1105/tpc.105.039651

Pradillo M, Evans D, and Graumann K. The nuclear envelope in higher plant mitosis and meiosis. Nucleus. 2019a:**10**(1):55–66. https://doi.org/10.1080/19491034.2019.1587277

Pradillo M, Evans D, and Graumann K. The nuclear envelope in higher plant mitosis and meiosis. Nucleus. 2019b:**10**(1):55–66. https://doi.org/10.1080/19491034.2019.1587277

Prusicki MA, Keizer EM, Van Rosmalen RP, Komaki S, Seifert F, Müller K, Wijnker E, Fleck C, and Schnittger A. Live cell imaging of meiosis in Arabidopsis thaliana. eLife. 2019:**8**:e42834. https://doi.org/10.7554/eLife.42834

Qu L-H and Sun M-X. The plant cell nucleus is constantly alert and highly sensitive to repetitive local mechanical stimulations. Plant Cell Rep. 2007:**26**(8):1187–1193. https://doi.org/10.1007/s00299-007-0343-6

Quarmby L and Mahjoub MR. Caught Nek-ing: Cilia and centrioles. Journal of cell science. 2005:**118**:5161–9. https://doi.org/10.1242/jcs.02681

Rayment I, Holden HM, Whittaker M, Yohn CB, Lorenz M, Holmes KC, and Milligan RA. Structure of the Actin-Myosin Complex and Its Implications for Muscle Contraction. Science. 1993:**261**(5117):58–65.

Rebocho AB, Southam P, Kennaway JR, Bangham JA, and Coen E. Generation of shape complexity through tissue conflict resolution. eLife. 2017:**6**:e20156. https://doi.org/10.7554/eLife.20156

Reichelt S, Knight AE, Hodge TP, Baluska F, Samaj J, Volkmann D, and Kendrick-Jones J. Characterization of the unconventional myosin VIII in plant cells and its localization at the post-cytokinetic cell wall. The Plant Journal. 1999:**19**(5):555–567. https://doi.org/10.1046/j.1365-313X.1999.00553.x

Reinhardt D, Frenz M, Mandel T, and Kuhlemeier C. Microsurgical and laser ablation analysis of interactions between the zones and layers of the tomato shoot apical meristem. Development (Cambridge, England). 2003a:**130**:4073–83. https://doi.org/10.1242/dev.00596

Reinhardt D, Mandel T, and Kuhlemeier C. Auxin Regulates the Initiation and Radial Position of Plant Lateral Organs. 2000.

Reinhardt D, Pesce E-R, Stieger P, Mandel T, Baltensperger K, Bennett M, Traas J, Friml J, and Kuhlemeier C. Regulation of phyllotaxis by polar auxin transport. Nature. 2003b:**426**(6964):255–260. https://doi.org/10.1038/nature02081

Ripoll J-J, Zhu M, Brocke S, Hon CT, Yanofsky MF, Boudaoud A, and Roeder AHK. Growth dynamics of the *Arabidopsis* fruit is mediated by cell expansion. Proc Natl Acad Sci USA. 2019:**116**(50):25333–25342. https://doi.org/10.1073/pnas.1914096116

Robinson S and Kuhlemeier C. Global Compression Reorients Cortical Microtubules in Arabidopsis Hypocotyl Epidermis and Promotes Growth. Current Biology. 2018:**28**(11):1794-1802.e2. https://doi.org/10.1016/j.cub.2018.04.028

Rodriguez RE, Debernardi JM, and Palatnik JF. Morphogenesis of simple leaves: regulation of leaf size and shape. WIREs Developmental Biology. 2014:**3**(1):41–57. https://doi.org/10.1002/wdev.115

Roeder AHK, Chickarmane V, Cunha A, Obara B, Manjunath BS, and Meyerowitz EM. Variability in the Control of Cell Division Underlies Sepal Epidermal Patterning in Arabidopsis thaliana. PLoS Biol. 2010:**8**(5):e1000367. https://doi.org/10.1371/journal.pbio.1000367

Rölleke U, Kumari P, Meyer R, and Köster S. The unique biomechanics of intermediate filaments – From single filaments to cells and tissues. Current Opinion in Cell Biology. 2023:**85**:102263. https://doi.org/10.1016/j.ceb.2023.102263

Romeiro Motta M, Biswas S, and Schaedel L. Beyond uniformity: Exploring the heterogeneous and dynamic nature of the microtubule lattice. European Journal of Cell Biology. 2023:**102**(4):151370. https://doi.org/10.1016/j.ejcb.2023.151370

Romeiro Motta M, Zhao X, Pastuglia M, Belcram K, Roodbarkelari F, Komaki M, Harashima H, Komaki S, Kumar M, Bulankova P, et al. B1-type cyclins control microtubule organization during cell division in *Arabidopsis*. EMBO Reports. 2022:**23**(1):e53995. https://doi.org/10.15252/embr.202153995

Roncero C and Sánchez Y. Cell separation and the maintenance of cell integrity during cytokinesis in yeast: the assembly of a septum. Yeast. 2010:**27**(8):521–530. https://doi.org/10.1002/yea.1779

Rong D, Zhao S, Tang W, Luo N, He H, Wang Z, Ma H, Huang Y, Yao X, Pan X, et al. ROP signaling regulates spatial pattern of cell division and specification of meristem notch. Proc Natl Acad Sci USA. 2022:**119**(47):e2117803119. https://doi.org/10.1073/pnas.2117803119

Rongpipi S, Ye D, Gomez ED, and Gomez EW. Progress and Opportunities in the Characterization of Cellulose – An Important Regulator of Cell Wall Growth and Mechanics. Front Plant Sci. 2019:**9**:1894. https://doi.org/10.3389/fpls.2018.01894

Ross MD. The influence of gravity on structure and function of animals. Advances in Space Research. 1984:**4**(12):305–314. https://doi.org/10.1016/0273-1177(84)90575-1

Rutten TLM and Derksen J. Organization of actin filaments in regenerating and outgrowing subprotoplasts from pollen tubes ofNicotiana tabacum L. Planta. 1990:**180**(4):471–479. https://doi.org/10.1007/BF02411443

Ryu KH, Huang L, Kang HM, and Schiefelbein J. Single-Cell RNA Sequencing Resolves Molecular Relationships Among Individual Plant Cells. Plant Physiol. 2019:**179**(4):1444–1456. https://doi.org/10.1104/pp.18.01482

Sablowski R and Gutierrez C. Cycling in a crowd: Coordination of plant cell division, growth, and cell fate. The Plant Cell. 2022:**34**(1):193–208. https://doi.org/10.1093/plcell/koab222

Sachs J. Uber die Anordnung der Zellen in jungsten Pflanzentheilen. Arbeiten des Botanisches Institut Wurzburg 2:46–104.

Sakai K, Charlot F, Le Saux T, Bonhomme S, Nogué F, Palauqui J-C, and Fattaccioli J. Design of a comprehensive microfluidic and microscopic toolbox for the ultra-wide spatio-temporal study of plant protoplasts development and physiology. Plant Methods. 2019:**15**(1):79. https://doi.org/10.1186/s13007-019-0459-z

Sakai T, Honing H van der, Nishioka M, Uehara Y, Takahashi M, Fujisawa N, Saji K, Seki M, Shinozaki K, Jones MA, et al. Armadillo repeat-containing kinesins and a NIMA-related kinase are required for epidermal-cell morphogenesis in Arabidopsis. The Plant Journal. 2008:**53**(1):157–171. https://doi.org/10.1111/j.1365-313X.2007.03327.x

Salbreux G, Charras G, and Paluch E. Actin cortex mechanics and cellular morphogenesis. Trends in Cell Biology. 2012:**22**(10):536–545. https://doi.org/10.1016/j.tcb.2012.07.001

Sambade A, Pratap A, Buschmann H, Morris RJ, and Lloyd C. The Influence of Light on Microtubule Dynamics and Alignment in the *Arabidopsis* Hypocotyl. The Plant Cell. 2012:**24**(1):192–201. https://doi.org/10.1105/tpc.111.093849

Sampathkumar A. Mechanical feedback-loop regulation of morphogenesis in plants. Development. 2020:**147**(16):dev177964. https://doi.org/10.1242/dev.177964

Sampathkumar A, Gutierrez R, McFarlane HE, Bringmann M, Lindeboom J, Emons A-M, Samuels L, Ketelaar T, Ehrhardt DW, and Persson S. Patterning and Lifetime of Plasma Membrane-Localized Cellulose Synthase Is Dependent on Actin Organization in Arabidopsis Interphase Cells. Plant Physiology. 2013:**162**(2):675–688. https://doi.org/10.1104/pp.113.215277

Sampathkumar A, Krupinski P, Wightman R, Milani P, Berquand A, Boudaoud A, Hamant O, Jönsson H, and Meyerowitz EM. Subcellular and supracellular mechanical stress prescribes cytoskeleton behavior in Arabidopsis cotyledon pavement cells. eLife. 2014:**3**:e01967. https://doi.org/10.7554/eLife.01967

Sampathkumar A, Lindeboom JJ, Debolt S, Gutierrez R, Ehrhardt DW, Ketelaar T, and Persson S. Live Cell Imaging Reveals Structural Associations between the Actin and

Microtubule Cytoskeleton in *Arabidopsis* . The Plant Cell. 2011:**23**(6):2302–2313. https://doi.org/10.1105/tpc.111.087940

Sanchez MDLP, Costas C, Sequeira-Mendes J, and Gutierrez C. Regulating DNA Replication in Plants. Cold Spring Harbor Perspectives in Biology. 2012:**4**(12):a010140–a010140. https://doi.org/10.1101/cshperspect.a010140

Sánchez-Huertas C, Freixo F, Viais R, Lacasa C, Soriano E, and Lüders J. Non-centrosomal nucleation mediated by augmin organizes microtubules in post-mitotic neurons and controls axonal microtubule polarity. Nat Commun. 2016:**7**(1):12187. https://doi.org/10.1038/ncomms12187

Sano T, Higaki T, Oda Y, Hayashi T, and Hasezawa S. Appearance of actin microfilament 'twin peaks' in mitosis and their function in cell plate formation, as visualized in tobacco BY-2 cells expressing GFP–fimbrin. The Plant Journal. 2005:**44**(4):595–605. https://doi.org/10.1111/j.1365-313X.2005.02558.x

Sasaki T, Tsutsumi M, Otomo K, Murata T, Yagi N, Nakamura M, Nemoto T, Hasebe M, and Oda Y. A Novel Katanin-Tethering Machinery Accelerates Cytokinesis. Current Biology. 2019:**29**(23):4060-4070.e3. https://doi.org/10.1016/j.cub.2019.09.049

Sassi M, Ali O, Boudon F, Cloarec G, Abad U, Cellier C, Chen X, Gilles B, Milani P, Friml J, et al. An Auxin-Mediated Shift toward Growth Isotropy Promotes Organ Formation at the Shoot Meristem in Arabidopsis. Current Biology. 2014:**24**(19):2335–2342. https://doi.org/10.1016/j.cub.2014.08.036

Sassi M and Vernoux T. Auxin and self-organization at the shoot apical meristem. Journal of Experimental Botany. 2013:**64**(9):2579–2592. https://doi.org/10.1093/jxb/ert101

Sauer M, Balla J, Luschnig C, Wiśniewska J, Reinöhl V, Friml J, and Benková E. Canalization of auxin flow by Aux/IAA-ARF-dependent feedback regulation of PIN polarity. Genes Dev. 2006:**20**(20):2902–2911. https://doi.org/10.1101/gad.390806

Savaldi-Goldstein S, Peto C, and Chory J. The epidermis both drives and restricts plant shoot growth. Nature. 2007:**446**(7132):199–202. https://doi.org/10.1038/nature05618

Savin T, Kurpios NA, Shyer AE, Florescu P, Liang H, Mahadevan L, and Tabin CJ. On the growth and form of the gut. Nature. 2011:**476**(7358):57–62. https://doi.org/10.1038/nature10277

Sawidis T, Quader H, Bopp M, and Schnepf E. Presence and absence of the preprophase band of microtubules in moss protonemata: a clue to understanding its function? Protoplasma. 1991:**163**(2–3):156–161. https://doi.org/10.1007/BF01323339

Scarpella E, Barkoulas M, and Tsiantis M. Control of Leaf and Vein Development by Auxin. Cold Spring Harbor Perspectives in Biology. 2010:**2**(1):a001511–a001511. https://doi.org/10.1101/cshperspect.a001511

Schaedel L, John K, Gaillard J, Nachury MV, Blanchoin L, and Théry M. Microtubules self-repair in response to mechanical stress. Nat Mater. 2015:**14**(11):1156–1163. https://doi.org/10.1038/nmat4396

Schaedel L, Triclin S, Chrétien D, Abrieu A, Aumeier C, Gaillard J, Blanchoin L, Théry M, and John K. Lattice defects induce microtubule self-renewal. Nat Phys. 2019:**15**(8):830–838. https://doi.org/10.1038/s41567-019-0542-4

Schaefer E, Belcram K, Uyttewaal M, Duroc Y, Goussot M, Legland D, Laruelle E, de Tauzia-Moreau M-L, Pastuglia M, and Bouchez D. The preprophase band of microtubules controls the robustness of division orientation in plants. Science. 2017:**356**(6334):186–189. https://doi.org/10.1126/science.aal3016

Schaller GE, Bishopp A, and Kieber JJ. The Yin-Yang of Hormones: Cytokinin and Auxin Interactions in Plant Development. Plant Cell. 2015:**27**(1):44–63. https://doi.org/10.1105/tpc.114.133595

Schiessl K, Muiño JM, and Sablowski R. Arabidopsis JAGGED links floral organ patterning to tissue growth by repressing Kip-related cell cycle inhibitors. Proc Natl Acad Sci USA. 2014:**111**(7):2830–2835. https://doi.org/10.1073/pnas.1320457111

Schiff PB and Horwitz SB. Taxol stabilizes microtubules in mouse fibroblast cells. Proc Natl Acad Sci USA. 1980:**77**(3):1561–1565. https://doi.org/10.1073/pnas.77.3.1561

Schneider R, Hanak T, Persson S, and Voigt CA. Cellulose and callose synthesis and organization in focus, what's new? Current Opinion in Plant Biology. 2016:**34**:9–16. https://doi.org/10.1016/j.pbi.2016.07.007

Schneider R, Klooster K van't, Picard KL, van der Gucht J, Demura T, Janson M, Sampathkumar A, Deinum EE, Ketelaar T, and Persson S. Long-term single-cell imaging and simulations of microtubules reveal principles behind wall patterning during proto-xylem development. Nat Commun. 2021:**12**(1):669. https://doi.org/10.1038/s41467-021-20894-1

Schneider R and Persson S. Connecting two arrays: the emerging role of actin-microtubule cross-linking motor proteins. Front Plant Sci. 2015:**6**. https://doi.org/10.3389/fpls.2015.00415

Schopfer P. Biomechanics of plant growth. American Journal of Botany. 2006:**93**(10):1415–1425. https://doi.org/10.3732/ajb.93.10.1415

Schwarz N and Leube RE. Plasticity of cytoplasmic intermediate filament architecture determines cellular functions. Current Opinion in Cell Biology. 2023:**85**:102270. https://doi.org/10.1016/j.ceb.2023.102270

Scofield S, Jones A, and Murray JAH. The plant cell cycle in context. Journal of Experimental Botany. 2014:**65**(10):2557–2562. https://doi.org/10.1093/jxb/eru188

Scott CB, Mjolsness E, Oyen D, Kodera C, Uyttewaal M, and Bouchez D. Graph metric learning quantifies morphological differences between two genotypes of shoot apical meristem cells in *Arabidopsis*. in silico Plants. 2023:**5**(1):diad001. https://doi.org/10.1093/insilicoplants/diad001

Sha W, Moore J, Chen K, Lassaletta AD, Yi C-S, Tyson JJ, and Sible JC. Hysteresis drives cell-cycle transitions in *Xenopus laevis* egg extracts. Proc Natl Acad Sci USA. 2003:**100**(3):975–980. https://doi.org/10.1073/pnas.0235349100

Sharir A, Stern T, Rot C, Shahar R, and Zelzer E. Muscle force regulates bone shaping for optimal load-bearing capacity during embryogenesis. Development. 2011:**138**(15):3247–3259. https://doi.org/10.1242/dev.063768

Shaw SL, Kamyar R, and Ehrhardt DW. Sustained Microtubule Treadmilling in *Arabidopsis* Cortical Arrays. Science. 2003:**300**(5626):1715–1718. https://doi.org/10.1126/science.1083529

Shimmen T and Yokota E. Cytoplasmic streaming in plants. Current Opinion in Cell Biology. 2004:**16**(1):68–72. https://doi.org/10.1016/j.ceb.2003.11.009

Shimotohno A, Aki SS, Takahashi N, and Umeda M. Regulation of the Plant Cell Cycle in Response to Hormones and the Environment. Annu Rev Plant Biol. 2021:**72**(1):273–296. https://doi.org/10.1146/annurev-arplant-080720-103739

Shoji T, Narita NN, Hayashi K, Asada J, Hamada T, Sonobe S, Nakajima K, and Hashimoto T. Plant-Specific Microtubule-Associated Protein SPIRAL2 Is Required for Anisotropic Growth in Arabidopsis. Plant Physiology. 2004:**136**(4):3933–3944. https://doi.org/10.1104/pp.104.051748

Shraiman BI. Mechanical feedback as a possible regulator of tissue growth. 2005. https://www.pnas.org/doi/epdf/10.1073/pnas.0404782102. Retrieved July 22, 2024

Shyer AE, Tallinen T, Nerurkar NL, Wei Z, Gil ES, Kaplan DL, Tabin CJ, and Mahadevan L. Villification: How the Gut Gets Its Villi. Science. 2013:**342**(6155):212–218. https://doi.org/10.1126/science.1238842

Simons M and Mlodzik M. Planar Cell Polarity Signaling: From Fly Development to Human Disease. Annual review of genetics. 2008:**42**:517–40. https://doi.org/10.1146/annurev.genet.42.110807.091432

Sinnott EW and Bloch R. The Relative Position of Cell Walls in Developing Plant Tissues. American Journal of Botany. 1941:**28**(7):607–617. https://doi.org/10.2307/2437010

Slautterback DB. CYTOPLASMIC MICROTUBULES. The Journal of Cell Biology. 1963:**18**(2):367–388. https://doi.org/10.1083/jcb.18.2.367

Smertenko A, Assaad F, Baluška F, Bezanilla M, Buschmann H, Drakakaki G, Hauser M-T, Janson M, Mineyuki Y, Moore I, et al. Plant Cytokinesis: Terminology for Structures and Processes. Trends in Cell Biology. 2017:**27**(12):885–894. https://doi.org/10.1016/j.tcb.2017.08.008

Smertenko AP, Chang H-Y, Sonobe S, Fenyk SI, Weingartner M, Bögre L, and Hussey PJ. Control of the AtMAP65-1 interaction with microtubules through the cell cycle. Journal of Cell Science. 2006:**119**(15):3227–3237. https://doi.org/10.1242/jcs.03051

Smirnova EA and Bajer AS. Spindle poles in higher plant mitosis. Cell Motility. 1992:**23**(1):1–7. https://doi.org/10.1002/cm.970230102

Smirnova EA and Bajer AS. Early stages of spindle formation and independence of chromosome and microtubule cycles in Haemanthus endosperm. Cell Motility. 1998:**40**(1):22–37. https://doi.org/10.1002/(SICI)1097-0169(1998)40:1<22::AID-CM3>3.0.CO;2-H

Smith LG. Plant cell division: building walls in the right places. Nat Rev Mol Cell Biol. 2001:**2**(1):33–39. https://doi.org/10.1038/35048050

Smith LG, Hake S, and Sylvester AW. The *tangled-1* mutation alters cell division orientations throughout maize leaf development without altering leaf shape. Development. 1996:**122**(2):481–489. https://doi.org/10.1242/dev.122.2.481

Smith LG and Oppenheimer DG. SPATIAL CONTROL OF CELL EXPANSION BY THE PLANT CYTOSKELETON. Annu Rev Cell Dev Biol. 2005:**21**(1):271–295. https://doi.org/10.1146/annurev.cellbio.21.122303.114901

Snowman BN, Kovar DR, Shevchenko G, Franklin-Tong VE, and Staiger CJ. Signal-Mediated Depolymerization of Actin in Pollen during the Self-Incompatibility Response. Plant Cell. 2002:**14**(10):2613–2626. https://doi.org/10.1105/tpc.002998

Sorrell D, Marchbank A, McMahon K, Dickinson R, Rogers H, and Francis D. A WEE1 homologue from Arabidopsis thaliana. Planta. 2002:**215**(3):518–522. https://doi.org/10.1007/s00425-002-0815-4

Spadafora ND, Doonan JH, Herbert RJ, Bitonti MB, Wallace E, Rogers HJ, and Francis D. Arabidopsis T-DNA insertional lines for CDC25 are hypersensitive to hydroxyurea but not to zeocin or salt stress. Annals of Botany. 2011:**107**(7):1183–1192. https://doi.org/10.1093/aob/mcq142

Spector I, Shochet N, Kashman Y, and Groweiss A. Latrunculins: novel marine toxins that disrupt microfilament organization in cultured cells. Science. 1983:**219**(4584):493–495. https://doi.org/10.1126/science.6681676

Spinner L, Gadeyne A, Belcram K, Goussot M, Moison M, Duroc Y, Eeckhout D, De Winne N, Schaefer E, Van De Slijke E, et al. A protein phosphatase 2A complex spatially controls plant cell division. Nat Commun. 2013:**4**(1):1863. https://doi.org/10.1038/ncomms2831

Staiger CJ and Blanchoin L. Actin dynamics: old friends with new stories. Current Opinion in Plant Biology. 2006:**9**(6):554–562. https://doi.org/10.1016/j.pbi.2006.09.013

Staiger CJ and Schliwa M. Actin localization and function in higher plants. Protoplasma. 1987:**141**(1):1–12. https://doi.org/10.1007/BF01276783

Staiger CJ, Sheahan MB, Khurana P, Wang X, McCurdy DW, and Blanchoin L. Actin filament dynamics are dominated by rapid growth and severing activity in the *Arabidopsis* cortical array. Journal of Cell Biology. 2009:**184**(2):269–280. https://doi.org/10.1083/jcb.200806185

Stals H, Bauwens S, Traas J, Van Montagu M, Engler G, and Inzé D. Plant CDC2 is not only targeted to the pre-prophase band, but also co-localizes with the spindle, phragmoplast, and chromosomes. FEBS Letters. 1997:**418**(3):229–234. https://doi.org/10.1016/S0014-5793(97)01368-9

Stamm K and Dirks J-H. Insect exoskeletons react to hypergravity. Proceedings of the Royal Society B. 2023. https://doi.org/10.1098/rspb.2023.2141

Stewart MP, Helenius J, Toyoda Y, Ramanathan SP, Muller DJ, and Hyman AA. Hydrostatic pressure and the actomyosin cortex drive mitotic cell rounding. Nature. 2011:**469**(7329):226–230. https://doi.org/10.1038/nature09642

Stieger PA, Reinhardt D, and Kuhlemeier C. The auxin influx carrier is essential for correct leaf positioning. The Plant Journal. 2002:**32**(4):509–517. https://doi.org/10.1046/j.1365-313X.2002.01448.x

Stöckle D, Reyes-Hernández BJ, Vilches Barro A, Nenadić M, Winter Z, Marc-Martin S, Bald L, Ursache R, Fujita S, Maizel A, et al. Microtubule-based perception of mechanical conflicts controls plant organ morphogenesis. SCIENCE ADVANCES. 2022.

Stoppin V, Vantard M, Schmit AC, and Lambert AM. Isolated Plant Nuclei Nucleate Microtubule Assembly: The Nuclear Surface in Higher Plants Has Centrosome-like Activity. Plant Cell. 1994:**6**(8):1099–1106. https://doi.org/10.1105/tpc.6.8.1099

Stoppin-Mellet V, Gaillard J, and Vantard M. Functional evidence for in vitro microtubule severing by the plant katanin homologue. Biochem J. 2002:**365**(Pt 2):337–342. https://doi.org/10.1042/BJ20020689

Stoppin-Mellet V, Gaillard J, and Vantard M. Katanin's severing activity favors bundling of cortical microtubules in plants. The Plant Journal. 2006:**46**(6):1009–1017. https://doi.org/10.1111/j.1365-313X.2006.02761.x

Strzalka W and Ziemienowicz A. Proliferating cell nuclear antigen (PCNA): a key factor in DNA replication and cell cycle regulation. Annals of Botany. 2011:**107**(7):1127–1140. https://doi.org/10.1093/aob/mcq243

Sugimoto K, Jiao Y, and Meyerowitz EM. Arabidopsis Regeneration from Multiple Tissues Occurs via a Root Development Pathway. Developmental Cell. 2010:**18**(3):463–471. https://doi.org/10.1016/j.devcel.2010.02.004

Sulimenko V, Hájková Z, Klebanovych A, and Draber P. Regulation of microtubule nucleation mediated by γ-tubulin complexes. Protoplasma. 2017:**254**. https://doi.org/10.1007/s00709-016-1070-z

Swarup K, Benková E, Swarup R, Casimiro I, Péret B, Yang Y, Parry G, Nielsen E, De Smet I, Vanneste S, et al. The auxin influx carrier LAX3 promotes lateral root emergence. Nat Cell Biol. 2008:**10**(8):946–954. https://doi.org/10.1038/ncb1754

Szekeres M, Németh K, Koncz-Kálmán Z, Mathur J, Kauschmann A, Altmann T, Rédei GP, Nagy F, Schell J, and Koncz C. Brassinosteroids Rescue the Deficiency of CYP90, a Cytochrome P450, Controlling Cell Elongation and De-etiolation in Arabidopsis. Cell. 1996:**85**(2):171–182. https://doi.org/10.1016/S0092-8674(00)81094-6

Tagawa S, Yamagishi Y, Watanabe U, Funada R, and Kondo T. Dynamics of structural polysaccharides deposition on the plasma-membrane surface of plant protoplasts during cell wall regeneration. J Wood Sci. 2019:**65**(1):47. https://doi.org/10.1186/s10086-019-1826-0

Takatani S, Ozawa S, Yagi N, Hotta T, Hashimoto T, Takahashi Y, Takahashi T, and Motose H. Directional cell expansion requires NIMA-related kinase 6 (NEK6)-mediated cortical microtubule destabilization. Sci Rep. 2017:**7**(1):7826. https://doi.org/10.1038/s41598-017-08453-5

Takatani S, Verger S, Okamoto T, Takahashi T, Hamant O, and Motose H. Microtubule Response to Tensile Stress Is Curbed by NEK6 to Buffer Growth Variation in the Arabidopsis Hypocotyl. Current Biology. 2020:**30**(8):1491-1503.e2. https://doi.org/10.1016/j.cub.2020.02.024

Takatsuka H and Umeda M. Hormonal control of cell division and elongation along differentiation trajectories in roots. Journal of Experimental Botany. 2014:**65**(10):2633–2643. https://doi.org/10.1093/jxb/ert485

Tatout C, Evans DE, Vanrobays E, Probst AV, and Graumann K. The plant LINC complex at the nuclear envelope. Chromosome Res. 2014:**22**(2):241–252. https://doi.org/10.1007/s10577-014-9419-7

Taubenberger AV, Baum B, and Matthews HK. The Mechanics of Mitotic Cell Rounding. Front Cell Dev Biol. 2020:**8**:687. https://doi.org/10.3389/fcell.2020.00687

Teale WD, Paponov IA, and Palme K. Auxin in action: signalling, transport and the control of plant growth and development. Nat Rev Mol Cell Biol. 2006:**7**(11):847–859. https://doi.org/10.1038/nrm2020

Thibaut B, Gril J, and Fournier M. Mechanics of wood and trees: some new highlights for an old story. Comptes Rendus de l'Académie des Sciences - Series IIB - Mechanics. 2001:**329**(9):701–716. https://doi.org/10.1016/S1620-7742(01)01380-0

Thimann KV and Schneider CL. Differential Growth in Plant Tissues. American Journal of Botany. 1938:**25**(8):627–641. https://doi.org/10.2307/2436524

Thomas C, Tholl S, Moes D, Dieterle M, Papuga J, Moreau F, and Steinmetz A. Actin bundling in plants. Cell Motility. 2009:**66**(11):940–957. https://doi.org/10.1002/cm.20389

Thompson D. On growth and form First edition. (Cambridge University Press).

Thorand E. Mechanical investigation of wall-less plant cells using microfluidics. 2018.

Tindemans SH, Hawkins RJ, and Mulder BM. Survival of the Aligned: Ordering of the Plant Cortical Microtubule Array. Phys Rev Lett. 2010:**104**(5):058103. https://doi.org/10.1103/PhysRevLett.104.058103

Tominaga M, Kimura A, Yokota E, Haraguchi T, Shimmen T, Yamamoto K, Nakano A, and Ito K. Cytoplasmic Streaming Velocity as a Plant Size Determinant. Developmental Cell. 2013:**27**(3):345–352. https://doi.org/10.1016/j.devcel.2013.10.005

Tournebize R, Popov A, Kinoshita K, Ashford AJ, Rybina S, Pozniakovsky A, Mayer TU, Walczak CE, Karsenti E, and Hyman AA. Control of microtubule dynamics by the antagonistic activities of XMAP215 and XKCM1 in Xenopus egg extracts. Nat Cell Biol. 2000:**2**(1):13–19. https://doi.org/10.1038/71330

Traas J, Bellini C, Nacry P, Kronenberger J, Bouchez D, and Caboche M. Normal differentiation patterns in plants lacking microtubular preprophase bands. Nature. 1995:**375**(6533):676–677. https://doi.org/10.1038/375676a0

Traas JA, Doonan JH, Rawlins DJ, Shaw PJ, Watts J, and Lloyd CW. An actin network is present in the cytoplasm throughout the cell cycle of carrot cells and associates with the dividing nucleus. The Journal of cell biology. 1987:**105**(1):387–395. https://doi.org/10.1083/jcb.105.1.387

Trinh D-C, Alonso-Serra J, Asaoka M, Colin L, Cortes M, Malivert A, Takatani S, Zhao F, Traas J, Trehin C, et al. How Mechanical Forces Shape Plant Organs. Current Biology. 2021:**31**(3):R143–R159. https://doi.org/10.1016/j.cub.2020.12.001

True JH and Shaw SL. Exogenous Auxin Induces Transverse Microtubule Arrays Through TRANSPORT INHIBITOR RESPONSE1/AUXIN SIGNALING F-BOX Receptors. Plant Physiol. 2020:**182**(2):892–907. https://doi.org/10.1104/pp.19.00928

Turner S and Kumar M. Cellulose synthase complex organization and cellulose microfibril structure. Royal Society of Publishing. 2018. https://doi.org/10.1098/rsta.2017.0048

Ueda H, Yokota E, Kutsuna N, Shimada T, Tamura K, Shimmen T, Hasezawa S, Dolja VV, and Hara-Nishimura I. Myosin-dependent endoplasmic reticulum motility and F-actin organization in plant cells. Proc Natl Acad Sci USA. 2010:**107**(15):6894–6899. https://doi.org/10.1073/pnas.0911482107

Uhlmann F, Wernic D, Poupart M-A, Koonin EV, and Nasmyth K. Cleavage of Cohesin by the CD Clan Protease Separin Triggers Anaphase in Yeast. Cell. 2000:**103**(3):375–386. https://doi.org/10.1016/S0092-8674(00)00130-6

Uyttewaal M, Burian A, Alim K, Landrein B, Borowska-Wykręt D, Dedieu A, Peaucelle A, Ludynia M, Traas J, Boudaoud A, et al. Mechanical Stress Acts via Katanin to Amplify Differences in Growth Rate between Adjacent Cells in Arabidopsis. Cell. 2012:**149**(2):439–451. https://doi.org/10.1016/j.cell.2012.02.048

Valster AH and Hepler PK. Caffeine inhibition of cytokinesis: effect on the phragmoplast cytoskeleton in livingTradescantia stamen hair cells. Protoplasma. 1997:**196**(3–4):155–166. https://doi.org/10.1007/BF01279564

Van Damme D, Van Poucke K, Boutant E, Ritzenthaler C, Inzé D, and Geelen D. In Vivo Dynamics and Differential Microtubule-Binding Activities of MAP65 Proteins. Plant Physiol. 2004:**136**(4):3956–3967. https://doi.org/10.1104/pp.104.051623

Van Damme D, Vanstraelen M, and Geelen D. Cortical division zone establishment in plant cells. Trends in Plant Science. 2007:**12**(10):458–464. https://doi.org/10.1016/j.tplants.2007.08.011

Verger S, Long Y, Boudaoud A, and Hamant O. A tension-adhesion feedback loop in plant epidermis. eLife. 2018:**7**:e34460. https://doi.org/10.7554/eLife.34460

Verma DPS. Cytokinesis and Building of the Cell Plate in Plants. Annu Rev Plant Physiol Plant Mol Biol. 2001:**52**(1):751–784. https://doi.org/10.1146/annurev.arplant.52.1.751

Vermot J, Forouhar AS, Liebling M, Wu D, Plummer D, Gharib M, and Fraser SE. Reversing Blood Flows Act through klf2a to Ensure Normal Valvulogenesis in the Developing Heart. PLoS Biol. 2009:**7**(11):e1000246. https://doi.org/10.1371/journal.pbio.1000246

Vernoux T, Besnard F, and Traas J. Auxin at the Shoot Apical Meristem. Cold Spring Harbor Perspectives in Biology. 2010:**2**(4):a001487–a001487. https://doi.org/10.1101/cshperspect.a001487

Vilches Barro A, Stöckle D, Thellmann M, Ruiz-Duarte P, Bald L, Louveaux M, Von Born P, Denninger P, Goh T, Fukaki H, et al. Cytoskeleton Dynamics Are Necessary for Early Events of Lateral Root Initiation in Arabidopsis. Current Biology. 2019:**29**(15):2443-2454.e5. https://doi.org/10.1016/j.cub.2019.06.039

Vinson CR, Conover S, and Adler PN. A Drosophila tissue polarity locus encodes a protein containing seven potential transmembrane domains. Nature. 1989:**338**(6212):263–264. https://doi.org/10.1038/338263a0

Viscosi V and Cardini A. Leaf Morphology, Taxonomy and Geometric Morphometrics: A Simplified Protocol for Beginners. PLoS ONE. 2011:**6**(10):e25630. https://doi.org/10.1371/journal.pone.0025630

Vogel S. Comparative Biomechanics: Life's Physical World - Second Edition (Princeton University Press).

Volkmann D and Baluska F. Actin cytoskeleton in plants: From transport networks to signaling networks. Microsc Res Tech. 1999:**47**(2):135–154. https://doi.org/10.1002/(SICI)1097-0029(19991015)47:2<135::AID-JEMT6>3.0.CO;2-1

Vos JW, Dogterom M, and Emons AMC. Microtubules become more dynamic but not shorter during preprophase band formation: A possible "search-and-capture" mechanism for microtubule translocation. Cell Motility. 2004:**57**(4):246–258. https://doi.org/10.1002/cm.10169

Waites R and Hudson A. PHANTASTICA: a gene required for dorsoventrality of leaves in Antirrhinum majus. Development. 1995:**121**:2143.

Walker KL, Müller S, Moss D, Ehrhardt DW, and Smith LG. Arabidopsis TANGLED Identifies the Division Plane throughout Mitosis and Cytokinesis. Current Biology. 2007:**17**(21):1827–1836. https://doi.org/10.1016/j.cub.2007.09.063

Walker RA, O'Brien ET, Pryer NK, Soboeiro MF, Voter WA, Erickson HP, and Salmon ED. Dynamic instability of individual microtubules analyzed by video light microscopy: rate constants and transition frequencies. The Journal of cell biology. 1988:**107**(4):1437–1448. https://doi.org/10.1083/jcb.107.4.1437

Walton KD, Freddo AM, Wang S, and Gumucio DL. Generation of intestinal surface: an absorbing tale. Development. 2016:**143**(13):2261–2272. https://doi.org/10.1242/dev.135400

Wan X, Cimini D, Cameron LA, and Salmon ED. The coupling between sister kinetochore directional instability and oscillations in centromere stretch in metaphase PtK1 cells. MBoC. 2012:**23**(6):1035–1046. https://doi.org/10.1091/mbc.e11-09-0767

Wang H-Y, Yu Y, Chen Z-L, and Xia G-X. Functional characterization of Gossypium hirsutum profilin 1 gene (GhPFN1) in tobacco suspension cells: Characterization of in vivo functions of a cotton profilin gene. Planta. 2005:**222**(4):594–603. https://doi.org/10.1007/s00425-005-0005-2

Wang T, Park YB, Cosgrove DJ, and Hong M. Cellulose-Pectin Spatial Contacts Are Inherent to Never-Dried Arabidopsis Primary Cell Walls: Evidence from Solid-State Nuclear Magnetic Resonance. Plant Physiol. 2015:**168**(3):871–884. https://doi.org/10.1104/pp.15.00665

Wang T, Zabotina O, and Hong M. Pectin–Cellulose Interactions in the *Arabidopsis* Primary Cell Wall from Two-Dimensional Magic-Angle-Spinning Solid-State Nuclear Magnetic Resonance. Biochemistry. 2012:**51**(49):9846–9856. https://doi.org/10.1021/bi3015532

Wang Y. Role of the actin cytoskeleton in cellular morphogenesis at the shoot apical meristem oh Arabidopsis thaliana.

Wang Y, Ji Y, Fu Y, and Guo H. Ethylene-induced microtubule reorientation is essential for fast inhibition of root elongation in Arabidopsis. Journal of Integrative Plant Biology. 2018:**60**(9):864–877. https://doi.org/10.1111/jipb.12666

Wasteneys G and Ambrose C. Spatial organization of plant cortical microtubules: Close encounters of the 2D kind. Trends in cell biology. 2009:**19**:62–71. https://doi.org/10.1016/j.tcb.2008.11.004

Wasteneys GO and Yang Z. New Views on the Plant Cytoskeleton. Plant Physiol. 2004:**136**(4):3884–3891. https://doi.org/10.1104/pp.104.900133

Weihmann T. Survey of biomechanical aspects of arthropod terrestrialisation – Substrate bound legged locomotion. Arthropod Structure & Development. 2020:**59**:100983. https://doi.org/10.1016/j.asd.2020.100983

Weingartner M, Pelayo H, Binarova P, Zwerger K, Melikant B, Torre C, and Heberle-Bors E. A plant cyclin B2 is degraded early in mitosis and its ectopic expression shortens G2-phase and alleviates the DNA-damage checkpoint. Journal of cell science. 2003:**116**:487–98.

Whitewoods C, Gonçalves B, Cheng J, Cui M, Kennaway R, Lee K, Bushell C, Yu M, Piao C, and Coen E. Evolution of carnivorous traps from planar leaves through simple shifts in gene expression. Science. 2020. https://doi.org/10.1126/science.aay5433

Wick S. Cytoskeletal Regulation of Plant Growth. J Plant Growth Regul. 2001:**20**(2):101–102. https://doi.org/10.1007/s003440010020

Wick SM and Duniec J. Immunofluorescence microscopy of tubulin and microtubule arrays in plant cells. I. Preprophase band development and concomitant appearance of nuclear envelope-associated tubulin. The Journal of cell biology. 1983:**97**(1):235–243. https://doi.org/10.1083/jcb.97.1.235

Wieschaus E. FROM MOLECULAR PATTERNS TO MORPHOGENESIS THE LESSONS FROM DROSOPHILA. 1995.

Wightman R, Chomicki G, Kumar M, Carr P, and Turner SR. SPIRAL2 Determines Plant Microtubule Organization by Modulating Microtubule Severing. Current Biology. 2013:**23**(19):1902–1907. https://doi.org/10.1016/j.cub.2013.07.061

Wightman R and Turner SR. Severing at sites of microtubule crossover contributes to microtubule alignment in cortical arrays. The Plant Journal. 2007:**52**(4):742–751. https://doi.org/10.1111/j.1365-313X.2007.03271.x

Wightman R and Turner SR. The roles of the cytoskeleton during cellulose deposition at the secondary cell wall. The Plant Journal. 2008:**54**(5):794–805. https://doi.org/10.1111/j.1365-313X.2008.03444.x

Willats WGT, Orfila C, Limberg G, Buchholt HC, Van Alebeek G-JWM, Voragen AG., Marcus SE, Christensen TMIE, Mikkelsen JD, Murray BS, et al. Modulation of the Degree and Pattern of Methyl-esterification of Pectic Homogalacturonan in Plant Cell Walls. Journal of Biological Chemistry. 2001:**276**(22):19404–19413. https://doi.org/10.1074/jbc.M011242200

Williams CB, Reese Næsborg R, and Dawson TE. Coping with gravity: the foliar water relations of giant sequoia. Tree Physiology. 2017:**37**(10):1312–1326. https://doi.org/10.1093/treephys/tpx074

Williamson GB and Wiemann MC. Measuring wood specific gravity…Correctly. American Journal of Botany. 2010:**97**(3):519–524. https://doi.org/10.3732/ajb.0900243

Willis L, Refahi Y, Wightman R, Landrein B, Teles J, Huang KC, Meyerowitz EM, and Jönsson H. Cell size and growth regulation in the *Arabidopsis thaliana* apical stem cell niche. Proc Natl Acad Sci USA. 2016:**113**(51). https://doi.org/10.1073/pnas.1616768113

Wilson BF. Root Growth Around Barriers. Botanical Gazette. 1967:**128**(2):79–82. https://doi.org/10.1086/336383

Winter JA, Allen TJ, and Proske U. Muscle spindle signals combine with the sense of effort to indicate limb position. The Journal of Physiology. 2005:**568**(3):1035–1046. https://doi.org/10.1113/jphysiol.2005.092619

Wolf S and Greiner S. Growth control by cell wall pectins. Protoplasma. 2012:**249**(S2):169–175. https://doi.org/10.1007/s00709-011-0371-5

Woo RA and Poon RYC. Cyclin-Dependent Kinases and S Phase Control in Mammalian Cells. Cell Cycle. 2003:**2**(4):315–323. https://doi.org/10.4161/cc.2.4.468

Woodruff JB, Drubin DG, and Barnes G. Mitotic spindle disassembly occurs via distinct subprocesses driven by the anaphase-promoting complex, Aurora B kinase, and kinesin-8. Journal of Cell Biology. 2010:**191**(4):795–808. https://doi.org/10.1083/jcb.201006028

Wormit A and Usadel B. The Multifaceted Role of Pectin Methylesterase Inhibitors (PMEIs). IJMS. 2018:**19**(10):2878. https://doi.org/10.3390/ijms19102878

Wu S-Z and Bezanilla M. Myosin VIII associates with microtubule ends and together with actin plays a role in guiding plant cell division. eLife. 2014:**3**:e03498. https://doi.org/10.7554/eLife.03498

Wydro M, Kozubek E, and Lehmann P. Optimization of transient Agrobacterium-mediated gene expression system in leaves of Nicotiana benthamiana. Acta Biochim Pol. 2006:**53**(2):289–298. https://doi.org/10.18388/abp.2006_3341

Xiao C, Zhang T, Zheng Y, Cosgrove DJ, and Anderson CT. Xyloglucan Deficiency Disrupts Microtubule Stability and Cellulose Biosynthesis in Arabidopsis, Altering Cell Growth and Morphogenesis. Plant Physiol. 2016:**170**(1):234–249. https://doi.org/10.1104/pp.15.01395

Xu J, Lee Y-RJ, and Liu B. Establishment of a mitotic model system by transient expression of the D-type cyclin in differentiated leaf cells of tobacco (Nicotiana benthamiana). New Phytologist. 2020:**226**(4):1213–1220. https://doi.org/10.1111/nph.16309

Xuan LT and Menczel L. Improved protoplast culture and plant regeneration from protoplast-derived callus in Arabidopsis thaliana. Zeitschrift für Pflanzenphysiologie. 1980:**96**(1):77–80. https://doi.org/10.1016/S0044-328X(80)80102-4

Yamada M and Goshima G. Mitotic Spindle Assembly in Land Plants: Molecules and Mechanisms. Biology. 2017:**6**(4):6. https://doi.org/10.3390/biology6010006

Yamada M and Goshima G. The KCH Kinesin Drives Nuclear Transport and Cytoskeletal Coalescence to Promote Tip Cell Growth in *Physcomitrella patens*. Plant Cell. 2018:**30**(7):1496–1510. https://doi.org/10.1105/tpc.18.00038

Yamada M, Tanaka-Takiguchi Y, Hayashi M, Nishina M, and Goshima G. Multiple kinesin-14 family members drive microtubule minus end–directed transport in plant cells. Journal of Cell Biology. 2017:**216**(6):1705–1714. https://doi.org/10.1083/jcb.201610065

Yamaguchi M, Fabian T, Sauter M, Bhalerao RP, Schrader J, Sandberg G, Umeda M, and Uchimiya H. Activation of CDK-activating kinase is dependent on interaction with H-type cyclins in plants. The Plant Journal. 2000:**24**(1):11–20. https://doi.org/10.1046/j.1365-313x.2000.00846.x

Yeoman MM and Brown R. Effects of Mechanical Stress on the Plane of Cell Division in Developing Callus Cultures. Annals of Botany. 1971:**35**(5):1102–1112. https://doi.org/10.1093/oxfordjournals.aob.a084545

Yi P and Goshima G. Microtubule nucleation and organization without centrosomes. Current Opinion in Plant Biology. 2018:**46**:1–7. https://doi.org/10.1016/j.pbi.2018.06.004

Yokoyama R, Hirakawa T, Hayashi S, Sakamoto T, and Matsunaga S. Dynamics of plant DNA replication based on PCNA visualization. Sci Rep. 2016:**6**(1):29657. https://doi.org/10.1038/srep29657

Yoneda A, Akatsuka M, Hoshino H, Kumagai F, and Hasezawa S. Decision of Spindle Poles and Division Plane by Double Preprophase Bands in a BY-2 Cell Line Expressing GFP–Tubulin. Plant and Cell Physiology. 2005:**46**(3):531–538. https://doi.org/10.1093/pcp/pci055

Yoo S-D, Cho Y-H, and Sheen J. Arabidopsis mesophyll protoplasts: A versatile cell system for transient gene expression analysis. Nature protocols. 2007:**2**:1565–72. https://doi.org/10.1038/nprot.2007.199

Yoshida S, Barbier de Reuille P, Lane B, Bassel GW, Prusinkiewicz P, Smith RS, and Weijers D. Genetic Control of Plant Development by Overriding a Geometric Division Rule. Developmental Cell. 2014:**29**(1):75–87. https://doi.org/10.1016/j.devcel.2014.02.002

Yoshida S, van der Schuren A, van Dop M, van Galen L, Saiga S, Adibi M, Möller B, ten Hove CA, Marhavy P, Smith R, et al. A SOSEKI-based coordinate system interprets global polarity cues in Arabidopsis. Nat Plants. 2019:**5**(2):160–166. https://doi.org/10.1038/s41477-019-0363-6

Young NM, Chong HJ, Hu D, Hallgrímsson B, and Marcucio RS. Quantitative analyses link modulation of sonic hedgehog signaling to continuous variation in facial growth and shape. Development. 2010:**137**(20):3405–3409. https://doi.org/10.1242/dev.052340

Yu Y, Song C, Zhang Q, DiMaggio PA, Garcia BA, York A, Carey MF, and Grunstein M. Histone H3 Lysine 56 Methylation Regulates DNA Replication through Its Interaction with PCNA. Molecular Cell. 2012:**46**(1):7–17. https://doi.org/10.1016/j.molcel.2012.01.019

Yuan G, Gao H, and Yang T. Exploring the Role of the Plant Actin Cytoskeleton: From Signaling to Cellular Functions. IJMS. 2023:**24**(20):15480. https://doi.org/10.3390/ijms242015480

Zhai N and Xu L. Pluripotency acquisition in the middle cell layer of callus is required for organ regeneration. Nat Plants. 2021:**7**(11):1453–1460. https://doi.org/10.1038/s41477-021-01015-8

Zhang L and Ambrose C. CLASP balances two competing cell division plane cues during leaf development. Nat Plants. 2022:**8**(6):682–693. https://doi.org/10.1038/s41477-022-01163-5

Zhang Q, Fishel E, Bertroche T, and Dixit R. Microtubule Severing at Crossover Sites by Katanin Generates Ordered Cortical Microtubule Arrays in Arabidopsis. Current Biology. 2013:**23**(21):2191–2195. https://doi.org/10.1016/j.cub.2013.09.018

Zhang Y, Iakovidis M, and Costa S. Control of patterns of symmetric cell division in the epidermal and cortical tissues of the Arabidopsis root. Development. 2016:dev.129502. https://doi.org/10.1242/dev.129502

Zhang Z, Runions A, Mentink RA, Kierzkowski D, Karady M, Hashemi B, Huijser P, Strauss S, Gan X, Ljung K, et al. A WOX/Auxin Biosynthesis Module Controls Growth to Shape Leaf Form. Current Biology. 2020:**30**(24):4857-4868.e6. https://doi.org/10.1016/j.cub.2020.09.037

Zhao F, Chen W, Sechet J, Martin M, Bovio S, Lionnet C, Long Y, Battu V, Mouille G, Monéger F, et al. Xyloglucans and Microtubules Synergistically Maintain Meristem Geometry and Phyllotaxis. Plant Physiol. 2019:**181**(3):1191–1206. https://doi.org/10.1104/pp.19.00608

Zhao F, Du F, Oliveri H, Zhou L, Ali O, Chen W, Feng S, Wang Q, Lü S, Long M, et al. Microtubule-Mediated Wall Anisotropy Contributes to Leaf Blade Flattening. Current Biology. 2020:**30**(20):3972-3985.e6. https://doi.org/10.1016/j.cub.2020.07.076

Zheng Y, Wong ML, and Alberts B. Nucleation of microtubule assembly by a y-tubulin-containing ring complex. 1995:**378**.

Zhong R, Cui D, and Ye Z-H. Secondary cell wall biosynthesis. New Phytologist. 2019:**221**(4):1703–1723. https://doi.org/10.1111/nph.15537

Zumdieck A, Lagomarsino MC, Tanase C, Kruse K, Mulder B, Dogterom M, and Jülicher F. Continuum Description of the Cytoskeleton: Ring Formation in the Cell Cortex. Phys Rev Lett. 2005:**95**(25):258103. https://doi.org/10.1103/PhysRevLett.95.258103

Zykwinska A, Thibault J-F, and Ralet M-C. Organization of pectic arabinan and galactan side chains in association with cellulose microfibrils in primary cell walls and related models envisaged. Journal of Experimental Botany. 2007:**58**(7):1795–1802. https://doi.org/10.1093/jxb/erm037